

Mechanisms and Machine Science 47

Giovanni Boschetti
Alessandro Gasparetto *Editors*

Advances in Italian Mechanism Science

Proceedings of the First International
Conference of IFToMM Italy

 Springer

Mechanisms and Machine Science

Volume 47

Series editor

Marco Ceccarelli

LARM: Laboratory of Robotics and Mechatronics

DICeM: University of Cassino and South Latium

Via Di Biasio 43, 03043 Cassino (Fr), Italy

e-mail: ceccarelli@unicas.it

More information about this series at <http://www.springer.com/series/8779>

Giovanni Boschetti · Alessandro Gasparetto
Editors

Advances in Italian Mechanism Science

Proceedings of the First International
Conference of IFToMM Italy

 Springer

Editors

Giovanni Boschetti
Department of Management
and Engineering
Università degli Studi di Padova
Vicenza
Italy

Alessandro Gasparetto
Dipartimento di Ingegneria Elettrica,
Gestionale e Meccanica
Università degli Studi di Udine
Udine
Italy

ISSN 2211-0984

Mechanisms and Machine Science

ISBN 978-3-319-48374-0

DOI 10.1007/978-3-319-48375-7

ISSN 2211-0992 (electronic)

ISBN 978-3-319-48375-7 (eBook)

Library of Congress Control Number: 2016954714

© Springer International Publishing AG 2017

This work is subject to copyright. All rights are reserved by the Publisher, whether the whole or part of the material is concerned, specifically the rights of translation, reprinting, reuse of illustrations, recitation, broadcasting, reproduction on microfilms or in any other physical way, and transmission or information storage and retrieval, electronic adaptation, computer software, or by similar or dissimilar methodology now known or hereafter developed.

The use of general descriptive names, registered names, trademarks, service marks, etc. in this publication does not imply, even in the absence of a specific statement, that such names are exempt from the relevant protective laws and regulations and therefore free for general use.

The publisher, the authors and the editors are safe to assume that the advice and information in this book are believed to be true and accurate at the date of publication. Neither the publisher nor the authors or the editors give a warranty, express or implied, with respect to the material contained herein or for any errors or omissions that may have been made.

Printed on acid-free paper

This Springer imprint is published by Springer Nature

The registered company is Springer International Publishing AG

The registered company address is: Gewerbestrasse 11, 6330 Cham, Switzerland

Preface

This book contains the Proceedings of the First International Conference of IFToMM ITALY (IFIT2016). IFToMM ITALY is the Italian branch of IFToMM, the International Federation for the Promotion of Mechanism and Machine Sciences.

The aim of this conference was to bring together researchers, industry professionals and students, from the Italian as well from the international community, in an intimate, collegial and stimulating environment. The sixty papers presented at the conference dealt with the topics belonging to a broad range of disciplines related to theory, design, practice and application of mechanism science, in particular, biomechanical engineering, history of mechanism and machine science, linkages and mechanical controls, multi-body dynamics, reliability, robotics and mechatronics, transportation machinery, tribology, and vibrations. Within the conference, a special session was organized in honor of Prof. Aldo Rossi (past Chair of IFToMM ITALY) in occasion of his 70th birthday celebration.

The First International Conference of IFToMM ITALY association was held at the Department of Management and Engineering (DTG) of the University of Padova, located in the town of Vicenza. The conference was organized under the patronage of International Federation for the Promotion of Mechanism and Machine Science (IFToMM), and was sponsored by the Department of Management and Engineering (DTG) of the University of Padova as well as by the Fondazione Studi Universitari (FSU).

We want to thank the authors for their interesting scientific contributions, the reviewers for their useful feedback, the scientific and the organizing committees for their work, and the people at Springer for their efficient support and help. Altogether, we made IFIT2016 a truly successful event.

Vicenza, Italy
Udine, Italy

Giovanni Boschetti
Alessandro Gasparetto

Committees

General Chair

Cesare Rossi, University of Napoli

Scientific Committee

Roberto Caracciolo, University of Padova
Giuseppe Carbone, University of Cassino
Enrico Ciulli, University of Pisa
Antonio Frisoli, Sant'Anna School
Alessandro Gasparetto, University of Udine
Domenico Mundo, University of Calabria
Paolo Pennacchi, Politecnico di Milano
Giuseppe Quaglia, Politecnico di Torino
Giulio Reina, University of Lecce
Cesare Rossi, University of Napoli
Alberto Trevisani, University of Padova

Organizing Committee

Paolo Boscariol, University of Padova
Giovanni Boschetti, University of Padova
Chiara Passarini, University of Padova
Dario Richiedei, University of Padova
Giulio Rosati, University of Padova

General Secretary

Giovanni Boschetti, University of Padova

Contents

Part I Biomechanical Engineering

Design and Implementation of a Low-Cost Mechatronic Shoe for Biomechanical Analysis of the Human Locomotion	3
P. Boscariol, A. Gasparetto, N. Giovanelli, S. Lazzer and L. Scalera	
A Study of Feasibility for a Limb Exercising Device	11
G. Carbone, C. Aróstegui Cavero, M. Ceccarelli and O. Altuzarra	
DARTAGNAN a Self-balanced Rehabilitation Robot Able to Work in Active and Passive Modes on Both Sides of Upper and Lower Limbs	23
M. Perrelli, P. Nudo, M. Iocco and G. Danieli	
Dynamic Analysis of Handcycling: Mathematical Modelling and Experimental Tests	33
G. Azizpour, A. Ousdad, G. Legnani, G. Incerti, M. Lancini and P. Gaffurini	
A Kinematic Solution of a Novel Leg Mechanism with Parallel Architecture	41
Matteo Russo and Marco Ceccarelli	
Multi-target Planar Needle Steering with a Bio-inspired Needle Design	51
Christopher Burrows, Fangde Liu, Alexander Leibinger, Riccardo Secoli and Ferdinando Rodriguez y Baena	
Development of an Active Force Plate for Testing Lower-Limb Prostheses	61
Cristiano Marinelli, Hermes Giberti and Ferruccio Resta	
Determination of the Human Arm Stiffness Efficiency with a Two Antagonist Muscles Model	71
Daniele Borzelli, Stefano Pastorelli and Laura Gastaldi	

Design of a Miniaturized Safety Clamping Device for Portable Kidney Replacement Systems	79
P. Boscariol, G. Boschetti, R. Caracciolo, M. Neri, D. Richiede, C. Ronco and A. Trevisani	
Conceptual Design of a Mechatronic Biomedical Wearable Device for Blood Ultrafiltration	89
G. Boschetti, A. Dalla Via, N. De Rossi, F. Garzotto, M. Neri, L. Pamato, C. Ronco and A. Trevisani	
Design of an Underactuated Hand Exoskeleton with Joint Estimation	97
Mine Sarac, Massimiliano Solazzi, Daniele Leonardis, Edoardo Sotgiu, Massimo Bergamasco and Antonio Frisoli	
Standard and Natural Motion Protocols for the Kinetic Measurements of the Squat	107
Nicola Sancisi, Marco Coconcelli, Riccardo Rubini and Vincenzo Parenti-Castelli	
Design and Simulation of an Assisting Mechanism for Arm Exercises	115
B. Chaparro-Rico, D. Cafolla, M. Ceccarelli and E. Castillo-Castaneda	
Part II History of Mechanism and Machine Science	
Role of Scientific-Technical Museums in the Future of Mechanical	127
Alberto Rovetta and Edoardo Rovida	
An Analysis of the Hydraulic Saw of Hierapolis	135
Cesare Rossi, Sergio Savino and Francesco Timpone	
Part III Linkages and Mechanical Controls	
Riccati Equation Based Nonlinear Filter: A Case Study for Hydraulic Actuators in the Presence of Dead-Zone	145
Salvatore Strano and Mario Terzo	
Trajectories Generation with Constant Extrusion Rate for Experimentations on AM Techniques and Extrusion Based Technologies	153
H. Giberti, L. Sbaglia and M. Parabiaghi	
Preliminary Design of a Simplified Pneumatic Actuator	161
G.A. Naselli, M. Zoppi and R. Molfino	

Part IV Multi-Body Dynamics

Multibody Model of Under-Actuated Tendon Driven Finger to Study the Antagonist Tendon 175
 Sergio Savino

A Model Reduction Strategy for Flexible-Link Multibody Systems 183
 Ilaria Palomba, Dario Richiedei and Alberto Trevisani

Part V Reliability

Topology Optimization and Analysis of Static Transmission Error in Lightweight Gears 195
 Jakub Korta, Domenico Mundo, Giuseppina Ambrogio, Barbara Folino, Shadi Shweiki and Luigino Filice

A Strategy for Moving Cable Driven Robots Safely in Case of Cable Failure 203
 Giovanni Boschetti, Chiara Passarini and Alberto Trevisani

Approaches to the Detectability of Faults in Railway Pantograph Mechanism. 213
 G. Santamato, M. Gabardi, M. Solazzi and A. Frisoli

Behaviour of Tilting-Pad Journal Bearings in Case of Large Manufacturing Errors 221
 Steven Chatterton, Phuoc Vinh Dang, Paolo Pennacchi and Andrea Vania

Part VI Robotics and Mechatronics

A New Automated 2 DOFs 3D Desktop Optical Scanner. 231
 Maria Cristina Valigi, Silvia Logozzo and Gabriele Canella

Adam’s Hand: An Underactuated Robotic End-Effector 239
 Giovanni Antonio Zappatore, Giulio Reina and Arcangelo Messina

Automatic System for Fibers Extraction from Brooms 247
 P.F. Greco, G. La Greca, G. Larocca, S. Meduri, B. Sinopoli, D. Battaglia, A. Caseti, A. Aloise, G. Chidichimo and G. Danieli

Functional Design of a Robotic Gripper for Adaptive Robotic Assembly 257
 F. Oscari, S. Minto and G. Rosati

Optimal Design of a Reconfigurable End-Effector for Cable-Suspended Parallel Robots 267
 Luca Barbazza, Damiano Zanotto, Giulio Rosati and Sunil K. Agrawal

Kinematic Optimization of a 2DoF PRRRP Manipulator 277
 Simone Cinquemani, Hermes Giberti and Giovanni Legnani

Optimized Trajectory Planning of Pick and Place Operations to Be Performed by Cable-Driven Parallel Robots	287
Luca Barbazza, Fabio Oscari, Simone Minto and Giulio Rosati	
An Innovative Method for Sizing Actuating Systems of Manipulators with Generic Tasks	297
E. Fiore, H. Giberti and G. Bonomi	
Experimentally Based Design of a Manually Operated Baler for Straw Bale Construction.	307
Walter Franco, Giuseppe Quaglia and Carlo Ferraresi	
Part VII Transportation Machinery	
Fast Calibration Procedure of the Dynamic Model of an Autonomous Underwater Vehicle from a Reduced Set of Experimental Data	317
Benedetto Allotta, Riccardo Costanzi, Luca Pugi, Alessandro Ridolfi and Andrea Rindi	
Braking Energy Recovery in High Speed Trains: An Innovative Model	327
Amedeo Frilli, Enrico Meli, Daniele Nocciolini, Simone Panconi, Luca Pugi and Andrea Rindi	
Dynamic Model and Instability Evaluation of an Articulated Mobile Agri-Robot	335
G. Carabin, R. Vidoni, F. Mazzetto and A. Gasparetto	
NVH Analysis of Automotive Components: A Carbon Fiber Suspension System Case	345
Alessandro Fasana, Massimiliana Carello, Alessandro Ferraris, Andrea Airale and Davide Berti Polato	
Dynamics of a Tethered Rover on Rough Terrain	355
Stefano Seriani, Paolo Gallina and Armin Wedler	
Wind Propulsion for Robot Surface Mobility	363
Mario Foglia, Giulio Reina and Giovanni Boschetti	
Anti-dive Front Suspension for Agricultural Tractors: Dynamic Model and Validation	371
Francesco Biral, Riccardo Pelanda and Alberto Cis	
Dynamic Model of an Independent Carts System.	379
Jacopo Cavalaglio Camargo Molano, Stefano Rossi, Marco Cocconcelli and Riccardo Rubini	

Tyre-Road Adherence Conditions Estimation for Intelligent Vehicle Safety Applications 389
 Mojtaba Sharifzadeh, Francesco Timpone, Arash Farnam, Adolfo Senatore and Ahmad Akbari

Part VIII Tribology

Tilting Pad Journal Bearing TEHD Analysis: An Innovative Model 401
 Amedeo Frilli, Enrico Meli, Daniele Nocciolini, Simone Panconi, Luca Pugi, Andrea Rindi and Stefano Rossin

Thermo-Hydrodynamic Analysis of Tilting Pad Journal Bearing with General Purpose CFD Software 411
 Marco Del Chiaro, Paola Forte, Francesco Torrigiani and Enrico Ciulli

Multiple Holes Rectangular Gas Thrust Bearing: Dynamic Stiffness Calculation with Lumped Parameters Approach 421
 Federico Colombo, Mona Moradi, Terenziano Raparelli, Andrea Trivella and Vladimir Viktorov

Theoretical and Experimental Study of a Rectangular Grooved Pocketed Air Pad 431
 Federico Colombo, Danial Ghodsiyeh, Terenziano Raparelli, Andrea Trivella and Vladimir Viktorov

Experimental Identification of an Aerostatic Thrust Bearing 441
 Federico Colombo, Luigi Lentini, Terenziano Raparelli and Vladimir Viktorov

Experimental Analysis of the Influence of the Electrical Arc on the Wear Rate of Contact Strip and Contact Wire in a.c. System. 449
 Giuseppe Bucca, Andrea Collina and Ezio Tanzi

Part IX Vibrations

Low-Cost Experimental Assessment of Forces in the Contact Bridge-Soundboard of Stringed Musical Instruments 459
 Enrico Ravina

Vibration Modes of Piezoelectric Bimorphs: A Sensitivity Analysis 467
 Alberto Borboni, Cinzia Amici, Valter Cappellini and Rodolfo Faglia

Concurrent Active Control and Dynamic Structural Modification in the Design and the Optimization of Vibrating Systems 475
 Roberto Belotti, Roberto Caracciolo and Dario Richiedei

A Vibration Isolator Based on Magneto-Rheological Elastomer	483
Renato Brancati, Giandomenico Di Massa and Stefano Pagano	
A Physical Analytical Model to Study the Elasto-Kinematic Behaviour of a MacPherson Suspension	491
Francesco Timpone	
A Smart System for Shock and Vibration Isolation of Sensitive Electronic Devices On-Board a Vehicle	503
M. De Michele, G. Di Massa, G. Frisella, S. Lippolis, S. Pagano, G. Pisani and S. Strano	
Wavelet Analysis of Gear Rattle Induced by a Multi-harmonic Excitation.	513
Renato Brancati, Ernesto Rocca, Sergio Savino and Francesco Timpone	
 Part X Special Session in Honor of Prof. Aldo Rossi for his 70th Birthday	
Analytical and Multibody Modelling of a Quick-Release Hook Mechanism.	523
Luca Bruzzone, Davide Bonatti, Giovanni Berselli and Pietro Fanghella	
Evolution of a Dynamic Model for Flexible Multibody Systems	533
P. Boscarriol, P. Gallina, A. Gasparetto, M. Giovagnoni, L. Scalera and R. Vidoni	
Anti-hedonistic Mechatronic Systems	543
Lorenzo Scalera, Paolo Gallina, Alessandro Gasparetto and Marco Giovagnoni	
On the Use of Cable-Driven Robots in Early Inpatient Stroke Rehabilitation	551
G. Rosati, S. Masiero and A. Rossi	

Part I
Biomechanical Engineering

Design and Implementation of a Low-Cost Mechatronic Shoe for Biomechanical Analysis of the Human Locomotion

P. Boscariol, A. Gasparetto, N. Giovanelli, S. Lazzer and L. Scalera

Abstract In this paper the development of a low-cost and easy wearable mechatronic system for the measurement of ground reaction forces (GRF) for the biomechanical analysis of the human locomotion is presented. The system consists of an insole, a conditioning device for the signals produced by the sensors applied to the insole and a data acquisition system connected to a USB portable storage. The sensors applied to the insole can measure the reaction forces in the horizontal and vertical directions during locomotion. The prototype was validated by comparing the data from the sensors with the values obtained using a force platform.

Keywords Mechatronic shoe · Biomechanical analysis · Human locomotion · Ground reaction forces · Sensors

1 Introduction

This work is part of a project carried out by an interdisciplinary team composed by researchers in Mechatronics as well as Biomedical Science. The aim of this study is the design and the implementation of a low-cost mechatronic insole, provided with sensors, to be inserted in a shoe, in order to measure horizontal and vertical ground

P. Boscariol
University of Padova, Padova, Italy
e-mail: paolo.boscariol@gmail.com

A. Gasparetto (✉) · N. Giovanelli · S. Lazzer · L. Scalera
University of Udine, Udine, Italy
e-mail: alessandro.gasparetto@uniud.it

N. Giovanelli
e-mail: nicola.giovanelli@uniud.it

S. Lazzer
e-mail: stefano.lazzer@uniud.it

L. Scalera
e-mail: scalera.lorenzo@spes.uniud.it

reaction forces (GRF) during locomotion (running or walking). GRF analysis is also used by athletic trainers in order to study the running performances of the athlete, by providing the possibility of intervention with specific training focused on improving the running efficiency [9–11, 17, 18, 23].

Nowadays it is possible to find systems, which can detect this kind of information, such as force boards, barometric plates [7] and insoles equipped with sensors. Ground reaction forces are often investigated in biomechanical studies on the human gait [1, 4, 5, 12, 13, 15, 22]. The analysis of these forces plays an important part in medicine during rehabilitation of patients hit by stroke [8] or for people with diabetes, in order to prevent the occurrence of ulcers on the foot. For example, instrumented shoes with a thin layer of strain gauge transducers [6], or piezoelectric copolymer film [19] or two sensors mounted beneath the forefoot and the rearfoot [16] have been built. However, these devices turn out to have a high cost and to be very cumbersome. Moreover, they greatly increase the thickness of the sole, as well as its weight, thus altering the correct gait [24].

The first studies on the motion analysis coincide with the birth of photography, because if it was possible to represent reality on a photographic plate, it would have been possible also to develop devices capable to take a series of pictures over a short period of time in order to record the motion. Subsequently, better results have been obtained by means of different cameras, which could capture the motion thanks to specific markers applied on the body of the person.

Nowadays, different technologies and methods for the biomechanical analysis of the step, in running or walking subjects, are available. The cheapest and most popular are based on software packages for the kinematic analysis, which allow to study the human motion by means of properly recorded video files. More information could be obtained from force platforms, which can detect the ground reaction forces in three directions. Different kind of devices, which provide useful information, could be integrated, such as accelerometers or gyroscopes, by means of which it is possible to calculate the external work by knowing the position of the Center of Mass (CoM). In the last few years, insoles that can provide the ground pressure of the foot [2, 3, 14, 21], considering the ground vertical reaction forces, have been developed. However, no similar system, which allows to obtain information on horizontal ground reaction forces, has been found in the literature. Measurement systems of horizontal reaction forces are still too cumbersome for a correct measurement during normal deambulation. To date, it is hard to record data during outdoor events, since installing force platforms on running tracks it is not always possible.

The paper is organized as follows: in Sect. 2 the design of the insole and of the accessory systems (data acquisition system, etc.), as well as the choice of sensors for the detection of horizontal and vertical forces, is explained. In Sect. 3 experimental results obtained from sensors mounted on the insole for a walking and a running step, as well as the comparison between these results and those obtained from a force platform, are described. In Sect. 4 conclusions are drawn.

2 Design of the Mechatronic Shoe

The CAD model of the insole was developed by means of SolidWorks™ environment. The resulting prototype was made of two half-insoles, which can slide one on the top of the other by means of guides. The prototype was designed so as to include the sensors for the measure of the reaction forces, namely five piezo-resistive sensors for the measure of vertical forces and a load cell for the measure of horizontal forces between the foot and the ground. The inserts for the five piezo-resistive sensors cables were built with the purpose of limiting the thickness after the components assembling (Fig. 1a). A prototype of the insole was realized by means of a 3D print, with a thermoplastic polyurethane elastomer 80 shore (TPU 80) printed with a 200 μm layer (Fig. 1b), which had a thickness of 7.8 mm and a mass of 0.175 g.

A piezo-resistive sensor is a kind of sensor made of a material that changes his own electrical resistance in proportion to the external force applied orthogonally to his sensitive surface. In this work Tekscan Flexiforce A401 sensors were used, in order to minimize the height of the insole and its total cost. Five sensors were positioned in coincidence of the first toe, the first, the third and the fifth metatarsus and under the heel, as suggested by [20]. With respect to other prototypes [8], bigger sensors have been used, because some preliminary experiments showed that with small sensors a more noisy signal was obtained.

The choice of the load cell turned out to be very complicated, considering the need to find a device that could be at the same time thin and robust: eventually, a Futek LSB200 load cell was chosen. Its dimensions are: 17 × 19 × 6.7 mm, and its thickness was considered suited to this application.

The data recorded by the load cell and the piezo-resistive sensors were registered at 1 kHz and logged into a portable acquisition device (MyRIO-1900 by National Instruments). The data acquisition software was developed in LabView™ environment. MyRIO was placed in a belt and powered by a 4 V batteries, which ensure the operation of the device for more than 2 h. So far, the capacity of the system is sufficient for the prototype-test phase, but in the future lithium-ion batteries with a larger capacity and a lower weight will be installed.

Fig. 1 The CAD model and the prototype of the sole with some piezo-resistive sensors and the I/O apparatus



Before every trial the sensors were calibrated using known weights. The calibration of the piezoresistive force sensors was performed after the sensors were fixed on the insole as suggested by the manufacturer.

3 Experimental Results

In order to verify the efficacy and the accuracy of the realized system, several experimental tests were made. The mechatronic shoe was worn by a subject, who was asked to walk on a Kistler force platform. Horizontal and vertical force signals obtained from the load cell and the piezo-resistive sensors were compared with those given by the platform.

The experimental were then post-processed with a dedicated program run in the MatLabTM environment. The program implemented a set of function for reading, analyzing and for graphically representing of data obtained from both the insole sensors and the force platform.

In Fig. 2 a typical trend of the forces measured by the force platform for one step is shown. The blue curve represents the trend of the vertical reaction force, in which the first peak matches the talon support and the second one to the forefoot. The red line represents the trend of the horizontal shear force, in which the first part corresponds to the braking phase and the second to the pushing. The green line, finally, represents the force perpendicular to the motion direction.

Experimental results are shown in the next figures. In Fig. 3 and in Fig. 4 two examples of vertical and horizontal forces measured by the sensors and the force platform respectively, in the case of a single walking step, are shown.

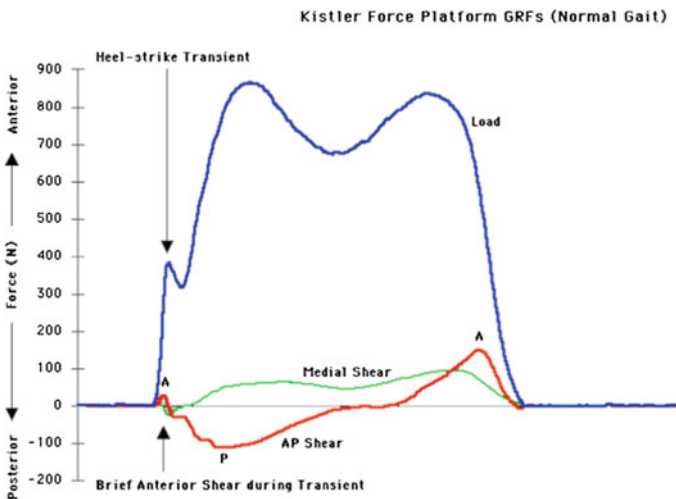


Fig. 2 Forces measured by the force platform for one step (normal walking gait)

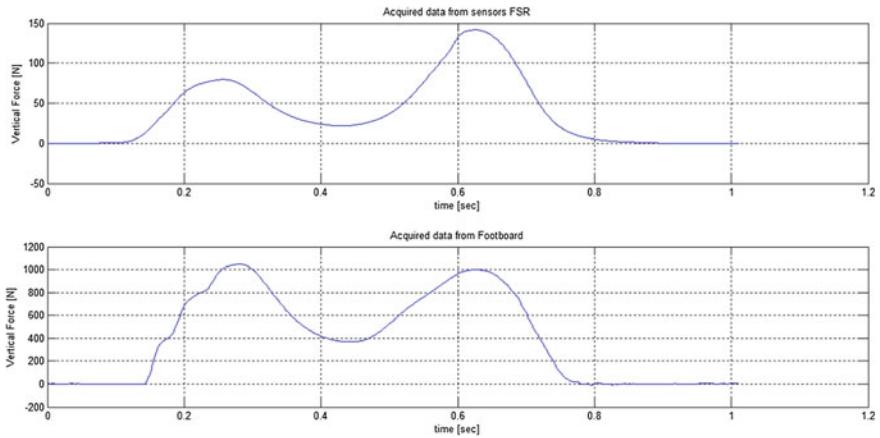


Fig. 3 Comparison of vertical forces during a step of walking (*top* piezoelectric sensors in the insole, *bottom* force platform)

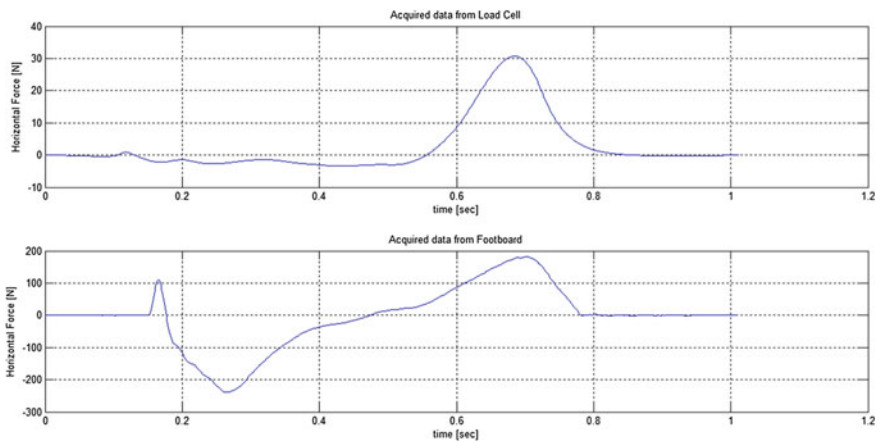


Fig. 4 Comparison of horizontal forces during a step of walking (*top* load cell in the insole, *bottom* force platform)

In Fig. 5 and in Fig. 6 two examples of vertical and horizontal forces revealed by the sensors and the footboard, in the case of a single running step, are shown.

The measurement of reaction forces gave satisfactory results, since it was possible to determine the contact times and the maximum force values determined from the insole sensors resulted very similar to those provided by the force platform. If we consider the shape of the signals, the trends of the vertical force during one step are quite close, even if the values are scaled. The offset resulting from the experiments was due to the difficulties encountered during the calibration phase, since the piezo-resistive sensors that were used turned out to be very sensitive with respect to

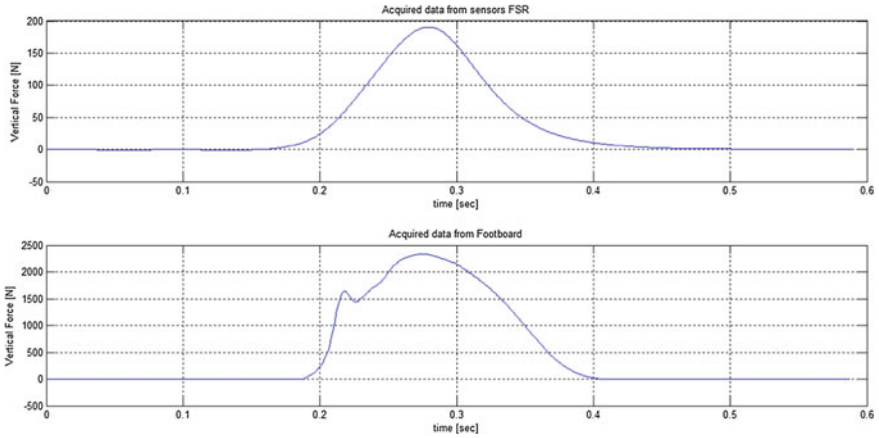


Fig. 5 Comparison of vertical forces during a step of running (*top* piezoelectric sensors in the insole, *bottom* force platform)

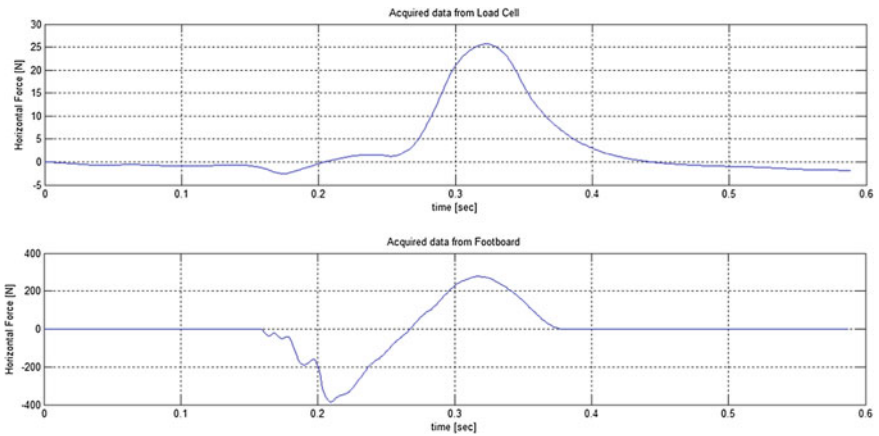


Fig. 6 Comparison of horizontal forces during a step of running (*top* load cell in the insole, *bottom* force platform)

the position to which the charge is applied. Indeed, every single individual distributes his load in a different way during the locomotion phase: therefore it is impossible to determine the optimal position to install the piezoelectric sensors in order to evaluate the vertical forces. Furthermore, a number of five sensors was not sufficient for a complete evaluation of the vertical forces involved.

Horizontal reaction forces gave more problems because from experimental tests it was not possible to find a perfect correspondence between the results obtained with the mechatronic insole and those obtained from the force platform. Namely, the peak related to the contact of the ball of the foot could be detected, whereas the

peak related to the contact of the talon could not be clearly identified. This fact could be due the structure of the insole: since the insole is placed inside the shoe, it moves adequately with the foot during the step phase but during the braking and pushing phases the sliding between the two semi-insoles is restricted.

4 Conclusions

In this paper, the development of a low cost and easy wearable mechatronic insole, which could be integrated inside a shoe during outdoor events, for the study of ground reaction forces in both horizontal and vertical directions, was presented.

The efficiency and the accuracy of this mechatronic system were tested by comparing the results obtained the sensors mounted on the insole (a load cell for the measurement of the horizontal force and five piezo-resistive for the measurement of the vertical forces) with the data obtained from a force platform. The experimental results pointed out that, while vertical forces were detected with good accuracy, for the horizontal forces it was not possible to find a perfect correspondence between the results obtained with the mechatronic insole and those obtained from the force platform. In other words, the peak related to the contact of the ball of the foot could be detected, whereas the peak related to the contact of the talon could not be clearly identified. Therefore, future work will be done, in order to improve the accuracy of the results given by the load cell, mainly by studying a design of the insole which is optimized with respect to this goal.

Acknowledgments The Authors would like to thank Mr. Daniele Zuccato, Mr. Riccardo Padoin and Mr. Stefano Biasi for their help in setting up the system.

References

1. Avogadro P, Chaux C, Bourdin M, Dalleau G, Belli A (2004) The use of treadmill ergometers for extensive calculation. *Eur J Appl Physiol* 4
2. Bamberg SJM, LaStayo P, Dibble L, Musselman J, Raghavendra SKD (2006) Development of a quantitative in-shoe measurement system for assessing balance: sixteen-sensor insoles. In: EMBS annual international conference
3. Bamberg SJM, Benbasat AY, Scarborough DM, Krebs DE, Paradiso JA (2008) Gait analysis using a shoe-integrated wireless sensor system. *IEEE Trans Inf Technol Biomed* 11
4. Blickhan R (1989) The spring-mass model for running and hopping. *J Biomech* 22: 1217–1227
5. Cavanagh PR, Lafortune MA (1980) Ground reaction forces in distance running. *J Biomech* 13:397–406
6. Davis BL, Perry JE, Neth DC, Waters KC (1998) A device for simultaneous measurement of pressure and shear force distribution on the plantar surface of the foot. *J Appl Biomech* 14: 93–104
7. Diasu Health Technologies, Baropodometro Flessibile. <http://www.diasu.com/it/pedane-pressorie/solette-flessibili/>

8. Edgar SRST, Fulk G, Sazonov ES (2010) Wearable shoe-based device for rehabilitation of stroke patients. In: Proceeding of 2010 annual international conference of the IEEE engineering in medicine and biology society (EMBC), Buenos Aires, Argentina
9. Farley CT, Gonzalez O (1996) Leg stiffness and stride frequency in human running. *J Biomech* 29(2):181–186
10. Giovanelli N, Ortiz AL, Henninger K, Kram R (2015a) Energetics of vertical kilometer foot races; is steeper cheaper? *J Appl Physiol* (1985): jap 00546 02015 doi:[10.1152/jappphysiol.00546.2015](https://doi.org/10.1152/jappphysiol.00546.2015)
11. Giovanelli N, Taboga P, Rejc E, Simunic B, Antonutto G, Lazzer S (2015) Effects of an uphill marathon on running mechanics and lower limb muscles fatigue. *Int J Sports Physiol Perform*. doi:[10.1123/ijspp.2014-0602](https://doi.org/10.1123/ijspp.2014-0602)
12. Girard O, Millet GP, Slawinski J, Racinais S, Micallef JP (2013) Changes in running mechanics and spring-mass behaviour during a 5-km time trial. *Int J Sports Med* 34:832–840. doi:[10.1055/s-0032-1329958](https://doi.org/10.1055/s-0032-1329958)
13. Gottschall JS, Kram R (2005) Ground reaction forces during downhill and uphill running. *J Biomech* 38:445–452. doi:[10.1016/j.jbiomech.2004.04.023](https://doi.org/10.1016/j.jbiomech.2004.04.023)
14. Howell AM, Kobayashi T, Hayes HA, Foreman KB, Bamberg SJM (2013) Kinetic gait analysis using a low-cost insole. *IEEE Trans Biomed Eng* 60(12)
15. Lieberman DE, Warrenner AG, Wang J, Castillo ER (2015) Effects of stride frequency and foot position at landing on braking force, hip torque, impact peak force and the metabolic cost of running in humans. *J Exp Biol* 218:3406–3414. doi:[10.1242/jeb.125500](https://doi.org/10.1242/jeb.125500)
16. Liedtke C, Fokkenrood SA, Menger JT, van der Kooij H, Veltink PH (2007) Evaluation of instrumented shoes for ambulatory assessment of ground reaction forces. *Gait Posture* 26: 39–47. doi:[10.1016/j.gaitpost.2006.07.017](https://doi.org/10.1016/j.gaitpost.2006.07.017)
17. Morin J-B, Dalleau G, Kyröläinen H, Jeannin T, Belli A (2005) A simple method for measuring stiffness during running. *J Appl Biomech* 15
18. Nikooyan A, Zadpoor A (2011) Mass-spring-damper modelling of the human body to study running and hopping—an overview. *Proc Inst Mech Eng Part H: J Eng Med* 15
19. Razian MA, Pepper MG (2003) Design, development, and characteristics of an in-shoe triaxial pressure measurement transducer utilizing a single element of piezoelectric copolymer film. *IEEE Trans Neural Syst Rehabil Eng* 11:288–293
20. Sazonov ES, Fulk G, Hill J, Schutz Y, Browning R (2011) Monitoring of posture allocations and activities by a shoe-based wearable sensor. *IEEE Trans Biomed Eng* 58:983–990. doi:[10.1109/TBME.2010.2046738](https://doi.org/10.1109/TBME.2010.2046738)
21. Shu L, Hua T, Wang Y, Li Q, Feng DD, Fellow IEEE, Tao X, Member IEEE (2010) In-shoe plantar pressure measurement and analysis system based on fabric pressure sensing array. *IEEE Trans Inf Technol Biomed* 14(3)
22. Tekscan, F-Scan System. <https://www.tekscan.com/products-solutions/systems/f-scan-system>
23. Tomazin JB, Edouard K, Millet P, Morin GY (2011) Changes in running mechanics and spring–mass behavior induced by a mountain ultra-marathon race. *J Biomech* 4
24. Veltink PH, Liedtke C, Droog E, van der Kooij H (2005) Ambulatory measurement of ground reaction forces. *IEEE Trans Neural Syst Rehabil Eng* 13:423–427. doi:[10.1109/TNSRE.2005.847359](https://doi.org/10.1109/TNSRE.2005.847359)

A Study of Feasibility for a Limb Exercising Device

G. Carbone, C. Aróstegui Cavero, M. Ceccarelli and O. Altuzarra

Abstract This paper deals with the design of a robotic device for limb exercising. The attached problem is outlined to identify the main limb exercising features as referring to upper limbs and cable driven robotic solutions. A novel design solution is proposed as consisting in a portable low-cost user-friendly cable driven manipulator. Numerical models and simulations are carried out to verify the feasibility of the proposed solution in terms of operation and motion ranges.

Keywords Robot design · Biomechanics · Limb exercising · Cable-driven robots

1 Introduction

Limb exercising has attracted significant research interest due to its practical usefulness for sport training and rehabilitation and there are even several patents proposing machines for limb exercising, or exoskeletons for human walking assistance or for rehabilitation purposes [1–4]. Some authors have also proposed the use of cable driven robots for limb exercising and physiotherapy applications. In fact, cable driven robots are a special class of parallel mechanisms, whose trusts consist of cables, [5]. This feature allows a significant reduction of inertia and a reduced risk in human robot interactions as well as reduced manufacturing costs, [5]. Significant examples of cable driven robot for rehabilitation can be NeReBot (NEuroREhabilitation robot), a three DOFs cable driven parallel robot for post stroke upper-limb rehabilitation, [6]; CALOWI (Cassino Low-Cost Wire Driven), a four cable robot for limb exercising and rehabilitation, [7]; MACARM (Multi-Axis

G. Carbone (✉) · M. Ceccarelli
University of Cassino and South Latium, Cassino, Italy
e-mail: carbone@unicas.it

C. Aróstegui Cavero · O. Altuzarra
University of the Basque Country, Bilbao, Spain
e-mail: oscar.altuzarra@ehu.es

Cartesian-based Arm Rehabilitation Machine), an eight cable robot for upper limb rehabilitation, [8].

Besides a wide literature on the topic there are still several issues to be addressed. For example, the structural frame of a cable driven robot can be significantly larger than the usable workspace. Instead, as users are often injured or disabled people, it is important that the size and shape of the structural frame facilitates the access to workspace area. Additionally, easy portability could allow the use of a robot in a home environments to increase users' motivation towards the training/rehabilitation process. For this purpose, the attached problem has been addressed aiming to identify a novel design solution being easily portable while having low-cost user-friendly features.

2 The Attached Problem

Limb exercising consists in motions that activate limb muscles in various ways to keep them fit. Physical rehabilitation is the process of helping patients in regaining control over parts of their body after an illness or a traumatic event. In particular, upper limbs rehabilitation after stroke consists mainly on physical repetitive exercises of the injured limb. These exercises include movements such as flexion and extension, pronation and supination, adduction and abduction and circular movements of shoulder and elbow, [9].

There are several reasons for this transition from conventional methods to a robot-oriented approach. For example, in the current ageing society, the demand for rehabilitation exercises is expected to grow considerably while available therapists are expected to slightly decline. Accordingly, the use of robots, several patients can be treated at the same time under the supervision of a single therapist, increasing productivity and efficiency. Moreover, robots can support long duration exercises keeping the required precision while tiredness can affect therapist treatment, [10]. Additionally, robotic systems can record information such as position, trajectory, force and velocity and then archive this data and compare it to check the progress of patients. They can also provide acoustic and visual feedback, helping the patient maintain a high level of attention during the session, allowing patients achieve autonomy in the exercises may increase motivation towards following the rehabilitative therapy. In short, rehabilitation robotics can provide high-intensity, repetitive, task-specific treatment of the injured limb and can help monitor patient progress, [11].

Among the different robotic structures existing, the cable driven parallel robots have characteristics that make them suitable for rehabilitation purposes. As already mentioned, they have large workspace and can be reconfigured by simply changing the attachment points or the actuators positions. These features allow the adaptation to different patients and different rehabilitation exercises. In fact, unlike other robots such as industrial ones, rehabilitation robots need to be adapted to the particular characteristics of each patient, taking into account not only the type of exercise

required, but also the physical characteristics, perception and pain threshold of each patient. Besides, their transportability makes them easy to be placed aside a wheelchair or a bed and easy to be stored after treatment. In terms of commercialization, they have a low cost mechanical structure and simple maintenance, which may also contribute to be used by patients at home. Furthermore, they are intrinsically safe for patients and therapists thanks to the use of cables instead of rigid links. Finally, the way in which the patient perceives the treatment is of great importance. In this regard, the use of wires increases the acceptability by the patient, who feels guided and not constrained by the machine, [10–12].

3 Cable Driven Robots Features

Cable driven parallel manipulators are a special class of parallel mechanisms, whose trusts consist of cables whose lengths are adjustable to control the end-effector's position and orientation [12]. That is, the pose of the end-effector, determined by its degrees of freedom (DOFs), is manipulated by actuating motors that extend or retract the cables. As [12] points out, the condition for a mobile platform with n DOFs to have a fully controlled motion is having, at least $m = n + 1$ cables. This derives from the fact that, due to their nature, cables require positive tension. They can only exert pulling action, being able to carry loads in tension but not in compression, so redundant cables are needed to avoid uncontrollable situations. Figure 1 shows the general structure of a spatial cable driven parallel robot and its main components.

4 Proposed Design Solution

A specific design procedure has been outlined as proposed in the flow-chart in Fig. 2 aiming to carry out the design of a proper mechanical structure as based on key aspects such as limb exercising/rehabilitation requirements, training motions as defined in medical protocols as well as constraints given by size limitation of home

Fig. 1 A scheme of a cable driven parallel robot with its main components

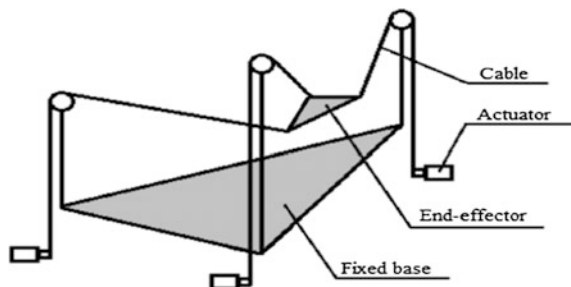
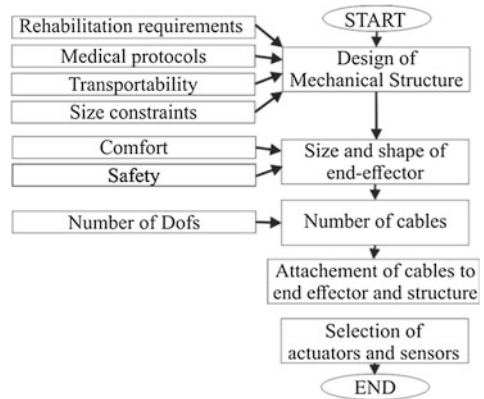


Fig. 2 A flow-chart of the design procedure



environments, easy operation, comfort, safety, transportability. Accordingly, the shape of the mechanical structure has been defined as shown in Fig. 3 also to achieve an easy placement of the device in a room edge and a wider easily accessible workspace as compared with cubic shapes of many existing cable driven parallel robots such as [7, 8]. The proposed structure can accommodate 6 or more cables. However, the more cables, the less low-cost easy-operation the robot becomes. Thus, a balance should be found between the number of DOFs under control and the complexity of the mechanism.

The proposed design has been thought to have a maximum of six cables. The way in which these cables are attached to the end-effector will determine which DOFs are under control. Depending on the kind of exercise, some cables could be disconnected. For instance, to provide flexion-extension movements four cables are enough. Gravity is another issue to be taken into account. A distinction should be made between acute stroke patients, whose limbs need to be totally guided as they do not have autonomy to move them, and patients who are able to move their limbs following the rehabilitative exercise. In the first case, gravity has to be considered as

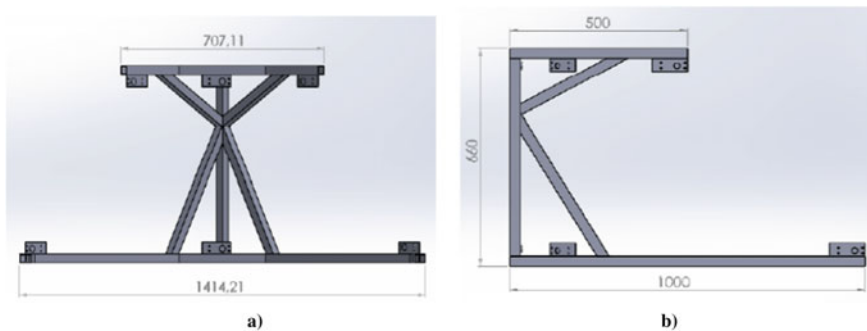


Fig. 3 A 3D model of the proposed mechanical structure with main sizes in mm: **a** front view; **b** side view

the limb is acting as deadweight. Focusing on the forearm, a first study will focus at elbow flexion-extension and horizontal adduction-abduction movements. Both of them are angular displacements of the forearm, being the elbow joint the centre of rotation of this motion. The trajectory followed by the wrist is a circumference arc along the plane defined by the median longitudinal plane of the arm. The difference between both movements is the orientation of that plane. While in the flexion-extension it is vertical, in the adduction-abduction it remains horizontal. Being the trajectory a circumference arc along the same plane, the degrees of freedom that need to be under control are two for the position of the center of gravity in that plane and one for the orientation of the reference system attached to the end-effector. Being the pose of the end-effector in the arm's plane defined by three degrees of freedom, the number of cables required by the kinematics is four: three on the top of the frame and one extra cable on the bottom to fulfil the positive tension requirement. The adjustment of the lengths of these cables makes the end-effector/upper limb, follow the desired trajectory.

A kinematic model can be established for the proposed design solution by expressing the position of the end-effector as function of the coordinates of the cable attachments to the mechanical structure and as function of the cable lengths. In particular, Fig. 4a, b, c show kinematic schemes as referring to a 3D view, plane X-Y, and plane X-Z, respectively. The Inverse Kinematics Problem (IKP) consists on finding the cable lengths as function of the end-effector degrees of freedom. As shown below, in both cases the length of each cable can be written in terms of difference of coordinates of its endpoints.

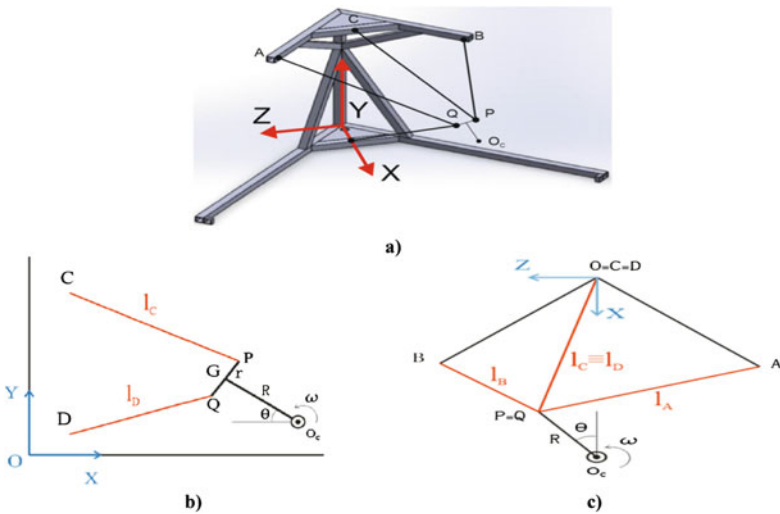


Fig. 4 Kinematic schemes: **a** a 3D view with reference frame and location of cable attachments; **b** X-Y (flexion-extension) plane; **c** X-Z (adduction-abduction) plane

Firstly, for the flexion-extension movement, the kinematic scheme of cables C and D is shown in Fig. 4b. Because of the symmetry of the structure and arm position it moves along plane π , so the IKP for this cables is simplified. The length of the cable, l_C , is defined by points C and P, which represent the attachment points of the cable to the motor and to the upper face of the end-effector, respectively. Two reference frames have been considered: OXY is the fixed frame and $G X_G Y_G$ is the moving frame associated to the end-effector center of gravity. Parameter R indicates the length of the forearm, while parameter r indicates the distance from the center of gravity of the end-effector to the attachment point P, this is, half the height of the frame arms. θ represents the angular displacement of the arm axis and also the orientation of the moving reference frame with respect to the fixed one. It is indeed one of the three DOFs to define the pose of the end-effector. The other two DOFs are related to the position of the frame arms in the plane, and could be defined by the coordinates of the center of gravity or by the coordinates of point P. Finally, since the trajectory followed by point G is a circumference arc, it is interesting to write the equations in terms of the coordinates of its rotation center, OC.

Thus, the following equations can be written for the kinematics of cable C by referring to a planar motion of the end effector within the plane shown in Fig. 4b,

$$l_C = \sqrt{\overline{CX}_P^2 + \overline{CY}_P^2} \quad (1)$$

$$\overline{CX}_P = X_P - X_C = X_{Oc} - R \cos \theta + r \sin \theta - X_C$$

$$\overline{CY}_P = Y_P - Y_C = Y_{Oc} + R \sin \theta + r \cos \theta - Y_C$$

where X_i and Y_i are the X and Y Cartesian coordinates of the i -th point; r and R are geometrical sizes of the end-effector and θ is the angular displacement of a limb in the X-Y plane, as shown in Fig. 4. Similar equations can be written for cable D. Cables A and B do not just move along plane π , but along the space in the three dimensions. However, the equations for their lengths l_A and l_B can be defined similarly to the ones of cables C and D, as difference of coordinates of their endpoints. Accordingly, for cable A one can write

$$l_A = \sqrt{\overline{AP}_X^2 + \overline{AP}_Y^2 + \overline{AP}_Z^2} \quad (2)$$

$$\overline{AX}_P = X_P - X_A = X_{Oc} - R \cos \theta + r \sin \theta - X_A$$

$$\overline{AY}_P = Y_P - Y_A = Y_{Oc} + R \sin \theta + r \cos \theta - Y_A$$

$$\overline{AZ}_P = Z_P - Z_A = -Z_A$$

A similar equation can be obtained for cable B. Accordingly, Eqs. (1) and (2) can be combined with the similar equations for cables B and C to provide a set of four equations in four unknown that are the kinematic relationship between cable

lengths and end-effector position and orientation for a planar motion of the end effector. The above-mentioned equations allow to calculate the cable lengths for any desired end effector pose for a planar motion of the end effector. Similar equations have been defined and solved for other planned motions of the end effector. The above-mentioned equations have been used for validating the operation of the proposed design solution within Solidworks Motion environment.

5 Numerical Simulations

Numerical simulations have been carried out both by using the models given by Eqs. (1) and (2) and a 3D CAD model within Solidworks Motion simulation toolbox. In particular, Fig. 5a, b, c show snapshots taken from the Solidworks Motion simulation of the adduction training movement: when the forearm is at 0°, 45°, and 90°, respectively. It is to note that the simulations have been carried out by using the values reported in Tables 1 and 2. In particular, Fig. 6a shows an angular motion of the forearm by 45° corresponding to a displacement of the wrist (point O_C) from 685 to 731 mm from the attachment of cables at point P. This motion range is within the feasible motion range of the chosen servomotors and pulleys. Several other training trajectories have been tested within Solidworks Motion

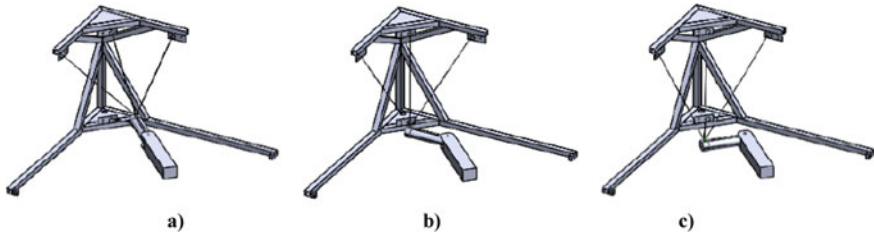


Fig. 5 Snapshots taken from a Solidworks Motion simulation of the adduction training movement: **a** forearm at 0°; **b** forearm at 45°; **c** forearm at 90°

Table 1 Values of main kinematic parameters used for the simulation of the extension mode

OCX [mm]	OCY [mm]	R [mm]	r [mm]
879.88	30	215	27

Table 2 Coordinates of attachment points of cables with pulleys

X_A [mm]	Y_A [mm]	Z_A [mm]	X_B [mm]	Y_B [mm]	Z_B [mm]	X_C [mm]	Y_C [mm]	X_D [mm]	Y_D [mm]
327.7	618.5	-279.7	356.7	618.5	308.6	196.4	618.5	196.4	58.5

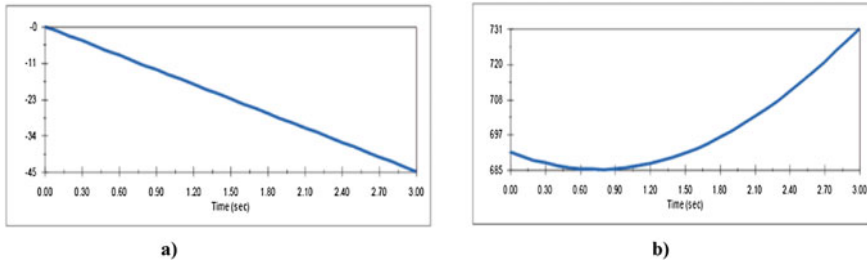


Fig. 6 Plot outputs from the simulation in Fig. 5: **a** angular displacement ($^{\circ}$) of the forearm over time (s); **b** distance (mm) of point O_C (attachment of the wrist) relative to point P (attachment of the first two cables) over time (s)

environment Data from the Solidworks Motion simulations have been also compared with results obtained by using Eqs. (1) and (2) with very good matching of results.

6 Preliminary Tests on a Built Prototype

Preliminary experimental tests have been carried out as shown in Fig. 7. In particular, Fig. 7a, b, c show snapshots taken from an experimental test of the adduction training movement: when the forearm is at -45° , 0° , and 45° , respectively. The achieved motion properly matches with the simulated operation in Fig. 5. Further work should be carried out for improving the control and of the used servomotors as well as for taking into account the flexibility of cables into the control loop as well as the effect of human limb weight and inertia.

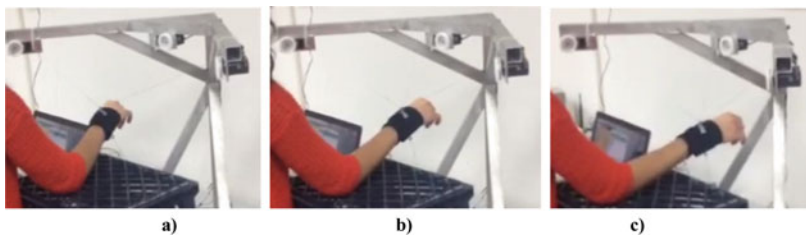


Fig. 7 Preliminary experimental tests of the adduction training movement at LARM in Cassino: **a** forearm at -45° ; **b** forearm at 0° ; **c** forearm at 45°

7 Conclusions

This paper deals with the development of a device for limb exercising. In particular, the main limb exercising features have been identified, mainly as referring to upper limbs. A novel cable driven parallel manipulator has been proposed as a solution for achieving a portable low-cost user-friendly upper limb exercising device. Numerical models and simulations as well as preliminary experimental tests have been carried out to verify the feasibility and practical usefulness of the proposed solution.

Per la presentazione (Figs. 8, 9, 10 and 11).

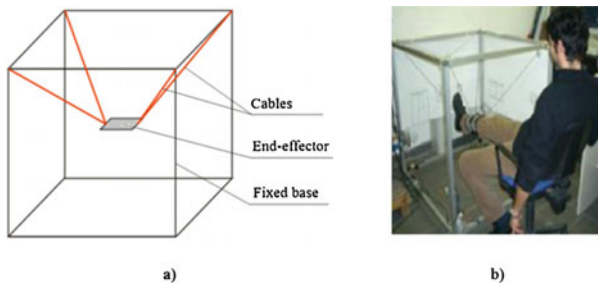


Fig. 8 A four cable driven parallel manipulator CALOWL: **a** structural diagram; **b** application as support for limb rehabilitation

Fig. 9 NeRebot: **a** structure diagram; **b** overall view [6]

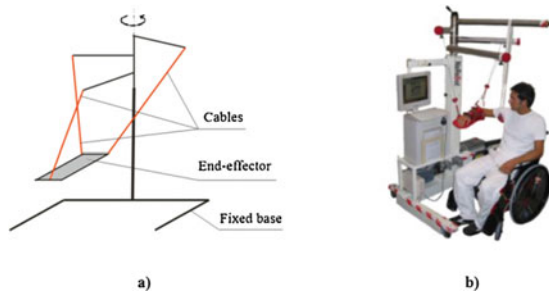
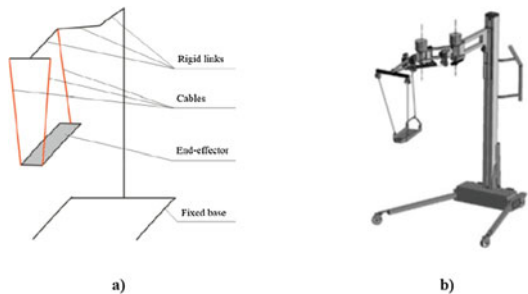
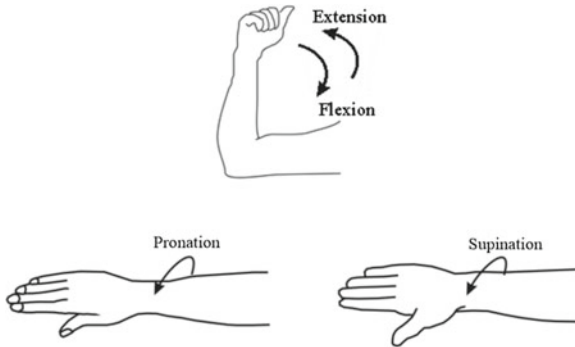


Fig. 10 MariBot rehabilitation robot: **a** Structural diagram; **b** design of the prototype





Elbow joint movements: Flexion-Extension; Pronation-Supination.

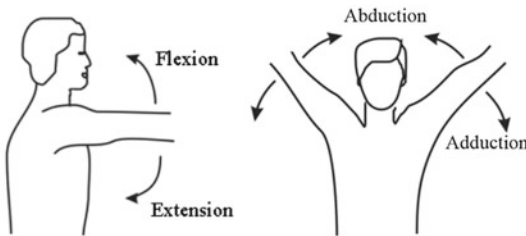


Fig. 11 Shoulder joint movement: Flexion-Extension; Abduction-Adduction

Acknowledgments The second Author has spent a period of study at LARM in 2015 with an Erasmus grant which is gratefully acknowledged.

References

1. Potash RL, Potash RJ, Kollet KW, Dugas GE (2014) Exercise system for physical rehabilitation and fitness. US Patent US 20140135174 A1
2. Gezari W, Gezari DY (1990) Muscle exercise and/or rehabilitation apparatus using linear motion. US Patent US 4907797 A
3. Smith J, Bhugra K (2012) Exoskeleton for gait assistance and rehabilitation. US Patent WO 2013019749 A
4. Agrawal S, Mao Y, Scholz J (2015) Wearable cable-driven exoskeleton for functional arm training. US Patent US 9144528 B2
5. Ceccarelli M (2004) Fundamentals of mechanics of robotic manipulation. Springer, Dordrecht
6. Rosati G, Gallina P, Masiero S (2007) Design, implementation and clinical tests of a wire-based robot for neurorehabilitation. *IEEE Trans Neural Syst Rehabil Eng* 15(4):560–569
7. Ceccarelli M (2013) Problems and experiences on cable-based service robots for physiotherapy applications. *New Trends Med Serv Robots* 16:27–42
8. Mayhew D, Bachrach B, Ryme WZ, Beer RF (2005) Development of the MACARM—a novel cable robot for upper limb neurorehabilitation. In: Proceedings of the 2005 IEEE 9th international conference on rehabilitation robotics, Chicago, pp 299–302

9. Prange GB, Jannink MJ, Groothuis-Oudshoorn CG, Hermens HJ, IJzerman MJ (2006) Systematic review of the effect of robot-aided therapy on recovery of the hemiparetic arm after stroke. *J Rehabil Res Dev* 43(2):171–184
10. Loureiro R, Colin C, Harwin W (2004) Robot aided therapy: challenges ahead for upper limb stroke rehabilitation. In: *Proceedings of 5th international conference on disability, virtual reality and associated technologies*, Oxford, pp 33–39
11. Cheverud J, Gordon C, Walker R, Jacquish C, Kohn L, Moore A, Yamashita L (1989) Anthropometric survey of U.S. personnel: summary statistics. Interim Report
12. Ceccarelli M, Romdhane L (2010) Design issues for human-machine platform interface in cable-based parallel manipulators for physiotherapy applications. *J Zhejiang Univ Sci A* 11(4):231–239

DARTAGNAN a Self-balanced Rehabilitation Robot Able to Work in Active and Passive Modes on Both Sides of Upper and Lower Limbs

M. Perrelli, P. Nudo, M. Iocco and G. Danieli

Abstract The article deals with a new six degrees of freedom system for rehabilitation, able to work, in active or passive modes, on upper and lower, left and rights limbs. This robot has an hybrid serial parallel structure, mechanically self-balanced thanks to the particular joints configuration. Performing a simple manual operation it's possible to change configuration of the robot, depending on the patient side on which the operator would act. The system is controlled by a multiprocessor distributed control system connected via CAN bus protocol. The control unit will also able to detect the force interactions between patient and manipulator, so that the system might behave as a 3D haptic system. Patents have been applied on this device [3–5].

Keywords Rehabilitation robot · Robot behaving as exoskeleton · Self-balanced robot

1 Introduction

In the rehabilitation field [2, 8, 12, 18–20] several robots exist able to provide rehabilitation services of upper or lower limbs, often ambidextrous or double, so as to enable the rehabilitation of both sides, but none able to provide all possible combinations of rehabilitation, as proposed by DARTAGNAN (Device for ARTiculAtion GeNeral rehAbilitationN), derived from a series of modifications to Navi-Robot as described in patent EP1843876 and related articles [6, 9, 10, 17]. As

M. Perrelli · P. Nudo · G. Danieli (✉)
Calabrian High Tech Srl, 87036 Rende, CS, Italy
e-mail: danieli@unical.it
URL: <http://www.chtsrl.com>

M. Perrelli · P. Nudo · G. Danieli
Università della Calabria, 87036 Rende, CS, Italy

M. Iocco
Università della Magna Graecia, 88100 Catanzaro, CZ, Italy

will be clear from the description, DARTAGNAN does not have an exoskeletal structure, such as Locomat [11, 15] robot capable of assisting the rehabilitation of the lower limbs, or ARAMIS (Automatic Recovery Arm Motility Integrated System) [2, 8] applied for the upper limbs, but thank to software behaves as such. Many other robots more specialized exist, such as the MIT Manus [13, 14], but their specialization is also their limit.

As well known, one of the main application fields of the robots in rehabilitation, is post-stroke motion recovery. In this particular case, robots are much more useful due to the peculiar disabilities of patients which suffer of force deficit and spasticity, as usually happen in the “neuron lesion syndrome”. It is to be noticed, furthermore, that also the alteration of proprio and exteroceptive sensibility can cause an anomalous and distorted sensitive state, in which the patient does not recognize spatial position and motion of his/her own body segments. Moreover, the possibility of storing the data of each performance, of monitoring their evolution in time and of correcting recurring errors while performing the exercises, explains the high interest for these instruments. Moreover, the availability of sensorial, acoustic or visual feedback helps the perception of the difference between the motion programmed by the brain and its actuation, allowing, after a very high number of repetitions of the specific motion exercise, the reorganization of the brain function. The rehabilitation process is also helped by assigning to the patient the attainment of specific objectives, by increasing the motivation and attention toward the correct execution of the exercises. This can be obtained also by giving to the patient the possibility of playing with video game specifically designed. Employing sensorized robots is thus fully motivated and justified. Moreover, the possibility of storing and post-processing the data of each performance, following their variation in time while observing recurring errors causes the rehabilitator’s keen interest for these instruments. And, as reported in [16], a long term exercise can even promote muscle reinnervation.

Naturally they can be applied as well to a variety of other problems where rehabilitation is needed.

2 The New Device

The basic idea is to provide an haptic system that can enable the greatest variety of rehabilitation patterns, thanks to the use of a structure bearing six self-balanced DOFs on which force sensors are applied, capable of measuring forces and torques applied to the end effector.

All joints are equipped with absolute encoders and motor reducer groups and can be either passively moved without offering resistance, or actively responding to a force or torque applied, the magnitude of which can be adjusted by the rehabilitator. For example it is possible to teach the robot the exercise attacking the patient to the machine and performing the exercise, while the machine learns the exercise itself and then is able to repeat it endlessly. In alternative a rehabilitator can perform the exercise and ask the robot to repeat on the patient, adapting it to the different

physical characteristics. A playful mode will also be introduced. In this mode the patient must drive the game with or without haptic guidance of the path to be followed.

This robot is not obviously a structure of exoskeletal type [11, 15], but behaves as such without the need for specific adjustments thanks to the specific control software designed. As can be seen in Fig. 1, the first three degrees of freedom (1–3) allow positioning the fourth hinge in any position in space in a cylindrical space around the first vertical hinge. Note that the second hinge moves a parallel arms four bar link, that allows changing the vertical position of the end effector while maintaining hinges (3) and (4) with vertical axes and hinge (5) horizontal. Moreover, the presence of counterweight (12) completely balances the entire structure.

The last three degrees instead allow positioning the final end effector with any direction within the workspace. Also note that the last end effector presents a handle (7) and a ring (8) on which the arm or leg should be fixed, in order to keep it aligned with the last robot’s end effector. Also note the position of the motor (10) chosen as to almost balance the last link about hinge (5).

Another interesting point is the possibility of working on both sides of the patient, thank to a double joint (18) that can allow turning the link 3–4 almost 180° about the joint 3 on both sides of the robot, as can be observed in Fig. 2.

Returning to the possibility of this robot behaving as an exoskeletal structure, it is enough to consider that if, as example, one wants to use it on the upper limbs, it is

Fig. 1 Scheme of DARTAGNAN

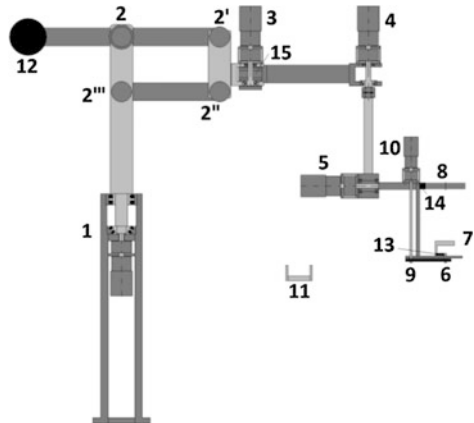
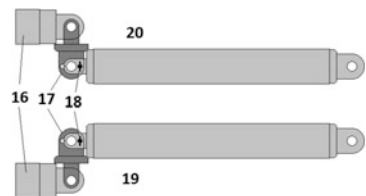


Fig. 2 Link 3–4 as seen from the top, showing the double joint



enough to lock initially the trunk and the arm moving the forearm. This allows determining the position of the elbow with respect of the end effector by using the robot in passive mode. Then, freeing the arm, while keeping the trunk fixed, also the position of the shoulder can be determined in the same way. In this way is then possible to calculate the length of arm and forearm of the user. Notice also that no mechanical adjustments are needed.

3 Actual DARTAGNAN Version

For the realization of the first prototype, we decided to use Maxon motors and reducers, 48 V DC (1 RE30, 1 RE50 and 4 RE40) for motion, controlled by EPOS2 boards with CAN bus interface, while the angles are measured by 16 bit absolute encoders by POSITAL, also controlled via EPOS2. The robot is controlled by an industrial PC, via MATLAB, using a touch screen placed on a wheeled chart for input. Next two Figs. 3 and 4 show the robot in right and left configuration, applied on a team member.

Fig. 3 DARTAGNAN for *right* arm

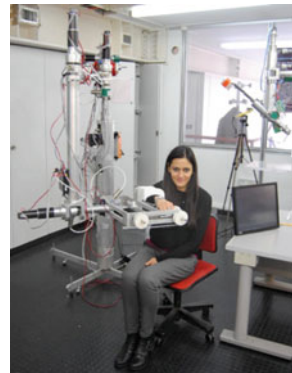
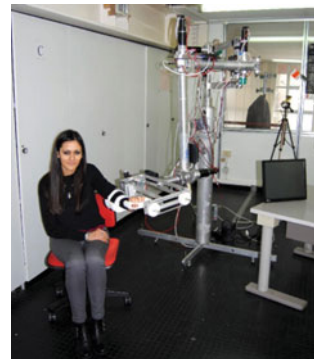


Fig. 4 DARTAGNAN for *left* arm



4 The Kinematic Models

Once the patient’s arm or leg lengths are known, then the computer is able to calculate their motion as direct kinematic, determining the position of the forearm or leg, which coincides with the robots end effector position. Figure 5 shows the direct kinematic model for the human arm with according to Denavit-Hartembreg [7].

The kinematic model of DARTAGNAN with the relative DH transformation table is visible in Fig. 6.

For the closed loop kinematic chain, showed in Fig. 7, it is not possible to apply the canonical Denavit-Hartemberg method. The transformation between frame 1 and 2, was so calculated by using the Denavit-Hartemberg method extended to closed loop kinematic chain obtaining the transformation matrix of Fig. 7.

Since the forearm represents the robot’s end effector position, the position in which the axis of the fifth joint crosses the end effector axis is well known. Calling x_h, y_h, z_h the hand coordinates and x_e, y_e, z_e those of the end effector point of

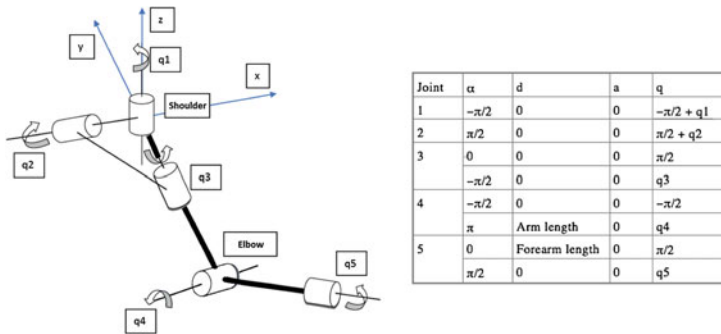


Fig. 5 Denavit Hartemberg model for human arm

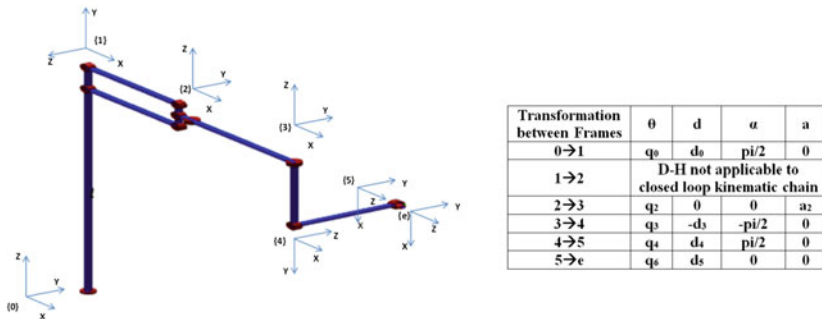


Fig. 6 Denavit Hartemberg model for DARTAGNAN

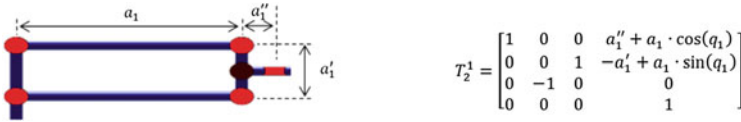


Fig. 7 Transformation for closed loop chain of DARTAGNAN

intersection with the fifth axis, knowing that the axis of the fifth joint will always be horizontal, we can determine the angle in the x, y reference frame $\{0\}$ as:

$$\theta = \arctan((x_h - x_e)/(y_e - y_h))$$

Knowing this, the position of the point in which the fourth joint axis will cross the fifth may be determined at a known distance from sixth joint axis and on the right side of said axis. This allows immediately determining the center of fourth joint, since the distance between these two is a design parameter.

From these coordinates it is possible to determine first the angle assumed by the rocker of the parallelogram, and its horizontal projection, and finally the coordinates of joint 3 by simply finding the intersection of one of the two circles representing the length of members 3–4 and 1–3.

At this point it is possible to easily compute all six angles to be assumed by the robot in order to allow the particular arm's motion desired. Naturally once this is programmed the computation described is practically instantaneous.

In order to fix the lengths of the various links of the robot to allow rehabilitation of any individual, first the member dimensions of a tall individual (two meters of heights) were established. In order to do so, even if from literature [1] is not so certain that on the average member's length is proportional to height, we just measured the length of the members of a few students to determine typical dimensions, multiplying then the lengths by the ratio between 2 and their height expressed in meters. In fact, a more precise analysis on this topic will be performed later, but at the moment is enough to establish starting values, that can be easily modified afterwards.

At this point we started simulations of the robot motion as a consequence of limbs motions, starting from an arm extension process in the horizontal plane. Figure 8 shows a sequence of positions of arm and forearm during this process as computed with MATLAB.

Next we fixed the robot to the elbow and we repeated the process computing the positions assumed by it. Figure 9 shows a 3D view of the process showing both the robot (thicker lines) and arm positions.

Next the robot angles (in radians) were computed during the process, as a function of the angle of horizontal arm rotation and are shown in Fig. 10, noticing that in this case only the first, third and fourth angles are subject to variations.

This is only an example, but is possible to simulate practically all types of exercises. As well as it will be possible on the robot to execute them.

Fig. 8 - Arm extension process in the horizontal plane as seen from the *top*

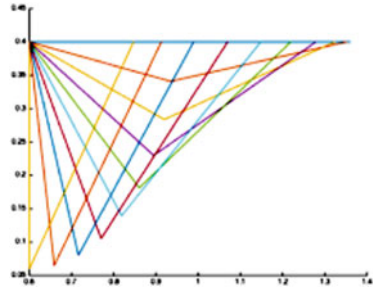


Fig. 9 Robot and arm assumed positions during the previous motion

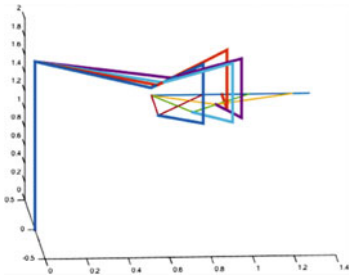
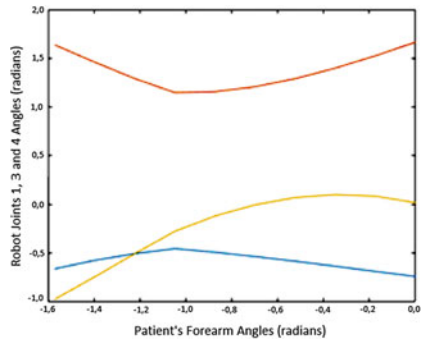


Fig. 10 Angles assumed by the robot during the previous procedure



Note also that it is possible for a rehabilitation operator to program special procedures simply choosing the option on the control PC and attaching his forearm or leg to the robot, then moving it according to the calibration procedure in order to supply the robot his/hers limb dimensions, then execute the desired exercise, while the robot records the motion in passive mode. At this point, placing the patient on the robot chair or bed, and repeating with the patient the calibration procedure (in reality a very fast one) the system will be ready to repeat the exercise in an endless way. And all this using the touch screen.

5 Conclusion

In this paper, a robot able to perform rehabilitative procedures was presented. The main advantage of the proposed system is the high reusability and the efforts necessary to build this system are justified by the possibility to execute, with the same instrumentation, the rehabilitation of upper and lower limbs. This peculiarity will introduce, also, a significant money saving for the rehabilitation Centres, with the consequent increasing diffusion of robotic systems in the rehabilitation field.

Acknowledgments The authors wish to acknowledge the great and patient work of Basilio Sinopoli and Attilio Caseti, which were fundamental for the construction of this robot. This work has been made possible by a grant of Regione Calabria, under project LOCUBIR rehab.

References

1. Bogin B, Varela-Silva MI (2010) Leg length, body proportion, and health: a review with a note on beauty. *Int J Environ Res Public Health* 7(3):1047–1075
2. Colizzi L, Lidonnici A, Pignolo L (2009) The ARAMIS project: a concept robot and technical design. *J Rehabil Med* 41:1011–1015
3. Danieli G (2015) Self balanced rehabilitation robot able to work both in active and passive modes on upper and lower limbs, left and rights. Italian patent application CS2015A000001, 18 Jan 2015
4. Danieli G (2016) Robot riabilitativo auto-bilanciato in gradi di lavorare sia in modo attivo che passivo sia su arti superiori che inferiori, sia destri che sinistri. CS2016A000001, 17 Jan 2016
5. Danieli G (2016) Robot riabilitativo auto-bilanciato in gradi di lavorare sia in modo attivo che passivo sia su arti superiori che inferiori, sia destri che sinistri. PCT, 18 Jan 2016
6. Danieli G, Fragomeni G, Gatti G, Merola A, Moschella D (2005) Navi-Robot, a navigator able to turn itself into a robot to reach the correct position for a given task during orthopaedic surgical procedures. *WSEAS Trans Syst* 4(7):1037–1045. ISSN: 1109-2777
7. Denavit L, Hartenberg RS (1955) A kinematic notation for lower-pair mechanism based on matrices. *ASME J Appl Mech* 77:215–221
8. Dobkin BH (2004) Strategies for stroke rehabilitation. *Lancet Neurol* 3:526–528
9. Donnici M, Lupinacci G, Nudo P, Perrelli M, Meduri S, Sinopoli B, Pulice D, Pace C, Danieli G (2012) Using Navi-Robot in conjunction with a CT equipment to guide precision biopsies. In: *Proceedings of the RAAD 2012, 17th international workshop on robotics in Alpe-Adria-Danube Region, 10–13 Sept 2012, Napoli, Italy*
10. Donnici M, Meduri S, Perrelli M, Battaglia D, Gatti G, Pace C, Danieli G (2014) Stochastic deterministic calibration of a self balanced hybrid parallel/serial robotic structure. *Probl Mech* 54(2):29–37
11. Esquenazi A, Lee S, Packel AT, Braitman L (2013) A randomized comparative study of manually assisted versus robotic-assisted body weight supported treadmill training in persons with a traumatic brain injury. *PM R* 5(4):280–290
12. Hidler J, Nichols D, Pelliccio M, Brady K (2005) Advances in the understanding and treatment of stroke impairment using robotic devices. *Top Stroke Rehabil* 12:22–33
13. Krebs HI, Hogan N, Volpe BT, Aisen ML, Edelstein L, Diels C (1999) Overview of clinical trials with MIT-MANUS, a robot aided neuro-rehabilitation facility. *Technol Health Care* 7:419–423

14. Krebs HI, Ferraro M, Buerger SP, Newbery MJ, Makiyama A, Sandmann M, Lynch D, Volpe BT, Hogan N (2004) Rehabilitation robotics: pilot trial of a spatial extension for MIT-Manus. *J NeuroEng Rehabil* 1:5
15. Mehrholz J, Elsner B, Werner C, Kugler J, Pohl M (2013) Electromechanical-assisted training for walking after stroke. *Cochrane Database Syst Rev* 25:7
16. Mosole S, Carraro U, Kern H, Loeffler S, Fruhmann H, Vogelauer M, Burggraf S, Mayr W, Krenn M, Paternostro-Sluga T, Hamar D, Cvecka J, Sedliak M, Tirpakova V, Sarabon N, Musarò A, Sandri M, Protasi F, Nori A, Pond A, Zampieri S (2004) Long-term high-level exercise promotes muscle reinnervation with age. *J Neuropathol Exp Neurol* 73(4):284–294
17. Perrelli M, Nudo P, Donnici M, Gatti G, Colacino FM, Pace C, Danieli G (2010) Navi-Robot, a multipurpose robot for medical applications. *Probl Mech* 41(4):22–33
18. Platz T (2003) Evidence-based arm rehabilitation. *Nervenarzt* 74:841–849
19. Van Peppen RP, Kwakkel G, Wood-Dauphinee S, Hendriks HJ, Van der Wees PJ, Dekker J (2004) The impact of physical therapy on functional outcomes after stroke: what's the evidence? *Clin Rehabil* 18:833–862
20. Volpe BT, Krebs HI, Hogan N (2001) Is robot-aided sensorimotor training in stroke rehabilitation a realistic option? *Curr Opin Neurol* 14:745–752

Dynamic Analysis of Handcycling: Mathematical Modelling and Experimental Tests

G. Azizpour, A. Ousdad, G. Legnani, G. Incerti, M. Lancini
and P. Gaffurini

Abstract The handbike is an upper body-powered vehicle used for sports and rehabilitation purposes. The advantages include improving patients physical activities and fitness level, as well as promoting an active lifestyle after rehabilitation duration. In this research the torques in shoulder and elbow joints have been determined during handbike motion from dynamic output and kinematics information. Therefore, a 2D model was presented. Data have been collected based on the output of experimental results obtained by sensors inserted on the handles of a cycle ergometer and by marker coordinates acquired by a vision system.

1 Introduction

Handbikes are three wheel vehicles used for transportation and recreation, but they are also widely used in rehabilitation programs for people with reduced mobility and in sport fields for disabled people.

In the last decade, researches have showed interest in different aspects of synchronous handcycling. Literature analyzes physiological responses with oxygen uptake, ventilation and respiratory rate to identify the effects of cadency and work rate [3, 4]. Furthermore, some studies performed biomechanical and force analyses which were conducted to identify two main efficiency indices. The first one is the fraction of effective force (FEF) [3, 5], associated with the effectiveness of the force application and the second one is the postural force production index (PFPI) [1], which evaluates the force generation capacity in all directions. However, these indices do not take into account gravity, inertia and the Coriolis effects, thus presenting a limitation in the efficiency evaluation. The aim of this study is to present a dynamic model that considers contributions of gravity, inertia and Coriolis effects

G. Azizpour (✉) · A. Ousdad · G. Legnani · G. Incerti · M. Lancini · P. Gaffurini
University of Brescia, Via Branze 38, 25123 Brescia, Italy
e-mail: g.azizpour@unibs.it

A. Ousdad
e-mail: a.ousdad@unibs.it

in order to associate the forces measured on handles to the corresponding shoulder and elbow torques. This allows the correction of the mentioned indices to give them more relevance.

2 Mathematical Modelling

In this study a planar model of the upper-limb has been developed, considering one rotation for the shoulder and the elbow respectively, whilst the wrist joint is considered fixed to the handle.

The dynamic study of the arm-forearm group was carried out by the matrix approach; denoting by $q = [\alpha \ \beta]^T$ the vector containing the angular positions of the upper and lower limb (see Fig. 1), the generalized motion equation can be written in the form [2]:

$$M_s(q)\ddot{q} + C(q, \dot{q}) - J_e^T F_{ext} = \tau \quad (1)$$

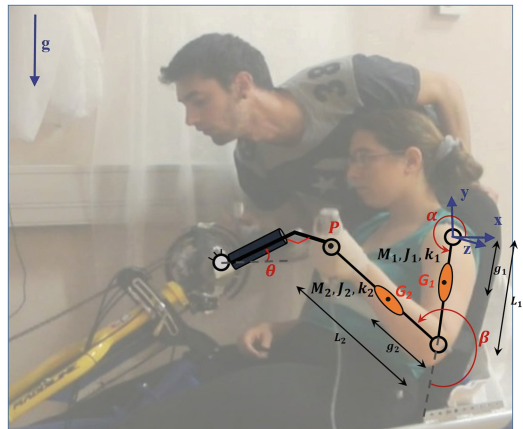
where $M_s(q)$ is the mass matrix, $C(q, \dot{q})$, the matrix containing the centrifugal and Coriolis effects, J_e the extended Jacobian matrix, F_{ext} the vector of the external forces and $\tau = [\tau_1 \ \tau_2]^T$ the vector of the joint torques. As is well known from the theory of mechanisms, the matrices $M_s(q)$ and $C(q, \dot{q})$ assume the following expressions:

$$M_s(q) = J_e^T M J_e \quad C(q, \dot{q}) = J_e^T M J_e \dot{q} \quad (2)$$

where M is a diagonal matrix containing the inertial parameters of the system. Assuming negligible the masses and the moment of inertia of the hand (i.e. the body located at point P in Fig. 1), this matrix assumes the following expression:

$$M = \text{diag} [0 \ 0 \ M_2 \ M_2 \ J_2 \ M_1 \ M_1 \ J_1] \quad (3)$$

Fig. 1 Details of the planar model of the upper-limb



The extended Jacobian matrix for the system under consideration is given by:

$$J_e(\alpha, \beta) = \begin{bmatrix} \frac{\partial S_1}{\partial \alpha} & \frac{\partial S_1}{\partial \beta} \\ \vdots & \vdots \\ \frac{\partial S_8}{\partial \alpha} & \frac{\partial S_8}{\partial \beta} \end{bmatrix} \quad (4)$$

where S_i ($i = 1, \dots, 8$) is the i th component of the vector S , that contains the relevant coordinates of the mechanical system (i.e. the Cartesian coordinates of the points P , G_1 , G_2 and the angular coordinates φ_1 and φ_2 of the limbs, measured counterclockwise from the horizontal reference):

$$S = \begin{bmatrix} S_1 \\ S_2 \\ S_3 \\ S_4 \\ S_5 \\ S_6 \\ S_7 \\ S_8 \end{bmatrix} = \begin{bmatrix} x_P \\ y_P \\ x_{G_2} \\ y_{G_2} \\ \varphi_2 \\ x_{G_1} \\ y_{G_1} \\ \varphi_1 \end{bmatrix} = \begin{bmatrix} L_1 \cos(\alpha) + L_2 \cos(\alpha + \beta) \\ L_1 \sin(\alpha) + L_2 \sin(\alpha + \beta) \\ L_1 \cos(\alpha) + g_2 \cos(\alpha + \beta) \\ L_1 \sin(\alpha) + g_2 \sin(\alpha + \beta) \\ \alpha + \beta \\ g_1 \cos(\alpha) \\ g_1 \sin(\alpha) \\ \alpha \end{bmatrix} \quad (5)$$

The time derivative of the Jacobian matrix can be synthetically written in the form:

$$\dot{J}_e = \frac{\partial J_e}{\partial \alpha} \dot{\alpha} + \frac{\partial J_e}{\partial \beta} \dot{\beta} \quad (6)$$

and it can be calculated without difficulties by using Eqs. (4) and (5).

The vector of the external forces F_{ext} is given by:

$$F_{ext} = F + F_{grav} \quad (7)$$

where:

$$F = [F_x \ F_y \ 0 \ 0 \ 0 \ 0 \ 0 \ 0]^T \quad (8)$$

is the vector containing the Cartesian components of the forces acting on the handle axis (point P) and

$$F_{grav} = [0 \ 0 \ 0 \ -M_2 g \ 0 \ 0 \ -M_1 g \ 0]^T \quad (9)$$

is the vector containing the weights of the limbs. Note that the components of the external forces must be inserted in the positions corresponding to the coordinates defined in the vector S . Substituting Eq. (7) into Eq. (1) and introducing the gravity vector $G(q) = -J_e^T F_{grav}$ we obtain:

$$M_s(q)\ddot{q} + C(q, \dot{q}) + G(q) - J_e^T F = \tau \quad (10)$$

Since only the first two components of the vector F are not null, the product $J_e^T F$ can be rewritten in the form $J^T F_h$, where $F_h = [F_x \ F_y]^T$ indicates the vector of the forces acting on the handle axis (point P), and J is the reduced Jacobian matrix, given by the following expression:

$$J(\alpha, \beta) = \begin{bmatrix} \frac{\partial S_1}{\partial \alpha} & \frac{\partial S_1}{\partial \beta} \\ \frac{\partial S_2}{\partial \alpha} & \frac{\partial S_2}{\partial \beta} \end{bmatrix} = \begin{bmatrix} \frac{\partial x_P}{\partial \alpha} & \frac{\partial x_P}{\partial \beta} \\ \frac{\partial y_P}{\partial \alpha} & \frac{\partial y_P}{\partial \beta} \end{bmatrix} \quad (11)$$

As regards the torques applied in correspondence of the joints (shoulder and elbow) it is important to emphasize that such torques are constituted by an active component τ_{m_i} ($i = 1, 2$), generated by the muscles and by a passive component, due to friction phenomena that occur at the joints. The present state of knowledge does not have detailed information on the type of friction present in the joints of the human body and therefore it was decided to adopt a combined Coulomb-viscous friction model; the torques acting in correspondence of the shoulder and the elbow can then be expressed by the following relationship:

$$\tau = \begin{bmatrix} \tau_1 \\ \tau_2 \end{bmatrix} = \begin{bmatrix} \tau_{m_1} - (k_{f1} \text{sign}(\dot{\alpha}) + k_{v1} \dot{\alpha}) \\ \tau_{m_2} - (k_{f2} \text{sign}(\dot{\beta}) + k_{v2} \dot{\beta}) \end{bmatrix} \quad (12)$$

where k_{f1} and k_{f2} are the Coulomb friction coefficients and k_{v1} and k_{v2} indicate the viscous friction constants.¹ Using matrix notation, Eq. (12) can be rewritten as:

$$\tau = \tau_m - K \quad (13)$$

where $\tau_m = [\tau_{m_1} \ \tau_{m_2}]^T$ and K is the vector containing the effects due to the Coulomb and viscous friction:

$$K = \begin{bmatrix} k_{f1} \text{sign}(\dot{\alpha}) + k_{v1} \dot{\alpha} \\ k_{f2} \text{sign}(\dot{\beta}) + k_{v2} \dot{\beta} \end{bmatrix} \quad (14)$$

According to these definitions, Eq. (10) takes the following form:

$$M_s(q)\ddot{q} + C(q, \dot{q}) + G(q) + K - J^T F_h = \tau_m \quad (15)$$

We can now observe that the first four terms on the left hand side of the Eq. (15) can be rewritten as a product of a matrix B and a vector P ; then we can write the following identity, which can be verified by symbolic computation:

$$BP \equiv M_s(q)\ddot{q} + C(q, \dot{q}) + G(q) + K \quad (16)$$

The components of the vector P are defined by the following expressions:

$$\begin{aligned} P_1 &= J_1 + M_1 g_1^2 + M_2 L_1^2 & P_5 &= k_{f1} \\ P_2 &= J_2 + M_2 g_2^2 & P_6 &= k_{f2} \\ P_3 &= M_2 g_2 & P_7 &= k_{v1} \\ P_4 &= M_1 g_1 + M_2 L_1 & P_8 &= k_{v2} \end{aligned} \quad (17)$$

and the matrix B is given by:

$$B = \begin{bmatrix} \ddot{\alpha} (\ddot{\alpha} + \ddot{\beta}) Z_1 g \cos \alpha \text{sign}(\dot{\alpha}) & 0 & \dot{\alpha} & 0 \\ 0 (\ddot{\alpha} + \ddot{\beta}) Z_2 & 0 & 0 & \text{sign}(\dot{\beta}) & 0 & \dot{\beta} \end{bmatrix} \quad (18)$$

¹The signum function is defined as follows:

$$\text{sign}(x) = \begin{cases} x/|x| & \text{if } x \neq 0 \\ 0 & \text{if } x = 0 \end{cases}.$$

where:

$$\begin{aligned} Z_1 &= L_1[(2\ddot{\alpha} + \ddot{\beta}) \cos \beta - (2\dot{\alpha}\dot{\beta} + \dot{\beta}^2) \sin \beta] + g \cos(\alpha + \beta) \\ Z_2 &= L_1(\ddot{\alpha} \cos \beta + \dot{\alpha}^2 \sin \beta) + g \cos(\alpha + \beta) \end{aligned} \quad (19)$$

The matrix B contains only two numerical parameters (the gravitational acceleration g and length L_1 of the upper-limb) and it is function of the kinematic variables that define the movement of the arms (the rotations α and β and their first and second time derivatives); the rotations can be measured at regular time instants by means of a vision system based on cameras, while the speed and angular accelerations can be obtained by numerical differentiation. The vector P has eight components and the first four of them contain the inertial and geometric characteristics of the limbs. Note that all components of the vector P linearly appear in the motion equation, which means that the system dynamics can be described by linear functions of the parameters P_i ($i = 1, \dots, 8$).

Taking into account the identity (16), the Eq. (15) becomes:

$$BP - J^T F_h = \tau_m \quad (20)$$

The estimation of the components of the vector P can be carried out by means of a passive test, in which the motion is generated by an external operator and the patient undergoing the test does not apply muscle force; in practice the patient is asked to grasp the instrumented handle, to remain completely relaxed and to maintain the movement of the limbs within the sagittal plane.

Being absent the contribution of muscle forces of the patient, the driving torques in the shoulder and elbow are null; setting $\tau_m = 0$ in Eq. (20), we get:

$$BP = J^T F_h \quad (21)$$

In this equation the matrix B , the reduced Jacobian J and the vector F_h of the forces acting on the handle axis are functions of time; using the subscript i to indicate their instantaneous values at the time instant t_i , we have:

$$B_i P = J_i^T F_{h_i} \quad (22)$$

The data collected at n different samplings during an experimental test can be collected together and are used to generate the following over constrained linear system:

$$WP = H \quad W = \begin{bmatrix} B_1 \\ B_2 \\ \dots \\ B_n \end{bmatrix} \quad H = \begin{bmatrix} J_1^T F_{h_1} \\ J_2^T F_{h_2} \\ \dots \\ J_n^T F_{h_n} \end{bmatrix} \quad (23)$$

that can be solved with the minimum squares criteria as:

$$P = (W^T W)^{-1} W^T H = W^+ H \quad (24)$$

where W^+ is the Moore-Penrose pseudoinverse.

As a verification, the estimated parameters can be inserted in Eq. (21) and the equation can be solved with respect to F_h , in order to obtain the estimated values $F_{h,es}$ of the forces on the handle axis:

$$F_{h,es} = (J^T)^{-1}BP \quad (25)$$

3 Results

In this phase of the study, a healthy right handed male subject was requested to perform the handcycling activity (Mass: 80.7 kg, Height: 186 cm). A vision system was used to determine 3D coordinates of the elbow and shoulder in the subject. In this case, the markers were placed on the right side of the subject on the following bony landmarks: one on acromion, one on elbow joint, one on hip, two on the handle, one on crank axis and two reference markers on the handbike frame.

In order to verify performance of the model and evaluate the results, two separate types of experiment were requested to be performed by the subject, which are described in the following subsections:

In the first experiment, passive tests were performed and vector P was estimated by assuming no voluntary muscle action is exerted (Eq. (24)). In this case the subject arm is fixed to the handle by a bandage. The subject was requested to keep his muscles relaxed throughout the test, while his arm was moved by an operator passively. In order to assure the null activity of the muscles during this experiment, an EMG measurement of some extensions and flexions made by muscles were recorded. The outcomes demonstrated that there was no significant EMG activity in those muscles during the passive movements (Table 1).

In addition, the xy components of the forces were estimated using Eq. (25), and then they were compared with those measured by the sensors. A sample result of comparison between the xy components of the measured and estimated forces is presented in Fig. 2.

The subject was asked to perform the passive tests three times and the results containing the lowest error was selected. This error was driven by comparing the measured force and the estimated force applied on the handle, as well as drawing comparisons between the torques generated by dynamic effects and the muscles. The P vector of this selected result was later used in active tests calculations.

Table 1 Comparing the dynamic parameters vector, obtained by anthropometric data (P_{ant}) and by estimated method (P_{est})

	P_1	P_2	P_3	P_4
P_{ant}	0.209661	0.019001	0.15118	0.789655
P_{est}	0.233705	0.083799	0.382064	0.969486

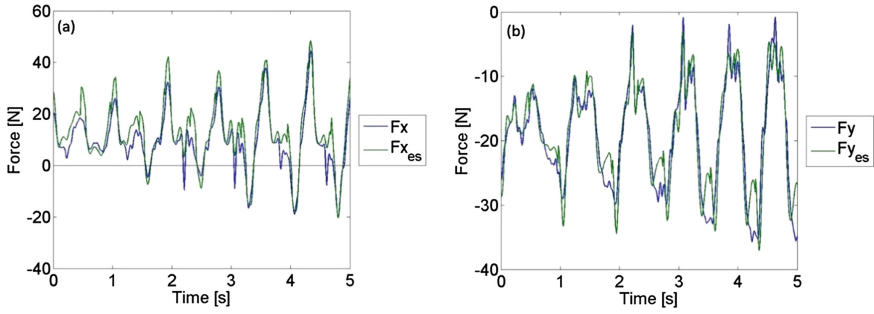
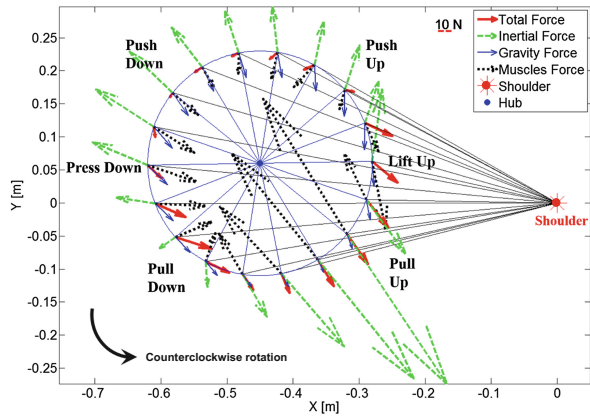


Fig. 2 Comparing the x component (a) and y component (b) of the estimated ($F_{x_{es}}, F_{y_{es}}$) and measured forces (F_x, F_y) during passive tests

Fig. 3 Force components over one cycle of handbike activity during an active test at 40 W input power



In the second series of experiments the subject is an active contributor; in this case, the handbike is equipped with a control system which guarantees a constant resistive power; three different constant resistive powers were considered for the subject: 0, 40 and 70 W. The vector of the shoulder and elbow torques τ_m during active handcycling motion can be obtained from Eq. (20), using the dynamic parameters vector P estimated in the passive test and the values of the measured forces F_h . The Matrix B and the reduced Jacobian J are calculated using the position data obtained from the vision system; the speed and angular accelerations are obtained by numerical differentiation. The graph in Fig. 3 illustrates performance of one cycle of handbike activity during an active test at 40 W input power. The red dot shows the shoulder position and the blue is for the crank hub. Each color of the arrows displays a different component of the force: The red arrows show the total measured forces, the blue vectors display the gravity components of the force, the green arrows illustrate the inertial parts of the force and finally the black arrows demonstrate the muscle forces generated to compensate for all the other components. It is visible that the maximum muscle forces have been generated in order to follow the propulsion

cycle while the dynamic forces have produced effects in contrast with the muscle forces. Besides, it is observable that during phases in which the dynamic forces produce effects compatible with the propulsion motion, the generated muscles force is decreased.

4 Conclusions

This work presents a passive handcycling test as a new method for estimating dynamic parameters of the arm. The suggested passive method facilitates a quick feasible method in order to estimate important dynamic parameters in human upper limbs. This is an important insight since this method is shown to estimate dynamic parameters directly driven from subjects data, while previous studies in the literature acquired their data mainly by regression curves as a function of body mass and height. The major problem found in those studies is that various factors such as age, sex or even body structures could significantly impact dynamic parameters values. In addition, the study provides the opportunity to study relationships between the forces applied on the handle, muscle forces, and the angular parameters of the upper body and thus, the overall understanding of handcycling movement and the corresponding patterns are to be improved. The joints torque generated during handcycling is computed by developing an analytic method which into account inertia, gravity and the Coriolis effects. The study reveals the effect of inertial torques as well as the torques generated by muscles, and draws a comparison between their levels of contribution to the total generated torques. Additionally, calculation of the mentioned indices (FEF) was modified by including the effects of dynamic contributions, and force weight in the procedure.

References

1. Jacquier-Bret J, Faupin A, Rezzoug N, Gorce PA (2013) A new postural force production index to assess propulsion effectiveness during handcycling. *J Appl Biomech* 29(6):798–803
2. Legnani G (2003) *Robotica Industriale*. C.E.A, Casa Editrice Ambrosiana, Milano
3. Powers SK, Beadle RE, Mangum M (1984) Exercise efficiency during arm ergometry: effects of speed and work rate. *J Appl Physiol Respir Environ Exerc Physiol* 56(2):495–499
4. Price MJ, Collins L, Smith PM, Goss-Sampson M (2007) The effects of cadence and power output upon physiological and biomechanical responses to incremental arm-crank ergometry. *Appl Physiol Nutr Metab* 32(4):686–692
5. Van Drongelen S, Arnet U, Van Der Woude LHV, Veeger HEJ (2010) *Propulsion effectiveness of synchronous handcycling, rehabilitation: mobility, exercise and sports*. IOS Press

A Kinematic Solution of a Novel Leg Mechanism with Parallel Architecture

Matteo Russo and Marco Ceccarelli

Abstract In this paper, a novel parallel mechanism for a biped robot leg is presented with the designed structure and its characteristics. The synthesis of the kinematic chain of the mechanism is described and the kinematic problem is solved.

Keywords Robot design · Leg mechanism design · Kinematics · Parallel robots

1 Introduction

In general, leg mechanisms for walking robots are based on serial mechanisms, such as the ones used in Honda's Asimo [1] and Nao [2]. Few bipeds with parallel architecture, such as the WL family [3] and LARM biped locomotor [4], can be found in literature, but no one has been as successful as the serial ones. One of the main advantages of serial legs is the dimension of their workspace, which is larger than the one of parallel structures when related to the size of the mechanism. The LARM biped locomotor, for example, has a step size that is equal to only 30 % of its height [4]. On the other hand, a parallel mechanism is more accurate and able to move a larger payload [5]. Therefore, a parallel structure is able to operate better than a serial one if properly designed for the target workspace.

This paper describes a novel parallel leg mechanism that is accurate and able to lift large payload while maintaining a workspace comparable to the one of a serial leg mechanism.

M. Russo (✉) · M. Ceccarelli
University of Cassino and Southern Latium, Cassino, Italy
e-mail: matteo.russo@unicas.it

M. Ceccarelli
e-mail: ceccarelli@unicas.it

2 Kinematic Design

The proposed mechanism is a 4 DoF parallel mechanism. Its kinematic chains are based on the kinematic inversion of the ones in the linear Delta robot [6] that is characterized by the three kinematic chains $\underline{3PR(2RR)R}$ in Fig. 1a. However, the workspace of this structure is too small when compared to the robot size, since the human gait is a motion on the sagittal plane (y-z plane in Fig. 3) that is characterised by a step length (along y-axis in Fig. 3) that is approximately 94 % of the leg length [7].

The conceptual design of the mechanism has evolved over 4 different conceptual designs, which are illustrated with the following chains:

1. $\underline{3(2RR)RPR}$, which is shown in Fig. 1b and in the structure in Fig. 2a. The workspace of this architecture is still too small for the task.
2. $\underline{3(2RR)RPR}$ with non-axisymmetric configuration as shown in the model in Fig. 2b. The workspace on the sagittal plane increases but it is still limited.
3. $\underline{2(2RR)RPR-R(2RPR)R}$. The lateral chain changes as in Figs. 1c and 2c. This structure presents an additional degree of freedom, which is described by the rotation of the moving platform within the sagittal plane.
4. $\underline{2PRPR-R(2RPR)R}$, which is shown in Fig. 3a, whose functionality is the same of the previous one. This structure uses less joints and therefore there are less friction forces in the mechanism.

The parameters a , l and h define the geometry of the base platform, while f and b describe the geometry of the moving platform by referring to Table 1 and Fig. 3a, b. The actuators are described by their total lengths s_b (rear), s_f (front),

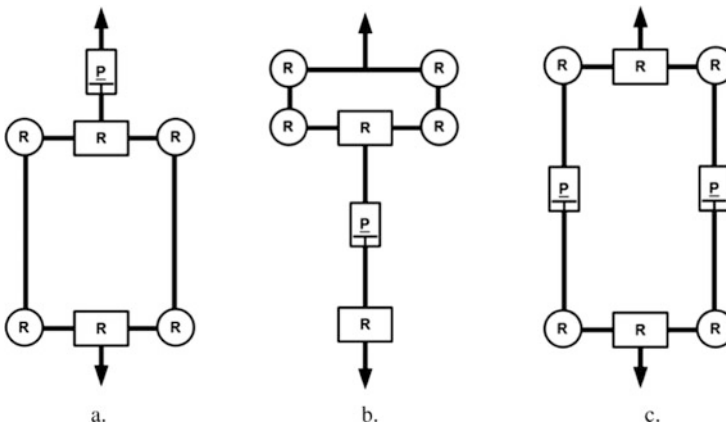


Fig. 1 Kinematic chains for parallel mechanisms: **a** Linear Delta robot; **b** first proposed chain; **c** second proposed chain (lateral chain) (R is for revolute joint, P is for prismatic joint and U is for universal joint, and the actuated joints are *underlined*)

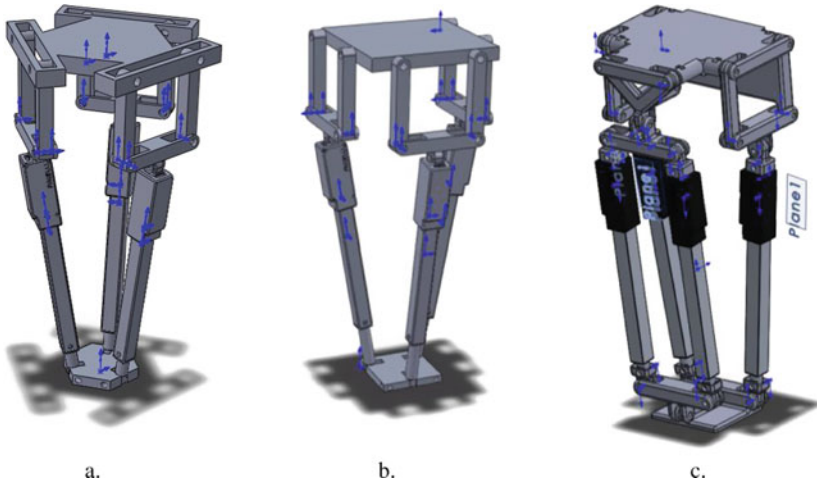


Fig. 2 Evolution of the CAD models of the proposed leg mechanism: **a** first solution; **b** second solution; **c** third solution

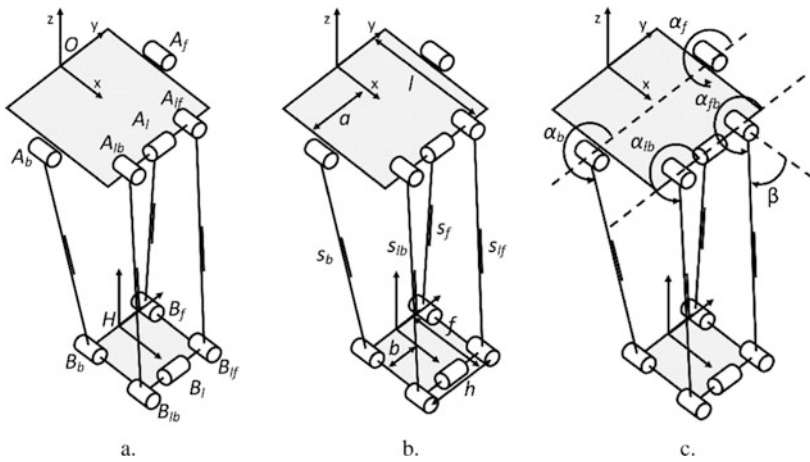


Fig. 3 Kinematic diagram of the proposed leg mechanism with its parameters: **a** Main points; **b** Geometric parameters; **c** Additional variables for the computation of kinematic equations

Table 1 Geometry of the mechanism

${}^0A_b = (x_H; -a; 0)$	${}^H B_b = (0; -b; 0)$	${}^0A_l = (l; 0; 0)$
${}^0A_f = (x_H; a; 0)$	${}^H B_f = (0; b; 0)$	${}^H B_l = (f; 0; 0)$
${}^0A_{ib} = (l; -h/2; 0)$	${}^H B_{ib} = (f; -h/2; 0)$	$AB = (0; s; 0)$
${}^0A_{if} = (l; h/2; 0)$	${}^H B_{if} = (f; h/2; 0)$	${}^0H = (x_H; y_H; z_H)$

s_{lb} (lateral-rear) and s_{lf} (lateral-front), which is defined as the distance between the centres of the revolute joints of each linear drive. Variables x_H , y_H and z_H define the position vector of the end-effector point, which is the centre of the reference frame of the moving platform. The orientation of the moving platform is defined by the rotation matrix $\mathbf{R}_x(\vartheta)$.

3 Forward and Inverse Kinematics

Forward and inverse kinematics can be solved through the computation of loop-closure equations [8]. The additional variables α_b , α_f , α_{lb} , α_{lf} and β , which describe the rotation of the actuators with respect to the $Oxyz$ frame, are described in Fig. 3c and they are needed to write loop-closure equations as

$${}^0A_b + \mathbf{R}_x(\alpha_b)AB_b - {}^0H - \mathbf{R}_x(\vartheta)^HB_b = \mathbf{0} \quad (1)$$

$${}^0A_f + \mathbf{R}_x(\alpha_f)AB_f - {}^0H - \mathbf{R}_x(\vartheta)^HB_f = \mathbf{0} \quad (2)$$

$${}^0A_{lb} + \mathbf{R}_y(\beta)\mathbf{R}_x(\alpha_{lb})AB_{lb} - {}^0H - \mathbf{R}_x(\vartheta)^HB_{lb} = \mathbf{0} \quad (3)$$

$${}^0A_{lf} + \mathbf{R}_y(\beta)\mathbf{R}_x(\alpha_{lf})AB_{lf} - {}^0H - \mathbf{R}_x(\vartheta)^HB_{lf} = \mathbf{0} \quad (4)$$

Therefore, a solution of forward and inverse kinematics can be obtained by solving the system of equations that is obtained by expanding and combining Eqs. 1–4 as

$$x_H + f = l + s_{lb} \sin \alpha_{lb} \sin \beta \quad (5)$$

$$y_H = 1/2(s_b \cos \alpha_b + s_f \cos \alpha_f) \quad (6)$$

$$z_H = 1/2(s_b \sin \alpha_b + s_f \sin \alpha_f) \quad (7)$$

$$s_b \cos \alpha_b + s_f \cos \alpha_f = s_{lb} \cos \alpha_{lb} + s_{lf} \cos \alpha_{lf} \quad (8)$$

$$s_b \sin \alpha_b + s_f \sin \alpha_f = s_{lb} \sin \alpha_{lb} \cos \beta + s_{lf} \sin \alpha_{lf} \cos \beta \quad (9)$$

$$s_{lb} \sin \alpha_{lb} \sin \beta = s_{lf} \sin \alpha_{lf} \cos \beta \quad (10)$$

$$-2b \cos \vartheta = -2a + s_b \cos \alpha_b - s_f \cos \alpha_f \quad (11)$$

$$-2b \sin \vartheta = s_b \sin \alpha_b - s_f \sin \alpha_f \quad (12)$$

$$-h \cos \vartheta = -h + s_{lb} \cos \alpha_{lb} - s_{lf} \cos \alpha_{lf} \quad (13)$$

Equations 5–13 describes a general configuration of the manipulator. The orientation of the moving platform is the same one of the fixed platform when

$$\mathbf{R}_x(\vartheta) = \mathbf{1} \quad (14)$$

This condition (14) is met when the two lateral actuators have the same length and the lateral chain behaves as an articulated parallelogram, to give

$$s_{lb} = s_{lf} = s_l \quad (15)$$

$$\alpha_{lb} = \alpha_{lf} = \alpha_l \quad (16)$$

By using Eqs. 14–16, the system in Eqs. 5–13 can be formulated as

$$x_H + f = l + s_l \sin \alpha_l \sin \beta \quad (17)$$

$$y_H = s_l \cos \alpha_l \quad (18)$$

$$z_H = s_b \sin \alpha_b \quad (19)$$

$$s_b \cos \alpha_b + s_f \cos \alpha_f = 2s_l \cos \alpha_l \quad (20)$$

$$s_f \sin \alpha_f = s_l \sin \alpha_l \cos \beta \quad (21)$$

$$s_f \cos \alpha_f = 2b - 2a + s_b \cos \alpha_b \quad (22)$$

$$s_f \sin \alpha_f = s_b \sin \alpha_b \quad (23)$$

3.1 Forward Kinematics

Forward kinematics refers to Eqs. 17–23 in order to compute the position of the end-effector ${}^0\mathbf{H}$ from known values of the joint parameters s_b , s_f , s_{lb} and s_{lf} . The expressions of α_b , α_f , α_l and β can be written as functions of the joint parameters from Eqs. 20–23 as

$$\cos \alpha_b = \frac{s_f^2 - s_b^2 - 4(b-a)^2}{4(b-a)s_b} \quad (24)$$

$$\cos \alpha_f = \frac{s_f^2 - s_b^2 + 4(b-a)^2}{4(b-a)s_f} \quad (25)$$

$$\cos \alpha_l = \frac{s_f^2 - s_b^2}{4(b-a)s_l} \quad (26)$$

$$\sin \beta = \sqrt{\frac{8(b-a)^2 [2s_l^2 - s_f^2 - s_b^2] + 16(b-a)^4}{[4(b-a)s_l]^2 - [s_f^2 - s_b^2]^2}} \quad (27)$$

Therefore, direct kinematics is solved by substituting Eqs. 24–27 into Eqs. 17–19 to give

$$x_H = l - f + \frac{\sqrt{2}}{2} \sqrt{2s_l^2 - s_f^2 - s_b^2 + 2(b-a)^2} \quad (28)$$

$$y_H = \frac{s_f^2 - s_b^2}{4(b-a)} \quad (29)$$

$$z_H = s_b \sqrt{1 - \left[\frac{s_f^2 - s_b^2 - 4(b-a)^2}{4(b-a)s_b} \right]^2} \quad (30)$$

3.2 Inverse Kinematics

Inverse kinematics refers to Eqs. 17–23 in order to compute the joint parameters s_b , s_f , s_{lb} and s_{lf} from a known position of the end-effector ${}^0\mathbf{H}$. The system in Eqs. 17–23 is used to solve this problem by expressing all the parameters as functions of the coordinates of the end effector to give

$$\sin^2 \beta = \frac{(x_H + f - l)^2}{z_H^2 + (x_H + f - l)^2} \quad (31)$$

$$\cos^2 \beta = \frac{z_H^2}{z_H^2 + (x_H + f - l)^2} \quad (32)$$

$$\frac{1}{\sin^2 \alpha_b} = \cot^2 \alpha_b + 1 = \frac{(y_H + a - b)^2 + z_H^2}{z_H^2} \quad (33)$$

$$\frac{1}{\sin^2 \alpha_f} = \cot^2 \alpha_f + 1 = \frac{(y_H - a + b)^2 + z_H^2}{z_H^2} \quad (34)$$

$$\frac{1}{\cos^2 \alpha_l} = \tan^2 \alpha_l + 1 = \frac{z_H^2 + (x_H + f - l)^2 + y_H^2}{y_H^2} \quad (35)$$

Therefore, the Inverse Kinematic solution can be written as

$$s_l = \sqrt{z_H^2 + (x_H + f - l)^2 + y_H^2} \quad (36)$$

$$s_b = \sqrt{(y_H + a - b)^2 + z_H^2} \quad (37)$$

$$s_f = \sqrt{(y_H - a + b)^2 + z_H^2} \quad (38)$$

4 A Numerical Evaluation

In order to characterize numerically the proposed mechanism, a CAD model is designed as function of available actuators [9] and for a future implementation in LARMbot humanoid robot [10]. The design parameters are listed in Table 2. The maximum step length of the mechanism with the chosen geometry is approximately 300 mm, as shown in the simulated stepping configuration in Fig. 4. The value is over 100 % of the leg height.

Furthermore, it is possible to compute the speed of the step as the velocity of the end-effector point along y -axis in the form

$$\dot{y}_H = \frac{s_f \dot{s}_f - s_b \dot{s}_b}{2(b - a)} \quad (39)$$

The typical speed of a commercial linear actuator is equal to 20 mm/s. Therefore, the velocity of the end-effector that can be computed through Eq. 39 for the chosen geometry is approximately 200 mm/s.

Table 2 An example geometry for a numerical characterization

${}^0A_b = (x_H; -50; 0)$	${}^H B_b = (0; -30; 0)$	${}^0A_l = (150; 0; 0)$
${}^0A_f = (x_H; 50; 0)$	${}^H B_f = (0; 30; 0)$	${}^H B_l = (50; 0; 0)$
${}^0A_{lb} = (l; -30; 0)$	${}^H B_{lb} = (50; -30; 0)$	$AB = (0; s; 0)$
${}^0A_{lf} = (l; 30; 0)$	${}^H B_{lf} = (50; 30; 0)$	${}^0H = (x_H; y_H; z_H)$

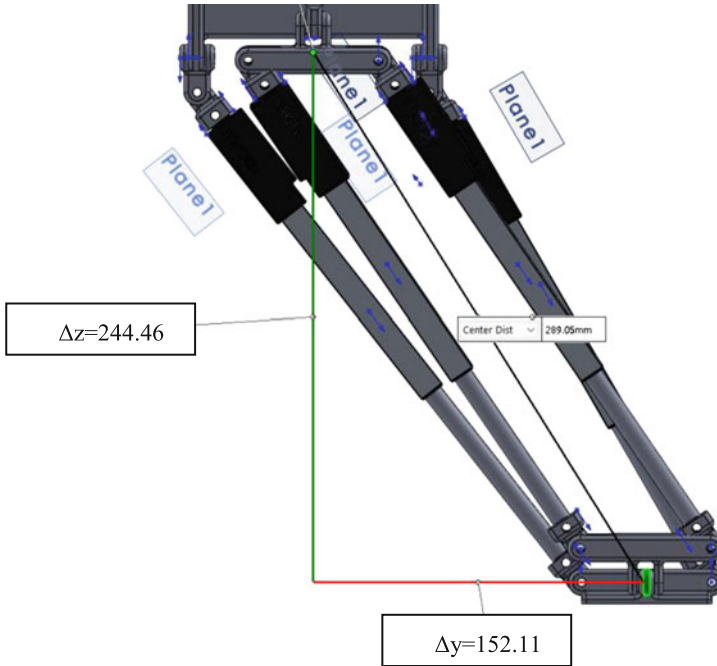


Fig. 4 Simulated maximum half-step length of the novel leg mechanism

5 Conclusions

This paper describes a kinematic design for a novel biped robot leg with parallel architecture. Forward and inverse kinematic problems are solved for the structure and a numerical characterization of its operation is reported as a study of feasibility. The mechanism improves considerably previous LARM designs, since its step length is approximately 100 % of the leg height. Future work on the mechanism design will improve the solution through multi-objective optimization and dynamic walking control.

References

1. Chestnutt J, Lau M, Cheung G, Kuffner J, Hodgins J, Kanade T (2005) Footstep planning for the Honda Asimo humanoid. In: Proceedings of the 2005 IEEE international conference on robotics and automation, 2005. ICRA 2005. IEEE, pp 629–634
2. Gouaillier D, Collette C, Kilner C (2010) Omni-directional closed-loop walk for NAO. In: 2010 10th IEEE-RAS international conference on humanoid robots (humanoids). IEEE, pp 448–454

3. Lim HO, Takanishi A (2007) Biped walking robots created at Waseda University: WL and WABIAN family. *Philos Trans R Soc Lond A: Math Phys Eng Sci* 365(1850):49–64
4. Wang M, Ceccarelli M (2015) Design and simulation of walking operation of a Cassino biped locomotor. In: *New trends in mechanism and machine science*. Springer International Publishing, pp 613–621
5. Merlet JP (2012) *Parallel robots*, vol 74. Springer Science & Business Media
6. Rey L, Clavel R (1999) The delta parallel robot. In: *Parallel kinematic machines*. Springer, London, pp 401–417
7. Knudson D (2007) *Fundamentals of biomechanics*. Springer Science & Business Media
8. Ceccarelli M (2004) *Fundamentals of mechanics of robotic manipulation*, vol 27. Springer Science & Business Media
9. Firgelli Website (2016) Firgelli L16-R Miniature Linear Servo. <http://www.firgelli.com>
10. Cafolla D, Wang M, Carbone G, Ceccarelli M (2016) LARMbot: a new humanoid robot with parallel mechanisms. In: *ROMANSY 2016 21st CISM-IFTOMM symposium on robot design, dynamics, and control* (In print)

Multi-target Planar Needle Steering with a Bio-inspired Needle Design

Christopher Burrows, Fangde Liu, Alexander Leibinger, Riccardo Secoli and Ferdinando Rodriguez y Baena

Abstract Percutaneous intervention is common practice in many diagnostic and therapeutic surgical procedures. Needle steering research aims to extend these by enabling therapies that are not possible with a straight rigid needle. Being able to address multiple targets in one insertion is an example of such a therapy, which would result in reduced overall trauma to the patient and surgery time. However, needle steering remains challenging, as soft tissue is highly compliant and deformable, and thus difficult to interact with. In this work, we develop a new biologically inspired needle design (4 mm outside diameter) and show its capabilities in multiple moving target scenarios. In vitro results in gelatin demonstrate accurate 2D tracking of two virtual targets over 3 target movement rates.

Keywords Needle steering · Bio-inspired · Medical robotics

1 Introduction

One of the potential technologies for improving minimally invasive surgery is needle steering, with research in this area growing significantly in recent years. Needle steering technologies offer an alternative means of therapy compared to standard percutaneous intervention techniques. Using a flexible needle and typically a robotic system, a needle can be guided along a curved path within the tissue. This potentially enables therapies that would otherwise not be available with a straight line path, for example steering around a critical region in the tissue, and alternative treatments for multiple lesions which could be accessed through a single insertion. Also, as the needle is able to steer, the trajectory of the needle can be adjusted in situ to compensate for moving targets due to the soft tissue deforming, as to reduce the final positional error and the need for reinsertion in the event that the target is missed. Being able to address multiple targets, such as in brachytherapy of the prostate, during one needle insertion is beneficial to the patient, as reducing the number of insertions results

C. Burrows · F. Liu · A. Leibinger · R. Secoli · F. Rodriguez y Baena (✉)
Imperial College, London, UK
e-mail: f.rodriguez@imperial.ac.uk

in decreased tissue trauma. This, in turn, minimizes recovery time and stress for the patient, while, from a surgical standpoint, this technique also reduces overall surgery time and cost.

Within this context, we aim to develop a steerable needle for the specific purpose of multi-target percutaneous access. Several needle steering technologies have been developed in order to produce curvilinear paths within tissue; however, these designs have drawbacks that make them unsuitable for certain clinical scenarios. For example, concentric tube based needle systems operate well inside a cavity but suffer from important kinematic constraints when used percutaneously [4, 12]. Bevel and kinked tip needle steering systems are accurate and have a good range of possible curvatures, but the needle must be rotated as it is inserted, causing additional trauma to the surrounding tissue [11] although in some tissues and scenarios this effect may be negligible [9]. In light of these weaknesses, our group has developed a flexible needle controlled using a biologically inspired multi-segment design [6]. Our Soft Tissue Intervention and Neurosurgical Guide (STING) has a unique actuation mechanism which employs a ‘programmable bevel’ in order to steer along arbitrary curvilinear paths. Recent prototypes produced by this research that have been published in the literature are a two segment needle prototype, with a 4 mm outer diameter (OD), which is capable of only planar steering, and a four segment needle prototype, with an 8 mm OD, capable of 3D steering but not of a clinically acceptable size. This paper describes the design and manufacture of a new four segment, 4 mm OD needle and its application to multi-target delivery. Our group has previously developed a system for reaching a single moving target, with on-line path planning on a plane [2]. Here, we describe the extension of this on-line path replanner to multiple moving targets and use it to assess the performance of the new needle design in vitro.

This paper is structured as follows: Sect. 2 presents the new needle design and Sect. 3 describes how the control system was developed to reach multiple targets. Sections 4 and 5 present the validation experiments performed to assess the system and a discussion of the results, respectively. Finally, Sect. 6 presents conclusions and future work.

2 Needle Design

In this work, we continue to miniaturize the STING needle toward a size that is realistic for clinical applications. The latest prototype prior to this work was a two segment needle prototype, 4 mm OD, only capable of planar steering [6]. Here, we present a new, four segment needle design, of the same OD, shown in Fig. 1. This needle is the first prototype of this size that is capable of steering in 3D, due to the four segment design. This was achieved by pushing the boundaries of the additive layer manufacturing technique used in this work. As with all of the previous designs, this needle was produced using rapid prototyping technology (Objet Connex, Stratasys Ltd.) however, a novel approach was required in order to produce a four segment needle at this scale.

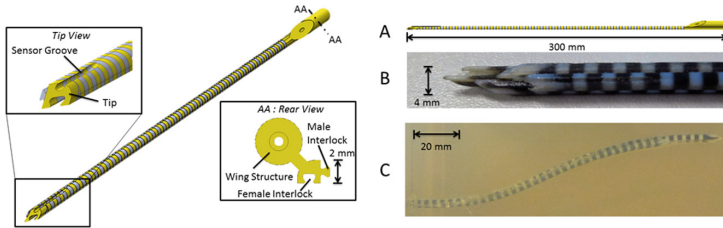


Fig. 1 3D render (*Left*) and side profile (*A*) of one of the segments of the new STING needle prototype, showing the wing and tip designs and the ‘composite’ body structure made up of soft (*black*) and rigid (*white*) sections. Picture of the needle tip (*B*) and the new needle performing a double bend trajectory (*C*)

The principal shape of the needle remains the same as in previous versions [1], with four ‘dovetail’ interlocked segments that can slide independently of each other; a 3D model of one of the segments and the assembled needle is shown in Fig. 1. The needle has a wing structure similar to the design in [6], which allows the needle to be actuated from the back. The cross section of the segments was optimized using the technique described in [7], where several parameters of the needle design are adjusted to create an interlock optimized against two failure modes. The cross section and wing structure can be seen in Fig. 1 AA: Rear View. The length of the needle is 300 mm and the tip of the needle is made of VeroWhitePlus (Stratasys Ltd.). A groove is present at the tip so that an electromagnetic sensor (Northern Digital Inc.) can be attached, to allow translational and rotational tracking of the needle tip during insertion.

The body of this design is made up of a ‘composite’ structure, with alternating rigid and soft sections, as shown in Fig. 1B. The soft sections are made from FLX9885 (Stratasys Ltd.) and the rigid sections VeroWhitePlus (Stratasys Ltd.). This ‘composite’ structure is required since, at the required dimensions, the interlock strength is not high enough to prevent the needle from failing due to the segments coming apart. The alternating structure prevents the smaller dimension dove-tail interlocking mechanism between segments from failing, [7], with the rigid sections along the length of the body in both the male and female sections adding strength to the interlocking mechanism. The soft regions interspersed between the rigid sections allow the prototype to remain flexible and able to bend.

3 Controlling to Multiple Targets

An on-line path planner based needle steering system developed to reach a moving target was first demonstrated in [2]. This planner produces locally optimal smooth continuous paths and can also constrain the curvature and the gradient of curvature

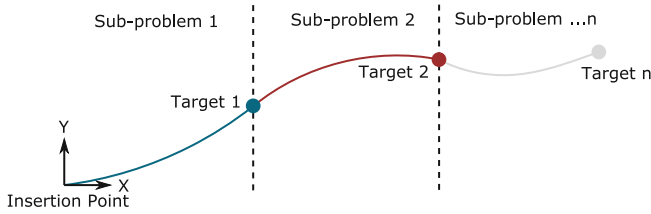


Fig. 2 Diagram of the process carried out by the planning system. Given n targets, each target is considered individually and sequentially and therefore, as a sub-problem. Upon reaching a target, the next target in the sequence is considered and this continues until all the targets have been reached

of the path online during an insertion. Here, this system is extended so that multiple targets can be addressed within one insertion.

To allow multiple targets to be reached, the overall plan that connects all of the targets is broken down into sub-objectives. Specifically, the path between the targets is divided up into n sub-problems, n being equal to the number of targets. This is shown in Fig. 2, where each target is considered sequentially ($i = 1, 2, \dots, n$) in its local frame, as separate control sub-problems which are iterated through. Currently, the system is limited to sub-problems where the direction of the curvature of the path between the current needle state and target remains the same. This requirement can be met by setting suitable constraints in the global pre-planner of the needle steering system, see [2] for more details. The direction of curvature to the target in the current sub-problem is determined from the local needle frame and the associated approach angle of each target (set from the pre-planner in the initial phase).

The algorithm from [2] is then used to replan the path between the needle and the target pose in each sub-problem as the target moves. This has the advantage that the replanning system used for the single moving target can be added into the multi-targeting system with little modification. The result of this system is that locally optimal paths (the shortest path that satisfies the constraints) for each target are produced, as the surgical scenario changes dynamically, under the effect of tool-tissue interactions.

4 In Vitro Testing

4.1 Experimental Setup

The experimental setup used to test the needle steering system is similar to that used in previous experiments [2, 6]. The actuation method for moving the needle consists of a set of linear actuators, motor driven lead screws connected to the needle by nitinol push rods, controlled via a CompactRIO controller programmed with

Table 1 Experimental parameters

Parameter	Symbol	Value
Preplan [6]		
Start state	$[x, y, \theta, \rho]$	$[0,0,0,0]$
Max. curvature (mm^{-1})	ρ_{max}	0.01
Max. deriv. curvature (mm^{-2})	$\dot{\rho}_{max}$	7.80×10^{-4}
Controller [5]		
Compensation coefficient	ϵ	2.4
Steering coefficient (mm^{-2})	κ	3.90×10^{-4}
Max. steering offset (mm)	δ_{max}	30
Sampling time (s)	T_p	2
Subsampling time (s)	T_s	0.25
Prediction horizon	N_p	10
Subsample prediction horizon	N_s	8
Deformation planner [2]		
Target movement threshold (mm)	D_{max}	0.2
Number of segments	n_{seg}	10
Max. curvature (mm^{-1})	ρ_{max}	0.01
Max. deriv. curvature (mm^{-2})	$\dot{\rho}_{max}$	7.80×10^{-4}

LabVIEW (National Instruments Corp.). The control system, as described in Sect. 3, was implemented in C++ and python. The controller for the needle, a MPC-based approach [5], was implemented in C++ using Quadprog++ as the quadratic programming solver. The Deformation planner was implemented using python (2.7) and the CVXOPT optimization library. An EM tracking sensor (Aurora 5 DOF sensor with 0.5 mm diameter and 8 mm length, Northern Digital Inc.), with a root-mean-square (RMS) accuracy of 0.7 mm, was attached to the sensor groove of one of the segments to measure the position of the needle tip. Bovine gelatin, 250 bloom (Sleaford Quality Foods, Sleaford, UK), 4.5 wt%, was used as the tissue phantom in the experiments, with a Young's modulus, $E = 7$ kPa. The parameters used for the control system are shown in Table 1.

4.2 Segment Offset Versus Curvature Calibration

Before determining the performance of the system, the needle prototype's steering performance was evaluated. Experiments with the new needle design were performed to ascertain the coefficient between segment offset and resultant path curvature, κ . It was previously shown that this coefficient is approximately linear [1, 5] and can be used to control the needle along curved trajectories by controlling segment

offset. Six insertion tests [1], with a constant steering offset between the segments (δ) of 5–30 mm (in 5 mm increments) were carried out, with the EM tracking system used to track the needle tip path, with a resulting $\kappa = 3.89 \times 10^{-4} \text{ mm}^{-2}$. With this linear coefficient, an offset of 25.7 mm would be required to produce a radius of curvature of 100 mm.

4.3 Experimental Scenarios

To evaluate the new needle design's ability to reach multiple moving targets, two scenarios were designed. The scenarios consist of guiding the needle to two moving virtual point targets that have varying degrees of target movement, as follows: (1) Two targets moving within the plane requiring curvature in a single direction, known as **2-Tar-SB**; (2) Two targets moving within the plane requiring a change in curvature direction after the first target (inflection point, S-Curve), known as **2-Tar-DB**. Each target has an associated 2D pose (x , y , approach angle) that the controller tries to drive the needle to. For **2-Tar-SB** the target poses were (100 mm, 20 mm, 27.4°) and (160 mm, 60 mm, 42.9°) respectively. For **2-Tar-DB** the target poses were (80 mm, 15 mm, 24.3°) and (160 mm, 42 mm, 7.8°) respectively. These target poses were chosen as they are near the edge of the needle workspace and therefore close to the constraint limits.

In order to test the system, the range of total displacements was chosen that matched the tissue values found in published studies [3, 8]. Three constant movement rates small (0.015 mm/s), medium (0.025 mm/s), large (0.05 mm/s) for the target displacements were then based on these values. The virtual target movement is then computed as a combination (sum) of two vectors. The constant movement vector, defined above, acts in the direction of the initial insertion axis of the needle. The second vector then acts in the direction of the tip axis with a rate of 0.075 mm/s when less than 20 mm away from the target. This is to simulate the deformation, in a simplified manner, seen from inserting the needle into soft tissue [10].

5 Results and Discussion

Each of the scenarios described in Sect. 4.3 was performed three times with each of the virtual target movement rates, resulting in a total of eighteen experiments.

Figure 3a and b show example results from **2-Tar-SB** and **2-Tar-DB** respectively. The tip position and angle error to each target was calculated for all the experiments. Across all movement rates, the mean positional errors for Target 1 and 2 were 0.3 mm and 0.6 mm, with SDs of 0.15 mm and 0.31 mm respectively. The positional error averaged over all targets and experiments was 0.46 mm with an SD of 0.17 mm.

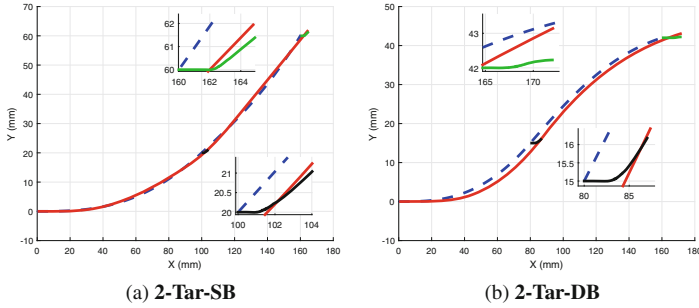


Fig. 3 Results from the experiments showing the performance in reaching two moving virtual targets: Initial path (*blue dashed*), smoothed needle path (*red*), and target paths (*black* for Target 1 and *green* for Target 2) with a large target movement rate. Insets show details of Target 1 (*bottom*) and Target 2 (*top*) paths

Across all movement rates, the mean approach angle errors for Target 1 and Target 2 were 1° and 1.1° , with SDs of 1.02° and 1.83° respectively. The approach angle error averaged over all targets and experiments was 1.05° , with an SD of 0.32° .

The results in Table 2 show that the new needle design is capable of similar steering performance to the two part needle of equal cross section, described in [6], where the mean targeting error was 0.51 mm and SD 0.85 mm. Additionally, the maximum bending performance was 19.4% worse than that obtained for the 2-part prototype [6], which had an offset coefficient $\kappa = 4.824 \times 10^{-4} \text{ mm}^{-2}$. This can be explained by the fact that, compared to the previous design, the new design is symmetrical, has rigid sections along the length of the body, and has more material in its cross section (greater bending stiffness) due to the interlock design and lack of working channel. Further refinement of this design will also improve steering performance. For both scenarios, qualitative analysis shows, the target position error increases for Target 2, as shown by the increase in total mean. This is likely due to the increased insertion length and therefore increased overall target displacement compared to Target 1, however this does not appear to be linked to the Target movement rate as the mean position error values for Target 2 are within a similar range across all the scenarios.

These results demonstrate that the new needle design used in this work can be used within a needle steering system and guided towards multiple moving targets in plane, across a range of movement rates, under path constraints (curvature and its derivative), with small position and angular errors. The rate of movement of the targets does not appear to affect the ability of the system to guide the needle to the target position, with all the errors within a similar range.

Table 2 Positional and angular error results

Scenario	Deformation	Target 1—Positional error (mm)		Target 1—Angle error (Deg.)		Target 2—Positional error (mm)		Target 2—Angle error (Deg.)	
		Mean	SD	Mean	SD	Mean	SD	Mean	SD
2-Tar-SB	Small	0.28	0.21	1.38	0.57	0.79	0.32	1.38	0.74
	Medium	0.23	0.17	0.69	1.15	0.53	0.21	1.09	2.86
	Large	0.39	0.12	1.2	0.60	0.63	0.62	0.69	1.09
2-Tar-DB	Small	0.30	0.24	1.20	0.8	0.36	0.17	0.74	1.15
	Medium	0.33	0.15	0.69	0.70	0.71	0.22	1.72	3.40
	Large	0.43	0.06	0.86	2.29	0.57	0.33	0.97	1.71
	Total mean	0.30	0.15	1.00	1.02	0.60	0.31	1.11	1.83

6 Conclusion and Future Work

This paper describes our latest work in developing a novel steerable needle for percutaneous intervention. A new 4 mm four-part, 3D steering capable, prototype with a novel ‘composite’ structure was developed. The new needle design was then tested experimentally by using an extension of an online path planner to guide the needle to two virtual moving targets over various scenarios. The experimental results showed a mean positional error of 0.46 mm and approach angle error of 1.05° over 18 experiments. This work sets significant scope for future improvements. The natural progression of this work is an extension to 3D, with the development of a controller and planning algorithm capable of following arbitrary trajectories across all three planes. Development of the needle designs will continue, with the OD of the needle reduced further, by exploring alternative manufacturing techniques.

Acknowledgments This work was supported by the European Research Council under the European Union’s Seventh Framework Programme (FP7/2007–2013)/ERC grant agreement no [258642-STING] and the Horizon 2020 Research and Innovation Programme under grant agreement no [688279].

References

1. Burrows C, Secoli R, Rodriguez y Baena F (2013) Experimental characterisation of a biologically inspired 3d steering needle. In: 2013 13th International conference on control, automation and systems (ICCAS). IEEE, pp 1252–1257
2. Burrows C, Liu F, Rodriguez y Baena F (2015) Smooth on-line path planning for needle steering with non-linear constraints. In: 2015 IEEE/RSJ international conference on intelligent robots and systems (IROS), pp 2653–2658. doi:[10.1109/IROS.2015.7353739](https://doi.org/10.1109/IROS.2015.7353739)
3. Deurloo EE, Gilhuijs KG, Kool LJS, Muller SH (2001) Displacement of breast tissue and needle deviations during stereotactic procedures. *Invest Radiol* 36(6):347–353
4. Dupont PE, Lock J, Itkowitz B, Butler E (2010) Design and control of concentric-tube robots. *IEEE Trans Robot* 26(2):209–225
5. Ko SY, Rodriguez y Baena F (2012) Trajectory following for a flexible probe with state/input constraints: an approach based on model predictive control. *Robot Auton Syst* 60(4):509–521
6. Ko SY, Rodriguez y Baena F (2013) Toward a miniaturized needle steering system with path planning for obstacle avoidance. *IEEE Trans Biomed Eng* 60(4):910–917
7. Leibinger A, Oldfield M, Rodriguez y Baena F (2014) Multi-objective design optimization for a steerable needle for soft tissue surgery. In: The 15th international conference on biomedical engineering. Springer, pp 420–423
8. Lobo JR, Moradi M, Chng N, Dehghan E, Morris WJ, Fichtinger G, Salcudean SE (2012) Use of needle track detection to quantify the displacement of stranded seeds following prostate brachytherapy. *IEEE Trans Med Imaging* 31(3):738–748
9. Majewicz A, Marra S, van Vledder M, Lin M, Choti M, Song D, Okamura A (2012) Behavior of tip-steerable needles in ex vivo and in vivo tissue. *IEEE Trans Biomed Eng* 59(10):2705–2715. doi:[10.1109/TBME.2012.2204749](https://doi.org/10.1109/TBME.2012.2204749)
10. Oldfield M, Burrows C, Kerl J, Frasson L, Parittotokkaporn T, Beyrau F, Rodriguez y Baena F (2014) Highly resolved strain imaging during needle insertion: results with a novel biologically inspired device. *J Mech Behav Biomed Mater* 30:50–60

11. Swaney PJ, Burgner J, Gilbert HB, Webster RJ (2013) A flexure-based steerable needle: high curvature with reduced tissue damage. *IEEE Trans Biomed Eng* 60(4):906–909
12. Webster RJ, Jones BA (2010) Design and kinematic modeling of constant curvature continuum robots: a review. *Int J Robot Res*

Development of an Active Force Plate for Testing Lower-Limb Prostheses

Cristiano Marinelli, Hermes Giberti and Ferruccio Resta

Abstract In the recent past, lower-limb prostheses technological advancement mostly concerned the possibility of integrating ever smaller and more powerful electronic components instead of new materials and topologies. Although sophisticated, products currently on the market do not guarantee the same opportunities of their biological counterpart. According to authors' opinion this deficiency is principally due to the lack of suitable development and verification methods. As a consequence, our research group is developing a bench for testing transfemoral prostheses. The setup is briefly recalled in this paper. Then, attention is focused on the subsystem designed for reproducing the loads acting on the foot due to reaction with the ground.

Keywords Prostheses · Test bench · Gait simulator · Force plate

1 Introduction

Different solutions have been proposed in the last two decades for replacing the lower limbs after amputation surgery. On the one hand, developing a commercially viable prosthesis that is humanlike as well as economical is a challenging design problem. On the other hand, suitable development and verification methods are missing. Indeed, the legislation in force (ISO 2006:10328 [1]) merely identifies structural tests to verify the prosthetics strength properties. The ISO itself acknowledges the

C. Marinelli (✉) · F. Resta
Politecnico di Milano, Milan, Italy
e-mail: cristiano.marinelli@polimi.it

F. Resta
e-mail: ferruccio.resta@polimi.it

H. Giberti
Università degli Studi di Pavia, Pavia, Italy
e-mail: hermes.giberti@unipv.it

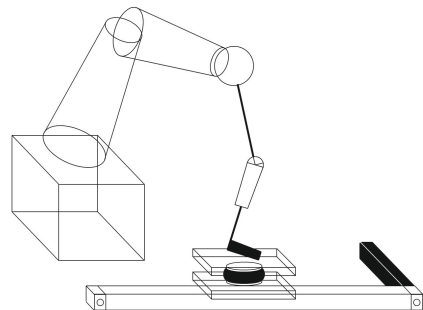
limits of the standard stating: “*Ideally, additional laboratory tests should be carried out to deal with function, . . . , and user activities as part of the evaluation procedure. There are no standards for such tests, so appropriate procedures will need to be determined.*”.

The need to introduce the user behavior in the development and verification process is not recent, several solutions have been proposed in the literature. Among these, in-vitro experimental procedures [2–4] demonstrate several advantages over in-vivo ones [5, 6] in terms of reliability, versatility and safety. It is therefore foreseen that robotic testing will play a greater role than human gait trials in the development process of prosthetics. However, there is no system yet able to completely achieve the aforementioned purpose. In particular, the possibility to apply full scale forces is still an open issue. As a consequence our research group is developing a novel bench for testing the functional properties of transfemoral prostheses considering working conditions more realistic than those achieved in the literature. The setup is briefly recalled. Further information may be found by the reader in [7]. Afterward, attention is focused on the innovative solution defined for reproducing the loads acting on the foot due to reaction with the ground.

2 System Mechanical Architecture

The gait simulator (Fig. 1) exhibits 8 degrees of freedom (DOFs) and consists of two main subsystems. These are respectively used to replicate the series of motion patterns performed by the residual segment of the limb and the trend of forces acting on the prosthetic foot due to reaction with the ground. The first task is accomplished through a 6-axis manipulator having suitable motion and payload capabilities. On the other hand, the second is accomplished through a custom 2-axis active force plate whose longitudinal and vertical progression are respectively driven through a toothed belt linear guide and an active air spring. The employment of this pneumatic actuator has not yet been evaluated by other authors even if two merits are related to its usage: the compressibility of the gas and the intrinsic stiffness of the bellows

Fig. 1 Schematic representation of the gait simulator



ensure a smooth transfer of the load during the initial contact phase enhancing the stability of the system; the high power to weight ratio of this kind of solution guarantees a mass reduction and therefore a stress attenuation at the electric motor driving the longitudinal progression of the carriage.

From a functional point of view, the solution proposed allows to define two independent control strategies in longitudinal and vertical direction. On the one hand, the use of a linear guide determines the need to alternately implement two control logics: force and position control. The former is active during the entire stance phase in order to reproduce the correct value of the force acting on the foot due to reaction with the ground in the longitudinal direction. The latter contributes instead to return the carriage to its initial position before the beginning of the next cycle, that is, before the end of the swing phase. The contact force in the vertical direction allows to detect the walking phase, either stance or swing, and therefore to choose the control strategy to be applied. In addition, the vertical force itself is used to modulate the selection matrix so as to change the control mode as smoothly as possible [8].

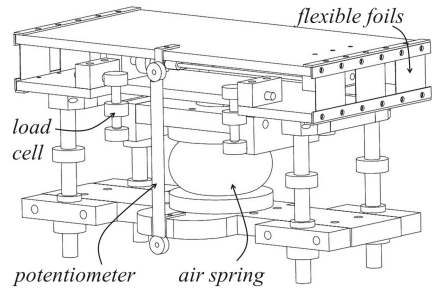
On the other hand, the intrinsic stiffness of the bellows allows to control the air spring exclusively in terms of force during all the phases of the test. During the swing phase the pneumatic actuator supply the force necessary to hold the force plate at the maximal vertical height, i.e. the force necessary to support the weight of the plate itself and the elastic return of the spring bellows. The same force is supplied during the initial contact stage while being dragged downward by the movement of the foot, which is subjected to an increasing force due to the simultaneous return of the spring to its resting length. When the force is high enough to ensure a stable contact condition the inner pressure is modulated so as to reproduce the correct gait analysis trend of vertical force. Finally, when the force drops below the predetermined offset value, the application of the initial constant force results in a gradual decrease of the load applied to the foot and the return of the platform to the initial height.

3 Mechanical Design of the Foot Loading Subsystem

Once identified a linear guide (NC Componenti LPA RH80-15) and an air spring (Norgren PM/31041) suitable for the application the active force plate is designed in order to: accommodate the air spring, fit the shape of the carriage of the linear guide and introduce the measurement equipment. In particular, the main quantities to be collected during the procedure are the contact force between the foot and the plate representing the ground and the vertical displacement of the plate itself. Apart from being useful parameters for evaluating the performance of the prosthesis under test, these quantities are indeed essential in terms of control purpose. In particular, it is necessary to design and build a force plate that can separately collect data along 2 axes in order to avoid measurement interferences.

The final solution satisfying these needs follows from the equipment presented in [9] for identifying the mass matrix of people standing in a quiet upright position. It consists of a horizontal rigid plate and two vertical flexible foils designed

Fig. 2 Perspective view of the active force plate architecture



to offer high rigidity in vertical direction and low rigidity in longitudinal one. As a consequence, the solution ensures complete transmission of the vertical force so that it can be successively measured, and access to the longitudinal force starting from the deflection of the structure. Both the force components are measured by means of strain gauge load cells (Honeywell Precision Miniature Load Cell). On the other hand, the vertical displacements is measured through a linear potentiometer (DSPM Industria CLS1322). A schematic representation of the solution is shown (Fig. 2). The dimensions of its structural components are assessed by performing finite-element (FE) simulations in SolidWorks.

4 Mathematical Model

The system may be modelled as a mass moving in the sagittal plane under the effect of the force supplied by the air spring and the linear guide as well as the load applied by the foot both in vertical and longitudinal direction. The equations are given below with reference to the following scheme (Fig. 3). The first term is significantly affected by the dynamic behavior of the air within the pneumatic circuit. In this case the use

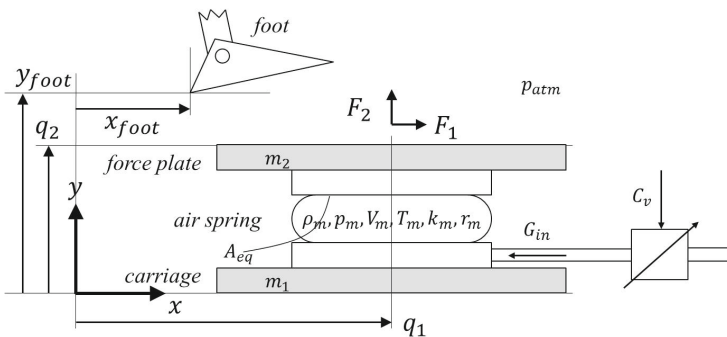


Fig. 3 Schematic representation of the problem under study

of reservoirs, compressors and long pipes is not expected. As a consequence, only the thermodynamic transformations of the gas within the air spring [10], the physical characteristic of the bellows and the mass flow-rate in the servo-valve are considered [11–13]. Their behavior is described by the following set of equations:

$$\begin{aligned}
 F_m &= A_{eq} (p_m - p_{atm}) - k_m (q_2, p_m) (q_2 - q_{20}) - r_m \dot{q}_2 \\
 \dot{p}_m V_m + k p_m \dot{V}_m &= k G_{in} R T_m \\
 V_m &= A_{eq} q_2 \\
 T_m &= \left(\frac{p_m}{p_{m0}} \right)^{\frac{k-1}{k}} T_{m0} \\
 G_V &= \begin{cases} C_V p_1, & \text{if } (p_2/p_1) \leq b_v \\ C_V p_1 \sqrt{1 - \left(\frac{(p_2/p_1) - b_v}{1 - b_v} \right)^2}, & \text{if } (p_2/p_1) > b_v \end{cases}
 \end{aligned}$$

where F_m is the air spring thrust force, p_m , V_m and T_m are the spring inner pressure, volume and temperature, k_m and r_m are the intrinsic stiffness and damping of the bellows, q_{20} is the spring length when $p_m = p_{atm}$, the atmospheric pressure, A_{eq} is the equivalent area, G_{in} is the mass flow-rate entering the air spring, C_V represents the valve opening, p_1 and p_2 are the upstream and downstream pressures of the valve, b_v is the critical pressure ratio, k is the specific heat ratio and R is the gas universal constant.

The second contribution is modeled neglecting many aspects that unnecessarily complicate the issue. For example, the model of the electric motor is not considered. Similarly, the dynamic effect of the flexibility of both the belt and the transmission is neglected as well as the backlash in the reducer unit. The force applied by the motor to the carriage can therefore be computed simply as $F_e = T_{ml}/R_p$ where T_{ml} is torque applied at the load shaft and R_p is the radius of the pulley. Finally, the reaction force due to contact of the foot with the plate are modeled. The Karnopp friction model is introduced in order to define the longitudinal force component [14]. The following set of three ordinary differential equations is considered:

$$F_{fric} = \begin{cases} -|F_t| \text{sign}(F_t), & \text{if } v_s = 0 \wedge |F_t| \leq F_{lim} \\ -\mu_s |F_n| \text{sign}(F_t), & v_s = 0 \wedge |F_t| > F_{lim} \\ -\mu_d |F_n| \text{sign}(v_s), & \text{else} \end{cases}$$

where F_t is the net force applied tangent to contact surface, F_n is the net force applied normal to contact surface, μ is the friction coefficient, $F_{lim} = \mu_s |F_n|$ is the static friction limit, v_s is the sliding velocity and v_{th} is the threshold velocity.

A penetration contact model is exploited instead to compute the vertical one. In particular, the vertical component is calculated as the sum of an elastic and a viscous contribution as follows:

$$F_c = -k_c d - r_c(d)\dot{d}$$

where k_c and r_c are the stiffness and damping contact coefficients and $d = q_2 - y_{foot}$ is the penetration value. The parameters and coefficient useful from the implementation point of view are obtained starting from the literature [15]. The gravitational and inertial forces are finally introduced to definitely compute F_1 and F_2 , i.e. the total amount of force acting on the system respectively in longitudinal and vertical direction:

$$\begin{aligned} F_1 &= F_e + F_{fric} - (m_1 + m_2)\ddot{q}_1 \\ F_2 &= F_m + F_c - m_2(g + \ddot{q}_2) \end{aligned}$$

The total mass is estimated starting from the CAD model of the force plate (Fig. 2) being known the density of its components: $m = m_1 + m_2 \approx 15$ kg.

5 Results

The nonlinear numerical model of the problem under study is developed using both the Simulink and SimMechanics. SimMechanics is used to model and simulate the mechanical properties and the motion possibilities of the bodies constituting the system, that is, the foot and the force plate. Simulink is used instead to implement the equations describing the behavior of the pneumatic actuator, to estimate the reaction forces according to the aforementioned contact model, to apply the PID controller, and to compute both the force and position reference signals online as a function of the current state of the system. During the experimental test procedure the behavior of the prosthetic device may indeed vary from cycle to cycle preventing the possibility to implement standard reference signals. In particular, during the stable contact condition the vertical reaction force is simply reproduced through a sine function. The longitudinal force is computed instead on-line as a function of the vertical reaction force based on a linear correlation found between the two components:

$$dF_x(t)/dt \approx AF_y(t) - B$$

Finally, the law of motion necessary to take the carriage back to the initial position is computed as a function of the actual position and velocity of the carriage itself at the end of the stance phase. Figures 4 and 5 show the trend of the reaction forces achieved respectively in vertical and longitudinal direction. These are comparable only qualitatively with the physiological trends reported in the literature about gait analysis. Despite small, the deviations are principally induced by the techniques used for computing the approximated force references on-line as a function of the state of the system. Anyway, greater affinity might be achieved using different strategies.

Fig. 4 Trends of the reference and actual vertical reaction force

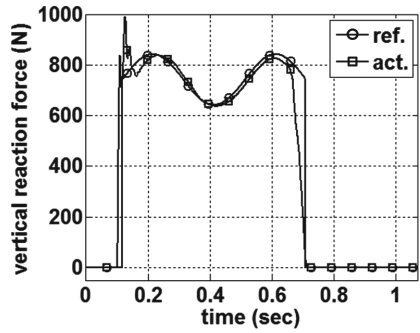


Fig. 5 Trends of the reference and actual longitudinal reaction force

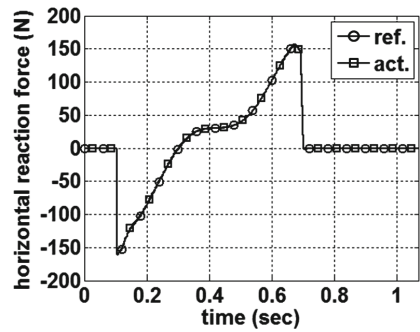
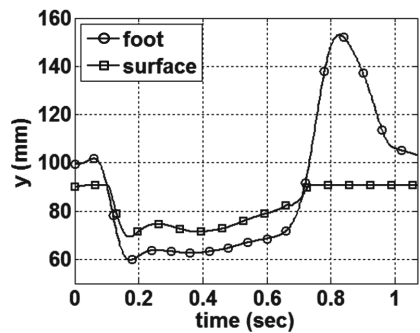


Fig. 6 Trend of the foot and contact surface vertical displacement



On the other hand, the hardware solution implemented allows to successfully reproduce the force components both in terms of amplitude and duration. Moreover, the pneumatic actuator allows to restrain the force peaks at the beginning of the contact stage.

Results are good also in terms of position. The subsystem is indeed able to recover both the vertical and longitudinal initial position before the beginning of the next cycle (Figs. 6, 7). Finally, the trend of the air spring inner pressure (Fig. 8) and the trend of the torque supplied by the motor (Fig. 9) are shown. Both the trends are

Fig. 7 Trend of the foot and contact surface longitudinal displacement

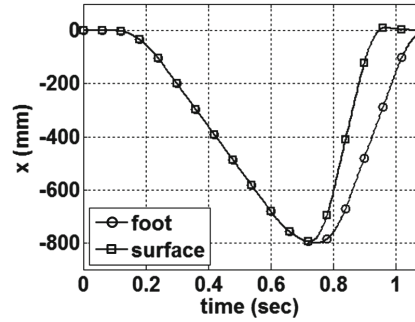


Fig. 8 Air spring absolute inner pressure

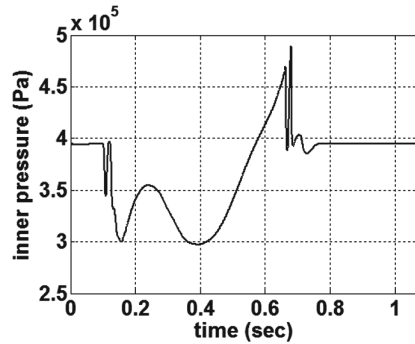
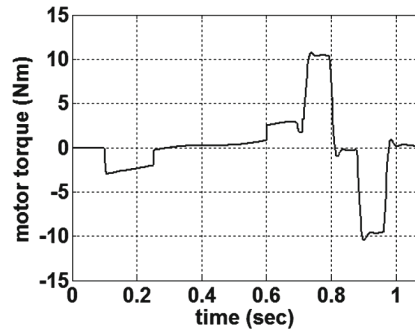


Fig. 9 Torque supplied by the motor



compliant with the commercially viable equipment. In addition, Fig. 9 demonstrates the ability of the selection matrix implemented in longitudinal direction to avoid sudden reference changes and therefore spikes that may jeopardize the stability of the system.

6 Conclusions

The research activity presented in this paper dealt with the development of a novel bench for assessing the functional performances of lower limb prostheses. The mechanical architecture of the rig was first introduced. Thereafter, the attention was focused on the mechanism necessary for reproducing the loads acting on the foot due to reaction with the ground during normal walking. Both the mechanical design and the operation procedure were reviewed. Then a numerical model was set up in order to assess the merits and limits of the proposed solution.

From this point of view the decision to reproduce the vertical reaction force through a pneumatic actuator resulted successful. Besides restraining the force peaks, the air spring has indeed a bandwidth wide enough for the application. Deviations from the physiological trend are more evident in longitudinal direction. However, better results may presumably be achieved by changing the strategy for computing the reference on-line as a function of the state of the system.

References

1. ISO 10328:2006 Prosthetics—structural testing of lower-limb prostheses—requirements and test methods
2. Hanz R, Dan S, Smith WA, Samorezov S (2015) Dynamic modeling, parameter estimation and control of a leg prosthesis test robot. *Appl Math Model* 39(2):559–573
3. Julius T, Simon G, Peter S, Marc K (2015) The gait simulator for lower limb exoprosthesis—overview and first measurements for comparison of microprocessor controlled knee joints. *Facta Universitatis, Ser: Mech Eng* 13(3):193–203
4. Zhang J, Shen L, Shen L, Li A (2010) Gait analysis of powered bionic lower prosthesis. In: 2010 IEEE international conference on robotics and biomimetics (ROBIO). IEEE, pp 25–29
5. Fite K, Mitchell J, Sup F, Goldfarb M (2007) Design and control of an electrically powered knee prosthesis. In: 2007 IEEE 10th International conference on rehabilitation robotics. IEEE, pp 902–905
6. Frank S, Amit B, Michael G (2008) Design and control of a powered transfemoral prosthesis. *Int J Robot Res* 27(2):263–273
7. Marinelli C, Giberti H, Resta F (2015) Conceptual design of a gait simulator for testing lower-limb active prostheses. In: 2015 16th international conference on, research and education in mechatronics (REM). IEEE, pp 314–320
8. Zhang H, Zhen Z, Wei Q, Chang W (2001) The position/force control with self-adjusting select-matrix for robot manipulators. In: IEEE international conference on robotics and automation, 2001. Proceedings 2001 ICRA, vol 4. IEEE, pp 3932–3936
9. Tarabini M, Solbiati S, Saggin B, Scaccabarozzi D (2015) Apparent mass matrix of standing subjects exposed to multi-axial whole-body vibration. *Ergonomics* 1–12
10. Righettini P, Giberti H, Strada R (2013) A novel in field method for determining the flow rate characteristics of pneumatic servo axes. *J Dyn Syst Meas Control Trans ASME* 135(4)
11. Giberti H, Cinquemani S (2011) Sliding mode controller for a 2 dof fully pneumatic parallel kinematic manipulator. In: IMETI 2011—4th international multi-conference on engineering and technological innovation, proceedings, vol 2, pp 122–127
12. McDonnell BW, Bobrow JE (1997) Modeling, identification, and control of a pneumatically actuated robot. In: 1997 IEEE international conference on robotics and automation, 1997. Proceedings, vol 1. IEEE, pp 124–129

13. Sanville FE et al (1971) A new method of specifying the flow capacity of pneumatic fluid power valves. *Hydraulic Pneum Power* 17(195):120–126
14. Schaper U, Sawodny O, Mahl T, Blessing U (2009) Modeling and torque estimation of an automotive dual mass flywheel. In: 2009 American control conference. IEEE, pp 1207–1212
15. Shandiz MA, Farahmand F, Osman NAA, Zohoor H (2013) A robotic model of transfemoral amputee locomotion for design optimization of knee controllers. *Int J Adv Robot Syst* 10

Determination of the Human Arm Stiffness Efficiency with a Two Antagonist Muscles Model

Daniele Borzelli, Stefano Pastorelli and Laura Gastaldi

Abstract In the last years, due the working age increase, more and more attention was given to the use of exoskeleton for industrial applications, such to reduce fatigue and the operator effort. Since in industrial practice, stiffening the joint is a requested action for those operations in which precision is needed, an exoskeleton whose stiffness could be controlled by the operator would reduce the operator discomfort. In this paper we attempt to study the stiffness of the elbow on which two muscles act as agonist-antagonist and we proposed an estimation of the efficiency.

Keywords Hill muscle · Ergonomy · Stiffness control · Efficiency

1 Introduction

Exoskeletons are robotic wearable devices that permit the information sharing between operator and machine. Electromyographic (EMG) signal was pointed as one of the most reliable way to control exoskeletons [19] and EMG-controlled exoskeletons were largely developed for rehabilitation purpose [4, 14, 20]. However, due to the increasing of the working age, more and more effort is reposed in developing exoskeleton for industrial purpose [23] because of their beneficial effects, in terms of ergonomy and fatigue, expecially during non-comfortable operations like the over-shoulder ones [22]. So far the main task exoskeletons were requested to satisfy, was to relive the operator when carrying a load. However, since the joint stiffening is achieved by co-activating muscles [1, 7], also this operation

D. Borzelli (✉) · S. Pastorelli · L. Gastaldi
Politecnico di Torino, Turin, Italy
e-mail: daniele.borzelli@polito.it

S. Pastorelli
e-mail: stefano.pastorelli@polito.it

L. Gastaldi
e-mail: laura.gastaldi@polito.it

would lead to fatigue and discomfort, with possible consequences of injuries. The development of an exoskeleton that can assure arm stiffness and controlled by the operator EMG signal would reduce fatigue, risk of injuries and would improve productivity. Exoskeletons whose stiffness was controlled by EMG signal were developed for rehabilitation purpose [12] while robotic devices whose stiffness was controlled by EMG, were developed for industrial purpose [2, 21]. However no exoskeletons whose stiffness could be modulated on the basis of the EMG signal, were developed for industrial purpose. Controlling the stiffness of an exoskeleton through the EMG activity needs a control law that should be tested on an analogue of musculo-tendon. This to study the mechanical behavior of the biological joints on which the exoskeleton is plan to work on [4, 5].

In this study we modeled and tested a simple model composed of two antagonist muscles acting on a joint. The proposed model could be used not only for testing the efficiency of an exoskeleton but also for testing others devices controlled by the operator stiffness, acquired by EMG signal. The muscles are modeled as Hill muscles [3, 6], the joint stiffness was calculated as in [17], and the joint rotational stiffness is defined as the ratio between the recorded torque and the deflection that generated it. In this study we evaluated the limitations of the model and we proposed an estimation of the efficiency of the muscle activation, intended as the ratio between the exerted joint stiffness and the norm of the muscle activations, in the generation of joint stiffness for different joint angles.

2 Methods

2.1 *Arm and Musculo-Tendon System Models*

The elbow joint is studied and treated as an hinge joint [16]. The authors use a two-links simplified model of the human elbow to study the behavior of the muscles when modulating the joint stiffness. The two links simulated the radius-ulna set and the humerus bones. Two actuators, that simulate the actions of muscles on the elbow joint, control the single degree of freedom (Fig. 1a). Since muscles could only exert pulling actions, they are approximated with wires. The musculo-tendon system law for force exertion is the one of Hill [6], a commonly used analogue of musculo-tendon when studying the mechanical behavior of biological joints. The Hill musculo-tendon model is composed of two segments (Fig. 1b) that model both muscle and tendon actions. The muscle segment (l_p) is composed of an active element (A) and a non-linear spring in parallel with A (parallel spring). The tendon segment (l_s) is composed of a non-linear spring in series with A (serial spring). Expressions and parameters used to calculate the forces exerted by each element are got from [13]. The equations that relate the force exerted by the active element (F_A) and by the parallel spring (F_p) with the muscle length (l_p), and the force exerted by the serial spring (F_s) with the tendon length (l_s) are:

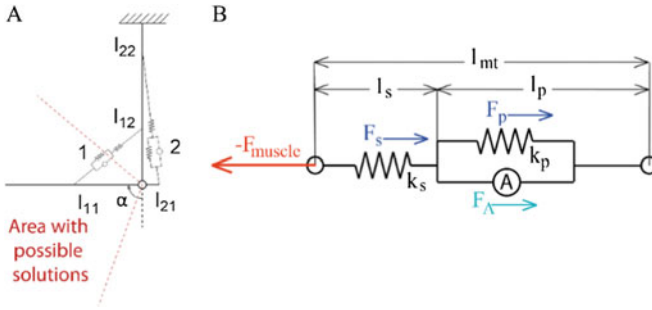


Fig. 1 Model of the elbow joint and of the musculo-tendon group. **a** Model of human joint. The range of elbow flexions in which solutions of equilibrium exist are comprised between the red dashed lines. **b** Hill muscle model used in the study

$$\begin{cases} F_A = m \cdot F_{MAX} \cdot \left[-a \cdot (l_p/l_{ceopt})^2 + 2a \cdot (l_p/l_{ceopt}) - a + 1 \right] \\ F_p = k_p \left[\max(0, l_p/l_{ceopt} - l_{p0}/l_{ceopt}) \right]^2 \\ F_s = k_s \left[\max(0, l_s - l_{s0}) \right]^2 \end{cases} \quad (1)$$

where l_{ceopt} is the optimal length at which the muscle exerted its maximum active force (F_{MAX}), m is the muscle activation, reported as a fraction of the Maximum Voluntary Contraction (MVC), $a = 1/\text{width}^2$ and $\text{width} = 0.66$, k_p is the stiffness of the muscle, that is chosen such that at $F_p = F_{MAX}$, $l_p/l_{ceopt} = 1 + \text{width}$, l_{p0} is the muscle relaxation length, that indicates the maximum length of the muscle for which the parallel spring does not exert any passive force (in this study $l_{p0} = l_{ceopt}$), k_s is the tendon stiffness, chosen such that at F_{MAX} , $l_s = 1.04 \cdot l_{s0}$, and l_{s0} is the tendon slack length, that indicates the maximum length of the tendon for which the serial spring does not exert any force. F_{MAX} , l_{ceopt} , and l_{s0} are muscle specific and their values, for the muscles used in this study, are got from literature [8] and reported in Table 1. The mono-articular antagonist muscles are chosen as in [18] and are the Brachioradialis (BRD, muscle 1), that acts as a flexor of the elbow, and the Lateral head of the Triceps (TriLat, muscle 2) that acts as an extensor of the elbow. Anthropometrical information on the attachment of the muscles on the bones are got from literature and are reported in Table 1 [8].

Table 1 Anatomical parameters used in the study

Muscle	l_{ceopt} (m)	l_{p0} (m)	l_{s0} (m)	F_{max} (N)
1: BRD	0.0858	0.0858	0.0535	261.33
2: TriLat	0.1138	0.1138	0.0980	624.3
Muscle	k_p (N/m)	k_s (N/m)	Attach on Radius-Ulna (m)	Attach on Humerus (m)
1: BRD	600	163×10^3	l_{11} : 0.1274	l_{12} : 0.1004
2: TriLat	1433	390×10^3	l_{21} : 0.0219	l_{22} : 0.1735

2.2 Equations for the Force Balancing

The only stiffness modulation is considered in this study. The equations that describes the equilibrium among the internal forces shared between the serial spring (F_{s_i}), the parallel spring (F_{p_i}), and the active element (F_{A_i}), for the muscle i , and among the torques exerted by the antagonist muscles are:

$$\begin{cases} F_{s1} = F_{p1} + F_{A1} \\ F_{s2} = F_{p2} + F_{A2} \\ m_{a_2}(F_{p2} + F_{A2}) = m_{a_1}(F_{p1} + F_{A1}) \end{cases} \quad (2)$$

where m_{a_i} is the moment arm of the muscle i . The force equations are coupled with the geometrical equations that defined the lengths of each segment and their attachments on the bones:

$$\begin{cases} l_{m_i} = l_{p_i} + l_{s_i} \\ l_{m_i} = \sqrt{l_{i1}^2 + l_{i2}^2 - 2 \cdot l_{i1} \cdot l_{i2} \cdot \cos \beta} \\ m_{a_i} = \frac{2}{l_{m_i}} \sqrt{\frac{P_i}{2} \left(\frac{P_i}{2} - l_{i1}\right) \left(\frac{P_i}{2} - l_{i2}\right) \left(\frac{P_i}{2} - l_{m_i}\right)} \end{cases} \quad (3)$$

where l_{m_i} , m_{a_i} , and P_i are respectively the length, the moment arm of the muscle i , and the perimeter of the triangle whose sides are l_{i1} , l_{i2} , and l_{m_i} . β is equal to $\pi - \alpha$ for muscle 1 and to α for muscle 2; where α is the angle of the elbow defined such that $\alpha = 0 \text{ rad}$ when the joint is completely extended and $\alpha = \pi \text{ rad}$ when the joint is completely flexed (Fig. 1a). The system, that is composed with geometric and force equations, together with the equations for the evaluation of the forces exerted by the muscle elements, was implemented in Matlab. Physiological range of the elbow flexion was set from 0° to 130° [10].

2.3 Stiffness Calculation and Efficiency

In this study the different levels of co-contraction is defined on the basis of the activation of muscle 1. The rotational stiffness of the musculo-tendon system i is defined as the derivative of displacement caused by imposed torque τ_i :

$$K_i = \frac{\partial \tau_i}{\partial \alpha} = \frac{\partial (m_{a_i} \cdot (F_{p_i} + F_{A_i}))}{\partial \alpha} = m_{a_i} \frac{\partial (F_{p_i} + F_{A_i})}{\partial \alpha} + (F_{p_i} + F_{A_i}) \frac{\partial m_{a_i}}{\partial \alpha} \quad (4)$$

A small deflection ($\partial \alpha = 0.01^\circ$) [9] is applied to the elbow joint in both positive and negative directions, while the activations of the muscles are maintained unchanged. Since the force exerted by the muscle depended on its length, a corresponding torque is exerted at the elbow. The elbow angle-torque relation could be approximated, around the unperturbed configuration, with a linear shape whose

slope represents the stiffness of the muscles. The rotational stiffness of the elbow is the difference between the slopes of the elbow angle-torque curves of muscle 1 respect with muscle 2. The efficiency is calculated as the ratio between the elbow stiffness, intended as the output of the system, and the norm of the muscle activation, intended as the input of the model.

3 Analysis

3.1 Musculo-Tendon System Characteristic and Angle Boundaries

The variation of the joint angle leads to a different variation of the antagonist muscles length. Since the torque-length of the muscle characteristic is specific for each muscle this behavior could be interpreted as a shifting of the characteristic of one muscle along the other such to match the lengths the two muscles assume at the specific joint angle. We may observe that this shifting permits the two muscles, which exert force along different range of length (between 0.09 and 0.20 m muscle 1 and between 0.17 and 0.21 muscle 2), to apply a force along the same range of angles (between 20° and 130°) (Fig. 2).

Two different joint angle boundaries could be identified: one is due to the joint angles at which intersections between the torque-angle characteristics of the two muscles does exist, like the lower boundary set to 20°, and the other is due to the physiological constraints, like the upper boundary set to 160°. The

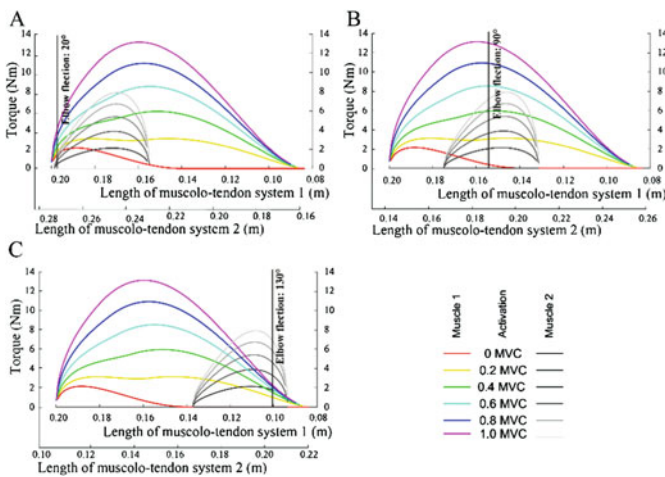
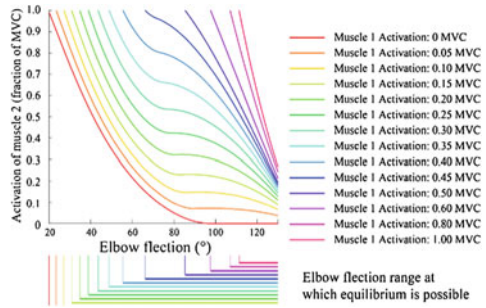


Fig. 2 Intersections of the characteristics of the torque, related to the musculo-tendon length, exerted by the two antagonistic muscles for different elbow flexions, at different level of activation of muscle 1 (colored) and 2 (gray scale)

Fig. 3 Activation of muscle 2 necessary to balance the torque exerted by muscle 1, in relation to the elbow flexions. Different colors identify different levels of muscle 1 activations



non-physiological lower boundary of 20° may be due to the approximation of the muscles with strings, while more complex geometries may occur, or to the limited number of muscles modeled. Figure 3 shows the joint angles at which co-activation of the antagonist muscles is possible for different levels of activations. It could be noticed that co-activating the antagonist muscle at a certain level is possible only for some joint angles. In particular higher activations of muscle 1 are feasible for higher joint angles. Intersections between two specific activations of muscles 1 and 2 are possible at most for one elbow flexion. In other words, the activations of the antagonist muscles univocally identify the elbow flexion if no torque was exerted by the elbow joint.

3.2 Arm Stiffness and Efficiency

Higher joint stiffness could be found for higher muscle activations (Fig. 4a). A peak due to the active element of muscle 1 could be found at a joint angle, close to 100° , that decreases with the increasing of the activation of the muscle 1. Another peak is close to 50° of elbow flexion and depends on the passive action of the parallel spring of muscle 1. A knee, that represents the elbow flexion at which the parallel spring ended exerting its action, could be found in all curves. The elbow flexion, at which the knee appears, decreases with muscle 1 activation growing. Since the balancing of the torque exerted by high activation of muscle 1 is possible only for some joint angles, the stiffness of higher muscle activations could be computed only for these angles.

The efficiency, intended as the ratio between the elbow stiffness and the norm of the muscle activations (Fig. 4b) shows minima between 70° and 90° . These minima depend on the muscle activations, and are found in correspondence of the joint angle at which the parallel spring of muscle 1 starts its action. Two peaks are found, except for the muscle activation equal to zero. The first peak corresponds to joint angle at which the parallel spring of the muscle 1 exerts a passive force (lower joint angles). The second peak corresponds to joint angles at which the parallel spring of the muscle 1 does not exert any force (higher joint angles). So we can find a range in which the system is more efficient in stiffening the joint.

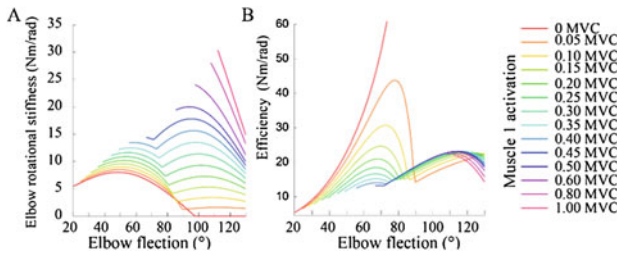


Fig. 4 Joint stiffness and efficiency of the model in relation to joint angle. **a** Values of the rotational stiffness in relation to the norm of the muscle activation for different activations of muscle 1, identified with different colors. **b** Relation between the efficiency, calculated as the ratio between the rotational stiffness and the norm of the muscle activation, respect with the elbow flexion for different values of muscle 1 activations

4 Discussion

The purpose of this study was the development of a simple model for the analysis of the stiffness exerted by two antagonist muscles acting on a joint. This model would be successively used for the testing the control law of robotic devices, such as exoskeletons, whose stiffness could be modulated by the recording of the operator EMG signal. The muscle model used in this study is one of the simplest ones and more complex models were developed [15]. However, this simple model is commonly used for the study of mechanical characteristics of human limb [11].

In this paper we introduced a device for the estimation of the efficiency at which the operator is working. This device could be used to define better joint angles in relation to the requested stiffness.

In future work we plan to add another joint, modeling the shoulder, and to increase the redundancy of the system, adding more muscles and using physiological laws to select the muscle activations.

References

1. Agostini V et al (2015) Does texting while walking really affect gait in young adults? *J NeuroEng Rehabil* 12(1):86
2. Ajoudani A et al (2012) Tele-Impedance: teleoperation with impedance regulation using a body-machine interface. *Int J Robot Res* 0(0):1–14 (2012)
3. Borzelli D et al (2016) Model of the human arm stiffness exerted by two antagonist muscles. In: 25th international conference on robotics in Alpe-Adria-Danube region RAAD 2016, Belgrade
4. Galetto M et al (2014) accuracy evaluation of a new stereophotogrammetry-based functional method for joint kinematic analysis in biomechanics. *Proc Inst Mech Eng Part H J Eng Med* 228(11):1183–92
5. Gastaldi L et al (2015) Evaluation of functional methods for human movement modelling. *Acta Bioeng Biomech* 17(4):31–38

6. Hill AV (1953) The mechanics of active muscle. *Proc Royal Soc B: Bio Sci* 141(902):104–117
7. Hogan N (1984) Adaptive control of mechanical impedance by coactivation of antagonist muscles. *IEEE Trans Autom Control AC* 29(8):681–690
8. Holzbaur KRS et al (2005) A model of the upper extremity for simulating musculoskeletal surgery and analyzing neuromuscular control. *Ann Biomed Eng* 33(6)
9. Hu X et al (2011) Muscle short-range stiffness can be used to estimate the endpoint stiffness of the human arm. *J Neurophysiol* 105(4):1633–1641
10. Iannotti JP, Parker RD (2013) The netter collections of medical illustrations: musculoskeletal system, Part I—upper limb. Frank H, Netter
11. Inouye JM, Valero-Cuevas FJ (2016) Muscle synergies heavily influence the neural control of arm endpoint stiffness and energy consumption. *PLoS Comput Biol* 12(2):e1004737
12. Karavas N, Ajoudani A (2013) Tele-impedance based stiffness and motion augmentation for a knee exoskeleton device. In: 2013 IEEE international conference on robotics and automation (ICRA), pp 2194–2200 (2013)
13. Kistemaker DA et al (2010) The Central nervous system does not minimize energy cost in arm movements. *J Neurophysiol* 104(6):2985–2994
14. Lee S, Sankai Y (2002) Power Assist control for walking aid with HAL-3 based on EMG and impedance adjustment around knee joint. In: IEEE/RSJ international conference on intelligent robots and system, IEEE, pp 1499–1504 (2002)
15. Lichtwark GA et al (2009) Intensity of activation and timing of deactivation modulate elastic energy storage and release in a pennate muscle and account for gait-specific initiation of limb protraction in the horse. *J Exp Biol* 212(15):2454–2463
16. Marieb EN, Hoehn K (2007) *Human Anatomy and Physiology*. Pearson Benjamin Cummings
17. Mussa-Ivaldi FA et al (1985) Neural, mechanical, and geometric factors subserving arm posture in humans. *J Neurosci* 5(10):2732–2743
18. Osu R, Gomi H (1999) Multijoint muscle regulation mechanisms examined by measured human arm stiffness and EMG signals. *J Neurophysiol* 81(4):1458–1468
19. Rosen J et al (2001) A myosignal-based powered exoskeleton system. *IEEE Trans Syst Man Cybern—Part A: Syst Humans* 31(3):210–222
20. Sacco K et al (2011) A combined robotic and cognitive training for locomotor rehabilitation: evidences of cerebral functional reorganization in two chronic traumatic brain injured patients. *Frontiers Human Neurosci* 5:146
21. Smith AMC et al (2015) Novel hybrid adaptive controller for manipulation in complex perturbation environments. *PLoS ONE* 10(6):e0129281
22. Sylla N et al (2014) Ergonomic contribution of ABLE exoskeleton in automotive industry. *Int J Ind Ergonomics* 44(4):475–481
23. van der Vorm J et al (2015) Safety and risk management in designing for the lifecycle of an exoskeleton: a novel process developed in the robo-mate project. In: *Procedia Manufacturing* 3(6th Int. Conf. on Applied Human Factors and Ergonomics (AHFE 2015) and the Affiliated Conferences, AHFE 2015), pp 1410–17

Design of a Miniaturized Safety Clamping Device for Portable Kidney Replacement Systems

P. Boscariol, G. Boschetti, R. Caracciolo, M. Neri, D. Richiedei, C. Ronco and A. Trevisani

Abstract In this paper the design of a miniaturized safety clamp to be used in portable/wearable kidney replacement systems and/or ultrafiltration devices is dealt with. These devices can be used to treat patients with renal deficiency by filtering the blood drawn through a specific vascular access, and by reinfusing it after the purification. A clamping device is essential to guarantee the safety of these devices, since it allows to occlude the external body blood circulation in case of a safety hazard, such as the formation of air bubbles, clots, and blood backflow. The clamp must be designed to provide adequate clamping force, while minimizing space occupation, weight and power consumption, since it is meant to be housed in a portable/wearable and battery-operated device. The novel design proposed is based on an articulated mechanism, whose dimensions have been optimized to meet the required specifications. The estimated power consumption constitutes a sensible improvement over commercially available devices.

Keywords Clamping device · Wearable ultrafiltration system · Design optimization · Miniaturized mechanism

P. Boscariol · G. Boschetti · R. Caracciolo · M. Neri ·
D. Richiedei · A. Trevisani (✉)
Department of Management and Engineering,
University of Padova, Vicenza, Italy
e-mail: alberto.trevisani@unipd.it

C. Ronco
Department of Nephrology, Dialysis and Transplantation,
S. Bortolo Hospital, Vicenza, Italy

C. Ronco
IRRIV, San Bortolo Hospital, Vicenza, Italy

1 Introduction

Patients suffering from chronic kidney disease need to be treated with support therapy involving blood purification. Blood ultrafiltration systems are capable of filtering blood taken from a specific vascular access, by passing it through a porous semipermeable membrane to remove the excess solutes and water, and re-infusing blood into the patient. Commonly, such therapies are performed on a semi-daily basis in hospitals, where specific machines and trained personnel can be found [3, 4]. Given the frequency and the length of treatments, which usually last several hours and are repeated at least three times per week, the possibility of performing the same treatments, or part of them, outside the hospital is considered of paramount importance. Indeed, this would reduce the interference of the therapies with patients' everyday life and in turn would allow improving their quality of life considerably [6]. Additionally, the economic impact of reduced hospital admissions and length of stays could be significant, with important savings for national health services [5]. For these reasons, the development of so-called miniaturized Wearable Artificial Kidneys (WAK) and of Wearable Ultra Filtration Systems (WUF) has been the focus of widespread research efforts, and has led to the development of a few devices and prototypes some of which are currently in clinical trial phase [3]. However, large-scale clinical applications and device commercialization are far from being reached. This fact combined with the existence of still open and relevant research issues, justifies further research effort in this field.

The requirement of combining safety and miniaturization imposes a thorough risk management analysis, and the development of specific safety strategies and devices. In particular, any portable device must drain and reinfuse blood from patients, who are therefore exposed to the risk of blood losses, blood clots, injection of air bubbles into the venous circulation systems and blood reverse flows. All these occurrences, when detected, should lead to an immediate occlusion of the extra-corporeal blood circulation. In the renal replacement devices used in hospitals, for example, this task is performed by an automatic pinch valve, usually referred to as "clamp". A clamp must be capable of occluding the circuit (often a disposable one) through which blood flows, thereby isolating the problem and significantly reducing direct and indirect risk to patients. Furthermore, a clamp should operate normally closed, i.e. it should automatically close the circuit whenever no actuation power is available, in order to cope with possible power supply or actuator failures. Commercially available safety clamps are usually unsuitable to portable/wearable devices being large, heavy and high power consuming, additionally, their not negligible power losses generally lead to high operation temperatures.

In this work the conceptual design, the synthesis, and geometric optimization of a novel miniaturized clamping system is proposed, with the aim of meeting the requirements for a wearable kidney replacement systems suitable for blood ultrafiltration, which can be basically summarized in terms of small dimensions, adequate clamping force exertion capability, efficient electric power consumption and normally closed operation. The focus of the design is on the careful synthesis of a

miniaturized articulated mechanism which is then optimized in order to make it possible to operate it by a small-size stepper motor. The aforementioned requirements are all met by the proposed design.

2 Design Specifications

The basic requirement to be met by the clamp of a portable/wearable ultrafiltration system is to ensure the maximum possible level of safety during its operation, in order to avoid any possible hazardous situation.

Clearly, a clamp cannot directly come into contact with blood but it needs to work by occluding the PVC tube into which blood flows. The wearability of the device imposes the use of batteries as power sources, therefore electric power consumption must be kept to a minimum. In order to provide the required normally-closed operation, safety clamps are currently designed as spring-loaded mechanisms, in which the spring preload is counteracted by an electric actuator that must be energized to allow blood to flow. Actuators are typically brushless motors [7] or voice-coil actuators [2]. As previously mentioned, such clamps, conceived for non-portable devices for ultrafiltration or dialysis, are of impractical use in portable devices, due to their high power consumption, weight and size. Just to provide an explicative example, if PVC tubes of external diameter 4.2 mm are supposed to be employed in the blood circuit of a portable device, according to the currently available datasheets [2], a voice-coil device would consume up to 4.2 W to keep the circuit open. This consumption is incompatible with the need to supply a wearable device through a battery for the whole duration of an ultrafiltration treatment, which can last as long as 24 h. As a matter of fact, this power consumption would require slightly more than 100 Wh battery capacity just for operating the clamp. Such a capacity would imply using batteries weighing between 500 g and 1 kg, on the basis of the average power density of lithium-ion batteries [8]. Even if the treatment lasted 12 h, the battery weight would be excessively high for a wearable device and the expected high temperature reached by the clamp would be likely to be uncomfortable.

A very restrictive specification of 1 W has therefore been set in this work for the maximum continuous power consumption of the clamp to be designed. Based on the experimental tests carried out at the initial stage of the design procedure, the chosen 4.2 mm PVC tubes need a pinch force by 25 N to be occluded. If a reasonable safety factor equal to 2 is used, the clamp should be capable of exerting a force equal to 50 N by means of the spring preload. The occluding response time must also be short enough to guarantee that no extra particles (air, clots) are infused into patient's vascular access after a safety hazard detection. Considering a maximum blood flow equal to 50 ml/min, the geometrical characteristics of the tube (with 2.6 mm inner diameter) and the expected distance between the last safety sensor and patient's vascular access (that should be about 150 mm), the necessary response time of the clamp (i.e. the time taken to pinch the tube) might be about 1 s,

since blood flow speed is 0.16 m/s. Considering a severe safety factor equal to 10, it has been decided that the clamp should be designed to occlude the tube in about 0.1 s from fault detection occurrence.

A novel clamp design meeting all the aforementioned specifications is introduced in the next section and its performances are discussed.

3 Mechanical Design and Optimization

The proposed design for the clamp mechanism is based on the use of the cascade of two four-bar linkages, as shown in Figs. 1 and 2. The use of an articulated multi-loop mechanism is suggested by the need to obtain a considerable force amplification in order to keep to a minimum the size of the actuator counteracting the preloaded spring used to guarantee the normally closed operation for the clamp. The electric actuator is assumed to exert the driving torque T_m about joint O and move link 1 directly. The coupling between the two four-bar linkages is assured by the ternary link BCD. The clamping force f_{CLAMP} is applied to the tube through a pin located at point F . The operation of the clamp in the absence of electric actuation is provided by an extension spring exerting force f_{EL} , whose moving end is located at point H while its fixed end is jointed at point N .

In the proposed design, the spring allows pinching the tube by promptly rotating the follower EH clockwise whenever the motor is switched off. The motor torque can instead keep the clamp open by inducing a counter-clockwise (positive) rotation of the same link. The two configurations are shown in Fig. 2.

On the basis of the requirements stated in Sect. 2, optimization should be accomplished to minimize the size of both the actuator and of the overall mechanism. The design procedure has involved the optimization of the lengths of some links, of the joint positions and of the spring parameters. In order to reduce the size of the actuator, and consequently its power consumption, the goal of the optimization is to minimize the maximum amplitude of motor torque along the usable workspace (denoted by Q : it basically corresponds to the range of angular rotation

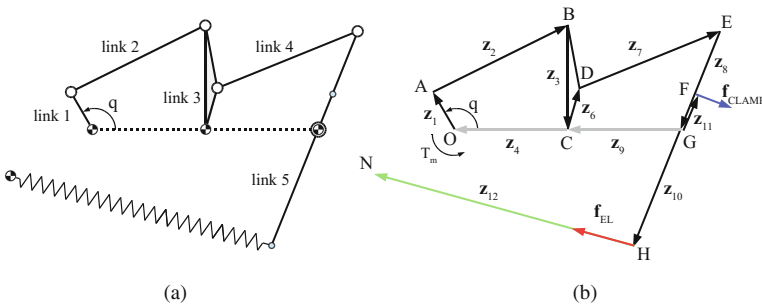


Fig. 1 Clamp: kinematic scheme and external forces exerted on the mechanism

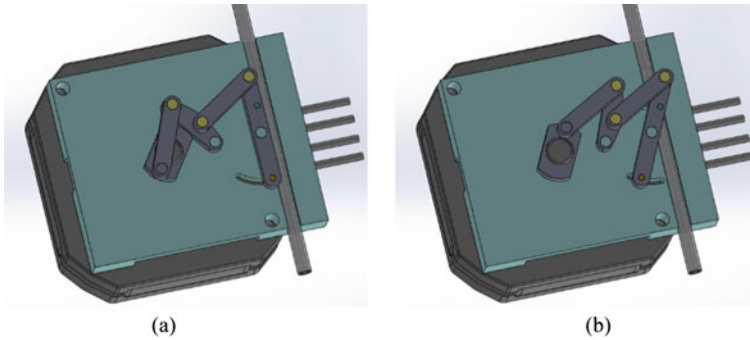


Fig. 2 Clamp: preliminary CAD design, open (a) and closed (b) configurations

of link 1 from the “closed” position to the “open” one, see Fig. 2, a proper definition is provided below), in the presence of constraints used to bound the overall size of the mechanism.

Other constraints have been imposed in the optimization in order to obtain only feasible designs. As a first constraint, the inner tube diameter imposes a minimum displacement of point F equal to 2.6 mm (denoted ΔF). Additionally, the mechanism should be able to exert an adequate force to pinch the tube when the clamp is closed. Such a force must be exerted by the spring, with the motor switched off. By expressing the static equilibrium of the whole mechanism through the principle of virtual works the magnitude of f_{CLAMP} can be evaluated for any configuration within the workspace as follows:

$$f_{EL} \begin{Bmatrix} \frac{\partial x_H}{\partial q} \\ \frac{\partial y_H}{\partial q} \end{Bmatrix} + f_{CLAMP} \begin{Bmatrix} \frac{\partial x_F}{\partial q} \\ \frac{\partial y_F}{\partial q} \end{Bmatrix} = 0 \tag{1}$$

The evaluation of the magnitude of f_{CLAMP} in the “closed” configuration is included in the optimization as a constraint. The static analysis also allows evaluating the magnitude of the motor torque needed to counteract the spring pull in the closed configuration:

$$f_{EL} \begin{Bmatrix} \frac{\partial x_H}{\partial q} \\ \frac{\partial y_H}{\partial q} \end{Bmatrix} + T_m = 0 \tag{2}$$

Although all the design parameters of the mechanism have a strong influence on its performances, the large number of possible design parameters suggests to include just a subset of them within the optimization parameters vector. Indeed the effectiveness and the convergence of a nonlinear constrained optimization routine is easily jeopardized by large scale problems. Therefore, the number of optimization parameters has been kept to a minimum by performing a preliminary design of the mechanism, which has involved the choice of the lengths of the links of the two

cascaded four-bar mechanisms. Such a preliminary design has been carried out considering that the mechanical advantage is directly proportional, among the others, to the ratios of the link length z_3/z_1 , z_6/z_{11} , z_3/z_6 , and z_8/z_{11} , which appear in the sensitivity coefficients $\partial x_F/\partial q$ and $\partial y_F/\partial q$. These ratios have therefore been set to be as high as possible, considering also the inevitable tradeoff between getting high force magnification and assuring an adequate displacement at point F, as well as the limitations related to the detailed design of the mechanism (e.g. link interference or collisions). The stiffness of the spring has been chosen by evaluating the trade-off between the overall size and the needed stiffness, considering that the latter should be quite high in order to provide a sufficiently large force with a limited displacement.

The feasibility of the optimization numerical routine is ensured by including the following parameters within the design parameters vector: the location of the fixed point N (in Cartesian coordinates x_N, y_N), the length of link z_{10} , the relative angle between vectors z_3 and z_6 (denoted $\gamma_{3,6}$), as well as the free length of the spring (denoted L_0):

$$\mathbf{x} = [x_N; y_N; L_0; z_{10}; \gamma_{3,6}] \quad (3)$$

Indeed, the combined influence of these parameters on the mechanism performance is difficult to be predicted a priori. The aforementioned design goals, as well as the design constraints that ensure feasibility, are included in the following optimization problem:

$$\begin{aligned} & \min_{q \in Q} \max T_m(q, \mathbf{x}) \\ & \text{subject to:} \\ & \begin{cases} f_{\text{CLAMP}} \geq 50 \text{ N} \\ \Delta F \geq 2.6 \text{ mm} \\ y_N \leq -5 \text{ mm} \end{cases} \end{aligned} \quad (4)$$

The optimization problem of Eq. (4) includes the nonlinear constraints that ensure adequate clamping force and displacement at point F . The analysis is extended to the usable workspace Q , computed as the subset of the whole workspace, for which the sensitivity coefficient $\partial \varphi_8/\partial q$ is larger than the threshold value arbitrarily chosen equal to 0.04. This limitation ensures that the mechanism is never operated too close to a singular configuration, in order to assure reversibility and that the torque needed to counteract the spring pull always takes positive values. The latter condition allows using T_m in Eq. (3), in lieu of its absolute value. It can be observed that an additional constraint is set on the position of point N , which is bounded to be at least 5 mm below the motor axis, in order to avoid interference between the spring and the motor shaft.

The design optimization has been performed by using a pattern search method based on the simplex algorithm. The outcome of the minimization procedure has been compared with the result of a genetic algorithm procedure [1], which has

Table 1 Optimized design parameters

$O = [0, 0]$ mm	$z_1 = 4$ mm	$z_2 = 12$ mm	$z_3 = 10$ mm
$C = [8.5, 0]$ mm	$z_6 = 4$ mm	$z_7 = 12$ mm	$z_8 = 10$ mm
$G = [17, 0]$ mm	$z_{10} = 8.5$ mm	$z_{11} = 5.3$ mm	$\gamma_{3,6} = 0.2187$ rad
$N = [-14, -5]$ mm	$K = 3000$ N/m	$L_0 = 16$ mm	

produced the same results, thus corroborating the convergence of the optimization. The optimized design parameters are shown in Table 1. The table lists also the position of the fixed revolute joints, the link lengths, the spring stiffness K and the spring free length L_0 .

The resulting motor torque is represented in Fig. 3a for all configurations within the usable workspace Q . It can be seen that the peak torque needed to achieve the equilibrium is lower than 70 mNm, therefore a relatively small size motor can be used and no gearboxes are necessary. The clamping force is shown in Fig. 3b. It also complies with the design specifications, since it is larger than 50 N for every configuration within the usable workspace Q .

On the basis of the computed torque, a pancake Sanyo Denki motor has been chosen as a reasonable example. The motor can provide the needed torque to keep the clamp in the open position, with a power consumption that is roughly equal to 143 mW. The design is therefore capable of meeting the design specification of reducing the continuous power consumption well below the 1 W threshold.

In order to verify that the complete closure of the pipe is obtained within the required maximum time, the dynamic response of the mechanism is investigated through forward dynamic analysis. This analysis is needed to evaluate whether the system can avoid the injection of an air bubble or a clot into the patient’s circulating system by occluding the pipe in a sufficiently small amount of time. In order to provide a reliable estimation, the system dynamics has been modeled by accounting for the spring force, the inertial contribution of the motor joint, and by representing

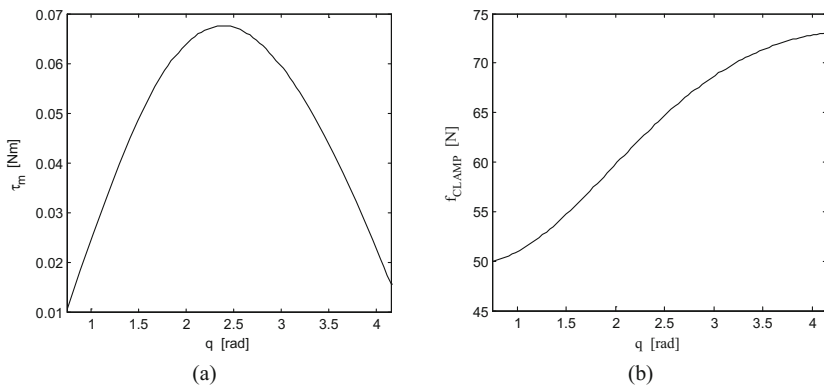


Fig. 3 Motor torque T_m versus free coordinate q (a), clamping force f_{CLAMP} (b)

the tube resistant force as a constant term equal to 25 N. Additionally, the detent torque (i.e. the torque required to rotate the motor shaft with no current applied to the windings) of the stepper motor has explicitly considered in the evaluation and estimated as 1/10 of the motor holding torque. In order to consider a worst-case scenario, an overall inertia J_{tot} equal to twice the motor one has been considered ($J_{tot} = 0.03 \times 10^{-4} \text{ kgm}^2$). The resulting equation of motion has been integrated numerically for the initial conditions $q = 4.153 \text{ rad}$ and $\dot{q} = 0 \text{ rad/s}$. The solution of the forward dynamics highlights that the complete pipe obstruction, which happens for $q = 0.7429 \text{ rad}$, is achieved after just 49 ms. Considering that the speed of blood along tubes is roughly equal to 0.16 m/s, air bubbles can only travel 7.8 mm after their detection. This assure that air bubbles can be stopped even before reaching the clamp, since the distance between the bubble detector and the clamp should be at least 5 cm.

4 Conclusions

In this paper the design of a novel clamp for portable kidney replacement systems and ultrafiltration devices is dealt with. The design of such a key component includes the synthesis of an articulated mechanism which can be driven by a small size electric motor without a gearbox. The design of the mechanism has been optimized to reduce the maximum torque the motor has to exert to open the clamp, while achieving good mechanical advantage in the open position of the clamp and assuring a prompt closing of the clamp in case of emergency. A small maximum torque guarantees that a small size or even miniaturized motor can be chosen; a good mechanical advantage allows keeping energy consumption to a minimum; a fast closing of the mechanism makes it suitable to assure patient's safety. We believe that the proposed design has considerable advantages over commercially available pinching devices, mainly in terms of power consumption, and that it can provide a fundamental contribution to the design of portable/wearable kidney replacement systems.

Acknowledgments The authors acknowledge the financial support by Fondazione Studi Universitari di Vicenza (FSU) and Fondazione Cariverona through a Ph.D. scholarship and the research grant "RAP".

References

1. Cabreara JA, Simon A, Prado M (2002) Optimal synthesis of mechanisms with genetic algorithms. *Mech Mach Theory* 37(10):1165–1177
2. Clippard Instrument Laboratory, Inc.—USA. www.clippard.com

3. Davenport A (2015) Portable and wearable dialysis devices for the treatment of patients with end-stage kidney failure: wishful thinking or just over the horizon? *Pediatr Nephrol* 30 (12):2053–2060
4. Drukker W, Parsons FM, Mahe JF (2012) Replacement of renal function by dialysis: a textbook of dialysis. Springer Science & Business Media
5. Gura V, Beizai M, Exon C, Rambod E (2006) Continuous renal replacement therapy for congestive heart failure: the wearable continuous ultrafiltration system. *ASAIO J* 52(1):59–61
6. Ronco C, Davenport A, Gura V (2011) The future of the artificial kidney: moving towards wearable and miniaturized devices. *Nefrologia (Madrid)* 31:9–16
7. SONCEBOZA SA—CH. www.sonceboz.com
8. Thackeray MM, Wolverton C, Isaacs ED (2012) Electrical energy storage for transportation—approaching the limits of, and going beyond, lithium-ion batteries. *Energy Environ Sci* 5 (7):7854–7863

Conceptual Design of a Mechatronic Biomedical Wearable Device for Blood Ultrafiltration

G. Boschetti, A. Dalla Via, N. De Rossi, F. Garzotto, M. Neri,
L. Pamato, C. Ronco and A. Trevisani

Abstract The industrialization of a wearable, mechatronic, biomedical device for blood ultrafiltration would represent an important step toward the achievement of tailored and improved care for kidney disease and congestive heart failure patients. In this article, the conceptual design of a novel and portable device is proposed. The necessary components are identified, and the most suitable technologies for pumps, sensors and control systems are selected, taking into account the basic requirement of minimizing the size and weight of the device in order to make it actually portable and wearable. The selection has also been driven by the results of a thorough risk analysis from a clinical point of view. Most components have been considered as disposables in order to ensure aseptic conditions and easy restoring operations for the device, which is believed to be essential to promote the use of wearable devices for blood purification in clinical practice.

Keywords Blood ultrafiltration · Mechatronic device · Wearable device

1 Introduction

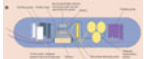





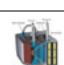
Kidney disease and congestive heart failure patients suffer from a pathological condition of over-hydration in which the body accumulates too much water. Over-hydrated patients need to be hospitalized and treated through extracorporeal blood ultrafiltration therapies delivered by bulky machines. Differently from

G. Boschetti · A. Dalla Via · N. De Rossi · M. Neri · L. Pamato · A. Trevisani (✉)
Department of Management and Engineering, University of Padova, Vicenza, Italy
e-mail: alberto.trevisani@unipd.it

F. Garzotto · C. Ronco
Department of Nephrology, Dialysis and Transplantation, S. Bortolo Hospital,
Vicenza, Italy

F. Garzotto · C. Ronco
International Renal Research Institute of Vicenza (IRRIV), S. Bortolo Hospital,
Vicenza, Italy

Table 1 Previous proposals of biomedical devices for blood ultrafiltration and dialysis

Name	Technological breakthroughs	Current status	Layout
The WAK [2]	Pulsatile pump REDY cartridge	Clinical trial	
ViWAK	Remote control Double lumen PD catheter	Prototype	
AWAK	REDY cartridge Protein regeneration	Before clinical trial	
The WHF	Double lumen PD catheter	Clinical trial	
WAKMAN [3]	Pump-filter unit Remote control	Prototype	
iNephron	Nanostructured sorbents ICT-integration	Prototype	
RAD (IAK) [4]	Nanostructured hemofilter Cell function	Prototype	

hemodialysis, that allows even a reduction of uremic toxins concentration, ultrafiltration is a therapy that aims to remove plasma water (the “ultrafiltrate”) from blood through a porous membrane applying a controlled pressure gradient.

A wearable ultrafiltration device (WUF) would have the potential to implement a not impetuous blood ultrafiltration therapy out of hospital over an extended period of time, making this process closer to natural body water removing, reducing total therapy costs and improving patients’ quality of life. Wearable systems can be broadly defined as mobile mechatronic devices that can be unobtrusively embedded in the user’s outfit as part of the clothing or an accessory.

Several prototypes with a similar therapeutic target have been developed to date (see Table 1 and [1]): although many of them have contributed to a scientific progress in this field, technological limitations still limit the potential clinical application and the industrialization of such devices. In particular, the main technological issues are related to the requirement of combining high levels of safety for patients together with miniaturization and low energy consumption.

This article introduces the conceptual design of a new mechatronic wearable system for blood ultrafiltration, designed to address the aforementioned requirements and conceived for an actual out of hospital use under remote supervision. This research is carried out within the framework of a cross-disciplinary project, named RAP, aimed to develop a miniaturized wearable/portable mechatronic device for blood ultrafiltration, and in which both the DTG of the University of Padova and the IRRIV of the S. Bortolo Hospital are involved.

2 Operative Requirements and Risk Management

A WUF must provide extracorporeal circulation of blood and ultrafiltrate removal by means of pumps. Typically, blood is directly taken from a patient by a specific vascular access, passed through a porous semipermeable membrane in order to remove ultrafiltrate by a pressure gradient, and finally re-infused into the patient. Clearly, a WUF should be wearable, wireless and independent from the electrical power outlet. In general, it is intended to be used for continuous ultrafiltration therapy, i.e. 24 h a day: in such a condition, the apparatus may consume large amounts of energy which imposes that adequate energy sources are available and a careful design of component to guarantee relevant energy savings.

The main operating parameters and the basic requirements of the system have been identified before starting its conceptual design: they are summarized in Table 2. They refer to three fundamental components that must be present in the device: the blood pump, the ultrafiltrate pump, and the filter. In addition to such requirements, miniaturization, low weight and energy consumption are obviously of paramount importance and need to be taken into account.

In the European Union, medical devices must comply the essential requirements laid down by the specific Directive [5]. In particular, devices must be designed and manufactured in such a way that they will not compromise the clinical safety of patients, ensuring that any hazardous situation which may be associated with their use determines acceptable risks when weighed against the benefits for the patient.

A thorough risk assessment has therefore been preliminary performed based on a top down fault tree analysis (FTA) [6]: a potential harm list for the patients has been identified from clinical and technical experience as well as literature. Various hazardous situations (circumstances in which the use of a WUF may lead to harms for patients) have furthermore been determined and classified. Severity and probability have been categorized using a numerical scale with five levels (from negligible to catastrophic for severity, from improbable to frequent for probability).

The risk, defined as the combination of the probability of occurrence of harm and its severity, has been finally associated to each hazard. Actions taken to mitigate the severity and probability of harms in case of unacceptable circumstances have been evaluated in order to find the most adequate technologies. Even if the

Table 2 Project specifications for a wearable blood ultrafiltration device

Blood pump	Ultrafiltrate (UF) pump	Membrane and filter
Max expected flow: 50 ml/min	Max expected flow: 7 ml/min	Hydraulic permeability: >1(ml/h)/mmHg
Resolution: 5 ml/min	Resolution: 1 ml/min	Contact surface area: >0.15 m ²
Tolerance: <10 %	Tolerance: <5 %	Priming Volume: ≈10 ml
Low hemolysis (damage of red blood cells)		Hemo-compatibility
Hemo-compatibility		

Table 3 Hazardous situations identified and technical solutions adopted to reduce risk

Unacceptable hazardous situation	Technical solutions to reduce the risk
Patient air infusion	Air bubble detector and air bubble removal system
Blood loss to the environment	Pressure sensors
Blood loss due to membrane leak	Blood leak detector sensor
Blood coagulation	Anticoagulation pump and blood flowmeter
Hypervolemia or hypovolemia due to inaccurate ultrafiltration volume/flow	Continuous feedback by fluid balance monitoring system
Infusion of air bubbles or clots	Electro-mechanical safety clamps
Malfunctioning of sensors or components, unplugged connectors	Control redundancy, emergency switch-off
Malfunction or failure of the control system	Control redundancy, watchdog code
Inaccuracy of therapy program and patient's inexperience in solving problems	Self-test and remote monitoring system

majority of the sensors and transducers proposed in our analysis are mandatory in such a device, its use out of the hospital introduces additional risks.

Table 3 summarizes the chief results of the risk analysis: the main unacceptable hazardous situations identified and the technical solutions chosen to delete or reduce risk are reported.

3 Chief Components for a WUF

The selection of the device components (still ongoing for a few of them, but mostly completed) has been based on the concept of the “single-treatment use”. Differently from most previous proposals appeared in literature, we have privileged the use of disposable components, whose cost keeps decreasing. The basic idea is collecting most of the components into a tidy and compact disposable kit, which will be replaced at the end of each treatment. The disposable kit must be connected to a set of non-disposable components by means of fast and safety plug connectors. The non-disposable components are those which are currently too expensive to replace or easy to keep not in direct contact with blood. In particular, in this preliminary design, the disposable kit is intended to be pre-assembled with the main hydraulic components of the device (e.g. tubes, pumps, filter, pressure transducers, ultrafiltration bag), while the non-disposable composed will comprise a set of electro-mechanical and electronic components whose need is further discussed below and derives from the aforementioned risk analysis (e.g. air bubble detector, blood leakage detector, signal conditioning hardware, micro controllers, safety clamps, plugs and electrical connections).

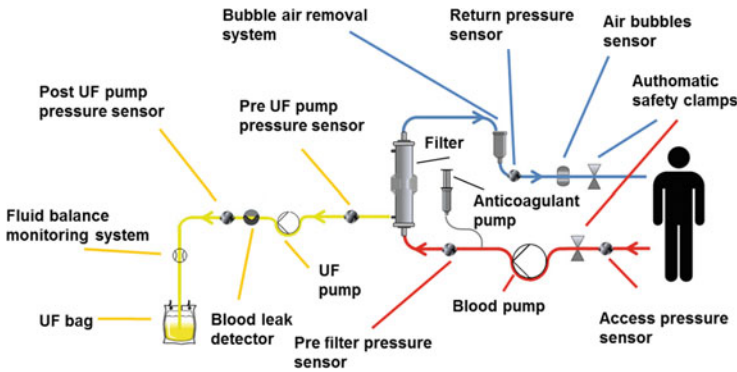


Fig. 1 Main components of the circuit and conceptual layout

Figure 1 shows the main components needed for the device and a basic conceptual layout. The blood pumping system is the core of the device and its choice is still a big research issue in the field of WUF devices. A specific investigation on such pumps is being carried out within the framework of the RAP project. Among the chief technologies that could be employed in a WUF, one could recall peristaltic, diaphragm and centrifugal pumps. Each of them has advantages and disadvantages, which, however are not discussed here, being beyond the scope of this paper. Generally speaking, if a diaphragm pump guaranteeing good efficiency, adequate hemo-compatibility, and low manufacturing cost is identified, it will be likely to represent the best choice in case of disposable use.

As far as the ultrafiltrate pump is concerned, a disposable volumetric diaphragm pump equipped with piezoelectric components should be employed. The maximum allowable flow should be 7 ml/min, which is compatible with the requirements listed in Table 2.

A further pump is shown in Fig. 1, which is the one for continuous infusion of anticoagulant (heparin). It must be very accurate in order to avoid under- or over-dosage of anticoagulant. Commercial devices in small size are available.

As for the filter, poly-ether-sulfone based membrane has an exchange surface area of 0.25 m², with a blood filling volume of 19 ml. Overall these features represent a good choice for the WUF.

Figure 1 shows that two electro-safety clamps need to be placed in the circuit: one in the access line in order to avoid blood backflow, one in the return line, mainly to avoid that air bubbles and clots are re-infused into the patient. Additionally, both clamps must occlude the circuit whenever any potential risk for the patient is detected. A new energy efficient and miniaturized prototype is being designed to this purpose and is the objective of a specific research effort.

All the sensors shown in Fig. 1 are used to reveal hazardous situations and to monitor the state of the device. Disposable pressure sensors can monitor pressure drops inside the circuit due to failure of tubes or connections. Such pressure sensors, based on piezo-electric transducers, are characterized by a good resolution and

thermal stability and a very low cost. Representative industrialized samples have already been successfully calibrated in a range between -500 mmHg (-66.6 kPa) and $+500$ mmHg ($+66.6$ kPa), which is the range of interest for the therapy. Unwanted air bubbles in the return line and red blood cells in the ultrafiltrate tube may be detected by means of respectively, an ultrasound transducer and an optical transducer. They are both off-the-shelf sensors, with a good degree of miniaturization. An air bubble removal system also needs to be integrated in the circuit in order to remove bubbles. Such a system is certainly necessary at the beginning of the therapy, when a considerable amount of air is still trapped into the circuit, but no evidence of its need during the whole therapy has been found yet.

Finally, a system suitable for measuring the amount of plasma water removed during the treatment is necessary: such measurements are needed by the control system to regulate the ultrafiltrate pump and keep the flow as constant as possible throughout the therapy. The usual gravimetric method making use of load cells cannot be used in a wearable device, hence either volumetric (e.g. capacitive) sensors or flowmeters should be employed. Flowmeters allow keeping size and weight to a minimum, but are generally expensive. An effort towards designing disposable devices is being made by a few companies. The actual availability of such disposable sensors will boost the possibility of industrializing a WUF.

4 Control Architecture

The core of the mechatronic system is its control architecture, which is shown in Fig. 2. The architecture has been carefully designed to meet both the restrictive requirements imposed by the application (the development of a miniaturized, energy efficient and wearable device which could be monitored remotely) and those imposed by the Directives and by the need to minimize risk for patients. As shown in Fig. 2 the architecture includes two main sections: the program application section and the electronic one. It has been verified that one microcomputer and two microcontrollers can successfully implement such an architecture.

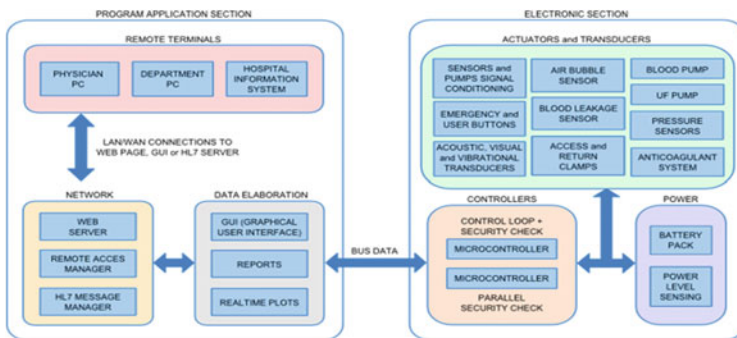


Fig. 2 WUF control architecture

The main tasks of the program application section are to set up the device on the basis of the treatment parameters, to manage network communication, to collect and sort therapy data, and to show the clinical treatment information using a clear Graphical User Interface (GUI) during the whole treatment, supporting remote monitoring. An off-the-shelf miniaturized microcomputer can perform all these tasks. Based on the peculiar field of application of the WUF, it has been chosen to make it possible to check therapy data and download reports and charts, in three ways:

- by visualizing the GUI from remote terminals through LAN/WAN connections;
- by opening a web page directly connected with the device;
- by using HL7 transmission protocol [7] to retrieve data through hospital information system.

The electronic section, instead, receives the reference commands from the GUI (and hence from the program application section), reads the feedback signals from the transducers, and basically suitably drives the actuators of the pumps to perform the treatment. It also returns information on the status of the system (pressure values, UF overall amount removed, etc.) to the GUI via a data bus. Two miniaturized microcontrollers can easily manage, in real-time, this process: a dual parallel safety-loop should be performed in order to implement redundancy control. The two microcontrollers must read the signals measured by the transducers and detect potential non-compliant situations. In order to improve the overall system safety, an additional safety monitoring, made by the microcomputer supervising the whole therapy, should detect possible faults in data bus communications. Moreover, a watchdog code should check the microcomputer status continuously.

The choice of off-the-shelf embedded boards meets power saving needs, with simple managing of prototype functionality and general purpose inputs/outputs, extremely spread documentation and advantages of cross-compiled code availability. As for the programming languages that should be chosen for the GUI, they are C++ and Python because of their versatility and software portability. With reference to the web environment, PHP, HTML and MySQL should be selected for the onboard web server: they allow encryption of patients' data and the possible scheduling of backup copies of all the device data, which are also downloadable through remote terminal via FTP server.

Since a WUF must also be managed by the treated patient, at least for switching it on and off or for receiving warning/alarm messages from the control system, the interface must include some additional hardware components including visual, audible and vibrational devices (i.e. buttons, LEDs, buzzers). Finally, the design should include at least two battery packs as power supply and a specific circuit for power level measurement (which should be monitored by microcontrollers, yielding an emergency signal if residual power is too low). The actual sizing of the batteries will be a matter of future investigations, but does not seem to be critical after having properly chosen the pumps and designed the clamps, which are current and relevant research activities.

5 Conclusions

The industrialization of a wearable mechatronic, biomedical device for blood ultrafiltration (WUF) may soon become possible, although some further technology improvements and experimental investigations are still required to get effective prototypes and assure a widespread use of such devices. Recent advances in sensor technologies, micro pumps, filtering materials, embedded systems, wireless networking have currently made available industrial grade components for the implementation of an actually portable WUF.

In this work the conceptual design of a safe and miniaturized WUF has been addressed. The strict requirements imposed by patients' safety, and recognized through an extensive specific risk management analysis, have been considered explicitly. Miniaturization through specific sensor and pump technologies, redundancy of control and remote monitoring of the therapy have been considered of primary importance since the very first step of the design phase, in order to assure adequate safety for patients. Additionally, the ever rising availability of low-cost, and hence disposable, sensors and pumps is believed to represent a critical factor for changing and improving the way of designing such wearable devices, and what is more important, to promote their deployment in clinical practice.

Acknowledgments The authors acknowledge the financial support by Fondazione Studi Universitari di Vicenza (FSU) and Fondazione Cariverona through a Ph.D. scholarship and the research grant "RAP".

References

1. Kim JC et al (2011) A wearable artificial kidney: technical requirements and potential solutions. *Expert Rev Med Devices* 8:567–579
2. Davenport A et al (2007) A wearable haemodialysis device for patients with end-stage renal failure: a pilot study. *Lancet* 370:2005–2010
3. Ronco C et al (2011) The future of the artificial kidney: moving towards wearable and miniaturized devices. *Nefrologia* 31:9–16
4. Humes HD et al (2004) Initial clinical results of the bioartificial kidney containing human cells in ICU patients with acute renal failure. *Kidney Int* 66:1578–1588
5. Medical Devices Directive 2007/47/EC of Sept. 5th, 2007, amending Council Directive 93/42/EEC. *Official J Eur Union* 247(L): 21–55, 2007
6. Lodi CA et al (2010) Multidisciplinary evaluation for severity of hazards applied to hemodialysis devices: an original risk analysis method. *Clin J Am Soc Nephrol* 5 (11):2004–2017
7. ISO 16527: Health informatics—HL7 Personal Health Record System Functional Model, 1nd Ed., Geneva, International Organization for Standardization, 2016

Design of an Underactuated Hand Exoskeleton with Joint Estimation

Mine Sarac, Massimiliano Solazzi, Daniele Leonardis, Edoardo Sotgiu, Massimo Bergamasco and Antonio Frisoli

Abstract In this study, we present an underactuated hand exoskeleton with the adaptation for the shape and the size of the objects during grasping tasks. The realism of the grasping tasks are improved by allowing only the normal transmission of the forces on the finger phalanges. The absence of the tangential forces allows the device to be attached to the user's finger in an easy and comfortable manner for the operation. Furthermore, the finger size adjustability can be ensured by the linkage-based design. Underactuation assures the automatic adjustability of the device for the grasping objects, while preventing the posture control of the finger phalanges. The undersensing disadvantage of the underactuation approach is suggested to be overcome by utilizing an additional potentiometer on the device in order to estimate the finger joints and the pose analysis of the mechanism during operation.

1 Introduction

Hand exoskeletons assist the human hand in a realistic and safe manner, as the force from the actuator is transmitted to the finger phalanges through the mechanical links of the exoskeleton. Even though some stationary devices provide assistance on the

M. Sarac (✉) · M. Solazzi · D. Leonardis · E. Sotgiu · M. Bergamasco · A. Frisoli
PERCRO Lab, Scuola Superiore Sant'Anna, Pisa, Italy
e-mail: m.sarac@sssup.it

M. Solazzi
e-mail: m.solazzi@sssup.it

D. Leonardis
e-mail: d.leonardis@sssup.it

E. Sotgiu
e-mail: e.sotgiu@sssup.it

M. Bergamasco
e-mail: m.bergamasco@sssup.it

A. Frisoli
e-mail: a.frisoli@sssup.it

fingertips for rehabilitation tasks [1], a generic hand exoskeleton should have the ability to assist the user to perform real grasping tasks for various applications.

Some exoskeletons utilize individual actuators for each finger joints [3, 5]. Independent joint control allows the device to adjust the finger pose for different objects to grasp, while increasing the complexity and the overall cost of the design. Utilizing a single actuator to move a single finger through the force transmission over adjustable links to impose different ratios between the finger joints decreases the design complexity and the device cost [4, 8, 9]. The adjustability for different objects require mechanical adjustments based on the information about the object to be grasped. Yet, these devices are low cost, portable and simple mechanisms to be used. Underactuation is an approach to achieve automatic adjustability for object size and shape using a single actuator. The underactuated devices simply move the finger joints based on the contact forces between the finger and the object to be grasped [2]. Since the number of controlled joints are higher than the number of actuators in underactuation, the undersensing of the approach prevents the finger joints to be measured during operation.

In this work, we present a novel underactuated hand exoskeleton utilized with an additional potentiometer in order to achieve automatic adjustability for the grasping objects while estimating the pose of the finger joints. The direction of the forces between the device and the finger is ensured to be normal to the finger phalanges with the motivation of improved realism during grasping tasks. Thanks to the linearly actuated linkage-based design, the mechanism is highly wearable and portable. The underactuation property controls the finger based on the contact forces, which allows the final pose to be adjusted by the shape and the size of the grasping object. To calculate the pose of the finger during operation, the measurements of the actuator and an additional potentiometer, which has been utilized at one of the passive joints of the mechanism. Furthermore, this additional sensor can be used to calculate the length of the first finger phalange, which is crucial for operation, in a pre-determined pose of the finger to improve the performance of the joint estimation.

The paper continues as follows: Sect. 2 introduces the characteristics of the design while Sect. 3 details the pose analysis. Section 4 presents the multi-finger implementation of the proposed device, joint estimation and a calibration procedure to estimate the finger sizes. Finally, Sect. 5 discusses the outputs and the future work.

2 Device Characteristics

Even though the human fingers have 4 Degrees of Freedom (DoFs) mobility with 3 joints, controlling the metacarpophalangeal (MCP) and the proximal interphalangeal (PIP) joints is sufficient for the grasping tasks. A generic hand exoskeleton should be comfortable, easily worn and efficient to transmit forces to the finger phalanges during operation. Moreover, the adjustment for the hand sizes and the grasping objects would increase the performance and the usability of the device. These requirements

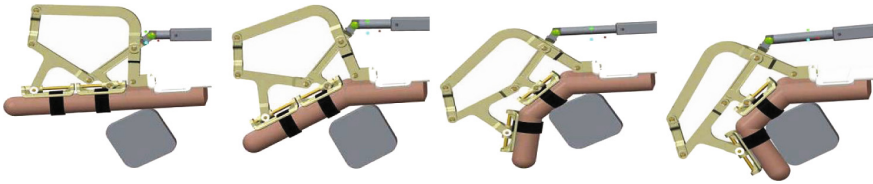


Fig. 1 The underactuation concept for grasping tasks

can be achieved by the kinematics decisions on the finger components of the hand exoskeleton.

The self-adjustability for the finger sizes might be achieved by assuming the finger as a part of the kinematic chain [7]. Not aligning the finger and the mechanical joints increase the safety of the force transmission as well as the finger size adjustability. Placing the device above the fingers allows the user to grasp real objects. The device exerts only normal forces to the finger phalanges during operation in order to prevent the tangential forces to be applied. The direction of the applied forces on the finger phalanges are limited through the connection links using a cylindrical joint and a rotational joint with perpendicular axis (see Fig. 2). Since the tangential forces move the passive sliders, the connection between the user and the device can be secured using simple straps.

Underactuation [6] controls multiple joints with a single actuator by adjusting the grasping tasks based on the objects with various shapes and sizes in a stable manner. Figure 1 presents the steps of the proposed hand exoskeleton performing a grasping task. In particular, the actuator starts to move the MCP joint, applying forces on the proximal phalange until the first finger phalange gets in touch with the grasping object. Then, the actuation is transferred through the mechanical links to the intermediate phalange to move the PIP joint; until the grasping is completed by flexing both joints. For opening the hand, the actuation starts to move the PIP and MCP joints in this order until both joints are completely extended to their physical limits. The proposed mechanism does not move the finger joints individually or with a predefined relation, but applies forces on the phalanges to open/close the hand while the relation between the finger joints are set by the contact forces automatically with no prior knowledge of the size and shape of the grasping object.

3 Pose Analysis

Figure 2 shows the design of the proposed linkage-based underactuated mechanism with the joints and the defined points superimposed on its CAD model. A linear actuator is attached to the device at point A with the corresponding displacement lx and to the base at point N . The MCP and the PIP joints are defined as points L and M respectively, with the displacements as q_{o1} and q_{o2} . The mechanism consists of

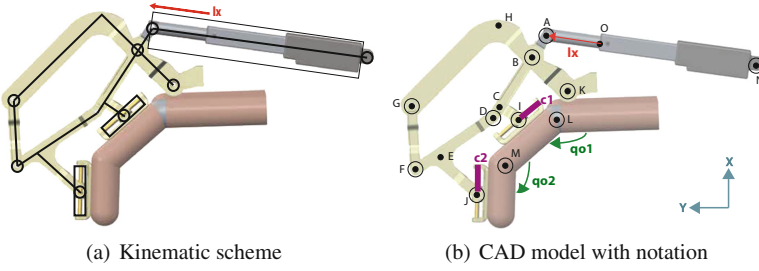


Fig. 2 CAD model and kinematic scheme of one finger device

9 passive revolute joints at points $A, B, D, F, G, I, J, K,$ and N , with the rotations q_i defined for the point i . The points I and J are the intersection points between the sliders attached to the finger phalanges with linear displacements c_1 and c_2 . The points C, E and H provide perpendicular connection between links. Finally, the point O shows the position of point A when the actuation stroke lx is zero.

Extra DoF introduced by the underactuation allows the finger joints to perform a constrained movement when the actuator is locked. Such extra mobility prevents the unique solution for the finger pose to be achieved using only the actuator displacement. To measure this extra mobility, an additional sensor has been utilized on one of the passive joints on the mechanism such that the finger pose can be calculated using two sensory measurements. In this work, the joint to be measured has been selected as q_B , since it is close to the base and it performs a wide range of rotation.

The whole mechanism can be defined using the sensory measurements $\{q_B, lx\}$, and 8 unknown parameters as $\{q_{o1}, q_{o2}, c_1, c_2, q_D, q_G, q_K, q_N\}$. Even though there are other passive revolute joints that perform rotation during operation as $\{q_A, q_F, q_I, q_J\}$, their rotations are not required to define the device configuration since they are constrained by the previously stated parameters. To find a unique solution for these 8 unknowns, 8 independent equations are obtained using the X and Y components of 4 loop equations as described in Fig. 3, where the loops between *Loop1* and *Loop4* show the vector chains along the mechanical links. In the equations, the notation \vec{r}_j^i is used to indicate the vectors connecting point i to point j , while q_k signifies the rotation along the point k . The proposed equations are used to calculate 8 unknowns numerically due to their nonlinearity.

$$\vec{r}_A^O + \vec{r}_B^A + \vec{r}_K^B + \vec{r}_N^K = \vec{0} \quad (1)$$

$$\vec{r}_B^K + \vec{r}_C^B + \vec{r}_I^C + \vec{r}_L^I + \vec{r}_K^L = \vec{0} \quad (2)$$

$$\vec{r}_B^K + \vec{r}_D^B + \vec{r}_E^D + \vec{r}_J^E + \vec{r}_M^J + \vec{r}_L^M + \vec{r}_K^L = \vec{0} \quad (3)$$

$$\vec{r}_H^B + \vec{r}_G^H + \vec{r}_F^G + \vec{r}_D^F + \vec{r}_B^D = \vec{0} \quad (4)$$

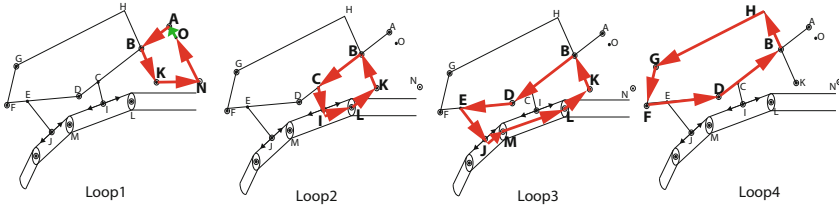


Fig. 3 Kinematic loops

The loops above have been chosen such that one cannot be obtained using the others among *Loop1–Loop4*. Furthermore, each loop provides at least one unique unknown parameter that is not covered by other loops as $\{q_N\}$ in *Loop1*, $\{c_1\}$ in *Loop2*, $\{c_2, q_{o2}\}$ in *Loop3* and $\{q_G\}$ in *Loop4*. The existence of these unique parameters can be stated as a proof of independency of the loop equations. Even though the loops above can be chosen in a different manner as well, the simplest paths have been chosen to satisfy the purpose of the loop.

4 Multi-Finger Exoskeleton

The first prototype of the hand exoskeleton has been produced by a 3D printer, such that the device is low-cost and light-weight. Firgelli L16 linear motors with 50 mm linear stroke for each finger have been placed on top of the hand without causing fatigue during operation. Table 1 presents the mechanical specifications of the device and the actuators.

Thanks to the strap based connection, the device can be worn in less than a minute, with no initial requirement about the pose of the human hand. Figure 4 shows the hand exoskeleton that is connected to the index, middle and ring fingers separately. During the grasping tasks, the thumb is left passive and the little finger is attached to the ring finger from the proximal phalanges by the straps. The control of the device is performed by a Delfino board with 1 kHz frequency to ensure the stability. The

Table 1 Specifications of the proposed exoskeleton and its actuators

Property	Value	Property	Value
RoM for MCP	80°	RoM for PIP	90°
Motor gear ratio	35:1	Stroke of the motor	50 mm
Max. cont force of the motor	40 N	Backdrive force	31 N
Max. torque on MCP	1485 Nmm	Max. torque on PIP	434 Nmm
Device Mass	≈300 g	Max. velocity	32 mm/s

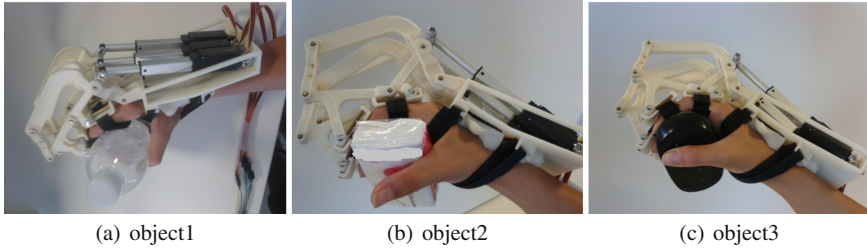


Fig. 4 The grasping by the multi-finger hand exoskeleton

ADC pins of the board is used to read the sensory measurements, while PWM pins run the motors through the Pololu motor driver carrier.

The feasibility of the device has been tested through the grasping tasks with various objects using a simple position control. Figure 4 shows that the users can grasp various objects with different sizes and shapes with no preliminary knowledge about the object.

4.1 Estimation of Finger Joints

In order to estimate the finger pose during operation, a low-cost, lightweight potentiometer (BOURNS 3382G-1-103G) has been utilized on each finger component. Thanks to its small size and the mounting type, it can be implemented on the mechanism easily without causing any mechanical interference and increasing the total weight as in Fig. 5a.

Figure 5b presents a scheme of the pose analysis described in Sect. 3 to estimate the finger joints during grasping tasks. The sensory measurements (l_x and q_B) and arrays of mechanical and anatomical constants (k_{mec} and k_{act}) are used to calculate the finger pose q_{o1} and q_{o2} along other passive unknowns q_{pas} using the nonlinear

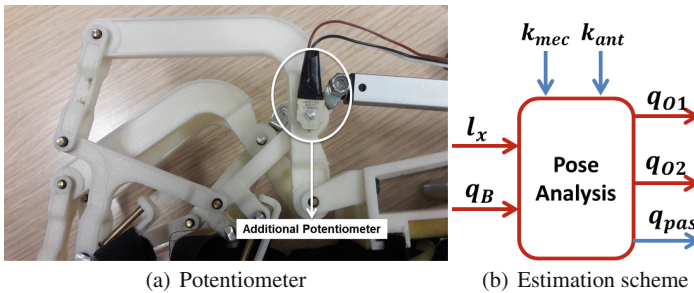


Fig. 5 Utilization of additional potentiometer for joint estimation

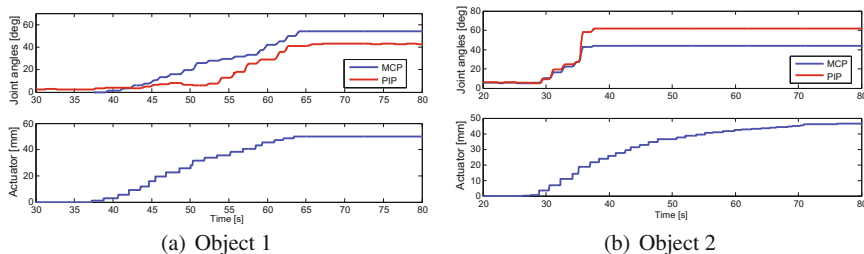


Fig. 6 Joint estimations while grasping different objects

equations (Eqs. (1)–(4)) simultaneously. In particular, k_{mec} describes the mechanical link lengths, while k_{act} is about the finger lengths and the location of the device attached to the finger.

Since grasping different objects require the adjustability of different relations between MCP and PIP joints, the joint estimation has been performed during the grasping tasks of real objects with various size and shapes. Figure 6 shows the MCP and PIP joint estimations, with the corresponding actuator displacement. Different relation between the MCP and PIP joints represent different grasping tasks. The second object to grasp has bigger size than the first object, therefore the finger joints reach their final states sooner and the actuator does not reach its physical limit.

4.2 Calibration for Finger Size

Since the finger phalanges are accepted as a part of the mechanism, the length of the finger phalanges acts as a significant parameter for the operation performance as well as the active workspace of the finger joints. Even though manually measuring the length of the first finger phalange might be the solution, it can be calculated by implementing additional sensors as well. Since the passive linear displacement on the second phalange and the proximal phalange length cause singularity when the PIP joint is fully extended, the proximal phalange length cannot be calculated during operation even if one more potentiometer is utilized for such estimation simultaneously.

In this work, an offline calibration process has been developed to estimate the phalange length when c_2 measurement are assumed to be maximum and the actuator displacement is kept constant as 42 as in Fig. 7a. Figure 7b represents the calibration scheme, where c_2 is a constant with its maximum range and l_{LM} represents the length of the proximal phalange, while l_x and q_B are the sensory measurements.

The calibration scheme has been tested on a single user on index finger only and its finger length has been measured as 49.19 mm, while the measurements with a ruler gave the result of 48.32 mm with an error rate of 1.77%. It is important to note

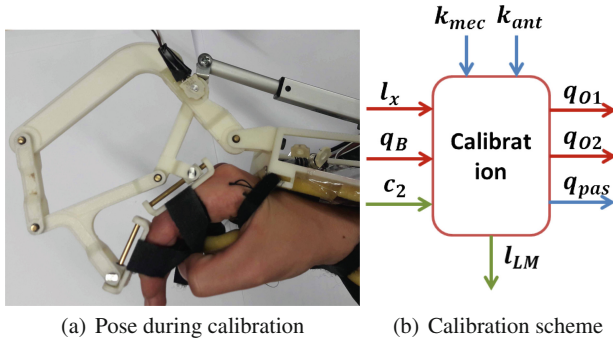


Fig. 7 Calibration for finger size

that since the initial guess and the pose of the finger should be close to each other, the initial guesses for the passive joints should be determined carefully in order to increase the efficacy of the analysis.

5 Conclusion and Future Work

In this paper, we have presented a novel, underactuated hand exoskeleton that performs flexion/extension for grasping tasks of various objects, while exerting only normal forces to the finger phalanges. The linkage based design is portable, wearable and possible to extend the finger component for multiple finger implementation. The first prototype of the hand exoskeleton has been manufactured for index, middle and ring fingers. The preliminary tests show that the device can be adjusted to the users with different hand sizes, as well as to assist grasping tasks for different objects in terms of size and shape, without any prior information. Implementing an additional potentiometer allows the MCP and PIP joints of the finger to be calculated using the pose analysis of the mechanism, as well as the length of the proximal finger phalanges with an initial requirement of the finger pose.⁹

In the future, the thumb and little finger components will be completed in order to achieve five-fingered hand exoskeleton. The backdriveability is aimed to be achieved by control in order to move the exoskeleton freely while attached to the user's hand. Regarding the adaptability of the device by different hand sizes, further experiments are required to understand the achieved workspace by each user. Currently, an integration between the virtual environment and the device is being implemented.

Acknowledgments This research was been funded from the project “WEARHAP WEARable HAPTics for humans and robots” of the European Union Seventh Framework Programme, grant agreement n 601165 and the EU Horizon2020 project n. 644839 CENTAURO.

References

1. Aubin P, Sallum H, Walsh C, Stirling L, Correia A (2013) A pediatric robotic thumb exoskeleton for at-home rehabilitation: the isolated orthosis for thumb actuation (IOTA). In: IEEE international conference on rehabilitation robotics (ICORR). pp 1–6 (2013)
2. Ertas IH, Hocaoglu E, Patoglu V (2014) AssistOn-Finger: an under-actuated finger exoskeleton for robot-assisted tendon therapy. *Robotica*
3. Hasegawa Y, Tokita J, Kamibayashi K, Sankai Y (2011) Evaluation of fingertip force accuracy in different support conditions of exoskeleton. In: IEEE international conference on robotics and automation (ICRA). pp 680–685
4. Iqbal J, Tsagarakis NG, Caldwell DG (2014) Human hand compatible underactuated exoskeleton robotic system. *Electron Lett* 50(7):494–496
5. Jones C, Wang F, Morrison R, Sarkar N, Kamper D (2014) Design and development of the cable actuated finger exoskeleton for hand rehabilitation following stroke. *IEEE/ASME Trans Mechatron* 19(1):131–140
6. Laliberte T, Birglen L, Gosselin C (2002) Underactuation in robotic grasping hands. *Mach Intell Rob Control* 4(3):1–11
7. Leonardi D, Barsotti M, Loconsole C, Solazzi M, Troncossi M, Mazzotti C, Parenti Castelli V, Procopio C, Lamola G, Chisari C et al (2015) An emg-controlled robotic hand exoskeleton for bilateral rehabilitation
8. Nycz CJ, Btzer T, Lambercy O, Arata J, Fischer GS, Gassert R (2016) Design and characterization of a lightweight and fully portable remote actuation system for use with a hand exoskeleton. *IEEE Robot Autom Lett* 1(2):976–983
9. Taheri H, Rowe JB, Gardner D, Chan V, Gray K, Bower C, Reinkensmeyer DJ, Wolbrecht ET (2014) Design and preliminary evaluation of the FINGER rehabilitation robot: controlling challenge and quantifying finger individuation during musical computer game play. *J NeuroEng Rehabil* 11(10):1–17

Standard and Natural Motion Protocols for the Kinetic Measurements of the Squat

Nicola Sancisi, Marco Cocconcelli, Riccardo Rubini
and Vincenzo Parenti-Castelli

Abstract Two motion protocols that describe the sequence of movements to be complied with by a subject to perform a controlled squat are presented. The protocols are intended to be used in gait analysis to obtain repeatable and reproducible results that can be compared among different studies. The first protocol (“standard”) is closer to other studies in the literature, in order to improve comparison with previous experimental results. The second protocol (“natural”) reproduces a squat movement more similar to natural conditions, also allowing a deeper knee flexion. The two motion protocols are tested by a volunteer on a gait lab. Results of experimental tests in terms of joint and foot-ground angles, ground reaction force and centre of pressure show the characteristics of the standard and natural squat, and the repeatability of the tests.

Keywords Gait analysis • Squat • Motion protocols

1 Introduction

In gait analysis, a protocol is defined as a to-do list for the initial setup, the execution of the tests, and the post-processing of the data, in order to obtain repeatability of experimental measurements. For example, a protocol defines the position of the markers on the patient body, the measurement technique, the defi-

N. Sancisi · V. Parenti-Castelli
University of Bologna, Bologna, Italy
e-mail: nicola.sancisi@unibo.it

V. Parenti-Castelli
e-mail: vincenzo.parenti@unibo.it

M. Cocconcelli (✉) · R. Rubini
University of Modena and Reggio Emilia, Modena, Italy
e-mail: marco.cocconcelli@unimore.it

R. Rubini
e-mail: riccardo.rubini@unimore.it

inition of the local reference systems, the motion task and how it is performed (hereinafter referred to as the motion protocol). For some motion tasks, such as the walking [1], different protocols were proposed but the motion protocol is almost standardized. Conversely, other tasks do not even have a standard motion protocol. The squat, which is the movement a subject does when he/she gets down from a standing position without moving the feet, is one of these. This is a common and important task: it features high flexion angles (namely, large femur-tibia relative rotations about a medial/lateral axis) and it is demanding for the subject. However, the literature clearly shows a lack of standardization in the definition of the squat. Dionisio et al. [2] defined two squat movements: in the semi-squat the subject starts from a straight position, bends the knees to 40° and then stops; the half squat is the same movement but maximum flexion angle is 70° . Hollman et al. [3] proposed a single leg movement, since the patient stands on a single leg and performs the movement. Nagura et al. [4] defined the squat as a deep flexion similar to kneeling: the subject knees rest on the ground at the end of the movement. Four different movements are proposed which significantly differs from the other protocols. Kongsgaard et al. [5] studied the differences in the squat on a flat or inclined (25°) surface.

These motion protocols optimize the acquisition of specific data, but the subject natural movement is sacrificed, since it is far from everyday life. Moreover, most of these protocols do not reach deep flexion, that is an important characteristic of squat. This paper proposes two motion protocols, namely “standard condition protocol” (SCP) and “natural condition protocol” (NCP), for the study of the squat. Both are developed in this study to maximize the repeatability and the standardization of the tests, and to reach high flexion angles. The two protocols are performed by a subject and results are presented.

2 Methods

2.1 Protocols

The SCP and NCP are presented in this Section. The SCP favors repeatability and comparison with results in the literature. The NCP makes the movement as close as possible to everyday life, while maintaining the repeatability of the trial. Moreover, the SCP allows a maximum knee flexion of approximately 90° , while in the NCP a higher knee flexion can be reached, approximately 120° – 140° .

Motion is measured by skin markers, while ground forces by two force platforms. The subject stands on the two force platforms, a foot on each platform. The complete squat cycle comprises a descent and ascent phase.

The SCP requirements are listed below:

1. Initial position

- the subject stands up with parallel feet
- the legs are slightly apart
- the feet are in full contact with the ground
- the arms are extended along the anterior part of the body

2. Squat movement

- the arms remain extended, while the hands move along the legs and are placed on the knees at the end
- the feet are always in full contact with the ground
- the descent phase ends when the femur and tibia form a 90° angle
- the ascent phase is similar, but is performed in reverse and ends with the subject in the straight position.

Figure 1 shows the initial and final position of the body for the SCP protocol.

The NCP requirements are listed below:

1. Initial setup position

- the subject stands up with his feet forming an angle of 20° – 30° with respect to the anterior direction of the body
- the legs are slightly apart
- the feet are in full contact with the ground
- the arms are extended along the body

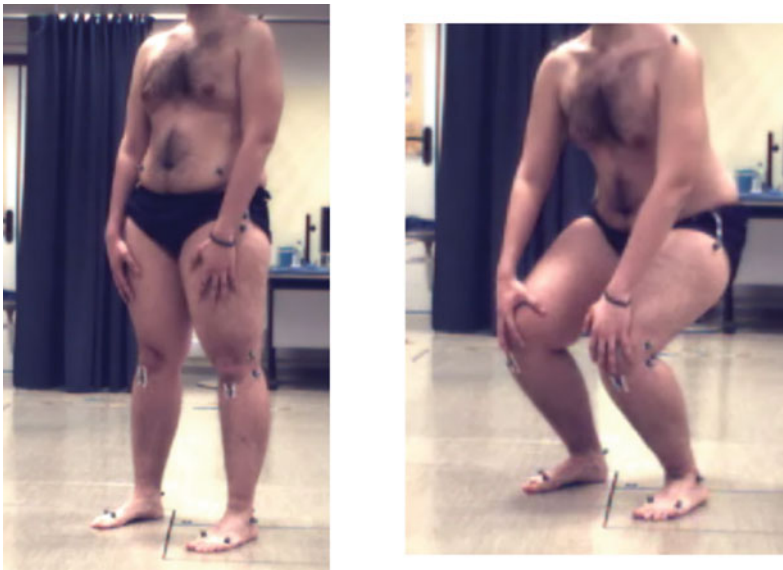


Fig. 1 SCP: initial (on the *left*) and final (on the *right*) position

2. Squat movement

- the torso remains approximately vertical
- the hands move along the legs and are placed on the knees at the end; at this position, hands are rotated facing one towards the other, while the arms are slightly flexed
- the torso remains approximately vertical
- during movement, the subject raises the heels and remains on tiptoes
- the descent phase ends at the lowest possible position
- the ascent phase is similar, but is performed in reverse and ends with the subject in the straight position.

Figure 2 shows the initial and final position of the body for the NCP protocol.

2.2 *Experimental Analysis*

Experimental tests on a volunteer were performed in a gait analysis laboratory by means of an optoelectronic system (Vicon Motion Systems Ltd) with six infrared cameras, passive markers and two force platforms (AMTI OR6). The markers were placed on the subject body according to the Total3Dgait protocol [1]. Each trial consisted of one squat cycle; each trial was repeated three times for the SCP and three times for the NCP.



Fig. 2 NCP: initial (on the *left*) and final (on the *right*) position

Experimental data were post-processed to obtain the knee and ankle flexion angles, the angle of foot with the ground, the ground reaction force (GRF) and the centre of pressure (COP). In particular, a global reference system had horizontal plane parallel to the ground, while a foot reference system was obtained from the foot markers, namely the markers on the calcaneus (P1), on the fifth (P2) and on the first (P3) metatarsal heads and the mid-point (P4) between P2 and P3. In particular, these points were projected on the global horizontal plane (P1*, ..., P4*) and the foot reference system was defined with origin P1*, anterior axis connecting P1* and P4*, medial axis on the horizontal plane, orthogonal to the anterior axis, pointing medially, vertical axis orthogonal to the horizontal plane, pointing up (coincident with the global vertical axis). Thus, the left and right foot reference systems are left and right handed respectively. The GRF and COP were represented with respect to the foot reference system. The foot-ground angle was the angle between the segment P1–P4 and the horizontal plane, offset by the same angle at the initial position. Flexion angles were defined according to the Total3Dgait protocol. The forces were scaled on the patient’s weight, while time was scaled on each cycle duration.

3 Results

Only results of left leg are presented for the sake of conciseness. The knee, ankle and foot-ground angles are shown in Fig. 3. The latter is always equal to zero during SCP, since the feet remain in contact with the ground, so it is not represented. In Fig. 3 the curve color represents a different trial repetition. Maximum knee flexion is significantly higher for NCP and reaches 150°. Maximum ankle

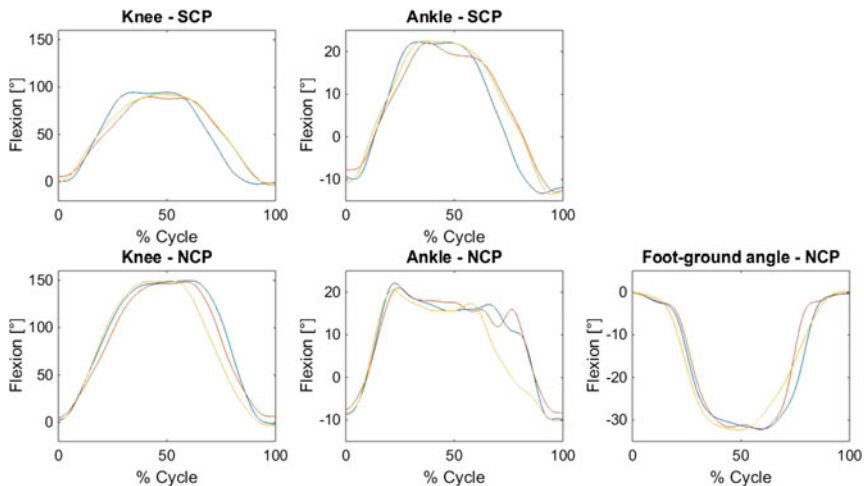


Fig. 3 Comparison of the flexion angles for the SCP and NCP in the *left* leg

flexion is similar for NCP and SCP: the ankle reaches maximum dorsiflexion in both cases, but during NCP the foot flexes and contributes to increase shank angle with the vertical axis, allowing a deeper knee flexion.

GRF components are shown in Fig. 4. The curve color represents a different trial repetition, as used in Fig. 3. GRF is prevalently vertical, pointing medially and posteriorly. Only a few significant differences are noticed between the two movements: a peak at 60 % of cycle for the vertical component of NCP, corresponding to the start of ascending phase (inertial force), and a greater posterior component for NCP.

COP trajectory on the foot is shown in Fig. 5. For both protocols, the COP trajectory is a closed curve with a significant difference between the ascending and descending phase. However, this curve is about the foot centre during SCP, but it extends forward and closer to foot fingers during NCP: this is the effect of foot flexion during movement.

In general, the two protocols were easily repeated by the volunteer after a few free trials. A visual inspection of the material recorded during the test shows very similar movements for all repetitions of each protocol. This qualitative analysis is confirmed quantitatively by the results: all curves look similar over different repetitions. The only significant difference is timing, that was not strictly controlled during each cycle. For instance, the standard deviation for the second peak value of the ankle flexion angle (60–80 % Cycle) is 1.7° and 1.0° for SCP and NCP respectively, but standard deviation between NCP curves at the same instant (e.g., 80 % Cycle) reaches 8.2° for NCP. A first possibility to improve this aspect is to better instruct the volunteer on a specific time sequence or to help him by beating the time, at the risk of a less natural movement of the subject. A second possibility is to choose a different parameter to represent different movements (such as the

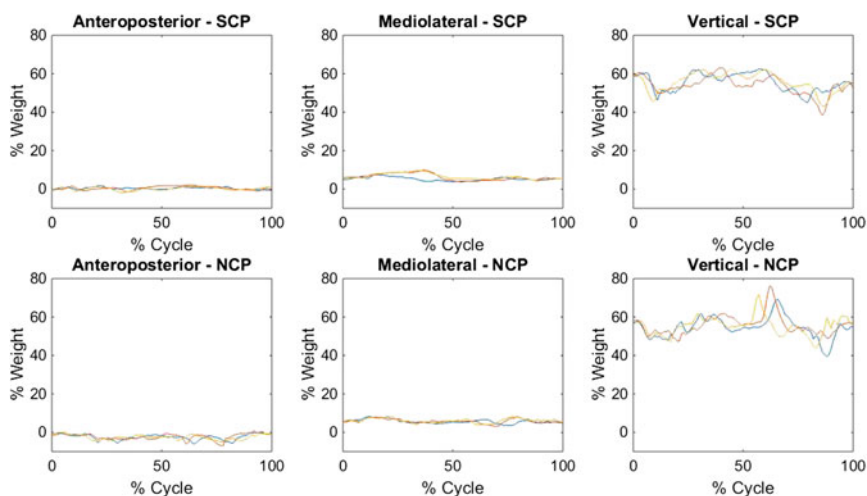


Fig. 4 Comparison of the ground forces for the SCP and NCP in the *left* leg

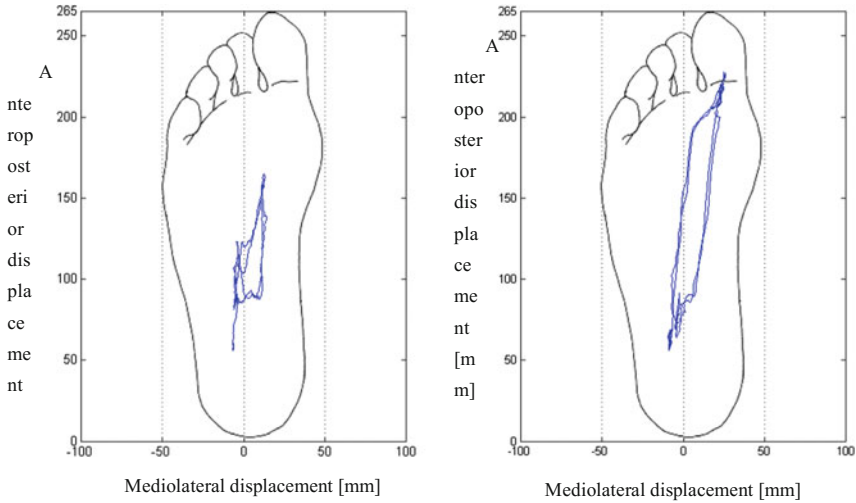


Fig. 5 Different COP trajectories for the standard (*left*) and natural (*right*) protocols

knee flexion angle) or to divide the recorded motion into several events that are synchronized for all repetitions, at the risk of biased data since speed of each test phase influences the results (GRF in particular) due to different inertial forces.

4 Conclusions

Two new protocols for the squat analysis are proposed in this paper. The “standard condition protocol” is developed to maximize the standardization and the repeatability of measurements, also with respect to previous studies in the literature. The “natural condition protocol” maintains the repeatability of the test but, in addition, is closer to the natural squat movement and allows a deeper knee flexion, that is one of the peculiar characteristics of the squat. Experimental measurements were performed in a gait analysis lab on a volunteer. The protocols were well accepted and easily learned by the subject. Results show repeatability over several trials and allow the analysis of the joint and foot-ground angles, of the ground reaction force and of the centre of pressure even at deep flexion. Timing could be improved, depending on the application of the data.

Acknowledgments The authors want to acknowledge Dr Alberto Ferrari, for his help during experimental measurements.

References

1. Ferrari A et al (2008) Quantitative comparison of five current protocols in gait analysis. *Gait Posture* 28:207–216
2. Dionisio VC et al (2008) Kinematic, kinetic and EMG patterns during downward squatting. *J Electromyogr Kinesiol* 18:134–143
3. Hollman JK et al (2014) Frontal and transverse plane hip kinematics and gluteus maximus recruitment correlate with frontal plane knee kinematics during single-leg squat tests in women. *Clin Biomech* 29:468–474
4. Nagura T et al (2002) Mechanical loads at the knee joint during deep flexion. *J Orthop Res* 20:881–886
5. Kongsgaard M et al (2006) Decline eccentric squats increases patellar tendon loading compared to standard eccentric squats. *Clin Biomech* 21:748–754

Design and Simulation of an Assisting Mechanism for Arm Exercises

**B. Chaparro-Rico, D. Cafolla, M. Ceccarelli
and E. Castillo-Castaneda**

Abstract A conceptual design of a novel mechanism is proposed to assist the training exercises for the human arm. The proposed mechanism is based on a mechanism of 2 degrees of freedom whose workspace has been amplified by using a pantograph mechanism. The proposed assisting mechanism can reproduce any trajectory for arm exercise within a large suitable space in a horizontal plane. Two configurations of the mechanism are presented with the conceptual features. Analysis of the displacement, velocities, accelerations and torques are worked out to compare two possible configurations and to characterize the mechanism solution as the feasible one for future developments.

Keywords Mechanical design · Dynamics simulation · Arm · Exercise device

1 Introduction

The human arm is essential to perform tasks of daily living and the exercises to human arm motion are imperative to keep up its health. Physical fitness of the arm prevents its early fatigue, damage, injury or disease. The human arms exercises are generally focused on amplify the range motion of the joints, strengthening and lubrication of the joints, flexing and extending of the muscles and the joints [13].

B. Chaparro-Rico (✉) · D. Cafolla · M. Ceccarelli
University of Cassino and Southern Latium, Cassino, Italy
e-mail: betsychaparro@hotmail.com

D. Cafolla
e-mail: cafolla@unicas.it

M. Ceccarelli
e-mail: ceccarelli@unicas.it

B. Chaparro-Rico · E. Castillo-Castaneda
National Polytechnic Institute – CICATA, Qro, Santiago de Querétaro, Mexico
e-mail: ecast63@yahoo.com

Several devices have been developed to assist the human arm exercises. However, the existing portable mechanisms cover a small workspace and offer only few typologies of exercises [1, 6, 15]. Other existing mechanisms have a large workspace but they are very difficult to transport, difficult to construct and the user-mechanism interaction is more invasive [2, 10, 11]. The proposed mechanism offers multiples advantages in a single apparatus: ability to reproduce multiple exercises into a large workspace; easy to replicate; the user-mechanism interaction is less invasive; the mechanism is portable and compact regarding to the large workspace that the mechanism should cover, among others.

2 Human Arm and Exercise Motion

Figure 1a shows a representation of the human arm that is composed by an upper arm, a forearm and a hand. The shoulder, the elbow and the wrist allow the human arm motion around the axes 1–7. The shoulder has three degrees of freedom (DOFs), the elbow two and the wrist two [8]. The workspace of the arm motion on the horizontal plane has worked up to follow training exercises, Fig. 1b; the space estimation has been calculated using averages of anthropometric parameters [7, 12]. The arm workspace has a maximum height of 667.5 mm and a maximum width of 1335.0 mm. However, one exercise has been selected in order to test the mechanism. The exercise consists of tracing the “figure of the number 8” with a tracing point of the hand, Fig. 1c. The exercise involves coordinated motions of the shoulder and the elbow. Since the proposed mechanism is a manipulator, the end-effector will be attached to the tracing point of the hand during the training; the patient’s hand will grasp the end-effector which will perform the desired rehabilitation trajectory together with a proper motion of the arm. Therefore, Cartesian parameters X and Y versus time of the path to tracing the “figure of number 8” have been obtained by using a database previously generated experimentally [5].

3 Conceptual Design

According to the human arm exercises feasible into the workspace in Fig. 1b, two degrees of freedom (DOFs) has been needed to control the Cartesian Components X and Y . A 5-bar mechanism of 2 DOFs has been selected, Fig. 2a. The L_1, L_2, L_3, L_4 are mobile links and the point E correspond to the end-effector position. L_5 is the fixed frame link of the mechanism. The active joints of the mechanism are the joint that connects L_1 to the fixed link L_5 , and the joint that connects L_4 to the fixed link L_5 . The angular displacements of the active joints have been delimited from 0° to 180° to avoid singularities. In addition, the mobile links have been considered symmetrical to obtain a larger workspace [3, 9]: $L_1 = L_2 = L_3 = L_4$. The workspace and link sizes of the 5-bar have been calculated by using the inverse

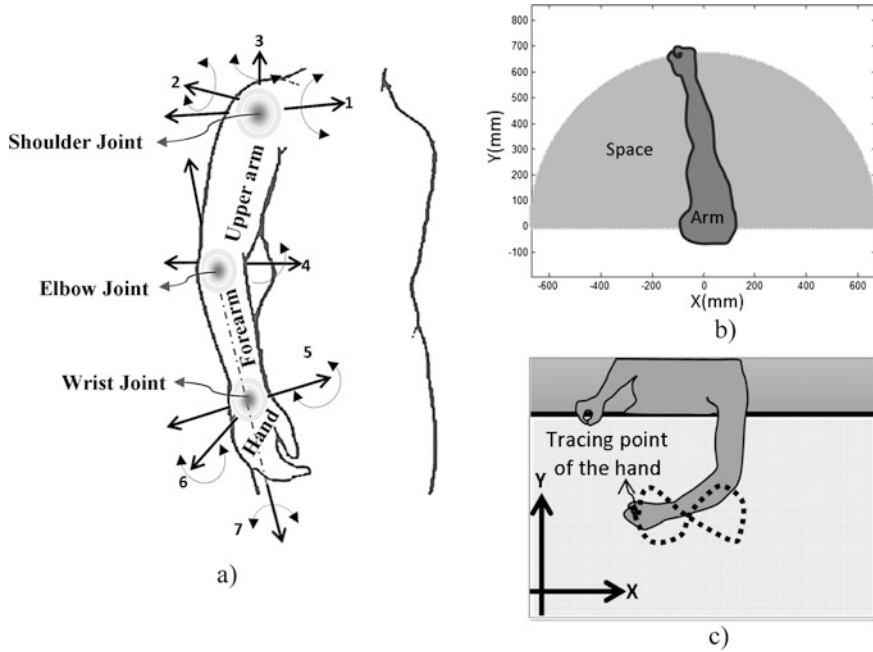


Fig. 1 Human arm and exercise motion: **a** Anatomy and principal parameters of motion [8]; **b** Workspace of the human arm motion on *horizontal* plane; **c** Illustrative drawing to tracing the “figure of number 8”

kinematic [4]. However, link lengths should be equal to 720 mm to cover the required workspace which are too large dimensions, therefore a pantograph mechanism has been considered in order to amplify the workspace and thus to use

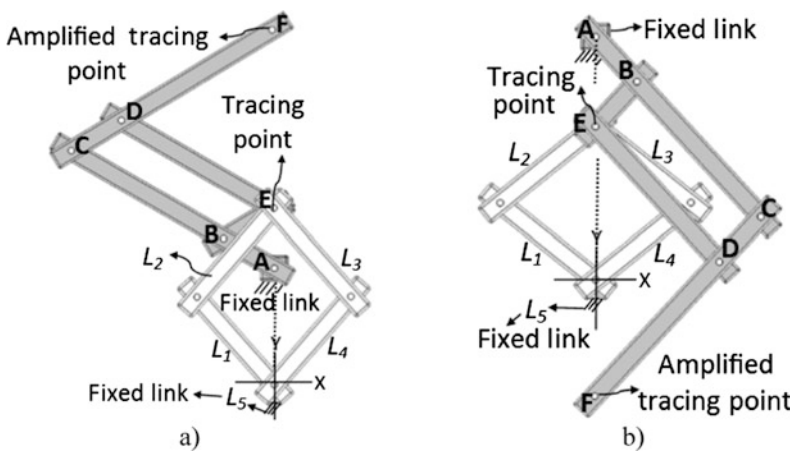
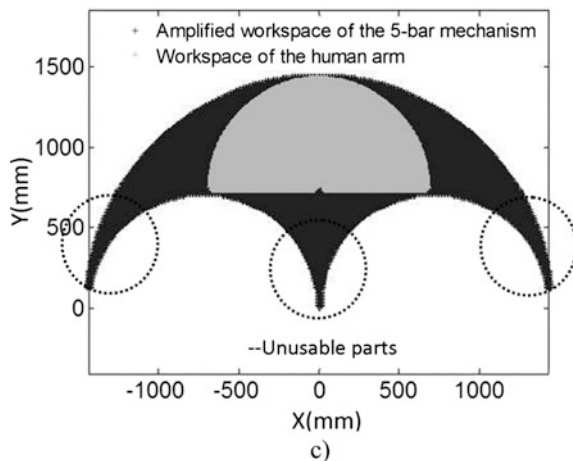


Fig. 2 Proposed solutions for the mechanism: **a** Solution A; **b** Solution B

Fig. 3 Amplified workspace of mechanism versus workspace of the human arm



smaller links, Fig. 2a. The point E traces the desired trajectory while point F traces the amplified trajectory. The amplification scale is obtained from distances: AC/AB . The pantograph should have the following dimensional relations: $BE = CD$; $BC = ED$ and $AC = CF$ [14]. A reduction scale $\times 1/4$ has been applied to the 5-bar, obtaining a length of 180 mm for each link. Therefore, the calculated distances to the pantograph are: $AB = BE = CD = 90$ mm; $BC = ED = 270$ mm; $AC = CF = 360$ mm. A solution A in Fig. 2a and a solution B in Fig. 2b have been proposed. In solution A, the amplified tracing keeps the same orientation; the fixed link of the pantograph has been attached under the workspace of the tracing point. In the solution B, the amplified tracing is rotated 180° ; the fixed link of the pantograph has been attached above the workspace of the tracing point. The solutions A and B provide the same workspace with different orientation. The tracing point of the pantograph has been attached to the end-effector of the 5-bar for both solutions A and B.

For the computation of the angular displacement of the active joints, X and Y axis in Fig. 2a and b have been taken as reference coordinates system respectively for solution A and solution B. The Zeros of the angular displacements related to the active joints begin aligned to Y axes and it is a counter-clockwise system. Figure 3 shows the amplified workspace versus the workspace of the human arm.

4 A Numerical Characterization via Simulation

The solutions A and B have been tested to evaluate their feasibility and to choose the most suitable one for the target application. The target of this study is to make the mechanism portable, low-cost and fairly easy to use. Both solutions have been simulated in ADAMS environment to run the chosen exercise. Since the trajectory

is complex enough to test the feasibility of the mechanism in terms of angular displacement, angular velocities, angular accelerations and the torques of the two motors that actuate the mechanism. A 1060 aluminium alloy with mass density of 2700 kg/m^3 has been chosen in the simulation environment. Each simulation considers the gravity and the friction between components. Body contact parameters have been assumed as: dynamic friction velocity $v_k = 10.16 \text{ mm/s}$; dynamic friction coefficient $\mu_k = 0.20 \text{ N/A}$; static friction velocity $v_s = 0.10 \text{ mm/s}$; and static friction coefficient $\mu_s = 0.25 \text{ N/A}$. In each simulation environment, the integrator step size is assumed of $1.0\text{E-}04$ with a minimum integrator step of $1.0\text{E-}11$ and a maximum integrator step of $1.0\text{E-}01$. The frames per seconds are assumed with a value of 800 to allow the solver to better compute the model behaviour. The accuracy of the simulations has been set to $1.0\text{E-}09$. Each simulation lasts 8 s as the experimental duration of the chosen exercise. Figure 4 shows the CAD designs for the solutions. In both solutions, a force F_a of 37 N has been applied acting on the point F, according to Fig. 2, simulating the average weight of the arm [7], Fig. 4. The acting forces are important to estimate the Stiffness of the mechanism and the torques needed by the actuators as real as possible. Referring to Fig. 4, v_1 is the input velocity for Motor 1 (M1) while v_2 is the input velocity of Motor 2 (M2).

The simulation of the solution A has been worked up; Fig. 5 shows some snapshots. Figure 6a shows the input motor velocities to outline the desired trajectory; v_1 has a range from $-14.75^\circ/\text{s}$ to $15.57^\circ/\text{s}$ and v_2 from $-14.55^\circ/\text{s}$ to $15.58^\circ/\text{s}$. The angular displacement in M1 has a range from 35.98° to 62.66° while in M2 from -29.20° to -63.81° , Fig. 6b. The trend of the plot shows the symmetric behavior of the mechanism. Furthermore, the computed values allow the use of commercial servo-motors. The angular accelerations have a range from $-122.42^\circ/\text{s}^2$ to $161.13^\circ/\text{s}^2$ in M1 and from $-163.69^\circ/\text{s}^2$ to $84.55^\circ/\text{s}^2$ in M2, Fig. 6c. The torque in M1 has a range from -222.71 to 130.08 N-mm and -737.05 to 467.02 N-mm in

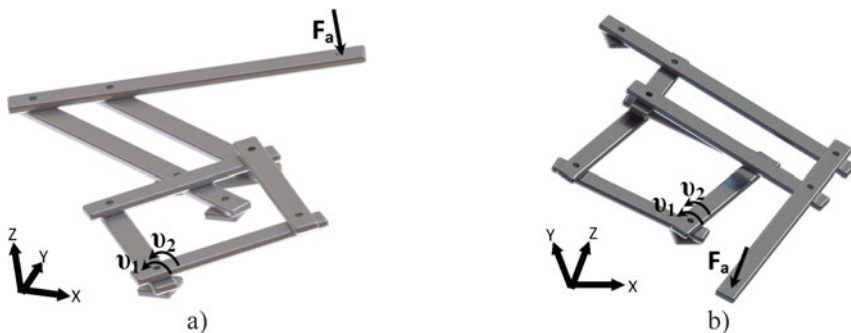


Fig. 4 CAD design, input velocities and acting force in the proposed solutions: **a** Solution A; **b** Solution B

M2, Fig. 6d. These computed torque values confirm that the use of commercial servo-motors is feasible. It is important to notice that all the computed values in angular acceleration and motor torques presents several change of direction and some spikes due to the complexity of the trajectory to trace. However, the solution A has shown a good behavior in achieving the desired objective.

The simulation of the solution B has been worked up, Fig. 7 shows some snapshots. A suitable angular velocity has been given as an input to each motor, Fig. 8; v_1 has a range from $-45.53^\circ/s$ to $63.92^\circ/s$ and v_2 from $-58.01^\circ/s$ to

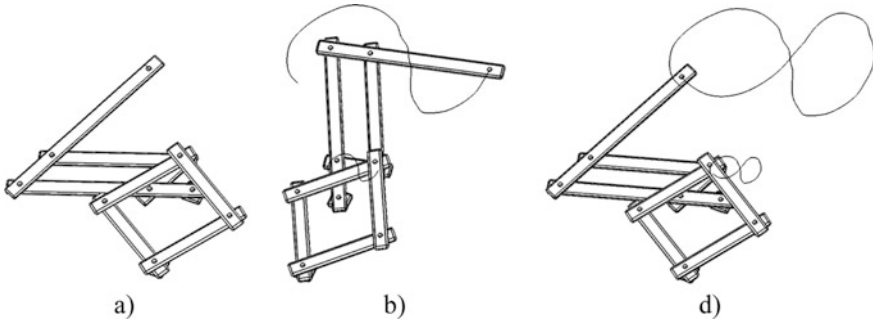


Fig. 5 Snapshots of simulation in the solution A: **a** At 0.00 s; **b** At 4.50 s; **c** At 8.00 s

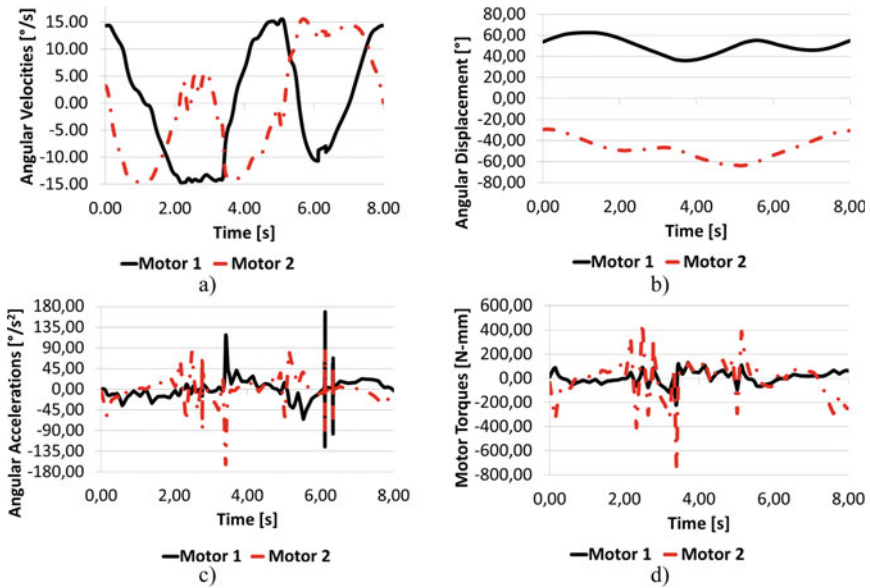


Fig. 6 Input velocities and computed results in the solution A simulation: **a** Input velocities; **b** Angular displacements; **c** Angular accelerations; **d** Motors torques

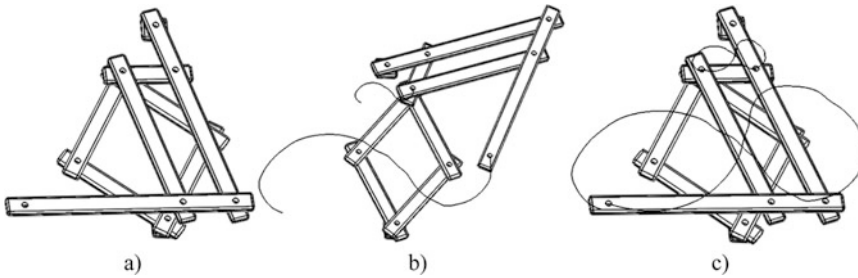


Fig. 7 Snapshots of the simulation in the solution B: **a** At 0.00 s; **b** At 3.10 s; **c** At 8.00 s

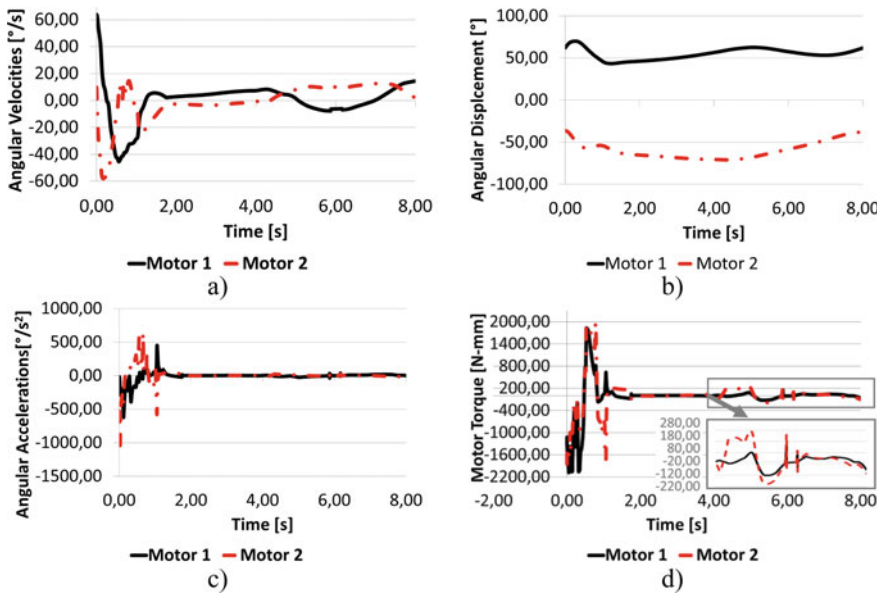


Fig. 8 Input velocities and computed results of the solution B simulation: **a** Input velocities; **b** Angular displacements; **c** Angular accelerations; **d** Motors torques

14.60°/s. The angular displacement obtained in M1 has a range from 43.45° to 70.12° while in M2 varies from -36.32° to -79.92°, Fig. 8b. The trend of the plot is similar to the solution A. Furthermore, the computed values allow the use of commercial servo-motors. The angular acceleration has a range from -622.61°/s² to 452.56°/s² in M1 while in M2 assumes values from -1077.56°/s² to 642.92°/s², Fig. 8c. It is important to notice that this solution produce higher acceleration than the solution A in the first step. However, after the first part of the trajectory the computed acceleration becomes lower than the computed acceleration in the solution A and it reduces until a constant value. The torque in M1 has a range from -2065.51 to 1832.11 N-mm while in M2 assumes values from -1903.92 to

1997.76 N-mm, Fig. 8d. It is important to notice that the computed torques values after a first step becomes smooth and low, this is a desired condition that allows the use of commercial servo-motor better than the solution A. The simulations show a better dynamic behavior for the solution B, in terms of accelerations and torques. This behavior allows the use of low-cost commercial servo-motors that can be controlled by a commercial control board such as Arduino. Furthermore, the solution B is more compact than the solution A. The mechanism in solution A can fit into a box of $(512 \times 240 \times 40)$ mm, while the mechanism in solution B can fit into a box of $(420 \times 90 \times 70)$ mm. Both solutions require a suitable space to work correctly of (1140×1395) mm; (668×1335) mm corresponds to the needed workspace for the arm motion and the remaining part is required for the mechanism motion.

5 Conclusions

A 2 DOFs mechanism has been proposed with two design solutions. Workspace analysis and dynamic simulations have been worked up for the design solutions. The mechanism workspace has been sized to cover the workspace of the human arm motion for the training exercises on a horizontal plane. In addition, since the proposed mechanism is a manipulator the user-mechanism interaction is less invasive than the exoskeletons. The two solutions show feasible designs but the solution B is more compact and the needed torques for the actuation ensures a solution for low-cost and fairly easy functioning with commercial servo-motors. Thus, the solution B will be worked for a prototype and future tests to evaluate its performances.

Acknowledgments The first author acknowledge CONACYT for the financial support during her one-year Ph.D. period of study at LARM, Cassino in 2016.

References

1. Annisa J et al (2014) Development of upper limb rehabilitation robot prototype for home setting. In: Engineering and Technology (BICET 2014) proceeding, 5th Brunei Conference, Bandar Seri Begawan, 1–3 Nov 2014
2. Ball SJ, Brown IE, Scott SH (2007) A planar 3DOF robotic exoskeleton for rehabilitation and assessment. In: Proceedings of the 29th annual conference of the IEEE EMBS Cité Internationale, Lyon, France, 23–26 Aug
3. Chaparro-Rico BDM (2014) Device for knee rehabilitation based on a parallel mechanism. Master thesis, National Polytechnic Institute (in Spanish)
4. Chaparro-Rico BDM, Castillo-Castaneda E (2016) Design of a 2DOF parallel mechanism to assist therapies for knee rehabilitation. *Ingeniería e Investigación Journal* 36(1):98–104

5. Chaparro-Rico BDM, Castillo-Castaneda E, Ceccarelli M, Cafolla D (2016) Design and test of therapy exercise for human arms. In: Proceedings of 5th international workshop on medical and service robots, Graz, 4–6 July 2016
6. Gao J, Li M, Alison G, Cui L (2015) Optimal dimensional synthesis of a symmetrical five-bar planar upper-extremity neuromotor device. *Chin J Mech Eng* 28(4):684–690
7. Hall, S. J: *Basic Biomechanics*, 6 ed, McGraw Hill, New York, 538 p (2012)
8. Kapandji I (2008) *The physiology of the joints*, vol 3. Churchill Livingstone, New York, 352 pp
9. Liu Xin-Jun, Wang Jinsong, Zheng Hao-Jun (2006) Optimum design of the 5R symmetrical parallel manipulator with a surrounded and good-condition workspace. *Robot Auton Syst* 54:221–233
10. Mao Y, Kumar-Agrawal S (2012) Design of a cable-driven arm exoskeleton (CAREX) for neural rehabilitation. *IEEE Trans Robot* 28(4):922–931
11. Moreira-Nunes W, Oliveira-Rodrigues LA, Paiva-Oliveira L, Ribeiro JF, João C (2011) Cable-based parallel manipulator for rehabilitation of shoulder and elbow movements. In: 2011 IEEE international conference on rehabilitation robotics rehab week Zurich, ETH Zurich Science City, Switzerland, 29 June–1 July 2011
12. Pineau JC, Delamarche P, Bozinovic S (2005) Average height of adolescents in the Dinaric Alps. *C R Biol* 328(9): 841–846 (in French)
13. Rippe J, McCarthy S, Abbott Waite M (2002) *The joint health prescription: 8 weeks to stronger, healthier, younger joints*. Ballantine Books, New York, 208 pp
14. Signh S (2012) *Theory of machines: kinematics and dynamics*. Pearson Education India, New Delhi, pp 209–210
15. Tommasino P, Masia L, GKC-Gamage W, Muhammad A, ML-Hughes H, Campolo C (2014) H-Man: characterization of a novel, portable, inexpensive planar robot for arm rehabilitation. In: Proceedings of 2014 5th IEEE RAS and EMBS international conference on biomedical robotics and biomechatronics (BioRob), São Paulo, 12–15 Aug 2014, pp 175–180

Part II
History of Mechanism
and Machine Science

Role of Scientific-Technical Museums in the Future of Mechanical

Alberto Rovetta and Edoardo Rovida

Abstract This paper deals with a red wire which connects the mechanisms and the historical museums and collections. Starting from the collection of mechanisms of the Politecnico di Milano, an application is described of an informatics method developed by the authors. Such method, based on neurological consideration about the management of knowledge by the human brain, realize a comparison between the interest of the potential user of museums or collections and the correspondent characteristics of the objects of the collection. The result is a classification of the exposed objects in relation to the interest of the user and, consequently, a criteria of visit.

Keywords Museums · Historical heritage · History of mechanisms

1 Today Knowledge for Growing the Science of Mechanics

Scientific Engineering faces the challenges of the new millennium with stunning methods, rich, powerful and efficient and with communication between people, between businesses, with cooperation for the theoretical knowledge, with the strength of database, with more friendly study methods. The scientific and technical knowledge of the theory of machines, mechanisms and the knowledge system projects into the future the human development also in the technique. It is a necessary basis for a more and more better quality of life. The knowledge is the fundamental basis for development, and the written statement of knowledge is entrusted to books and digital data for the numerical and technical information, and

A. Rovetta · E. Rovida (✉)
Politecnico di Milano, Milan, Italy
e-mail: edoardo.rovida@polimi.it

A. Rovetta
e-mail: alberto.rovetta@polimi.it

to existing and stored objects, for a real view of products. Objects and products are rooted in the reality of everyday life. They express their essence, which is lived and shared by engineers and scientists, and with equal weight and intensity is experienced by all people with different interests and passion. The knowledge offered by the Museums and collections complete the actual knowledge. Now currently it is also expanded in time and in technical history, which can allow the knowledge of design and construction also for the future design and invention. Museums are sources of future actions.

Meanwhile, the technical world and the daily life evolve in an unbelievable extent in recent years. The curiosity opens new ways of being and thinking. Some people believe a lot of things will be passing, but the reality of intense and profound today daily life brings each person into play, and everyone is involved in the reality of life in the world. The professional in the center of New York and the farmer in Korea, the scientist in Finland and the mechanical manufacturer in Brazil, all act now with immense technological possibilities and communication. This key fact never happened in human history, and it is necessary to take note of the new reality in order to be immersed and to be encouraging developments. For knowledge, the museums and collections techniques, together with engineered products, are the absolute and unique references. The spread of data and the immense amount of data provided by all the books, documents, photographs make the memory and the libraries/museums an invaluable intelligence tool to manage knowledge.

Since few years the intelligence of objects is studied and understood in its deep meaning. Human nature is to penetrate into the intelligence of the objects to build, design, invent, browse through the past and present, and offer the best solution, dictated by technology and science today. Today the real reality does not forgive the inability and ignorance.

2 A Realization for Growing the Scientific Knowledge in Mechanical Sciences by Museums

The Interest increases about objects intelligence. The hidden objects in distant locations, all gathered to express a story, make up the Museums. Never word is so obsolete and appealing as Museum, in the years after 2010, when the social world has changed speed. The acceleration in everyday life has affected the actions, thoughts, and emotions. The facts have been overwhelmed by the immediacy of communication, and the memories are generated in the cloud, social networks, and billions of people—not just the technology experts—use them spasmodically and in a valuable manner. Knowledge has changed profile and those born these days will have a completely indefinite future, of peace or of war, of happiness or despair. The Museums, as they are today, are archaic reality. What sense does he/she go to see, moving from home with all the complications of moving, to see an object or even to watch a string of objects, often unknown, of which there is small interest? To meet

the knowledge from a long series of objects with no real appealing in mind and in heart? No, it does not. Aristotle in 340 BC wrote: *The fourth kind of quality is each object is said to possess a quality. All the qualities you say affective quality, for the fact that each of them produces a disease in the senses* [1].

Today, the visit to the Museum is still a walk through objects, described with signs or movies, which require a personal interpretation, often unclear and not always complete, so as to make and create true “knowledge”. The way, crossed by some, is to see the Museum as the Environment of Knowledge.

3 The Collection of Mechanisms at Department of Mechanical Engineering, Politecnico di Milano

The Mechanical Department of Politecnico di Milano has first origins with the foundation of Politecnico di Milano in 1863 [2]. Many historical documents, machines, mechanisms and mechanical parts remained in the Department, as witnesses of its long history, with the idea of preserving and enhancing the heritage [3]. Particularly interesting is the collection of mechanisms by Ottorino Sesini, who taught Applied Mechanics to generations of students. The mechanisms collection was used continuously by the main mechanical teachers e.g., by Emilio Massa, Rector of Politecnico [4].

Such mechanisms were used for decades, until the application of the virtual models progressively substituted the “real” models. The collection of the mechanisms is now an important witness to study the history of mechanics and, also, the history of teaching of mechanics. Figure 1 is relative to samples of the collection of mechanisms, as mechanical transmission elements (bevel and square gears), cranks, gear trains, and joints. There is also a Watt’s regulator model.



Fig. 1 Some examples from the mechanisms collections, department of mechanical engineering, Politecnico di Milano

4 The Proposed Choice Method

The evolutionary and revolutionary approach is presented [5–8]. It will be used in the collection, which is not easily accessible to students of engineering, technicians and experts. The reasons for the changes are as follows:

1. Allow all to observe, learn, investigate as a model, make for possible insights and innovations, to know in detail the objects, intelligent in their real existence in engineering centuries.
2. Let everyone know also the objects in storage and in archives, which by law cannot be made public except with special authorization.
3. Enrich the intelligent object descriptions files, movies, multimedia for knowledge and redesign.
4. Enrich the subject of a technical knowledge, also specialists, indicating possible new materials, new uses, etc.

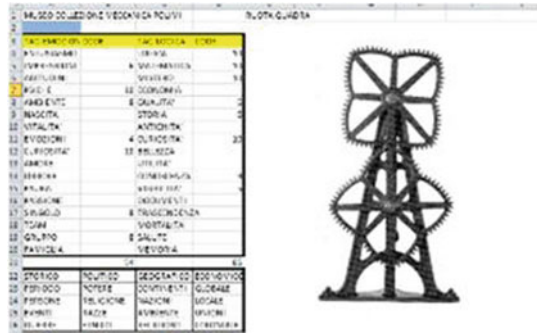
The modern knowledge force can overcome all obstacles of time, distance, environment and culture, if well guided and with precise objectives. In short, we pulled out all the knowledge of computer design, communication design, data management, virtual and multimedia representations, multivariate mathematics, to show how more and more each person can be brought to the museum reality. Not only considering the programmed path set but also the free choice of knowledge and participation, with intelligence and passion. In this way, the visitor finds him-self in front of the intelligent object, work of art, archaeological find, scientific instrument, and other. The quality of the items (as already wrote Aristotle in 330 BC) attracts human attention, in logic, in emotional and vital participation. It is a parallel contribution to the imposed and programmed path, which remains effective for a priori suggested knowledge.

The here presented project “DYNAMIC MUSEUMS” radically transforms the use of Museums involving visitor with his/her personality through logical cognitive aspects and through his/her emotions, expressed in daily life by the action respectively of the left and right brain hemispheres. The DYNAMIC MUSEUMS project would enhance the visitor interest with logical/emotional convergence with participation by computer of the curator of the museum. Potential Visitor can use computers, cell phones, tablets, and each communication device, as well as a location in the Museum itself (Fig. 2).

Fig. 2 Table for logical and emotional interests by visitor

VISITOR	NOME	COGNOME	NAZIONE
CODICE	ETA'	SESSO	PROFESSIONE
TAG EMOZIONI	CODE	TAG LOGICA	CODE
ENTUSIASMO		LOGICA	
IMPRESSIONI		MATEMATICA	
ABITUDINI		MISTERO	
PSICHE		ECONOMIA	
AMBITI		CRISTIANITA'	
NASCITA		STORIA	
VITALITA'		ANTICHITA'	
EMOZIONI		CURIOSITA'	
CURIOSITA'		BELLEZZA	
AMORE		UTILITA'	

Fig. 3 Example of evaluation given by the collection curator



Through mathematical algorithms the project DYNAMIC MUSEUMS generates a numerical-physical platform with suggested results to the visitor. It lists the collected most pleasing objects, interesting and pleased by the potential visitor. Example of the collection of mechanisms is presented in Fig. 3. The platform also serves for the reconfiguration of Museums themselves and for the reconfiguration of the museum routes, which can be prepared for each individual visitor. The new service offered for the new use of the Museums takes place with identification of the Museum paths between multiple museums, offering on-line all the necessary information to reach, access, collect documentation and obtaining all the necessary facilities for a comfortable and appealing use. The result for each visitor can also be produced as printing photos, holography, 3D printing, getting the documentation right of those museum objects most liked and interesting to the visitor.

The process is very simple: the willing visitor compiles a table on mobile phone, on tablet, computer or even on the printed sheet, table which can express his/her interest in logic and emotional involvement. The Program “DYNAMIC MUSEUMS” now contains data from Italian Museums, which, for large packages of Museum objects, indicate the logic and emotional value. The intersection of the logical and emotional data Visitor with the logical and emotional data for selected objects, as reported by the Museum Curator, brings out a ranking of favorite items, which correspond to the logical and emotional desires of the visitor. The ranking appears on the computer system of the visitor, with a recommended route, and with the ability to receive all the tourist signs and the route based on his/her preferences.

Figure 4 shows the numerical results of the suggestions. The scoreboard shows the final results, so that the potential visitor receives on his/her electronic device (computer, mobile tablet and any other system on the network) the classification suggested for the linked objects in the database project. The objectives of the “DYNAMIC MUSEUMS” Program, through the methods of the most advanced performance offered today by new technologies, are:

1. Exploitation Program “DYNAMIC MUSEUMS” by the Italian state and non-state museums, for a spread of participatory activities of Museum objects in close relation with cultural and emotional demands of potential visitors,

Fig. 4 Final table for mechanisms museum

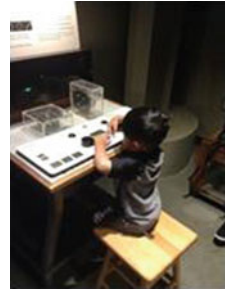
- extended to the Italian territory, and refer also to foreign visitors, for the widest possible enjoyment of the Museums in Italy.
2. Development of attention to small museums, not incorporated in full in the Museum tourist routes.
 3. Possibility of collaboration with foreign companies to promote the use of the Program DYNAMIC MUSEUMS to the visits and cultural tourism in Italy.

Mechanics Science was and still is the basis of any industrial evolution and in the most advanced sectors must be known and loved. This means an interpretation of the past, to gather new ideas and suggestions, maybe not exhausted earlier in addition, the basic mechanics relies on mechatronics, robotics, with the task of bypassing and adjustment to the new reality of life.

5 Conclusions

Preserving the artistic heritage keeps alive the resources useful to tourist activities and thus increase not only the entrance torn tickets but also to multiply the revenue related to the sectors linked to it such as transport, catering, accommodation, communication and merchandising. Many foreigners are systematically visiting Italy, reaching places of personal interest and recall. However much of—too much of—the Italian culture and the museum is not known by foreigners and Italians. The ambitious goal of Project DYNAMIC MUSEUMS is to increase the income from tourism, creating a visitor service available for museum that is sustainable and can be applied at various levels. Basically, a New Cultural Service is designed and offered as a new road suggesting museums throughout Italy with improved relationships with their visitors. Talking to many different tourists: Italian, foreigners, educated or interested in the beauty, art or technique, Project DYNAMIC MUSEUMS suggest their objects and routes, information and knowledge that can

Fig. 5 Exploiting future, exploratorium museum, USA



make even more exciting to visit the museum. Digital technology allows sharing information and feelings. PC, Tablet and Smartphone, connected to the network allow considerably expanding the catchment area of application. Huge spaces covered by objects from the past, living new lives in the memory of those who live today, surround us [9, 10]. Some are ennobled by a beautiful building, with a careful and inviting arrangement of objects, a description reminiscent of the past and connects each object to the present. Curiosity about things and people is the main push today to learn, which is transformed into new products with intelligent things (Fig. 5). Intelligence of objects is from some years the discipline that explains the things we use in daily life. Knowledge of objects takes out a new intelligence, and human knowledge, devoted to “connecting minds” through the knowledge and creativity obtained from the Museums.

References

1. Aristotle: Categories, 8, 9 (330 B.C.)
2. Curami A, Rovida E, Zappa E (2013) Storia del Dipartimento di Meccanica. Politecnico di Milano, Milan
3. De Alberti L, Rovida E (2013) Patrimonio storico del Dipartimento di Meccanica, Milan
4. Massa E (1999) una vita per il Politecnico, Milan
5. Eccles JC (1966) Brain and conscious experience. Springer, Gottingen
6. Levi Montalcini R (2004) Courage of knowledge. Milan
7. Rovetta A (1987) Voice control, encyclopedia of robotics, vol III, Ed. Dorf
8. Antinucci F (2011) Words and images. Rome
9. Raghianti CL (1974) Art, making and vision. Florence
10. Antinucci F (2014) Communication in museum. Rome

An Analysis of the Hydraulic Saw of Hierapolis

Cesare Rossi, Sergio Savino and Francesco Timpone

Abstract A mechanical analysis of the hydraulic saw of Hierapolis is presented. The device is the oldest example of saw moved by a water wheel and using a crank and rod mechanism. A bas relief representing the machine was found in Hierapolis, Phrygia, now Turkey, and was studied by the Italian Archaeological Mission in Hierapolis. The bas relief was dated III Century A.D. The paper starts from the archaeological studies of the find and from the early reconstructions that were proposed and presents a new pictorial reconstruction, a mechanical model and a model made by means of WM 2D™; the latter permitted to easily obtain the mechanical behavior of the machine. The water wheel was also modeled starting from archaeological relict found at Venafro, Italy.

Keywords History of mechanism and machine science · Roman technology · Ancient water powered machines

1 Introduction

The Hellenistic Age represents a real revolution in the Classic Age in any fields; in addition to the many fields of the Arts, the technical-scientific knowledge is among the main fields in which this cultural revolution occurs in ancient times [1–21]. During that period, in fact, a very wide number of new inventions was made; see e.g. the repeating weapons [2, 3, 10, 11], the siege towers and charts in general [1, 12], the throwing machines [2–4, 7, 10–15, 18] and the automatic devices [10, 11, 17–19].

In this paper the study of the mechanical behavior of an hydraulic saw is presented, that was invented at the end of the Hellenistic age.

It can be interesting to cite that Decimus Magnus Ausonius (310–395 A.D.), a Gallic-Roman poet, in his poem “Mosella” [22] tells about saws used to cut the

C. Rossi (✉) · S. Savino · F. Timpone
D.I.I. University of Naples, Naples, Italy
e-mail: cesare.rossi@unina.it

marble and moved by water wheel on the river Mosella, producing loud noise. This poem was sometimes considered not by Ausonius but by a much later poet of the Middle Age since the crank and rod mechanism, it was thought, wasn't invented before the late Middle Age.

The discovery of a bas relief on a sarcophagus in Hierapolis showing an hydraulic saw and dated to the III Century A.D., clarified the matter.

2 The Hydraulic Saw

In Fig. 1, on the left, a particular of the sarcophagus is reported; on the right a block of marble is shown the cut of which was just started [9].

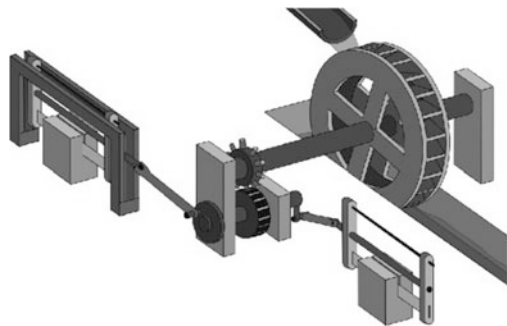
The bas relief was found on a cover of a sarcophagus at Hierapolis of Frigia (Turkey) and the picture (Archivio MAIER—Missione Archeologica Italiana a Hierapolis di Frigia) is reported with the kind permission of Prof. F. D'Andria, director of the Italian Archaeological Mission at Hierapolis. It was dated by Professor Tullia Ritti (University of Naples "Federico II") [9] to the 3rd Century A.D.

In Fig. 2 a virtual perspective reconstruction of the machine by Klaus Grewe, Paul Kessener [9, 23, 24] is shown.



Fig. 1 Bas-relief of the saw (*left*), cuts in a block of marble (*right*)

Fig. 2 Virtual perspective reconstruction by Klaus Grewe and Paul Kessener



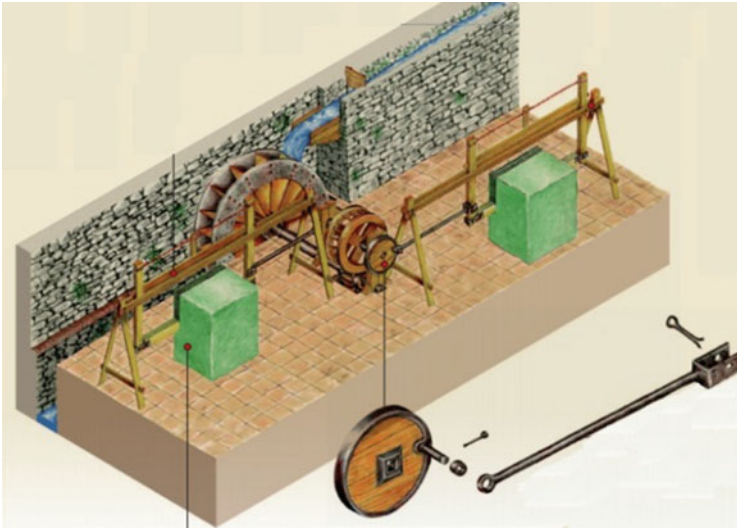


Fig. 3 Virtual reconstruction of the machine by F. Russo and C. Rossi

In Fig. 3 the virtual reconstruction of the machine by Dr. Ing. F. Russo and C. Rossi is reported.

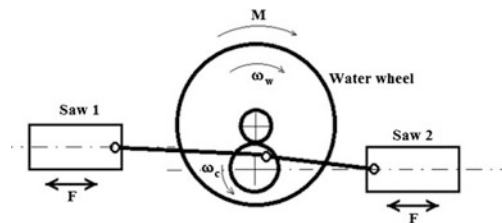
The machine consists in a crank moved by a water wheel through a geared reducer. The crank is linked to two connecting rods and each of them is linked to a saw. The latter, used to cut the marble block in sheets, consists in a toothless copper blade; between the copper blade and the marble some water and sand is put continuously so that almost the same cutting force is exerted in both the saw strokes.

3 The Mechanical Model

In Fig. 4 a simple scheme of the mechanism is shown.

Masses, forces and dimensions are reported in the next sub-paragraphs.

Fig. 4 Simple scheme of the mechanism



3.1 The Water Wheel

In order to consider the data of the water wheel, we considered the one that was found in 1908 near Venafro, Isernia, Italy since it was suitable for such applications and was built during the Roman Empire. In Fig. 5 a virtual reconstruction, a reconstruction in 1:1 scale and a technical drawing, by Dr. Ing. F. Russo are shown.

The mass of the wheel built by Dr. Ing. F. Russo was about 300 kg and considering its dimensions, the radius of gyration can be supposed to be about 1 m, hence the mass moment of inertia of the wheel is roughly 300 kg m^2 .

In order to evaluate the torque given by the wheel, the studies by Dr. Ing. L. Jacono [25] on the wheel of Venafro were considered. According with this study, the following parameters values were assumed:

Water flow $Q = 0.093 \text{ m}^3/\text{s}$

Water speed $V = 8.85 \text{ m/s}$

It was then supposed that the wheel was a high breast shot water wheel as shown in Fig. 6.

Hence an efficiency η from 45 to 65 % can be considered [5, 8], In the following it was considered $\eta = 0.5$.

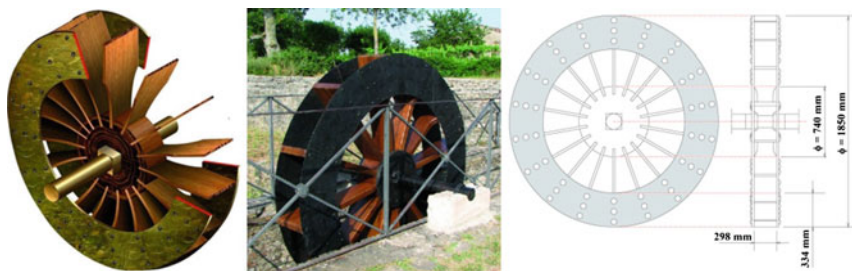
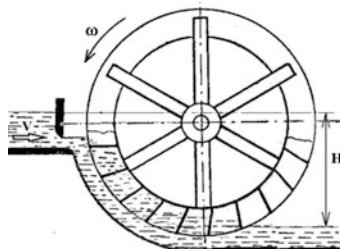


Fig. 5 Virtual reconstruction (*left*), reconstruction in 1:1 scale (*center*) and a technical drawing (*right*) by Dr. Ing. F. Russo

Fig. 6 Scheme of an high breast shot water wheel



The power by a water wheel can be computed as follows:

$$P = \frac{L}{t} = Q \rho g H \eta \quad (1)$$

Where ρ is the density of the liquid.

Hence:

$$P = 0.093 \times 998 \times 9.81 \times 0.9 \times 0.5 = 410 \text{ W} \quad (2)$$

If we suppose that the mean wheel speed v_{med} is one half of speed of the water stream, we have:

$$v_{med} = 4.43 \text{ m/s}$$

Being the mean radius of the blades $r_{med} = 0,76$ we obtain that the wheel angular speed is:

$$P = 5.82 \text{ rad/s} \cong 60 \text{ rpm}$$

Hence the torque given by the water motor is:

$$M_{mot} = 410/5.82 = 70.5 \text{ Nm}$$

3.2 The Saw Mechanism

As for the mechanism, we suppose that:

- the gear ratio was $\varepsilon = 2$.
- the efficiency of the geared reducer and the crank and rod mechanism together was $\eta_m = 0.5$.
- the length of the crank $r_m = 0,5$ m, hence the saw stroke was $s_c = 1$ m.

The energy available to the saws is:

$$M_{mot} = \varepsilon \eta_m 2 \pi = F 2 s_c \quad (3)$$

From the equation above we obtain the force acting on the saws blades:

$$F = \frac{M_{mot} \varepsilon \eta_m}{s_c} = 70.520,5 \pi = 221.5 \text{ N}$$

That is to say about 111 N for each of the saws.

3.3 The WM Model

The study of the mechanical behavior of the device could be done starting from the well-known kinematic equation for a crank and rod mechanism. Nevertheless, in the present investigation, we choose to arrange a simple multibody model by means of Working Model 2D™. This, in fact, permits to obtain a tool that permits, first of all to observe the movements and also all the kinematic and dynamical data can be easily obtained. In Fig. 7 the model is shown.

On the body representing the water wheel a motor was linked; in order to observe a transient, the torque of this motor was considered as a decreasing function of the angular speed ω , given by the following polynomial:

$$M(\omega) = 66 - 4\omega - 0.213\omega^2 \tag{4}$$

that gives the computed torque on the crankshaft at the steady-state speed.

On each of the two bodies, having 10 kg mass, that represents a saw, two force of 111 N each were considered; one of the two forces acts when that saw speed is positive and the other when that saw speed is negative.

In Fig. 8 the computed saw displacement, velocity and acceleration are reported as a function of the crank rotation.

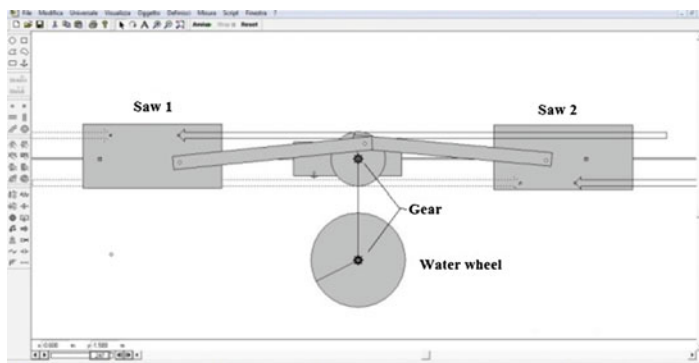
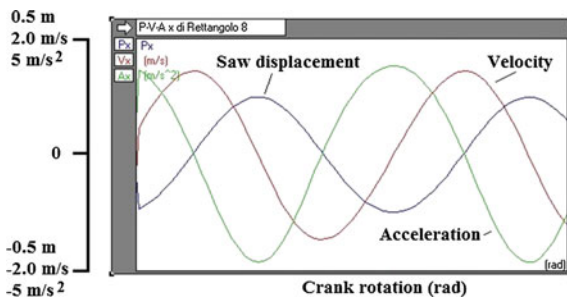


Fig. 7 Model of the machine by Working Model 2D™

Fig. 8 Displacement, velocity and acceleration of the saw versus the crank position



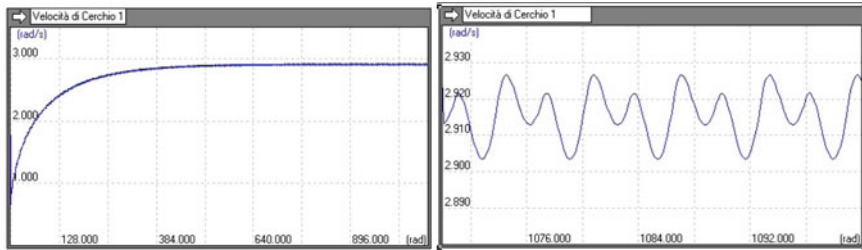


Fig. 9 Crank angular velocity during the transient

In Fig. 9, on the left, the crank angular velocity is reported as a function of the crank rotation during the transient; on the right the same velocity is reported, but for 5 crank rotation after the machine had reached steady state conditions.

From the figures above we can conclude that the machine worked satisfactorily and that the high mass momentum of inertia of the water wheel was able to significantly contain the periodical variation of crank velocity.

Moreover, a water wheel like the one found at Venafro, was able to move two saws exerting a force of 111 N to each of them in both the senses along a 1 m stroke, doing about 30 stokes per minute.

4 Conclusions

A first study of an ancient water mill saw was presented, based on a bas relief dated III Century A.D.

The study was carried on by means of a model Working Model 2D™ and showed that the machine satisfactorily worked by exerting on the saws blades a suitable force to cut marble blocks.

Further investigation will compare these performances to those by later reciprocating saws up to the Renaissance.

References

1. Chondros TG, Milidonis K, Paipetis S, Rossi C (2015) The Trojan Horse reconstruction. *Mech Mach Theor* 90:261–282. ISSN: 0094-114X
2. Marsden EW (1969) *Greek and Roman artillery historical development*, Oxford University Press II
3. Marsden EW (1971) *Greek and roman artillery. Technical treatises*, Oxford, pp 106–184
4. Messina A, Rossi C (2015) Mechanical behavior and performance of the Onager. *J Mech Des* 137(3), 034501 (5 pages); Paper No: MD-14-1276. doi:[10.1115/1.4029319](https://doi.org/10.1115/1.4029319)

5. Müller G, Wolter C (2004) The breastshot waterwheel: design and model tests. *Proc ICE-Eng Sustain* 157(4):203–211. <http://www.steffenreichel.homepage.t-online.de/Muehlen/Infos/ModernWaterwheels.pdf>
6. Özis Ü, Türkman A, Özdemir Y (2005) Historical waterworks in Turkey. In Ninth international water technology conference, IWTC9 2005, Sharm El-Sheikh, Egypt, pp 291–309
7. Penta F, Rossi C, Savino S (2014) Mechanical behavior of the imperial carroballista. *Mech Mach Theor* 80:142–150. ISSN: 0094-114X
8. Quaranta E, Fontan S, Cavagnero P, Revelli R (2015) Efficiency of traditional water wheels. In E-proceedings of the 36th IAHR World Congress, 28 June–3 July, 2015, The Hague, the Netherlands 1
9. Ritti Tullia, Grewe Klaus, Kessener Paul (2007) A relief of a water-powered stone saw mill on a sarcophagus at hierapolis and its implications. *J Roman Archaeol* 20:138–163
10. Rossi C, Russo F, Russo F (2009) Ancient engineers' inventions. Springer, Precursors of the present. ISBN 978-90-481-2252-3
11. Rossi C, Russo F (2010) A reconstruction of the Greek-Roman repeating catapult. *Mech Mach Theor* 45(1):36–45. ISSN:0094-114X
12. Rossi C, Pagano S (2011). A study on possible motors for siege towers. *J Mech Des* 133:1–8. ISSN:1050-0472)
13. Rossi C (2012). Ancient throwing machines: a method to compute their performances. *Mech Mach Theor* 51:1–13. ISSN:0094-114X
14. Rossi C (2013) Guest editorial “On Designs by Ancient Engineers”. *J Mech Des Trans ASME* 135(6), art. no. 060301. doi:10.1115/1.4024
15. Rossi C, Pagano S (2013) Improvement in ballistae design from eutitonon to palintonon: a study on the mechanical advantages. *J Mech Design Trans ASME* 135(8), art. no. 081006
16. Rossi C, Unich A (2013) A study on possible archimede's Cannon. *Rivista Storica dell'Antichità*. Vol. XLIII. ISSN 0300-340X
17. Rossi C (2014) Some examples of the hellenistic surprising knowledge: its possible origin from the east and its influence on later arab and European engineers. *Rivista Storica dell'Antichità*, XLIV, 2014, pp 61–84. ISSN 0300-340X
18. Rossi C, Messina A, Savino S, Reina G (2015) Performance of Greek-Roman Artillery. *Arms and Armour*. *J Royal Armouries* 12(1):66–88. ISSN: 1741-6124, Online ISSN: 1749-6268
19. Russo L (1996) *La Rivoluzione dimenticata*. Feltrinelli, Milano. ISBN 88-07-81644-X
20. Sharkey N (2007) The programmable robot of ancient Greece—*New Scientist* issue 2611, July 4, 2007, pp 32–35
21. Webb B. The first mobile Robot?—*Proc. TIMR 99 Towards intell*Rossi C., Russo F, Russo F (2009)—Ancient Engineers' Inventions, Precursors of the present. Springer ISBN: 978-90-481-2252-3
22. Decimius Magnus Ausonius (III Century A.D.) Mosella
23. Grewe K, Kessener P (2006) A stone relief of a water-powered stone saw at Hierapolis, Phrygia—a first consideration and reconstruction attempt. In D'Andria F, Caggia MP, Hierapolis di Frigia I: Le attività della Missione Archeologica Italiana a Hierapolis. Campagne 2000–2003. Atti del Convegno di Cavallino (Le), Convento dei Domenicani, Lecce 9-10 luglio 2004. Lecce 2006. Also published in *Énergie hydraulique et machines élévatrices d'eau dans l'Antiquité*, pp 227–234
24. Grewe K (2010) “La máquina romana de serrar piedras. La representación en bajorrelieve de una sierra de piedras de la antigüedad, en Hierópolis de Frigia y su relevancia para la historia técnica (translation by Miguel Ordóñez)”, *Las técnicas y las construcciones de la Ingeniería Romana* (PDF), V Congreso de las Obras Públicas Romanas (in Spanish), pp 381–401
25. Jacono L (1938) “La ruota idraulica di Venafro” *L'Ingegnere*, n.12, 15 dic. 1938 Stucchi, Milano

Part III
Linkages and Mechanical Controls

Riccati Equation Based Nonlinear Filter: A Case Study for Hydraulic Actuators in the Presence of Dead-Zone

Salvatore Strano and Mario Terzo

Abstract One of the most common hard nonlinearities in hydraulic actuator is the dead-zone. More specifically, dead-zone characterizes hydraulic control valves when its spool occludes the orifice with an overlap, so that for a range of spool positions there is no fluid flow. This paper focuses on an alternative nonlinear estimation method that is able to fully take into account dead-zone hard nonlinearity and measurement noise. The estimator is based on the State-Dependent-Riccati-Equation (SDRE).

Keywords Nonlinear state estimation • Hydraulic actuator • Dead-zone

1 Introduction

Typical usage of hydraulic actuators concerns seismic test rig, positioning systems, vibration control [1]. The state estimation of such systems is fundamental for their operation. The design of state observers should take into account the nonlinear dynamics of hydraulic actuators. One of the most common hard nonlinearities is the dead-zone. Dead-zone is a hard nonlinearity, frequently encountered in many actuators of industrial control systems, especially those containing some very common components, such as hydraulic or pneumatic valves and electric motors. Other common nonlinearities are, for example, hysteresis and friction [2]. The dead zone nonlinearity is common in closed center valves when the land width is greater than the port width at neutral spool position. Several approaches have been proposed in literature for the state estimation in hydraulic actuators [3].

This paper investigates on an alternative nonlinear technique for the state estimates of the hydraulic actuators. The approach is based on the

S. Strano · M. Terzo (✉)
University of Naples Federico II, Naples, Italy
e-mail: mario.terzo@unina.it

S. Strano
e-mail: salvatore.strano@unina.it

State-Dependent-Riccati-Equation (SDRE) nonlinear filtering formulation. The SDRE techniques are recently emerging for optimal nonlinear control and filtering techniques. The SDRE filter (SDREF) originates from a suboptimal nonlinear regulator technique that uses parameterization to bring the nonlinear system into a linear-like structure with state-dependent coefficients (SDC) and is characterized by the structure of the steady state Kalman filter and the Kalman gain is obtained by solving an algebraic Riccati equation. Simulations have been conducted in order to analyse the effect of the dead-zone characteristic on the estimator performance, showing a comparison with the widely used Extended Kalman Filter (EKF) that is based on a local linearization of the system.

2 Dynamic Model

The hydraulic actuation system under consideration consists mostly of a double-rod hydraulic cylinder and a proportional valve. The hydraulic cylinder is linked to a mass that moves on a linear guide (Fig. 1).

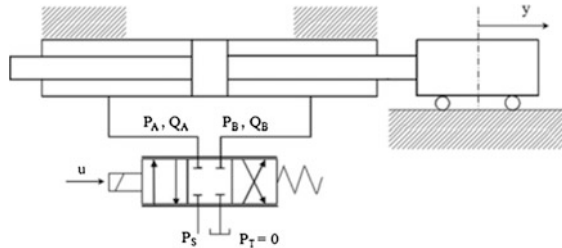
For the derivation of the mathematical model, some assumptions are made: the tank pressure P_T is equal to zero, the fluid properties are not dependent on the temperature, the piston areas and the chamber volumes are equal, the internal and external fluid leakages are negligible. The dynamic model is here briefly recalled [4, 5].

The nonlinear system can be written in the following form:

$$\begin{cases} \ddot{y} = -\frac{\sigma}{m}\dot{y} - \frac{F_f(\dot{y})}{m\dot{v}_e}v_e + \frac{A_p P_L}{m} \\ \dot{P}_L = -\frac{2\beta A_p}{V_0}\dot{y} + \frac{2\beta\Psi(\bar{v}_e)\sqrt{P_s - |P_L|}}{V_0}v_e \\ \dot{v}_e = -2\xi_v\omega_{nv}\dot{v}_e - \left(1 - \frac{v_e\omega}{\bar{v}_e}\right)\omega_{nv}^2 v_e + \omega_{nv}^2 k_e u \end{cases} \quad (1)$$

where y is the movable mass displacement, m is the mass of the load, σ is the viscous friction coefficient, F_f is the friction force, A_p is the piston area, $P_L = P_A - P_B$ is the load pressure, P_A and P_B are the pressures inside the two chambers of the cylinder, v_e is the displacement signal of the spool valve, $\Psi(v_e)$ is a gain that depends on the geometry of the adopted proportional valve, V_0 is the volume of each chamber for the centered position of the piston, $Q_L = (Q_A + Q_B)/2$ is the load

Fig. 1 Schematic diagram of the hydraulic actuation system



flow, β is the effective Bulk modulus, ω_{nv} and ξ_v are the natural frequency and the damping ratio of the valve respectively, v_{e0} is the spool position bias, k_e is the input gain and u is the valve command.

The system (1), whose state vector is given by $x = [\dot{y} \ y \ P_L \ \dot{v}_e \ v_e]^T$, is nonlinear in the state and autonomous. In order to prevent divisions by zero, the variable $\tilde{v}_e = v_e + \varepsilon$ has been introduced, where ε is given by:

$$\varepsilon = \begin{cases} \Delta v_e & v_e = 0 \\ 0 & \text{otherwise} \end{cases} \quad (2)$$

where the value of Δv_e can be assumed less than the discrimination threshold of the valve spool position sensor.

3 Riccati Equation Based Nonlinear Filter

SDRE techniques are used as control and filtering design methods and are based on state dependent coefficient (SDC) factorization. Infinite-horizon nonlinear regulator problem is a generalization of time invariant infinite-horizon linear quadratic regulator problem where all system coefficient matrices are state-dependent. When the coefficient matrices are constant, the SDRE control method changes into the steady-state linear regulator. Filtering counterpart of the SDRE control algorithm is obtained by taking the dual system of the steady-state linear regulator and then allowing coefficient matrices of the dual system to be state-dependent. Starting from the nonlinear system of Eq. (1), there are infinite solutions to transform this nonlinear system into an SDC form as:

$$\dot{\mathbf{x}}(t) = \mathbf{F}(\mathbf{x}(t), \mathbf{u}(t))\mathbf{x} + \boldsymbol{\psi} \quad (3)$$

$$\mathbf{z}(t) = \mathbf{H}(\mathbf{x}(t), \mathbf{u}(t))\mathbf{x} + \mathbf{g} \quad (4)$$

where

$$\mathbf{f}(\mathbf{x}(t), \mathbf{u}(t)) = \mathbf{F}(\mathbf{x}(t), \mathbf{u}(t))\mathbf{x} \text{ and } \mathbf{h}(\mathbf{x}(t), \mathbf{u}(t)) = \mathbf{H}(\mathbf{x}(t), \mathbf{u}(t))\mathbf{x} \quad (5)$$

$\boldsymbol{\psi}$ is the process noise with covariance \mathbf{Q} , and \mathbf{g} is the Gaussian white measurement noise with covariance \mathbf{R} .

Starting from the SDC form, the derivative of the state estimate is given by:

$$\dot{\hat{\mathbf{x}}} = \mathbf{F}(\hat{\mathbf{x}}, \mathbf{u})\hat{\mathbf{x}} + \mathbf{K}_f(\hat{\mathbf{x}})[\mathbf{z}(\mathbf{x}) - \mathbf{H}(\hat{\mathbf{x}}, \mathbf{u})\hat{\mathbf{x}}] \quad (6)$$

where

$$\mathbf{K}_f(\hat{\mathbf{x}}) = \mathbf{P}(\mathbf{x})\mathbf{H}^T(\hat{\mathbf{x}}, \mathbf{u})\mathbf{R}^{-1} \quad (7)$$

and \mathbf{P} is the positive definite solution of the algebraic Riccati equation (8).

$$\mathbf{F}(\hat{\mathbf{x}}, \mathbf{u})\mathbf{P}(\hat{\mathbf{x}}) + \mathbf{P}(\hat{\mathbf{x}})\mathbf{F}^T(\hat{\mathbf{x}}, \mathbf{u}) - \mathbf{P}(\hat{\mathbf{x}})\mathbf{H}^T(\hat{\mathbf{x}}, \mathbf{u})\mathbf{R}^{-1}\mathbf{H}(\hat{\mathbf{x}}, \mathbf{u})\mathbf{P}(\hat{\mathbf{x}}) + \mathbf{Q} = \mathbf{0} \quad (8)$$

The highly nonlinear equations (1) have been parameterized in SDC form with the following choice:

$$\mathbf{F}(\mathbf{x}, \mathbf{u}) = \begin{bmatrix} -\frac{\sigma}{m} & 0 & \frac{A_p}{m} & 0 & -\frac{F_f(\dot{y})}{m\dot{v}_e} \\ 1 & 0 & 0 & 0 & 0 \\ -\frac{2\beta A_p}{V_0} & 0 & 0 & 0 & \frac{2\beta\Psi(\tilde{v}_e)\sqrt{P_s - P_L}}{V_0} \\ 0 & 0 & 0 & -2\xi_v\omega_{nv} & -\left(1 - \frac{v_{e0}}{\dot{v}_e}\right)\omega_{nv}^2 + \frac{\omega_{nv}^2 k_e u}{\dot{v}_e} \\ 0 & 0 & 0 & 1 & 0 \end{bmatrix} \quad (9)$$

$$\mathbf{H}(\mathbf{x}, \mathbf{u}) = \mathbf{H} = \begin{bmatrix} 0 & 1 & 0 & 0 & 0 \\ 0 & 0 & 1 & 0 & 0 \\ 0 & 0 & 0 & 0 & 1 \end{bmatrix} \quad (10)$$

4 Simulation Results

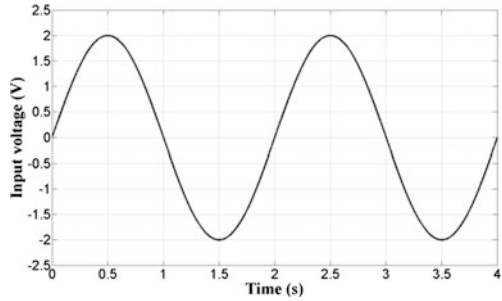
In order to evaluate the benefits of the proposed estimator, simulations have been carried out on the mathematical model of a hydraulic actuator. The hydraulic actuator has been modelled by means of Eq. (1), in which the parameters have been determined through of an identification procedure and are:

$$\begin{aligned} m &= 440 \text{ kg}, \quad \sigma = 23555 \frac{\text{N} \cdot \text{s}}{\text{m}}, \quad F_C = F_{C0} = 950 \text{ N}, \quad \mu = \mu_0 = 0.01 \\ A_p &= 0.01 \text{ m}^2, \quad V_0 = 0.004 \text{ m}^3, \quad \beta = 1\text{e}9 \text{ Pa}, \quad v_{e0} = 0.01 \text{ V}, \quad k_e = 0.49, \\ \omega_{nv} &= 152 \text{ rad/s}, \quad \xi_v = 0.92, \quad P_s = 6\text{e}6 \text{ Pa}. \end{aligned}$$

The simulated experiment refers to a hydraulic actuator characterized by a symmetric dead-zone that has been taken into account through the function $\Psi(\tilde{v}_e)$:

$$\Psi(\tilde{v}_e) = \begin{cases} k_{qp} \left[1 + \left(\frac{k_{q0}}{k_{qp}} - 1 \right) \frac{v_{ep}}{\tilde{v}_e} \right] & v_e > v_{ep} \\ k_{q0} & v_{en} \leq v_e \leq v_{ep} \\ k_{qn} \left[1 + \left(\frac{k_{q0}}{k_{qn}} - 1 \right) \frac{v_{en}}{\tilde{v}_e} \right] & v_e < v_{en} \end{cases} \quad (11)$$

Fig. 2 Input voltage



where $k_{q0} = 1e - 12 \frac{m^3}{s \cdot V \cdot Pa^2}$, $k_{qp} = 6.15e - 7 \frac{m^3}{s \cdot V \cdot Pa^2}$, $k_{qn} = 5.86e - 7 \frac{m^3}{s \cdot V \cdot Pa^2}$, $v_{ep} = 0.21 \text{ V}$, $v_{en} = -0.21 \text{ V}$.

The performance of the SDREF will be evaluated through a comparison with the EKF estimator and the real state. The observers have been designed taking into account as input the signal u and the measurements given by displacement y , the load pressure P_L and the spool valve displacement v_e .

The simulated results have been obtained by means of open loop tests employing a sine wave as input (Fig. 2). The parameters adopted in the observers are the same of the hydraulic actuator model.

The first important result is shown in Fig. 3, where the capability of the SDREF is easily visible: indeed, the comparison with the EKF technique highlights substantial differences due to the linearization process. The nonlinearities of the system are fully considered in the SDREF and, consequently, all the null speed zones, caused by the dead-zone, are well estimated. This result finds an important application for fault detection algorithm and in velocity feedback control in which, for example, the speed sensor is not adopted.

With the particular reference to the hydraulic actuators, the nonlinearities involve the load velocity equation and the load pressure one. As a consequence, the

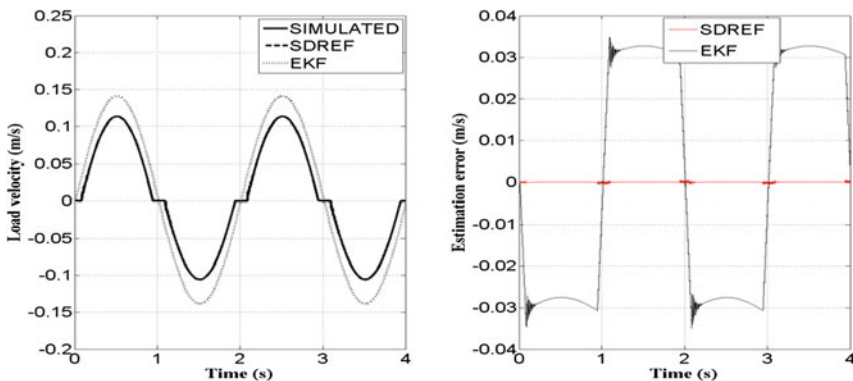


Fig. 3 Load velocity

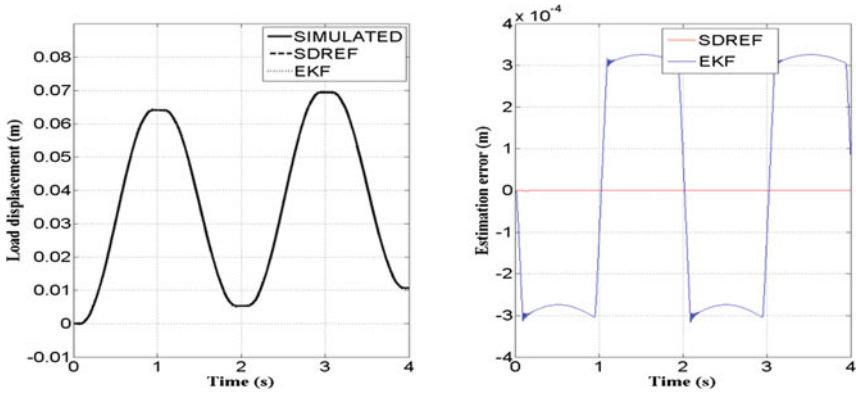


Fig. 4 Load displacement

differences between the EKF and the SDREF are evident if the time histories of the estimates of the cited states are evaluated. In any case, with the aim of completeness of the discussion, the comparisons for all the states are shown in the following. Figure 4 exhibits the comparison in terms of load displacement, Fig. 5 shows the comparison for the load pressure.

While the estimates obtained with the two techniques are comparable for the load displacement, the differences are visible for the load pressure. Indeed, as for the load velocity, the SDREF gives an estimate that appears practically superimposed to the actual one. The result confirms the goodness of the technique in presence of not negligible nonlinearities and allows to consider it a valid alternative to the installation of sensors.

Figures 6 and 7 show the spool valve velocity and the spool valve displacement, respectively.

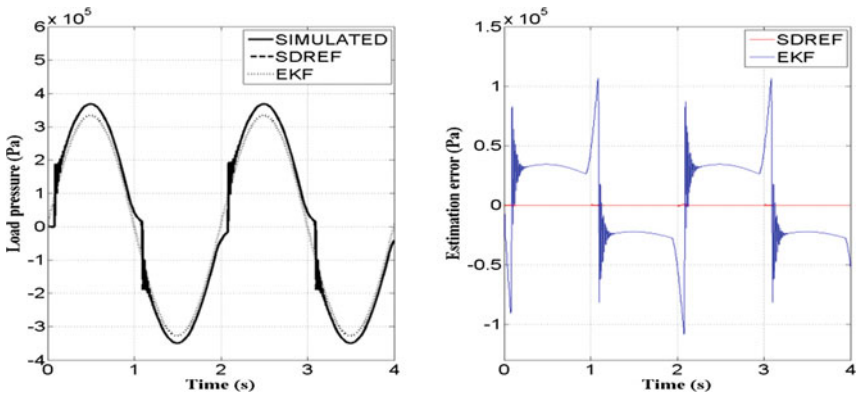


Fig. 5 Load pressure

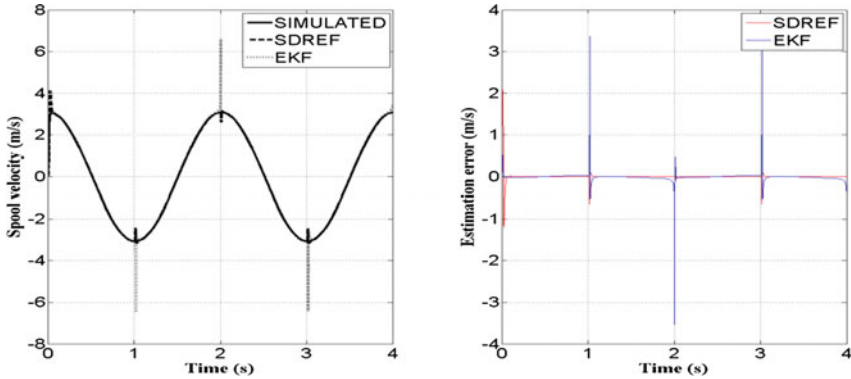


Fig. 6 Spool velocity

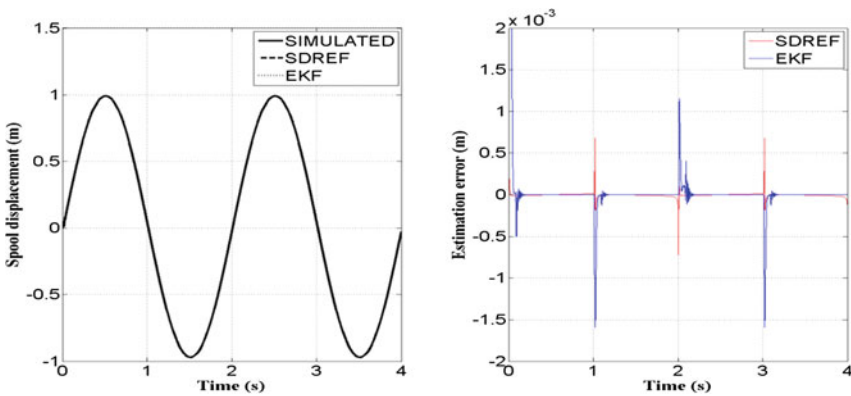


Fig. 7 Spool displacement

5 Conclusions

A Riccati equation based nonlinear filter has been proposed for the state estimation of a hydraulic actuator. The effectiveness of the filter has been evaluated by means of simulations that show a comparison with the EKF technique. The results show the advantages in terms of state estimates for all the states depending on nonlinearities. Consequently, the effectiveness of the SDREF is clearly visible for the load velocity and for the load pressure estimates. Taking into account the performances of the technique, its main contributions can be found in fault detection algorithms or as alternative solution to the installation of velocity sensors.

References

1. Calabrese A, Serino G, Strano S, Terzo M (2013) Investigation of the seismic performances of an FRBs base isolated steel frame through hybrid testing. In: Lecture notes in engineering and computer science: proceedings of the world congress on engineering 2013, London, U.K., 3–5 July, 1974–1978
2. Farroni F, Russo M, Russo R, Timpone F (2012) Tyre-road interaction: experimental investigations about the friction coefficient dependence on contact pressure, road roughness, slide velocity and temperature. In: ASME 2012 11th biennial conference on engineering systems design and analysis, ESDA 2012, vol 4, pp 521–529
3. Yu D (1995) Fault diagnosis for a hydraulic drive system using a parameter estimation method. *Control Eng Pract* 5(9):1283–1291
4. Strano S, Terzo M (2014) A multi-purpose seismic test rig control via a sliding mode approach. *Struct Control Health Monit* 21(8):1193–1207
5. Strano S, Terzo M (2015) A SDRE-based tracking control for a hydraulic actuation system. *Mech Syst Signal Process* 60–61:715–726

Trajectories Generation with Constant Extrusion Rate for Experimentations on AM Techniques and Extrusion Based Technologies

H. Giberti, L. Sbaglia and M. Parabiaghi

Abstract AM techniques based on material extrusion are currently under experiments in the pursuance of printing new materials related with new printing techniques. For these studies it would be helpful a trajectory with constant feed rate, in order to guarantee a uniform distribution of material with a constant extrusion feed rate. For this purpose a model for trajectories generation is developed exploiting Bézier curves. This model can be helpful for AM experiments and technologies where a uniform material deposition is needed as painting, gluing and sealing. At the end of the paper an example is presented.

Keywords Trajectories generation • Bézier curves • Constant feed rate • Constant extrusion rate • Additive manufacturing

1 Introduction

Additive manufacturing (AM) is becoming an established technology nowadays with a continuous growth and often subject of experiments. Research in AM is mainly focused on the possibility of printing new materials and the related techniques. Among AM techniques the ones based on the extrusion of material, as FDM, are one of the most studied in particular after that Stratasys patent [11] about its technology is expired and so making spread this technique in the market. Roberson et al. [10] show the use of an FDM technique for new materials in the manufacture of electromechanical and electromagnetic applications, Volpato et al. [13] show an

H. Giberti · L. Sbaglia (✉)

Dipartimento di Ingegneria Industriale e dell'Informazione, Università degli Studi di Pavia, Via A. Ferrata 5, 27100 Pavia, Italy
e-mail: luca.sbaglia@studenti.unipv.it

H. Giberti
e-mail: hermes.giberti@unipv.it

M. Parabiaghi
Mechanical Department, Politecnico di Milano, via la Masa 1, 20156 Milano, Italy
e-mail: marco.parabiaghi@mail.polimi.it

innovative piston-driven extrusion head that can extrude polypropylene granules into a filament and in previous works Fiore et al. [3], Giberti et al. [4, 5] show several studies on a new 3D printing solution for metal parts based on a MIM technique. Many studies are related to parameters optimization of these techniques, [9], or to attempt to model particular characteristics of this process, [2, 7]. In all these studies the importance of constant extrusion rate is highlighted for instance by Jiang and Gu [6] in order to obtain a uniform-distributed material width which is fundamental for the accuracy of this process. Without the control of this parameter these studies are affected by uncertainties which are not evaluable.

To guarantee a uniform material deposition for extrusion systems with a constant feed rate can help these experimental studies. A Direction-Parallel Tool-Path (DP) can be used for a direct and immediate feedback on technological process characterized by the control parameters variation.

Some articles are available in literature which propose DP deposition trajectories using lines and parabolas approach, moving the tool with constant feed rate for a major part of the trajectory. Thompson et al. [12] shows constant material flow trajectories for straight lines using a constant acceleration to modify velocity for two consecutive lines with different velocity: in this way is introduced an error on absolute velocity as bigger as smaller is the angle between the two consecutive lines leading to the necessity to change the material flow during the parabolic segments. Jin et al. [8] suggests a straight lines and parabolas trajectory based entirely on the curvilinear abscissa velocity control. Defining two lines typologies (type I for lines which intersects the deposition profile, and type II for lines adjacent to the profile boundaries) a different absolute velocity is imposed on the two types: usually velocity I is doubler than velocity II and a constant acceleration profile is used to link the two lines on the curvilinear abscissa. The extruder motion profile is created taking into account the velocity variations of the control parameter. This strategy leads to limited accelerations on active joints during curved paths keeping a good printing velocity.

In this article is proposed a trajectory generation based on Bézier curves in order to guarantee a uniform material deposition in combination with a constant extrusion rate and feed rate in all deposition points. This will be helpful not only for studies on AM techniques but for all processes based on material extrusion as painting, gluing and sealing where a uniform distribution of material is requested. A straight and parabolic lines interpolation technique is developed describing the trajectory with the use of only one parameter. On this parameter is applied a trapezoidal velocity profile allowing to move a tool center point, TCP, with constant velocity during its trajectory. It's possible to reach different parametric velocities according to particular needs derived on the specific application and so allowing material deposition experiments not affected by material flow variations. Parametric curves are initially presented and after the explanation is focused on the Bézier curves which are exploited for the generation of a straight lines-parabolas interpolator that it's used for an example showed in the final part of this paper.

2 Curve Parametrization

To define a trajectory in a cartesian space (XYZ) is necessary to define a parametric geometrical path, as defined by [1]:

$$\mathbf{p} = \mathbf{p}(u), \quad u \in [u_{min}, u_{max}] \quad (1)$$

where $\mathbf{p}(u)$ is a continuous vectorial function (3×1) which describes the path inside the workspace as a function of the independent variable u . We take into account 3 Dofs, but we can extend the definition of \mathbf{p} in order to include more Dofs.

The so defined vector function is controlled imposing a motion profile on parameter $u = u(t)$ which describes the tool trajectory along its path.

In particular:

$$|\dot{\tilde{\mathbf{p}}}(t)| = v_c = constant \quad (2)$$

where $\tilde{\mathbf{p}}(t) = (\mathbf{p} \circ u)(t)$, and for velocity and acceleration we derive the last equation.

It's not needed to analytical obtain function $u(t)$, its value $u(t_k) = u_k$ can be computed with a temporal discretization $t_k = kT_s$, with T_s sample time. We can obtain u_k with $k = 0, 1, 2, \dots$, using a Taylor series with a second order approximation. Deriving respect to the time the following conditions are obtained:

$$\dot{u}(t) = \frac{v_c}{\left| \frac{d\mathbf{p}}{du} \right|} \quad \ddot{u}(t) = -v_c^2 \frac{\frac{d\mathbf{p}^T}{du} \cdot \frac{d^2\mathbf{p}}{du^2}}{\left| \frac{d\mathbf{p}}{du} \right|^4} \quad (3)$$

considering a second order approximation the variable value u at time $(k + 1)T_s$ can be determined as:

$$u_{k+1} = u_k + \frac{v_c T_s}{\left| \frac{d\mathbf{p}}{du} \right|_{u_k}} - \frac{(v_c T_s)^2}{2} \left[\frac{\frac{d\mathbf{p}^T}{du} \cdot \frac{d^2\mathbf{p}}{du^2}}{\left| \frac{d\mathbf{p}}{du} \right|^4} \right]_{u_k} \quad (4)$$

In order to achieve a constant velocity trajectory in the initial and final part of the path there is a non-zero acceleration. Considering a trapezoidal velocity the computing of u_{k+1} is modified as follow:

$$u_{k+1} = u_k + \frac{v_k T_s}{\left| \frac{d\mathbf{p}}{du} \right|_{u_k}} + \frac{T_s^2}{2} \left\{ \frac{a_k}{\left| \frac{d\mathbf{p}}{du} \right|_{u_k}} - v_k^2 \left[\frac{\frac{d\mathbf{p}^T}{du} \cdot \frac{d^2\mathbf{p}}{du^2}}{\left| \frac{d\mathbf{p}}{du} \right|^4} \right]_{u_k} \right\} \quad (5)$$

where $a_k = a(t_k)$ and $v_k = v(t_k)$ are respectively acceleration and velocity at instant $t_k = k \cdot T_s$.

To define a deposition trajectory which guarantees a constant feed rate of the tool in necessary to implement a parametric curve defined in the tool workspace. In order to achieve this goal *Bézier curves*, are exploited to generate a parametric path made of straight lines and parabolas.

A *Bézier curve* of m degree is defined as:

$$\mathbf{b}(u) = \sum_{j=0}^m B_j^m(u) \mathbf{p}_j, \quad 0 \leq u \leq 1 \quad (6)$$

where coefficients \mathbf{p}_j are control points, and functions $B_j^m(u)$ are *Bernstein polynomials* defined as $B_j^m(u) = \binom{m}{j} u^j (1-u)^{m-j}$.

The Binomial coefficient, for $j = 0, 1, \dots, m$, defines the rows of the *Pascal triangle*. A *Bézier curve* derivative respect to variable u of m degree is still a *Bézier curve* of degree $m - 1$ defined as:

$$\frac{d\mathbf{b}(u)}{du} = m \sum_{i=0}^{m-1} B_i^{m-1}(u) (\mathbf{p}_{i+1} - \mathbf{p}_i) \quad (7)$$

3 Motion Curve Design

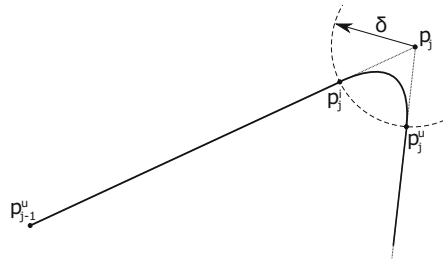
Straight lines and parabolas interpolation is used starting from *Bézier curves* of first and second degree. They are evaluated in the following manner:

$$\begin{aligned} \mathbf{b}(u) &= (1-u)\mathbf{p}_{j-1}^u + u\mathbf{p}_j^e && \text{line} \\ \mathbf{b}(u) &= (1-u)^2\mathbf{p}_j^e + 2u(1-u)\mathbf{p}_j + u^2\mathbf{p}_j^u && \text{parabola} \end{aligned} \quad (8)$$

The entire trajectory is created merging one after one straight lines and parabolas which are parametrized independently one from the other using a parameter range $u \in [0, 1]$. This method simplifies the trajectory equation creation even though the evaluation of the motion profile of parameter u is get complicated as will be shown latter.

In Fig. 1 is possible to see the control points \mathbf{p}_j defined in the workspace. They are used to interpolate the trajectory, linking straight lines with parabola trajectories in order to obtain a smooth path. The parabola trajectories are geometrically constructed defining points \mathbf{p}_j^i and \mathbf{p}_j^u which define input and output of the trajectory. They are obtained using construction lines intersected with circles with δ radius centered on vertices defined by \mathbf{p}_j . For a further generalization of the trajectory for the 3D space, and not only for the plane, suffices intersect the previous segments with spheres of δ radius centered in the vertices and correctly select the intersection

Fig. 1 Control points



points. To link straight lines using parabolas trajectories leads to final straight lines limited by points \mathbf{p}_{j-1}^u and points \mathbf{p}_j^i as it's easily understandable.

It's possible to evaluate derivatives of Eq. 8 respect to variable u using formula 7.

Computing for straight and parabola lines $d\mathbf{b}/du$ and $d^2\mathbf{b}/du^2$ and exploiting Eq. 3, $\dot{u}(t)$ and $\ddot{u}(t)$ are obtained.

In this way all instruments needed to evaluate temporal derivatives of *Bézier curves* through the use of Eq. 3 are made available. Respectively for **straight** and **parabolic lines**:

$$\dot{\mathbf{b}}(t) = \left(-\mathbf{p}_{j-1}^u + \mathbf{p}_j^e \right) \dot{u} \qquad \ddot{\mathbf{b}}(t) = \left(-\mathbf{p}_{j-1}^u + \mathbf{p}_j^e \right) \ddot{u} \qquad (9)$$

$$\begin{aligned} \dot{\mathbf{b}}(t) &= -2(1-u)\dot{u}\mathbf{p}_j^e + [2\dot{u}(1-u) - 2u\dot{u}] \mathbf{p}_j + 2u\dot{u}\mathbf{p}_j^u \\ \ddot{\mathbf{b}}(t) &= [\dot{u}^2 - 2(1-u)\ddot{u}] \mathbf{p}_j^e + [2\ddot{u}(1-u) - 2\dot{u}^2 - 2u\ddot{u}] \mathbf{p}_j + (2\dot{u}^2 + 2u\ddot{u}) \mathbf{p}_j^u \end{aligned} \qquad (10)$$

Now it's possible to evaluate the motion profile computing the $u(t)$ values in every instant considering the time discretization with sample time T_s . The goal is to generate a TVP¹ for parameter $u(t)$ in order to guarantee a constant material flow in all trajectory points. For part with constant acceleration Eq. 5 is used whereas for the central part of the path Eq. 4 is used. Pulling together straight and parabolic segments a velocity variation of the parametric variable is generated in the first point of the new segment when passing from the previous to the following. That's caused by the fact that in the crossing point the parametric value is not $u = 1$ but it's lower as shown by Fig. 2a. Since every segment is defined by a starting parametric value $u = 0$ a spatial distance is generated along the path $\Delta s < \Delta b$ between the last point of the straight line and the initial point of the parabolic line. It's necessary to attribute a suitable value of u to the first point of the parabolic line in order to obtain equally spaced points along the path, equal to Δb . Having as reference Fig. 2b, and being aware that $\Delta b = v_c \cdot T_s$ and $\Delta r = b_{line}(u = 1) - b_{line}(u_f)$ it's necessary to evaluate the right variable u_2 to collocate the first point of the parabolic line to a distance equal to Δb along the curve evaluated as $\Delta p = \Delta b - \Delta r$.

¹Trapezoidal velocity profile.

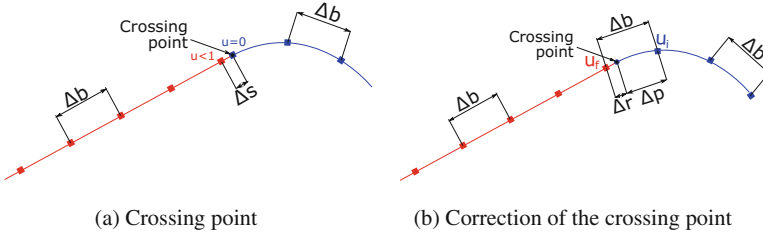


Fig. 2 Deposition trajectory

Rewriting conveniently Eq. 4 for the parabolic line u_i is obtained as follow:

$$u_i = \frac{\Delta p}{\left| \frac{d\mathbf{b}}{du} \right|_{u=0}} - \frac{\Delta p^2}{2} \left[\frac{\frac{d\mathbf{b}^T}{du} \cdot \frac{d^2\mathbf{b}}{du^2}}{\left| \frac{d\mathbf{b}}{du} \right|^4} \right]_{u=0} \quad (11)$$

The same procedure with same rules is used for the crossing point from a parabolic to a straight line. It's possible to evaluate $\Delta r = \Delta b - \Delta p$ where $\Delta b = v_c \cdot T_s$ whereas for the evaluation of Δb is necessary to recall Eq. 4 replacing $u_{k+1} = 1$, $u_k = u_f$ and $v_c \cdot T_s = \Delta p$.

Replacing and rewriting an equation of second degree for the variable Δp is obtained:

$$\frac{1}{2} \left[\frac{\frac{d\mathbf{b}^T}{du} \cdot \frac{d^2\mathbf{b}}{du^2}}{\left| \frac{d\mathbf{b}}{du} \right|^4} \right]_{u_f} \Delta p^2 - \frac{1}{\left| \frac{d\mathbf{b}}{du} \right|_{u_f}} \Delta p + 1 - u_f = 0 \quad (12)$$

Solving with respect to Δp is computed u_i on the straight line replacing it in the Eq. 4:

$$u_i = \frac{\Delta r}{\left| \frac{d\mathbf{b}}{du} \right|_{u=0}} \quad (13)$$

4 Application

The trajectories generation proposed can be implemented in material deposition techniques with constant extrusion rate. In Fig. 3d is shown a trajectory for a gluing deposition system where a straight lines and parabolas technique is used starting \mathbf{p}_j points (red in Fig. 3d) defining a possible trajectory. To define the trajectory the

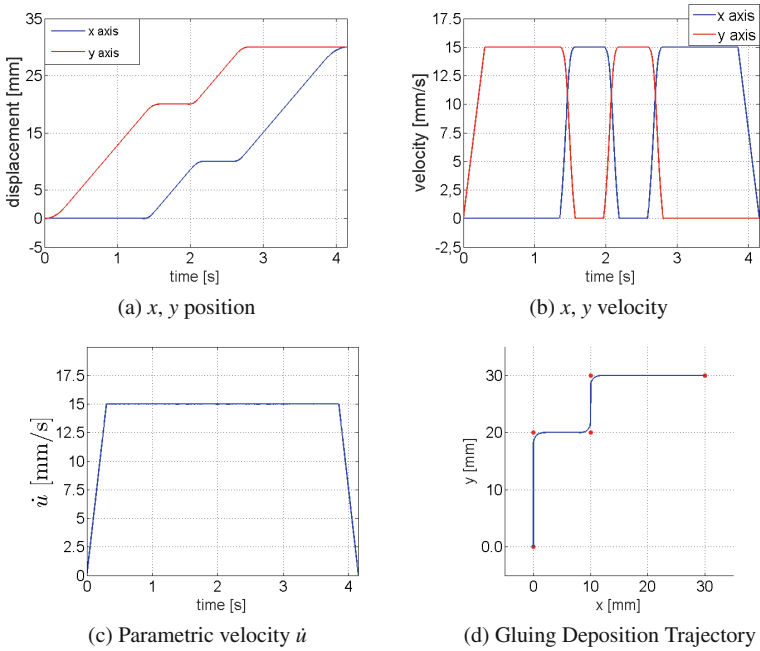


Fig. 3 Gluing deposition motion profiles

values $\delta = 2$ mm, $\dot{u}_{max} = 15$ mm/s and $\ddot{u}_c = 50$ mm/s² as been used. To notice how the trajectory doesn't pass exactly over the red points \mathbf{p}_j , but near as much as δ is low; if the filament width of the material deposited is bigger than the radius δ the points of interest will be covered anyway during the trajectory deposition. δ must be chosen in accordance with the application needs and the acceleration limits on active joints; with a constant velocity \dot{u} a lower δ leads to bigger accelerations required on the machine actuators which could be over their possibilities.

In the others figures is possible to see the actual trajectory generated, x and y position and velocity and the parametric velocity \dot{u} . It's possible to see the TVP motion profile which guarantees a constant velocity along all the central part of the TCP path.

5 Conclusions

In the field of extrusion system techniques experimental studies can be affected by problems related to uniform material distribution as showed. Helpful can be a trajectories generation model with constant feed rate. A technique based on Bézier curves and a straight lines and parabolas interpolator has been developed; this technique is capable to guarantee a constant feed rate along a parametric curve which defines

the trajectory and so allowing a uniform material deposition for extrusion systems with constant material rate. Defining the trajectory parameters is possible to have an immediate feedback on the specific technological process studied. The use of this model has been shown in an actual example of a gluing deposition system. The trajectories generation model can be advantageous in all experiments related to AM techniques and technologies based on material extrusion.

References

1. Biagiotti L, Melchiorri C (2008) Trajectory planning for automatic machines and robots. Springer, Heidelberg, p 514
2. Boschetto A, Giordano V, Veniali F (2012) Modelling micro geometrical profiles in fused deposition process. *Int J Adv Manuf Technol* 61:945–956
3. Fiore E, Giberti H, Sbaglia L (2015) Dimensional synthesis of a 5-DOF parallel kinematic manipulator for a 3d printer. In: 16th international conference on research and education in mechatronics, REM 2015—Proceedings, art. no. 7380372, pp 41–52
4. Giberti H, Strano M, Annoni M (2016) An innovative machine for fused deposition modeling of metals and advanced ceramics. *MATEC Web Conf* 43:03003
5. Giberti H, Fiore E, Sbaglia L (2016) Kinematic synthesis of a new 3D printing solution. *MATEC Web Conf* 45:04013
6. Jiang KY, Gu YH (2004) Controlling parameters for polymer melting and extrusion in FDM. *Key Eng Mater*
7. Jin Y, Zhang J, Wang Y, Zhu Z (2009) Filament geometrical model and nozzle trajectory analysis in the fused deposition modeling process. *J Zhejiang Univ Sci A*
8. Jin et al (2014) Optimization of tool-path generation for material extrusion-based additive manufacturing technology. *Add Manuf* 1:32–47
9. Mohamed OA, Masood SH, Bhowmik JL (2016) Optimization of fused deposition modeling process parameters for dimensional accuracy using I-optimality criterion. *Measurement* 81:174–196
10. Roberson D, Shemelya CM, MacDonald E, Wicker R (2015) Expanding the applicability of FDM-type technologies through materials development. *Rapid Prototyping J* 21(2):137–143
11. Stratasys Inc. assignee, US Patent 5340433, date 23/08/1994, Modeling apparatus for three-dimensional objects
12. Thompson et al (2014) Efficient path planning algorithm for additive manufacturing systems. *IEEE Trans Compon Packag Manuf Technol* 4(9):1555–1563
13. Volpato N, Kretschek D, Foggia JA, Gomez da Silva Cruz CM (2015) Experimental analysis of an extrusion system for additive manufacturing based on polymer pellets. *Int J Adv Manuf Technol* 81:1519–1531

Preliminary Design of a Simplified Pneumatic Actuator

G.A. Naselli, M. Zoppi and R. Molfino

Abstract A major topic of soft robotics is the design of pneumatic actuators made of hyperelastic materials, such as silicone rubber. So far, many efforts have been made in the creation of prototypes, exploiting commercial silicone rubber, mainly to perform manipulation tasks or locomotion. However, there is a lack of methods for the design of such actuators. In this paper, we present the results of a preliminary work, aimed at the development of a method for the synthesis of a single chamber pneumatic actuator. The work is based on the use of finite elements and exploits two different algorithms to find the optimal shape of the actuator such that a prescribed deformation is obtained.

1 Introduction

In the last years, there has been an increasing interest in the field of *soft robotics*. Unlike rigid-linked conventional robots, soft robots are characterized by a distributed elasticity and, therefore, a number of degrees of freedom much greater. Soft robots are usually made of materials with low modulus of elasticity (e.g., polymers) and their reduced weight and high compliance are considered remarkable qualities in terms of safety in human-robot interaction. In particular, there have been relevant achievements in the creation of soft robots pneumatically actuated: this kind of robots is generally made of bodies with one or more internal chambers, which are inflated with a fluid. The result is a change of shape and volume that allows the robots to perform some task.

So far, researchers have designed soft robots able to perform locomotion and manipulation tasks. For instance, the soft gripper described in [5] is able to grasp objects of any shape, thanks to its compliance. Other examples of soft grippers can be found in literature (e.g., [6, 10]). All of them are actuated by inflating soft bodies with air. Their deformed shape results from a non-uniform distribution of the material over the volume of the actuator, and/or, in some cases, of the combination of

G.A. Naselli (✉) · M. Zoppi · R. Molfino
University of Genoa, DIME, Via all'Opera Pia 15A, 16145 Genoa, Italy
e-mail: naselli@dimec.unige.it

different materials. An example of soft robot able to crawl on the ground and pass beneath an obstacle is provided in [12]: the actuation principle is the same employed for the grippers, and also for the pneumatic actuators described in [8, 11]. Due to the characteristics of such actuators, some authors have performed finite element simulations to evaluate the performances, such as in [2]. However, there is a lack of methods for the design of such actuators, due to the novelty of the field.

The aim of this paper is to show the results obtained employing two different algorithms to calculate the optimal shape of the actuator. The goal is to achieve a prescribed deformation under hydrostatic pressure of given value. The optimization is performed both with a genetic algorithm, which does not require an initial point as input parameter, and a constrained optimization algorithm. In the past, the former has been widely employed by other authors to perform structural optimization (see, e.g., [1, 3, 7, 13]); the latter has been used, among other applications, to design compliant mechanisms (as shown, for instance, in [4]). The objective function is generated within the implementation of a finite element model of the actuator.

The paper is organized as follows: Sect. 2 presents the problem of the synthesis of a pneumatic actuator in general; in Sect. 3, the model created is described; in Sect. 4, the results obtained are presented and discussed. The conclusions of our work are summarized in Sect. 5.

2 Description of the Problem

The problem under investigation can be briefly summarized as follows: given a pneumatic actuator, made of a precise hyperelastic material, which must be its geometry in order to obtain a wanted deformed shape, under the action of a hydrostatic pressure?

If the pneumatic actuator has only one internal chamber (see Fig. 1), this means that the distribution of the thickness of the wall must be found.

The main difficulties are due to the nonlinear behaviour of the material employed to build such actuators; moreover, further complications arise due to large deformations.

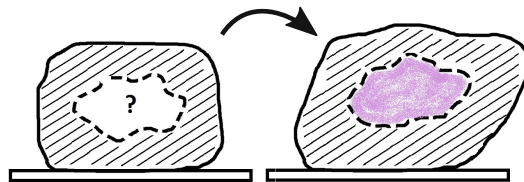


Fig. 1 Idealization of a pneumatic actuator with a single internal chamber. The shape of the chamber is unknown (*left*), and must be determined in order to obtain the wanted change of shape and/or volume (*right*) when an internal hydrostatic pressure is applied

At this stage of the work, some necessary simplifications have been introduced, as explained in the next section.

3 Model

For the purposes of this work, a two-dimensional model is employed. This is equivalent to consider the cross section of a cylindrical pneumatic actuator, neglecting the effect of the hydrostatic pressure along the axial direction. Of course, this assumption will be removed in future works, since real pneumatic actuators have usually sphere-like shapes.

The 2D system considered has been modelled by recurring to the finite elements technique. Since the geometry under investigation is a ring (see Fig. 2), we have employed only two-nodes beam elements to create the mesh. Each node has three degrees of freedom (*dof*): two translations on the plane and one rotation along the axis orthogonal to the plane; therefore, each beam element has six *dof*.

The N nodes belong to the circle of radius R , represented by the blue dash-dot line in Fig. 2. Since a pneumatic actuator is usually constrained to a frame, two nodes are considered clamped, and the mesh turns out to be made of $N - 1$ elements. The portion of the ring between the constrained nodes also represents the section through which the fluid is pumped inside the chamber.

The mesh adopted for this work is shown in Fig. 3: it is made of nineteen elements (we have set $N = 20$). The beam elements have rectangular section of width b . The influence of this dimension will be discussed further. For the moment, let the focus be on the height h_i of the generic i th beam element: such height is unknown. The

Fig. 2 Cross section of a single chamber pneumatic actuator. The chamber is filled with a fluid, introduced through the pipe represented on the left

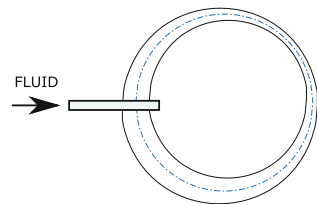
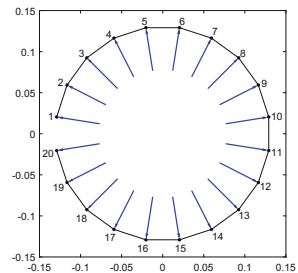


Fig. 3 Finite element model of the actuator. The mesh is made of nineteen element. Nodes n. 1 and 20 are clamped. The blue arrows represent the load applied



heights of the elements of the mesh are collected in the array \mathbf{h} and are the design variables. In other words, the variation of the thickness of the ring in the hoop direction is modelled with the different heights of the beams of the mesh. The number of elements considered allows to represent enough accurately the variability of the thickness in the ring.

In this way, each local stiffness matrix $\mathbf{K}_i^{(i)}$ depends on h_i , which represents the i th design variable, and on the other geometrical and material parameters of the beam element (length, Young's modulus, width of the cross section); hence, the global stiffness matrix of the whole structure depends on \mathbf{h} and the Hooke's law is written as:

$$\mathbf{F} = \mathbf{K}_g(\mathbf{h}) \cdot \mathbf{u} \quad (1)$$

remarking the dependence on the design variables. The vectors \mathbf{F} and \mathbf{u} contain respectively the nodal forces and the nodal displacements. In the problem described in this paper, the former is known, since the body is actuated with hydrostatic pressure; therefore, \mathbf{F} represents a uniformly distributed load acting on the nodes in radial direction. Some of the entries of the latter are prescribed, according to the wanted deformed shape of the actuator. Hence, if n is the number of prescribed entries in \mathbf{u} , the problem is to find \mathbf{h} such that $u_j = u_j^P$ for each $j = 1, 2, \dots, n$.

In order to solve the problem, we have defined the objective function

$$f(\mathbf{h}) = \sum_{j=1}^n |u_j(\mathbf{h}) - u_j^P| \quad (2)$$

and we have searched for its minimum by using two different algorithms. In both cases, the problem has been solved keeping into account the set of constraints:

$$h_{min} < h_i < h_{max}, \quad \forall i \quad (3)$$

The numerical values of the parameters adopted for this work are listed in Table 1. It is worth noticing that the quantities b and f appear linearly in Eq. 1, so the major role is played by their ratio, which can be treated as a scale factor. Moreover, these values does not affect the convergence of the calculation, unless unreasonable values are chosen.

Since the whole work has been implemented in Matlab®, we have employed two functions provided within the Global Optimization Toolbox of the software ([9]). On the one hand, we have performed the optimization by recurring to a genetic algorithm (the *ga* function). In this case, the optimization process does not require an initial point for \mathbf{h} as input. On the other hand, we have used the function *fmincon*, which finds the minimum for a constrained nonlinear function starting from an initial solution that must be assigned as input.

We have tested both the algorithm for different sets of prescribed displacements, on a mesh made of 19 elements. We report the results obtained for the following particular prescribed displacements:

Table 1 Geometrical and material parameters

Par.	Description	Value
R	Radius of the circle	130 mm
b	Width of the beam cross section	10 mm
E	Young's modulus	5 MPa
N	Number of nodes	20
f	Load applied on each node in radial direction	10 N/m
h_{min}	Minimum thickness admissible	1 mm
h_{max}	Maximum thickness admissible	30 mm

Table 2 Prescribed displacements

Case	Node	u_x (mm)	u_y (mm)
1	11	20	5
	17	10	-7
2	11	20	5
	16	Free	-10
	17	10	Free
3	9	10	7
	14	30	20
	16	10	-7

1. the translation of 11th and 17th nodes (*case 1*);
2. the translation of 11th node, the horizontal displacement of 17th node and the vertical displacement of 16th node (*case 2*);
3. the translation of 9th, 14th and 16th nodes (*case 3*).

The prescribed displacements for each case are listed in Table 2. The latter are referred to a cartesian system of coordinates in which the horizontal direction is denoted by x and the vertical (upwards) by y .

For each of the three cases listed above, *fmincon* function has been tested twice, with two different initial points: once, assuming $h_i = h_{min}$ (condition I) and then $h_i = h_{max}$ (condition II) for any i . In the next section, the results obtained are presented and discussed.

4 Results and Discussion

In this section, we report the results obtained to achieve a comparison between the effectiveness of the genetic algorithm and the *fmincon* function for the problem under consideration.

4.1 Case 1

The results obtained in the first case are reported in Table 3. Both the algorithms have been able to achieve a solution within the constraint tolerance.

As it is evident, the choice of the initial point does not have a relevant influence of the solution when *fmincon* is employed. In both cases, the solution was found in a short time: 10.3 and 11.2 s with initial point *I* and *II*, respectively. The time required for the genetic algorithm to find a solution has been considerably higher: 127.4 s on the same computer (Intel@Core™i7 processor, 2.0 GHz, 4 GB RAM). Moreover, the final value for the objective function has been greater when the calculation has been performed recurring to the genetic algorithm: such value is of the same order of magnitude of the prescribed displacements, which makes *fmincon* a more advantageous choice than the genetic algorithm. In addition, the solution found by means of the genetic algorithm presents a high number of abrupt variations of the thickness in the hoop direction, which should be avoided when building a prototype, if possible. This fact can be observed also in the other two cases presented.

4.2 Case 2

For the second case under investigation, the same considerations arisen for Case 1 are valid: also in this case the use of the genetic algorithm has been inconvenient, because of the time required for the computation and the final value of the objective function. The results are reported in Table 4.

4.3 Case 3

Also for the last case reported in this paper, the considerations made above are valid. However, due to the higher number of prescribed displacements, the final value of the objective function minimized with *fmincon* has been higher than in Cases 1 and 2: 2.9 mm against 0.002 mm achieved in Case 1. The results are listed in Table 5.

It is worth saying that we have tried to prescribe a higher number of displacements, but depending on the wanted deformed shape imposed, in some cases no solution has been found for the problem as constrained. This depends on the characteristics of the problem: due to the typology of the load applied to the structure, some requirements on the deformed configuration are not achievable. In other words, there is no possible geometry when the required deformed shape is not feasible. The most obvious example might be a compression of the actuator, impossible to achieve if the applied pressure inside the chamber is positive.

Table 3 Case 1 results: values (in mm) obtained using the genetic algorithm (g.a.) and the *fmincon* function with initial point *I* (f.m.) and *II* (f.M.)

alg.	h_1	h_2	h_3	h_4	h_5	h_6	h_7	h_8	h_9	h_{10}	h_{11}	h_{12}	h_{13}	h_{14}	h_{15}	h_{16}	h_{17}	h_{18}	h_{19}
g.a.	27.8	3.8	12.3	7.3	17.3	9.4	8.1	10.3	15.3	25.2	4.4	6.4	26.5	5.0	15.5	22.4	2.8	28.4	29.0
f.m.	19.9	19.5	19.0	3.0	18.1	18.2	18.3	18.6	19.5	20.1	19.6	18.8	17.9	7.4	4.7	17.5	2.7	18.3	17.9
f.M.	19.4	18.9	16.3	3.4	15.5	14.6	16.1	19.8	18.9	22.2	20.5	20.0	19.0	6.0	5.6	13.9	2.6	19.3	19.9

Table 4 Case 2 results: values (in mm) obtained using the genetic algorithm (g.a.) and the *fmincon* function with initial point *I* (f.m.) and *II* (f.M.)

alg.	h_1	h_2	h_3	h_4	h_5	h_6	h_7	h_8	h_9	h_{10}	h_{11}	h_{12}	h_{13}	h_{14}	h_{15}	h_{16}	h_{17}	h_{18}	h_{19}
g.a.	26.8	27.2	3.9	27.8	28.3	27.6	3.9	28.5	27.8	27.4	5.7	28.0	26.9	3.5	28.0	4.3	3.3	5.2	28.6
f.m.	20.6	19.0	18.8	10.9	16.1	17.4	9.0	19.1	21.1	20.8	20.2	18.9	16.9	7.5	3.9	5.1	4.1	4.0	15.0
f.M.	22.0	20.5	20.2	19.4	13.4	8.6	18.5	16.5	19.6	20.6	18.7	10.2	4.0	7.9	9.3	7.2	2.3	19.7	19.6

Table 5 Case 3 results: values (in mm) obtained using the genetic algorithm (g.a.) and the *fmincon* function with initial point *I* (f.m.) and *II* (f.M.)

alg.	h_1	h_2	h_3	h_4	h_5	h_6	h_7	h_8	h_9	h_{10}	h_{11}	h_{12}	h_{13}	h_{14}	h_{15}	h_{16}	h_{17}	h_{18}	h_{19}
g.a.	26.8	29.2	28.4	10.2	24.5	24.6	21.5	5.1	28.7	28.7	2.7	5.9	3.9	2.2	3.5	2.5	28.4	25.6	23.2
f.m.	18.2	20.1	18.7	19.9	16.5	17.5	18.8	17.7	1.5	7.3	12.8	10.1	11.5	24.5	1.2	4.3	14.9	26.8	29.9
f.M.	12.0	15.0	15.4	16.7	18.7	18.24	18.8	19.8	4.4	19.4	20.0	20.3	20.6	20.3	1.3	6.6	2.6	18.5	20.3

5 Conclusions

In this paper, we have presented an extremely simple finite element model for the design of a pneumatic actuator. The aim of the work has been to test the feasibility of the resolution of a constrained optimization, employing two different algorithms and comparing the results obtained. So far, the best choice seems to be to perform a constrained optimization without recurring to a genetic algorithm, since the initial point does not play a relevant role in the optimization process (at least, in the case under investigation).

In future works, we will improve the model, adopting a mesh made of shell elements and considering the thickness of each element as a design variable. Another remarkable improvement will consist in the implementation of a nonlinear model, since nonlinearity is a major feature of pneumatic actuators made of hyperelastic material.

Furthermore, the set of the feasible prescribed configurations will be determined: as expected, we have observed that, depending on the set of prescribed displacements of the nodes of the actuator, the solution may not exist.

Acknowledgments A sincere thank is due to colleague Barbara Bruno, PhD, for useful discussions about the use of the genetic algorithm and the computational burden involved.

References

1. Chen TY, Chiou YH (2013) Structural topology optimization using genetic algorithms. In: Proceedings of the world congress on engineering, vol 3
2. Elsayed Y, Vincensi A, Lekakou C, Geng T, Saaj CM, Ranzani T, Cianchetti M, Menciassi A (2014) Finite element analysis and design optimization of a pneumatically actuating silicone module for robotic surgery applications. *Soft Robot* 1(4)
3. Erbaturo F, Hasancebi O, Tutuncu I, Kilic H (2000) Optimal design of planar and space structures with genetic algorithms. *Comput Struct* 75:209–224
4. Howell LL (2001) Compliant mechanisms. Wiley. ISBN: 0–471–38478–X
5. Ilievski F, Mazzeo AD, Shepherd RF, Chen X, Whitesides GM (2011) Soft robotics for chemists. *Angew Chem Int Ed* 50(8):1890–1895
6. Katzschmann RK, Marchese AD, Daniela Rus D (2015) Autonomous object manipulation using a soft planar grasping manipulator. *Soft Robot* 2(4)
7. Lagaros ND, Papadrakakis M, Kokossalakis G (2002) Structural optimization using evolutionary algorithms. *Comput Struct* 80:571–589
8. Martinez RV, Branch JL, Fish CR, Shepherd RF, Nunes RMD, Suo Z, Whitesides GM (2013) Robotic tentacles with three-dimensional mobility based on flexible elastomers. *Adv Mater* 25:205–212
9. MATLAB R2014b and Global Optimization Toolbox. The MathWorks, Inc., Natick, Massachusetts, United States
10. Niiyama R, Sun X, Sung C, An B, Rus D, Kim S (2015) Pouch motors: printable soft actuators integrated with computational design. *Soft Robot* 2(2)
11. Shapiro Y, Gabor K, Wolf A (2015) Modeling a hyperflexible planar bending actuator as an inextensible eulerbernoulli beam for use in flexible robots. *Soft Robot* 2(2)

12. Shepherd RF, Ilievski F, Choi W, Morin SA, Stokes AA, Mazzeo AD, Chen X, Wang M, Whitesides GM Multigait soft robot. PNAS, vol 108 no 51, pp 20400–20403 doi:[10.1073/pnas.1116564108](https://doi.org/10.1073/pnas.1116564108)
13. Tai K, Akhtar S (2005) Structural topology optimization using a genetic algorithm with a morphological geometric representation scheme. Struct Multidisc Optim 30:113–127

Part IV
Multi-Body Dynamics

Multibody Model of Under-Actuated Tendon Driven Finger to Study the Antagonist Tendon

Sergio Savino

Abstract In this paper is presented a study on the antagonist tendon of an underactuated finger that is actuated by means of a traction tendon. The study is carried out developing a multibody model in which are applied the force that the tendons exert. The study and the model are part of a research activity to develop a mechanical hand with prosthetic purposes. The different types of antagonists tendons, that achieve different dynamic behaviours of the finger, are shown and described in the paper.

Keywords Multibody dynamics • Mechanical hand • Tendon driven systems • Underactuated system

1 Introduction

Simulation is one of the most important tools to analyze the behaviour of robotic systems, [1]. The multibody model of a system allows to study the dynamic behaviour of the system itself. The evolutions, that occurred in multibody dynamics, allowed it to become an important tool in the design, development and simulation of articulated mechanical systems, [2], and so also in simulation of human body. This modeling tool has been introduced in the study of different aspects, like to estimate the load of skeletal muscle during human activities, [3]; or to develop a dynamic model of the whole body, driven by the muscles, in order to study human tasks, [4–6]. Several toolboxes have been presented for the modelling and control of robot systems, [7–9], and many simulators have been dedicated to the study of the hand with the purpose to develop a tool for human and robot grasping evaluation, [10–12].

In this study a multibody model of an underactuated hand, developed and prototyped at the department “DII” of the University of Naples “Federico II”, is

S. Savino (✉)

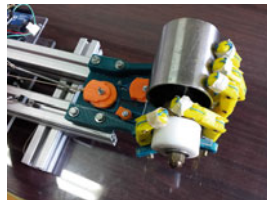
Department of Industrial Engineering, University of Naples Federico II, Naples, Italy
e-mail: sergio.savino@fastwebnet.it; sergio.savino@unina.it

© Springer International Publishing AG 2017

G. Boschetti and A. Gasparetto (eds.), *Advances in Italian Mechanism Science*,
Mechanisms and Machine Science 47, DOI 10.1007/978-3-319-48375-7_19

175

Fig. 1 The underactuated self adapting mechanical hand prostheses



introduced. The underactuated hand was described in previous papers of the authors [13–19], and its peculiarities are:

- simple mechanical system;
- differential system to transfer the motion to all the fingers;
- one motor to activate 15 d.o.f.

A prototype of the above hand is shown in Fig. 1.

The multibody model was developed to study the behaviour of the hand and all its components. The aim of such modelling is to analyze the dynamic behavior to optimize the design choose. In particular in this paper, some studies on the behaviour of a single finger are presented. In these studies it is shown the influence of different types of antagonists tendons on the dynamic behavior of underactuated finger.

2 Multibody Finger Model

A 3D model of an under-actuated finger for a five finger hand, Fig. 2a, has been developed and the working schemes of this finger model is reported in Fig. 2b.

Input parameters of each phalanx are: length (L), width (W), thickness (T), peg-hole radius (R). The scheme of each finger consists of three main subsystems for the three phalanx: “proximal”, “medial”, “distal”. By means of three revolute joints, the phalanges move between them. The multibody model allows to analyze all the parameters of the system during its dynamic behavior.

2.1 Action of the Traction Tendon

In order to simulate the presence of tendons inside the fingers, forces have been applied at points of entry and exit of the guides of the tendon itself. In Fig. 3 a

Fig. 2 Multibody model: **a** five fingers hand; **b** one finger

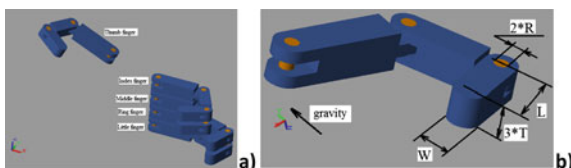


Fig. 3 Actions of traction tendon

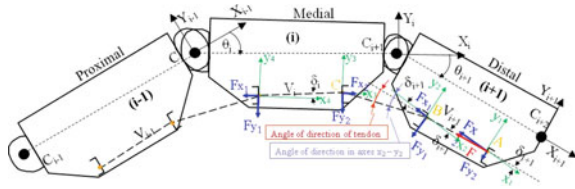


diagram of the actions of the actuator tendon, is shown. In each phalanx the action of the tendon was substituted with four forces that have the direction of the axis x and y of the reference system of the phalanx itself. The module of this forces depends on traction force, F, applied by tendon, geometrical parameters of the phalanx (like position of the tendon guides) and the rotation angle, θ_i, of the phalanx.

The force F, exerted by tendon, in the real prototype of the hand, is applied by means a motor that pull the tendon. Because the system is underactuated, the only control parameter of the motor is the displacement of the tendon. By assigning a displacement, the motor pulls the tendon that exerts its actions on the phalanges and these rotate.

3 Dynamic Behaviour of the Finger

In Table 1 the geometrical and inertial parameters of the finger are reported.

In the simulations, the distance from the joints along the Y axis, of the traction tendon guide, in all the phalanges, is the same and it is equal to 5 mm.

3.1 Free Simulation

A free simulation of the finger was carried out by neglecting the action of the antagonistic tendon. The tendon is actuated by a motor controlled on the error displacement of the traction tendon, like it is shown in the diagram of Fig. 4. In this simulation, the model of finger is actuated in such a way that the motor pulls the tendon according to a displacement ramp, which in 0.5 s, ensures the displacement of the tendon which is necessary to the complete closing of the finger. In Fig. 5 the

Table 1 Parameters of finger model

Phalanx	L (m)	W (m)	T (m)	Mass (kg)
Proximal	4.5×10^{-2}	1.4×10^{-2}	$1.4/3 = 4.67 \times 10^{-3}$	0.01
Medial	3×10^{-2}	1.4×10^{-2}	4.67×10^{-3}	0.0055
Distal	2×10^{-2}	1.4×10^{-2}	4.33×10^{-3}	0.0030

Fig. 4 Diagram of finger in “free simulation”

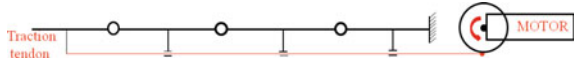
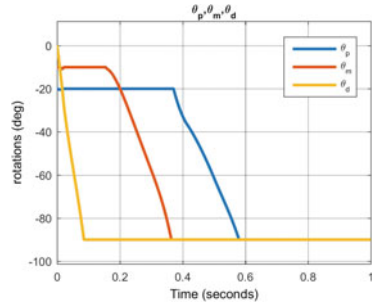


Fig. 5 Rotation angles of the three phalanges in “free simulation”



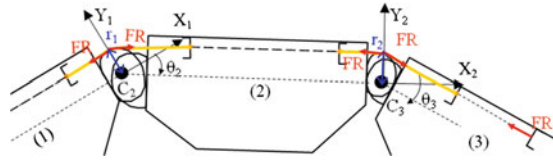
rotation angles of the three phalanges are shown. A such closing sequence of the phalanges of the finger, is not preferable in grasping tasks, in fact with this sequence the finger closes on itself and is not capable of grasping any object.

In this simulation it is evident that the traction tendon exerts a force only to start the movement of each phalanx. Because no other force acts on the phalanges, the closing sequence of the finger must necessarily be “distal-medial-proximal”. By modifying the geometric parameters of the phalanges and in particular the position of the tendon guides, it is possible to achieve different closing sequences, as discussed in [16].

4 Action of the Antagonist Tendon

The antagonist tendon opposes to the traction tendon action and allows to restore the finger in extended configuration, Fig. 6. This tendon is fixed to the last phalanx, the distal one, and it flows in guides positioned on the upper side of the finger. The medial phalanx and the proximal phalanx terminate with a pulley on which the antagonist tendon wraps itself. So, the actions that the antagonist tendon generates on the phalanges are different for the distal phalanx and for the medial and proximal phalanx. On the distal phalanx the action of antagonist tendon has the direction x and a value FR , and its point of application is the tendon attachment point, Fig. 6. On the medial and proximal phalanges the action of the antagonist tendon has a direction that depends on the rotation angle of successive phalanx and its point of application is in the hinge of the successive phalanx, Fig. 6. In Eq. (1) the antagonist tendon actions on the three phalanges are reported. Where FR is the action of antagonist tendon; F_{Aix} is the component of the action of the antagonist tendon on

Fig. 6 Actions of antagonist tendon



phalanx i in direction x ; F_{Aiy} is the component of the action of the antagonist tendon on phalanx i in direction y ; θ_i is the rotation angle of phalanx (i) .

$$\begin{aligned}
 F_{A3x} &= FR; F_{A3y} = 0; F_{A2x} = FR(1 - \cos \theta_3); F_{A2y} = FR \sin \theta_3; \\
 F_{A1x} &= FR(1 - \cos \theta_2); F_{A1y} = FR \sin \theta_2
 \end{aligned}
 \tag{1}$$

In the following, two different methods of application of the antagonist tendon force FR , were analyzed by means of the multibody model of the finger.

4.1 Antagonist Tendon Force

In the simplest case, the force of the antagonist tendon, FR , is implemented by a spring element with a stiffness k . In Fig. 7 a diagram of the actuation of the finger is shown.

In this case, the antagonist tendon always exerts a force which is increasing with the displacement of the tendon itself, simultaneously, the actuator tendon can never cancel its action even when the final configuration of the finger has been reached. Another consequence of the antagonist tendon type with fixed elastic element is that the motor, as in the case of “free simulation”, can only directly control the actuator tendon and thus the closure of the finger. In no case the control may act to reopen the finger. To ensure more control on the closing of the finger and also to act on its reopening, it is necessary to control the antagonist tendon. The solution that is presented in the following, provides that the antagonist tendon is connected to the

Fig. 7 Diagram of finger with antagonist tendon linked to spring element



Fig. 8 Diagram of finger with antagonist tendon actuated by the motor



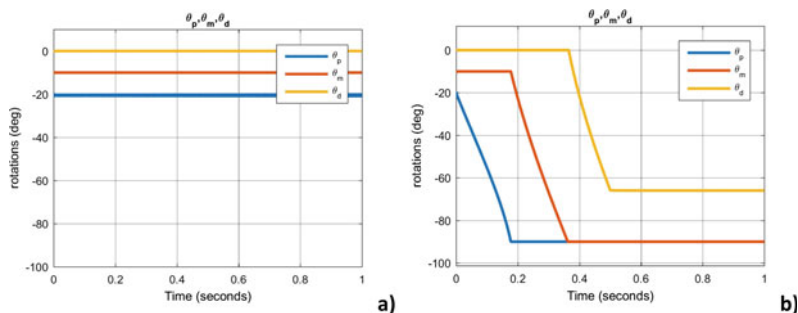


Fig. 9 Rotation angles of the three phalanges with antagonist tendon with stiffness spring elements: **a** stiffness of 280000 N/mm; **b** stiffness of 2.8 N/mm

same motor of the actuator tendon. This makes it possible to operate complete control on the actuator tendon displacement.

In general, in a given configuration of the finger, the displacements of the actuator tendon and of the antagonist tendon are different, because of the geometry of the finger itself. In order not to obstruct this difference in displacements, it is necessary to introduce an elastic element. Figure 8 shows a diagram of the finger as described above.

If it does not consider the presence of an elastic element, the finger stops when the displacement of the antagonist tendon is greater than that of the actuator tendon. This situation is shown in Fig. 9a, in which are represented the rotations of the phalanges with an extremely large stiffness of the elastic element.

An extremely large stiffness, $k = 280000$ N/mm, of the elastic element of the antagonist tendon stops the rotations of the phalanges like an inextensible tendon. With a stiffness $k = 2.8$ N/mm, the displacement of antagonist tendon can be greater than the displacement of traction tendon, and the finger can complete its closing sequence. The simulation of the model in the same conditions of the “free simulation”, shows that the finger reaches a configuration that corresponds to the desired displacement of the actuator tendon. The rotations of the phalanges are shown in the Fig. 9b.

The controlled antagonist tendon allows to follow a motion law for the displacement of the actuator tendon. The use of this type of antagonist tendon, introduces a possibility of greater control for the underactuated finger. In Fig. 10 the displacement of the actuator tendon (blue) is shown for the three types of antagonist tendon, and compared with desired law of motion (red). In the “free simulation”, Fig. 10a, the displacement of the actuator tendon cannot be controlled because there is not control on the over closing of the finger. When there is the action of an antagonist tendon with a fixed spring element, Fig. 10b, the final position of the actuator tendon is reached, but its law of motion is different by the desired one. With an actuated antagonist tendon, Fig. 10c, the final position of the actuator tendon is reached and also the displacement of actuator tendon is controlled. In this last case, the actuator does not need to exert a continuous force to counteract the action of the antagonist tendon.

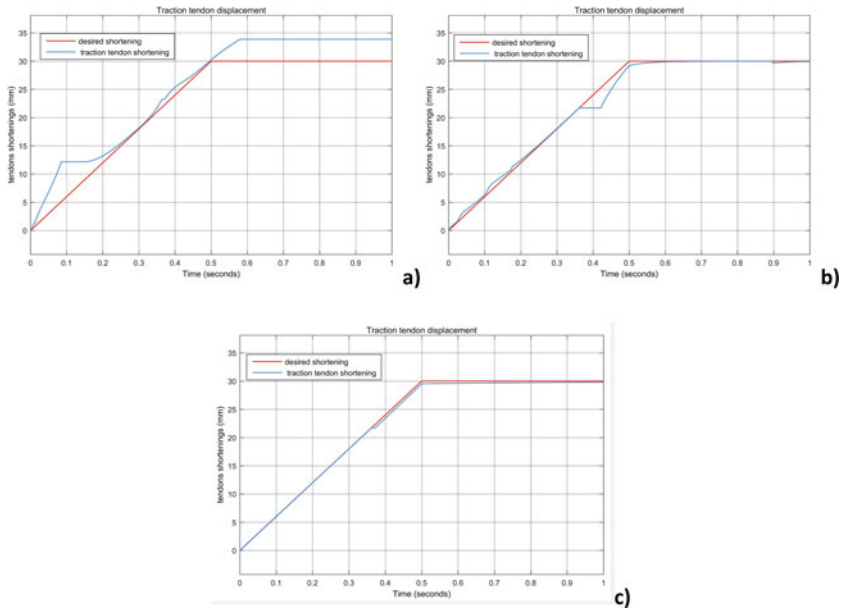


Fig. 10 Displacement of actuator tendon (*blue*) versus desired one (*red*): **a** free simulation; **b** antagonist tendon with fixed spring element; **c** actuated antagonist tendon

5 Conclusion

This study is part of the research activity of Department of Industrial Engineering of University of Naples “Federico II” on a mechanical hand, that has also prosthetic purpose. The hand is underactuated and it is tendon driven.

A multibody model of the under actuated finger was presented and it was used to study the effect of different type of antagonist tendon on the dynamic behaviour of the finger itself. Some results derived by simulations was presented. The model simulations was used to test the efficiency of a design choice based on an antagonist tendon actuated by the same motor of the actuator tendon. The results that are showed in this paper, demonstrate that the actuated antagonist tendon is a good solution to control the law of motion of the displacement of the actuator tendon. This solution was implemented in prototyping of the mechanical hand showed in Fig. 1. The multibody model is a good investigative tool for the study of the dynamic behavior of the finger. Future studies will focus on the analysis of the effect of the motion laws assigned to the motor on the dynamics of the finger, performing also experimental tests, and taking advantage the results of previously conducted investigations [20–23].

References

1. Žlajpah L (2008) Simulation in robotics. *Math Comput Simul* 79(4):879–897. ISSN 0378-4754
2. Amirouche F (2006) *Fundamentals of multibody dynamics: theory and applications*. Chicago
3. Veloso A, Esteves G, Silva S, Ferreira C, Brandao F (2006) Biomechanics modelling of human musculoskeletal using Adams multibody dynamics package. In: *Proceedings of the 24th IASTED international multi conference biomedical engineering*, Innsbruck, Austria, February 15–17, 2006, pp 401–407
4. Chao EY (2003) Graphic-based musculoskeletal model for biomechanical analyses and animation. *Med Eng Phys* 25(3):201–212
5. Pandy MG, Sasaki K, Kim S (1998) A three-dimensional musculoskeletal model of the human knee joint. Part 1: Theoretical construct. *Comput Methods Biomech Biomed Eng* 1(2):87–108
6. Stylianou AP, Guess TM, Kia M (2013) Multibody muscle driven model of an instrumented prosthetic knee during squat and toe rise motions. *J Biomech Eng* 135(4)
7. Chinello F, Scheggi S, Morbidi F, Prattichizzo D (2011) Kuka control toolbox. *IEEE Robot Autom Mag* 18(4):69–79
8. Corke P (1996) A robotics toolbox for MATLAB. *IEEE Robot Autom Mag* 3(1):24–32
9. Mariottini G, Prattichizzo D (2005) EGT for multiple view geometry and visual servoing: robotics and vision with pinhole and panoramic cameras. *IEEE Robot Autom Mag* 12(4):26–39
10. Le´on B, Ulbrich S, Diankov R, Puche G, Przybylski M, Morales A, Asfour T, Moisio S, Bohg J, Kuffner J. et al (2010) Opengrasp: a toolkit for robot grasping simulation, Simulation, modeling, and programming for autonomous robots, pp 109–120
11. Malvezzi M, Gioioso G, Salvietti G, Prattichizzo D, Bicchi A (2013) SynGrasp: a MATLAB toolbox for grasp analysis of human and robotic hands. In: *Proceedings of IEEE international conference on robotics and automation*, Karlsruhe, Germany
12. Miller A, Allen P (2004) Graspit! a versatile simulator for robotic grasping. *IEEE Robot Autom Mag* 11(4):110–122
13. Carbone G, Rossi C, Savino S (2015) Performance comparison between FEDERICA Hand and LARM Hand. *Int J Adv Robot Syst* 12
14. Niola V, Penta F, Rossi C, Savino S (2015) An underactuated mechanical hand: theoretical studies and prototyping. *Int J Mech Control* 16(1):11–19. ISSN: 15908844
15. Niola V, Rossi C, Savino S (2014) A new mechanical hand: theoretical studies and first prototyping. *Int Rev Mech Eng* 8(5):835–844
16. Penta F, Rossi C, Savino S (2014) An underactuated finger for a robotic hand. *Int J Mech Control* 15(2). ISSN: 1590-8844
17. Rossi C, Savino S (2013) Mechanical model of a single tendon finger. In: *Proceedings of ICNAAM 2013: 11th international conference of numerical analysis and applied mathematics*, Rhodes, Greece, Sep 21–27
18. Rossi C, Savino S (2014) An underactuated multi-finger grasping device. *Int J Adv Robot Syst* 11(1), Article number 20
19. Rossi C, Savino S, Niola V, Troncone S (2015) A study of a robotic hand with tendon driven fingers. *Robotica*. ISSN: 0263-5747. doi:[10.1017/S0263574714001179](https://doi.org/10.1017/S0263574714001179)
20. Brancati R, Rossi C, Timpone F (2007) Dynamic behavior and motion planning of a robot arm with non-rigid transmission. *Mech Based Des Struct Mach* 35(4):347–362
21. Niola V, Rossi C, Savino S (2010) A new real-time shape acquisition with a laser scanner: first test results. *Robot Comput Integr Manuf* 26(6):543–550
22. Niola V, Rossi C, Savino S, Strano S (2010) Robot trajectory planning by points and tangents. In: *Proceedings of the 10th WSEAS international conference on robotics, control and manufacturing technology, ROCOM '10*, Hangzhou, China, April 11–13, 2010, pp 91–96
23. Rossi C, Savino S (2013) Robot trajectory planning by assigning positions and tangential velocities. *Robot Comput Integr Manuf* 29(1):139–156. doi:[10.1016/j.rcim.2012.04.003](https://doi.org/10.1016/j.rcim.2012.04.003)

A Model Reduction Strategy for Flexible-Link Multibody Systems

Ilaria Palomba, Dario Richiedei and Alberto Trevisani

Abstract In this paper a novel strategy is presented to perform the reduction at system level of flexible-link multibody models based on the equivalent rigid-link system modeling approach. Such a strategy is aimed at obtaining reduced models ensuring an accurate description of the full-order model dynamics in a frequency range of interest and in a wide subset of the workspace. Starting from the well-known Craig-Bampton reduction technique, and the interior mode ranking method a configuration-dependent reduction transformation is formulated, which allows obtaining a minimum-size reduced model, accurately describing the dynamics of interest. The proposed strategy has been validated by applying it to the model of a flexible-link planar manipulator driven by three motors.

Keywords Model reduction · Flexible-link multibody systems · Craig-Bampton method · Interior mode ranking method · Equivalent rigid-link system

1 Introduction

Flexible-link multibody systems (FLMBSs) are increasingly used, since light weight systems promise smaller power consumption and improved dynamic performances compared to rigid-link multibody systems.

The modeling of FLMBSs imposes the use of a large number of coordinates representing the system elasticity. The resulting models have high dimensions and require

I. Palomba (✉)

Faculty of Science and Technology, Free University of Bozen-Bolzano,
Piazza Università 5, Bolzano, Italy
e-mail: Iaria.Palomba@unibz.it

D. Richiedei · A. Trevisani

Department of Management and Engineering (DTG), Università Degli
Studi di Padova, Stradella S. Nicola 3, 36100 Vicenza, Italy
e-mail: dario.richiedei@unipd.it

A. Trevisani

e-mail: alberto.trevisani@unipd.it

© Springer International Publishing AG 2017

G. Boschetti and A. Gasparetto (eds.), *Advances in Italian Mechanism Science*,
Mechanisms and Machine Science 47, DOI 10.1007/978-3-319-48375-7_20

considerable computational efforts, so they are not suitable for model-based design or for state estimation and real-time control. Therefore, the use of model reduction techniques is often necessary. Numerous contributions can be found in the literature on the reduction of linear time-invariant models [1], but they cannot be employed directly since the dynamic models of FLMBs are highly nonlinear.

A common way, to reduce the model size of FLMBs and to exploit the state-of-the-art reduction techniques developed for linear systems, consists in generating a reduced linear finite element (FE) sub-model of each link, and then in embedding such reduced models in a floating frame [7], in a co-rotational frame [5], or in a moving reference configuration [8] in order to allow for large displacements and rotations. Such an approach based on the concept of component mode synthesis [1] is at the single component level. However, a reduction at the full system level can improve the accuracy of reduced models while keeping the size to a minimum [2].

In this paper a novel strategy is presented to perform the reduction at the full system level of FLMB models. Such a strategy is aimed at obtaining reduced models ensuring an accurate description of the full-order model dynamics in a frequency range of interest and in a wide subset of the workspace. In order to obtain such a goal, the new strategy suitably modifies and combines the Equivalent Rigid Link System (ERLS) approach [9], the well-known Craig-Bampton reduction technique [3], and the Interior Mode Ranking (IMR) method [6].

The remainder of the paper is organized as follows. In Sect. 2 the proposed reduction strategy is presented. In Sect. 3 it is applied to reduce the model of a flexible-link planar manipulator driven by three motors, and its validity is proved. Concluding remarks are given in the Sect. 4.

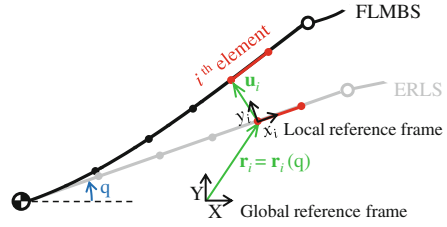
2 Reduction of ERLS-Based Dynamic Models

Let us consider a FLMB with holonomic and scleronomous constraints. The total motion of such a system can be notionally separated into two motions mutually influenced: the large rigid-body motion of the ERLS, whose generalized coordinates are denoted $\vec{q} \in \mathbb{R}^{n_q}$, and the small elastic displacements $\vec{u} \in \mathbb{R}^{n_u}$ of the flexible links with respect to the ERLS itself [9], as schematically represented in Fig. 1. Follows this representation, the system nonlinear motion equations can be written as below:

$$\begin{aligned} & \begin{bmatrix} \mathbf{K}(\mathbf{q}) & \mathbf{0} \\ \mathbf{0} & \vec{\mathbf{0}} \end{bmatrix} \begin{Bmatrix} \mathbf{u} \\ \mathbf{q} \end{Bmatrix} + \begin{bmatrix} 2\mathbf{M}_G(\mathbf{q}) + \mathbf{C}(\mathbf{q}) & \mathbf{M}(\mathbf{q})\dot{\mathbf{S}}(\mathbf{q}, \dot{\mathbf{q}}) \\ \mathbf{S}^T(\mathbf{q})(2\mathbf{M}_G(\mathbf{q}) + \mathbf{C}(\mathbf{q})) & \mathbf{S}^T(\mathbf{q})\mathbf{M}(\mathbf{q})\dot{\mathbf{S}}(\mathbf{q}, \dot{\mathbf{q}}) \end{bmatrix} \begin{Bmatrix} \dot{\mathbf{u}} \\ \dot{\mathbf{q}} \end{Bmatrix} + \\ & + \begin{bmatrix} \mathbf{M}(\mathbf{q}) & \mathbf{M}(\mathbf{q})\mathbf{S}(\mathbf{q}) \\ \mathbf{S}^T(\mathbf{q})\mathbf{M}(\mathbf{q}) & \mathbf{S}^T(\mathbf{q})\mathbf{M}(\mathbf{q})\mathbf{S}(\vec{q}) \end{bmatrix} \begin{Bmatrix} \ddot{\mathbf{u}} \\ \ddot{\mathbf{q}} \end{Bmatrix} = \begin{bmatrix} \mathbf{M}(\mathbf{q}) & \mathbf{I} \\ (\mathbf{S}^T(\mathbf{q})\mathbf{M}(\mathbf{q})) & \mathbf{S}(\mathbf{q})^T \end{bmatrix} \begin{Bmatrix} \mathbf{g}(\vec{q}) \\ \mathbf{f}(\mathbf{q}) \end{Bmatrix} \quad (1) \end{aligned}$$

where \vec{K} , \vec{C} , and \vec{M} are the stiffness, damping and mass matrices obtained by assembling the consistent matrices of the FEs; matrix \vec{M}_G represents the centrifugal and

Fig. 1 ERLS definition



Coriolis effects; \vec{S} is the ERLS sensitivity coefficient matrix for all the nodes of the FEs, which relates the velocities of the ERLS generalized coordinates \vec{q} to the velocities of all the nodes of the ERLS \vec{r} ($\dot{\vec{r}} = \vec{S}(\vec{q})\dot{\vec{q}}$); \vec{g} is the gravity acceleration vector, and \vec{f} is the external force vector. Hereafter, the three matrices on the left-hand side of Eq. (1) will be denoted, respectively, as \vec{K} , \vec{C} , and \vec{M} .

The application of the CB method requires to split the degrees of freedom (dofs) into master and slave dofs and to partition the motion equations accordingly. In particular, all the ERLS coordinates \vec{q} have to be selected as master dofs. The set of the master dofs should be also expanded to include some meaningful elastic coordinates, such as the ones of those nodes where external forces may be applied or where sensors are located. By partitioning \mathbf{u} into $\mathbf{u}_m \in \mathbb{R}^\mu$ and $\mathbf{u}_s \in \mathbb{R}^\varsigma$ ($\mu + \varsigma = n_u$), which denote the elastic coordinates chosen as, respectively, the master and the slave dofs, the vector of master dofs is therefore $\vec{x}_m = \{\mathbf{q}^T \quad \mathbf{u}_m^T\}^T$. Such a selection of the master dofs leads to a subsystem related to the slave dofs \vec{u}_s , which is linear and depending on the configuration, i.e. on \vec{q} . This allows performing a local modal analysis for the computation of the so-called interior mode matrix Φ . In particular, Φ is computed by placing the ERLS at a given equilibrium configuration \mathbf{q}^* (i.e. by setting $\dot{\mathbf{q}} = \ddot{\mathbf{q}} = \mathbf{0}$):

$$\begin{aligned} & \left(\vec{K}_s(\mathbf{q}^*) - \omega_i \vec{M}_s(\mathbf{q}^*) \right) \phi_i = \mathbf{0}, \quad i = 1, \dots, \varsigma \\ \Phi &= [\phi_1 \dots \phi_i \dots \phi_\varsigma], \quad \Phi^T \vec{M}_s(\mathbf{q}^*) \Phi = \mathbf{I}, \quad \Phi^T \vec{K}_s(\mathbf{q}^*) \Phi = \Omega \end{aligned} \quad (2)$$

where the subscript s denotes the matrix partitions corresponding to the slave dofs, while Ω is a diagonal matrix whose entries are the eigenvalues of $\vec{M}_s^{-1} \vec{K}_s$.

In order to reduce model dimension, the set of interior modes should be truncated. To this end the most important interior modes, $\tilde{\Phi} \in \mathbb{R}^{\varsigma \times \tau}$ ($\tau \ll \varsigma$) are selected according to the IMR method [6]. Such a method ranks and selects the interior modes which provide the highest contributions to all the vibration modes of the complete system with actual boundary conditions in the frequency range of interest.

It is worth noticing that matrix $\tilde{\Phi}$ is configuration-dependent: $\tilde{\Phi} = \tilde{\Phi}(\vec{q})$. Hence it only has a local validity. This is due to the definition of the elastic variables assumed in the model: they are defined with respect to an ERLS, which follows the gross motion of the FLMBS. Therefore, when the system moves, the ERLS follows its

motion, and then the elastic coordinates must be re-defined in the new ERLS. In order to use the interior modes computed at the equilibrium configuration \mathbf{q}^* in a wide subset of the workspace, they have to be projected onto the actual, instantaneous ERLS by means of a transformation matrix.

Let $\mathbf{R} \in \mathbb{R}^{c \times c}$ be a block-diagonal matrix expressing the rotation of the slave dofs from the local reference frames of each FE $\{x_i; y_i\}$ (see Fig. 1) to the global one $\{X; Y\}$, the configuration-dependent interior mode matrix $\tilde{\Psi}$ can be defined as:

$$\tilde{\Psi}(\mathbf{q}) = \mathbf{R}(\mathbf{q})\mathbf{R}^T(\mathbf{q}^*)\tilde{\Phi}(\mathbf{q}^*) = \mathbf{R}(\mathbf{q} - \mathbf{q}^*)\tilde{\Phi}(\mathbf{q}^*) \quad (3)$$

with \mathbf{q} the actual system configuration and \mathbf{q}^* the one where $\tilde{\Phi}$ has been computed.

Finally, the configuration-dependent CB reduction matrix is defined as follows:

$$\mathbf{H}(\mathbf{q}) = \begin{bmatrix} \mathbf{I} & \mathbf{0} \\ \mathbf{B}(\mathbf{q}) & \tilde{\Psi}(\mathbf{q}) \end{bmatrix} \quad (4)$$

In Eq. (4) $\mathbf{B}(\vec{q}) = -\overline{\mathbf{K}}_s^{-1}(\vec{q})\overline{\mathbf{K}}_{sm}(\vec{q})$ is the Guyan's condensation (the double subscripts denote the matrix partition corresponding to the coupling terms between slave and master dofs), here defined as a configuration-dependent matrix. Such a definition of the Guyan's matrix requires to know the inverse of $\overline{\mathbf{K}}_s \in \mathbb{R}^{c \times c}$ for each value of \mathbf{q} . $\overline{\mathbf{K}}_s$ is a stiffness matrix arising from a FE model, therefore it is typically a block and sparse matrix. As a consequence, its inverse can be easily computed analytically in advance (pre-processed) by means of Schur complements or other well-known linear algebra methods [4]. Once an analytical formulation of $\overline{\mathbf{K}}_s^{-1}$ is available it is possible to set an analytical configuration-dependent formulation of \mathbf{B} . However, if the number of slave dofs is large, it might not be possible, or at least it could be not convenient, to compute the inverse of $\overline{\mathbf{K}}_s$ analytically. Numerical methods should be employed. In this case, matrix inversion must be performed for each variation of \mathbf{q} . Although such an operation decreases the computational efficiency of the reduced model, the use of reduced models is generally still extremely advantageous compared to the use of full-order models.

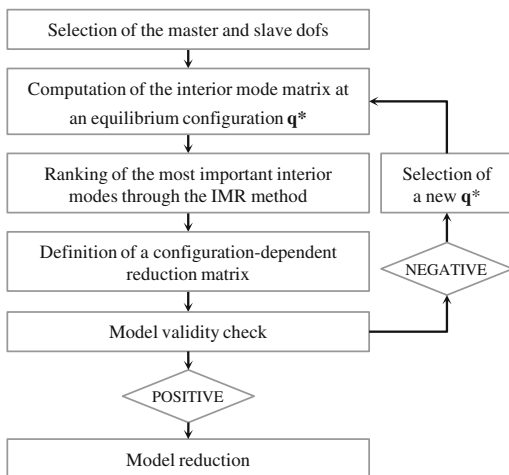
By transforming the system matrices in Eq. (1) through $\tilde{\mathbf{H}}$, the reduced nonlinear model is obtained as follows:

$$\mathbf{H}^T \overline{\mathbf{K}} \mathbf{H} \begin{Bmatrix} \mathbf{x}_m \\ \boldsymbol{\eta} \end{Bmatrix} + \mathbf{H}^T \overline{\mathbf{C}} \mathbf{H} \begin{Bmatrix} \dot{\mathbf{x}}_m \\ \dot{\boldsymbol{\eta}} \end{Bmatrix} + \mathbf{H}^T \overline{\mathbf{M}} \mathbf{H} \begin{Bmatrix} \ddot{\mathbf{x}}_m \\ \ddot{\boldsymbol{\eta}} \end{Bmatrix} = \mathbf{H}^T \overline{\mathbf{F}} \quad (5)$$

where vector $\boldsymbol{\eta} \in \mathbb{R}^r$ collects the modal coordinates associated to the retained interior modes, and $\overline{\mathbf{F}}$ represents the term on the right-hand side in Eq. (1).

The resulting reduced-order model is able to represent the nonlinearities of the full-order model, its dependence on configuration, and to model correctly the system dynamics in a finite neighborhood of the equilibrium configuration \vec{q}^* .

Fig. 2 Main steps for FLMBs model reduction



In order to check the validity of the reduced model far from \vec{q}^* , a simple analysis can be made. In particular, since the interior modes have been normalized with respect to the mass matrix (see Eq. 2), the model consistency may just be based on verifying that the projected interior modes are still $\bar{\mathbf{M}}_s$ -orthogonal: $\tilde{\Psi}^T(\mathbf{q})\bar{\mathbf{M}}_s(\mathbf{q})\tilde{\Psi}(\mathbf{q}) \approx \mathbf{I}$. When such a verification fails, Φ must be calculated in a new configuration \vec{q}^* .

The main steps of the strategy proposed here are summarized in Fig. 2.

3 Validation and Assessment

The new reduction strategy has been validated by applying it to the reduction of the model of a planar manipulator with flexible links lying on the horizontal plane. A schematic representation of the manipulator is shown in Fig. 3. Such a topology is often employed in industrial robots designed for material handling. The manipulator consists of five rods with circular cross-sections, which are supposed to be made of Aluminum Anticorodal (Young's modulus 69 GPa, mass density 2700 kg/m³). All the links have been modeled with classical two-node and six-degree-of freedom beam elements. The geometric parameters of the links are listed in Table 1. The links are connected to each other by means of revolute joints with negligible clearance and friction losses. Three motors are supposed to drive links 1, 2 and 4–5. Lumped masses and inertias are used to account for the moving joints, and for the brakes and the rotors of the motors, as indicated in Table 2. The full-order dynamic model synthesized for such a manipulator has 30 dofs, of which three are the generalized coordinates of the ERLS, $\mathbf{q} = \{q_1 \ q_2 \ q_3\}^T$, and 27 are elastic dofs.

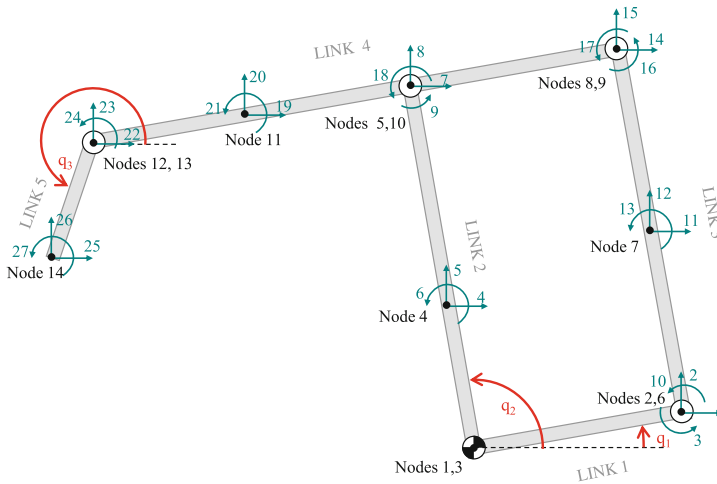


Fig. 3 Finite element model of the studied manipulator

Table 1 Geometric parameters

Link	Length (m)	Diameter (mm)
1	0.5	30
2	0.85	30
3	0.85	16
4	1.2	24
5	0.282	20

Table 2 Lumped masses and inertia

Node	Mass (kg)	Inertia (kgm ²)	Node	Mass (kg)	Inertia (kgm ²)
1	7.644	0.013	8	0.383	0
2	0.392	0	9	0.658	0
3	9.517	0.0229	10	0.308	0
4	0.4	0	12	1.537	0
5	0.648	0	13	0.095	0.0015
6	0.671	0	14	0.046	0

The aim is to get a reduced model capable to represent correctly the system dynamics in the frequency range 0–180 Hz, basically, corresponding to motor bandwidth and to the range within which active vibration control could be reasonably achieved. In the frequency range of interest there are 3 rigid-body modes and 6 elastic vibration modes. As far as the rigid modes are concerned, they are always represented correctly, since the rigid body variables are all collected in the master dofs.

In order to satisfy the test aim, the first 6 elastic eigenvectors of the system must be properly approximated by the chosen subset of interior modes.

The master dofs selected are the three ERLS coordinates, i.e. the angular positions of the actuated links, and other six elastic coordinates (dofs 4, 5, 14, 15, 25, and 26 in Fig. 3); hence the 30 dofs are split into 9 master dofs and 21 slave dofs.

After the application of the proposed reduction strategy very good level of accuracy has been achieved with a model with just 13 dofs, i.e. comprising 4 out of 21 slave dofs. As a consequence the model dimension has been reduced by 56%, while guaranteeing a perfect match between the dynamics of interest represented by the

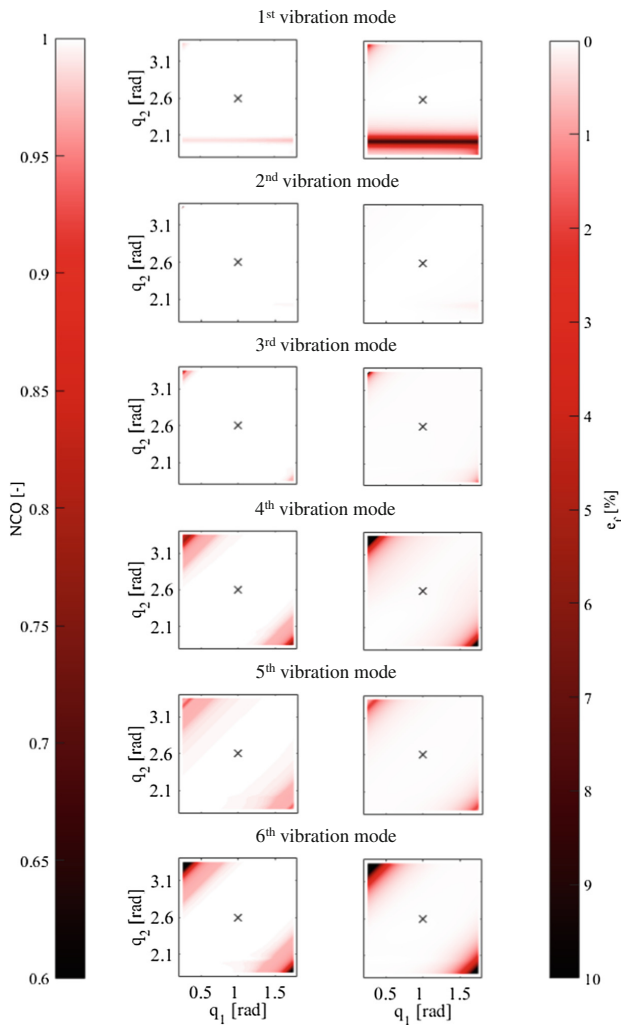


Fig. 4 NCO (left), e_f (right) for the six vibration modes in the bandwidth of interest

full-order model and the reduced one. The comparison between the two models has been made in terms of eigenvectors (through the NCO: a squared cosine between the two eigenvectors computed by using the mass matrix as the scalar product) and eigenfrequencies (through a relative percentage error: e_f). In Fig. 4 these two evaluation parameters are shown for each of the six vibration modes in the frequency range of interest. For clarity of representation, the indices are plotted versus just two coordinates, (q_3 is constant), however, very similar results have been obtained when all the coordinates vary. An example of reduced model has been synthesized at the equilibrium configuration $\mathbf{q}^* = \{1.0 \ 2.6 \ 1.5\pi\}^T$ rad, indicated by a black cross in each plot. Then, the model has been evaluated in a neighborhood of such a configuration. It is worth noticing that in each plot both the coordinates q_1 and q_2 have been varied from the values at the reference configuration by as much as ± 0.75 rad. Apparently such changes do not affect evaluation indices considerably: indices keep values which are very close to their target values (i.e. one for the NCO and zero for the e_f). Therefore, it is proved that the 13-dof reduced model represents correctly the dynamics of interest in a wide subset of the manipulator workspace.

4 Conclusions

In this paper a novel strategy has been presented to perform the reduction at system level of FLMBSSs modeled by based on the equivalent rigid link system. The strategy consists in using the well-known Craig-Bampton (CB) method suitably modified (in order to cope with nonlinearities of FLMB models) together with the Interior Mode Ranking method, which allows ranking and selecting the interior vibrational modes of the CB method that guarantee obtaining a minimum-size reduced model, accurately describing the dynamics of the system in a frequency range of interest. The new strategy leads to the formulation of a configuration-dependent reduction transformation capable of representing the nonlinearities of the full-order model, and its dependence on configuration.

The proposed strategy has been validated by applying it to the reduction of the model of a flexible-link planar manipulator with hybrid topology and driven by three motors. The results obtained are satisfactory: the technique developed has led to a significant reduction in the size of the model while keeping a very accurate representation of the system dynamics in the frequency range of interest.

References

1. Besselink B, Tabak U, Lutowska A, van de Wouw N, Nijmeijer H, Rixen D, Hochstenbach M, Schilders W (2013) A comparison of model reduction techniques from structural dynamics, numerical mathematics and systems and control. *J Sound Vib* 332(19):4403–4422

2. Bruls O, Duysinx P, Golinval JC (2007) The global modal parameterization for non-linear model-order reduction in flexible multibody dynamics. *Int J Numer Methods Eng* 69(5):948–977
3. Craig R, Bampton M (1968) Coupling of substructures for dynamic analyses. *AIAA J* 6(7):1313–1319
4. Hogben L (2006) *Handbook of linear algebra*. CRC Press
5. Kadawathagedara STW, Rixen DJ (2011) Model reduction in co-rotated multi-body dynamics based on the dual Craig-Bampton method. In: 52nd AIAA/ASME/ASCE/AHS/ASC Structures, structural dynamics and materials conference. AIAA, pp 1869–1886
6. Palomba I, Richiedei D, Trevisani A (2014) A ranking method for the selection of the interior modes of reduced order resonant system models. In: ASME 2014 12th biennial conference on engineering systems design and analysis, ESDA 2014, vol 2. ASME
7. Shabana AA, Wehage RA (1983) A coordinate reduction technique for dynamic analysis of spatial substructures with large angular rotations. *J Struct Mech* 11(3):401–431
8. Vidoni R, Gallina P, Boscarol P, Gasparetto A, Giovagnoni M (2015) Modeling the vibration of spatial flexible mechanisms through an equivalent rigid-link system/component mode synthesis approach. *J Vib Control* 1077546315604495
9. Vidoni R, Gasparetto A, Giovagnoni M (2014) A method for modeling of three-dimensional flexible mechanisms based on an equivalent rigid-link system. *J Vib Control* 483–500

Part V

Reliability

Topology Optimization and Analysis of Static Transmission Error in Lightweight Gears

Jakub Korta, Domenico Mundo, Giuseppina Ambrogio,
Barbara Folino, Shadi Shweiki and Luigino Filice

Abstract In this paper, the influence of gear-body lightweighting on the static transmission error (STE) for a pair of spur gears is investigated by using the Finite Element (FE) method. The transmission error, in fact, is recognized as one of the main internal excitation sources in a mechanical transmission and the minimization of its variability along the meshing cycle is considered as a design target to improve the N&V behaviour of the full transmission. The case study analysed in this paper is derived from a gearbox typically used in helicopter transmissions. The FE model of three different variants of the same gear pair, one solid model and two lightweight models, are generated and analysed by non-linear FE static simulations. By deriving the STE curves for each of the gear pairs, the impact of the increased flexibility caused by material removal in the two lightweight models is investigated.

Keywords Gears • Mechanical transmissions • Transmission error • Finite element method • Nonlinear static analysis

J. Korta · D. Mundo (✉) · G. Ambrogio · B. Folino · S. Shweiki · L. Filice
University of Calabria, Rende, Italy
e-mail: domenico.mundo@unical.it

J. Korta
e-mail: jakub.korta@unical.it

G. Ambrogio
e-mail: giuseppina.ambrogio@unical.it

S. Shweiki
e-mail: shadi.shweiki@unical.it

L. Filice
e-mail: luigino.filice@unical.it

J. Korta
AGH University of Science and Technology, Kraków, Poland

1 Introduction

During the development process of a mechanical transmission a large number of factors must be taken under consideration in order to achieve a good quality design, which meets all the design targets and constraints.

System weight represents one of the main structural constraints in many areas of mechanical engineering and design. Especially in some fields of the transportation industry, weight reduction is the key for engineers to meet stringent design targets and constraints linked to system efficiency and sustainability. Being key mechanical components in most of the industrial applications in those areas, mechanical transmissions, and specifically gearboxes, are often targeted as system's regions where material must be reduced. Gear lightweighting is quite common in those application areas, such as aerospace engineering, where huge mechanical transmissions are employed and severe quests for mass reduction apply. It is typically achieved by removing material from the central part of the gear, i.e. the gear body, where holes are manufactured in order to reduce the mass.

Predicting the influence of design variables, such as teeth macro and micro-geometry, gear material and dimensional characteristics, on the dynamic behavior of the full transmission is a non-trivial task and requires the availability of proper simulations tools. Such tools support the development process from the earliest phases of concept design up to refinement engineering, enabling a significant reduction of physical prototyping and hence reducing development costs and time.

The design and development of mechanical transmissions are even more challenging when system lightweighting is targeted due to the huge impact that material removal has on gear meshing stiffness and, in general, on system flexibility. The variability of the former along the meshing cycle, in fact, is recognized as one of the main sources of system excitation and cause of significant non-linear, load-dependent phenomena, such as clearance-type non-linearity [2, 5] and rattle noise [3, 4]. Strictly linked to the variable meshing stiffness is the so called Transmission Error (TE) [10]. The TE is defined as a deviation of the real gear motion from the nominal case of perfectly conjugated meshing teeth, which can be caused by different reasons: misalignments, teeth deflection under load, manufacturing inaccuracies and others. One the most accurate approaches to estimate the TE curve in a gear pair is based on the use of the FE method [6]. However, its major drawback, i.e., the simulation time, precludes its application to demanding dynamic problems analyzed in the time domain. Several studies proposed the use of non-linear static FE simulations to estimate the transmission error of a gear pair under static loads. STE curves can be thus generated to provide a basic characterization of the gear meshing process and, eventually, can be used subsequently in analytical one-dimensional [8] or multi-body three-dimensional [7] formulations to predict the dynamic response.

In this paper, we propose the use of topology optimization [1] in combination with static FE simulations as a tool for the design of lightweight gears. Based on

design indications given by the results of the topology optimization, a new model of lightweight gear is generated and analysed in comparison with an existing model taken from the literature. The case study analysed in the paper consists of a pair of spur gears derived from a gearbox, which is typically used in helicopter transmissions [9]. In order to investigate the influence of the proposed approach for gear body mass reduction, the FE models of two lightweight gears are built. By applying static loads, STE curves are derived and subsequently used for a comparative analysis of the variability of the meshing stiffness along multiple meshing cycles in the solid, in the classical and in the newly proposed lightweight models.

2 Gear Topology Optimization

Topology optimization was used for achieving a design that allows reducing the weight of a gear. This type of procedure is aimed at finding optimal mass distribution within the specified design domain, under strength or stiffness constraints [1]. The variable in this type of procedure is element stiffness, which is controlled by a normalized value of the so-called density parameter, according to Eq. (1):

$$\begin{aligned}
 &K_e(E_e), \\
 &E_e = E_0\rho(e)^p, \\
 &p > 1, \quad e = 1, \dots, n, \quad 0 \leq \rho \leq 1
 \end{aligned}
 \tag{1}$$

where K_e is the element stiffness, E_e is resultant material Young’s modulus, E_0 denotes basic material Young’s modulus, ρ is the so-called density parameter and p is the control parameter, which facilitates result filtering.

The gear model used for the optimization purposes is presented in Fig. 1a. It was divided into three main sections: hub, body and toothed crown. The design domain

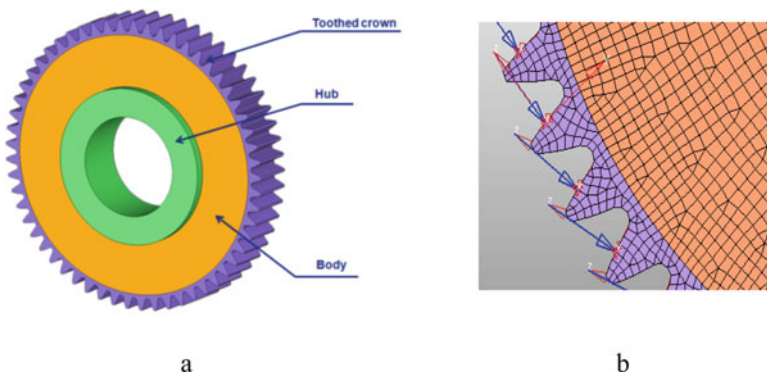


Fig. 1 Model prepared for topology optimization (a) and representation of the static load case applied to the modified gear (b)

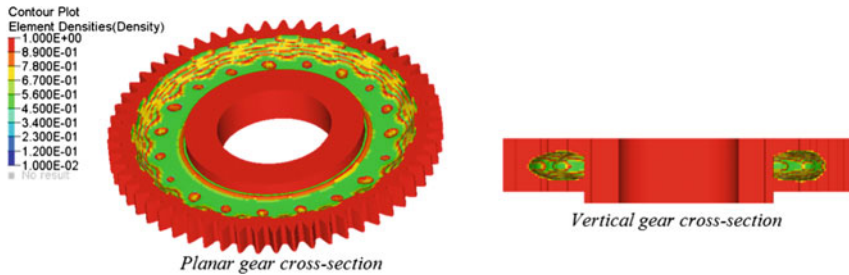


Fig. 2 Results of the topology optimization applied to the gear hub

was specified in the body, because this region provides significant mass reduction possibilities in typical gear pairs.

The model was loaded by 350 Nm torque, which was distributed on the teeth flank at the pitch circle along the line of action. It was assumed that only one tooth remains in contact at a time, i.e., the contact ratio is equal to 1. The constraint limiting the gear deflection was defined on teeth upper edge. The imposed limiting factor was defined as 110 % of the teeth deflection calculated for a full-body gear loaded by the same torque. The optimization objective was defined as minimization of the gear weight.

Each iteration of the optimization process consisted of as many separate linear static simulations as the teeth number of the gear, providing essential information regarding the static behavior of the gear structure. The optimization run was terminated by reaching limiting number of iterations (50) or by achieving improvement in the objective function below a given convergence threshold.

The result of the procedure is shown in Fig. 2. The material was extracted from the inner part of the gear, leaving a cavity in the design domain. After 27 iteration, the procedure converged to the result of reducing the gear weight by 15.5 %.

The gear which is studied in Sect. 3 was built in accordance to this result, i.e., it was hollowed with a square-based toroidal cavity (compare Fig. 4). This type of lightweighting approach was compared with classical approach based on holes in the gear body.

3 Case Study Description

In order to characterize different lightweighting approaches in terms of internal system excitation, FEM analysis is used to estimate the STE for different design alternatives of a lightweight gear. The initial case study is a pair of spur cylindrical gears with involute tooth profiles, similar to the one used in aerospace applications, for which the main geometric parameters are extrapolated from [9] and summarized in Table 1. AISI9310 is assumed as gear material.

Table 1 Gear specifications [9]

Parameter	Pinion	Gear
Number of teeth	27	176
Pitch diameter (mm)	68.60	447.00
Facewidth (mm)	66.00	59.90
Normal pressure angle (°)	25.00	25.00
Normal module (mm)	2.54	
Gear ratio t	6.5185	

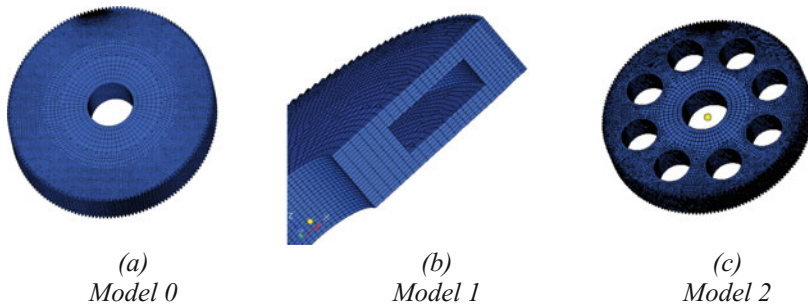


Fig. 3 FE models of the solid gear (a) and of the two lightweight gears (b, c)

Three different FE models of this transmission, with the three gear models shown in Fig. 3, were built varying the geometry of the gear body: in the first model, referred to as *Model 0*, the gear has a solid blank, without any body lightweighting, and represents the reference model (Fig. 3a); in the other two models, named *Model 1* and *Model 2*, lightweight design for the transmission is obtained by using two alternative approaches. In the gear of *Model 1*, which is shown in Fig. 3b, mass reduction is obtained by considering a hollow volume inside the blank. The gear of *Model 2* is a typical lightweight gear, where mass reduction is achieved through 8 holes symmetrically distributed along the blank with an angular period of 45° (Fig. 3c). Gears in *Model 1* and *Model 2* have been designed as to have the same total mass, which is 27 % lower than the one of the reference model.

As concerns the mesh generation, the models were discretized by hexagonal elements. The size of the elements in the three models was properly set through a convergence analysis and varies from a minimum length of 0.02 mm, in correspondence of meshing teeth flanks, up to a maximum of 3 mm in the central region of the gear. A set of one-dimensional rigid elements were modeled in order to simulate the physical presence of the shafts supporting the gear and the pinion, which are supposed to be infinitely rigid.

In order to estimate the STE, a set of non-linear static FEM simulations were performed, using Altair OptiStruct software, for each of the three models, in which

a constant torque value of 500 Nm was applied to the pinion, while the rotational degree of freedom of the gear was constrained.

Subsequent FEM simulations were carried out by dividing each meshing cycle into 33 angular steps. In each simulation, the pinion was rotated by an angle $\varnothing_1 = 0.4^\circ$, while the driven gear rotation was calculated based on the gear ratio τ , according to Eq. 2:

$$\varnothing_2 = \frac{\varnothing_1}{\tau} = 0.061^\circ \quad (2)$$

which resulted in maintaining the same gap between the teeth in each analysis.

The transmission error can be defined as the difference between the actual position of the gear and the one that it would occupy in case of perfect meshing process, i.e. in absence of elastic deflections in the gears and in the supporting shafts, of manufacturing and assembly errors, of tooth profile modifications. Such information on a difference between rotational displacements is typically converted in a linear displacement of the contact point along the line of action [10].

Being the rotation of the gear equal to zero for the boundary conditions set in the model, each simulation allowed computing one point of the STE curve as:

$$\text{STE} = r_{b1} \vartheta_1 \quad (3)$$

where r_{b1} and ϑ_1 are the base radius and the rotation of the pinion respectively.

4 Results

The STE curves estimated for *Model 0* and *Model 1* are shown in Fig. 4. Being the gears in both models axisymmetric, the STE angular period equals the length of the meshing cycle. In both curves, a region with high values of STE and a region with low values of STE can be observed. This effect derives from the variable number of meshing teeth: when two teeth pairs are in contact at the same time, the overall meshing stiffness is higher, which determines a reduction of the STE. For Fig. 4 it can be also noticed that the material removal from the inner part of the gear blank has a significant impact on the average value of the STE, which is about 10 % lower in *Model 1* with respect to the reference model. This is due to an overall reduction of the meshing stiffness in *Model 1*, caused by material removal from the inner part of the gear blank. Less important is the effect of gear lightweighting on STE peak-to-peak value.

On the contrary of the first two models, the gear in *Model 2* is not axisymmetric, due to the presence of eight holes in the blank. As a consequence of the non-homogenous mass distribution, the average value of the overall meshing

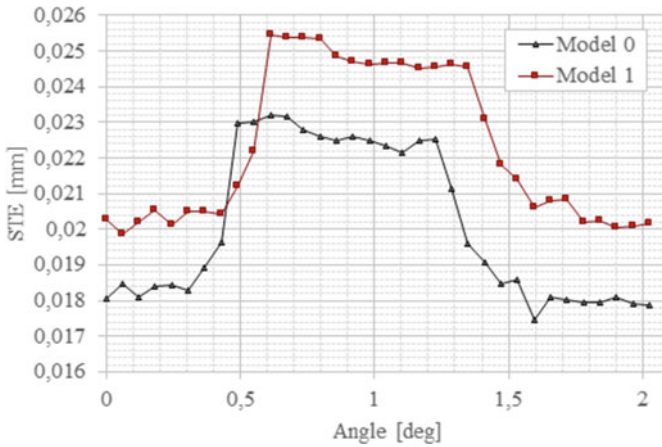


Fig. 4 STE curves obtained for Model 0 and Model 1

stiffness varies along each 45° sector. For this reason, the angular period of the STE for this model is not coincident with the length of the meshing cycle, as shown in Fig. 5, where the STE values calculated along a number of meshing cycles are reported. By comparing the STE curve shown in Fig. 5 with the two curves of Fig. 4, it can be noticed that the average value of the STE along the meshing cycle is variable for Model 2 and always higher than the ones estimated for Model 0 and Model 1. No significant differences in peak-to-peak values are to be pointed out.

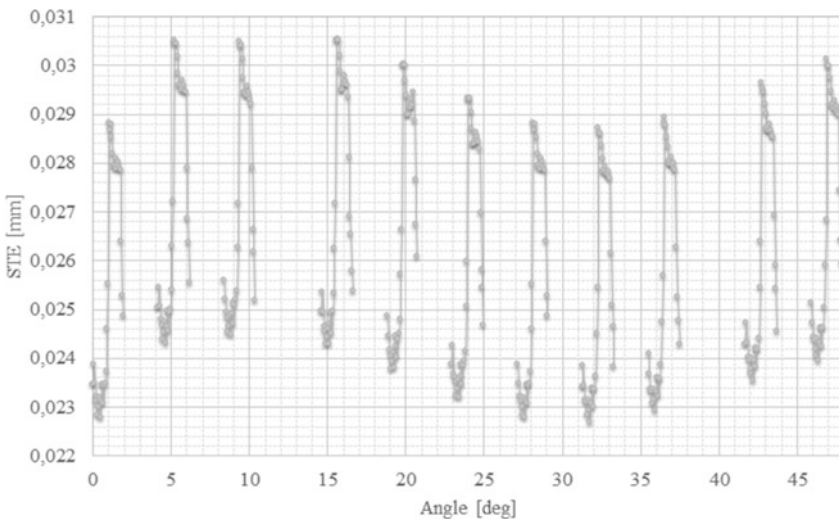


Fig. 5 STE curve obtained for Model 2

5 Conclusions

In this paper elastic non-linear static FE analyses were carried out to compare the performance of three different gear models in terms of meshing stiffness and STE. In particular, the static behavior of a solid gear has been compared with the one of two lightweight gears, designed by using two different approaches for material removal, but with the same overall mass reduction of the reference model.

The achieved results show that the two different lightweight designs have a huge impact on the STE curves. In both cases, the average value of the STE is significantly higher than the one estimated for the reference model. Moreover, for the transmission with the non-axisymmetric lightweight gear a fluctuation in the STE curve was also observed, which is due to the variability of the contribution of the gear blank to the overall meshing stiffness of the gear pair.

Next steps of this research are scheduled in order to assess the impact of the observed STE modifications on the dynamic behavior of lightweight gear trains.

Acknowledgments The research leading to these results has received funding from the People Programme (Marie Curie Actions) of the European Union's Seventh Framework Programme FP7/2007-2013 under REA grant agreement no 324336 DEMETRA: Design of Mechanical Transmissions: Efficiency, Noise and Durability Optimization.

References

1. Bendsoe MP, Sigmund O (2013) *Topology optimization: theory, methods, and applications*. Springer
2. Blankenship GW, Kahraman A (1995) Steady state forced response of a mechanical oscillator with combined parametric excitation and clearance type non-linearity. *J Sound Vib* 185 (5):743–765
3. Brancati R, Rocca E, Savino S, Farroni F (2013) Analysis of gear rattle by means of a wavelet-based signal processing procedure. *Meccanica* 48–6:1399–1413
4. Brancati R, Rocca E, Savino S (2015) A gear rattle metric based on the wavelet multi-resolution analysis: Experimental investigation. *Mech Syst Signal Process* 50–51: 161–173
5. Cai Y (1995) Simulation on the rotational vibration of helical gears in consideration of the tooth separation phenomenon (a new stiffness function of helical involute tooth pair). *J Mech Des* 117:460–469
6. Litvin FL, Fuentes A (2004) *Gear geometry and applied theory*. Cambridge University Press
7. Palermo A, Mundo D, Hadjit R, Desmet W (2013) Multibody element for spur and helical gear meshing based on detailed three-dimensional contact calculations. *Mech Mach Theory* 62:13–30
8. Parker RG, Vijayakar SM, Imajo T (2000) Non-linear dynamic response of a spur gear pair: modelling and experimental comparisons. *J Sound Vib* 237(3):435–455
9. Rashidi M, Krantz T (1992) Dynamics of a split torque helicopter transmission. In: *Sixth international power transmission and gearing conference*, Scottsdale, Arizona
10. Smith JD (2003) *Gear noise and vibration*. Marcel Dekker, Cambridge

A Strategy for Moving Cable Driven Robots Safely in Case of Cable Failure

Giovani Boschetti, Chiara Passarini and Alberto Trevisani

Abstract Cable driven robots are often suggested for applications in which they operate close to, or even in contact with, human operators. The well known broadcasting and rehabilitation use are just two representative examples. Safety is therefore a critical issue. The aim of this paper is to introduce a motion planning strategy for leading a cable robot to a safe position of the workspace in case one or more cables brake or become slack during the motion. The strategy is addressed to redundant cable robots and guarantees that the tensions of the unbroken cables are kept positive and bounded along the whole path toward a safe position. The strategy is then applied to a point-mass planar cable robot, with two translational degrees of freedom to prove its effectiveness.

Keywords Cable robots · Cable failure · Safety · Motion planning

1 Introduction

Cable driven robots, or just “cable robots”, are basically parallel robots in which the end-effector is connected to the base platform through cables instead of rigid links. In the last decades, cable driven robots have been increasingly studied, thanks to their peculiar advantages over conventional robots, which may include possessing a wide workspace, high load capacity, low moving masses, and/or operating at high speed. Beside all these advantages, cable driven robots introduce an additional constraint to motion planning and control due to the peculiar unilateral force exertion capability of cables (i.e. they can obviously just pull the end-effector).

G. Boschetti · C. Passarini · A. Trevisani (✉)
University of Padova, Padua, Italy
e-mail: alberto.trevisani@unipd.it

G. Boschetti
e-mail: giovanni.boschetti@unipd.it

C. Passarini
e-mail: chiara.passarini@phd.unipd.it

Indeed a cable robot operates properly only when cable tensions are maintained positive. Such a constraint makes trajectory planning and motion control particularly challenging [1].

For their peculiar properties, not only have cable robots been suggested for industrial applications [2], but also for home assistance and rehabilitation applications [3]. Independently from the application, nowadays the need of direct interaction with human is increasing, making safety a major concern and a primary research issue.

Managing safety in cable driven robots is more difficult than in conventional robots with rigid links. In such robots, for example, an abrupt emergency stop of the robot can be obtained by just dropping motor voltage and braking the actuated joints. This is usually enough to stop a traditional robot promptly but does not represent a strategy that can be used with cable robots: in particular braking motors is not a sufficient condition to make the end-effector reach a static equilibrium configuration.

A very basic approach which can be followed at the design stage to improve safety in case of cable failure, consists in increasing the number of cables far beyond the minimum needed number: indeed cable robots with many degrees of redundancy can more easily cope with cable failures and in particular, with a broken cable. However, this approach has some major limitations, first of all it is expensive, additionally cables tend to obstruct the workspace and sometimes cable interference can be difficult to avoid. Therefore it is interesting investigating how a cable robot should be moved to assure safety in case of cable failure, without introducing excessive cable redundancy.

The failure issue for cable driven robots was firstly investigated in [4] by studying the impact of removing a cable on the robot ability to achieve static equilibrium. In [5] different types of failures were classified with respect to the so called wrench-feasible workspace, dividing failures due to exceeding upper tension bounds, from failures due to slack cables (i.e. with tensions below the lower bounds). In [6] a classification of the possible failure modes is discussed and a methodology to recover the lost wrench is proposed in [7]. Finally, in [8] a preliminary evaluation of the failure consequences is presented. Such a work aims to study an optimal robot design minimizing the differences in cable tensions before and after failure.

In this paper a novel motion planning strategy is introduced for leading the end-effector of a cable robot to a safe position of the workspace in case one or more cables brake or become slack during the motion. Just these types of failures are considered in this preliminary work. The strategy can be applied to any cable robot topology (i.e. to under actuated, fully actuated or redundant cable robots) in presence of any number of broken cables, provided that a not-null static equilibrium workspace is available after cable failure. The static equilibrium workspace (SEW) is the set of end-effector poses for which static equilibrium can be obtained while maintaining tension in all cables [1]. The proposed after failure recovery algorithm takes into account the modification of the SEW induced by cable failure, identifies a “safe pose” where static equilibrium can be achieved and then plans a

feasible motion aimed at leading the end-effector toward the safe pose and stopping it there. The motion is split into two parts addressing different motion requirements. Such an algorithm takes advantage of state-of-the-art studies on cable robot performance evaluation [9, 10].

The paper is organized as follows: in Sect. 2, the strategy proposed to manage cable failure is presented by referring to a generic redundant, planar and translational cable robot. In Sect. 3 numerical results are presented to prove the effectiveness of the proposed algorithm. Final remarks are given in the Conclusions.

2 After Failure Motion Strategy

Without lack of generality, the motion strategy is here presented by referring to a point-mass, translational, planar and redundant cable robot and assuming that just a single cable brakes. These assumptions have been chosen because they lead to a very clear and illustrative condition after failure which simplifies the description of the proposed strategy. This is basically a consequence of the fact that the cable robot is still fully constrained and with a single degree of redundancy after cable failure. Such a configuration gives the possibility of computing the position, velocity and acceleration of the end-effector, without using a separate metrology system, but merely exploiting the known angular positions of the winch actuators. Nonetheless, the method could be adopted also in less restrictive conditions provided that a suitable metrology system was available for measuring the end-effector position, and that a SEW existed after failure.

Generally speaking, in cable robots, the structure matrix S defines the relation between the wrench w exerted by the cables on the end-effector and the tension vector τ containing the cable forces. In other words, the relation $w = S\tau$ describes the static behavior of a generic cable robot. For a point-mass cable robot, the structure matrix can be written as $S = [u_1 \ u_2 \ \dots \ u_m]$ where u_i is the i th cable unit vector (oriented from the point-mass toward the cable output point on the fixed frame) and m is the number of cables. Having assumed that the end-effector is a point mass, the wrench vector w reduces to just a force vector f and no rotations can be imposed. Hence, without lack of generality, the following simplified notation will be used henceforth: $f = S\tau$.

The after failure real-time motion strategy proposed in this paper consists in promptly driving the end-effector to a pre-computed safe pose (actually a “safe point” in the case of a point-mass cable robot) where the robot can be stopped, in a time that should be kept to a minimum. The safe point can be chosen arbitrarily, depending on some special needs (i.e. to move the end-effector far from human operators) or desired after failure performances (i.e. to stop as quick as possible). In absence of specific needs or expected performances, a reasonable choice for the safe point could be the point with the maximum isotropy in terms of exertable force in the after-failure SEW. Indeed, such a point is expected to offer the best performance

in terms of end-effector braking capacity irrespective of the direction the end-effector comes from.

In order to simplify the task of minimizing the time needed to reach the safe point while keeping always positive and bounded cable tensions, it is essential to plan the motion along a geometrically simple path: a reasonable choice would obviously be a straight line path from the position where failure takes place toward the safe point. However, in general, such a straight path cannot be followed immediately after failure, since the initial (i.e. after failure) conditions of the end-effector would prevent tracking such a path. Hence, a short connecting path is needed between the point where failure takes place and a point, identified dynamically, from which a precise straight line path toward the safe point can be planned and accurately tracked. The connecting path is discussed in the following Sect. 2.1. As for the straight path, which is discussed in Sect. 2.2, it is worth observing that it takes advantage of a performance index called WEC [10]. This index allows computing the wrench exertion capability of a cable robot along a given direction. The use of such an index allows identifying the maximum and the minimum forces that can be exerted by the unbroken cables on the end-effector after failure, in any point of the workspace toward the safe point. Since the use of the WEC for this purpose may take long computational times, it is here suggested to carry out the analysis off-line, considering each possible failure scenario.

2.1 The Connecting Path

As previously mentioned, in order to reach a desired safe point through a linear path, an initial connecting path must be generated from the point where the failure took place to a point from which a straight line path can actually be planned and tracked. Along such a connecting path, a new and ever changing tension configuration of the cables is applied to the end-effector in order to change its direction of motion and make it point the safe point.

Suppose that the starting condition at the failure instant is described in Fig. 1. Henceforth the unit vector r will be used to describe the desired direction of motion

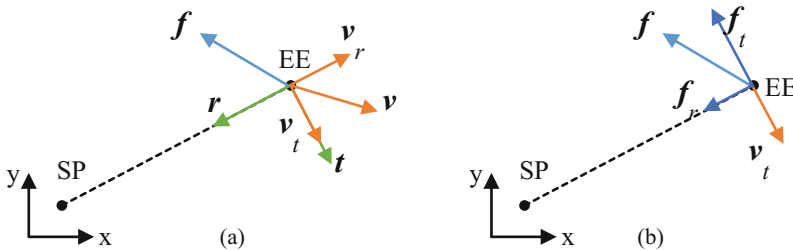


Fig. 1 The end-effector velocity (a) and force (b) configuration at the failure instant

corresponding to the straight line connecting, at each time instant, the end-effector EE with the chosen safe SP: \mathbf{r} keeps changing along the connecting path.

Let us introduce a moving reference frame identified by the unit vectors \mathbf{r} and \mathbf{t} as depicted in Fig. 1a by means of green arrows. Vector \mathbf{v} identifies the velocity of the end-effector at the failure instant while v_r and v_t represent its projections along the moving reference frame axes. A connecting path is generated as long as the tangential velocity component v_t differs from zero considerably. Afterwards the motion along a straight line path along the \mathbf{r} direction can be planned. To this purpose a suitable force \mathbf{f} must be exerted by the unbroken cables. The force vector \mathbf{f} and its projections f_r and f_t along \mathbf{r} and \mathbf{t} are depicted in Fig. 1b with blue arrows.

Let us denote with \mathbf{R} the rotation matrix that describes the orientation of the moving reference frame with respect to the absolute reference frame. The translational velocity \mathbf{v} of the end-effector and the exerted force \mathbf{f} can be expressed in the moving reference frame by means of the following relations:

$$\begin{bmatrix} v_r \\ v_t \\ 0 \end{bmatrix} = \mathbf{R}^T \begin{bmatrix} v_x \\ v_y \\ 0 \end{bmatrix}; \quad \begin{bmatrix} f_r \\ f_t \\ 0 \end{bmatrix} = \mathbf{R}^T \begin{bmatrix} f_x \\ f_y \\ 0 \end{bmatrix} = \mathbf{R}^T \mathbf{S} \boldsymbol{\tau} = \begin{bmatrix} s_r^T \\ s_t^T \\ 0 \end{bmatrix} \boldsymbol{\tau} \quad (1)$$

The main goal along the connecting path is reducing $|v_t|$ to a small value v_t^* close to zero (i.e. achieving $|v_t| < v_t^*$). At each time step, a new cable tension configuration must therefore be sought maximizing f_t in order to reduce $|v_t|$ promptly. Such a tension configuration can be found by solving the following linear programming (LP) problem:

$$\text{maximize: } (-\text{sgn}(v_t) * f_t) = -\text{sgn}(v_t) * s_t^T \boldsymbol{\tau} \quad (2)$$

$$\text{s.t.: } \begin{cases} s_r^T \boldsymbol{\tau} \geq 0 \\ \tau_{\min} \leq \tau \leq \tau_{\max} \quad \forall \tau \neq \tau_f \\ \tau_f = 0 \end{cases} \quad (3)$$

where the first constraint ensures that the force exerted is directed toward the chosen safe point; while the constraints involving cable tensions ensure positive and bounded tensions in all the cables apart from the broken one, for which tension (τ_f) is set to zero. The LP problem is iterated until $|v_t| \geq v_t^*$.

2.2 Motion Planning Along a Straight Line Path

Once v_t has been set close to zero it is possible to plan a safe and feasible motion along a straight line toward the safe point. Feasibility implies positive and bounded tensions in all the unbroken cables. By using the WEC index, it is possible to identify for each point of the direction of interest, the maximum and minimum exertable forces, and hence the force bounds for the planned motion.

Unfortunately the after failure straight line path is not known a priori since it depends on the connecting path which in turn depends on the failure conditions. Hence the aforementioned analysis should be executed on-line, which is likely to be very time consuming and not compatible with a real-time use of the strategy. To overcome such an issue, the analysis performed by means of the WEC index is here proposed to be extended off-line, applied to a sheaf of straight lines through each pre-computed safe point of the SEW. In this way, force bounds can be computed for each failure scenario and then for each possible path.

Once the force bounds are available, a conservative choice consists in planning a trajectory respecting the most restrictive limits. Such a condition ensures planning a certainly feasible trajectory regardless of the chosen motion law. Since the robot behavior may significantly differ throughout the workspace, the trajectory planned can be over conservative and hence too long lasting. Therefore, it is here suggested to split the workspace into radial sectors centered in the chosen safe points. Then, following the reasoning stated above, force limits can be computed for each sector, and just the limits of the sector of interest should be considered when planning the straight line path. In this way, a more accurate description of the residual exertion capability can be achieved.

3 Simulation

The strategy described above is here applied to a point-mass planar cable robot, with four cables and two translational degrees of freedom. The initial SEW of the robot is a square with 2 m side length. The origin of the reference frame is located in the centroid of the square. The workspace vertices coincide with the cable anchor points. In this analysis it will be assumed that a single cable brakes. Four reasonable safe points have been identified: $SP = (\mp\sqrt{3}/3m, \mp\sqrt{3}/3m)$. The sign of the coordinates depends on the cable broken. For example if the failed cable is the one attached to vertex B, then the SP is the point with the maximum isotropy in the 3rd quadrant, since the SEW after failure coincides with the triangle with vertices A-D-C. Maximum and minimum tension limits have been set equal, respectively, to 10 N and 0.5 N, while the mass of the end-effector has been set equal to 3 kg. In order to prevent excessive cable stresses, the maximum tension limit has been reduced to 7.5 N for after failure motion planning.

Suppose that the cable attached to vertex B breaks; the corresponding residual force exertion capability throughout the original (square) SEW is depicted in Fig. 2. In practice, the original SEW of the robot has been discretized through a regular and thick grid. Subsequently, by means of a linear interpolation, the isolines of the maximum and minimum exertable forces that can be exerted along the direction

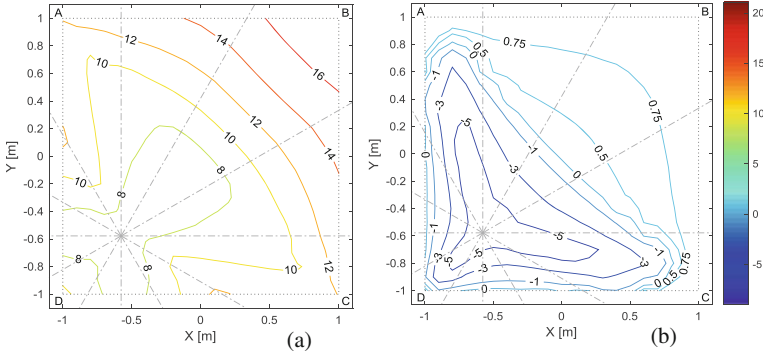


Fig. 2 Maximum (a) and minimum (b) exertable forces along the directions toward the SP

toward the safe point have been computed, and plotted in Fig. 2a, b respectively. Negative values refer to the outward radial direction. In both the figures the forces take the lower values nearby the SP, and increase significantly when moving radially from this point. Clearly, only in the subspace where negative lower bounds are available it is possible decelerating the EE.

It has been chosen to split the square SEW (delimited in Fig. 2 by dashed black lines) into twelve sectors about the SP. The sectors are delimited by grey dash-dotted lines. Force bounds have then be computed for each sector off-line.

A cable break has been simulated. The failure is assumed to take place at time t_f along a linear path. Table 1 summarizes the position and the velocity of the EE at t_f . The same table also shows the EE position and velocity achieved at the end of the connecting path (i.e. at the time t_e). In this simulation v_t^* was set equal to 10^{-3} m/s. In particular, the distance d from the SP and the velocity v_r at t_e represent the inputs for straight line trajectory planning. At time t_e , the EE is located in the central sector of the first quadrant. The force bounds computed off-line for this sector are depicted with red lines in Fig. 3b. Several motion laws [11, 12] can be adopted to optimize the last path satisfying these force bounds. Without lack of generality the trajectory toward the SP was planned by using a 5th order polynomial. The fastest trajectory computed is plotted in Fig. 3a in terms of distance from the SP, modulus of the velocity v_r and of the acceleration a_r .

Then the force exerted to perform such a trajectory is depicted in green line in Fig. 3b proving that it satisfies the force bounds. Finally, in Fig. 4a the whole path traversed by the end-effector is depicted. The path before failure (1), the connecting path (2) and the straight line path to the SP (3) are plotted in different colors. The

Table 1 Position and velocity of the end-effector

	x (m)	y (m)	d (m)	v_x (m/s)	v_y (m/s)	v_r (m/s)	v_t (m/s)
t_f	0.54	0.46	1.52	0.37	-0.37	-0.02	0.52
t_e	0.55	0.38	1.48	-0.25	-0.22	0.33	0.8×10^{-3}

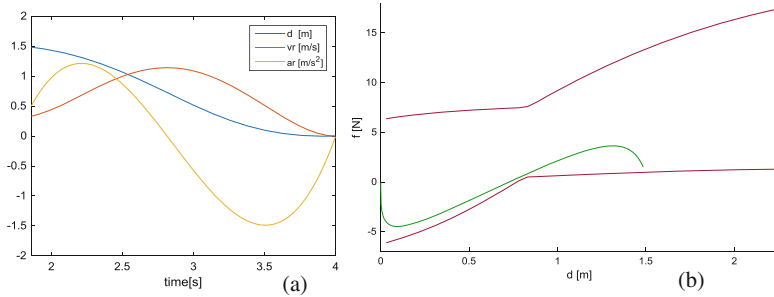


Fig. 3 The straight trajectory: the motion law (a) the exerted force and its bounds (b)

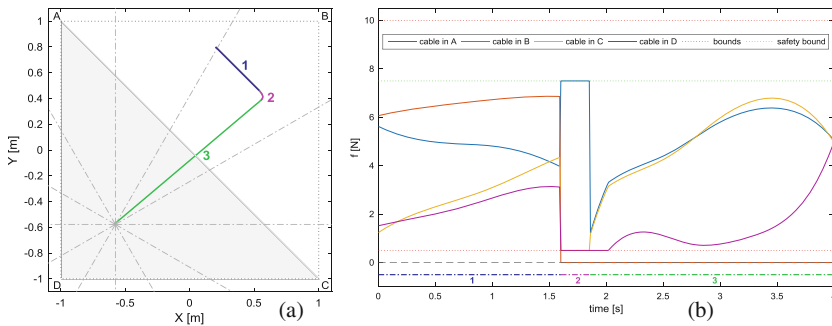


Fig. 4 Path (a) and cable tensions (b) during the whole motion

triangular SEW holding after failure is highlighted too. Finally, the cable tension distributions during the whole path are plotted in Fig. 4b: it is proved that tensions are always kept within the bounds.

4 Conclusions

A novel strategy for moving cable driven robots safely in case of cable failures has been presented and then applied to a planar over-constrained point-mass cable robot. The proposed after failure recovery algorithm takes into account the modification of the static equilibrium workspace induced by cable failure, identifies a “safe pose” and then plans a feasible motion aimed at leading the end-effector toward the safe pose and stopping it there. Such an algorithm takes advantage of state-of-the-art studies on cable robot performance evaluation and allows keeping always positive and bounded cable tensions. Numerical results are presented to prove the effectiveness of the proposed strategy.

References

1. Trevisani A (2010) Underconstrained planar cable-direct-driven robots: a trajectory planning method ensuring positive and bounded cable tensions. *Mechatronics* 20:113–127
2. Albus JS, Bostelman R, Dagalakis NG (1993) The NIST ROBOCRANE. *J Robotic Syst* 10 (5):709–724
3. Rosati G, Gallina P, Rossi A, Masiero S (2006) Wire-based robots for upper-limb rehabilitation. *Int J Assist Robot Mechatron* 7(2):3–10
4. Roberts RG, Graham T, Lippitt T (1998) On the inverse kinematics, statics, and fault tolerance of cable-suspended robots. *J Robot Syst* 15(10):581–597
5. Bosscher P, Ebert-Uphoff I (2004) Wrench-based analysis of cable-driven robots. In: *Proceeding of ICRA 2004 the IEEE international conference on robotics and automation (2004)*
6. Notash L (2012) Failure recovery for wrench capability of wire-actuated parallel manipulators. *Robotica* 30(06):941–950
7. Notash L (2013) Wrench recovery for wire-actuated parallel manipulators. In: *Proceedings of robot design, dynamics and control, Romansy 19*. Springer Vienna, pp 201–208
8. Ghaffar A, Hassan M (2014) Failure analysis of cable based parallel manipulators. *Appl Mech Mater* 736 (2014)
9. Boschetti G, Trevisani A (2014) Performance evaluation for cable direct driven robot. In: *Proceedings of ESDA 2014 conference on engineering systems design and analysis*
10. Boschetti G, Trevisani A (2015) On the use of the wrench exertion capability as a performance index for cable driver robot. In: *Proceedings of ECCOMAS thematic conference on multibody dynamics (2015)*
11. Behzadipour S, Khajepour A (2006) Time-optimal trajectory planning in cable-based manipulators. *IEEE Trans Robot* 22(3):559–563
12. Boschetti G (2016) A picking strategy for circular conveyor tracking. *J Intell Robot Syst: Theory Appl* 81(2):241–255

Approaches to the Detectability of Faults in Railway Pantograph Mechanism

G. Santamato, M. Gabardi, M. Solazzi and A. Frisoli

Abstract Vibration-based condition monitoring is a leading field in both research and industrial world. Systems features and boundary conditions makes detectability highly case-sensitive and hence each application demands for a specific strategy. In this paper we introduce a project meant to develop a robotic tool for the assessment of railway pantographs health under strong customer requirements, such as limited frequency bandwidth and few sensors allowed. The lack of historical data and the unavailability of specimens make the case-study particularly challenging. Considerations were hence derived through numerical simulations. We took into account leakage in dashpot and clearance in a joint to investigate how faults afflict both global and local modes. The way specifications limit the suitability of frequency domain methods is pursued using the extended Modal Assurance Criterion (MACX). Phase plots shapes alteration were observed collecting responses of two points to a cosine chirp force with the aim to compare the effectiveness of this simple method with MACX performance. Structural damage is identified by both techniques but only the latter detects the leakage in the dashpot. Phase plots use needs to be delved deeper to test the suitability for the real application.

1 Introduction

1.1 Literature Review

Detection method of faults have been widely adopted in different fields during last 30 years; despite of that it does not exist a general-purpose technique [2, 5, 9].

Vibration based strategies are classified depending on whether they work in frequency or time domain [2, 5]. The former look for modifications in natural frequencies, modal vectors and modal energy. Literature suggested Modal Assurance Criterion (MAC) as a tool proving that local changes has occurred [1, 4, 12]. At the

G. Santamato (✉) · M. Gabardi · M. Solazzi · A. Frisoli
PERCRO Laboratory Scuola Superiore Sant'Anna, Pisa, Italy
e-mail: giancarlo.santamato@sssup.it

same time its evolutions such as Coordinate Modal Assurance Criterion (COMAC) are meant to precisely locate the damage [3]. To deal with non proportionally damped structures the extended Modal Assurance Criterion (MACX) method was addressed thoroughly [11]. In recent years time series analyses are being deepened as more sensitive to damage and less sensitive to noise [7]. Online condition monitoring is prone to employ phase plots changes as excellent candidates to recognize faults like cracks [7], degradation of stiffness [10], joint and bolt preload loss [6, 8].

1.2 Case Study

This paper deals with a funded project in partnership with Trenitalia Spa. It is meant to develop a robotic tool for periodic automatic monitoring tests to be executed on condition. The machine will assess pantographs health through the analyses of its response; vibrations will be induced from the application of a dynamic load. In addition portability and ease in use are strong customer requirements. In particular:

1. force should be applied along the vertical direction to a fixed point;
2. equipment set-up must not alter permanently pantograph frame, so the robot will be simply clamped to the structure;
3. sensors number has to be kept as low as possible.

Defects can modify the dynamic behavior of a system in terms of amplitude of motion, mode shapes and number of degrees of freedom (dof). Since the robot will exert a vertical force, independently of the monitoring approach, it would detect only those faults related with that direction. What is more to accomplish portability, a light equipment is demanded and thus dynamic forces would be properly exerted in a limited band, i.e. 0–20 Hz; hence among the structural modes involving the vertical direction only those belonging to this range would be observable. Few sensors makes the identification of local changes further arduous. Other critical aspects are the lack of historical data on faults and that actually pantographs specimens are not available. Furthermore, the mechanism does not comply with the classical assumptions of structural dynamics because of the presence of a dashpot.

1.3 Motivations

In this paper we introduce two approaches for the detectability of faults. Considerations will be carried out from numerical simulations performed on a Finite Element Method (FEM) model of the mechanism. We opted for leakage in the dashpot and clearance in joint as examples of damages affecting global and local properties respectively. The first aim of this study is to judge how a limited number of sensors restricts MACX effectiveness in the frequency band of interest. Eigenvectors

reconstruction was then simulated by taking only 6 nodes as necessary measurement points; they were located at joint coordinates to monitor suspected damages effect. Estimation of eigenvectors was conducted by means of numerical modal analysis. The latter goal is to prove if the investigation of phase plots shapes alterations is able to detect the same aforementioned faults. Consequently we simulated the application of a dynamic load and responses were collected in just two points. This very simple approach was therefore counterposed to the model-based one to trace straightforward a feasibility study.

2 Models

The modeled pantograph is shown in Fig. 1; its mechanism presents: (i) a lower suspension made up of a couple of springs and a pneumatic dashpot; (ii) upper elastic suspensions.

The following hypotheses were adopted to built the FEM model:

1. all constraints act like ideal holonomous hinges;
2. the system is linear subjected to viscous damping;
3. the mechanism exhibits small displacements.

Table 1 collects the main dynamical parameters.

Two faults have thus been considered. The former simply modifies the existing properties; it is a leakage in the dashpot seal, quantified in a reduction of 90 % of the damping coefficient c_p . Clearance in a joint changes the response but also introduces new dof; under the small-displacements assumption a no-contact condition expresses this alteration. This scenario was located at point A (see Fig. 1).

We analyzed the effects of faults in the frequency domain, with the MACX criterion and in the time domain, looking for discrepancies in the shape of phase-plots. Complex modal vectors were estimated by general-damped modal analyses, while phase plots were built from the simulated response to a transient load.



Fig. 1 Pantograph under consideration; *left* a picture (courtesy of Trenitalia); *right* FEM model

Table 1 Main dynamical properties of the mechanism

Parameter	Symbol	Value	Unit
Principal spring stiffness	k_p	9236	N/m
Secondary spring stiffness	k_s	1621	N/m
Dashpot damping coefficient	c_p	6944	Ns/m
Pantograph mass	m_p	59	kg
Pan head mass	m_s	15	kg

The input force was a cosine chirp applied to point E in Fig. 1 so as to excite all the modes in the frequency range of interest. Simulated time was chosen so as to optimize frequency resolution and computational time; an interval of 10 s was therefore adopted. We opted for a sampling frequency of 400 Hz, corresponding to 20 times the last spectral line; this choice was meant to mitigate the effect of discretization.

3 Results

Eigenvectors were evaluated at points A–F in Fig. 1. Per each damaged system, modal vectors were compared against the undamaged mechanism set. MACX matrices are depicted in Figs. 2 and 3 showing the consistency between couples of corre-

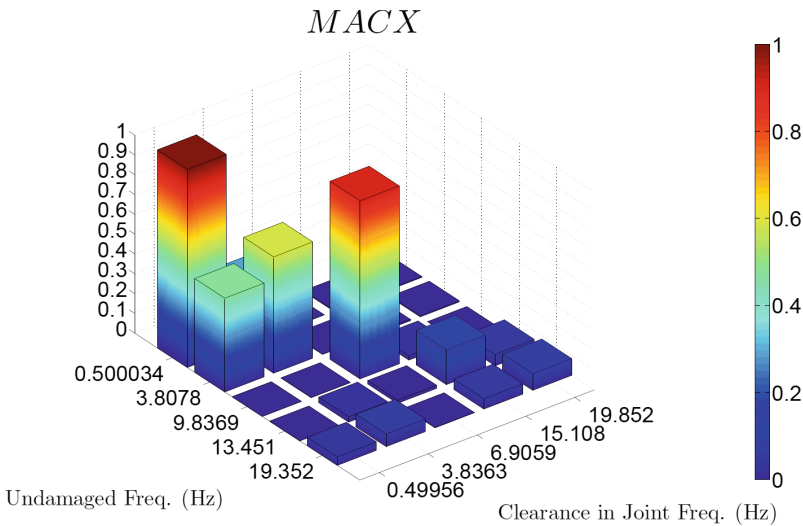


Fig. 2 MACX matrix: sets of eigenvectors refer to the undamaged system and damaged one with clearance in joint

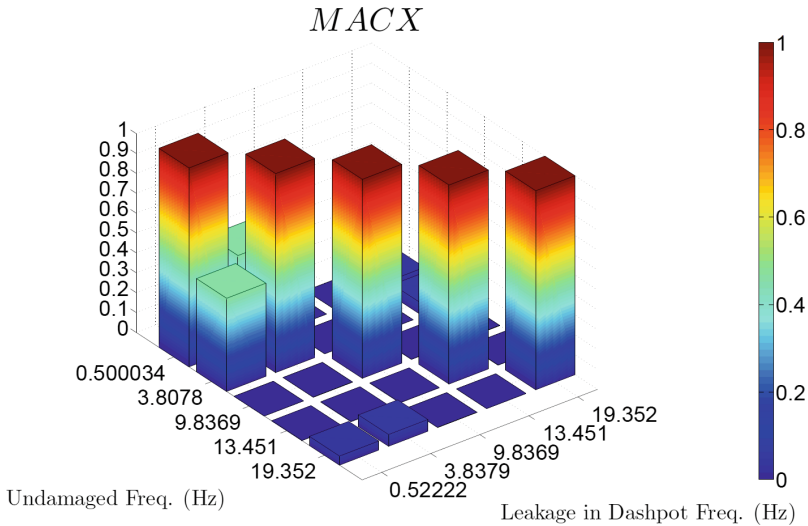


Fig. 3 MACX matrix: sets of eigenvectors refer to the undamaged system and damaged one with leakage in dashpot

sponding vectors. From Fig. 2 it seems that MACX is really effective in detecting the clearance and it is even more sensitive for the last two local mode shapes. Except for the first and the third mode MACX values are under the 60 %, proving uncorrelation. Figure 3 shows instead that leakage is not recognizable even though the reduction of damping is relevant; on the principal diagonal values are about 100 %. It is also interesting to notice that clearance is even responsible for a relevant frequency shift for the third and fourth mode.

Vertical displacements s_1, s_2 and their derivatives \dot{s}_1, \dot{s}_2 were collected from the transient response at just two points (E and F respectively in Fig. 1), so the system is modeled with the two dof status: $[s_1, s_2, \dot{s}_1, \dot{s}_2]^T$. The use of phase-plots powerfully renders the difference between the dashpot damaged system and the undamaged one as shown in Fig. 4. Under the excitation the system undergoes considerable displacements due to loss of damping. Clearance in joint has a time-varying relevance in phase plots which need to be split, according to amplitudes decrement; after 6 s the undamaged system responses are less than a determined value and then the time threshold is chosen. When the response is mainly governed by the principal modes just little discrepancies emerge due to fault (left diagrams of Fig. 5); once the global motion has been damped diagrams (right of Fig. 5) differ from damaged and undamaged specimen. This structural defect is in fact responsible for the appearance of a local mode, at 4 Hz, involving the upper half of the mechanism; since the dashpot is not collocated with that portion, this mode is undamped. Hence for the s_1 dof phase plot is subjected to deformation shape due to this mode contribution. For the s_2 dof phase plot is determined just from the input and no effect on shape are noticeable while is evident an increase in amplitude.

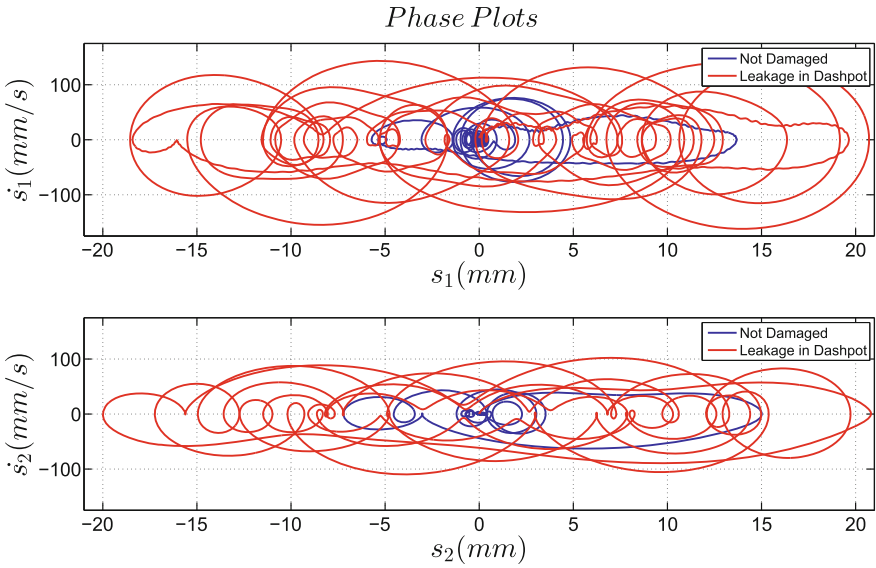


Fig. 4 Transient responses phase plots; *blue trajectories* refer to the undamaged system; *red trajectories* relate to the pantograph with leakage in dashpot

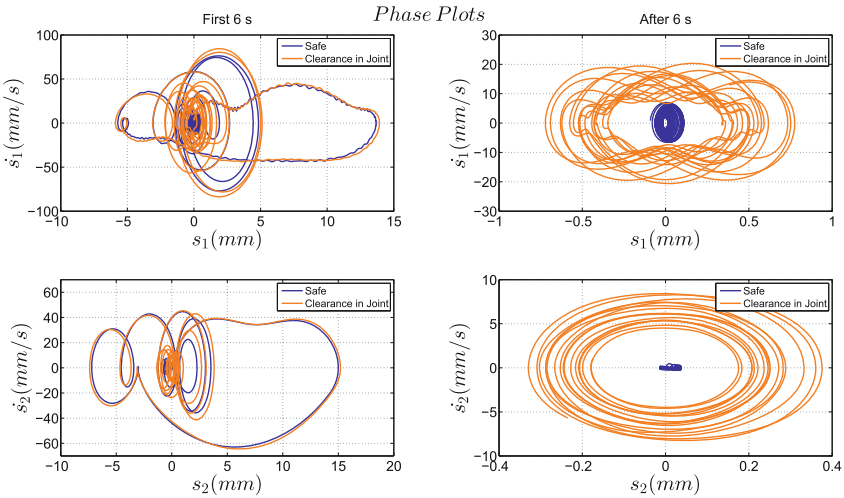


Fig. 5 Transient responses phase plots; *blue trajectories* refer to the undamaged system; *orange trajectories* relate to the pantograph with clearance in joint

4 Conclusions

Intensive efforts have been focused in last 30 years on detectability of faults by means of vibrations analyses. In this paper MACX and phase plots are proposed as methods to inspect railway pantographs health under strong customer requirements. Main issues were outlined through numerical simulations. MACX as an example of frequency domain technique detects the presence of damage and gives an information on its location. On the other side frequency methods need for a more demanding identification to characterize both the undamaged mechanism and the system under inspection. It is though really hard to perform a real-time-on-condition modal analysis especially in terms of time needed for the set-up of sensors. Furthermore MACX also requires a basilar knowledge on how damages affect modal vectors so as to choose number and location of sensors. It seems that the method is insensitive towards severe fault in dashpot. Phase plots inspection needs less measurement points and just one dof per each sensor to recognize both global and local modes related damages. Moreover no clue about the location of detected damage is provided. In addition noise effects have to be further investigated. As a conclusion, time domain method seems to be more efficient than frequency ones for what concerns cost and detectability of faults.

Acknowledgments The authors would like to thank Trenitalia Spa for the support given during the development of the research activities.

References

1. Allemang RJ (2003) The modal assurance criterion—twenty years of use and abuse. *Sound Vib* 37(8):14–23
2. Carden EP, Fanning P (2004) Vibration based condition monitoring: a review. *Struct Health Monit* 3(4):355–377
3. dos Santos F, Peeters B, Van der Auweraer H, Góes L, Desmet W (2016) Vibration-based damage detection for a composite helicopter main rotor blade. *Case Stud Mech Syst Signal Process* 3:22–27
4. Farrar C, Doebling S (1999) Damage detection and evaluation ii. In: *Modal analysis and testing*. Springer, pp 345–378
5. Krawczuk M, Ostachowicz W (1996) Damage indicators for diagnostic of fatigue cracks in structures by vibration measurements—a survey. *J Theoret Appl Mech* 34(2):307–326
6. Nichols J, Todd M, Wait J (2003) Using state space predictive modeling with chaotic interrogation in detecting joint preload loss in a frame structure experiment. *Smart Mater Struct* 12(4):580
7. Nie Z, Hao H, Ma H (2012) Using vibration phase space topology changes for structural damage detection. *Struct Health Monitor* 11(5):538–557
8. Overbey L, Olson C, Todd M (2007) A parametric investigation of state-space-based prediction error methods with stochastic excitation for structural health monitoring. *Smart Mater Struct* 16(5):1621
9. Peeters B, Lowet G, Van der Auweraer H, Leuridan J (2004) A new procedure for modal parameter estimation. *Sound Vib* 38(1):24–29

10. Todd M, Nichols J, Pecora L, Virgin L (2001) Vibration-based damage assessment utilizing state space geometry changes: local attractor variance ratio. *Smart Mater Struct* 10(5):1000
11. Vacher P, Jacquier B, Buchard A (2010) Extensions of the mac criterion to complex modes. In: *Proceedings of ISMA international conference on noise and vibration engineering*, Leuven, Belgium
12. West WM (1986) Illustration of the use of modal assurance criterion to detect structural changes in an orbiter test specimen. In: *Proceedings of 4th international modal analysis conference*, Los Angeles, CA, vol. 1, pp 1–6

Behaviour of Tilting-Pad Journal Bearings in Case of Large Manufacturing Errors

Steven Chatterton, Phuoc Vinh Dang, Paolo Pennacchi
and Andrea Vania

Abstract The behavior of five-pad tilting-pad journal bearings in case of large manufacturing errors, is investigated by means of a parametric analysis in this paper. The sensitivity analysis was performed for several combinations of pad thickness in both load-on-pad (LOP) and load-between-pad (LBP) configuration using a TEHD model. Pad thickness machining errors cause different preload factor or clearance for each pad. Several cases of thickness variation and different rotational speed were studied. Numerical results show that machining errors have a strong influence on the dynamic coefficients and on the static behaviour.

Keywords Manufacturing error · Bearing clearance · TEHD model

1 Introduction

Since Lund [1] developed a numerical method for calculating dynamic coefficients for TPJBs, extensive theoretical and experimental studies on dynamic and stability analysis have been conducted [2, 3]. Jones et al. [4] studied theoretically the effects of bearing clearance and pad clearance on the steady-state and dynamic behavior in TPJBs.

S. Chatterton (✉) · P.V. Dang · P. Pennacchi · A. Vania
Department of Mechanical Engineering, Politecnico di Milano,
Via La Masa 1, 20156 Milan, Italy
e-mail: steven.chatterton@polimi.it

P.V. Dang
e-mail: phuocvinh.dang@polimi.it

P. Pennacchi
e-mail: paolo.pennacchi@polimi.it

A. Vania
e-mail: andrea.vania@polimi.it

Strzelecki [5] investigated the static and dynamic features of five-pad TPJBs which has a non-symmetric pad support using Reynolds equation and an adiabatic model for the oil film.

Moreover, most of the papers in the literature evaluate the static and dynamic characteristics of TPJBs by means of simulations and assuming nominal dimensions for all bearing pads; that is, the pads have the same nominal geometry, which corresponds to a circular periodicity of the bearing geometry. In real applications, the manufacturing tolerances for the pads can be of the same order of magnitude as the oil-film thickness and an actual non-nominal geometry can occur [6–10].

Fillon, in [11, 12], simulated the effect of manufacturing tolerances on the static and dynamic characteristics of a five-pad TPJB using the same geometry for all pads. The effect of pad clearance and preload variation on dynamic coefficients of a five-pad TPJB was investigated using a numerical model in [13, 14].

In this paper, the effects of machining error on one pad individually and two pads simultaneously, i.e., the effects of geometry asymmetry, on TPJBs performances such as dynamic coefficients and shaft locus, have been evaluated using a thermo-elasto-hydro-dynamic (TEHD) model. The bearing with uniform dimensions is used as the reference.

2 Thermo-Elasto-Hydro-Dynamic Model

A thorough description of the mathematical model for evaluating static as well as dynamic coefficients is given in [10]. The bearing model includes the effect of the pad inertia and the pivot stiffness [15], the hydrodynamic lubrication model for the pressure distribution, a finite element model for the pad static deformation, and a simple thermal model for the effect of the temperature distribution on the oil viscosity. In particular, the viscosity μ and the density ρ of the lubricating oil are assumed functions of only the temperature T .

In order to calculate pad total deformation including pad bending and elastic deformation, a finite element model of each pad configuration is considered.

For a given static load, the following conditions must be satisfied:

- convergence of the pressure distribution in each pad;
- convergence of the temperature distribution in each pad;
- equilibrium of the forces on each pad;
- equilibrium of the forces on the shaft for the given static load.

3 Bearing Description

Numerical investigations were performed on the five-pad TPJBs with line contact rocker-back pad pivots by considering two cases of thickness variation as shown in Fig. 1: (a) thickness variations on one pad individually—LOP configuration and (b) thickness variations on two pads simultaneously—LBP configuration.

The thickness tolerances of pads have been chosen in a range of $\pm 30 \mu\text{m}$. These tolerances might be somewhat larger than those used by bearing companies and manufacturers. Nevertheless, deviations from the nominal dimensions vary during the working period, due to the wear on the pad surface. The geometric and operating parameters of the bearings are listed in Table 1.

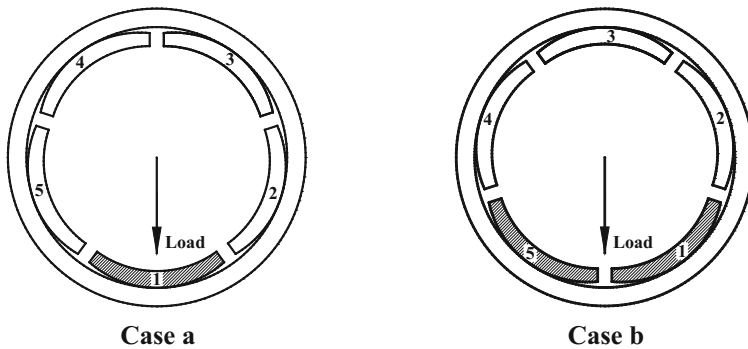


Fig. 1 Two cases of thickness variation are considered for parametric study

Table 1 Bearing geometric characteristics and operating conditions

Item	Symbol	Unit	Value/Span
Number of pads	–	–	5
Configuration w.r.t bearing housing	–	–	LOP
Bearing diameter	D	mm	100
Bearing length	L	mm	70
Nominal machined clearance	C_p	mm	0.130
Lubricant	–	–	ISO VG46
Static load	–	kN	5
Nominal pad thickness	t	mm	16.000

4 Results and Discussions

4.1 Shaft Locus

For convenience, the simulated bearing will be dubbed by the thickness value of pad #1, i.e., the name of bearing with thickness of pad #1 of 15.970 mm is 15.97-bearing. Note that the 16.00-bearing can be also called as the nominal bearing.

It is clearly seen that, when rotational speed increases, the center of shaft tends to “climb” to the equilibrium position of the bearing center (Fig. 2).

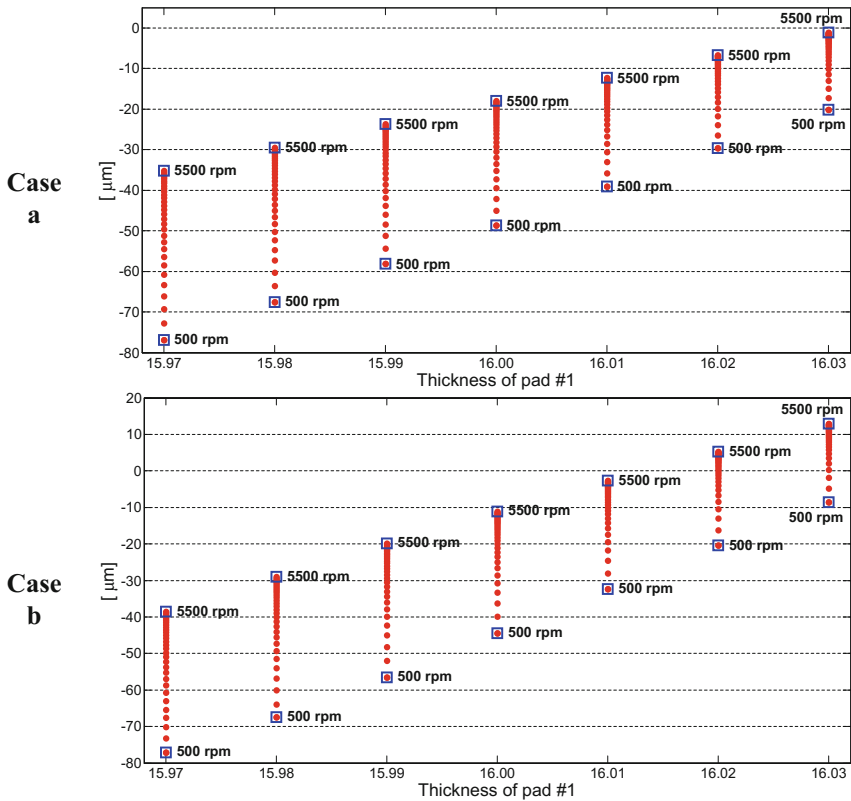


Fig. 2 Static position of the shaft center versus rotational speed

4.2 Dynamic Coefficients

Figure 3 shows the dynamic stiffness and Fig. 4 the damping coefficients of all bearings as a function of the rotational speed. For the sake of simplicity, only the direct terms of the dynamic coefficients are presented. By considering for instance the Case a, the direct stiffness coefficients, k_{xx} and k_{yy} , increase more or less linearly with the increasing of the rotational speed. The effect of geometry asymmetry on the k_{xx} is the same in the range of rotational speed. This effect is more obvious for the stiffness coefficient in the loaded direction k_{yy} .

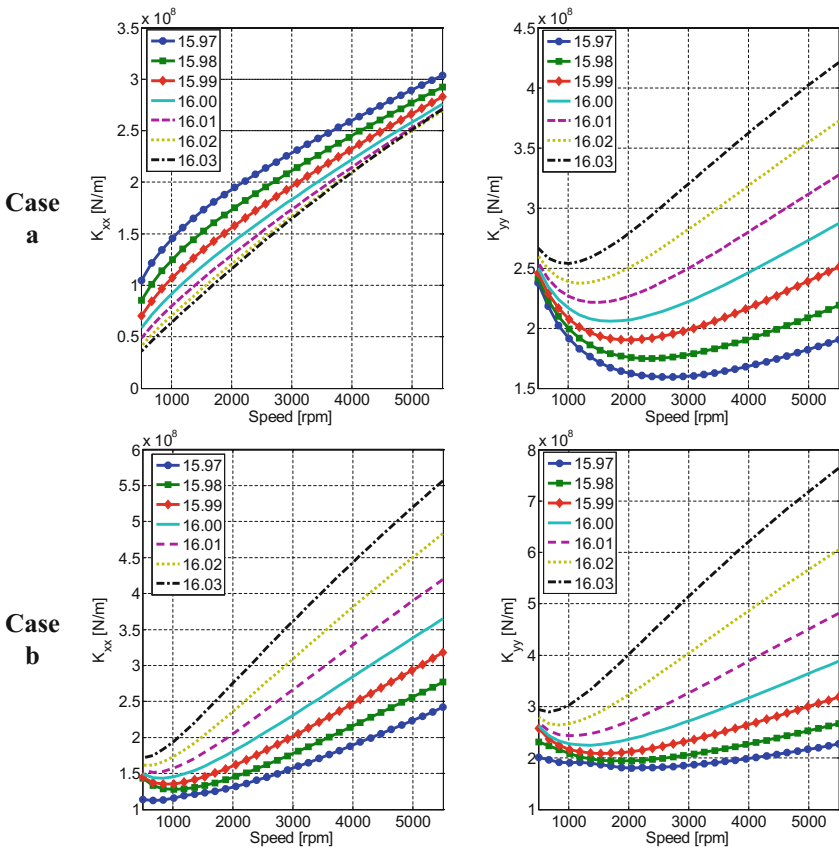


Fig. 3 Stiffness coefficients (direct terms) versus rotational speed (vertical static load)

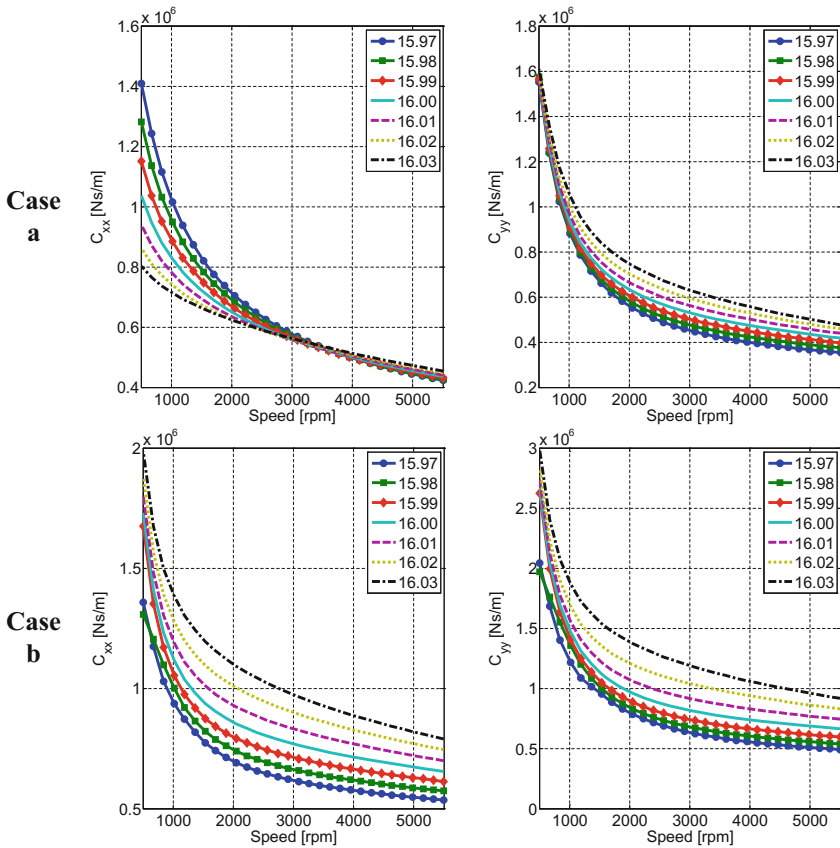


Fig. 4 Damping coefficients (direct terms) versus rotational speed (vertical static load)

5 Conclusions

The paper presents the effects of large manufacturing errors on pads on static as well as dynamic characteristics of five-pad TPJBs. In particular, the asymmetry of the bearing geometry leads to unexpected behavior of the bearing for TPJBs. In fact by considering the direct stiffness coefficient k_{yy} along the vertical direction, that is also the term that strongly influence the dynamic behavior of rotating machines, in case of large manufacturing error, it can double or halve the corresponding theoretical value for a nominal bearing. Two cases of thickness variation were considered for parametric study: (i) thickness variations on one pad individually—LOP configuration; (ii) thickness variations on two pads simultaneously—LBP configuration. The machining errors on the pad has a great influence on shaft locus and on the dynamic coefficients.

References

1. Lund JW (1967) Spring and damping coefficients for tilting pad journal bearing. *Trans ASLE* 7:342–352. <https://dx.doi.org/10.1080/05698196408972064>
2. Yan Z, Wang L, Qiao G, Zheng T (2010) An analytical model for complete dynamical coefficients of a tilting-pad journal bearing. *Tribol Int* 43:7–15. <https://dx.doi.org/10.1016/j.triboint.2009.03.010>
3. Qiuying C, Peiran Y, Yonggang M, Shizhu W (2002) Thermoelastohydrodynamic analysis of the static performance of tilting-pad journal bearings with the Newton–Raphson method. *Tribol Int* 35(4):225–234. [https://dx.doi.org/10.1016/S0301-679X\(01\)00108-6](https://dx.doi.org/10.1016/S0301-679X(01)00108-6)
4. Jones GJ, Martin FA (1978) Geometry effects in tilting-pad journal bearings. The 33rd annual meeting in Dearborn, Michigan
5. Strzelecki S (2002) Dynamic characteristics of tilting 5-pads journal bearing with asymmetric support of pads. In: Sixth international conference on rotor dynamics (IFTToMM), University of New South Wales, Sydney, Australia, pp 807–814
6. Dang PV, Chatterton S, Pennacchi P, Vania A, Cangioli F (2015) Behavior of a tilting–pad journal bearing with different load directions. In: Proceedings of the ASME 2015 International Design Engineering Technical Conferences & Computers and Information in Engineering Conference IDETC/CIE 2015 2–5 Aug 2015, Boston, Massachusetts, USA Paper No. DETC2015-46598. <http://dx.doi.org/10.1115/DETC2015-46598>
7. Dang PV, Chatterton S, Pennacchi P, Vania A, Cangioli F (2015) Eccentricity measurements on a five-pad tilting pad journal bearing. In: Proceedings of the 14th IFTToMM World Congress; 2015 October 25–30; Taipei, Taiwan. doi:10.6567/IFTToMM.14TH.WC.OS14.020
8. Chatterton S, Pennacchi P, Dang PV, Vania A (2014) A test rig for evaluating tilting-pad journal bearing characteristics. In: Proceedings of 9th International Conference on Rotor Dynamics (IFTToMM), 22–25 Sep 2014, Milan, Italy. *Mechanisms and Machine Science* 2015, vol. 21, pp 921–930. doi:10.1007/978-3-319-06590-8_75
9. Chatterton S, Pennacchi P, Dang PV, Vania A (2014) Identification dynamic force coefficients of a five-pad tilting–pad journal bearing. In: Proceedings of 9th International Conference on Rotor Dynamics (IFTToMM), 22–25 Sep 2014, Milan, Italy. *Mechanisms and Machine Science* 2015, vol 21, pp 931–941. doi:10.1007/978-3-319-06590-8_76
10. Dang PV, Chatterton S, Pennacchi P, Vania A (2016) Effect of the load direction on non-nominal five-pad tilting-pad journal bearings. *Tribology Int* 98:197–211. <https://dx.doi.org/10.1016/j.triboint.2016.02.028>
11. Fillon M, Dmochowski W, Dadouche A (2007) Numerical study of the sensitivity of tilting pad journal bearing performance characteristics to manufacturing tolerances: steady-state analysis. *Tribol Trans* 50:387–400. <https://dx.doi.org/10.1080/10402000701429246>
12. Dmochowski W, Dadouche A, Fillon M (2008) Numerical study of the sensitivity of tilting pad journal bearing performance characteristics to manufacturing tolerances: dynamic analysis. *Tribol Trans* 51:573–580. <https://dx.doi.org/10.1080/10402000801947709>
13. Gómez JL, Pineda S, Díaz SE (2013) On the effect of pad clearance and preload manufacturing tolerances on tilting pad bearings rotordynamic coefficients. ASME Turbo Expo 2013, Paper No. GT 2013-95214
14. Quintini JCR, Pineda S, Matute JA, Medina LU, Gómez JL, Díaz SE (2014) Determining the effect of bearing clearance and preload uncertainties on tilting pad bearings rotordynamic coefficients. ASME Turbo Expo 2014, Paper No. GT 2014-26773
15. Wilkes JC, Childs DW (2012) Tilting pad journal bearing—a discussion on stability calculation, frequency dependence, and pad and pivot. *J Eng Gas Turbines Power* 134 (12):122508. <https://dx.doi.org/10.1115/1.4007369>

Part VI
Robotics and Mechatronics

A New Automated 2 DOFs 3D Desktop Optical Scanner

Maria Cristina Valigi, Silvia Logozzo and Gabriele Canella

Abstract The goal of this research work was to create a completely automated desktop 3D optical measuring system for parts having freeform and complex surfaces, with high and certifiable resolution, precision and accuracy to be suitable for metrology. The proposed device is based on the principle of structured light active triangulation. The hardware system consists of an optical system, with a 2 degrees of freedom (DOFs) motorized tilt-rotational table and a framework providing fixtures for a proper location of the target specimen. The software module is able to synchronize the optical and mechanical systems after optical and mechanical calibrations. The mesh representing the measured object is registered automatically by stitching together all the single 3D data sets acquired at each movement of the positioning system. The quality of the result is evaluated by checking the difference between a certified reference model and the measured data.

Keywords 3D optical scanner • Automated mechanics and machines • Structured light active triangulation • Calibration

1 Introduction

Three-dimensional optical scanning of objects is required in a large variety of applications and procedures in mechanical, craft and medical industries, heritage preservation, archeology, architecture, environmental and civil engineering, art, media and entertainment.

M.C. Valigi (✉) · S. Logozzo
University of Perugia, Perugia, Italy
e-mail: mariacristina.valigi@unipg.it

S. Logozzo
e-mail: silvia.logozzo@unipg.it; silvia.logozzo@vger.eu

S. Logozzo · G. Canella
V-GER. S.R.L., Prunaro di Budrio (BO), Budrio, Italy
e-mail: gabriele.canella@vger.eu

Examples of applications in the mechanical industry are [13–15]: development of industrial design components, deformation and geometry analysis and measurement, quality control, reverse engineering, surface inspection and wear evaluation, prototyping and 3D printing, robotics.

In the medical industry 3D optical scanners are required in order to realize custom-tailored components like shoes or sport suits or to design orthopedic eso-prostheses and endo-prostheses or dental restorations [8, 11]. Body scanning is also needed to plan and guide aesthetic interventions [1]. In the field of craft and art, a typical application is the jewel manufacturing process, as the 3D scanning is useful to make reconstructions and series production of hand made and precious artifacts.

In heritage preservation and archeology 3D scanning and modeling is useful to restore monuments and artifacts, to detect and monitoring the status of preservation [4, 6] and to reproduce evidences in order to build virtual museum through the augmented reality. In the field of environmental and civil engineering typical applications are infrastructures and quarry monitoring or excavation planning [2, 9], monitoring of the structural status of ancient buildings. 3D scanning for media and entertainment is required to realize scenic design, characters of movies, cartoons and videogames or nice 3D portraits. The device presented in this paper is typically used for quality control and inspection applications, tribological and metrological evaluations, reverse engineering operations, dental applications and jewelry fabrication.

2 The Automated Tilt-Rotational 3D Optical Scanner: ScanRider

The instrument proposed in this paper has been called ScanRider (Fig. 1). It is a desktop 3D optical scanner based on the principle of structured light active triangulation. The device is configurable and modular and is basically composed by four parts: the optical assembly, the 1 or 2 degrees of freedom mechanics, the electronics and the software.

According to the goal of the research the scanner has been designed with an extendable framework with fixtures in order to get always the right working distance and positioning for objects of several sizes, from the size of about 5 mm (as a small pendant for instance) to the size of about 530 mm. ScanRider has been studied to work with four different scanning volumes and can be equipped with a single axis rotary table or with a two axes tilt-rotational system (Fig. 2).

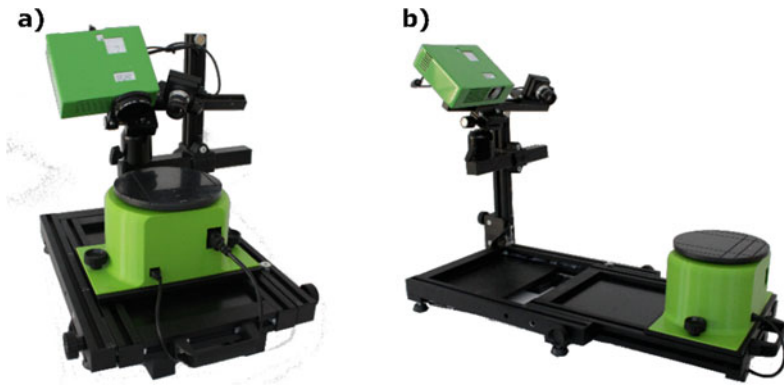


Fig. 1 ScanRider, a Volume 1 configuration, b Volume 3 configuration

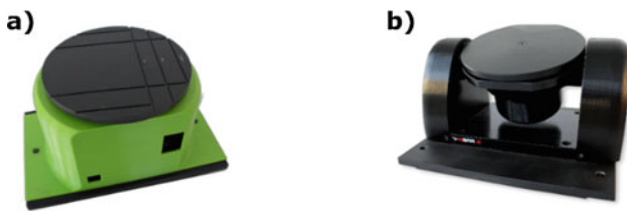


Fig. 2 Mechanisms, a single DOF, b two DOFs

2.1 Optical Assembly and Calibration

The optical assembly has been built with a led light source and one industrial black/white camera. The light emitter is a color light projector, projecting coded patterns of stripes onto the scene. The patterns are codified as a grey code in the first steps of the projection, while in the final stage they are codified applying the phase shift principle.

An innovative characteristic of the device is that different light colors (white, red, green, blue) can be projected. This allows to take the advantage of the optical natural features of the different target surfaces, in order to enhance the quality of the scan in terms of noise reduction.

Another advantage of the studied scanner is that the projector has a luminous flux of 500 lm and an high contrast. This allows to be able to acquire also reflective objects. The camera has a resolution of 1.3 MP. The camera and the projector are mounted on an aluminum guide. The projector is fixed, while the camera is mounted on proper slabs that assure the right positioning with respect to the projector and to the scene by moving in three ways. In-fact the camera can slide closer or farther to the projector, it can rotate around an axis perpendicular to the guide and it can tilt by using four grub screws.

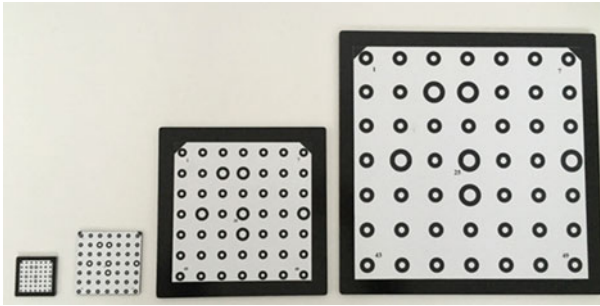


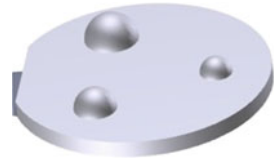
Fig. 3 Calibration plates

The guide is mounted on an adjustable ball joint to grant the right positioning of the entire optical assembly with respect to the scene.

After choosing the specimen the scanner must be configured to cover the correspondent scanning volume. As already mentioned, the framework is equipped with specific fixtures in order to find the right extension of the base, the position of the mechanical system and the height of the optical assembly depending on the size of the specimen (see Fig. 1). After positioning the framework according to the chosen volume, the optical system must be located properly and calibrated in order to define camera's intrinsic and extrinsic parameters and compensate distortions as explained in [12] and considering a camera model as in [3, 5, 7]. To do this four calibration plates can be used, one for each scanning volume (Fig. 3). The point-point distance is certified for every plate and annotated on the back side. First of all, the ball joint is used to position the center of the projection onto the center of the chosen calibration plate and the projector is brought into focus. After this the camera is moved on the guide to match the right distance from the projector (marked by specific reference signs), rotated and tilted in order to be centered with the center of the projection. Then the camera is brought into focus and the exposure is adjusted in order to guarantee the correct acquisition. After this, the optical system must be calibrated by following a procedure guided by the scanning software. The procedure is performed by taking eleven snaps in different positions of the calibration plate on the worktable. This optical calibration allows to assess the real precision of the instrument at each measurement and to ensure the accuracy reported in the following chapters.

The scanner is also equipped with a reference component (Fig. 4), certified by a metrological laboratory in order to be able to assess the real precision and accuracy of the measuring device after any calibration procedure, by comparing the difference between the certified reference model and the measured data.

Fig. 4 Reference phantom



2.2 Mechanical Positioning System

As already mentioned ScanRider can be equipped with a single axis rotary table or with a two axes tilt-rotational system, as shown in Fig. 2. The different worktables are used depending on the complexity of the surfaces to analyze. For objects with complex surfaces and undercuts or occlusions the scanner is equipped with the 2 DOFs table. In this paper we focus on this 2 DOFs mechanical system.

The two degrees of freedom are the rotations around the axes x and z (Fig. 5).

The reference system $Oxyz$ is the absolute and fixed system, centered on the center O of the worktable and oriented as the table in the start position. The reference system $Ox'y'z'$ is the system integral with the table during the motion and it is rotated and tilted with respect to the absolute system by the angles β and α . Therefore, the rotational matrixes are Eq. (1):

$$R_x = \begin{bmatrix} 1 & 0 & 0 \\ 0 & \cos\alpha & -\sin\alpha \\ 0 & \sin\alpha & \cos\alpha \end{bmatrix} \quad R_z = \begin{bmatrix} \cos\beta & -\sin\beta & 0 \\ \sin\beta & \cos\beta & 0 \\ 0 & 0 & 1 \end{bmatrix} \quad (1)$$

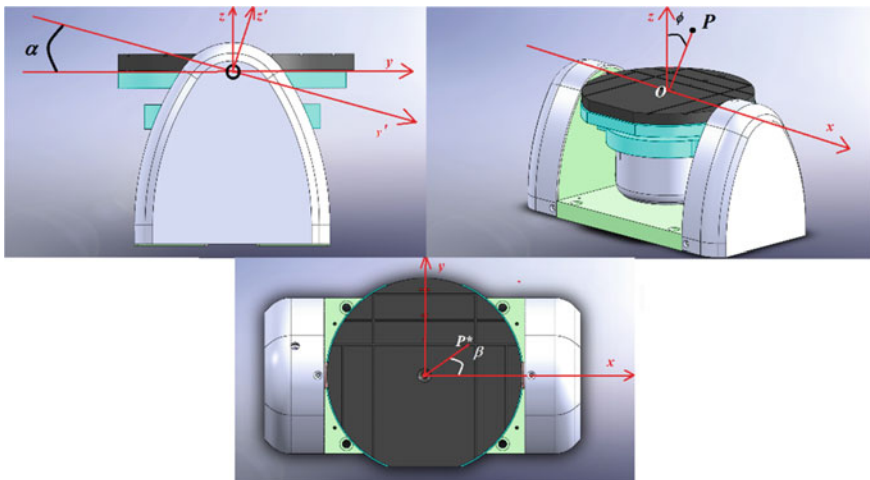


Fig. 5 Tilt-rotational worktable's reference systems and DOFs

Table 1 Technical specifications and scanning volumes

Specs	Volume 1	Volume 2	Volume 3	Volume 4
Scanning volume (mm ³)	66 × 50 × 50	133 × 100 × 100	300 × 225 × 225	530 × 400 × 400
Resolution (mm)	<0.05	<0.1	<0.23	<0.41
Precision/accuracy (mm)	<0.03	<0.07	<0.15	<0.27
Working distance (mm)	120	200	520	900

Also the mechanical system must be calibrated in order to be correctly recognized by the optics during the scanning stage. To do this an automatic procedure can be launched by the software after positioning the proper calibration plate on the worktable. This allows any point in the system Oxyz to be expressed in the camera system by means of the rotational and translational matrixes already known from the camera model [3, 10, 12].

2.3 Achieved Performance Parameters and Specs

The obtained scanner's technical specifications and the configurable scanning volumes are reported in Table 1.

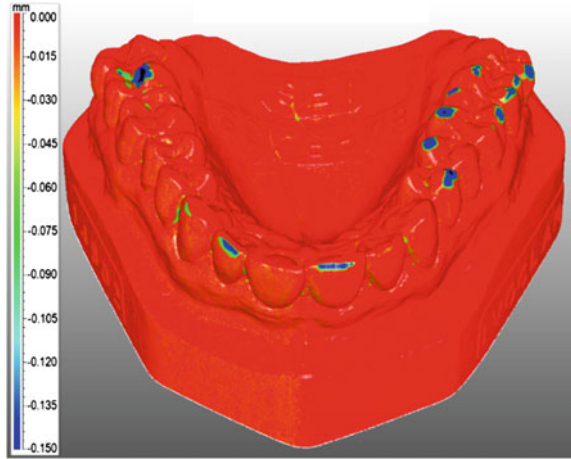
The device is able to acquire up to 2500000 triangles for each frame, and to output the watertight mesh of a full object in an STL format in less than three minutes. No physical targets are needed to scan.

3 Application

Here we present a medical application dealing with the study and evaluation of wear of teeth. In this study the scanned 3D model of the worn teeth has been compared with a reference 3D model of the non-worn teeth. In this case the reference model was the scanned 3D model of the teeth at the beginning of the study.

The comparison procedure was performed by: aligning and superimposing the worn and the reference in order to evaluate the deviations; calculating the difference of volume between the worn and non-worn models in order to assess the wear rate; the color 3D wear map is built Fig. 6. It represents the distribution of the deviations between the surfaces in the reference and in the worn models.

In the calculation of the wear rate the specimen is supposed to be homogeneous.

Fig. 6 3D wear map of teeth

The alignment procedure was performed by registration software by minimizing a distance criterion. The wear rate can be calculated according to Eq. (2):

$$\chi = \frac{V_i - V_f}{V_i} \% \quad (2)$$

where V_i is the volume measured in the reference model and V_f is the volume measured in the 3D model of the worn component [13, 14]. The obtained wear rate is 0.004 % and the difference between the initial and worn volumes is 3 mm³.

4 Conclusions

In this paper the design and development of an innovative automated desktop 3D optical metrological scanner is presented with particular attention to the optical and mechanical assemblies. The authors are going to deepen the dynamic behavior and the control system of the device.

References

1. Clarkson S et al (2016) Assessment of a Microsoft Kinect-based 3D scanning system for taking body segment girth measurements: a comparison to ISAK and ISO standards. *J Sports Sci* 34(11):1006–1014
2. Deliormanli H et al (2014) Using terrestrial 3D lasers scanning and optical methods to determine orientations of discontinuities at a granite quarry. *Int J Rock Mech Min Sci* 66:41–48

3. Fioravanti D et al (2008) Image based visual servoing for robot positioning tasks. *Meccanica* 43:291–305
4. Gallo A et al (2014) 3D reconstruction of small sized objects from a sequence of multi-focused images. *J Cult Herit* 15:173–182
5. Genta G et al (2016) Calibration procedure for a laser triangulation scanner with uncertainty evaluation. *Opt Lasers Eng* 86:11–19
6. Lerma J, Muir C (2014) Evaluating the 3D documentation of an early Christian upright stone with carvings from Scotland with multiples images. *J Archaeol Sci* 46:311–318
7. Niola V et al (2010) A New Real Time Shape Acquisition with a Laser Scanner: First Test Results. *Robot Comput-Integr. Manuf.* 26(6):543–550
8. Persson A et al (2006) A three-dimensional evaluation of a laser scanner and a touch-probe scanner. *J Prosthet Dent* 95(3):194–200
9. Sengoz B et al (2012) Comparison of pavement surface texture determination by sand patch test and 3D laser scanning. *Civ Eng* 56(1):73–78
10. Son S et al (2002) Automated laser scanning system for reverse engineering and inspection. *Int J Mach Tools Manuf* 42:889–897
11. Szymor P et al (2016) Accuracy of open-source software segmentation and paper-based printed three-dimensional models. *J Craniomaxillofac Surg* 44:202–209
12. Tsai R (1987) A versatile camera calibration technique for high-accuracy 3d machine vision metrology using off-the-shelf TV cameras and lenses. *IEEE J Robot Autom* 3(4):323–344
13. Valigi MC et al (2015) Study of wear of planetary concrete mixer blades using a 3d optical scanner. In: *Proceedings of the International Mechanical Engineering Congress & Exposition, IMECE2015, Houston, Texas, USA*
14. Valigi MC (2016) Wear resistance of blades in planetary concrete mixers. Part II: 3D validation of a new mixing blade design and efficiency evaluation. *Tribol Int* in press (2016)
15. Zhongxu H et al (2007) Automatic surface roughing with 3D machine vision and cooperative robot control. *Robot Auton Syst* 55:552–560

Adam's Hand: An Underactuated Robotic End-Effector

Giovanni Antonio Zappatore, Giulio Reina and Arcangelo Messina

Abstract This paper describes recent efforts by the authors in the development of a robotic hand, referred to as the Adam's hand. The end-effector is underactuated through a multiple bevel-gear differential system that is used to operate all five fingers, resulting in 15 degrees of freedom actuated by just 1 degree of actuation. Special focus is devoted to the transmission ratios and gear dimensions of the system to maintain the kinematic behaviour and the dimensions of the prototype as close as possible to that of human hand.

1 Introduction

A robotic hand refers to an end-effector with an anthropomorphic “inspiration”. However, matching the performance of the human hand poses many challenges [1]. Several examples of robotic hands have been proposed in the literature. They can be broadly classified into two main categories based on the number of their degrees of freedom (DOFs) compared to that of their degrees of actuation (DOAs): fully-actuated and underactuated. Notable fully-actuated hands are the DLR Hand [2] and the Shadow C3 Hand [11]. Complex robotic hands, while capable of efficient grasping, are overdesigned for this task and they suffer from high costs and overall lack of robustness. This is the main reason why in recent years there has been a growing interest in underactuated designs. The idea behind underactuation in robotic grasping is to use a mechanical system that can conform automatically to the specific shape of the object so that fewer actuators than DOFs are required. This results in simpler control systems and in a reduction of prototype cost. The underactuation concept for

G.A. Zappatore · G. Reina (✉) · A. Messina
Dipartimento di Ingegneria Dell'Innovazione, Università del Salento,
Via Arnesano, 73100 Lecce, Italy
e-mail: giulio.reina@unisalento.it

G.A. Zappatore
e-mail: giovanniantonio.zappatore@gmail.com

A. Messina
e-mail: arcangelo.messina@unisalento.it

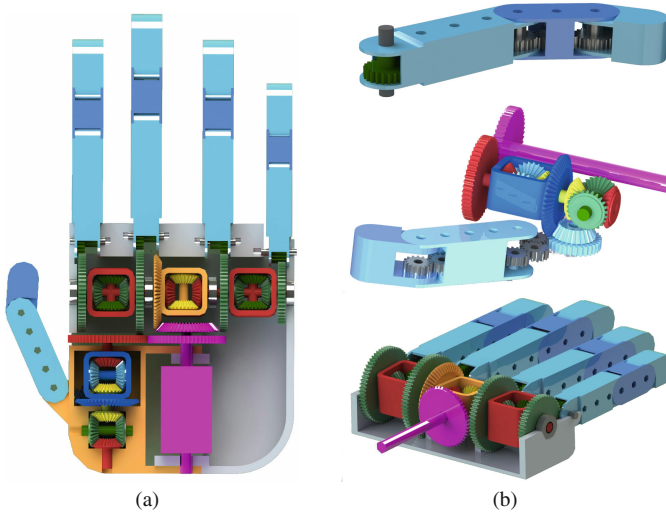


Fig. 1 3D CAD model of the Adam's hand: **a** entire actuation system, **b** from *top to bottom* middle finger, thumb actuation sub-system (Block I), actuation sub-system of the fingers from index to pinkie (Block II)

a robotic finger was presented for the first time in [4]. Since then, many examples of underactuated hands have been proposed, including the SARAH Hand [8], and FEDERICA and LARM Hand [3, 9, 10]. This paper presents preliminary results in the design and prototyping of the Adam's hand, a new concept of underactuated robotic system that mimics the human hand functionality using only one actuator (1 DOA). This is achieved drawing from the principle of differential systems, i.e. by automatically distributing one input to various output, the ratio between the different output being set by the design parameters and the output states themselves. The main goal is to reduce complexity and cost, while preserving the human hand functionality. The Adam's hand is composed of five fingers that are connected via revolute joints to a fixed frame (metacarpus) that is similar to a human palm, as shown in the 3D CAD model of Fig. 1. The palm hides the multiple differential stages that allow the hand to operate as explained in the remainder of this paper.

2 Hand Modeling

Due to complexity of human hand, the creation of a mechanism that can exactly reproduce its functions poses many challenges. The first step towards the prototype design is the definition of a suitable model. A kinematic scheme of the hand structure can be obtained by matching a link to each phalanx of the five fingers (referred to as I to V from thumb to the pinkie) and a joint to each articulation, without considering

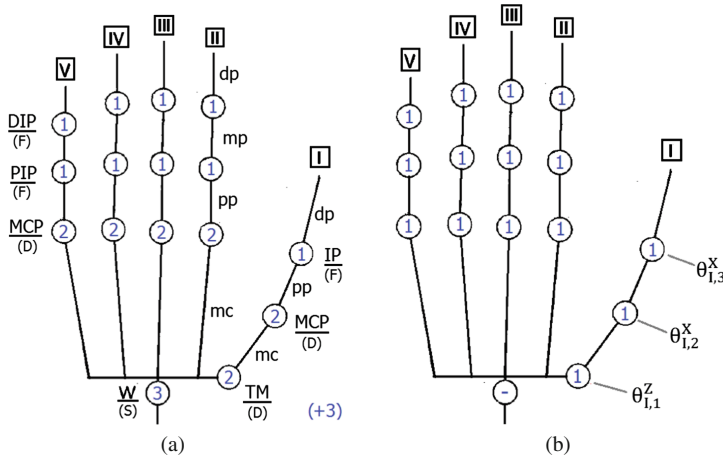


Fig. 2 Right hand scheme, palmar view: **a** full model (27 DOFs), **b** simplified model (15 DOFs)

Table 1 Nomenclature used in Fig. 2

Links (or bones)	Joints	Joint categories
dp: distal phalanx	DIP: distal interphalangeal	F: Flexion/Extension—1 DOF
mp: middle phalanx	PIP: proximal interphalangeal	A: Abduction/Adduction—1 DOF
pp: proximal phalanx	IP: interphalangeal	T: Twist (rotation)—1 DOF
mc: metacarpus	MCP: metacarpophalangeal	D: Directive (sum of F and A)—2 DOF
	TM: trapeziometacarpal	S: Spherical (sum of D and T)—3 DOF
	W: wrist	

wrist bones. Each finger is therefore modeled as a kinematic chain in which the DOFs correspond to the angles formed by the rotational joints [7], as shown in Fig. 2a. Corresponding nomenclature is explained in Table 1. The resulting model assigns 27 DOFs to the hand as follows:

- 4 DOFs for fingers II to V, corresponding to abduction/adduction of MCP joint, flexion/extension of MCP, PIP and DIP joints;
- 5 DOFs for finger I, corresponding to abduction/adduction of MCP and TM joints, flexion/extension of MCP, TM and IP joints;
- 6 DOFs needed to position and orientate the hand in the reference system, three of which in the wrist (flexion/extension, abduction/adduction and rotation).

Considering the limitations related to hand anatomy and joint behaviour during finger movements [5], the model has been further simplified by excluding the abduction/adduction of the MCP joint for fingers II-IV, and the flexion/extension of the TM joint and the abduction/adduction of the MCP joint for finger I. Fixing also the

hand in the reference system (translations and wrist rotations) the model is reduced to 15 DOFs (Fig. 2). To univocally define the model's DOFs, the variable $\theta_{i,j}^k$ is introduced: it refers to the rotation of the j -th joint ($j = 1, 2, 3$, from the wrist to the tip) of the finger $i = \text{I, II, ... , V}$. The superscript k refers to flexion/extension ($k = X$) or abduction/adduction ($k = Z$) angles, respectively. For ease of understanding, the DOFs of finger I are indicated in Fig. 2.

3 System Analysis

Although the model presented in the previous section represents well human hand dexterity, the design of an end-effector that is able to manage such a large number of DOFs by means of an equal number of actuators would be extremely complex and costly. This issue can be addressed by resorting to the principle of underactuation, i.e. handling a large number of DOFs through a limited number of actuators. One possible solution to the underactuation problem is the use of differential mechanisms. According to the IFToMM terminology [6] a differential mechanism is a “mechanism for which the degree of freedom is two and which may accept two inputs to produce one output or, may resolve a single input into two outputs”. To obtain more than two output, multiple differential modules can be stacked, each adding 1 DOF to the system. In general, $(n - 1)$ differential stages are required to obtain n output. These stages can be connected in series or symmetrically. The serial “nature” of human fingers suggests the use of serial underactuated transmission within a finger prototype, while underactuation between fingers can be reached through a symmetrical structure, that allows as well a more compact overall design.

The architecture of the proposed system is shown in Fig. 3 expressed as a functional scheme, where the strictly serial transmission tree within each finger and the symmetrical configuration between different fingers can be observed. For example, underactuation between fingers II and V is managed through differential stages 1, 2 and 3, whereas the serial transmission train in the middle finger III is handled by stage_{III,1} and stage_{III,2}. Details of the serial transmission along finger I and finger II are shown in Fig. 4a, b, respectively. The full kinematic scheme of the symmetrical differential structure of the Adam's hand is shown in Fig. 5. Stages in charge of the underactuation between the fingers are bevel gear differential systems, two of which (stages 4 and 5 in Block I of Fig. 3) are stacked serially to control thumb's TM abduction/adduction and thumb's MCP flexion/extension, and the remaining three (stages 1, 2, and 3 in Block II) are stacked symmetrically to control fingers II-V (not shown in Fig. 5). Block I and Block II are both powered by the only actuator (one electrical motor) of the system. Let us focus on Block II at first. Planet carrier P_1 is driven by the actuator through the conical coupling with gear M_1 . Output from the differential stage 1 are the left and right solar gears, respectively, $S_{1,L}$ and $S_{1,R}$. In turn, they serve as planet carriers for differential stage 2 and stage 3, respectively. Output from stage 2 are the left and right solar gears $S_{2,L}$ and $S_{2,R}$ that control the serial transmis-

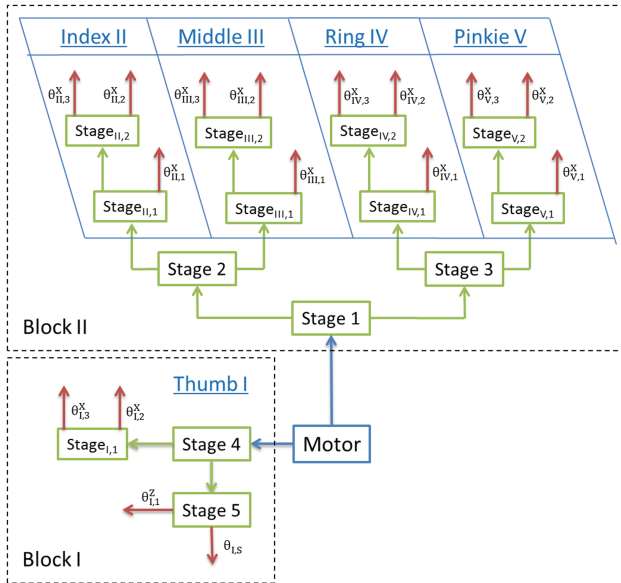


Fig. 3 Connection tree implemented in the Adam's hand: 14 differential stages leads to 15 DOFs. Block I refers to finger I. Block II refers to fingers II–V

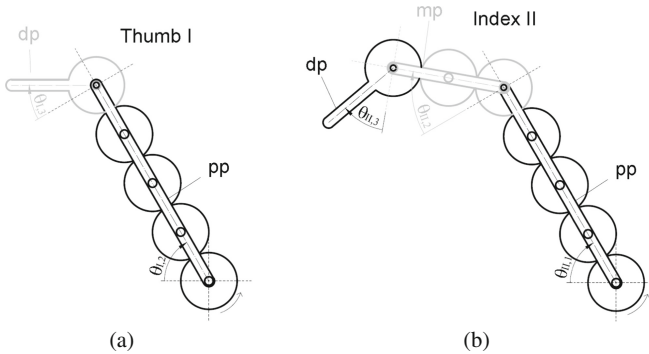


Fig. 4 Details of the transmission tree along: **a** Thumb (finger I), and **b** Index (finger II)

sion tree along finger II and III, respectively. Similarly, finger IV and V are driven by the solar gears output of stage 3, i.e. $S_{3,L}$ and $S_{3,R}$. Block I refers to the actuation of thumb, instead. Differential stage 4 receives motion from the actuator through the coupling between gear M_2 and input solar gear $S_{4,R}$. Output from stage 4 are the solar gear $S_{4,L}$ that serves as input solar gear for stage 5 and planet carrier P_4 that engages with bevel gear C_1 (represented by its primitive circle marked by a dashed orange line). Then, C_1 transfers motion to the serial transmission tree of finger I for flexion/extension. Finally, abduction/adduction is performed through rotation of the whole planet carrier P_5 about the axis a_1 .

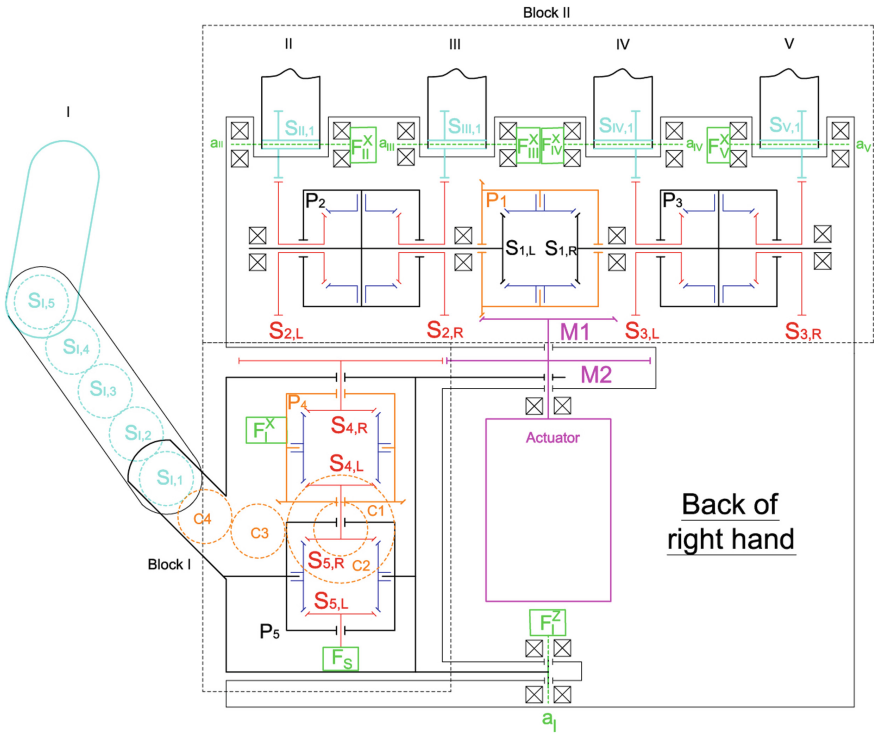


Fig. 5 Kinematic scheme of the Adam's hand

3.1 Discussion

The choice of using gear transmission is aimed to overcome the limits of tendon-based transmission. The latter is limited to small forces and exhibits large internal friction, whereas gears allow for a better overall robustness, reliability and control. Moreover, although tendons tend to enhance the compactness of the device as well as to imitate the human muscular principle, they are characterized by the unidirectionality of the actuation, for which at least $2n$ actuators are theoretically required to actively control n DOFs. The passive control, e.g. the return of the phalanges to the base position, can be in fact performed with springs. In contrast, using gear bidirectional movements, the same number of DOFs can be actively controlled with n actuators. The use of a gear-based mechanism allows the device to be designed with a modular approach. The fingers are plug&play (then easily replaceable in case of damage or upgrade), while the differential stages can be considered as “cumulative”, i.e. the differential assembly that drives fingers II-V can be modified so that the number of fingers can be easily changed according to the desired task. This property is not available in tendon-driven system, since the connections of the tendons in the palm are necessarily more complex. Differential gear systems are also characterised

by the independence of the output force from their kinematic state (i.e., they are force-isotropic), ensuring constant performance over the workspace and resulting in enhanced grasp stability. In addition, the high grade of underactuation implemented in our device allows objects to be grasped using a simple control, rather than having to command and coordinate several actions. It should be noted that the proposed solution allows independent control of each finger flexion/extension and of the thumb abduction/adduction through the use of dedicated clutches. Generally, two cases of force transmission between the fingers are of interest: all output of the system close to being equal (when the grasp configuration is symmetrical as in pinch or spherical grasps) or one output close to the sum of all others (as thumb in opposition to all the other fingers). The proposed design allows either cases to be fulfilled.

3.2 Gear Ratios

Under steady-state conditions and unitary efficiency, the following relationships hold for the differential stage i ,

$$\begin{aligned}\omega_{P_i} &= \frac{\omega_{S_{i,L}} + \omega_{S_{i,R}}}{2} \\ C_{P_i} &= C_{S_{i,L}} + C_{S_{i,R}} \\ C_{S_{i,L}} &= C_{S_{i,R}}\end{aligned}\quad (1)$$

where ω and C refer, respectively, to the angular velocity and the torque applied to the given gear. By adopting a unitary gear ratio between M_1 and P_1 and an equal gear ratio between the output gears from the symmetrical differential stages and the input gears to the serial differential stages, e.g. $\tau = \frac{\omega_{S_{II,1}}}{\omega_{S_{2,L}}} = -2$, the following relationships can be obtained between the actuator motion and the finger II-V flexion/extension:

$$\begin{cases} \omega_{M_1} = \omega_{P_1} = -\frac{\omega_{S_{II,1}} + \omega_{S_{III,1}} + \omega_{S_{IV,1}} + \omega_{S_{V,1}}}{8} \\ C_{M_1} = C_{P_1} = 2(C_{S_{II,1}} + C_{S_{III,1}} + C_{S_{IV,1}} + C_{S_{V,1}}) \end{cases}\quad (2)$$

Similar relationships can be obtained for Block I. In this paper, for simplicity, only the flexion/extension of finger I is considered, i.e. motion of the planet carrier P_5 and of the solar gear $S_{5,L}$ is prevented by brake F_1^Z and F_S , respectively (refer to Fig. 5). Therefore, ω_{P_5} and $\omega_{S_{5,L}}$ are null and it holds:

$$\begin{cases} \omega_{M_2} = -\omega_{S_{4,R}} = -2\omega_{P_4} = -\frac{\omega_{S_{1,1}}}{2} \\ C_{M_2} = C_{S_{4,R}} = 2C_{S_{1,1}} \end{cases}\quad (3)$$

Finally, the motor will provide the total torque:

$$C_M = C_{M_1} + C_{M_2} = 2(C_{S_{I,1}} + C_{S_{II,1}} + C_{S_{III,1}} + C_{S_{IV,1}} + C_{S_{V,1}}) \quad (4)$$

Since the motor actuates the two blocks at the same time, i.e. $\omega_{M_1} = \omega_{M_2}$, the following relationship holds between the five fingers:

$$\omega_{S_{I,1}} = \frac{\omega_{S_{II,1}} + \omega_{S_{III,1}} + \omega_{S_{IV,1}} + \omega_{S_{V,1}}}{4} \quad (5)$$

4 Conclusions

This paper presented preliminary results in the development of the robotic Adam's hand. The proposed end-effector is underactuated through a multiple bevel-gear differential system that is used to operate all five fingers, resulting in 15 DOFs actuated by just 1 DOA.

Acknowledgments The financial support of the ERA-NET ICT-AGRI2 through the grant Simultaneous Safety and Surveying for Collaborative Agricultural Vehicles (S3-CAV) is acknowledged.

References

1. Birglen L, Lalibert T, Gosselin C (2008) Underactuated Robotic hands. Springer, Berlin, Heidelberg
2. Butterfass J et al (2001) DLR-hand II: Next generation of a dexterous robot hand. In: IEEE international conference on robotics and automation, pp 109–114
3. Carbone G, Rossi C, Savino S (2015) Performance comparison between FEDERICA hand and LARM hand. *Int J Adv Rob Syst* 12(90):1–12
4. Hirose S, Umetani Y (1978) The development of soft gripper for the versatile robot hand. *Mech. Mach. Theory* 13:351–358
5. Huang TJ, Lin J, Wo Y (2000) Modeling the constraints of human hand motion. In: Workshop on human motion, pp 121–126
6. IFToMM: Terminology for the theory of machines and mechanisms. *Mech Mach Theory* 26(5):435–539
7. Kunii TL, Lee J (1995) Model-based analysis of hand posture. *IEEE Comput Graph Appl* 15(5):77–86
8. Martin E, Desbiens A, Laliberte O, Gosselin C (2004) SARAH hand used for space operation on STVF robot. In: *Intelligent Manipulation and Grasping*, pp 279–284
9. Niola V, Penta F, Rossi C, Savino S (2015) An underactuated mechanical hand: theoretical studies and prototyping. *Int J Mech Cont* 16(1):11–19
10. Niola V, Rossi C, Savino S (2014) A new mechanical hand: theoretical studies and first prototyping. *Int Rev Mech Eng* 8(5):835–844
11. Shadow Robot Company (2016) Shadow dexterous hand. <https://www.shadowrobot.com/products/dexterous-hand/>. Accessed 19 May 2016

Automatic System for Fibers Extraction from Brooms

P.F. Greco, G. La Greca, G. Larocca, S. Meduri, B. Sinopoli,
D. Battaglia, A. Caseti, A. Aloise, G. Chidichimo and G. Danieli

Abstract This paper presents an automatic system for fibers extraction from brooms, realized by Calabrian High Tech S.r.l. in the framework of PON MATRECO. Base of this system is a suspended rail from which a series of hoists are hanging, pulled by a chain. Six work stations are devoted to perform each a specific task, from hanging the plants manually to bars, placing them in position and pushing a button, to immerge them in a maceration bath held at 80° where the plants must be kept for about 20 min, to lift them, then rinse, detach fibers and finally discard the plants to restart the process. The entire cycle, controlled by a PC, will need only one person in operation, even if at the moment, being yet in an experimental phase, more people are involved. Broom is an endemic plant in Calabria, with good mechanical properties and long fibers, but fibers extraction was up to now extremely labor intensive, thus too expensive. Other fibers extraction, such as those of hemp or flax, require simpler treatments, even if the sequence of operations described in this paper, with minor modifications, could be adopted to treat all of them, obtaining long fibers. A patent application has been filed on this plant scheme, taking into account a number of possible variations [7], and a second patent is about to be deposited.

Keywords Broom fiber extraction · Automatic fiber extraction from plants

P.F. Greco · G. La Greca · G. Larocca · S. Meduri · B. Sinopoli · D. Battaglia · A. Caseti
· G. Danieli

Calabrian High Tech Srl, Via Ponte Pietro Bucci Cibo 45C, 87036 Rende (CS), Italy

P.F. Greco · G. Danieli (✉)

DIMEG – Dipartimento di Ingegneria Meccanica, Energetica e Gestionale,

Arcavacata di Rende (CS), Italy

e-mail: danieli@unical.it

URL: <http://www.chtsrl.com>

G. La Greca · D. Battaglia · A. Aloise · G. Chidichimo

CTC – Dipartimento di Chimica e Tecnologie Chimiche, Università della Calabria,

Via Ponte Pietro Bucci Cibo 45C, 87036 Rende (CS), Italy

© Springer International Publishing AG 2017

G. Boschetti and A. Gasparetto (eds.), *Advances in Italian Mechanism Science*,

Mechanisms and Machine Science 47, DOI 10.1007/978-3-319-48375-7_27

1 Introduction

Brooms were used for ages for fiber extraction. In fact broom fibers are almost as strong as cotton, and broom is an endemic plant in southern Italy, often considered an invasive shrub in other counties [4–11]. However the problem was extremely labor intensive, so that it became unbearable. In fact brooms were used quite extensively in Italy in the period immediately preceding the second world war as a substitute for jute, whose import was blocked by the sanctions arising from the invasion of Ethiopia [1]. But as the war ended, so did the sanctions, and the use of brooms, just because of the rising cost of manpower. However there is still a limited production of broom fibers in some villages of Albanian origin. Besides that, there is a number of possible applications that make again broom fibers extraction potentially interesting [2–5].

2 Generalities About the Design

We started from the analysis of the possible sequence of the operations to extract the cellulose fiber, main product, also separating the branches, that could be used as thermal insulator, from the trunk, to be used to generate heat. We then passed to define the sequence of operations, which must start from hooking a certain number of brooms (four at the moment, in the future twice as much) to a bar, which must be used to transfer the plants from one work station to the next. In order to reduce to a minimum the cost of labor, only the first operation will be actuated by a worker, while all remaining will be automated.

It was also thought to divide the different operations in physically separate processing stations, and, since the necessity of using chemical reagents, almost all the components are made of stainless steel. Moreover, it was thought to use a kind of assembly line in a closed circuit, which starts from the loading station and ends with the station of separation of branches from logs, to restart the cycle immediately after. The assembly line, had to leave the bar holding brooms to macerate for some time in a suitable reservoir, picking next another bar with already soaked brooms.

Furthermore, the brooms were to be raised and lowered continuously between a work station and the next. And hence the idea of a train equipped with electric hoists individually controlled and able to hook and unhook the bar-holding broom arose.

Basic element of this plant, the bar holding broom, shown in Fig. 1. Note the snap closure of each of the four slots, and as all the four slots can be opened by acting simultaneously on the pins release, placed on the upper side, right of each slot, as will be better clarified in the following.

To understand how the slots are closed, blocking the brooms, we look at the first work station (Fig. 2), which receives a bar with hatches open to host the new brooms. As can be seen, the operator manually enters the broom into the slot and



Fig. 1 The bar holding brooms



Fig. 2 First work station

Fig. 3 The travelling hoist and its grasping device



Fig. 4 The assembly line as seen from the floor



hits a button that produces a roller, driven by a worm, to advance, closing the hatch, otherwise held open by a spring. Closing the hatch compresses the broom against an element sitting in the back of the slot, in turn, pushed out by two pre-loaded springs. Immediately after the advancement of the hatch closing roller, the system stops due to the presence of a contact, placing it in waiting state for the next manual command. Then again the roller will advance to the next hatch closing it, repeating the operation till the fourth hatch is closed. At this point the hoist raises bar and brooms, and goes to the second station. Once the process of raising the bar is completed, the roller returns to the initial position. On the first station, the bar arrives already empty, and is lowered from above by the system shown in Fig. 3, which comprises a carriage sliding on a suspended rail, a hoist which controls two cables, supporting a light motorized bar presenting two rotating fingers, bent at 90° , which grasp the broom holder bar in the central portion, but close to the side plates. The Fig. 4 shows the entire assembly line as seen from the below, with the six hoists and relative bars hanging from these. Note that one bar is missing, and this will be clarified later.

3 The System Mechanical Components

Before being introduced in the maceration bath, however, the brooms are to be compacted in order to fit them in the bath. After having studied several possibilities, a mechanism based on the use of rotating drums was preferred to reduce the overall required height of the plant. The two drums are sitting above the insulated and covered tank containing the maceration bath held at 80°C , and the system is shown in Fig. 5.

Fig. 5 The second station, the rotating drums and the bar translation chain



Fig. 6 The third station and the squeezing drums



Note that there is some space between the tank and its cover, in order to leave room for two chains used to move the bars with their brooms from one extreme to the other of the tank, advancing of about 30 cm each time a new bar holding the plants is introduced, while on the other extreme a bar with soaked plants is lifted. A couple of smaller drums pressed by springs are positioned at the other extreme of the tank, in order to squeeze the brooms at the exit of the tank, recuperating as much as possible both the maceration liquid and its heat (Fig. 6).

The fourth station is dedicated to rinsing (with nozzles shown in the figure) and squeezing the plants, where two plates driven by four chains are pressed one against the other (Figs. 7 and 8).

Fig. 7 The fourth station for rinsing and squeezing

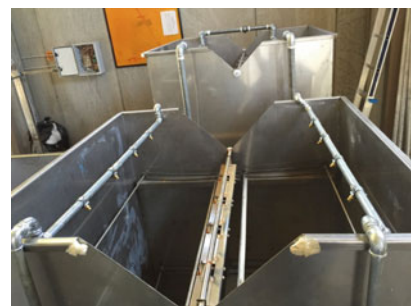
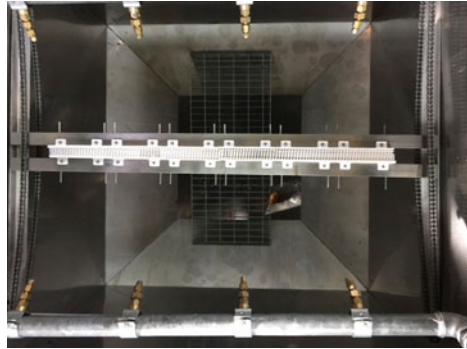


Fig. 8 The fifth station for fibers separation



The fifth station presents two rows of brushes with long plastic teeth that are pushed one against the other to detach the fibers. This is also matter for a new patent application.

4 The Electronic Control System

In order to function, the extraction system needs a large number of control devices. These drive the various components in function of various feedbacks supplied from a series of sensors arranged in the key points of the plant. Thanks to them the facility is able to fulfill the various processes in complete safety, following a predetermined logic. As they must comply with industry standards, a data communication protocol that was as robust and simple as possible was adopted.

The choice fell on the RS-485 standard, perfectly compatible with the rotating contact (Figs. 10 and 11). The RS-485 standard gives the possibility of daisy-chain connections, which allow the direct access, by the master, to the single slave without passing through the previous slaves. Doing so in case of breakage of a slave, the master is always able to communicate with others. As regards the control of the system itself, the choice fell on microcontroller electronic boards designed and manufactured specifically (Fig. 9). The hoists are driven directly by the master computer, through an algorithm written in Lab VIEW (Fig. 12), as they reach each

Fig. 9 The set of specially designed boards



Fig. 10 The rotating contact



Fig. 11 The rotating contact working scheme

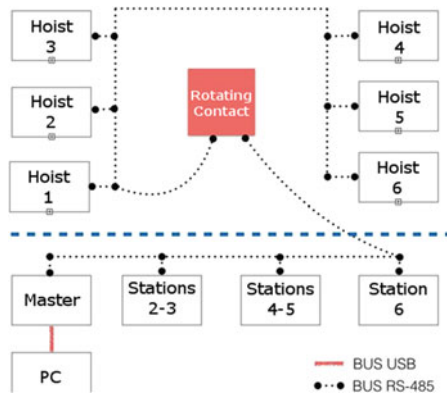
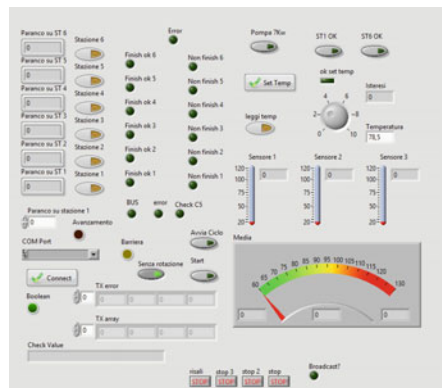


Fig. 12 Lab VIEW control panel



station, executing a series of commands which depend on the station itself. The correct hoist-station alignment is guaranteed by a double check: an infrared sensor and a mechanical stop.

5 The Heating and Temperature Control System

The auxiliary heating system (Fig. 13) has the task of providing the necessary hot water, so that the soaking tub meets the thermodynamic conditions necessary for a smooth operation of the broom maceration process.

Following the ministry guidelines, it was decided to allocate for use by the thermal power plant, the room adjacent to the installation of fiber extraction. It hosts many of the auxiliary thermal components, such as, heat generator, circulation pumps, expansion tanks, control and safety organs.

For the plant energy production, several alternatives were evaluated, including the use of solar collectors. But the cost of purchase and installation was not convenient for testing purposes. So it was decided to use LPG fuel as source of energy. Also, choosing water as thermo-vector fluid, the heat generator must be constituted by the boiler-burner pair.

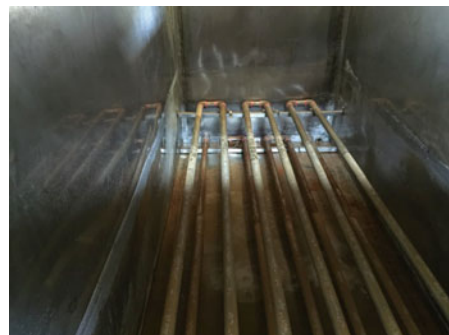
The thermal load on the maceration tub is supplied by an immersed heat exchanger (Fig. 14). Among the different types, the one consisting of a single tube was chosen, that entering and exiting from the same short side of the tub, runs through it several times throughout its length.

For the sizing of the heat exchanger, an iterative method was used.

Fig. 13 Heating and temperature control system



Fig. 14 Immersed heat exchanger



These iterations led to obtain a heat exchanger with 4.79 m² of surface, formed by a 1 ¼" single tube, 36 m long.

Since the heat exchanger has to be immersed in the maceration tank, it was realized in AISI 316 steel.

6 Conclusions

Concluding, this plant is starting to produce fibers, but at the moment not in satisfying quantities, and a lot of improvements are possible. Thus, still a lot of work is needed to obtain something of industrial value.

Acknowledgments The authors wish to acknowledge the work of Renato Bentrovato, Ernesto Ramundo and Diego Pulice of DIMEG Machine Lab, which helped in the initial part of this work. This work was financed by PON MATRECO.

References

1. Antoniani C (1940) Broom fibre extraction and its commercial possibilities. *Italia Agricola* 77:189–197
2. Avella M, Casale L, Dell'Erba R, Martuscelli E (1998) Broom fibers as reinforcement for thermoplastic matrices. *Macromol Symp* 127:211–218
3. Bellingham PJ, Coomes DA (2003) Grazing and community structure as determinants of invasion success by Scotch broom in a New Zealand montane scrubland. *Divers Distrib* 9:19–28
4. Bellingham PJ (1998) Shrub succession and invasibility in a New Zealand montane grassland. *Aust J Ecol* 23:562–572
5. Cassano R, Trombino S, Bloise E, Muzzalupo R, Iemma F, Chidichimo G, Picci N (2007) New broom fiber (*Spartium junceum* L.) derivatives: preparation and characterization. *J Agric Food Chem* 55:9489–9495
6. Downey PO, Smith JMB (2000) Demography of the invasive shrub Scotch broom (*Cytisus scoparius*) at Barrington Tops, New South Wales: insights for management. *Austral Ecol* 25:477–485
7. Greco PF, Danieli G, Aloise A, Chidichimo G, Nudo P, De Rango A, Impianto automatizzato per l'estrazione di fibre vegetali da piante. Italian Patent Application CS2014A000021
8. Kang M, Buckley YM, Lowe AJ (2007) Testing the role of genetic factors across multiple independent invasions of the shrub Scotch broom (*Cytisus scoparius*). *Mol Ecol* 16:4662–4673
9. Nekkaa S, Chebira F, Haddaoui N (2006) Effect of fiber treatment on the mechanical and rheological properties of polypropylene/broom fiber spartium junceum composites. *J Eng Appl Sci* 1:278–283
10. Paynter Q, Downey PO, Sheppard AW (2003) Age structure and growth of the woody legume weed *Cytisus scoparius* in native and exotic habitats: implications for control. *J Appl Ecol* 40:470–480
11. Rees M, Paynter Q (1977) Biological control of scotch broom: modeling the determinants of abundance and the potential impact of introduced insect herbivores. *J Appl Econ* 34:203–1221

Functional Design of a Robotic Gripper for Adaptive Robotic Assembly

F. Oscari, S. Minto and G. Rosati

Abstract Nowadays, automated production systems are rapidly changing to increase flexibility. However, robot end effectors are usually designed to accomplish specific tasks and to handle a limited family of parts, and flexibility can only be obtained by using tool changing systems. The main drawbacks of such systems are increased cost of automation and reduced productivity. This paper presents the functional design of a flexible robotic gripper, capable of adaptively changing its aperture (grasp width) to different handling demands, without affecting the cycle time of the production system, as it can be actuated in hidden time. The solution proposed consists of (1) an electrically-actuated mechanism for adapting aperture, which allows to satisfy the flexibility requirements; (2) a pneumatically-actuated mechanism for open/close operations, which ensures comparably fast motion of jaws if compared to traditional, non-adaptive robotic grippers.

1 Introduction

Today's fast changing market situation is characterized by reducing product life cycles and increasing the number of product variants. Flexibility in production is the key issue that industries increasingly requires to handle a wide variety of products, perform quickly and easily frequent model changeovers, process multiple parts and models simultaneously, and be quickly responsive to part design changes [21]. The flexible automation and robotics are a viable investment strategy to compete economically in the global market, evidenced by sales of industrial robots increased by 9 % every year since 2008 to 12 % in 2013 [8, 13].

To achieve these aims, industrial manipulators need to be able to pick parts of significantly different sizes in order to ensure the desirable flexibility [2, 12]. Robot grippers represent therefore a crucial part both for the traditional flexible assembly systems (FAS), when automated by means of a robot, and the latest fully-flexible

F. Oscari · S. Minto · G. Rosati (✉)
Department of Management and Engineering, University of Padua,
via Venezia 1, 35131 Padova, Italy
e-mail: giulio.rosati@unipd.it

assembly systems (F-FAS) [7, 14, 15]. However, in manufacturing applications, general purpose grippers are not very diffuse and, on the contrary, end effectors are designed for very specific and focused task with a strongly limited versatility [4]. The common practice is to resort to the employ of a different tool for each family of parts. Tools are stored in a tool magazine allocated in the workcell and an automated tool changing system allows the robot to rapidly replace the tool on the end effector when it must process a different family. However, such systems are expensive and their use may heavily affect productivity [16].

On the other hand, flexibility is one of the biggest differentiators and the common denominator in the latest EOAT (End-Of-Arm Tooling) trends [5]. In fact, lately, research has shown wide interest in the development of innovative and flexible grippers in many area of use [4, 17, 19, 20], some of them for more specific fields, such as micro-assembly line and others [3, 11].

This paper presents the functional design of a flexible, potentially cost-effective gripper, capable of adapting its aperture to different handling demands but without affecting the working-cycle time of a flexible robotized production system. The solution proposed consists of a mechanism with two degrees of freedom: the first one, which will be electrically actuated, will be used for the regulation of the aperture (grasp width); a second part, pneumatically actuated, for open/close operations. The electrical actuator allows for continuous regulation of gripper aperture, whereas pneumatic on/off actuation of jaws assures high speed opening and closing.

2 Synthesis of the Mechanism

The first important design aspect of the mechanism proposed here is the path followed by the gripper jaws when they are moved by the two different actuators. We opted for: a parallel gripper [10] with short transverse stroke of the jaws; a continuous regulation of the aperture that allows the jaws to be closed along the same grasping line for any aperture selected (see Fig. 1). The maximum variation in part widths to handle (aperture regulation) is fixed of 100 mm (e.g., $5 \div 105$ mm). The transverse velocity of the parallel jaws, with respect to the grasping line during the grasping movement (opening-closing), is desired negligible. Finally, we consider a maximum size of the gripper fixed to $h \times l \leq 150 \times 200$ mm in order to ensure compactness.

The topology considered is based on a four-bar linkage, as shown in Fig. 1 ($ABCD$). Link DC works as the crank whilst the connecting rod consists of a ternary link, in which the end point P represents the revolute joint of the coupling to the jaw (PGQ). By acting on the crank (first d.o.f., electrical actuation), the end point P can be moved in order to regulate the aperture (regulation movement).

For grasping movements, a second d.o.f. (pneumatic actuation) was added by introducing a slider (either horizontal or vertical) in A . By keeping fixed the crank DC , the mechanism ABC results in a slider-crank linkage in which the pneumatic cylinder allows a rapid rotation of link BPC , which in turn produces the grasping movement of the jaw.

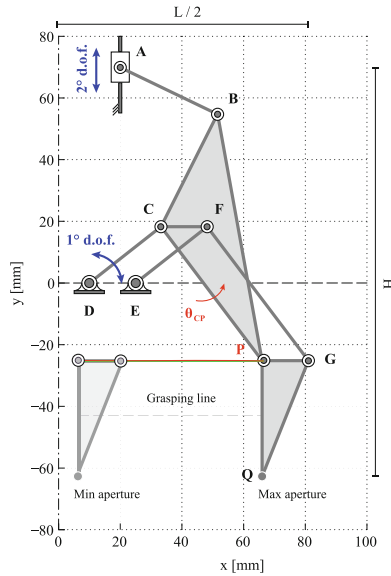


Fig. 1 Four-bar linkage based mechanism in the optimal solution provided with vertical slider and jaws closed ($\Delta A_y = 0$)

Two additional four-bar linkages, precisely the parallelograms $DCFE$ and $CFGP$, were attached to the mechanism. These supplements have the function of holding the jaw’s side PQ always perpendicular to the grasping line.

Different jaw roto-translations may be obtained by either imposing different link lengths to $DC-EF$ or $CF-GP$, or by using DE rotation (joint E no fixed to the frame) as second d.o.f. instead of a A translation (in this case, an angular gripper would be obtained [10]).

The synthesis of the entire mechanism was performed by employing an optimization-based, numerical mechanism synthesis method. This type of synthesis involves the minimization of structural error function $f(\mathbf{Z})$, subject to a set of size and geometric constraints such as Grashof and crank rocker conditions. Then, the optimization problem is given by:

$$\min \{f(\mathbf{Z})\} \quad \mathbf{Z} \in \mathbb{R}^k \tag{1}$$

subject to

$$g_j(\mathbf{Z}) \leq 0 \quad j = 1, \dots, m \tag{2}$$

$$Z_r \in [li_r, ls_r] \quad r = 1, \dots, k \tag{3}$$

where f is the goal function while the vector $\mathbf{Z} \in \mathbb{R}^k$ contains the search (design) variables Z_r ; $g_j(\mathbf{Z})$ denotes the constraints defining the searching space, and $[l_{i,r}, l_{s,r}]$ represents the boundary values of the design variables.

The computational approach used to minimize function $f(\mathbf{Z})$ dealt with two sequential algorithms applied iteratively in order to increase the possibility of providing global convergence within the solution. The first step consisted in finding the initial value of the design variables by using the genetic algorithm as implemented in MathWorks MatLab[®] (function *ga*) [6]. Then, the set of values from the first step was used as initial selection for the pattern search algorithm (second step), as implemented in MathWorks MatLab[®] (function *patternsearch*) [1, 9] with the aim of getting close to the global minimum. The objective function $f(\mathbf{Z})$ was evaluated at each iteration. In order to find a new solution, the kinematic analysis of the found mechanism had to be computed by using the new set of the design variables.

A motion generation synthesis [18] was considered for the design of this mechanism. Here, the ternary link *PBCP* was guided through a prescribed motion sequence.

As shown in Fig. 1, the desired path of pivot P , discretized in n target points (P_{x,d_i}, P_{y,d_i} $i = 1, \dots, n$), was prescribed to move along an horizontal line (green line) during the regulation movement of the aperture (rotation of crank *AB* as degree of freedom; slider *A* fixed). Precisely, the x coordinates of the desired path of P were uniformly distributed between the min (P_{x,d_1}) and max stroke value (P_{x,d_n}); the y coordinate of the desired path of P was defined as:

$$P_{y,d_i} = \text{mean}(P_{y_i})_{\forall i=1, \dots, n} \quad (4)$$

where P_{y_i} are the actual y coordinates of P obtained by the resulting mechanism.

The rotations of the ternary link were also defined. However, instead of the rotations during the regulation movement (θ_{CP}), the rotation of *PBC* from jaw closed to open $\Delta\theta_{CP}$ ¹ (opening movement) was prescribed for each point of the desired path of P . This movement is due to a translation of slider *A* considered in this case as the input for the mechanism motion, holding the crank *AB* fixed. The desired values for these rotations were set to

$$\Delta\theta_{CP,d_i} = 0 \quad \forall i = 1, \dots, n \quad (5)$$

This condition was applied in order to minimize the velocity of P along the y axis during the grasping/releasing movement.

The structural error between the obtained and desired motion was computed as a measure of the objective function to be minimized, which was defined as follows:

$$f(\mathbf{Z}) = \sum_{h=1}^3 ss_h \cdot w_h + \sum_{j=1}^4 g_j \cdot k_j \quad (6)$$

¹In the paper operator Δ indicates a rotation or a displacement due to the releasing movement of the gripper, i.e., from the configuration of jaws closed (grasp) to open (release), computed as open – closed.

where

$$ss_1 = \sum_{i=1, n} (P_{x, d_i} - P_{x_i})^2 \tag{7}$$

$$ss_2 = \sum_{i=1}^n (P_{y, d_i} - P_{y_i})^2 \tag{8}$$

$$ss_3 = \sum_{i=1}^n (\Delta\theta_{CP, d_i} - \Delta\theta_{CP_i})^2 \tag{9}$$

Each function g_j assumes value 1 when the condition is non satisfied ($k_j = 10^{15} \quad \forall j = 1, \dots, 4$) otherwise 0. The constraints considered are: (1) the satisfaction of the Grashof’s criterion, (2) the specifications on the overall gripper size (L_{max}, H_{max}), (3) the guarantee of the minimum jaw travel that corresponds to the stroke per gripper jaw ($\Delta P_{x, min}$), and (4) the condition on the sign of the jaw’s position along y during the opening movement ($\Delta P_y \geq 0$) to avoid higher quotas of the jaws when the gripper is closed.

The thirteen design variables used are: $\theta_{DC_1}, \theta_{DC_n}, z_{DC}, D_x, A_x, A_y, z_{CB}, z_{CP}, \gamma_{PCB}, z_{AB}, z_{DE}, \text{cfg}_{ABC}$ (the configuration of the RRR chain ABC , either “down” or “up”), and dirn_A (the movement direction of the slider in A for the second d.o.f., either horizontal or vertical). All the design variables were bounded ($[li_r, ls_r]$). The numerical values imposed for the upper and lower bounds, as well as the values and assumptions for the other parameters defined before are reported in Table 1.

Table 1 Numerical values of the fixed scalar parameters and boundaries for the design variables of the four-bar linkage based mechanism

Fixed scalar parameters			Variable scalar parameters		
Symbol	Value	Unit	Symbol	Boundary	Unit
n	100		θ_{DC_1}	[80, 110]	°
L_{max}	170	mm	θ_{DC_n}	[30, 60]	°
H_{max}	135	mm	z_{DC}	[15, 80]	mm
$\Delta P_{x, min}$	2.5	mm	D_x	[5, 50]	mm
P_{x, d_1}	5	mm	A_x	[5, 50]	mm
P_{x, d_n}	55	mm	A_y	[-80, 80]	mm
ΔA_x^*	-5	mm	z_{CB}	[15, 80]	mm
ΔA_y^{**}	5	mm	z_{CP}	[15, 80]	mm
D_y	0	mm	γ_{PCB}	[95, 170]	°
E_y	0	mm	z_{AB}	[15, 80]	mm
z_{PQ}	37.5	mm	z_{DE}	[10, 40]	mm
θ_{PQ}	270	°	cfg_{ABCA}	[0, 1]	
θ_{DE}	0	°	dirn_A	[0, 1]	

*The parameter was used for solutions with a horizontal slider

**The parameter was used for solutions with a vertical slider

3 Results and Discussion

The optimal solution for the mechanism was found by running the optimization algorithm, regardless of the direction of the slider movement (pivot A). Figure 1 shows the resulting mechanism, provided with a vertical slider; Table 2 reports the resulting values of the design variables. The aperture can be regulated from the minimum to the maximum value by means of a clockwise rotation of the crank DC from $\theta_{DC} = \theta_{DC_1} = 93.5^\circ$ to $\theta_{DC} = \theta_{DC_n} = 50^\circ$. Positive increments of A_y from $A_y = 70.4$ mm ($\Delta A_y = 0$) to $A_y = 75.4$ mm ($\Delta A_y = 5$ mm) open the jaws.

This optimized mechanism made a total score of $f(\mathbf{Z}) = 0.573$, resulting from partial scores of $ss_1w_1 = 0.0045$, $ss_2w_2 = 0.1192$, and $ss_3w_3 = 0.4493$. The first two partial scores (ss_1w_1 , ss_2w_2) regards the trajectory of pivot P with respect to that desired during the regulation of the aperture. The resulting path x - y of pivot P is plotted in Fig. 2a. The x coordinate of pivot P indicates that such mechanism allows apertures from about 10 mm to about 110 mm. The y coordinate lets small oscillations around the average value, in the order of a tenth of millimeter. Also, the error on both the minimum and maximum apertures that can be set up appears negligible. Therefore, the mechanism allows for regulations of the aperture within almost the entire desired range; moreover, the end effector does not need a compensation of the y tool coordinate (height), whenever the aperture of the gripper changes.

The last partial score (ss_3w_3) is the major one. This parameter measures the rotations of the ternary connecting rod during the releasing movement for each aperture considered. Although these rotations are necessary for the movement, we found that the maximum rotation of the ternary link, $\Delta\theta_{CP}$, is limited to about $3 \div 4^\circ$. This leads

Table 2 Resulting values for the design variables of the four-based linkage mechanism

Variable scalar parameters: results		
Symbol	Value	Unit
θ_{DC_1}	93.5	°
θ_{DC_n}	50.4	°
z_{DC}	29.5	mm
D_x	9.9	mm
A_x	19.5	mm
A_y	70.4	mm
z_{CB}	40.9	mm
z_{CP}	54.4	mm
γ_{PCB}	116.3	°
z_{AB}	35.4	mm
z_{DE}	14.8	mm
$cf_{g_{ABC}}$	0	
$dirn_A$	1	

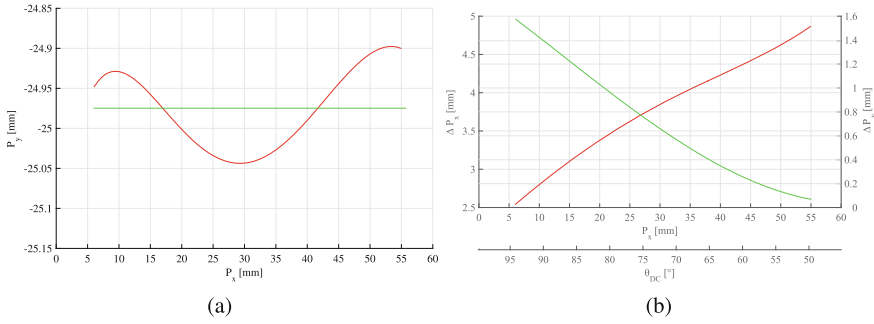


Fig. 2 Performance of the resulting four-bar linkage based mechanism: **a** the path of pivot P (right jaw of the gripper) in the x - y plane both desired (green line) and obtained (red line) during the regulation movement of the aperture; **b** the graph of the stroke per jaw ΔP_x (red line) and the undesired variations in height ΔP_y (green line) for the end effector during the opening movement, for each value of either the aperture per jaw P_x (main axis) or the crank angle θ_{DC} (first d.o.f., secondary axis)

to small variations along the y axis during grasping movements, up to a maximum value of about 1.5 mm, as shown on Fig. 2b (red line). It is worth also noticing that, specifically, the curve of ΔP_y is a monotonically increasing function with the aperture, which in turn means higher values at higher apertures, i.e., for larger and usually higher objects.

Figure 2b also depicts (green line) the stroke per jaw (open/close). It presents a well-shaped curve with values higher than $\Delta P_{x,\min} = 2.5$ mm. Notice as, at the minimum aperture of about 10 mm, the stroke per jaw measures about $\Delta P_x = 5$ mm achieving a complete closing of the jaws. This makes the gripper able to also grasp objects with width smaller than 10 mm, without designing properly jaws that recover the offset (keeping the same maximum aperture). On the whole, the mechanism seems to also have good performance in releasing/grasping movements.

4 Conclusion

The functional design of a flexible robotic gripper with two degrees of freedom was presented. The resulting mechanism fulfils all the initial requirements. With a proper mechanical design, it may be effectively used in robotized workcells. In fact, the electrical actuation allows the regulation of the aperture in hidden time, providing better productivity with respect to tool changing systems. Instead, the pneumatic actuation ensures performance in terms of force and closing times.

A limit of our design is the y movement of the jaws during opening/closing. More complex kinematics should be investigated in order to reduce/eliminate this issue, nonetheless it represents a good trade-off between mechanism simplicity and performance.

Next step will be the definition of mechanical design, the selection of actuators and prototype testing for experimental assessment of regulation and open/close times.

Acknowledgments The authors would like to acknowledge the great contribution of Andrea Carli to the project, in collaboration with Prof. J. Michael McCarthy of the Department of Mechanical and Aerospace Engineering at the University of California, Irvine.

References

1. Audet C, Dennis JE Jr (2003) Analysis of generalized pattern searches. *SIAM J Optim* 13(3):889–903
2. Boschetti G (2016) A picking strategy for circular conveyor tracking. *J Intell Robot Syst* 81(2):241–255
3. Bruzzone L, Bozzini G (2010) A flexible joints microassembly robot with metamorphic gripper. *Assembly Autom* 30(3):240–247
4. Canali C, Cannella F, Chen F, Hauptman T, Sofia G, Caldwell D, Eytan A (2014) High reconfigurable robotic gripper for flexible assembly. In: ASME 2014 international design engineering technical conferences and computers and information in engineering conference, pp V05BT08A019–V05BT08A019. American Society of Mechanical Engineers
5. Chaudhari N, Shinde VB (2014) Recent trends in robotic end of arm tooling (gripper). *Int J Mech Eng Robot Res* 3(2):171
6. Deep K, Singh KP, Kansal ML, Mohan C (2009) A real coded genetic algorithm for solving integer and mixed integer optimization problems. *Appl Math Comput* 212(2):505–518
7. Finetto C, Faccio M, Rosati G, Rossi A (2014) Mixed-model sequencing optimization for an automated single-station fully flexible assembly. *Int J Adv Manuf Technol* 70(5–8):797–812
8. International federation of robotics, world robotics 2015 industrial robots. <http://www.ifr.org/industrial-robots/statistics>
9. Kolda TG, Lewis RM, Torczon V (2003) Optimization by direct search: new perspectives on some classical and modern methods. *SIAM Rev* 45(3):385–482
10. Monkman GJ, Hesse S, Steinmann R, Schunk H (2007) *Robot Grippers*. Wiley-VCH
11. Qingsong X (2015) Design of asymmetric flexible micro-gripper mechanism based on flexure hinges. *Advances in Mechanical Engineering* 7(6):1687814015590331
12. Rosati G, Boschetti G, Biondi A, Rossi A (2009) On-line dimensional measurement of small components on the eyeglasses assembly line. *Opt Lasers Eng* 47(3–4):320–328
13. Robotics 2020 multi-annual roadmap for robotics in europe, horizon 2020 call ict-2016 (ict-25 & ict-26). <http://www.eu-robotics.net>
14. Rosati G, Faccio M, Carli A, Rossi A (2013) Fully flexible assembly systems (f-fas): a new concept in flexible automation. *Assembly Autom* 33(1):8–21
15. Rosati G, Faccio M, Finetto C, Carli A (2013) Modeling and optimization of fully flexible assembly systems (f-fas). *Assembly Autom* 33(2):156–174
16. Rosati G, Oscari F, Barbazza L, Faccio M (2016) Throughput maximization and buffer design of robotized flexible production systems with feeder renewals and priority rules. *Int J Adv Manuf Technol* 85(1–4):891–907
17. Sam R, Nefti S (2011) A novel, flexible and multi-functional handling device based on bernoulli principle. In: 2011 IEEE international conference on system engineering and technology (ICSET), pp. 166–171. IEEE
18. Sandor GN, Erdman AG (1997) *Advanced mechanism design: analysis and synthesis*. Prentice Hall

19. Tavakoli M, Marques L, De Almeida AT (2013) Flexirigid, a novel two phase flexible gripper. In: 2013 IEEE/RSJ international conference on intelligent robots and systems (IROS), pp 5046–5051. IEEE
20. Udupa G, Sreedharan P, Sai Dinesh P, Kim D (2014) Asymmetric bellow flexible pneumatic actuator for miniature robotic soft gripper. *J Robot* 2014
21. Wolfson W, Gordon SJ (1997) Designing a parts feeding system for maximum flexibility. *Assembly Autom* 17(2):116–121

Optimal Design of a Reconfigurable End-Effector for Cable-Suspended Parallel Robots

Luca Barbazza, Damiano Zanotto, Giulio Rosati and Sunil K. Agrawal

Abstract In this paper, a new cable-suspended parallel robot (CSPR) with reconfigurable end-effector is presented. The system has been conceived for pick and place operations in industrial environments where the ability to avoid obstacles and to maximize the performance are the main requirements. The proposed system has the capability of dynamically modifying the configuration of the cable anchor points on the end-effector to avoid collisions with obstacles in the approaching/departing phases, while reducing the movement time in the rest of the trajectory. Kinematic and dynamic models of the reconfigurable CSPR are derived and an optimal design of the end-effector is presented. The optimization aims at minimizing the force required by the linear actuator to modify the position of the cable anchor points during a pick and place task. The results reveal the predominant effect of the end-effector mass distribution on the force exerted by the linear actuator.

1 Introduction and Literature Review

Cable-Driven Parallel Robots (CDPRs) are a particular class of parallel robots wherein rigid links are replaced with cables. Compared to rigid serial and parallel robots, CDPRs have several advantages [2, 5]. High speed manipulation and load handling tasks are particularly suitable applications for CDPRs, thanks to their advantages in terms of large workspaces and high payload per unit weight [3]. Furthermore, CDPRs feature simple designs that make them relatively inexpensive,

L. Barbazza · G. Rosati (✉)
Department of Management and Engineering,
University of Padua, via Venezia 1, 35131 Padova, Italy
e-mail: giulio.rosati@unipd.it

D. Zanotto · S.K. Agrawal
Department of Mechanical Engineering,
Columbia University, New York, NY 10027, USA

modular, transportable and easily reconfigurable. For such applications, an interesting solution is represented by under-constrained cable-suspended parallel robots (CSPRs), that feature a suspended mobile platform connected to a overhead frame, making the workspace below the platform cable-free [4, 6].

An interesting point to address when a CDPR is specifically designed for pick and place applications regards the choice of the best cable configuration to improve the efficiency of the required task. Generally, pick and place movements consist of two main phases: the pick/release of a part and the robot transfer between two locations. During the approaching and departing phases, the system must be able to operate in proximity of obstacles, such as a worker that waits for a part. During the transfer movement, instead, the requirements are high performance (e.g., minimum movement time). When approaching an operator or an obstacle, cables should be arranged such as to avoid collisions with the environment. On the other hand, during the transfer movement, the configuration of the cables should be the one that guarantees maximum performance. Recently, researchers studied new types of CDPRs which can be reconfigured by changing the cable layout [1, 6–8, 11, 13], but none of these previous works have analyzed the possibility to reconfigure the cable anchor points on the end-effector.

In this paper, we introduce the model of a 7-DOF¹ reconfigurable CSPR for pick and place applications that has the capability of modifying the position of the cable anchor points on the end-effector using a linear actuator. The possibility of adapting the position of the cable anchor points on the end-effector is a promising solution to reduce the risk of collisions between cables and obstacles and is the major novelty of this work.

This paper is organized as follows. Section 2 introduces the kinematic and dynamic models of the CSPR with reconfigurable anchor points on the end-effector. Section 3 describes the trajectory planning for the CSPR along a path specified in the operational space and presents an optimal design of the reconfigurable end-effector which minimizes size and cost of the linear actuator. The forces and tensions required to obtain the desired movement are reported and analyzed. Finally, conclusions and future work are presented in Sect. 4.

2 Equations of Motion

2.1 Kinematic Model

Let us consider the model of a reconfigurable CSPR with 7-DOF and 8 cables as shown in Fig. 1. The end-effector consists of two rigid bodies: the main supporting structure, here defined as *Body 1*, and the translating platform, here defined as *Body 2*. The upper cables are connected to the main structure of the end-effector; the lower

¹Degrees Of Freedom.

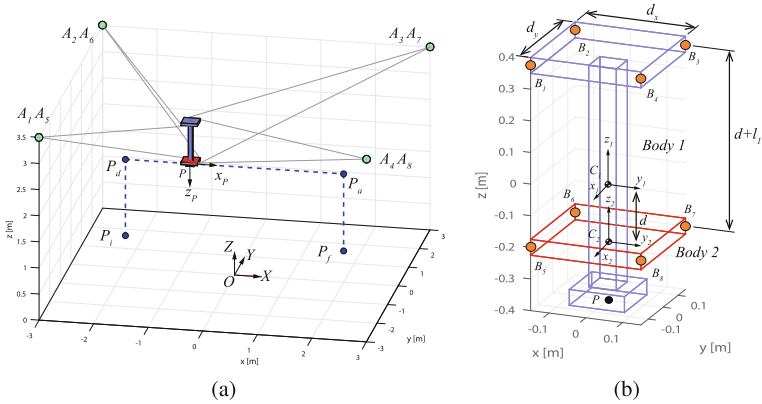


Fig. 1 **a** Layout of the CSPR. The path used for the trajectory planning is composed by three linear movements (*blue dashed line*). **b** Layout of the reconfigurable end-effector. The lower anchor points B_5, B_6, B_7, B_8 can translate along z_2

cables are connected to the translating platform, which can slide along a linear axis through a prismatic joint. As a result, the position of the lower anchor points with respect to the upper anchor points can be modified dynamically. The configuration of the cable anchor points is based on the optimal layout presented by Lamaury et al. [4]. This layout guarantees very good orientation capabilities and increases the stiffness of the robot.

Let ${}^0\mathbf{p}_1 = [x, y, z]^T$ be the position vector of the center of mass \mathbf{C}_1 of *Body 1* relative to the base frame $\{O\} = \mathbf{O} - \mathbf{XYZ}$. The orientation of the reference frame $\{C_1\} = \mathbf{C}_1 - \mathbf{x}_1\mathbf{y}_1\mathbf{z}_1$ can be expressed by means of the rotational matrix ${}^0\mathbf{R}(\alpha, \beta, \gamma)$ where α, β and γ are rotations about the fixed axes of the base frame $\{O\}$. The linear velocity of *Body 1* is ${}^0\mathbf{v}_1 = [\dot{x}, \dot{y}, \dot{z}]^T$ whereas the angular velocity is ${}^0\boldsymbol{\omega}_1 = [\dot{\alpha}, \dot{\beta}, \dot{\gamma}]^T$. Let d be the relative position of the reference frame $\{C_2\} = \mathbf{C}_2 - \mathbf{x}_2\mathbf{y}_2\mathbf{z}_2$ of *Body 2* with respect to $\{C_1\}$. Position and velocity of *Body 2* can be defined as follows:

$${}^0\mathbf{p}_2 = {}^0\mathbf{p}_1 + {}^0\mathbf{R}(\alpha, \beta, \gamma)[0, 0, d]^T \tag{1}$$

$${}^0\mathbf{v}_2 = {}^0\mathbf{v}_1 + {}^0\mathbf{R}(\alpha, \beta, \gamma)[0, 0, \dot{d}]^T + {}^0\boldsymbol{\omega}_1 \times ({}^0\mathbf{p}_2 - {}^0\mathbf{p}_1) \tag{2}$$

The configuration of the end-effector can be described by the set of independent variables $\mathbf{q} = [x, y, z, \alpha, \beta, \gamma, d]^T$. The position of the tool center point P (to be used for the trajectory planning) can be calculated as follows:

$${}^0\mathbf{p} = {}^0\mathbf{p}_1 + {}^0\mathbf{R}(\alpha, \beta, \gamma)[0, 0, -(l_1 + l_L)]^T \tag{3}$$

2.2 Dynamic Model

The dynamic model of the reconfigurable CSPR presented in the following has been developed based on [5], which was modified to account for the additional degree of freedom. The resultant wrench exerted by the four upper cables on *Body 1* is \mathbf{w}_{t1} , whereas \mathbf{w}_{t2} is the wrench exerted by the four lower cables on *Body 2*:

$$\mathbf{w}_{t1} = [\mathbf{f}_{t1}, \mathbf{n}_{t1}]^T = \mathbf{S}_1 \mathbf{t}_1 \quad \text{and} \quad \mathbf{w}_{t2} = [\mathbf{f}_{t2}, \mathbf{n}_{t2}]^T = \mathbf{S}_2 \mathbf{t}_2 \quad (4)$$

where $\mathbf{S}_1, \mathbf{S}_2 \in \mathbb{R}^{6 \times 4}$ are the structure matrices [12] relative to the center of mass of *Body 1* and *Body 2*, respectively. $\mathbf{t}_1 = [\tau_1, \tau_2, \tau_3, \tau_4]^T$ and $\mathbf{t}_2 = [\tau_5, \tau_6, \tau_7, \tau_8]^T$ are the vectors of the cable tensions applied to the bodies. Since the end-effector is suspended, the component of the force exerted by the cables on the translating platform along the upward direction must be non negative. To counteract the force applied by the cables on *Body 2*, a spring is inserted between *Body 1* and *Body 2*. *Body 1* and *Body 2* can be modeled as two rigid bodies having mass matrices $\mathbf{M}_1 = m_1 \mathbf{I}_3$ and $\mathbf{M}_2 = m_2 \mathbf{I}_3$ and inertia tensors ${}^{C_1} \mathbf{I}_1$ and ${}^{C_2} \mathbf{I}_2$ written in the reference frames $\{C_1\}$ and $\{C_2\}$. The payload is considered as a part of *Body 1*.

Using Newton-Euler approach, the general form of the equations of motion for the reconfigurable CSPR can be obtained in Cartesian space [9]. The force-balance and moment-balance equations can be expressed as follows:

$$\begin{cases} \mathbf{M}_1 {}^O \dot{\mathbf{v}}_1 = {}^O \mathbf{f}_{t1} + {}^O \mathbf{f}_{g1} - {}^O \mathbf{f}_2 - {}^O \mathbf{f}_k \\ {}^O \mathbf{I}_1 {}^O \dot{\boldsymbol{\omega}}_1 + {}^O \boldsymbol{\omega}_1 \times {}^O \mathbf{I}_1 {}^O \boldsymbol{\omega}_1 = {}^O \mathbf{n}_{t1} - {}^O \mathbf{n}_2 - ({}^O \mathbf{p}_2 - {}^O \mathbf{p}_1) \times {}^O \mathbf{f}_2 \end{cases} \quad (5)$$

and

$$\begin{cases} \mathbf{M}_2 {}^O \dot{\mathbf{v}}_2 = {}^O \mathbf{f}_2 + {}^O \mathbf{f}_k + {}^O \mathbf{f}_{t2} + {}^O \mathbf{f}_{g2} \\ {}^O \mathbf{I}_2 {}^O \dot{\boldsymbol{\omega}}_2 + {}^O \boldsymbol{\omega}_2 \times {}^O \mathbf{I}_2 {}^O \boldsymbol{\omega}_2 = {}^O \mathbf{n}_2 + {}^O \mathbf{n}_{t2} \end{cases} \quad (6)$$

where the inertia tensors with respect to the base frame are ${}^O \mathbf{I}_1 = {}_{C_1}^O \mathbf{R} {}^{C_1} \mathbf{I}_1 {}_{C_1}^O \mathbf{R}^T$ and ${}^O \mathbf{I}_2 = {}_{C_2}^O \mathbf{R} {}^{C_2} \mathbf{I}_2 {}_{C_2}^O \mathbf{R}^T$. The gravity forces are \mathbf{f}_{g1} and \mathbf{f}_{g2} whereas \mathbf{f}_k is the force exerted by the spring along \mathbf{z}_2 . The magnitude of \mathbf{f}_k can be modeled by the linear law $f_k = k \cdot (d_0 + d)$ where d_0 is the free length of the spring and k is the spring constant. \mathbf{f}_2 and \mathbf{n}_2 represent the force and moment that *Body 1* exerts on *Body 2*, respectively. Combining the equations above, we obtain:

$$\begin{cases} \mathbf{M}_1 {}^O \dot{\mathbf{v}}_1 + \mathbf{M}_2 {}^O \dot{\mathbf{v}}_2 = {}^O \mathbf{f}_{t1} + {}^O \mathbf{f}_{t2} + {}^O \mathbf{f}_{g1} + {}^O \mathbf{f}_{g2} \\ {}^O \mathbf{I}_1 {}^O \dot{\boldsymbol{\omega}}_1 + {}^O \boldsymbol{\omega}_1 \times {}^O \mathbf{I}_1 {}^O \boldsymbol{\omega}_1 + {}^O \mathbf{I}_2 {}^O \dot{\boldsymbol{\omega}}_2 + {}^O \boldsymbol{\omega}_2 \times {}^O \mathbf{I}_2 {}^O \boldsymbol{\omega}_2 = \\ = {}^O \mathbf{n}_{t1} + {}^O \mathbf{n}_{t2} - ({}^O \mathbf{p}_2 - {}^O \mathbf{p}_1) \times [\mathbf{M}_2 {}^O \dot{\mathbf{v}}_2 - {}^O \mathbf{f}_{t2} - {}^O \mathbf{f}_{g2} - {}^O \mathbf{f}_k] \end{cases} \quad (7)$$

The force required by the linear actuator is found by taking the component of the force applied by *Body 1* on *Body 2* along \mathbf{z}_2 :

$$f_d = {}^0\mathbf{f}_2 \cdot {}^0\mathbf{z}_2 = [\mathbf{M}_2 {}^0\dot{\mathbf{v}}_2 - {}^0\mathbf{f}_{t2} - {}^0\mathbf{f}_{g2} - {}^0\mathbf{f}_k] \cdot {}^0\mathbf{z}_2 \tag{8}$$

3 Optimal Design of the Reconfigurable End-Effector of CSPR for Pick and Place Applications

Pick and place operations are very common in many industrial applications and CSPRs can be a valid alternative to conventional crane systems [6]. Let P_i and P_f be the pick and the release point expressed in the base frame, respectively. Since the CSPR must avoid obstacles, the best option is to plan the path of the tool center point in the operational space. To simplify the pick and place operation, we consider three movements, each represented by a linear segment: vertical depart, transfer movement and vertical approach. We combine the ability to avoid obstacles during the approach/depart movements with the ability to exert high wrenches during the transfer motion by dynamically reshaping the configuration of the lower anchors points as shown in Fig. 1a. Once the task has been defined in terms of planned trajectory, we can optimize the design of the reconfigurable end-effector.

The optimal design aims at minimizing the size of the linear actuator required to dynamically reconfigure the lower anchor points of the end-effector. Using the planned trajectory as input for the inverse dynamics, we calculate the cable tensions and the force required by the linear actuator f_d . We identify three design variables that affect the linear force f_d : the mass distribution (expressed as the ratio $r_m = m_2/(m_1 + m_2)$), the spring constant (k) and the free length of the spring (d_0). The optimization problem consists in finding the optimal set of design variables $x = [r_m, k, d_0]^T$ that minimizes the following objective function during the pick and place movement:

$$\phi = \sqrt[2]{\frac{1}{T} \int_0^T [f_d(t)]^2 dt} \quad \text{subject to} \quad \begin{cases} 0 < r_m < 1 \\ k \geq 0 \\ d_0 \geq 0 \end{cases} \tag{9}$$

where the sum of the masses m_1 and m_2 is fixed and T is the total time of the movement.

The layout of the reconfigurable CSPR is shown in Fig. 1a, b. Table 1 reports the position of the cable exit points (A_i) and the cable anchor points (B_i). The parameters describing initial and final positions of the tool center point as well as the orientation of *Body 1* (assumed constant along the path) are listed in Table 1. The trajectory profiles of *Body 1* and *Body 2* are obtained with three linear movements in the operational space where position is planned with a fifth-order polynomial time law. The total time of the movement is: $T = T_{dep} + T_{trans} + T_{app}$. This trajectory ensures con-

Table 1 (a) Cable exit points A_i and cable anchor points B_i . (b) Kinematic and inertial parameters of the reconfigurable end-effector. (c) Trajectory parameters for the movement task

(a)		
Parameter	Value (m)	
${}^oA_1, {}^oA_5$	(-3, -3, 3.5)	
${}^oA_2, {}^oA_6$	(3, -3, 3.5)	
${}^oA_3, {}^oA_7$	(3, 3, 3.5)	
${}^oA_4, {}^oA_8$	(-3, 3, 3.5)	
${}^{c_1}B_1$	$(d_x, -d_y, L_1)$	
${}^{c_1}B_2$	(d_x, d_y, L_1)	
${}^{c_1}B_3$	$(-d_x, d_y, L_1)$	
${}^{c_1}B_4$	$(-d_x, -d_y, L_1)$	
${}^{c_1}B_5$	$(-d_x, d_y, d)$	
${}^{c_1}B_6$	$(-d_x, -d_y, d)$	
${}^{c_1}B_7$	$(d_x, -d_y, d)$	
${}^{c_1}B_8$	(d_x, d_y, d)	
(b)		
Parameter	Value	Unit
$m_1 + m_2$	7	kg
$I_{1_{xx}}, I_{1_{yy}}$	$m_1[0.050, 0.050]$	kg m ²
$I_{1_{zz}}$	$m_1[0.007]$	kg m ²
$I_{1_{xy}}, I_{1_{xz}}, I_{1_{yz}}$	0	kg m ²
$I_{2_{xx}}, I_{2_{yy}}$	$m_2[0.003, 0.003]$	kg m ²
$I_{2_{zz}}$	$m_2[0.007]$	kg m ²
$I_{2_{xy}}, I_{2_{xz}}, I_{2_{yz}}$	0	kg m ²
d_x	0.2	m
d_y	0.2	m
l_1	0.4	m
l_L	0.05	m
(c)		
Parameter	Value	Unit
${}^oP_{in}$	(-2, 0, 0.6)	m
oP_d	(-2, 0, 2.1)	m
oP_a	(2, 0, 2.1)	m
${}^oP_{fin}$	(2, 0, 0.6)	m
α	0	deg
β	0	deg
γ	0	deg
T_{dep}	1.0	s
T_{trans}	1.0	s
T_{app}	1.0	s

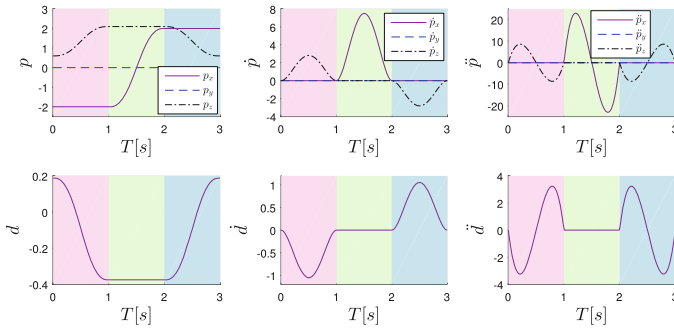


Fig. 2 Trajectory profiles of *Body 1* and *Body 2* in terms of position of the tool center point \mathbf{p} and relative position d . The three parts of the movement are highlighted

tinuity and assigned initial and final position, velocities and accelerations. Position, velocity and acceleration are shown in Fig. 2.

The optimization problem was solved by using the Global Search Algorithm proposed by Ugray et al. [10]. The optimal set of design variables that minimizes the objective function ϕ is $x_{opt} = [0.584, 0.0024 \text{ N/m}, 99.8 \text{ m}]^T$. The value of the objective function for the optimal design is $\phi = 3.205 \text{ N}$.

To compare the effect of the design variables on the objective function, we define two sub-optimal designs:

- *Design 1*: $r_m = 0.171, k = 0 \text{ N/m}, d_0 = 0 \text{ m}$;
- *Design 2*: $r_m = 0.171, k = 30 \text{ N/m}, d_0 = 1.15 \text{ m}$.

Design 1 represents a sample design with a low value of r_m and null values of k and d_0 . With respect to *Design 1*, *Design 2* is obtained with the same value of r_m and optimized values of k and d_0 . The root mean square (RMS) of the linear actuator force f_d obtained with the optimal design is 91.6% lower than *Design 1* and 76.2% lower than *Design 2*. Figure 3a represents the cable tensions corresponding

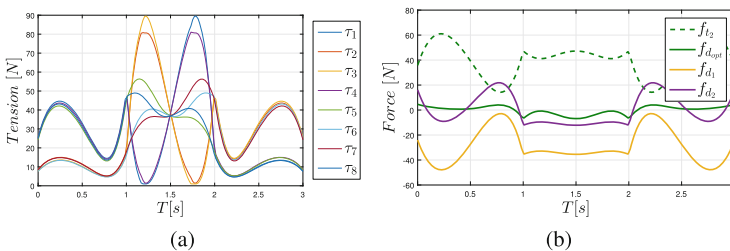


Fig. 3 **a** Cable tensions for the planned trajectory. **b** Linear actuator force for the planned trajectory. *Green solid line* represents the force f_d for the optimal layout. *Yellow and purple lines* represent the force f_d for *Design 1* and *Design 2*, respectively. *Green dashed lines* is the force exerted by the cables to *Body 2* for the optimal layout

the planned movements for the optimal design. The results show a non-negative and continuous tension distribution along the whole trajectory. Figure 3b illustrates the linear actuator force (Eq. 8). Since the end-effector is suspended, the upward component of the force exerted by the cables on *Body 2* must be non negative. Furthermore, the value of \mathbf{f}_{12} must satisfy Eq. 7. On the other hand, the force of gravity (f_{g2}) and the spring force (f_k) can be optimized to counteract the force exerted by the lower cables $\mathbf{f}_{12}^T \cdot \mathbf{z}_2$ (green dashed line in Fig. 3b) and minimize the force of the linear actuator (f_d). These observations explain the high values of r_m and d_0 obtained with the optimization. High values of r_m reduce the amplitude of the linear actuator force and shift the curve towards a null average value as shown by the green line in Fig. 3b. For a fixed value of r_m , the spring allows to reduce the RMS of the force f_d as shown by the yellow and purple lines in Fig. 3b. Furthermore, the higher r_m , the higher the maximum tension exerted by the cables during the movement. For example, the maximum cable tension with the optimal design is 20.2% greater than the maximum cable tension calculated for *Design 1* and *Design 2*. The final solution will be a trade-off between the RMS of the linear actuator force and the maximum cable tensions.

4 Discussion

The motivation behind this work was to present a novel subclass of Cable-Driven parallel Robots featuring a reconfigurable end-effector. This design shows promise in pick and place applications. We considered a system with 7-DOFs and 8 cables which has the capability of modifying the position of the cable anchor points on the end-effector using a linear actuator. The possibility of dynamically adapting the position of the anchor points during a pick and place movement is a promising way to avoid collisions with obstacles and increase the performance of the system. The model of the reconfigurable end-effector consists of a main structure and a translating platform which can slide along a linear axis. A simple pick and place task composed of three linear movements was defined and the design of the end-effector was optimized to minimize the linear actuator force. Among the design variables that affect the linear actuator force, mass distribution was found to be the most significant one. Future works will extend the current optimization framework by considering arbitrary paths where the orientation of the end-effector can be fixed or varying. The pose of the reconfigurable end-effector can affect the kinematic and dynamic behavior of the system influencing the cable tensions and the linear actuator force. Different strategies for trajectory planning and cable tension distribution will also be analyzed and tested.

Acknowledgments This work was supported by the Italian Ministry of University and Research (MIUR), call PRIN 2012, grant no. 20124SMZ88.

References

1. Gagliardini L, Caro S, Gouttefarde M, Girin A (2015) A reconfiguration strategy for reconfigurable cable-driven parallel robots. In: 2015 IEEE international conference on robotics and automation (ICRA), pp 1613–1620
2. Gosselin C (2014) Cable-driven parallel mechanisms: state of the art and perspectives. *Mech Eng Rev* 1(1):1–17
3. Izard J-B, Gouttefarde M, Michelin M, Tempier O, Baradat C (2013) A reconfigurable robot for cable-driven parallel robotic research and industrial scenario proofing. In: *Cable-driven parallel robots*, pp 135–148. Springer
4. Lamaury J, Gouttefarde M, Michelin M, Tempier O (2012) Design and control of a redundant suspended cable-driven parallel robots. In: *Latest advances in robot kinematics*, pp 237–244. Springer
5. Mustafa SK, Lim WB, Yang G, Yeo SH, Lin W, Agrawal SK (2015) Cable-driven robots. *Handbook of manufacturing engineering and technology*
6. Nguyen DQ, Gouttefarde M, Company O, Pierrot F (2014) On the analysis of large-dimension reconfigurable suspended cable-driven parallel robots. In *Robotics and Automation (ICRA), 2014 IEEE International Conference on*, pages 5728–5735
7. Rosati G, Zanutto D (2009) A novel perspective in the design of cable-driven systems. In: *ASME international mechanical engineering congress and exposition, Proceedings*, vol 12, pp 617–625
8. Rosati G, Zanutto D, Agrawal S (2011) On the design of adaptive cable-driven systems. *J Mech Robot* 3(2). cited By 22
9. Sciavicco L, Siciliano B (2012) *Modelling and control of robot manipulators*. Springer Science & Business Media
10. Ugray Z, Lasdon L, Plummer J, Glover F, Kelly J, Martí R (2007) Scatter search and local nlp solvers: a multistart framework for global optimization. *INFORMS J Comput* 19(3):328–340
11. Zanutto D, Rosati G, Minto S, Rossi A (2014) Sophia-3: a semiadaptive cable-driven rehabilitation device with a tilting working plane. *IEEE Trans Robot* 30(4):974–979
12. Zarebidoki M, Lotfavar A, Fahham H (2011) Dynamic modeling and adaptive control of a cable-suspended robot. In: *Proceedings of the world congress on engineering*, vol 3
13. Zhou X, Jun S-K, Krovi V (2014) Tension distribution shaping via reconfigurable attachment in planar mobile cable robots. *Robotica* 32(02):245–256

Kinematic Optimization of a 2DoF PRRRP Manipulator

Simone Cinquemani, Hermes Giberti and Giovanni Legnani

Abstract Parallel Kinematic Machines (PKM) are interesting in industrial field because of their ability to ensure high dynamic performance, stiffness, accuracy and precision. One of the options in the design of a manipulator is the opportunity to ensure isotropy performance within the workspace. Generally each PKM has a limited number of isotropy configurations. This paper shows that some 2 DoF PKMs may be designed to have an infinite numbers of kinematic configurations that constitute one or more continuous loci. These machines have the possibility to work at (or near) their ideal kinematic conditions in a large part of their working area. The paper presents a methodology to graphically identify the points of isotropy of a planar manipulator and defines the geometrical conditions to maximize their number.

1 Introduction

Parallel Kinematic Machines attract researchers and companies, as they are claimed to offer several advantages over their serial counterparts, like high structural rigidity and high dynamic performance. Indeed, the parallel kinematic arrangement of the links provides higher stiffness and lower moving masses, thus reducing inertia effects. PKM have better dynamic performance, however, most of them have a complex geometrical workspace shape and highly non linear input/output relations.

S. Cinquemani

Politecnico di Milano, Dipartimento di Meccanica, via La Masa 1, Milan, Italy
e-mail: simone.cinquemani@polimi.it

H. Giberti

Dipartimento di Ingegneria Industriale e dell'Informazione,
Università degli Studi di Pavia, Via A. Ferrata 5, 27100 Pavia, Italy
e-mail: hermes.giberti@unipv.it

G. Legnani (✉)

Dipartimento di Ingegneria Meccanica e Industriale,
Università degli Studi di Brescia, Via Branze 38, Brescia, Italy
e-mail: giovanni.legnani@unibs.it

The five-bar mechanism is the simplest and the most used 2-DoF parallel kinematic manipulator: it is generally used in “pick and place” operations or to place a point on a plane. Despite its simplicity, the design and the kinematic optimization of a manipulator of this type is a complex operation [3, 8–11, 15] and it is still a topic of great interest in industrial and academic field.

Two degrees of freedom parallel kinematic manipulators are widely studied in industrial and academic field especially regarding their workspace dimensions and shape. On the other side, the kinematic performances of a robot are evaluated both in terms of singularity and isotropy. The first is deeply analyzed in [2, 9, 16] following numerical and geometrical approaches. Isotropic properties of a 2-DoF PKM are investigated by [17], with particular interest on the so called isotropy continuum [12] (i.e. a locus of end-effector positions where isotropy can be achieved continuously).

This paper deepens the kinematic optimization of a 2-DoF PRRRP PKM in terms of isotropy performance. It presents an innovative graphical approach to highlight isotropic behavior and to optimize the robot configuration in order to reach the maximum number of points of isotropy achievable continuously. The simplicity of this approach allows an immediate understanding of the behavior of a planar manipulator and allows to have clear indications on its layout to optimize the isotropic properties. The approach is proposed for planar manipulators, but it could be extended to robots with a higher number of degrees of freedom. However, such an extension would require a considerable increase of the complexity, thus losing the distinguishing feature that is the simplicity.

After an introduction on the concept of isotropy and ellipses of manipulability, the paper investigates an interesting configuration of a 2-DoF PKM and demonstrates how it can be optimized to reach continuum isotropy loci. Achieving this goal ensures the efforts related to the design of a manipulator are paid in terms of ability to work, as much as possible, with ideal kinematic conditions.

2 Isotropy

Isotropy is defined as the ability of a robot to have identical kinetostatic properties along each direction [6, 7, 14]. This behavior can be analyzed through some indexes related to the Jacobian matrix.

A common definition of isotropy is based on the conditioning number of the jacobian matrix [4, 5] that is the ratio between the maximum and the minimum singular values

$$\frac{\sigma_{max}}{\sigma_{min}} = \sqrt{\frac{\lambda_{max}}{\lambda_{min}}} = \text{cond}(J) \quad (1)$$

where λ_i are the eigenvalues of the matrix $J^T J$.

The i th singular value $\sigma_i(J)$ of the jacobian matrix can be interpreted as Velocity Amplification Factors (VAF) between the actuated joints velocities and the end effector ones

$$\sigma_i(J) = \sqrt{\lambda_i(J^T J)} \text{ with } \lambda_i \geq 0 \quad (2)$$

When it is verified $\text{cond}(J) = 1$, the minimum and the maximum eigenvalues coincide and all the VAF are equal. In this case the manipulator is defined as isotropic. It worth to note that isotropy is not related to the absolute values of the VAFs, but only to their ratio.

Likewise, isotropy can also be expressed as [4, 5, 13, 14]:

$$J^T J = kI \quad (3)$$

where k is a scalar and I is the identity matrix. A graphical representation of these conditions can be obtained through the ellipses of manipulability. The lengths of the principal axes of the ellipse, which correspond to the inverse of minimum and maximum eigenvalues of $J^T J$, represent the minimum and maximum velocity amplification factor (VAFs), while eigenvectors of $J^T J$ represent the direction of the principal axes of the ellipse. No matter the dimensions of the ellipses, isotropy is achieved when ellipses become circles (i.e. all the VAFs are equal, regardless their absolute values).

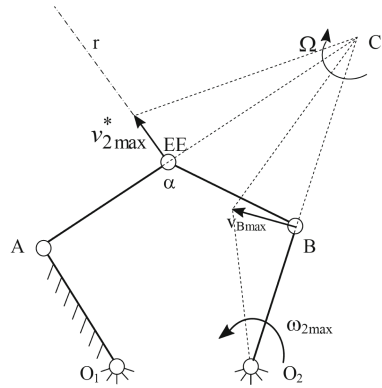
3 Graphical Evaluation of Isotropy for a 2 DoF Manipulator

The conditions of isotropy for a manipulator can be graphically identified, considering the relative kinematic of the links. As the ellipses of manipulability in velocity approximate the speed achievable by the end effector along different directions, to get them one can impose the end effector (EE) to move along a given direction at its maximum speed by pushing up the motors. The contribution of each motor depends on the direction to follow. Consider the manipulator depicted in Fig. 1. Suppose, for example, one wants to move the end-effector along the direction r orthogonal to the link $A - EE$. To achieve the maximum speed ($v_{2,max}^*$) in this direction the system is required to hold the motor 1, while moving the motor 2 at its maximum speed ($\omega_{2,max}$). Knowing the pose of the robot one gets:

$$\underline{v}_{B,max} = \underline{\omega}_{2,max} \times \underline{O_2B} \quad (4)$$

$$\underline{v}_{B,max} = \underline{\Omega} \times \underline{CB} \quad (5)$$

Fig. 1 Maximum velocity along direction r



where C is the instant center of rotation of the link $B - EE$ and $\underline{\Omega}$ its absolute angular speed, whose modulus is:

$$|\underline{\Omega}| = \left| \omega_{2,max} \frac{O_2B}{CB} \right| \tag{6}$$

Finally the maximum speed along direction r is:

$$v_{2,max}^* = \underline{\Omega} \times \underline{EEC} \tag{7}$$

Similar considerations can be done if one wants to reach the maximum speed along a direction orthogonal to $B - EE$. To move the end effector along different directions, both the two motors have to contribute to the motion.

By repeating this for all directions, the locus of points is represented by a polygon. For convenience of representation, it is usual to approximate these polygons respectively with ellipses, or with circles (Fig. 2). Ellipses are inscribed into the polygon and tangent to it in the middle point of each side.

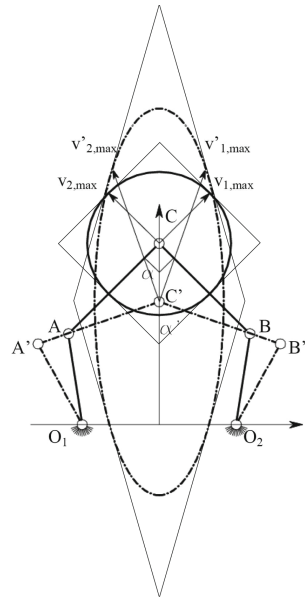
Obviously, depending on the configuration of the robot, the ellipse of manipulability in velocity has different shapes and sizes. When the manipulator is in an isotropic configuration the polygon is a square and the corresponding ellipse degenerates into a circle (Fig. 2). It worth to note that isotropy is not related to the dimension of the circle, but only to its shape. For this reason, it may happen that in two different isotropic poses, the EE of the manipulator may have different speeds, while for each configuration they are constant along all the directions.

Looking at Fig. 2, the considered manipulator is in an isotropic configuration if, and only if:

$$|v_{1,max}^*| = |v_{2,max}^*| \tag{8}$$

$$\alpha = 90^\circ \tag{9}$$

Fig. 2 Ellipses of manipulability in velocity in isotropic and non-isotropic configurations



These simple geometrical considerations can be extremely useful to evaluate the behavior of the manipulator inside its workspace [6]. Once the condition expressed in Eq. (9) is verified, the triangle $A - EE - B$ is defined. Its position and orientation to reach isotropy can be determined knowing the features of the actuators and the geometrical dimensions of the links in order to verify Eq. (8).

4 Kinematic Optimization of a 2 DoF PRRRP Manipulator

A very common 2 DoF PKM is the one represented in Fig. 3. The robot has 2 prismatic joints on the ground, and 3 revolute ones (PRRRP). Each prismatic joint is driven by an actuator characterized by a maximum achievable speed and maximum force. In its generic configuration, the two sliders may have a relative angle.

To guarantee isotropy it has to be $|v_{1,max}^*| = |v_{2,max}^*|$ when the two links connected to the end effector are orthogonal. For this robot it has been demonstrated [1] that this two condition can be verified if the two sliders are parallel and their distance is

Fig. 3 Layout of a 2DoF PKM (PRRRP)

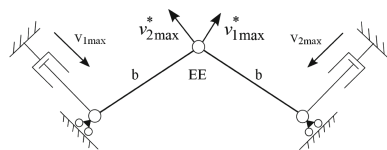
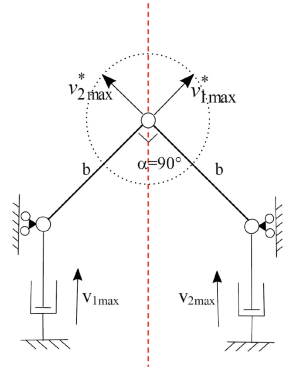


Fig. 4 Continuum isotropy locus



equal to $\sqrt{2} \cdot b$ (Fig. 4). The locus of continuum isotropy is a line, whose direction is parallel to the directions of the actuators, at the same distance from those. This configuration is interesting as it is the only one providing the maximum VAFs constant along the continuum isotropy locus. That means we can have the best performance of the machine along each direction for all the poses of the EE on that line.

Despite this is the only configuration ensuring maximum constant VAFs along a continuous set of positions, it is interesting to evaluate the performance of the manipulator according to the general definition expressed in Eqs. (8) and (9).

Let's consider a generic pose of the manipulator and impose $\alpha = 90^\circ$ as shown in Fig. 5.

According to Fig. 5 the position of the EE can be obtained as:

$$\underline{EE} = \begin{bmatrix} x \\ y \end{bmatrix} = \begin{bmatrix} r + a \cos \phi - b \sin \phi \\ a \sin \phi + b \cos \phi \end{bmatrix} \tag{10}$$

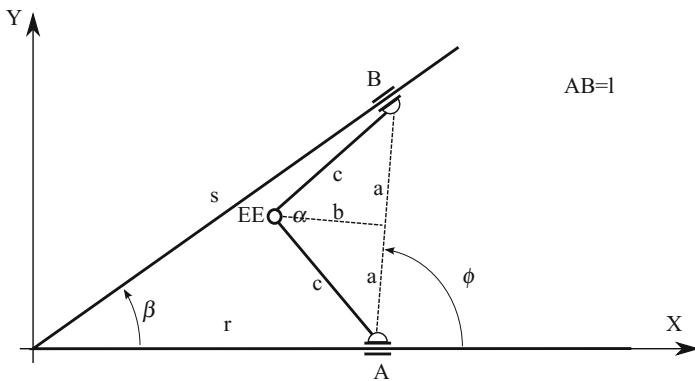


Fig. 5 Layout of a 2DoF PKM (PRRRP)

where r and s can be obtained from trigonometric relationships as:

$$\begin{cases} s \sin \beta = l \sin \phi \\ s \cos \alpha = r + l \cos \phi \end{cases} \quad (11)$$

Equation 10 becomes

$$\begin{bmatrix} x \\ y \end{bmatrix} = \begin{bmatrix} \frac{l}{\tan \beta} - b & a - l \\ a & b \end{bmatrix} \begin{bmatrix} \sin \phi \\ \cos \phi \end{bmatrix} = [A] \underline{\Phi} \quad (12)$$

As it has to be $\underline{\Phi}^T \underline{\Phi} = 1$ one gets

$$\begin{bmatrix} x & y \end{bmatrix} [A]^{-T} [A]^{-1} \begin{bmatrix} x \\ y \end{bmatrix}^T = 1 \quad (13)$$

By imposing $\alpha = 90^\circ$, we may substitute $a = b = l/2$. Equation (13) becomes:

$$x^2 + \left(2 - \frac{1}{\tan \beta}\right) xy + \frac{1}{2} y^2 - \frac{l^2}{2 \tan \beta} = 0 \quad (14)$$

that is the equation of a conic. This trajectory is an ellipse except for $\beta = 90^\circ$ where it degenerates in a line. As a matter of fact, the third invariant of the cubic results:

$$I_3 = \frac{l^2}{\tan \beta} \left(\frac{1}{4} - \frac{1}{2 \tan \beta} + \frac{1}{8 \tan \beta} \right) \quad (15)$$

that is equal to zero for $\beta = 90^\circ$.

Once the set of poses, where the condition in Eq. (9) is verified, is known, it is necessary to verify if the size of the manipulability ellipses (circles in this case) are the same for all the poses or if they change. If the circles are all of the same size (as in Fig. 4) the performances of the manipulator in terms of maximum velocity does not change on the different point of the locus. Opposite in the case of Fig. 6b, the locus of isotropy is a segment (dashed in the figure) but the maximum velocity performances depend on the position.

According to Fig. 6a it can be noted that, whatever is the angle between the sliders, the speed of the end effector is constant along different directions if, and only if, it is:

$$v_{1,max}^* = v_{2,max}^* \quad \Leftrightarrow \quad \cos \phi_1 = \cos \phi_2 \quad (16)$$

It can be easily observed that, if the two sliders have a generic angle $\beta \neq 90^\circ$ this condition can be obtained only for a limited number of poses. On the contrary, for orthogonal sliders, it can be demonstrated that condition in Eq. (16) stands for all the poses (Fig. 6b) thus reaching a continuum isotropy locus. The condition stands even if manipulators have arms with different lengths. Obviously, for each configuration,

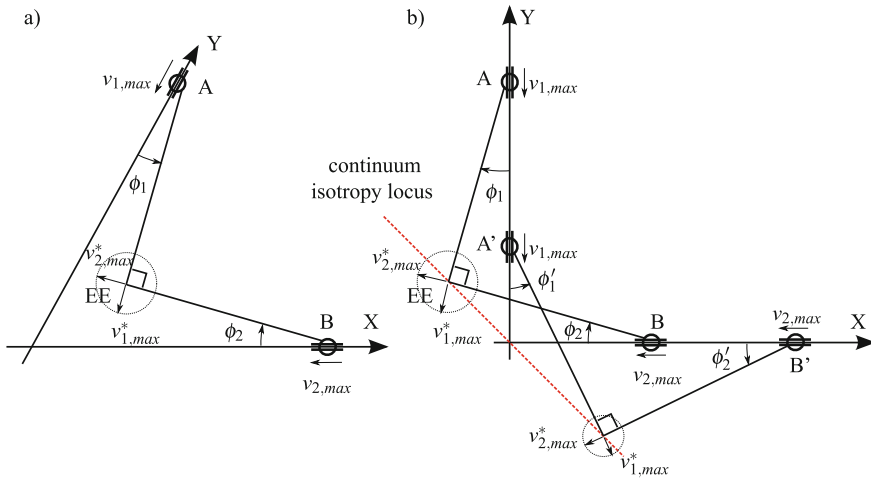


Fig. 6 Graphical representation of the condition in Eq. (16)

the VAFs are mutually identical, but different from their maximum values. That means the manipulator has an isotropic behaviour, even if it can not reach its maximum performance.

5 Conclusions

Isotropy is one of the most interesting properties of a manipulator, since it defines its ability of reaching the same performance along each direction. An innovative approach based on the instant center has been introduced to identify the geometrical conditions to achieve isotropy. The kinematic optimization of a manipulator in terms of isotropy has been introduced through a graphical representation, identifying the configurations of the robot that allows reaching the maximum number of point of isotropy continuously. The approach has been applied to a PRRRP manipulator, finding promising configurations where the robot can work close to its ideal kinematic conditions.

References

1. Cinquemani S, Giberti H, Legnani G (2012) Continuum isotropy loci of a 2-dof parallel kinematic manipulator. In: Proceedings of the 11th biennial conference on engineering systems design and analysis, Paper No. ESDA2012-82514, pp. 283–291
2. Di Gregorio R (2009) A novel method for the singularity analysis of planar mechanisms with more than one degree of freedom. *Mech Mach Theory* 44:83102

3. Gosselin CM, Angeles J (1989) The optimum kinematic design of a spherical three degree-of-freedom parallel manipulator. *ASME J Mech Transm Autom Des* 111:202207
4. Gosselin C (1990) Stiffness mapping for parallel manipulator. *IEEE Trans Robot Autom* 6–3:377–382
5. Gosselin C, Angeles J (1990) Singularity analysis of closed loop kinematic chains. *ASME J Mech Des* 112–3:331–336
6. Legnani G, Tosi D, Fassi I, Giberti H, Cinquemani S (2010) The point of isotropy and other properties of serial and parallel manipulators. *Mech Mach Theory* 45(10):1407–1423
7. Legnani G, Tosi D, Fassi I, Giberti H, Cinquemani S (2012) A new isotropic and decoupled 6-dof parallel manipulator. *Mech Mach Theory* 58:64–81
8. Liu XJ, Wang J, Zheng HJ (2006) Performance atlases and optimum design of planar 5R symmetrical parallel mechanisms. *Mech Mach Theory* 41:119144
9. Liu XJ, Wang J, Zheng HJ (2006) Optimum design of the 5R symmetrical parallel manipulator with a surrounded and good-condition workspace. *Robot Auton Syst* 54:221233
10. Liu XJ, Wang J, Pritschow G (2006) On the optimal kinematic design of the PRRRP 2-DoF parallel mechanism. *Mech Mach Theory* 41:11111130
11. Liu XJ, Wang J (2007) A new methodology for optimal kinematic design of parallel mechanisms. *Mech Mach Theory* 42:12101224
12. Majou F, Wenger P, Chablat D (2002) A novel method for the design of 2-dof parallel mechanisms for machining applications. In: 8th international symposium on advances in robot kinematics, pp 1–11
13. Merlet JP (2000) *Parallel robots*. Kluwer Academic Publishers, The Netherlands
14. Merlet JP (2006) Jacobian, manipulability, condition number and accuracy of parallel robots. *J Mech Des* 28:199–206
15. Ottaviano E, Ceccarelli M (2002) Optimal design of CaPaMan (Cassino Parallel Manipulator) with a specified orientation workspace. *Robotica* 20:159166
16. Park FC, Kim JW (1999) Singularity analysis of closed kinematic chains. *J Mech Des* 121:3238
17. Tsai KY, Lin PY, Lee TK (2008) 4R spatial and 5R parallel manipulators that can reach maximum number of isotropic positions. *Mech Mach Theory* 43:6879

Optimized Trajectory Planning of Pick and Place Operations to Be Performed by Cable-Driven Parallel Robots

Luca Barbazza, Fabio Oscari, Simone Minto and Giulio Rosati

Abstract Cable driven parallel robots (CDPRs) have large workspace and versatile layouts which make them an interesting solution for high speed manipulation tasks. On the other hand, the available wrench set varies widely among the workspace, thus hardly affecting the performance of the system. For this reason, trajectory planning is a crucial aspect in CDPRs, and motion performance can be optimized only by considering the variability of wrench all along the path. In this paper, an optimized trajectory planning algorithm for CDPRs is proposed, which implements a pick and place task in the operational space. The algorithm, based on the calculation of the effective wrench capabilities of the robot in a set of control points along the path, allows to find the trajectory with the optimal trade-off between movement time and smoothness. The algorithm was tested in the case of an under-constrained suspended CDPR with 3-DOF and 4 cables conceived for pick and place applications. Results show that the optimal trajectory allows the CDPR to achieve values of acceleration and velocity near to the maximum allowable values defined by the polytopes of the CDPR.

1 Introduction and Literature Review

Cable-Driven Parallel Robots represent a particular class of parallel robots whose links are cables. Compared to rigid serial and parallel robots, they have several advantages such as large workspaces, high payloads per unit of weight, ease of construction, flexible layouts and reconfigurability, affordable costs [7, 11]. Therefore, applications that require a combination of such features are good candidates for the use of CDPRs [1, 9, 12, 13, 17]. Thanks specifically to their advantages in terms of large workspaces, versatility and high payloads per unit of weight, CDPRs are particularly indicated for high speed manipulation tasks [8, 18], such as pick and place applications. Since the performance of CDPRs for pick and place applications

L. Barbazza · F. Oscari · S. Minto · G. Rosati (✉)
Department of Management and Engineering, University of Padua,
via Venezia 1, 35131 Padova, Italy
e-mail: giulio.rosati@unipd.it

are strongly related to the cable configuration [2, 14], the possibility of evaluating and maximizing the performance of different layouts is fundamental. The possibility of computing the available set of wrenches for a CDPR [15] can be a valid way to generate optimal trajectory planning. To this end, we were inspired by Gasparetto and Zanotto [5, 6] and Fahham et al. [3]. The first proposed an algorithm for the optimal trajectory planning of robotic manipulators based on the minimization of an objective function that takes into account the execution time and the integral of the squared jerk along the whole trajectory. The latter presented an algorithm to study the optimal trajectory tracking of redundant planar cable-suspended robot considering the limits in terms of cable tensions and cable velocities. The algorithm is based on the Pontryagin principle which states that at any point of a time optimal trajectory, at least one of the actuators exerts maximum or minimum input (bang-bang control).

In this paper, we introduce a trajectory planning algorithm to optimize the performance of CDPRs in pick and place operations. The movement is planned in the operational space, considering acceleration and velocity constraints.

The paper is organized as follows. Section 2 presents the manipulability of a generic CDPR. Section 3 describes the optimal trajectory planning algorithm. In Sect. 4 the method is applied to a three-DOF under-constrained suspended CDPR, comparing two different trajectories. Finally, conclusions and future works are presented in Sect. 5.

2 Manipulability of CDPRs

Let us consider the model of a generic CDPR with n degrees of freedom (DOFs) and N cables. A main issue when designing a cable-based system is to determine appropriate indices able to characterize its performance. Manipulability is a widely adopted index as a measure of the performance of a robotic system in the force domain, usually described by means of an ellipsoid or polytopes [4, 15, 16].

Let $\mathbf{W} \in \mathbb{R}^n$ be the resultant of all forces and moments acting on the end-effector. The resultant wrench \mathbf{W} can be expressed as the sum of two contributions: the wrench exerted by the cables \mathbf{W}_{tens} and the external wrench applied to the end-effector \mathbf{W}_{ext} :

$$\mathbf{W} = \mathbf{W}_{\text{tens}} + \mathbf{W}_{\text{ext}} = \mathbf{S} \mathbf{T} + \mathbf{W}_{\text{ext}} \quad (1)$$

where $\mathbf{T} = [T_1, \dots, T_N]^T$ is the cable tension vector and $\mathbf{S} \in \mathbb{R}^{n \times N}$ is the structure matrix [7]. Due to motor torque capabilities, each component T_i of vector \mathbf{T} is constrained by an upper bound T_{max_i} , so that a limited set of vectors \mathbf{W}_{tens} can be obtained at the end-effector that, in turn, means a limited \mathbf{W} . As a result, an actual system is not able to exert all the possible combinations of forces and moments. To account for gravity, its contribution can be included in the term containing the external wrenches \mathbf{W}_{ext} .

Given the maximum tension of the cables that the actuators can generate, it is possible to obtain the set of generalized forces that the system can exert to the

end-effector. To achieve this, the N-dimensional hypercube representing the set of available tensions must be transformed, via the linear transformation \mathbf{S} , to the n-dimensional convex polytope characterizing the set of available wrenches [4, 15]. The same approach can be used to define the available set of velocities for the end-effector of a CDPR [10] where the Jacobian matrix is used to compute the velocity polytope.

In the following section, we define a simple pick and place task in the operative space, and we introduce an optimized trajectory planning algorithm for CDPRs which makes use of the force and velocity polytopes to compute the force and velocity constraints in a set of control points along the path. In this way, the resulting trajectory (in particular, the time law) is tailored to the effective capabilities of the CDPR.

3 Optimized Trajectory Planning Algorithm

Consider a generic robotic task of pick and place. This type of operation is typically composed of three movements: vertical depart, transfer movement and vertical approach. Let P_{in} and P_{fin} be the pick and the release point, expressed in the global reference frame, respectively. Hypothesizing that the CDPR must avoid obstacles, we chose to plan the path of the tool center point P of the end-effector in the operational space.

The trajectory consists of three point-to-point linear motions in the operational space connected by two arc segments (the depart arc and the approach arc) between the vertical movements and the transfer motion (Fig. 1b). The trajectory planning problem consists in generating a trajectory $\mathbf{p}(t)$, where \mathbf{p} is the vector describing the position of the tool center point in the workspace (Fig. 1b), that satisfies for each segment, the following constraints:

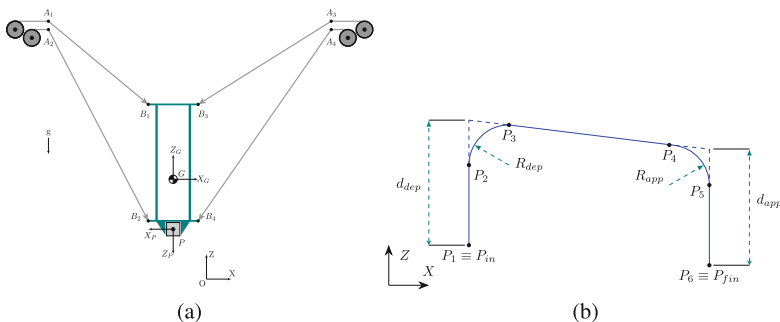


Fig. 1 **a** Layout of the three-DOF under-constrained suspended CDPR. **b** Description of the pick and place movement

- initial position, velocity and acceleration;
- final position, velocity and acceleration;
- acceleration bounded all along the path;
- velocity bounded all along the path.

We propose here to compute the acceleration and velocity constraints by using the polytopes generated by the structure matrix and by the Jacobian matrix of the C DPR. We analyze arc and linear segments separately.

To simplify the model, we assume null values of the tangential accelerations along the depart and the approach arcs. We discretize the arcs into r points, and for each intermediate point we compute the maximum value of the force that the cables can exert towards the center of the curve by using the polytope of the C DPR. Converting the maximum force into acceleration by means of the dynamic model of the C DPR, we compute the maximum allowable centripetal acceleration along the entire arc, which we impose constant:

$$\ddot{p}_{dep} = \min \left(\max \left(\ddot{p}_{dep_i} \right) \right) \Big|_{i=1, \dots, r} = \text{const.} \quad (2)$$

$$\ddot{p}_{app} = \min \left(\max \left(\ddot{p}_{app_i} \right) \right) \Big|_{i=1, \dots, r} = \text{const.} \quad (3)$$

Finally, since the centripetal accelerations are related to the tangential velocities as:

$$\ddot{p}_{dep} = \frac{\dot{p}_{dep}^2}{r_{dep}} \quad \ddot{p}_{app} = \frac{\dot{p}_{app}^2}{r_{app}} \quad (4)$$

we can calculate \dot{p}_{dep} that is the final velocity of the depart movement, and \dot{p}_{app} that is the initial velocity of the approach movement respectively. Clearly, \dot{p}_{dep} and \dot{p}_{app} represent also the initial and the final velocity of the transfer motion, respectively. The calculation of the trajectory of the point P along the arcs is then straightforward.

The parametric description of each linear segment is given by a function of the arch length (s): $\mathbf{p} = f(s(t))$. If we consider a linear segment connecting two points, \mathbf{p}_i and \mathbf{p}_f , the parametric representation of the path is:

$$\mathbf{p}(s) = \mathbf{p}_i + \frac{s}{\|\mathbf{p}_f - \mathbf{p}_i\|} (\mathbf{p}_f - \mathbf{p}_i) \quad (5)$$

We propose here to apply to the function $s(t)$ a modified version of the algorithm for time-jerk optimal planning proposed by Gasparetto et al. [5]. To do so, we discretize each linear segment into $m - 1$ sections and, for each section, the function $s_i(t)$ is planned with a third-order polynomial time law. Via points are equally-spaced along s , whereas the duration of motion in each section can be modified to optimize a cost function.

Let us define $h_i = t_{i+1} - t_i$ with $i = 1, \dots, m + 1$ as the time required to reach s_{i+1} from s_i . The expression of the generic polynomial for each section $s_i(t)$ is a cubic function:

$$s_i(t) = \frac{\ddot{s}_i(t_i)}{6h_i} (t_{i+1} - t)^3 + \frac{\ddot{s}_i(t_{i+1})}{6h_i} (t - t_i)^3 + \left(\frac{s_i(t_{i+1})}{h_i} - \frac{h_i \ddot{s}_i(t_{i+1})}{6} \right) (t - t_i) + \left(\frac{s_i(t_i)}{h_i} - \frac{h_i \ddot{s}_i(t_i)}{6} \right) (t_{i+1} - t) \quad i = 1, \dots, m + 1 \quad (6)$$

The linear system to solve consists of m equations defined to guarantee the continuity of the velocities in the via points:

$$\begin{cases} \dot{s}_1(t_2) = \dot{s}_2(t_2) \\ \vdots \\ \dot{s}_m(t_{m+1}) = \dot{s}_{m+1}(t_{m+1}) \end{cases} \quad (7)$$

where the m unknowns are the accelerations in the via points $\ddot{s}_i(t_i)$. The system can be also expressed in a matrix form as:

$$\mathbf{A} \left[\ddot{s}_2(t_2) \dots \ddot{s}_{m+1}(t_{m+1}) \right]^T = \mathbf{b} \quad (8)$$

where \mathbf{b} is the vector of the known terms whereas \mathbf{A} is a non-singular coefficient matrix with tridiagonal structure. The solution of the system has to satisfy the following boundary constraints

$$\begin{cases} \ddot{s}_{i,min} \leq \ddot{s}_i(t) \leq \ddot{s}_{i,max} & i = 1, \dots, m + 2 \\ \dot{s}_{i,min} \leq \dot{s}_i(t) \leq \dot{s}_{i,max} & i = 1, \dots, m + 2 \end{cases} \quad (9)$$

The values of the boundary constraints are computed for each point by using the force and velocity polytopes of the CDP, respectively. The optimal trajectory planning problem consists in finding, for each linear segment, the function $s(t)$ that minimizes the following objective function:

$$\Omega = \alpha_T T + \alpha_J \int_0^T (\ddot{s}(t))^2 dt \quad (10)$$

$$T = \sum_{i=1}^m h_i \quad \text{with} \quad h_i \geq 0 \quad i = 1, \dots, m + 1 \quad (11)$$

The optimization variables are h_i . By varying the weights α_T and α_J it is possible to find the desired trade-off between quickness and smoothness. Anyway, since the constraints (9) are defined by calculating the polytopes in a set of points along the path, we will obtain a trajectory tailored to the effective force and velocity capabilities of the CDP along the whole path.

4 Simulation Tests and Results

In order to evaluate the effectiveness of the proposed optimization algorithm, simulation tests were implemented and performed on the three-DOF under-constrained suspended CDPR shown in Fig. 1a. Table 1a, b show the values of the parameters used for the CDPR, whereas Table 1c reports the values of the movement task used in the simulations, with reference to Fig. 1b.

Figure 2 shows two examples of trajectory optimization with different weights α_J and α_T . Figure 2a represents position, velocity and acceleration obtained for a smoother trajectory ($\alpha_J \gg \alpha_T$). On the other hand, Fig. 2b shows the same parameters calculated for quicker trajectory ($\alpha_T \gg \alpha_J$). Dashed lines represent the maximum values of acceleration and deceleration achievable by the system during the movement. As expected, the maximum values of acceleration and deceleration vary along the path as described in Sect. 2.

By comparing Fig. 2a, b, it can be seen that there is a great difference in terms of total movement time and smoothness. When $\alpha_J \gg \alpha_T$ the acceleration profiles are smoother and they do not reach the maximum values of acceleration/deceleration. On the other hand, the acceleration profiles shown in Fig. 2b reveal the ability of the algorithm to exploit the maximum accelerations achievable by the cable robot when $\alpha_T \gg \alpha_J$. It is interesting to point out that the maximum acceleration towards the negative direction of Z is 9.81 m/s^2 (gravity acceleration) since the cables can exert force only towards the positive direction of Z.

Table 1 (a) Cable exit points A_i and cable anchor points B_i of the CDPR shown in Fig. 1. The points are expressed in the X-Z plane (b) Kinematic and inertial parameters of the end-effector. (c) Trajectory parameters for the movement task

(a)		(b)			(c)		
Parameter	Value (m)	Parameter	Value	Unit	Parameter	Value	Unit
${}^oA_1, {}^oA_2$	(-2.25, 2.4)	M	5	kg	${}^oP_{in}$	(-1, 0.3)	m
${}^oA_3, {}^oA_4$	(2.25, 2.4)	cI_y	0.061	kg m ²	${}^oP_{fin}$	(1, 0)	m
cB_1	(0.06, 0.21)	r_p	0.035	m	d_{dep}	1.5	m
cB_2	(-0.06, 0.21)	T_{max}	114.3	N	d_{app}	1.5	m
cB_3	(-0.06, -0.09)	\dot{l}_{max}	11.0	m/s	R_{dep}	0.3	m
cB_4	(0.06, -0.09)	g	9.81	m/s ²	R_{app}	0.3	m

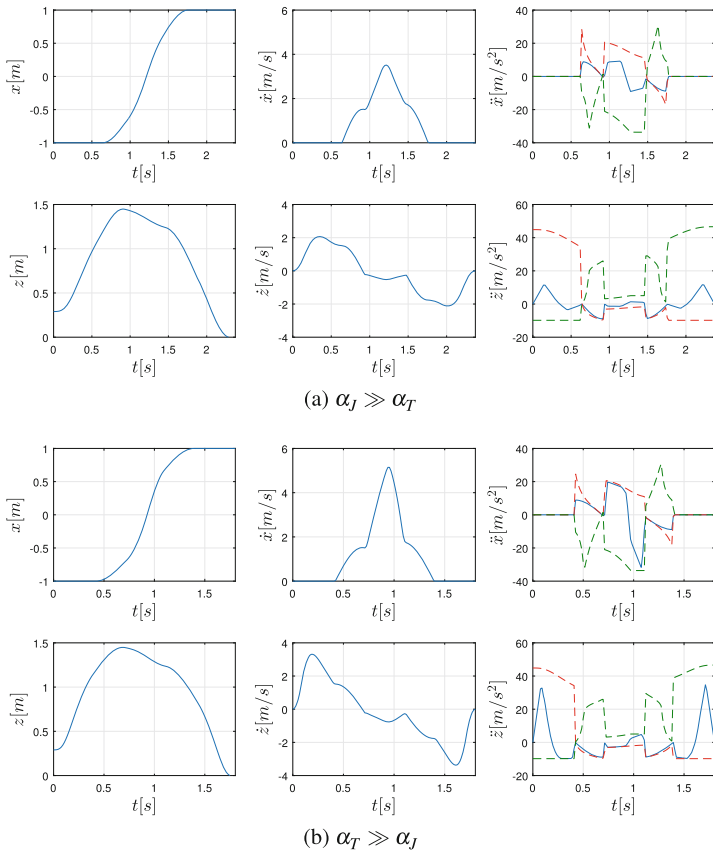


Fig. 2 Position, velocity, and acceleration profiles of the optimized trajectories. The *red dashed lines* and *green dashed lines* represent the maximum acceleration and the maximum deceleration along the motion direction, respectively

5 Conclusion

CDPRs have versatile layouts and they can be reconfigured to improve the efficiency of the task to accomplish. On the other hand, the performance of a CDPR are strongly related to the layout of cables, which directly affects the available wrench set. For this reason, trajectory planning is particularly important in CDPRs, and it should be performed taking into account the effective wrench capabilities of the robot all along the path.

In this work, we defined a pick and place task in the operational space which was composed by three linear segments connected by two arcs and we defined an optimization algorithm to find an optimal trade-off between movement time and smoothness. The algorithm was applied to an under-constrained suspended CDPR

with 3-DOF and 4 cables. Results show that the optimal trajectory allows the CDPR to achieve values of acceleration and velocity near to the maximum allowable values defined by the polytopes of the CDPR. As a result, the system can exert the maximum allowable forces and velocities all along the path, minimizing the movement times.

Acknowledgments This work was supported by the Italian Ministry of University and Research (MIUR), call PRIN 2012, grant no. 20124SMZ88.

References

1. Boschetti G, Caracciolo R, Richiedei D, Trevisani A (2014) Moving the suspended load of an overhead crane along a pre-specified path: a non-time based approach. *Robot Comput-Integr Manuf* 30(3):256–264
2. Boschetti G, Trevisani A (2014) Performance evaluation for cable direct driven robot. In: ASME 2014 12th Biennial conference on engineering systems design and analysis, pp V003T17A014–V003T17A014. American Society of Mechanical Engineers
3. Fahham HR, Farid M, Khooran M (2011) Time optimal trajectory tracking of redundant planar cable-suspended robots considering both tension and velocity constraints. *J Dyn Syst Meas Control* 133(1):011004
4. Gallina P, Rosati G (2002) Manipulability of a planar wire driven haptic device. *Mech Mach Theory* 37(2):215–228
5. Gasparetto A, Zanotto V (2008) A technique for time-jerk optimal planning of robot trajectories. *Robot Comput-Integr Manuf* 24(3):415–426
6. Gasparetto A, Zanotto V (2010) Optimal trajectory planning for industrial robots. *Adv Eng Softw* 41(4):548–556
7. Gosselin C (2014) Cable-driven parallel mechanisms: state of the art and perspectives. *Mech Eng Rev* 1(1):1–17
8. Holland CS, Cannon DJ (2004) Cable array robot for material handling. US Patent 6,826,452
9. Izard JB, Gouttefarde M, Michelin M, Tempier O, Baradat C (2013) A reconfigurable robot for cable-driven parallel robotic research and industrial scenario proofing. In: *Cable-driven parallel robots*, pp 135–148. Springer
10. Krut S, Pierrot F et al (2004) Velocity performance indices for parallel mechanisms with actuation redundancy. *Robotica* 22(02):129–139
11. Mustafa SK, Lim WB, Yang G, Yeo SH, Lin W, Agrawal SK (2015) Cable-driven robots. *Handbook of manufacturing engineering and technology*
12. Nguyen DQ, Gouttefarde M, Company O, Pierrot F (2014) On the analysis of large-dimension reconfigurable suspended cable-driven parallel robots. In: *2014 IEEE international conference on robotics and automation (ICRA)*, pp 5728–5735. IEEE
13. Pott A, Meyer C, Verl A (2010) Large-scale assembly of solar power plants with parallel cable robots. In: *2010 41st international symposium on and 2010 6th German conference on robotics (ROBOTIK) robotics (ISR)*, pp 1–6. VDE
14. Rosati G, Zanotto D, Agrawal SK (2011) On the design of adaptive cable-driven systems. *J Mech Robot* 3(2):021004
15. Rosati G, Zanotto D, Rossi A (2008) Performance assessment of a 3d cable-driven haptic device. In: *ASME 2008 international mechanical engineering congress and exposition*, pp 597–606. American Society of Mechanical Engineers

16. Shen Y, Osumi H, Arai T (1994) Set of manipulating forces in wire driven systems. In: Intelligent robots and systems' 94'. Advanced robotic systems and the real world'. IROS'94. Proceedings of the IEEE/RSJ/GI international conference on, vol 3, pp 1626–1631
17. Zanotto D, Rosati G, Minto S, Rossi A (2014) Sophia-3: a semi-adaptive cable-driven rehabilitation device with tilting working plane. *IEEE Trans Robot* 30(4):974–979
18. Zhang N, Shang W (2016) Dynamic trajectory planning of a 3-dof under-constrained cable-driven parallel robot. *Mech Mach Theory* 98:21–35

An Innovative Method for Sizing Actuating Systems of Manipulators with Generic Tasks

E. Fiore, H. Giberti and G. Bonomi

Abstract This paper describes an innovative method for the design of the driving system for manipulators whose task is a generic handling within a workspace, in particular robotic simulators. For those mechanisms the choice of an actuating system of the correct size is particularly arduous. As a matter of fact, typically the requirements for the machine are described in the workspace, but the intrinsically complex kinematics make difficult to understand which is the case that requires the highest dynamic performances. Analyzing all the possible combinations of the parameters that characterize the motion of the end-effector would require an incredible computational burden, and that's the reason why a statistical method is taken into account: in particular the sizing process described in this paper relies on the Monte Carlo Method. In order to show the its effectiveness, its implementation in a particular application is presented.

1 Introduction

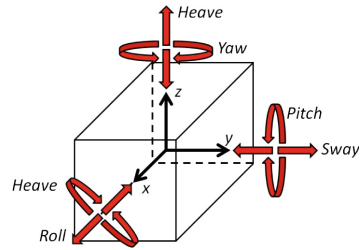
Usually the sizing of the actuating system of a robotic platform requires a deep knowledge of the desired motions the end-effector will be subjected to. However when it comes to estimate the size of the motor-reducer group for a simulator, it could be very difficult to have a precise estimation of the motion laws; indeed in most of the cases the technical specifications in terms of maximum displacements and bandwidth are given in the workspace of the machine, but, due to the complex kinematic relationships between end effector motion and actuating system displacements, it is not possible to foresee which motion requires the highest performances.

E. Fiore (✉) · G. Bonomi
Politecnico di Milano, Dipartimento di Meccanica,
Campus Bovisa Sud, via La Masa 1, 20156 Milan, Italy
e-mail: enrico.fiore@polimi.it

H. Giberti
Dipartimento di Ingegneria Industriale e dell'Informazione,
Università di Pavia, via Ferrata 5, 27100 Pavia, Italy
e-mail: hermes.giberti@unipv.it

Table 1 Workspace

DoF	Symbol	Value
Surge	$L_{wsd,x}$	± 110 mm
Sway	$L_{wsd,y}$	± 60 mm
Heave	$L_{wsd,z}$	± 60 mm
Roll	$L_{wsd,\alpha}$	$\pm 5^\circ$
Pitch	$L_{wsd,\beta}$	$\pm 5^\circ$
Yaw	$L_{wsd,\gamma}$	$\pm 1^\circ$

Fig. 1 Workspace

This paper presents an innovative approach based on the Monte Carlo Method for the dimensioning of the actuating system of a generic machine whose task is not known in advance. In order to show the potentialities of this method its application to a specific manipulator is presented in the following: the sizing of the motor-reducer group of a 6-DoF parallel kinematic manipulator designed to perform HIL (Hardware In the Loop) simulations in the wind tunnel of Politecnico di Milano involving a floating offshore wind turbine scale model [1–4]: in particular, the task the manipulator has to perform is to reproduce the motion induced by sea waves on aerodynamic models subjected to aerodynamic loads. The technical specifications are represented by the maximum dimensions of the workspace (Table 1; Fig. 1) and by the maximum excitation frequency $f_{max} = 3$ Hz for both translations and rotations.

2 Robot Description

Given the application the manipulator is required to have: high precisions and dynamic performances to correctly simulate the floater motion; a sufficiently rigid structure so that the behavior of the aeroelastic model remains unaffected [5, 6]; a low vertical size in order to keep the top of the scale model as low as possible due to the turbulent flow near the ceiling. The chosen architecture is called Hexaslide and belongs to the 6-PUS PKM (parallel kinematics manipulator) family [7, 8]. This architecture is made up of 6 independent kinematic chains, each of them characterized by a series of a prismatic actuated joint, a passive universal joint and a passive spherical joint. The actuation is provided by means of 6 linear transmission

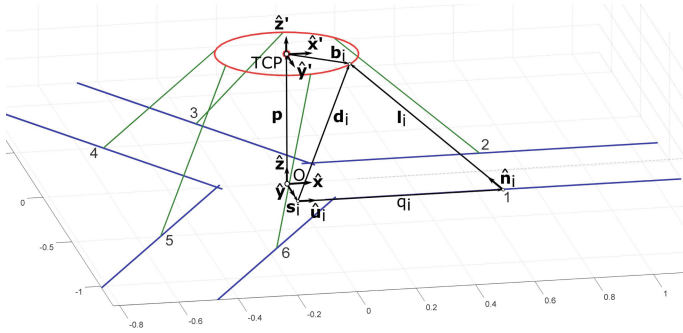


Fig. 2 Kinematics

units organized as three couples of parallel transmission units out of phase of 120° by the z-axis. Robot characteristic parameters are computed after a kinetostatic optimization process which takes into account kinematic, kinetostatic and geometric constraints [9]. During the optimization the cost function to be minimized is represented by the portion of the desired working volume that the machine is not able to cover. With reference to Fig. 2 two reference systems are defined: a global one (denoted by unitary vectors $\hat{x}, \hat{y}, \hat{z}$); a local reference system rigidly attached to the mobile platform (denoted by unitary vectors $\hat{x}', \hat{y}', \hat{z}'$). In order to solve the inverse kinematic problem it is possible to use two kinematic chains:

$$\mathbf{l}_i = \mathbf{d}_i - q_i \hat{\mathbf{u}}_i \quad \text{and} \quad \mathbf{d}_i = \mathbf{p} + [R] \mathbf{b}'_i - \mathbf{s}_i \tag{1}$$

from which it's possible to calculate joint coordinates q_i as:

$$q_i = \mathbf{d}_i^T \hat{\mathbf{u}}_i + \sqrt{\mathbf{d}_i^T (\hat{\mathbf{u}}_i \hat{\mathbf{u}}_i^T - I) \mathbf{d}_i + l_i^2} \tag{2}$$

The kinetostatic problem can be solved using Jacobian matrix $[J]$:

$$\boldsymbol{\tau}_{actuators} = -[J]^T \mathbf{f}_{e,C} \tag{3}$$

At the end of the optimization process a first sketch of the machine has been realized using Solidworks (Fig. 3a) with two purposes: having a quantitative measure of the size of the machine; estimating the inertial properties of each component of the machine for the subsequent dynamic analyses. A dynamic model of the robot (Fig. 3b) is developed using the geometric parameters computed during the optimization and the inertial properties from the CAD model. Geometric structure of the manipulator is made as simple as possible and simulations are performed under the assumption that bodies composing the structure are infinitely rigid. The multi-body model includes also the aerodynamic model.

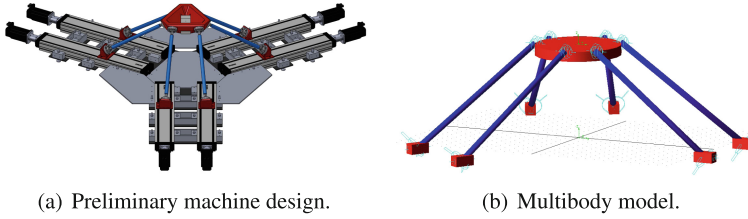


Fig. 3 Preliminary design

The dynamic analysis of the system requires a simplified model of the floater motion that the robot has to reproduce. In [10–12] the authors state that the time history of the sea level can be expressed as:

$$\zeta(t) = \text{Re}\{\rho(t)e^{\varphi(t)}e^{i\omega t}\} = \rho(t)\cos(i\omega t + \varphi(t)) \quad (4)$$

where ρ is the amplitude, ω the frequency and φ the phase. Since both amplitude and phase change very slowly, it is reasonable to keep them constant during the simulations. So for the j -th DoF it is possible to write:

$$j(t) = A_j \cos(2\pi f_j t + \phi_j) \quad (\text{with } j = x, y, z, \alpha, \beta, \gamma) \quad (5)$$

The TCP (Tool Center Point) motion is assumed to be a combination of six sinusoidal motions (three translations and three rotations), each of them characterized by the following expression:

$$j(t) = A_{0,j} + A_j \cos(2\pi f_j t + \phi_j) \quad (\text{with } j = x, y, z, \alpha, \beta, \gamma) \quad (6)$$

The offset $A_{0,j}$ is used to take into account the initial position of the robot.

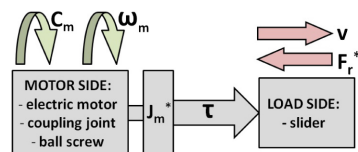
3 Method Explanation

Due to the complex kinematic constraints and to the 24 parameters needed to characterize the TCP motion it is impossible to know a priori which is the worst combination of the six sinusoidal movements in terms of torque demanding. If all the possible combinations of parameters were to be analyzed the computational burden would be too high. That's the reason why a statistical approach is taken into account. In particular the approach that will be used relies on the Monte Carlo Method (MCM) [13–15]. This method is based on the probability density functions of the variables involved. In the specific application described in this paper, the MCM can be divided into the following steps:

1. Choice of the total number of simulations M to be executed on the model: the statistical sample must be sufficiently big and reliable.
2. Definition of the PDF (Probability Density Function) for each of the input quantities involved: due to the arbitrariness of the motion law applied to TCP, the approach followed tends to be as general as possible. For this reason each combination of the six cosinusoidal functions defined by Eq. 6 is considered valid, with the only constraint of having the entire motion inscribed within the working volume. Thus it is possible to assume that at the beginning of the simulation the TCP has the same probability to be in whatever point within the workspace with whatever orientation. No assumptions are made regarding the phase and frequency. The PDF used to describe the variables involved are:
 - Initial position: uniform distribution in the range between $-L_{wsd,j}$ and $+L_{wsd,j}$;
 - Frequency: uniform distribution in the range between 0 and f_{max} ;
 - Phase: uniform distribution in the range between 0 and $2\pi rad$;
 - Amplitude: the value associated with the amplitude must satisfy the relation $|A_{0,j} \pm A_j| < L_{wsd,j}$, where $L_{wsd,j}$ represents half of the total range of the j -th DoF. The distribution of the amplitude is assumed to follow the Rayleigh distribution; there is no guarantee that the constraint on the limits of the workspace are respected, and thus all the simulations for which $|A_{0,j} \pm A_j|$ is greater than $L_{wsd,j}$ for at least one DoF are automatically excluded.
3. Repeated sampling of the PDFs: for each simulation a random value is assigned to each quantity according to its PDF. The result is a file containing M vectors, each of them containing 24 parameters.
4. Solution of the inverse kinematic problem to find the 6 time histories of the sliders displacements.
5. Computation of the forces and moments as the result of multibody simulations on the system under investigation.
6. Dimensioning of the motor-reducer group.

The adopted procedure to choose the driving system is based on the methodology presented in [16–18], applied to the system schematically represented in Fig. 4. The coupling between the motor and ball screw is assumed to be direct; for this reason an equivalent inertia value J_m^* , which is the sum of the three contributions given by the screw, the motor and the coupling joint, is considered. The transmission ratio is the nut-screw coupling $\tau = p/2\pi$, where p is the pitch of the screw. The only element on load side is the slider on which acts an equivalent resistant force F_r^* , composed by two contributions: the former is the inertial contribution of the robot, while the

Fig. 4 Power balance



latter is the result of the force exerted by the aerodynamic model on the end-effector. F_r^* could also be increased by a friction contribute, but in a first approximation it could also be considered negligible. Applied to the MCM, the procedure described in [16–18] is performed in accordance with the following steps:

1. Calculation of load factor β for each simulation:

$$\beta = 2[a_{rms} F_{r,rms}^* + (a F_r^*)_{mean}] \quad (7)$$

2. Analysis of the PDF of β results.
3. Choice of the value β_{99} which is the one such that cumulative distribution function reaches the value 0.99: sizing will be developed using a load factor that covers 99% of cases. The simulation in which β is the most similar to β_{99} will be used in next steps.
4. Computation of equivalent inertia J_m^* using data from catalogues and then calculation of accelerating factor $\alpha = \frac{C_n^2}{J_m^*}$ for each motor.
5. Computation of the transmission ratio admissible range for those motors with $\alpha > \beta$

$$\tau_{min,max} = \frac{\sqrt{\alpha - \beta + 4F_{r,rms}^* a_{rms}} \pm \sqrt{\alpha - \beta}}{2F_{r,rms}^*} \quad \text{and} \quad (8)$$

$$\tau_{lim,m} = \frac{\max |v(t)|}{\omega_{m,max}} \quad \text{and} \quad \tau_{lim,g} = \frac{\max |v(t)|}{\omega_{g,max}}$$

τ_{min} and τ_{max} are respectively lower bound and upper bound of the range in which the accelerating factor α is bigger than the load factor β . Once known the bounds of the admissible range of τ , it is easy to compute the corresponding limits in terms of the pitch p of the ball-screw.

6. Verification of the maximum torque limit:

$$\max |C_m(t)| < \min(C_{m,max}, C_{g,max}) \quad (9)$$

in which $\max |C_m(t)|$ is measured during simulation and threshold values $C_{m,max}$, $C_{g,max}$ are specific for each motor and transmission unit.

7. Choice of the smallest size actuating system among the ones that are able to meet the requirements.

The process to find the PDF that represents at best the distribution among the simulations should be repeated also for maximum torque and maximum speed. Indeed it is not possible to state that the worst case for maximum torque and maximum speed is the one recorded during the simulation whose load factor is equal to β_{99} .

The generation procedure of motions (Eq. 6) is performed in calculation environment (Matlab) and then data are imported in the simulation environment (Adams). After assigning the 6-DoF motion to the end-effector a first 30 s long simulation is

executed in order to record sliders displacement. The time histories of these displacements are stored into 6 spline, which will be used to define motion during a second simulation: this process corresponds to solve the inverse kinematic problem. During this simulation some measure are performed: motion forces along linear transmission units, reaction forces on linear transmission units and on spherical joints. Time histories of these quantities are stored in text files, in order to be acquired in calculation environment to perform design and verification process. This procedure is cyclically repeated M times. The value of M should be chosen carefully; as a matter of fact a low number of simulations would lead to inconsistent results, while a too high value would increase the computational burden. 1000 simulations represent a good compromise for the application under investigation.

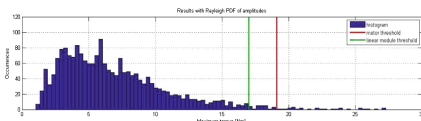
4 Results and Discussion

Examining load factor results, the PDF that represents their distribution at best is Birnbaum-Saunders distribution. The β_{99} parameter assumes a value of $2.7 \cdot 10^4$ W/s. The lower size motor and transmission unit that ensure a 99 % coverage of the considered cases are respectively *HG-JR 203B* motor by *Mitsubishi* and *CKK 20-145* linear transmission unit by *Bosch Rexroth* with 20 mm pitch. Main characteristics of electric drive and ball screw transmission unit are collected in Table 2.

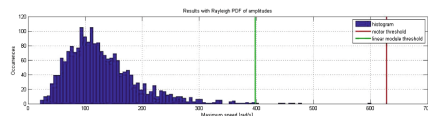
In Fig. 5a is shown the maximum torque distribution. The most restricting limit is the one imposed by transmission units: the test is satisfied in 94.7 % of the cases. Although the coverage is less than 99 % the current actuating system is considered acceptable in order to not have an excessive size. Figure 5b shows the distribution for rotation speed. Also in this case the most restricting limit is imposed by the linear transmission: since this value is greater than 99 %, this test is passed.

Table 2 Mitsubishi HG-JR 203B and Bosch Rexroth CKK 20-145: technical data

Quantity	Symbol	HG-JR 203B	CKK 20-145
Rated torque (Nm)	C_n	6.4	—
Maximum torque (Nm)	$C_{m,max}$	19.1	17
Maximum speed (rpm)	$\omega_{m,max}$	6000	3800



(a) Maximum torque



(b) Maximum speed

Fig. 5 First type of test on actuating system

5 Conclusions

This paper presents an innovative method based on a statistical approach for sizing the motor and transmission units for those machines whose task is not likely to be known in advance. The use of the Montecarlo Method allows to consider all possible motions admitted in the workspace and therefore a strict dimensioning of an actuating system which will be able to perform all possible tasks. MCM also enables to deal with tests of the mechanical components in a statistical way: critical issues related to sizing spherical joints in parallel kinematic machine design emerged from this analysis.

References

1. Bayati I, Belloli M, Bernini L, Fiore E, Giberti H, Zasso A (2016) On the functional design of the DTU10 MW wind turbine scale model within LIFES50+ project. *Journal of physics, conference series, the science of making torque from wind*
2. Bayati I, Belloli M, Facchinetti A, Giappino S (2012) Wind tunnel tests on floating offshore wind turbines: a proposal for hardware-in-the-loop approach to validate numerical codes. *Wind Eng*
3. Bayati I, Belloli M, Ferrari D, Fossati F, Giberti H (2014) Design of a 6-dof robotic platform for wind tunnel tests of floating wind turbines. *Energy Proc*
4. Bayati I, Belloli M, Ferrari D, Fossati F, Giberti H (2014) Wind tunnel tests on floating offshore wind turbines: Design of a 6-dof robotic platform for floating motion simulation. In: *European wind energy association conference and exhibition 2014, EWEA 2014*
5. Fiore E, Giberti H, Ferrari D (2016) Dynamics modeling and accuracy evaluation of a 6-DoF Hexaslide robot. In: *Conference proceedings of the society for experimental mechanics series, vol 1*, pp 473–479
6. Negahbani N, Giberti H, Fiore E (2016) Error analysis and adaptive-robust control of a 6-dof parallel robot with ball-screw drive actuators, vol 2016
7. Merlet JP (2006) *Parallel robots*, 2nd edn. Springer
8. Giberti H, Ferrari D (2015) A novel hardware-in-the-loop device for floating offshore wind turbines and sailing boats. *Mech Mach Theory* 85:82–105
9. Fiore E, Giberti H (2016) Optimization and comparison between two 6-DoF parallel kinematic machines for HIL simulations in wind tunnel. In: *MATEC web of conferences, vol 45*
10. Longuet-Higgins MS (1952) On the statistical distribution of the height of sea waves. *J Mar Res* 11(3):245–266
11. Longuet-Higgins MS (1957) The statistical analysis of a random moving surface. *Philos Trans R Soc Lond A* 249:321–387
12. Xu D, Li X, Zhang L, Hu N, Lu H (2004) On the distributions of wave periods, wavelengths, and amplitudes in a random wave field. *J Geophys Res* 109:C05016. doi:[10.1029/2003JC002073](https://doi.org/10.1029/2003JC002073)
13. International Organization of Legal Metrology (2008) Evaluation of measurement data—Supplement 1 to the “Guide to the expression of uncertainty in measurement”—propagation of distributions using a Monte Carlo method, OIML G 1-101 Edition 2008 (E)
14. Norma UNI CEI ENV 13005, “Guida all’espressione dell’incertezza di misura”
15. Moschioni G, Saggin B, Tarabini M, Hald J, Morkholt J (2010) Use of design of experiments and Monte Carlo method for instruments optimal design. *Measurement* 46(2013):976–984
16. Giberti H, Cinquemani S, Legnani G (2010) Effects of transmission mechanical characteristics on the choice of a motor-reducer. *Mechatr Elsevier J* 20:604–610

17. Giberti H, Cinquemani S, Legnani G (2011) A practical approach to the selection of the motor-reducer unit in electric drive systems. *Mech Based Des Struct Mach* 39(3):303–319
18. Giberti H, Clerici A, Cinquemani S (2014) Specific accelerating factor: one more tool in motor sizing projects. *Mechatr Elsevier J*. ISSN 0957–4158. doi:[10.1016/j.mechatronics.2013.11.007](https://doi.org/10.1016/j.mechatronics.2013.11.007). Accessed 16 Dec 2013

Experimentally Based Design of a Manually Operated Baler for Straw Bale Construction

Walter Franco, Giuseppe Quaglia and Carlo Ferraresi

Abstract Straw bale construction is considered an appropriate technique for improving housing condition in developing Countries and for rebuilding in emergency condition. However, balers suitable for this purpose are not available nowadays. This paper presents a method for functional design of a human powered baler for straw bale building, based on the straw mechanical characteristic, experimentally measured. A prototype has been realized and tested.

Keywords Straw bale construction • Slider crank mechanism synthesis • Human powered baler • Hand-operated machine • Straw mechanical characteristics

Nomenclature

A	Compression plate area, m^2
b	Connecting rod length, m
C	Operating torque, Nm
F	Compression force, N
F_{op}	Operating force, N
$F_{op\ max}$	Maximum force exertable by the operator, N
$F_{op\ peak}$	Peak of the operating force, N
k	Stiffness constant of the straw, $Pa\ m^3/kg$
l	Operating lever length, m
l_f	Final length of the compression chamber, m
l_o	Initial length of the compression chamber, m
L_c	Compression work per cycle, J
$L_{op\ max}$	Maximum input mechanical work that an operator can do in one compacting cycle, J
m	Crank length, m

W. Franco (✉) · G. Quaglia · C. Ferraresi
Politecnico di Torino, Turin, Italy
e-mail: walter.franco@polito.it

m_c	Mass of the straw loaded in the loading chamber between each compaction cycle, kg
m_{tot}	Total bale mass, kg
n_c	Number of compaction cycles necessary to realize a bale
p	Compression pressure, Pa
p_f	Straw compression pressure at final density ρ_f , Pa
y	Compression plate (piston) displacement, m
y_c	Compression plate (piston) stroke in one compaction cycle, m
α	Rotation angle of the crank (operating lever), rad
α_c	Rotation angle of the crank (operating lever) for one complete compaction cycle, rad
α_o	Initial crank (operating lever) angle, rad
λ	m/b, dimensionless parameter, mechanism's proportions
ρ	Density of the straw, kg/m ³
ρ_f	Final density of the straw bale, kg/m ³
ρ_o	Initial density of the straw, kg/m ³

1 Introduction

Straw-bale construction is a building method that uses bales of straw as walls infill or structural elements [1–4]. In the last years, with the increasing attention for green building, interest towards straw bale construction technique has grown. Indeed, straw is a sustainable material, naturally renewable, widespread, cheap and with great insulating proprieties. Building with straw bale is energy-efficient, durable, fire-resistant, smart, and comfortable [1, 5].

Due to the availability and low cost of the straw, and easy implementation in auto-constructing projects, the straw bale building technique is also considered one of the most appropriate for improving of the housing conditions in developing countries and for the reconstruction in post-emergency conditions [6, 7]. In these contexts, motorized balers are often not available, because fossil fuels are expensive and difficult to find and the distribution of electrical energy is intermittent. Therefore, developing of appropriate manually-operated balers, simple, low-cost, easy to use, self-constructible, could be advantageous.

The paper deals with the design of a straw manually operated press able to produce bales to be used as infill material for constructions. The authors developed a design method of such a baler, in support of an international cooperation project, developed by Architettura Senza Frontiere Piemonte (ASF, Architects Without Borders Piemonte) [6, 8], consisting in building a straw warehouse for rice farmers cooperative in Haiti. In the paper the design requirement of the press are listed. Then an experimentally-based calculation method of the functional parameters of the actuating mechanism of the press is described. Finally, the realized prototype is briefly presented and some conclusions are provided.

2 Design Specifications

The press must produce a rice straw bale sized $0.3 \times 0.45 \times 0.9$ m, with density $\rho_f = 90 \text{ kg/m}^3$ [2] and total mass $m_{tot} = 10.9$ kg. The initial density of the straw rice is of about $\rho_o = 30 \text{ kg/m}^3$.

The press must be able to operate in rural areas of developing countries, even in emergency conditions (re-building operations after earthquakes, tsunami, hurricanes etc.). For this reasons it must operate without electricity or fuels, i.e. it must be manually operated.

According to the appropriate technology approach, a purpose of the project is to involve local communities and to foster a self-constructing and sustainable technology process at a local level. Therefore, the baler has to be simple, ergonomic and easy to build; it has to be made using materials and components that can be found on site. Ultimately, in the design phase it is necessary to take into account the restrictions imposed by the technologies of the local community, in this case the one of Bocozele, Saint Marc, Haiti.

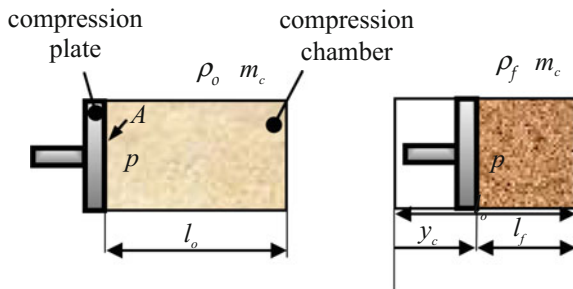
3 Functional Design of the Baler

The press must be capable of producing the straw bale in n_c compression cycles. For each compression cycle, a straw mass m_c , of ρ_o density, is placed in a compression chamber of initial length l_o (Fig. 1). Then the compression plate is moved with a stroke y_c , the compression chamber length is reduced to a length l_f and the straw reaches the desired density ρ_f . At the end of each compression cycle, the bottom of the compression chamber is manually moved, so the geometry of the compression chamber is restored.

The work necessary to compress the straw, for each compaction cycle, is:

$$L_c = \int_0^{y_c} p(\rho)A \, dy \tag{1}$$

Fig. 1 Press compression chamber scheme



where A is the compression plate area, y the compression plate displacement and p the compression pressure, depending on the straw density.

3.1 Experimental Mechanical Characterization of Straw

There are many works regarding the modeling of the straw mechanical characteristic [9–11], unfortunately not applicable in our study due to heterogeneity of the results.

Therefore, the mechanical characteristic of the rice straw, in term of compression pressure p versus the straw density ρ , has been experimentally measured. A mass of about 0.8 kg of rice straw has been inserted in a steel box (Fig. 2b). Then a compression plate of 0.162 m² area (0.36 × 0.45 m) was moved at 3 mm/s, and the compression force and the plate displacement were measured. Figure 2a shows the mechanical characteristic obtained in four different tests.

3.2 Slider-Crank Actuation Mechanism Synthesis

Knowing the mechanical characteristic of the straw, and numerically integrating the Eq. (1), it is possible to calculate the relationship between the stroke of the compression plate y_c and the compression work per cycle L_c (Fig. 3).

Obviously, the compression work per cycle L_c must be less than the maximum input mechanical work that an operator can do in one compacting cycle. In the case of lever operating (Fig. 4), the latter must be calculated as:

$$L_{op\ max} = F_{op\ max} l \cdot \alpha_c \quad (2)$$

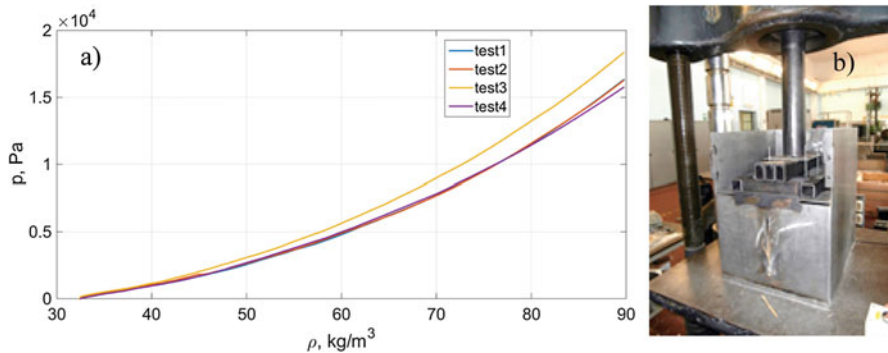
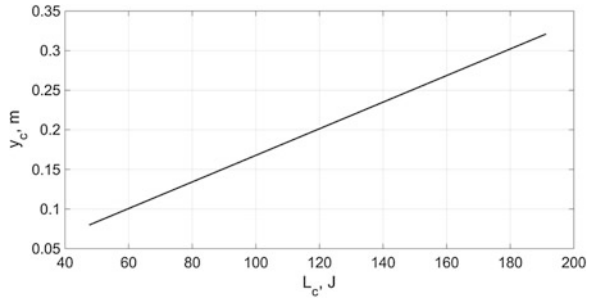


Fig. 2 a Mechanical characteristic of the rice straw. b Experimental setup

Fig. 3 Piston stroke y_c versus the compression work per cycle L_c

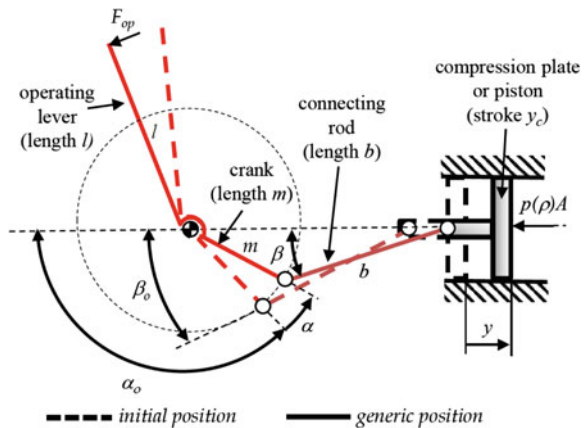


where $F_{op\ max}$ is the maximum acceptable force that a human operator can apply at the end of the actuating lever of length l , and α_c is the angular rotation of the lever that corresponds to one single compaction cycle. Set the maximum input mechanical work that an operator can do, it is possible to estimate the compression work at each compaction cycle compatible with the human-powered actuation of the press, and then the stroke of the compression plate.

Due to the simplicity, a centered slider-crank mechanism has been chosen as transmission mechanism of the press (Fig. 4). The operating lever is rigidly connected to the crank. It is assumed that the crank length is m , and the connecting rod length b . The crank has an initial angular position α_o and rotates of an angle α , until reaching a maximum value α_c ($0 < \alpha < \alpha_c$) corresponding to the stroke y_c of the piston. The aim of the synthesis methodology is to choose the length of the crank m , the length of the rod b , and the initial angle of the lever α_o , that allow to perform the desired stroke of the piston y_c , applying a limited force to the lever $F_{op} < F_{op\ max}$.

The lever length l was chosen equal to 2 m, considering that an operator has to be able to grab it even in a vertical position. The rotation angle for one compaction cycle α_c was fixed equal to 80° so that the operator can easily hold the lever, and can rotate it from an almost vertical position to a horizontal one.

Fig. 4 Baler slider-crank mechanism



Referring to Fig. 4 it is possible to obtain the stroke of the compression plate y_c :

$$y_c = b(\cos \beta_c - \cos \beta_o) + m(\cos \alpha_o - \cos(\alpha_o + \alpha_c)) \quad (3)$$

where:

$$\lambda = m/b \quad \beta_o = \arcsin(\lambda \sin(\alpha_o)) \quad \beta_c = \arcsin(\lambda \sin(\alpha_o + \alpha_c)) \quad (4)$$

Elaborating Eq. (3) and taking into account Eq. (4) we can calculate the crank length m as a function of the initial crank angle α_o , once the piston stroke y_c has been chosen, as previously discussed, and the parameter λ and the maximum rotating angle of the lever α_c have been fixed:

$$m = \frac{y_c}{1/\lambda(\cos \beta_c - \cos \beta_o) + \cos \alpha_o - \cos(\alpha_o + \alpha_c)} \quad (5)$$

The choice of parameter λ affects the minimum transmission angle that has to be as high as possible in order to reduce the force component normal to the frame; it was fixed $\lambda = 0.42$.

In order to calculate the force applied by the operator at the lever end, we can consider that:

$$F_{op} = \frac{p(\rho)A}{\eta l} \frac{dy}{d\alpha} = \frac{p(\rho)A}{\eta l} m [1/\lambda \cos \beta - \cos(\alpha_o + \alpha)] \tan \beta \quad (6)$$

where η is the efficiency of the transmission, and dy/da the geometrical speed of the output link.

The design methodology is articulated in the following phases:

- (a) setting the admissible compression work L_c ;
- (b) calculating the piston stroke y_c using the graph of Fig. 3;
- (c) assuming the design parameters l , α_c and λ , as reported in Table 1;
- (d) calculating the crank length, for each initial lever angle α_o , using Eqs. (4) and (5) and computing the correspondent connecting rod length $b = m/\lambda$;

Table 1 Design parameters

<i>Assumed design parameters</i>	
Compression work per cycle	$L_c = 185 \text{ J}$
Actuating lever length	$l = 2 \text{ m}$
Rotation angle of the lever per cycle	$\alpha_c = 80^\circ$
Ratio between crank and rod lengths	$\lambda = 0.42$
<i>Calculated design parameters</i>	
Piston stroke	$y_c = 0.31 \text{ m}$
Crank length	$m = 0.3$
Connecting rod length	$b = 0.7$
Initial crank (operating lever) angle	$\alpha_o = 100^\circ$

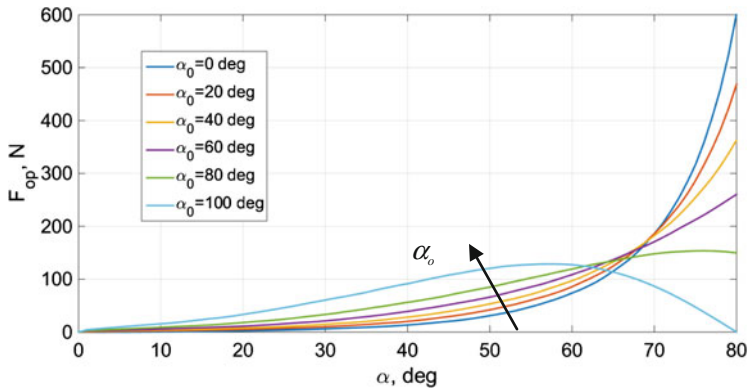


Fig. 5 Operating force F_{op} versus the rotation angle of the lever α ($\rho_o \approx 32 \text{ kg/m}^3$; $\rho_f = 90 \text{ kg/m}^3$; $\alpha_c = 80^\circ$; $\lambda = 0.42$; $l = 2 \text{ m}$; $L_c = 185 \text{ J}$; $\eta = 0.95$)

- (e) calculating, using Eq. (6) and the experimental characteristic of the straw, the operator force F_{op} versus the rotation angle of the lever α for each initial angles of the lever α_o (Fig. 5);
- (f) choosing the initial angle of the lever that minimizes the operator force; in our case it is $\alpha_o = 100^\circ$.

4 The Prototype of the Baler

Figure 6 shows a 3D image of the designed press and the first prototype realized. The straw to be pressed for each cycle is put into the loading chamber. The operator actuates the lever that moves the piston by means of the slider-crank mechanism. The extraction of the bale is done by means of the unloading door. An image of the prototype realized, called Anpil Pay 1.0, is reported in Fig. 6.

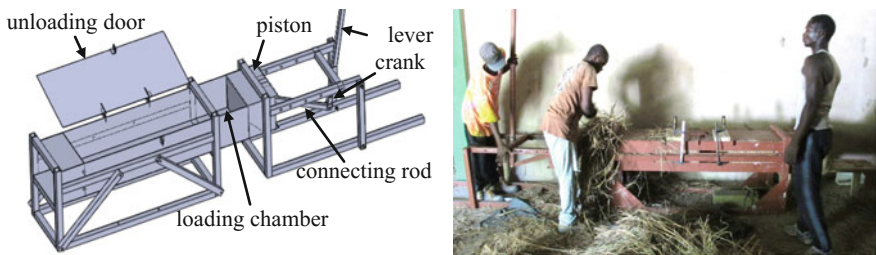


Fig. 6 The detailed design and the prototype of the baler

5 Conclusions

An experimentally based design method for hand-powered press used for producing straw bales was developed. The method has proven effective and allowed the realization of a press able to accomplish the project scope.

Acknowledgments Our gratitude goes to eng. Federico Iarussi for the collaboration in the detailed design of the press, the student team Anpil Pay 2.0 for the experimental tests and the Architetti Senza Frontiere Piemonte (ASF) association, in the person of Valeria Cottino, Annalisa Masetto and Veronica Brugaletta for the realization of the prototype.

References

1. Jones B (2009) Building with straw bales: a practical guide for the U. K. and Ireland, Green Books Totnes
2. King B (2006) Design of straw bale buildings. The state of art. Green Building Press
3. Lerner K, Theis B, Smith D (2000) Straw-bale, alternative construction: contemporary natural building materials. In: Elizabeth L, Adams C (eds) Wiley, New York, pp 209–34
4. Magwood C, Mack P (2000) Straw bale building: how to plan, design and build with straw. New Society Publishers, Gabriola Island, B.C.
5. Ashour T, Georg H, Wu W (2011) Performance of straw bale wall: a case study. *Energy Build* 43:1960–1967
6. Piemonte ASF (2013) Haiti |2| Re-start from straw, III Congress of the University Network for Development Cooperation (CUCS Torino 2013), Torino, 19–21 September 2013, p 318
7. Bonoli A, Rizzo S, Chiavetta C (2015) Straw as construction material for sustainable buildings: life cycle assessment of a post-earthquake reconstruction. In: Vernacular architecture: to-towards a sustainable future. CRC Press, pp 143–146
8. Franco W, Iarussi F, Quaglia G (2016) Human powered press for producing straw bales for use in construction during post-emergency conditions. *Biosyst Eng* 150:170–181
9. Afzalnia S, Roberge M (2013) Modeling of the pressure-density relationship in a large cubic baler. *J Agr Sci Tech* 15:35–44
10. Ferrero A, Horabik J, Molenda M (1990) Density-pressure relationship in compaction of straw. *Can Ag Eng* 33(1):107–111
11. Nona K, Lenaerts B, Kayacan E, Saeys W (2014) Bulk compression characteristics of straw and hay. *Biosyst Eng* 118:194–202

Part VII
Transportation Machinery

Fast Calibration Procedure of the Dynamic Model of an Autonomous Underwater Vehicle from a Reduced Set of Experimental Data

**Benedetto Allotta, Riccardo Costanzi, Luca Pugi, Alessandro Ridolfi
and Andrea Rindi**

Abstract AUVs (Autonomous Underwater Vehicles) represent an interesting industrial product with applications ranging from the monitoring of cultural and natural heritage to the inspection of underwater plants for the Oil and Gas industry. Development of AUVs also represents an interesting challenge for researchers and engineers involving a melting of different competences of robotics, mechanics and mechatronics. In particular, this paper is focused on the simulation, identification and validation of simplified hydrodynamic models that can be used for the overall verification and simulation of vehicle performances including aspects related to manoeuvrability and controllability of the system. The identification and validation process described in this work is based on past experiences with the Typhoon AUV built by the MDM Lab (Mechatronics and Dynamic Modelling Laboratory) of the University of Florence, Italy.

Keywords Autonomous Underwater Vehicles • Marine propulsion system • Simulation of dynamical systems • Marine robotics

B. Allotta · L. Pugi · A. Ridolfi (✉) · A. Rindi
Department of Industrial Engineering, University of Florence, Florence, Italy
e-mail: a.ridolfi@unifi.it

B. Allotta
e-mail: benedetto.allotta@unifi.it

L. Pugi
e-mail: luca.pugi@unifi.it

A. Rindi
e-mail: andrea.rindi@unifi.it

R. Costanzi
Department of Information Engineering and Centro Enrico Piaggio,
University of Pisa, Pisa, Italy
e-mail: riccardo.costanzi@unipi.it

1 Introduction

An accurate modelling of the dynamic response of the thrusters used to control ROVs (Remotely Operated Vehicles) and AUVs (Autonomous Underwater Vehicles) is fundamental to obtain a meaningful simulation of the behaviour of the vehicle and in particular for a simulation of the vehicle navigation and control system. Possible applications range from model based navigation and localization systems to estimation filters for the prediction of partially unknown disturbances such as marine currents. Typically, two complementary aspects of the problem are investigated:

- Identification of hydrodynamic coefficients of the hull;
- Identification of the behaviour of thrusters and of the whole propulsion system.

For the description of the hydrodynamic behavior of the hull the most commonly approach is summarized by Fossen in [5]. Hydrodynamic coefficients describing the behaviour of the vehicle can be first approximated using simplified correlations available on handbooks. Thanks to the development of CFD (Computational Fluid Dynamics) tools many recent works have been also focused on FEM (Finite Element Method) models for the calculation of hydrodynamic coefficients of the Hull [6]. However even considering the recent improvement of CFD sciences, there is still the need of an accurate identification of vehicle behavior from experimental results as stated by recent works where the identification of vehicle parameters is performed through different techniques such as Kalman filtering, neural networks, or modal techniques based on the concept of self-oscillations. The reason for such an interest in experimental identification techniques, despite the recent progress of CFD calculations, could be easily understood considering the following factors:

- The real hydrodynamic behaviour of an AUV can be heavily affected by various un-modelled phenomena including the interaction with the propulsion system which still represents a quite hard task for numerical models;
- Most of the AUVs used for scientific research have a modular architecture, involving variable geometric and mass properties according to the mission profile and the onboard payload;
- Finally, a non-secondary aspect is represented by the fact that autonomous vehicles are nowadays complex mechatronic systems designed by team of robotic and mechatronic engineers, so CFD competences represent an additional heterogeneous competence affordable only for a few research groups.

As previously introduced, the identification of the behaviour of the propellers is quite important, since the behaviour of the propellers, in terms of developed thrust and corresponding reaction torques transmitted to the hull, is widely influenced by the surrounding field of motion of the fluid and consequently by the interaction with hull dynamics. In particular, in literature the problem is studied in the following terms:

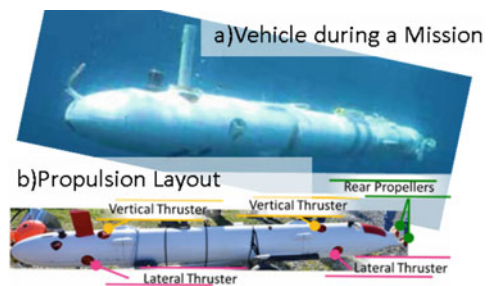
- Steady state response of the propeller is studied with respect to different operational conditions considering single quadrant operation or four quadrant ones;
- Transient response: steady state response of the propeller can be further refined considering time transient introduced by inertial behaviour of the propeller driveshaft coupled with the dynamic behavior of the motor;
- Sensitivity to cross fluxes: relevant cross fluxes of water can influence the behavior of the propeller.

The authors have focused their attention to the identification and simulation of the main hydrodynamic parameters of Typhoon AUV (Autonomous Underwater Vehicle) including its propulsion system. In particular, Typhoon AUV, visible in Fig. 1 is an innovative torpedo-shaped vehicle dedicated to localization, investigation and surveillance of archeological underwater sites whose design has been widely discussed in previously published works [1–3].

The propulsion layout of Typhoon AUV is visible in Fig. 1: two rear propellers are used for standard-straight navigation and a certain number of tunnel thrusters (two vertical and two lateral) are used to control vehicle orientation or to perform hovering over an assigned target. Considering the high number of controlled independent actuators, six in this case, fixed pitch propellers are adopted in order to reasonably reduce costs and increase the reliability of the whole system.

Methodologies and results obtained on the Typhoon benchmark could be easily extended to a wide variety of different vehicles and applications. The aim of this work is to propose identification procedures and models that are a reasonable trade-off between simplified and generalized models needed for preliminary design of propulsion, control and navigation systems and the huge amount of numeric simulations and experimental activities available in literature. In particular the authors have tried to optimize the proposed procedure to minimize time and cost needed to reasonably identify and reproduce the dynamic behaviour of a real AUV.

Fig. 1 Typhoon AUV: the vehicle navigating during a mission (a) and its propulsion layout (b)



2 Four Quadrants Model of Main Propellers and Thrusters

In order to study four quadrants operation of the propeller [7], the use of the advance, thrust and torque coefficients J, K_t, K_q is quite impractical. In particular null values and sign inversions of V_a and n lead to numerically inconsistent descriptions of J, K_t, K_q . For this reason, propellers advance is expressed in terms of the advance angle β defined according to (1) where the advance speed V_a is scaled with respect to the propeller tangential speed calculated at the 70 % of the propeller tip radius:

$$\beta = \tan^{-1} \frac{V_a}{0.7\pi nD} = \tan^{-1} \frac{J}{0.7\pi} \tag{1}$$

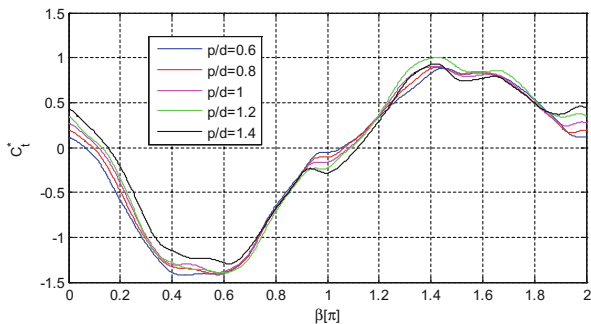
In particular, referring to the bladed disc model β is equal to the α angle of the blade. With respect to β , thrust and torque are expressed in term of the modified coefficients C_t^* and C_q^* in which Q and T are scaled with respect to kinetic energy associated to the inlet relative speed w_{1_07} referred again to the 70 % of the propeller tip radius:

$$C_t^* = \frac{T}{\left(\frac{1}{2}A_{disc}\rho w_{1_07}^2\right)} = \frac{K_t}{\frac{\pi}{8}(J^2 + 0.49\pi^2)} \tag{2}$$

$$C_q^* = \frac{Q}{\left(\frac{1}{2}A_{disc}\rho w_{1_07}^2\right)d} = \frac{K_q}{\frac{\pi}{8}(J^2 + 0.49\pi^2)} \tag{3}$$

C_t^* and C_q^* coefficients are typically approximated in terms of Fourier series (4) whose coefficients of some widely diffused propeller series are available in literature [4]. On Typhoon AUV propeller profiles are Ka 4-70 ducted in a 19-A accelerating nozzle. Some results for the Typhoon propellers are shown in Fig. 2; these results are referred to the first 21 terms of the sum ($n = 20$).

Fig. 2 C_t^* for a Ka 4-70 propeller ducted on a 19-A nozzle according to Oerstveld



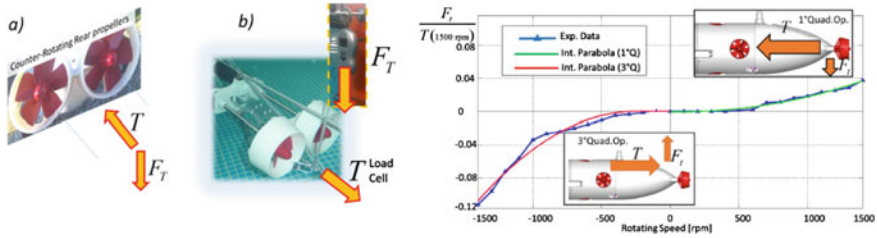


Fig. 3 Example of thruster identification tests performed in the pool of the MDM Lab, Pistoia, Italy

$$C_t^* = \sum_{k=1}^n A_k \cos \beta k + B_k \sin \beta k; \quad C_Q^* = \sum_{k=1}^n C_k \cos \beta k + D_k \sin \beta k \quad (4)$$

Results from literature [2] are refined with pool tests which are useful to calibrate models and to introduce and measure additional forces arising from the mutual interactions among the thrusters, as shown in the example of Fig. 3.

3 Experimental Tests and Model Calibration

The hydrodynamic behaviour of the hull is described following the classical approach described by Fossen in [5]. According to the SNAME convention, the adopted body and fixed reference systems are described in Fig. 4. Hull dynamics is consequently described with respect to a body constrained reference system by (5)

$$M\dot{\nu} + C(\nu)\nu + D(\nu)\nu + g(\eta) = \tau \quad (5)$$

where the following symbols are adopted:

- M 6×6 Matrix accounting for inertial effects;
- C 6×6 Matrix corresponding to the contribution of Coriolis forces;
- D 6×6 Matrix corresponding to viscous/dissipative effects;

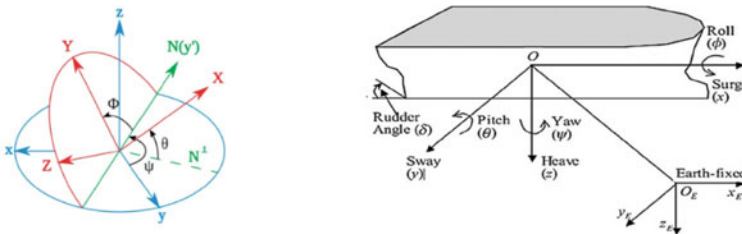


Fig. 4 Adopted reference systems and notation according to the SNAME convention

- g a six elements vector corresponding to the contribution of volumetric forces like the gravitational one (the weight) and the buoyancy;
- τ a six elements vector composed of the contribution of external forces and torques (6):

$$\tau = [\tau_1^T, \tau_2^T]^T; \quad \tau_1 = [X, Y, Z]^T; \quad \tau_2 = [K, L, M]^T \tag{6}$$

- Position and speed vectors η, ν are defined respectively according (7) and (8); the corresponding reference systems are described in Fig. 4.

$$\eta = [\eta_1^T, \eta_2^T]^T; \quad \eta_1 = [x, y, z]^T; \quad \eta_2 = [\phi, \theta, \psi]^T \tag{7}$$

$$\nu = [\nu_1^T, \nu_2^T]^T; \quad \nu_1 = [u, v, w]^T; \quad \nu_2 = [p, q, r]^T \tag{8}$$

Despite to the high number of coefficients related to (5) the dynamical behaviour of the system can be accurately described by a limited number of coefficients, especially if point to point navigation at limited speed is considered (common situation in real scenarios).

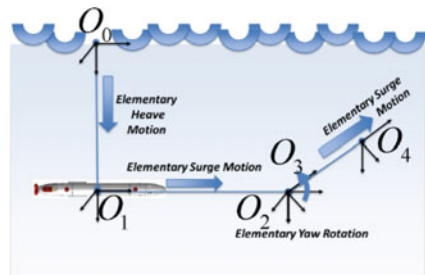
As clearly visible in the scheme of Fig. 5 a typical point to point navigation can be split into a sequence of elementary motions: heave motions (9), surge motions (10), yaw rotations (11)

$$M_{33}\dot{w} + D_{33}(w)w + g_3 = Z \tag{9}$$

where M_{33} and D_{33} are respectively the elements corresponding to the third row and the third column of the matrix M and D . g_3 represents the third element of the g vector. Similarly we can write down:

$$M_{11}\dot{u} + D_{11}(u)u = X \tag{10}$$

Fig. 5 Point to point motion, decomposition in a sequence of elementary motions



$$M_{66}\dot{r} + D_{66}(r)r = M \tag{11}$$

In Fig. 6, a typical example of mission profile performed by Typhoon AUV during some tests performed in October 2014 in Croatia (in Biograd na Moru during the Breaking the Surface 2014 International Workshop) is shown: the vehicle performed a square closed loop trajectory which can be easily decomposed in a sequence of the above described elementary motions. In particular, the vehicle starts moving on surface from WP1 (green line in Fig. 6); then at WP3 through an elementary heave manoeuvre the vehicle reaches the operating depth and starts its underwater mission in order to reach in sequence WP4 and WP5 where the vehicle returns to surface (red line in Fig. 6).

The vehicle during the test is equipped with a DVL (Doppler Velocity Log) measuring the absolute AUV speed with respect to the sea bottom, as visible from the experimental data reported in Fig. 7 (longitudinal speed). The vehicle is also equipped with an IMU (Inertial Measurement Unit) able to estimate 3D vehicle accelerations and rotations.

Also synchronized data concerning the rotation speed of rear propellers and thrusters are available from the field test logs.

Using the simplified model of each propeller described in Sect. 2, it is possible to estimate the exerted thrust $f_i(t)$ and the reaction torque $q_i(t)$ produced by the i -th thruster/propeller. Knowing the vector $F(t)$ and $Q(t)$ of forces and torques exerted

Fig. 6 Example of mission path during the experimental tests performed in Croatia, in October 2014

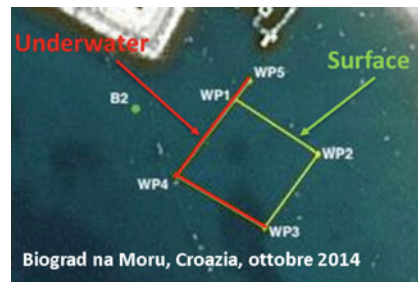


Fig. 7 Longitudinal body velocity u measured during the mission by the onboard DVL

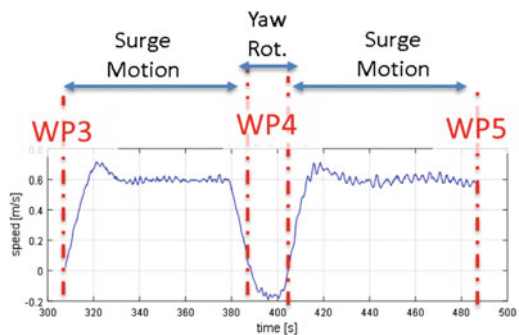
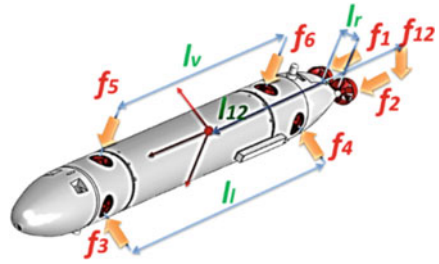


Fig. 8 Forces exerted by the rear propellers and thrusters



by propellers it is possible to calculate the corresponding vector estimated vector τ according to (12): it is worth noting that to take into account the transversal force caused by the interaction between the two rear propellers a seventh vector force called f_{12} is introduced. Relations corresponding to system are coherent with the scheme of Fig. 8. For the proposed application which should be treated as a constrained minimization of a functional with respect to a set of parameters, the authors implemented a standard least squares estimation procedure.

The optimization is performed considering admissible intervals of estimated values (hydrodynamics parameters) in order to avoid the identification of parameters with physically unfeasible or unrealistic values: as example mass and damping parameters have to be positive real numbers, their values should not exceed a maximum value which is obtained by multiplying of a factor of ten the expected results obtained from literature [5]. This procedure was repeated for the three elementary motions (surge motion, heave motion and yaw rotation) performed during the experimental campaign obtaining the estimated values M_{33}^* , M_{11}^* , M_{66}^* , D_{33}^* , D_{11}^* and D_{66}^* given in Table 1.

In order to validate the performed identification, the authors inserted the identified parameters in a 3D model of the vehicle developed in Matlab-Simulink™ [1–3].

The simulated trajectory of the full three-dimensional model imposing the same input speeds of the propellers is then compared with the known, experimental one as visible in Fig. 9, obtaining a good fitting in terms of vehicle trajectory. The maximum error (Euclidean distance) between the real trajectory of the vehicle and the simulated one is equal to 2.3 m.

Table 1 Estimated values for the main hydrodynamic parameters

M_{33}^*	M_{11}^*	M_{66}^*	D_{33t}^*	D_{11t}^*	D_{66t}^*
180 (kg)	180 (kg)	279 (kgm ²)	1230 (Ns ² m ⁻²)	58.7 (Ns ² m ⁻²)	1830 (Nms ²)

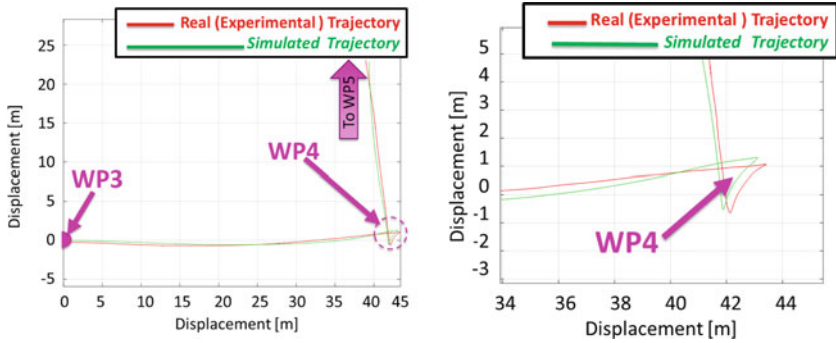


Fig. 9 Comparison between experimental trajectory of the vehicle and corresponding simulation results (on the left), detail of the rotation around WP4

$$\begin{bmatrix}
 1 & 1 & 0 & 0 & 0 & 0 & 0 & 0 & 0 & 0 & 0 & 0 & 0 & 0 & 0 \\
 0 & 0 & 1 & 1 & 0 & 0 & 0 & 0 & 0 & 0 & 0 & 0 & 0 & 0 & 0 \\
 0 & 0 & 0 & 0 & 1 & 1 & 1 & 0 & 0 & 0 & 0 & 0 & 0 & 0 & 0 \\
 0 & 0 & 0 & 0 & 0 & 0 & 0 & 1 & 1 & 0 & 0 & 0 & 0 & 0 & 0 \\
 0 & 0 & 0 & 0 & -\frac{l_v}{2} & \frac{l_v}{2} & l_{12} & 0 & 0 & 1 & 1 & 0 & 0 & 0 & 0 \\
 -\frac{l_r}{2} & \frac{l_r}{2} & \frac{l_r}{2} & -\frac{l_r}{2} & 0 & 0 & 0 & 0 & 0 & 0 & 0 & 0 & 1 & 1 & 0
 \end{bmatrix}
 \begin{matrix}
 F(t) \begin{cases} f_1(t) \\ f_2(t) \\ f_3(t) \\ f_4(t) \\ f_5(t) \\ f_6(t) \\ f_{12}(t) \end{cases} \\
 Q(t) \begin{cases} q_1(t) \\ q_2(t) \\ q_3(t) \\ q_4(t) \\ q_5(t) \\ q_6(t) \end{cases}
 \end{matrix}
 =
 \begin{bmatrix} X \\ Y \\ Z \\ K \\ L \\ M \end{bmatrix}
 \Bigg\}
 \tau
 \tag{12}$$

4 Conclusion and Future Developments

In this paper the authors introduced a fast procedure for the identification of the main hydrodynamic parameters of an AUV obtaining a good matching with the available experimental data at sea; further activities will be performed in order to verify the proposed approach on a wider population of data.

Acknowledgments This work has been supported by the European ARROWS project (www.arrowsproject.eu), that has received funding from the European Union’s Seventh Framework Programme for research, technological development and demonstration under grant agreement no. 308724.

References

1. Allotta B, Pugi L, Bartolini F, Costanzi R, Ridolfi A, Monni N, Gelli J, Vettori G, Gualdesi L, Natalini M (2013) The THESAURUS project: a long range AUV for extended exploration, surveillance and monitoring of archaeological sites. In: Proceedings of the 5th International Conference on Computational Methods in Marine Engineering V, MARINE V, pp 760–771
2. Allotta B, Pugi L, Bartolini F, Ridolfi A, Costanzi R, Monni N, Gelli J (2015) Preliminary design and fast prototyping of an autonomous underwater vehicle propulsion system. Proceedings of the Institution of Mechanical Engineers Part M: Journal of Engineering for the Maritime Environment 229(3):248–272
3. Allotta B, Caiti A, Costanzi R, Fanelli F, Fenucci D, Meli E, Ridolfi A (2016) A new AUV navigation system exploiting unscented Kalman filter. Ocean Eng 113:121–132
4. Carlton JS (2007) Marine propellers and propulsion, 2nd edn. Elsevier, Burlington, USA
5. Fossen TI (1994) Guidance and control of ocean vehicles, Wiley. ISBN 0–471-94113-1
6. Phillips AB, Turnock SR, Furlong M (2010) The use of computational fluid dynamics to aid cost-effective hydrodynamic design of autonomous underwater vehicles. Proceedings of IMechE, Part M: J Engineering for the Maritime Environment 224:239–254
7. Pivano L, Johansen TA, Smogeli ØN (2009) A four-quadrant thrust controller for marine propellers with loss estimation and anti-spin: theory and experiments. Marine Technol. 46:229–242

Braking Energy Recovery in High Speed Trains: An Innovative Model

Amedeo Frilli, Enrico Meli, Daniele Nocciolini, Simone Panconi,
Luca Pugi and Andrea Rindi

Abstract Modern railway development trend is pushing towards a strong enhancement of the energy efficiency of lines and vehicles, with particular attention to braking energy recovery. In this research work the authors have developed an innovative and numerically efficient vehicle-line coupled model, using the object oriented Simscape language: the model has been validated considering a set of experimental measurements concerning the Italian High Speed train ETR 1000 and has then be used to analyze the feasibility of the application of energy storage systems in high speed application. This analysis has shown that the use of stationary energy storage devices can provide significant energy savings even in high speed applications.

1 Introduction

Nowadays transportation still represents a significant source of CO_2 emissions worldwide [1, 2]: from this point of view, railway has started from a favorable position but its competitors (i.e. planes and cars sectors) are strongly pushing towards ever higher energetic and environmental efficiencies. Hence, there is a growing interest in the possibility to enhance the energetic performances of railway vehicles. Furthermore,

A. Frilli · E. Meli · D. Nocciolini · S. Panconi · L. Pugi (✉) · A. Rindi
Department of Industrial Engineering, University of Florence, Florence, Italy
e-mail: luca.pugi@unifi.it

A. Frilli
e-mail: amedeo.frilli@unifi.it

E. Meli
e-mail: enrico.meli@unifi.it

D. Nocciolini
e-mail: daniele.nocciolini@unifi.it

S. Panconi
e-mail: simone.panconi@unifi.it

A. Rindi
e-mail: andrea.rindi@unifi.it

due to the recent liberalization process in the railway sector and to interoperability issue, the interest to accurately calculate and measure the actual trains energy consumptions is ever increasing.

One of the most important possibility to seek for better energetic efficiencies in modern railways is the recovery of braking energy [3]: this technique is particularly interesting due to the great diffusion of train with distributed traction system. Regenerative braking allows to reduce energy consumption and also to get significant savings in terms of reduced wear and maintenance and design costs [4, 5].

The use of regenerative braking in tramways and light urban railways has been widely investigated in literature [6–9], due to the obvious advantages of such systems (e.g. the great number of braking phases); in this research work the authors have developed an innovative model useful for the analysis of the application of energy recovery systems on high speed trains, which still represents an open filed of research. The proposed model is composed of two fundamental sub-models, i.e. a train longitudinal dynamics model and a line electrical model, and is able to analyse the interactions between these different physical phenomena. The model has been developed with a modular architecture (in order to easily investigate different vehicles and lines) based on Matlab-Simulink™ and on Matlab-Simscape™, an innovative object oriented language characterized by a great numerical efficiency that allows to obtain a bidirectional correspondence between the model topology and the considered physical system (i.e. the model elements are implemented in terms of balance equations, according to the Bond-Graph approach).

The proposed coupled model has been validated considering a set of experimental measurements concerning the performances of the Italian High Speed train ETR 1000 on the Roma–Firenze High Speed line (usually denoted as “*Direttissima*”); the main characteristics of both train and line are reported in Table 1.

Table 1 Main characteristics of the ETR 1000 high speed train and of the “*Direttissima*” high speed line

Train mass	500 (t)
Axle load	17 (t)
Rotating inertia respect to train mass	4 %
UIC classification	BoBo+22+BoBo+22 +22+BoBo+22+BoBo
Motorized weight fraction	0.5 [-]
Supported electrification standards	25 kV 50 Hz, 15 kV 16.7 Hz, 3 kV DC, 1.5 kV DC
Nominal Power	9.8 (MW)
Max tractive effort	(standstill) 370 (kN)
Max speed (commercial)	360 (km/h)
Acceleration/Dec. performances	0.7 (ms ⁻²) (acc.)/1.2 (ms ⁻²) (dec.)
Line impedance ρ	About 0.05 (Ohm/km)
ESS no load voltage	3700 (V)
ESS Eq. impedance	About 0.09 (Ohm)
Mean distance between ESSs	14.7 (km)

2 Model Description

The proposed model includes a mechanical sub-model developed in Matlab-Simulink™ (see Fig. 1) which analyzes the train longitudinal dynamics and an electrical sub-model developed in Matlab-Simscape™ (see Fig. 2) which analyzes the behaviour of the electrical line, including electrical substations and stationary or on-board energy storage devices.

The longitudinal dynamics of the vehicle is calculated through a lumped parameters approach [10], using the following equation of motion:

$$m_i \ddot{x} = T - mg \sin \alpha - m (a\dot{x}^2 + b\dot{x} + c + d(r)), \tag{1}$$

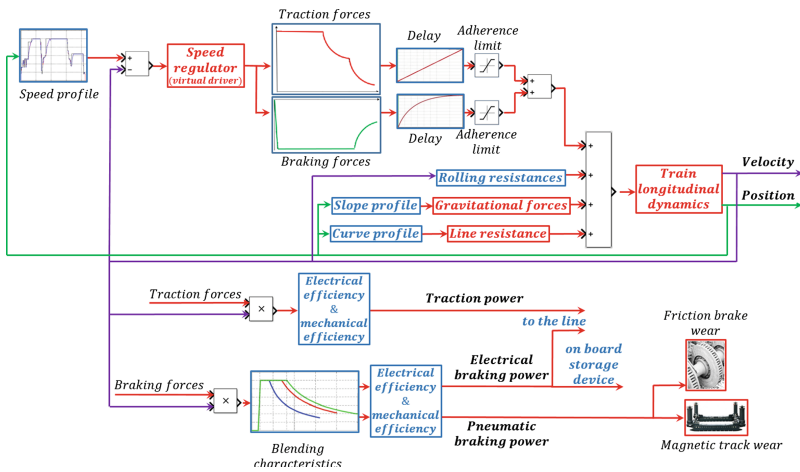
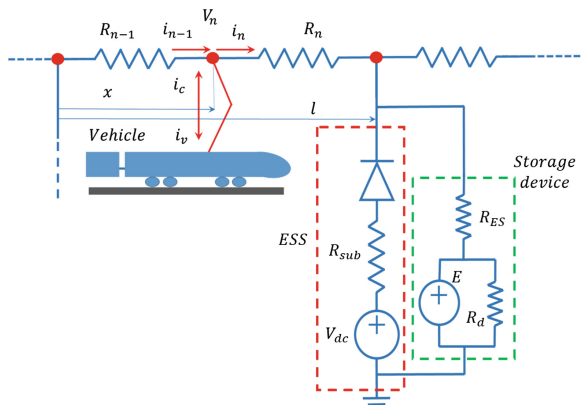


Fig. 1 Architecture of the mechanical sub-model

Fig. 2 Architecture of the electrical sub-model



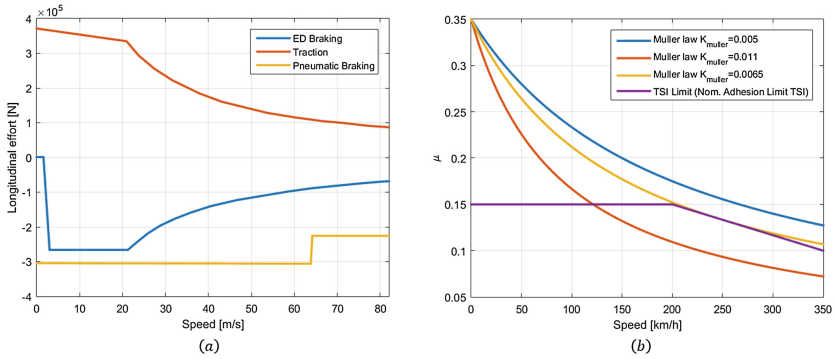


Fig. 3 Traction and braking performances of ETR 1000 high speed train (referred to 3 kV DC line)

where m_i is the train mass of the vehicle, x is the vehicle position, $\alpha(x)$ is the line slope, $a, b, c, d(r)$ are coefficients employed in the calculation of motion resistances and T are the longitudinal efforts due to the traction and braking system. Traction and braking effort are calculated according to the train performances as a function of the vehicle speed (see Fig. 3a); a further limitation due to limited wheel-rail adhesion along the line can be introduced considering TSI (acronym of Technical Specifications for Interoperability) limits or the Muller model (see Fig. 3b):

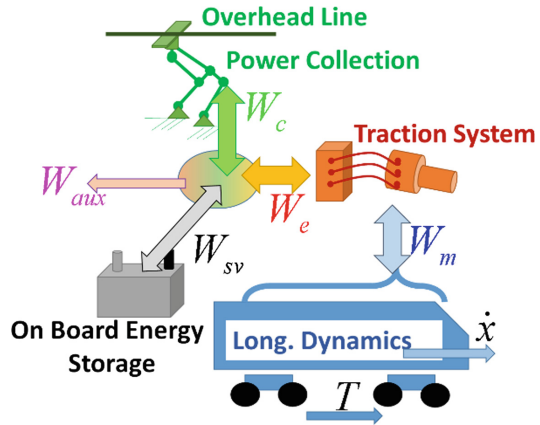
$$\begin{aligned}
 T_T &\leq T_{Tmax} = k_m m g \mu = k_m \frac{\mu_0}{1 + K_{muller} \dot{x}_{kmh}}, \\
 T_T &\geq T_{Bmax} = -m g \mu = -m g \frac{\mu_0}{1 + K_{muller} \dot{x}_{kmh}},
 \end{aligned}
 \tag{2}$$

where k_m is the ratio between the vertical load on motorized axis and the total weight of the train and μ_0 is the static friction factor.

The train kinetic energy dissipation during the braking phases can be due both to traction systems and conventional brakes (the model allows to choose the blending strategy). The complete power balance between the vehicle and the line is reported in Fig. 4: the power part handled by the traction system can be reused (i.e. the fraction W_c is transferred to the line while the part W_{sv} is stored in proper devices) or dissipated on on-board resistors; furthermore, the power contribution denoted as W_{aux} is used to fed on-board auxiliary systems.

The electrical sub-model includes the contact line and the Electrical Sub-Stations (ESSs), which have been represented as ideal voltage generators connected in series with a resistance and a diode. The mechanical sub-model provides as input to the line the power W_c collected in correspondence of the pantograph (the line is able both to provide the power required by the train during traction phases and to receive the power produced by the train during the braking phases); furthermore, the vehicle divides the contact line (within two adjacent substations) in two longitudinal sections, whose impedance values can be calculated as follows:

Fig. 4 Power fluxes at the pantograph involved in the vehicle dynamics, considering the interactions with the electrical line



$$\begin{aligned} R_1 &= \rho x, \\ R_2 &= \rho (l - x), \end{aligned} \tag{3}$$

where ρ is the linear resistivity of the line. The pantograph node electrical balance can be written as follows (see Fig. 2):

$$\begin{aligned} i_{n-1} - i_n &= i_v + i_c \\ V_{n+1} &= V_n - R_n \cdot i_n, \end{aligned} \tag{4}$$

where i_n is the current leaving the node, V_n is the voltage, i_v is current provided to the train, i_c is the current due to a possible on-board storage device and R_n is the impedance of the considered line part. The stationary energy storage devices which can be connected in parallel with the ESSs (i.e. batteries and supercapacitors) are shown in Fig. 2 and have been modelled as ideal voltage generators (whose voltage value is proportional to the integral of current) with a parallel and a series resistance.

3 Experimental Validation and Energy Storage Feasibility Analysis

The proposed model has been experimentally validated considering a traction manoeuvre of the ETR 1000 high speed train within the “*Direttissima*” line: the train starts from standstill and accelerates with a full traction effort to a speed equal to 250 km/h. Figure 5 shows the experimental validation in terms of vehicle speed: it is possible to highlight how the calculated speed profile is in good agreement with the measured one. The biggest error can be found in a speed range where during the tests some axle skidding phenomena occurred (i.e. the proposed model does not

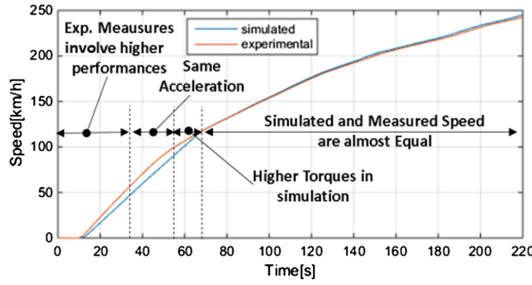


Fig. 5 Comparison between the measured and numerical speed profile (ETR 1000 on the Firenze–Roma high speed line)

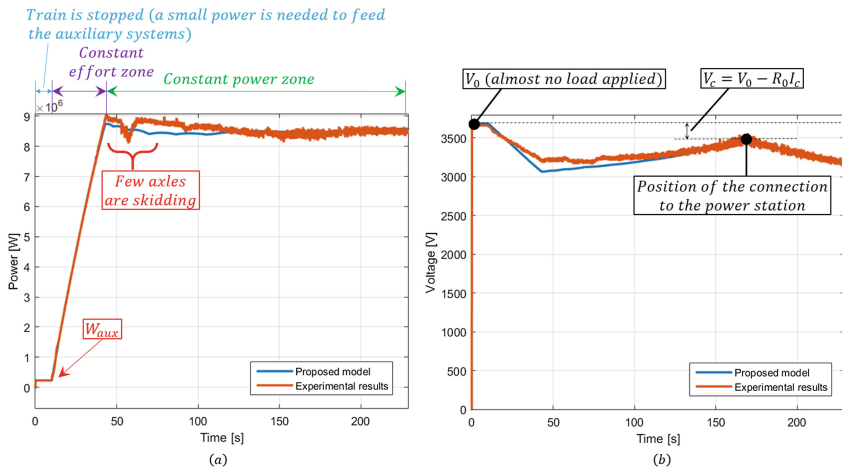


Fig. 6 Comparison between the measured and calculated power consumption W_c (a) and voltage V_c (b)

include an axle skidding controller yet). Figure 6a, b show the comparison between the numerical and experimental power consumption and line voltage: there is a good agreement between experimental and simulated results and it is possible to highlight how the mechanical and electrical efficiencies and the no-load voltage V_0 considered in the model provide a good approximation of the behaviour of the real train-line system. In the first part of the test, i.e. while the train is stopped, the only power consumption is due to on-board auxiliary systems.

After the validation phase, the model has been used to investigate the feasibility of energy storage systems within a high speed line performing a set of simulations considering the ETR 1000 and the “Direttissima” line, with a speed profile which includes a first acceleration to 70 m/s, a coasting phase and a final braking. For the sake of synthesis only the results referred to the most promising solution (i.e. stationary energy storage devices in correspondence of the ESSs) are reported. Figure 7a

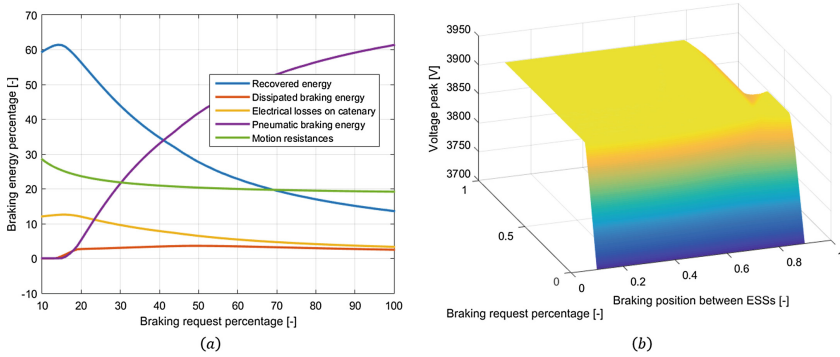


Fig. 7 Braking energy percentages as a function of the braking effort percentage (a) and braking line voltage peak as a function of the braking effort percentage and of the braking position, voltage peak limited to 3900 V

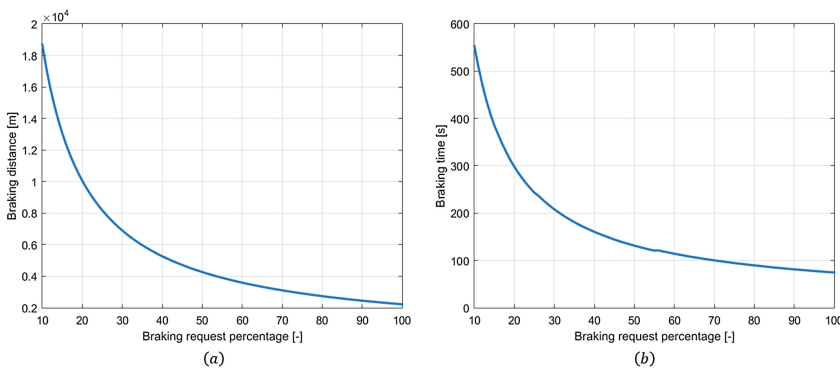


Fig. 8 Braking distance (a) and time (b) as a function of the braking effort percentage

shows the energy fluxes involved in the braking phase as a function of the braking effort request: the recovered energy shows a maximum with a braking request of about 20 %; however in that operating condition the braking distance and the braking time (see Fig. 8a, b) are too high to be acceptable. A good compromise from the energy recovery point of view can be found with a braking effort equal to about 50 %, where the recovered energy still represents a significant percentage and the braking distance and time are consistent with high speed application. Figure 7b shows the line voltage peak in correspondence of the braking phase as a function of the braking request percentage and of the position of the braking starting point between two adjacent ESSs, using a voltage peak limiter set to 3900 V to better represent the behaviour of the real line. The peak value increases steeply up to a 20 % braking request and then is saturated by the voltage limiter. Considering the braking starting point, the voltage is below the limit value only near the initial substation, where the storage device can manage all the energy flux provided by the train.

The proposed model proved to be highly efficient from the computational point of view, allowing to simulate the behaviour of the train in the entire line (about 250 km) in about 5 s.

4 Conclusions and Future Developments

Nowadays the interest towards energetic optimization of railway systems is constantly increasing, thanks to the new possibilities offered by regenerative braking. In this research work the authors developed an innovative coupled train-line model useful to investigate the effect of energy storage devices on energy consumption. The model has been validated considering a set of experimental data concerning the Italian high speed train ETR 1000 and has then been used to investigate the feasibility of braking energy recovery within a high speed line. The model, characterized by a high numerical efficiency, has shown that stationary storage device can provide significant savings even with high speed trains.

The research work will continue in order to further validate the proposed model with new test cases and to further develop the model itself, including more sophisticated representations of the energy storage devices and the possibility to simulate the simultaneous passage of more than a single train.

References

1. Fridell E et al (2011) On-board measurements of particulate matter emissions from a passenger train. *Proc Inst Mech Eng Part F J Rail Rapid Transit* 225(1):99–106
2. Kamal WA (1997) Improving energy efficiency—the cost-effective way to mitigate global warming. *Energy Convers Manag* 38(1):39–59
3. Hillmansen S, Roberts C (2007) Energy storage devices in hybrid railway vehicles: a kinematic analysis. *Proc Inst Mech Eng Part F J Rail Rapid Transit* 221:135–143
4. Barrero R, Tackoen X, Van Mierlo J (2010) Stationary or onboard energy storage systems for energy consumption reduction in a metro network. *Proc Inst Mech Eng Part F J Rail Rapid Transit* 224:207–225
5. Ceraolo M, Lutzemberger G (2014) Stationary and on-board storage systems to enhance energy and cost efficiency of tramways. *J Power Sour* 264(15):128–139
6. Falvo MC et al (2016) Energy savings in metro-transit systems: a comparison between operational Italian and Spanish lines. *Proc Inst Mech Eng Part F J Rail Rapid Transit* 230(2):345–359
7. González-Gil A, Palacin R, Batty P (2014) Optimal energy management of urban rail systems: key performance indicators. *Energy Convers Manag* 90:282–291
8. Peña-Alcaraz M et al (2012) Optimal underground timetable design based on power flow for maximizing the use of regenerative-braking energy. *Proc Inst Mech Eng Part F J Rail Rapid Transit* 226(4):397–408
9. Ware DK, Jones RNH (1992) Recent developments in light rail systems. *Proc Inst Mech Eng Part F J Rail Rapid Transit* 206(1):47–65
10. Allotta B, Pugi L (2013) *Meccatronica: Elementi di Trazione Elettrica*. Esculapio Editore, Bologna

Dynamic Model and Instability Evaluation of an Articulated Mobile Agri-Robot

G. Carabin, R. Vidoni, F. Mazzetto and A. Gasparetto

Abstract Stability, in particular in outdoor sloped conditions, is one of the most important requirements for design safe and effective future mobile robotic platforms. In this work, the authors' recent results on the study and development of an articulated mobile robot for agricultural and forestry activities in hilly/mountain environments are presented. First of all, a dynamic model for the stability analysis of a generic articulated platform has been designed and implemented. Then, different practical working conditions have been simulated to assess the stability of the system; possible stabilizing actions when travelling on a sloped surface on the steering angle, velocity and central joint have been finally evaluated and discussed.

Keywords Articulated joint · Mobile robot · Stability · Agricultural robotics

1 Introduction

Among different possible mobile robot architectures, the 4-wheeled articulated kinematics is one of the most promising [1]. Basically, it is composed of two main parts, i.e. front (f) and rear (r), interconnected by an articulated 2 Degrees of Freedom (DoF) joint. The first DoF, i.e. yaw angle, is controlled and allows steering. The second DoF is passive, i.e. roll angle, allowing to adapt to uneven terrains.

G. Carabin · R. Vidoni (✉) · F. Mazzetto
FaST (Faculty of Science and Technology), Free University of Bolzano,
39100 Bolzano, Italy
e-mail: renato.vidoni@unibz.it

G. Carabin
e-mail: giovanni.carabin@unibz.it

F. Mazzetto
e-mail: fabrizio.mazzetto@unibz.it

A. Gasparetto
DPIA (Dipartimento Politecnico di Ingegneria e Architettura), University of Udine,
33100 Udine, Italy
e-mail: gasparetto@uniud.it

With this architecture a minimal steering radius, if compared with other classical kinematics, is achievable. In literature, monitoring and predicting the stability of a mobile platform is a well treated problem. Indeed, the stability of multi-legged or -wheeled robots has been widely investigated since the sixties, e.g. [2], in particular for rigid chassis machines. Two main classes of stability criteria have been proposed: (quasi-)static and dynamics-based criteria. These can also be grouped in: *distance-based* [2], *angle-based* [3], *energy-based* [4], *moment-based* [5] and *force-based* criteria [6], according to the idea behind the formulation. Recent stability studies on articulated architectures refer to tractors/machines with the joint on the front axle [7, 8] demonstrated how, in addition to the “standard” stability condition (type II instability), the passive roll DoF creates a second critical stability condition that results in the triangle which is made by considering the position of two wheels of a vehicle half and the joint (type I instability).

2 Articulated Mobile Robot Model

The kinematic and dynamic model is based on the main basic hypothesis of the Guzzomi’s work [7] except for the robot speed. These are: (a) the roll DoF of the articulated joint is considered frictionless; (b) the robot does not slide down the slope, due to a non-limiting coefficient of friction between surface and tyres; (c) tyres are considered stiff, so the contact surfaces result in discrete points (not areas); (d) the joint mass is negligible, so it does not affect the dynamic behaviour.

By referring at Fig. 1a, the articulated robot kinematics can be explained. The front “F” and rear “r” parts are connected by a 2 DoF joint made of a first revolute DoF, i.e. the yaw β angle, and a second passive revolute DoF, i.e. the roll α angle. In Table 1, the geometric parameters of the model shown in Fig. 1a are explained.

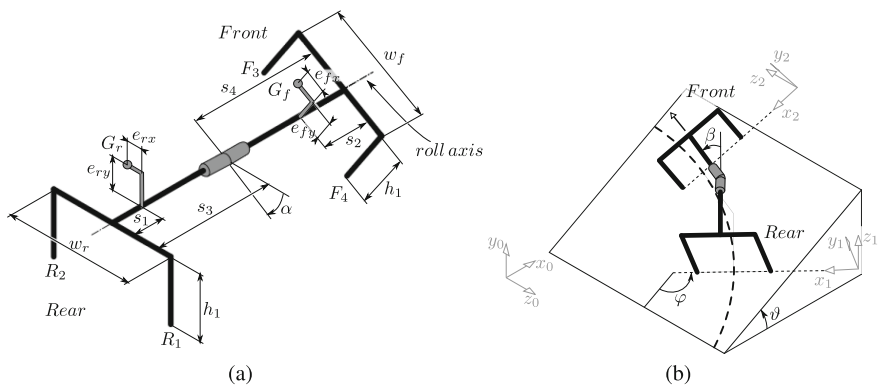


Fig. 1 Articulated robot: **a** kinematic model ($\alpha \neq 0$ and $\beta = 0$), **b** orientation angles and reference systems ($\alpha = 0$ and $\beta \neq 0$)

Table 1 Main parameters of the kinematic model

G_r	CoG of the rear part	s_4	Distance from front axle to central joint
G_f	CoG of the front part	s_1	Rear CoG distance from rear axle
R_1	Contact point between rear wheel 1 and surface	e_{rx}	Rear CoG x distance from rear midplane
		e_{ry}	Rear CoG y height above roll axis
R_2	Contact point between rear wheel 2 and surface	s_2	Front CoG distance from front axle
		e_{fx}	Front CoG x distance from front midplane
F_3	Contact point between front wheel 3 and surface	e_{fy}	Front CoG y height above roll axis
		w_r	Rear track width
F_4	Contact point between front wheel 4 and surface	w_f	Front track width
		h_1	Roll axis height from ground
α	Roll angle between rear and front part	m_r	Rear mass
β	Yaw angle between rear and front part	m_f	Front mass
s_3	Distance from rear axle to central joint		

In order to study the system configurations, both travelling along a slope and turning among different rows, the robot has been considered travelling a circle with a constant speed v on a sloped surface, i.e. ϑ . A global coordinate system $(x_0 y_0 z_0)$ and two local ones $(x_1 y_1 z_1)$ and $(x_2 y_2 z_2)$, rigidly attached on the moving rear and front robot parts respectively, are defined. By naming φ the robot orientation with respect to the maximum slope direction, β the trajectory followed by the robot and α the surface conformation ($\alpha = 0$ implies a plane surface), see Fig. 1b, the kinematics of the motion can be represented.

2.1 Dynamic Model

The instability of an articulated robot can be subdivided in phase I and II [7]. By increasing the slope, the force distribution on the four wheels changes according to the configuration and system properties. Instability occurs when one of the four reaction forces falls to zero. After that, the roll moment equilibrium is not satisfied, one wheel loses the contact and the phase I instability occurs.

As drawn in Fig. 2a, b, two \mathbf{F}_{Gr} and \mathbf{F}_{Gf} forces are present on the rear and front CoGs, given by the vectorial sum between weight \mathbf{P}_i and centrifugal \mathbf{F}_{ci} forces. These are counteracted by the four reaction forces \mathbf{F}_{r1} , \mathbf{F}_{r2} , \mathbf{F}_{f3} and \mathbf{F}_{f4} . Through the central joint, both forces (\mathbf{F}_{jr} and \mathbf{F}_{jf}) and moments (\mathbf{M}_r e \mathbf{M}_f) are exchanged. The two forces \mathbf{F}_{Gr} and \mathbf{F}_{Gf} and, due to the absence of friction, the moment $M_{f,z}$ are known.

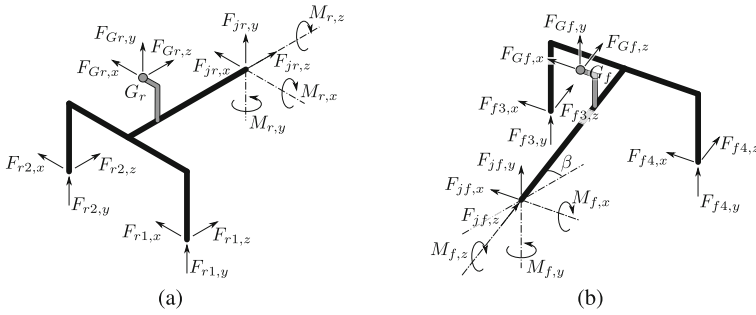


Fig. 2 Dynamic model: **a** rear part, **b** front part

To study the stability, the four normal force components acting on the wheels, i.e. $F_{r1,y}$, $F_{r2,y}$, $F_{f3,y}$ and $F_{f4,y}$, are needed. Thus, it is advisable to reduce the system dimension to improve the computational speed with respect to solve the whole system made of 23 equations. By exploiting the joint forces and torques relationships as well as the ones between the exchanged forces on the wheels and those acting on the CoGs, the problem can be reformulated and simplified from the initial 23 to 6 unknowns: F_{r1} , F_{r2} , F_{f3} , F_{f4} , $M_{f,x}$ and $M_{f,y}$. In such a manner, six equilibrium equations in 6 unknowns (F_{r1} , F_{r2} , F_{f3} , F_{f4} , $M_{f,x}$ and $M_{f,y}$) can be written:

$$F_{r1} + F_{r2} + F_{f3} + F_{f4} = -F_{Gr} - F_{Gf} \quad (1)$$

$$M_{f,x} + F_{f3} (-k_{f3}s_4 - k_{fz}h_1) + F_{f4} (-k_{f3}s_4 - k_{fz}h_1) = F_{gf} [k_{fy} (s_4 - s_2) + k_{fz}e_{fy}] \quad (2)$$

$$M_{f,y} + F_{f3} \left(k_{fx}s_4 - k_{fz} \frac{w_f}{2} \right) + F_{f4} \left(k_{fx}s_4 + k_{fz} \frac{w_f}{2} \right) = F_{gf} [-k_{fx} (s_4 - s_2) + k_{fz}e_{fx}] \quad (3)$$

$$M_{f,z} + F_{f3} \left(k_{fx}h_1 + k_{fy} \frac{w_f}{2} \right) + F_{f4} \left(k_{fx}h_1 - k_{fy} \frac{w_f}{2} \right) = F_{gf} (k_{fx}e_{fy} - k_{fy}e_{fx}) \quad (4)$$

$$M_{r,x} + F_{r1} (k_{ry}s_3 - k_{rz}h_1) + F_{r2} (k_{ry}s_3 - k_{rz}h_1) = F_{gr} [-k_{ry} (s_3 - s_1) - k_{rz}e_{ry}] \quad (5)$$

$$M_{r,z} + F_{r1} \left(k_{rx}h_1 - k_{ry} \frac{w_r}{2} \right) + F_{r2} \left(k_{rx}h_1 + k_{ry} \frac{w_r}{2} \right) = F_{gr} (k_{rx}e_{ry} - k_{ry}e_{rx}) \quad (6)$$

where $M_{f,z} = 0$, $M_{r,x} = -M_{f,x} \cos \alpha \cos \beta + M_{f,y} \sin \alpha \cos \beta$, $M_{r,z} = M_{f,x} \cos \alpha \sin \beta - M_{f,y} \sin \alpha \sin \beta$, $(k_{rx}, k_{ry}, k_{rz}) = \frac{\mathbf{F}_{Gr}}{\|\mathbf{F}_{Gr}\|}$, and $(k_{fx}, k_{fy}, k_{fz}) = \frac{\mathbf{F}_{Gf}}{\|\mathbf{F}_{Gf}\|}$.

The rear and front weight forces components can then be computed. Moreover, the rear and front centrifugal forces components while, see Fig. 3a, are:

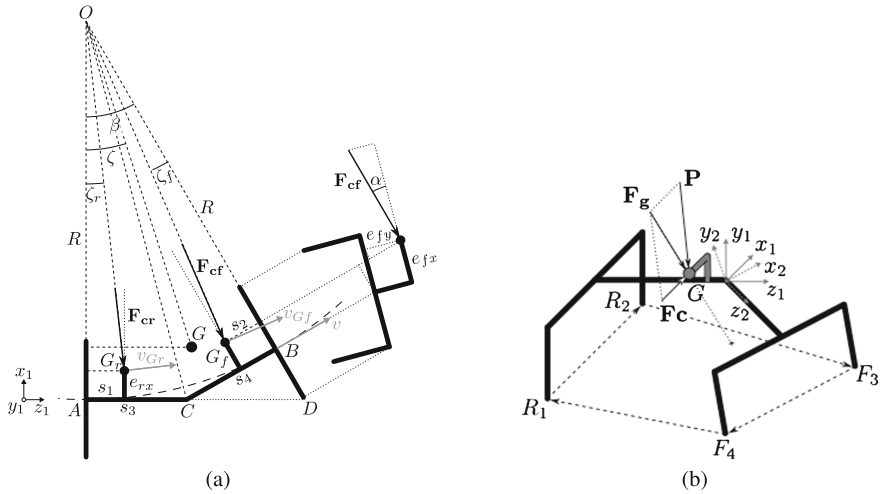


Fig. 3 a Centrifugal forces. b Phase II instability

$$\begin{cases} F_{cr,x} \\ F_{cr,y} \\ F_{cr,z} \end{cases} = F_{cr} \begin{cases} -\cos \zeta_r \\ 0 \\ \sin \zeta_r \end{cases} \quad \begin{cases} F_{cf,x} \\ F_{cf,y} \\ F_{cf,z} \end{cases} = F_{cf} \begin{cases} -\cos \zeta_f \cos \alpha \\ \sin \alpha \\ -\sin \zeta_f \cos \alpha \end{cases} \quad (7)$$

where ζ_r and ζ_f angles are computed as:

$$\zeta_r = \arctan \left(\frac{s_1}{R - e_{rx}} \right) \quad \zeta_f = \arctan \left(\frac{s_2}{R - e_{fx} \cos \alpha + e_{fy} \sin \alpha} \right) \quad (8)$$

Given a β angle, it is possible to compute the steering radius R in the following manner (see Fig. 3a):

$$R = \frac{\overline{AD}}{\tan \beta} = \frac{\overline{AC} + \frac{\overline{BC}}{\cos \beta}}{\tan \beta} = \frac{s_3 \cos \beta + s_4}{\sin \beta} \quad (9)$$

Now, by considering as reference the rear/front axle central point speed v , the CoGs speeds v_{G_r} and v_{G_f} and the centrifugal forces can be computed (see Fig. 3):

$$v_{Gi} = v \frac{R_{Gi}}{R} \quad R_{Gi} = \frac{s_j}{\sin \zeta_i} \quad F_{ci} = \frac{m_i v_{Gi}^2}{R_{Gi}} = \frac{m_i v^2 R_{Gi}}{R^2} \quad (10)$$

with $i = r, f$ and $j = 1, 2$. The vectorial sum between weight and centrifugal forces allows then to compute the two forces F_{G_r} and F_{G_f} .

The phase II instability detection method is based on force moments evaluation. The dashed lines in Fig. 3b represent the four oriented axes that pass through the four contact points. The robot could rotate around these axes, if there is no moment equilibrium. The force \mathbf{F}_g , that acts on the overall Center of Gravity G , generates four different moments on every axis. So, in a given robot configuration, if all the moments are positive, there is stability; if one of the moments becomes negative, the robot starts overturning. The global CoG coordinates can be obtained starting from G_r and G_f and, then, the force \mathbf{F}_g , expressed with respect to the $(x_1 y_1 z_1)$ reference system, can be computed as $\mathbf{F}_g = \mathbf{P} + \mathbf{F}_c$, where $P = (m_r + m_f)g$, and $F_c = \frac{(m_r + m_f)v^2 R_G}{R^2}$ with $R_G = \frac{G_z}{\sin \zeta}$ (see Fig. 3a).

3 Numerical Evaluation

The stability model has been implemented in a Matlab™ simulator. Given information on the geometric and physical parameters of the robot (see Table 2), and on the configuration in terms of α , β and φ angles, via an iterative method the stability limit angles of phase I, i.e. $\vartheta_{lim,I}$, and phase II, i.e. $\vartheta_{lim,II}$, are found. In Fig. 4, the output of the simulator is reported: the top plot refers to the limit stability angles while the central plot indicates which wheel firstly detaches from the terrain when phase I instability occurs; finally, the plot on the bottom reports the angular difference between phase II and phase I critical angles.

Now, the centrifugal terms influence on the emulator stability is evaluated. A constant steering angle, i.e. $\beta = 15^\circ$, and three different speeds ($v = 0 \text{ m/s}$, $v = 0.75 \text{ m/s}$ and $v = 1.5 \text{ m/s}$) are considered. In Fig. 4, the curve with no centrifugal influence, i.e. $v = 0 \text{ m/s}$ quasi-static approach, and the others are reported.

In the simulated case it can be easily highlighted how the centrifugal force plays against stability, both in phase I and II, when φ is inside the range of about $-80^\circ (280^\circ) \div 80^\circ$ (i.e. centrifugal forces are directed downstream). Furthermore this range tends to become larger if the speed increases. Varying the robot speed could represent a driving strategy, or a part of it, combined with a blocking action on the joint free DoF; indeed, in that manner, a safer stability state could be reached while maintaining the same configuration. Considering the range where the centrifugal effect plays against the stability, decreasing the speed helps increasing the stability. This strategy, if $v > 0.75 \text{ m/s}$, guarantees a higher angular margin with respect to blocking the joint. Below that speed the two effects are comparable. Outside this

Table 2 Robot emulator geometric and physical parameters

s_1 [mm]	s_2 [mm]	s_3 [mm]	s_4 [mm]	w_r [mm]	w_f [mm]	h_1 [mm]	e_{rx} [mm]	e_{fx} [mm]	e_{ry} [mm]	e_{fy} [mm]	m_r [kg]	m_f [kg]
26	55	200	200	240	180	94	0	0	20	14	1.34	1.84

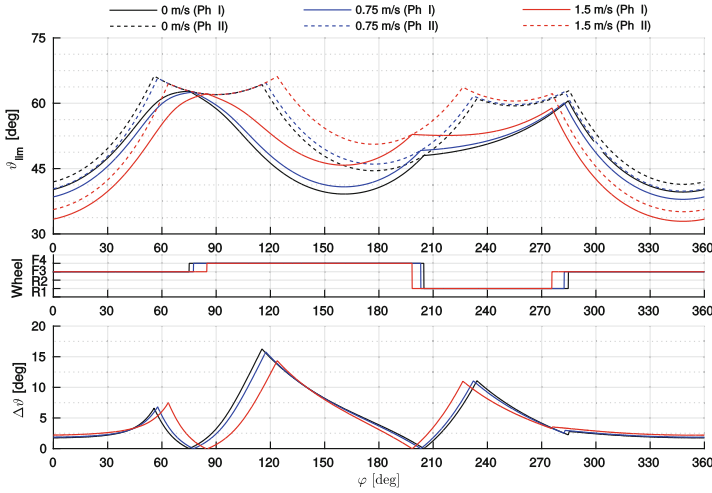


Fig. 4 Stability maps at different speeds ($\beta = 15^\circ$)

range, decreasing the speed becomes a dangerous manoeuvre. Considering $\varphi \simeq 0$, i.e. the robot on the lower point of the circular trajectory, the centrifugal effect is maximum. In this condition, it is interesting to evaluate this stability angle reduction. At speed $v = 0 \text{ m/s}$, the phase I stability angle is about 40° , at $v = 0.75 \text{ m/s}$ the reduction is about 2° , and at $v = 1.5 \text{ m/s}$ it is about 7° . For the phase II case, the values are almost the same. Now, if the angular margin that is gained by blocking the free joint DoF (see the bottom plot of Fig. 4), it could be seen that the centrifugal forces affect only the curves offset.

The transition between different sloped surfaces is another important case to be evaluated. In order to do so, the following condition has been considered:

- the base surface is inclined by an angle of $\vartheta = 15^\circ$;
- the robot runs crosswise the slope ($\varphi = 0^\circ$);
- on the base surface it is located another plane (obstacle) that gradually increases its inclination from ϑ to $\vartheta + \alpha$;
- this obstacle is overcome firstly by the front part, and then by the rear one.

In Fig. 5 the results are presented. Firstly considering the front part overcoming the obstacle, by increasing α , i.e. higher obstacle inclination, the angular margin for the roll-over decreases. However, the phase I and phase II have different negative slopes (less in the second case), so it is possible to gain stability margin by blocking the free DoF. It can be noticed how the instability concerns only the front part, but with the base inclination considered, $\vartheta = 15^\circ$, the roll-over does not occur (i.e. the $\vartheta_{lim} - \vartheta$ values reported in the figure is always positive). When the rear part overcomes the obstacle, two different phase I instability behaviours can be observed. Until $\alpha < 8^\circ$, the angle at which instability occurs remains constant; indeed, in this configuration, the front part is the one more critical and it is not influenced by an α

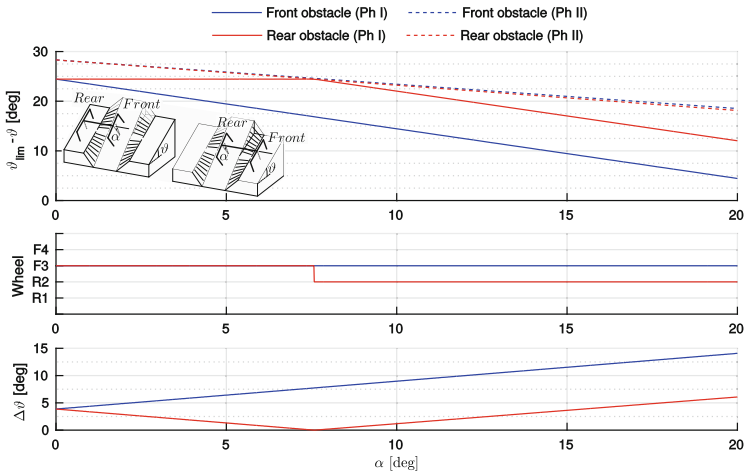


Fig. 5 Front and rear parts passing the obstacle (15° of plane inclination)

variation. When $\alpha > 8^\circ$, the rear part becomes the most critical in terms of phase I stability and the angular margin decreases with α . Also in this case the phase II has a negative constant slope, thus the support polygon reduces its area and the stability margin is reduced.

4 Conclusion

In this paper, an articulated kinematics has been chosen as basis of a future mobile robot able to operate in hilly terrains. After the definition of the dynamic model, the two main instabilities of the chosen platform has been discussed and a stability criterion chosen. The implemented model have been exploited for evaluating the critical configurations on different slopes; after that, given the importance of the working speed and of the current slope, the possible stabilizing effect of speed and steering angle variation, together with a blocking of the joint passive DoF have been simulated and highlighted.

References

1. Vidoni R, Bietesato M, Gasparetto A, Mazzetto F (2015) Evaluation and stability comparison of different vehicle configurations for robotic agricultural operations on side-slopes. *Biosyst Eng* 129:197–211
2. McGhee R, Frank A (1968) On the stability properties of quadruped creeping gaits. *Math. Biosci.* 3:331–351

3. Papadopoulos E, Rey D (2000) The force-angle measure of tipover stability margin for mobile manipulators. *Veh Syst Dyn* 33:29–48
4. Davidson JK, Schweitzer G (1990) A mechanics-based computer algorithm for displaying the margin of static stability in four-legged vehicles. *Trans ASME J Mech Des* 112:480–487
5. Lee J, Park J, Lee B (2009) Turnover prevention of a mobile robot on uneven terrain using concept of stability space. *Robotica* 27:641–652
6. Agheli M, Nestinger S (2012) Study of the foot force stability margin for multi-legged/wheeled robots under dynamic situations. In: 2012 IEEE/ASME International Conference on Mechatronics and embedded systems and applications (MESA), pp 99–104, July 2012
7. Baker V, Guzzomi AL (2013) A model and comparison of 4-wheel-drive fixed-chassis tractor rollover during phase I. *Biosyst Eng* 116(2):179–189
8. Li Z, Mitsuokab M, Inoueb E, Okayasub T, Hiraib Y (2015) Development of stability indicators for dynamic phase I overturn of conventional farm tractors with front axle pivot. *Biosyst Eng* 134:55–57

NVH Analysis of Automotive Components: A Carbon Fiber Suspension System Case

Alessandro Fasana, Massimiliana Carello, Alessandro Ferraris,
Andrea Airale and Davide Berti Polato

Abstract This paper presents the application of a modal parameter estimation technique, namely the Linear Identification by Polynomial Expansion in the Z-domain (LIPEZ) method, to automotive carbon fibre components. In particular, a leaf spring was chosen for its simple geometry and a door panel of an electric vehicle for its high influence in global NVH characteristics of vehicles. Both elements were experimentally tested with free-free boundary conditions under a random input force; the same test is reproduced at simulation level in order to perform a results correlation.

Keywords Modal parameter identification · Z-domain · FEM · NVH · FRF · CFRP component

1 Introduction

Over the last few decades, a number of papers dealing with the problem of modal parameters estimation of vibrating structures has been presented. As a matter of fact, both the complexity of the methods and the expectations of the analysts have increased and is now compulsory to be able to cope with Multi Input Multi

A. Fasana · M. Carello (✉) · A. Ferraris · A. Airale · D.B. Polato
Politecnico di Torino, Torino, Italy
e-mail: massimiliana.carello@polito.it

A. Fasana
e-mail: alessandro.fasana@polito.it

A. Ferraris
e-mail: alessandro.ferraris@polito.it

A. Airale
e-mail: andrea.airale@polito.it

D.B. Polato
e-mail: davide.ber ti.polato@polito.it

Output MIMO (and even output only) systems and large data sets. The LIPEZ method adopted in this paper starts from the rational fraction polynomials (RFP) representation of the frequency response function (FRF) and, with the aim of defining a small and well-conditioned set of linear equations, expounds a total least square method in the Z-domain. In particular, the method is applied to two automotive components which are also reproduced at simulation level with FEM software in order to perform a correlation analysis. The chosen automotive components include a leaf spring, because of its simple geometry, and a door panel, because of its influence in vehicle global NVH characteristics. Both components are made with structural CFRP whose mechanical properties has been previously defined according to the Oberst test method [1–3].

2 Outline of the LIPEZ Method

For a linear and time invariant system with n degrees of freedom (DOFs), the FRF $H(\Omega)$ can be expressed in the form [4]:

$$H_k = \sum_{r=1}^{2n} A_r \frac{z_k}{z_k - z_r} \quad (1)$$

$$H_k = H(i\Omega_k)$$

$$\Omega_k = (k-1)\Delta\Omega = (k-1)2\pi\Delta f = \pi f_s(k-1)/(N-1)$$

$$i = \sqrt{-1}$$

Δf is the frequency resolution, N is the number of spectral lines and $k = 1, \dots, N$. The terms related to the Z-transform are:

$$z_r = e^{s_r \Delta t} \quad (2)$$

$$z_k = e^{i(k-1)\Delta\Omega\Delta t} = e^{i\pi(k-1)(N-1)} \quad (3)$$

where the poles s_r are linked to the natural angular frequencies ω_r and damping ratios ξ_r by the expression $s_r = -\xi_r \omega_r + i\omega_r \sqrt{1 - \xi_r^2}$. The sum in Eq. (1) can be converted in the following RFP expression:

$$H_k = \frac{b_1 z_k + \dots + b_{2n} z_k^{2n}}{a_0 + a_1 z_k + \dots + a_{2n-1} z_k^{2n-1} + z_k^{2n}} \quad (4)$$

where the $4n$ unknown coefficients a_0, \dots, a_{2n-1} and b_1, \dots, b_{2n} are real valued [4]. Equation (4) can be written for N spectral lines to get:

$$\begin{bmatrix} H_1 & H_1 z_1 & \dots & H_1 z_1^{2n-1} \\ H_2 & H_2 z_2 & \dots & H_2 z_2^{2n-1} \\ \vdots & \vdots & \ddots & \vdots \\ H_N & H_N z_N & \dots & H_N z_N^{2n-1} \end{bmatrix} \begin{Bmatrix} a_1 \\ a_2 \\ \vdots \\ a_{2n-1} \end{Bmatrix} - \begin{bmatrix} z_1 & z_1^2 & \dots & z_1^{2n} \\ z_2 & z_2^2 & \dots & z_2^{2n} \\ \vdots & \vdots & \ddots & \vdots \\ z_N & z_N^2 & \dots & z_N^{2n} \end{bmatrix} \begin{Bmatrix} b_1 \\ b_2 \\ \vdots \\ b_{2n} \end{Bmatrix} = \begin{Bmatrix} H_1 z_1^{2n} \\ H_2 z_2^{2n} \\ \vdots \\ H_N z_N^{2n} \end{Bmatrix} \tag{5}$$

or, in a more compact form:

$$[\mathbf{A} - \mathbf{B}] \begin{Bmatrix} \mathbf{a} \\ \mathbf{b} \end{Bmatrix} = \mathbf{w} \tag{6}$$

When many FRFs are considered, e.g. NFRF, matrix \mathbf{B} and vector \mathbf{a} do not change and the system becomes:

$$\begin{bmatrix} \mathbf{A}_1 \\ \vdots \\ \mathbf{A}_{NFRF} \end{bmatrix} \mathbf{a} + \begin{bmatrix} -\mathbf{B} & \dots & 0 \\ \vdots & \ddots & \vdots \\ 0 & \dots & -\mathbf{B} \end{bmatrix} \begin{Bmatrix} \mathbf{b}_1 \\ \vdots \\ \mathbf{b}_{NFRF} \end{Bmatrix} = \begin{Bmatrix} \mathbf{w}_1 \\ \vdots \\ \mathbf{w}_{NFRF} \end{Bmatrix} \tag{7}$$

The linear system of Eq. (7) has $2n(NFRF + 1)$ unknowns, i.e. the elements of the vectors \mathbf{a} and \mathbf{b}_m , and can be solved if $N \geq 2n(1 + 1/NFRF)$. The above procedure is indeed correct but can be time consuming while implementing, especially when large data sets are analyzed ($NFRF \gg 1$) and n has to vary (e.g. to define a stabilization chart). It is possible to develop a least square procedure to solve Eq. (7) with very good numerical performances [4]. The problem boils down to:

$$\mathbf{R}\mathbf{a} = \mathbf{r} \tag{8}$$

Matrix $\mathbf{R} \in \mathfrak{R}^{2n \times 2n}$ and vector $\mathbf{r} \in \mathfrak{R}^{2n \times 1}$ contains the information of all the measured FRFs but a system of only $2n$ real linear equations has to be solved. Moreover, because of the formulation in the Z -domain, matrix \mathbf{R} is well conditioned and the solution vector \mathbf{a} is very reliable. The poles $s_r = \ln z_r / \Delta t$ can then be obtained by using the equation:

$$a_0 + a_1 z + \dots + a_{2n-1} z^{2n-1} + z^{2n} = 0 \tag{9}$$

Any vector \mathbf{b}_m and the related modal constants A_r , and eventually the mode shapes, can then be recovered from Eq. (6).

3 Leaf Spring Case

3.1 Leaf Spring Experimental Tests

This test aims at computing the modal response of the system, through the study of frequency response as described in [5–7]. The results provided by the test are the inertance of the system, the ratio between the acceleration measured in 23 points, and the force applied on a single point of the structure. These quantities permit the computation of the system's receptance and then the extraction of the modal parameters of the component by the LIPEZ method. In order to obtain the free–free condition, the component was suspended by elastic supports that should not influence the experiment as shown in Fig. 1. The leaf spring was excited with an electromagnetic shaker rigidly connected to the component; the input was a white noise signal in a frequency range from 0 Hz up to 1000 Hz. A 24 channels signal acquisition board (OROS OR38) was used to record the responses of 23 piezoelectric accelerometers (outputs) and the force was detected by a load cell (input) positioned in one of the four corners. Considering the leaf spring dimensions, one set of accelerometers properly distributed on the component is sufficient to investigate the vibration behaviour.

Time domain input and output data have been processed according to the Hv estimator [8] to produce the FRFs, which are the necessary inputs for the LIPEZ method. The coherence functions (not reported here for the sake of brevity) confirm the validity of the FRFs, showing local minima much lower than unity only at resonances and anti-resonances. A Matlab[®] implementation of the procedure described in Sect. 2 leads to the identification of modal parameters. The unknown model order n , which is necessary from the very first equation, is increased from a minimum value—3 in the following examples—to a maximum, in order to define stabilization charts, with the aim of separating physical and computational modes. Figures 2 and 3 present the stabilization diagrams of natural frequencies and damping ratios, overlaid on the sum of the moduli of all FRFs. Very stable frequency lines can be observed in Fig. 2, even at low orders. A slight scatter of damping ratios is observed in Fig. 3, due to a slower convergence and higher model orders are required to define the final reliable values.

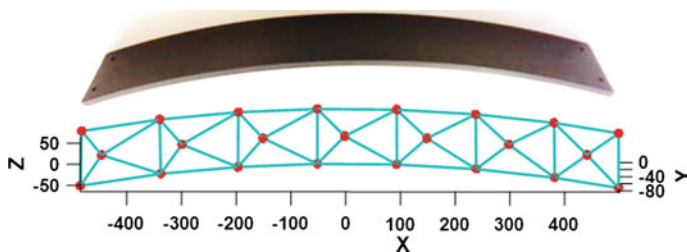


Fig. 1 Leaf spring component and experimental map

Fig. 2 Stabilization diagram for the natural frequencies. Each “+” corresponds to an estimated frequency in the selected band, given the model order n (ranging from 3 to 20)

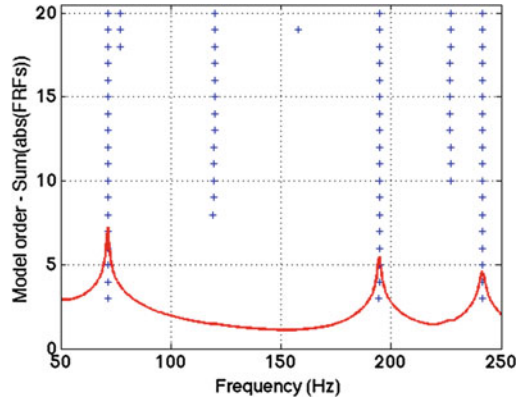
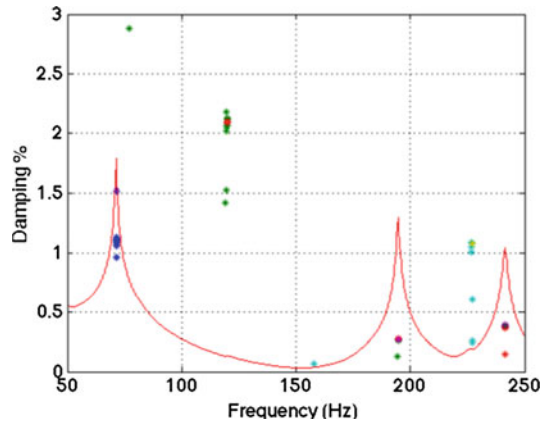


Fig. 3 Each “*” corresponds to the pair natural frequency damping ratio, given the model order n (ranging from 3 to 20)



3.2 Leaf Spring Simulation Tests

The same test has been reproduced at simulation level with a FE model: Hypermesh software was used, using Optistruct solver as specified in [9, 10]. It has been possible to exactly model the component due to the simplicity of its geometry and well-known production process, which allows for a precise definition of the stacking sequence and orientation of CFRP plies. The mechanical properties of the CFRP plies have previously been experimentally defined according to the Oberst test method [1, 2], using the facilities of the laboratories of the Department of Mechanical and Aerospace Engineering.

The Lanczos algorithm [11, 12] is used to solve the undamped eigenvalue problem:

$$[K - \lambda M]x = 0 \tag{10}$$

The damping matrix is disregarded not only to reduce the numerical issues but also for the limited damping capabilities of CFRP material.

3.3 Leaf Spring Test Correlation

The Modal Assurance Criterion (MAC) is adopted, as described in [5, 6], to evaluate the correlation between numerical analysis and experimental results:

$$MAC_{TS} = \frac{|\{\psi_T\}^T \{\psi_S\}^*|^2}{(\{\psi_T\}^T \{\psi_T\}^*)(\{\psi_S\}^T \{\psi_S\}^*)} \tag{11}$$

This index indicates the similarity between the modes shapes and is equal to one when two compared modes have exactly the same shape. Correlation is considered acceptable when value of MAC is higher than 0.6: computed MAC values are always higher than 0.8 for the first 10 analyzed modes (Fig. 4 and Table 1), confirming the validity of the FE model.

Table 1 gives the list of the experimental and numerical natural frequencies, showing a quite good correlation. As expected modal damping ratios are very limited, confirming the assumption of Eq. (10).

In Fig. 5 an example of mode shape (namely n.5) is reported in its FEM and experimental representations. The visual comparison confirms the similarity of modes shapes, already certified by the high MAC values.

Fig. 4 Leaf spring test MAC coefficient

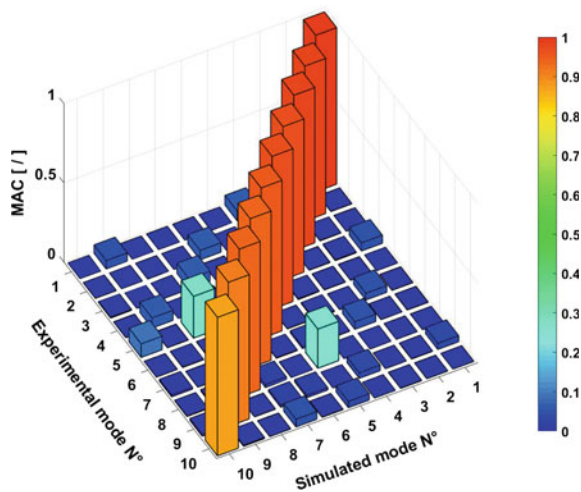


Table 1 Leaf spring frequency comparison

Mode	f_{FEM} [Hz]	f_{LIPEZ} [Hz]	Δf (%)	ζ_{LIPEZ}	diag(MAC)
1	67.8	71.31	-5.16	1.11	0.98
2	188.35	194.66	-3.34	0.27	0.97
3	238.26	241.42	-1.30	0.39	0.97
4	370.8	375.34	-1.24	1.59	0.96
5	452.4	441.92	2.30	1.37	0.96
6	614.57	614.30	0.03	0.44	0.95
7	748.77	720.31	3.83	0.90	0.93
8	828.3	851.41	-2.81	4.86	0.84
9	919.81	897.26	2.44	2.65	0.91
10	1053.9	994.38	5.66	2.52	0.87

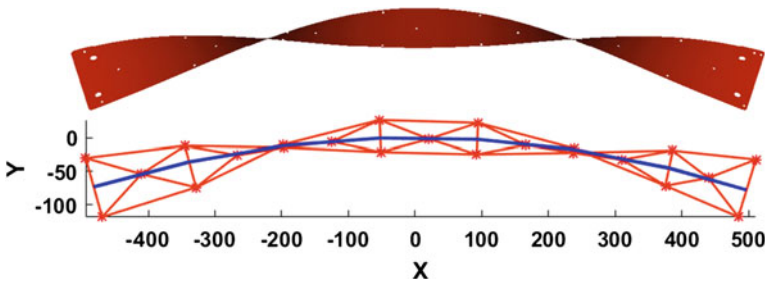


Fig. 5 Mode shape 5: FEM (*Top*) and LIPEZ method (*Bottom*)

4 Door Panel Case

4.1 Door Panel Experimental Tests

Based on the favorable results from the test on the leaf spring, the same procedure was used to study the behavior of a door panel of an electric prototype vehicle. This component was chosen because of its high influence in the global NVH characteristic of vehicle. The door panel is formed by two independently produced shells of CFRP material, glued to each other on their outer borders; a Lexan made window occupies the upper third of the door and is glued directly on the doorframe. The structural materials are well defined but the staking sequence data and its fiber orientation are lacking. Also the characteristics of the door opening mechanism, positioned between the two shells, are unknown. The component was tested in free-free condition, with a white noise excitation force given through an electro-magnetic shaker. The same 23 accelerometers and load cell were used to record the response but in this case three set were needed to measure 66 points on the component because of its larger dimensions. The load cell was applied in a rigid area as

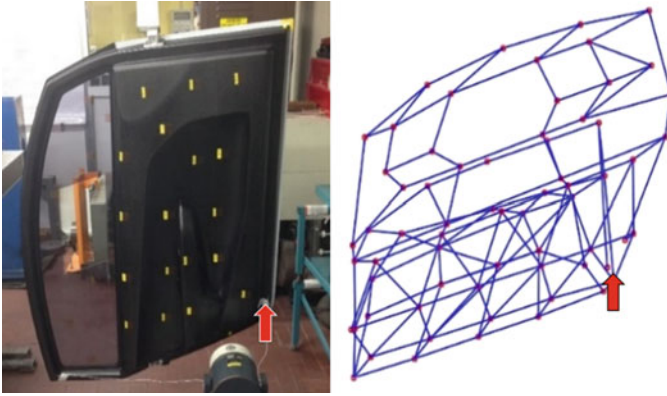


Fig. 6 Door panel component and experimental map

shown by the red arrow in Fig. 6. The procedure followed for data processing is the same as the test on the leaf spring and again coherence remain almost one in all the analyzed frequency range, giving an indication of goodness of experimental results.

4.2 Door Panel Simulation Tests

The component has been manufactured by a handmade distribution of the CFRP layers, which introduces a high variability in CFRP orientation; because of this limited information, a constant orientation of the fibers has been simulated. Also the thickness of the shells was approximated to a constant value because it is not possible to obtain this data from the final assembled component. The component has been modeled with the same procedure as the leaf spring giving extra attention to the connection of the two material shells. Another approximation was then introduced as it is not possible to exactly reproduce the real connection, which is far from perfection in some areas. A modal-based frequency response analysis was performed similar to the analysis on the leaf spring, but in a frequency range from 0 to 200 Hz. The choice of narrower frequency band is due to the fact that the test aims is to analyze the structural vibration frequency range. A set of nodes that reproduces the accelerometer position is used to compare the output response.

4.3 Door Panel Correlations

The experimental modal analysis procedure defines fourteen modes in the range 0–200 Hz: very stable frequency and damping ratios are achieved which allow computing reliable mode shapes. Unfortunately, both the visual inspection and the

MAC matrix proof that the correlation of FEM results and the experimentally defined mode shapes is very poor. Some natural frequencies are similar but the sequence and the deformations of the mode shapes are very different, which makes the comparison disappointing.

5 Conclusions

Structural materials properties have, been determined by the Oberst beam test, defining a database which permits reliable reproduction of experimental tests at a software level. Component manufactured with the same composite material have been tested numerically and experimentally. The correlation of results for a leaf spring, performed by MAC calculation and frequency response comparison, is very good and confirms the correctness of the FEM approach and the material data base. A similar test performed on a door panel shows a major difference in order to define a reliable model. Inadequate information on the two CFRP shells including their couplings and the door opening inner mechanism restricts designing an accurate model. Future work will be devoted to the analysis of the outer shell of the door, to verify the importance of an accurate knowledge of the layers disposition and material thickness on the modal parameters.

Acknowledgments The authors want to acknowledge Serena Cermelli for the cooperation during the activity and Altair-Italy Engineering S.R.L. for the Software.

References

1. American Society for Testing and Materials International: ASTM E756–05 (Reapproved 2010). Standard Test Method for Measuring Vibration-Damping Properties of Materials (2010)
2. SAE International: SAE J1637 (1993) Laboratory measurement of the composite vibration damping properties of materials on a supporting steel bar
3. Erdoğan G, Bayraktar F (2003) Measurement of dynamic properties of materials. Istanbul
4. Fasana A (2009) Modal parameters estimation in the Z-domain. *Mech Syst Signal Process* 23 (1):217–225. doi:[10.1016/j.ymssp.2008.03.015](https://doi.org/10.1016/j.ymssp.2008.03.015)
5. Maia NMM, Silva JMM (1998) Theoretical and experimental modal analysis. Taylor & Francis Inc.
6. Ewins DJ (2000) Modal testing: theory, practice and application, 2nd edn
7. Peeters B, Van der Auweraer H, Guillaume P, Leuridan J (2004) The PolyMAX frequency-domain method: a new standard for a modal parameter estimation? *Shock Vib* 11:395–409
8. Shin K, Hammond JK (2008) Fundamentals of signal processing for sound and vibration engineers. Wiley
9. Altair Engineering (2015) Practical aspect of Finite Element Simulation, 3rd edn
10. Altair Engineering (2015) Pre and post-processing for finite element analysis, guidebook

11. Rydh J (2007) Very large symmetric eigenvalue problems solved by Lanczos and multiple relatively robust representations for tridiagonals. Stockholm University
12. Yin J, Voss H, Chen P (2012) Combining automated multilevel sub-structuring and subspace iteration for huge gyroscopic eigenproblems

Dynamics of a Tethered Rover on Rough Terrain

Stefano Seriani, Paolo Gallina and Armin Wedler

Abstract The deployment of a complex modular cable robot is investigated. The act is performed by a supporting rover that drives on rough terrain while pulling—and unwinding—one of the tethers. In order to avoid rebounds and stress spikes, the cable must be kept in tension by the feeding mechanism. In this work, a constant torque control system is evaluated. A numerical simulation is carried out by direct time-integration of the dynamics equation of the cable and the drive. Results show that a constant torque applied by the motor unit is able to produce a tension in the cable that is well within the cable's yield limits, while at the same time being consistently larger than zero. This shows the viability of this technology for the deployment of cable structures by rovers in extreme environments.

Keywords Cable robot • Deployment • Robot • Dynamics • Tether

1 Introduction

The way the exploration of planetary bodies and other celestial objects is carried out is beginning to change. Since this endeavor began, in the sixties, the general methodology called for solitary, one-package probes or rovers [1, 2]. It is apparent that these systems are predominantly focused on the on-board scientific payload. In the last decade though, the focus has begun to change dramatically, with the emergence of a more varied set of objectives, such as ISRU (In Situ Resource

S. Seriani (✉) · A. Wedler
Robotik und Mechatronik Zentrum, Deutsches Zentrum für Luft- und Raumfahrt e.V. (DLR),
Köln, Germany
e-mail: stefano.seriani@dlr.de

A. Wedler
e-mail: armin.wedler@dlr.de

P. Gallina
University of Trieste, Trieste, Italy
e-mail: pgallina@units.it

Utilization) [3], or even preparation of a base for manned exploration [4]. In this framework, robots actually constitute and support a modular, multi-expertise environment for complex planetary activities [5].

CDPRs form a class of robots that exploit tethered mechanisms to manipulate the end-effector; in many cases, the end-effector is suspended with cables and, by varying the lengths of unwound cable, a set of winches handles the actuation [6–9]. With a few notable exceptions, CDPRs have seen scarce implementation in space; a notable example is the NIST Robocrane [8]. In the ROBEX framework, a Cable Driven Parallel Robot (CDPR) was described by Seriani et al., in [10]. The complex system is designed to operate in the context of planetary exploration; along with a supporting rover, it takes advantage of a modular architecture in order to increase efficiency in inspection and light manipulation activities.

In this paper we present an analysis of the deployment procedure of the CDPR described originally in [10]. A critical aspect of this is the unwinding of the cable when the rover performs the end-effector deployment; a preliminary analysis on the dynamics of this process is presented. Special care is given to the motion of the rover on a surface that can be far from ideally flat.

2 Description of the System

The general layout of the robot, along with its main components, is shown in Fig. 1. The modules are self-contained units that can be placed on the ground by a suitable rover, i.e. equipped with a manipulator able to perform the deployment. The extendable mast allows the cable feeding mechanism to reach a suitable height for the operation of the CDPR, as described in detail in the paper from Seriani et al. The end-effector is equipped with four docking interfaces, three of which are for the cables and one is to allow it to be picked up by the rover (which is equipped accordingly).

The deployment procedure is a two-phase process and is shown in detail in Fig. 2. In order for the rover to connect the end-effector to the cables, this should be brought to the cable-feed mechanism of each module and connected to the wound-up cables. Referring to the example in Fig. 2c, after connecting the first cable to the end-effector in P_4 , the rover is supposed to travel to point P_5 to connect the second cable. This requires the cable to be unwound during the rover's motion.

A few issues can be identified in this endeavor:

- The deployment procedure calls for the cable to be released simultaneously to the motion of the rover,
- The terrain upon which the rover threads can be rough, leading to oscillatory stresses in the cable,
- The cable can become jammed if tension is too low.

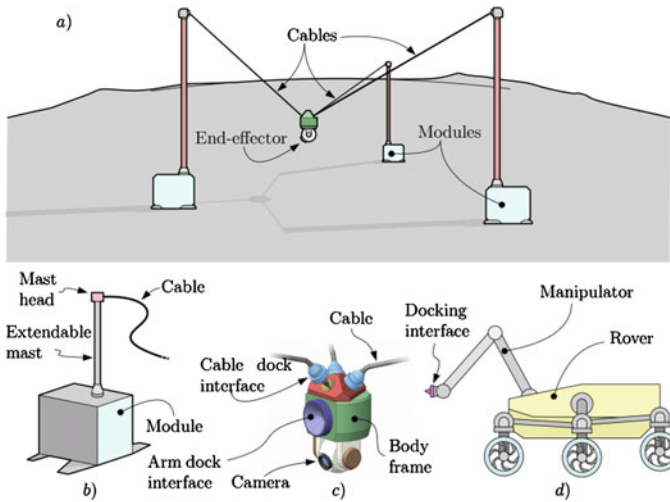


Fig. 1 Overview of the modular CDRP for inspection and light manipulation on celestial bodies (a). Main devices: in **b** a general module is illustrated, in **c** the end-effector is shown, along with its subsystems, and in **d** the manipulator-equipped rover is depicted

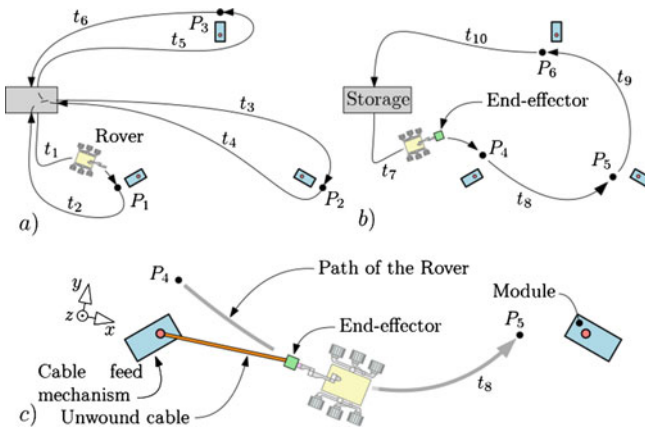


Fig. 2 Deployment procedure of the modular CDRP. In **a** the module placement phase is shown: the points $P_{1,2,3}$ indicate where the rover stops to deploy the modules; the first 6 path segments are shown (t_1 to t_6); in **b** the end-effector deployment is illustrated, with path segments t_7 to t_{10} , and in **c** a detailed view of segment t_8 is shown. In this last view, the unwinding of the cable—produced by the rover motion—is visible

By referring to Fig. 3a, one can see the general situation arising from the case of path segment t_8 . From the considerations above, it appears paramount that the tension τ in the cable remain within a set interval. The maximum value of said interval is given by the yield strength of the cable, whereas the lower limit can be

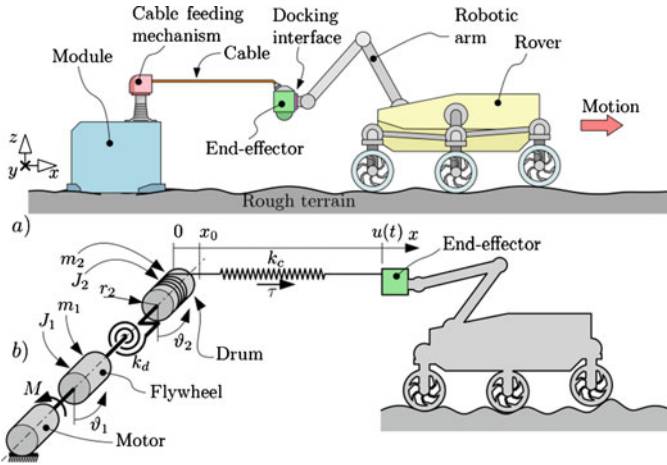


Fig. 3 Layout of the unwinding of the cable during the locomotion of the rover. In **a** a side-view of the situation seen in segment t_8 is illustrated. In **b** instead, the proposed solution is shown and the main values are indicated

assumed equal to zero, since if the cable should become loose, the consequent tension spike could easily cause the severance of the cable. Let us define the maximum force as $\tau_{max} = A_c \sigma_{yield} / \eta \cong 72.80 \text{ N}$, with a safety-coefficient $\eta = 2$, and a total area of the AWG 17 cables of $A_c = 2.08$. The ultimate yield coefficient of copper is $\sigma_{yield} = 70 \text{ MPa}$. Thus $\tau \in [0, 72.80] \text{ N}$. Additionally, a loosening of the cable can cause jamming events in the feed mechanism.

A constant-torque actuation combined with a torsional spring-damper system on the drum can mitigate the problem considerably without needing complex control architectures like force-feedback loops. In the next section a model for this solution is given and its dynamics is analyzed.

3 Model

In Fig. 3b, the cable is considered as elastic and non-sagging. The elastic constant is based on the length of the portion of cable that is unwound: $k_c = E_c A_c / (L_c)$, where E_c is the cable’s Young modulus, A_c is the section area, and $L_c(\vartheta_2) = x_0 - \vartheta_2 r_2$ is the unwound portion of cable, where x_0 is the minimal unwound portion. Therefore, if $u(t)$ is the coordinate of the end-effector over time the dynamic equations are as follows:

$$\begin{cases} J_1 \ddot{\vartheta}_1 + k_1(\vartheta_2 - \vartheta_1) + c\dot{\vartheta}_1 + M = 0 \\ J_2 \ddot{\vartheta}_2 + k_1(\vartheta_1 - \vartheta_2) + \tau r_2 = 0 \\ \tau = k_c[u(t) - L_c(\vartheta_2)] \\ J_2 = J_{drum} + J_{woundupcable} = J_{drum} + \rho_c r_2^2(L_{c,tot} - u(t)) \end{cases}, \quad (1)$$

where c is the rotational damping coefficient due to the friction of the bearings, and ρ_c is the linear density of the cable and $L_{c,tot}$ is the total length of the cable.

Note that the value of c is estimated in the relevant interval, since rolling friction is generally not a linear function of speed. The 4th equation reflects that the drum's inertia J_2 is a result of both the drum itself and the portion of winded-up cable. A non-linearity is present in the 3rd equation of the system; in fact $\tau = f(\vartheta_2^{-1})$. A direct sub-iterated time-integration of the dynamics equations in Eq. 2 is employed. The k_c term is purposely left out of the sub-iteration cycles since the non-linearity is comparably small at timestep scale.

In order to simulate the oscillation of the coordinate $u(t)$ caused by the traveling conditions of the rover on a rough terrain, the following input function is used,

$$u(t) = x_0 + vt + \mu \sin(\omega t), \quad (2)$$

where v is the linear speed of the rover, μ and ω are, respectively, the amplitude and frequency of the oscillation. Given a general size λ of the obstacles encountered by the rover, the disturbance frequency is given by $\omega = v/\lambda$. In order to avoid jerking at $t = 0$, a constant acceleration ramp of duration t_{ramp} was applied to v .

4 Results and Discussion

In Table 1, the main parameters used in the simulation are summarized.

In Fig. 4, the results of the simulation are shown with two different values of the motor torque M . The main oscillation seen in both Δx and τ is directly due to the oscillation of $u(t)$, and thus to the rough terrain the rover is traversing. It is apparent that the value of M impacts heavily on the value of τ . In fact, by applying a certain amount of constant torque, the cable can be efficiency kept in tension, thus avoiding

Table 1 Values of the main parameters

E_c	A_c	x_0	r_2	k_1	c	J_1	J_{drum}
[GPa]	[mm ²]	[m]	[m]	[N/m]	[Nms]	[kg m ²]	[kg m ²]
120	6.28	0.1	0.03	10	6.7E-5	4E-5	6.75E-5
ρ_c	$L_{c,tot}$	v	μ	λ	ω	Δt	t_{ramp}
[kg/m]	[m]	[m/s]	[m]	[m]	[1/s]	[s]	[s]
0.016	10	0.1	0.1	0.02	10	1E-5	0.5

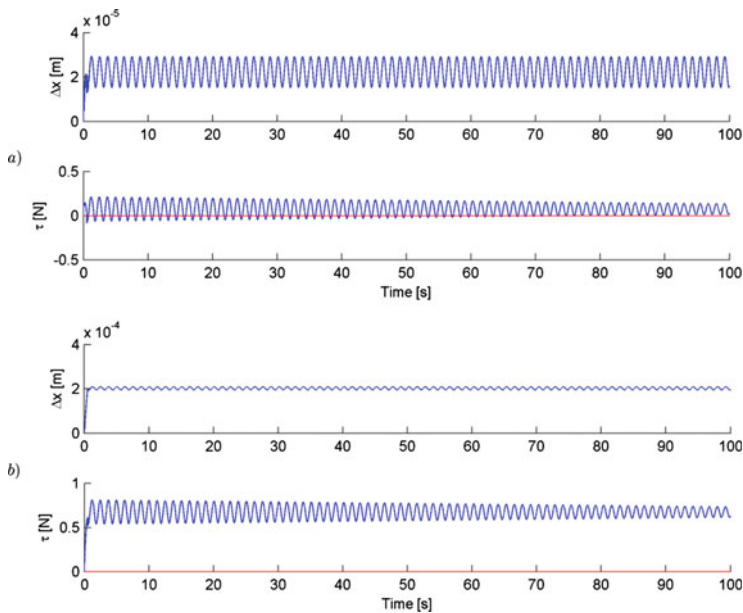


Fig. 4 Results of the simulation. In **a** a motor torque $M=0.002$ Nm is applied, whereas in **b** $M=0.02$ Nm are produced by the motor

loss of tension—which is, instead, present in (a)—and the consequent rebounds and stress spikes. An increase in torque M also has the effect of pre-loading k_1 , thus raising the stiffness of the drive, which, in turn, leads to the noticeable decrease in the amplitude of the oscillation in Δx that is visible in (b).

It should be noted that the tension τ in the cable is considerably lower than the τ_{max} calculated in Sect. 2.

Finally, the non-negligible influence of the wound-up cable on the inertia of the drum is appreciable by looking at the tapering amplitude of the main oscillation in τ . This would, in fact, be counteracted by the inertia of the unwound cable itself, albeit this is not included in our simulation.

The oscillation due to the elasticity of the cable itself is effectively damped by the friction from the ball-bearings the drive is mounted on.

5 Conclusion

The deployment of a cable robot by a rover is investigated; in particular, the dynamical aspects of the cable feeding system are simulated by direct integration of the non-linear motion equations. The drive is composed of a motor unit, which is coupled to a drum via a torsion spring. The cable is wound around the drum, and,

during the deployment phase, the rover actively pulls it out, unwinding it. A constant torque is applied by the motor unit on the drum, in an effort to keep the cable in tension.

Results show that the application of a constant torque on the drum allows the cable to remain properly tensioned, thus avoiding rebounds and the consequent stress spikes in the cable itself.

Future work may include a multiple cable deployment case, where the rover is itself considered as a dynamics constituent, but this work indicates that this type of constant-torque control might be convenient and effective.

References

1. Grotzinger JP, Crisp J, Vasavada AR, Anderson RC, Baker CJ, Barry R, Blake DF, Conrad P, Edgett KS, Ferdowski B, Gellert R, Gilbert JB, Golombek M, Gómez-Elvira J, Hassler DM, Jandura L, Litvak M, Mahaffy P, Maki J, Meyer M, Malin MC, Mitrofanov I, Simmonds JJ, Vaniman D, Welch RV, Wiens RC (2012) Mars Science Laboratory mission and science investigation. *Space Sci Rev* 170(1–4):5–56
2. Vago J, Gardini B, Kminek G, Baglioni P, Gianfiglio G, Santovincenzo A, Bayón S, Van Winnendael M (2006) ExoMars: searching for life on the red planet. *Eur Space Agency Bull* 126:16–23
3. Muscatello A, Santiago-Maldonado E (2012) Mars in situ resource utilization technology evaluation. In: *Proceedings of the 50th AIAA aerospace sciences meeting including the new horizons forum and aerospace exposition*, Nashville, Tennessee, 9–12 Jan 2012
4. Levrino L, Gatto G, Hall S, Wellons J, Gargioli E, Hoffman JA, Maggiore P, Viola N, Viscio MA (2014) Human life support in permanent lunar base architectures. In: *Proceedings of the 65th international astronomical congress IAC*, Toronto, Canada, Sept–Oct 2014, pp 9690–9700
5. Fink W, Baker VR, Schulze-Makuch D, Hamilton CW, Tarbell MA (2015) Autonomous exploration of planetary lava tubes using a multi-rover framework. In: *Proceedings of the 2015 IEEE aerospace conference*, June 2015, pp 1–9
6. Lamaury J, Gouttefarde M, Michelin M, Tempier O (2012) Design and control of a redundant suspended cable-driven parallel robots. In: Lenarcic J, Husty M (eds) *Latest advances in robot kinematics*. Springer, Netherlands, pp 237–244
7. Albus J, Bostelman R, Dagalakis N (1993) The NIST Robocrane. *J Robotic Syst* 10:709–724
8. Bostelman R, Albus J, Murphy K, Tsai TM, Amatucci E (1994) A Stewart platform lunar rover. In: *Proceedings of the space '94 conference*, Albuquerque, New Mexico
9. Campbell PD, Swaim PL, Thompson CJ (1995) Charlotte™ robot technology for space and terrestrial applications. In: *Proceedings of the 25th international conference on environmental systems*, San Diego, California, 10–13 July 1995
10. Seriani S, Gallina P, Wedler A (2016) A modular cable robot for inspection and light manipulation on celestial bodies. *Acta Astronaut* 123:145–153

Wind Propulsion for Robot Surface Mobility

Mario Foglia, Giulio Reina and Giovanni Boschetti

Abstract This paper investigates new solutions for robot mobility based on wind propulsion. Different wind energy-conversion configurations are presented that can be employed to propel a land vehicle. The proposed system is based on a vertical multi-wing solution that can be mechanically configured to work as either a wind mill or a sail. The model of a three-wheel robot in wind-sail mode is also recalled showing the influence of wind intensity and direction on the vehicle's performance.

Keywords Wind-driven vehicles • Energy conversion • Mobile robotics • Dynamic modeling

1 Introduction

Wind energy is a green, available, and economical alternative source of energy. For centuries, it has been used for transportation in air- and water-crafts. Whereas in airplanes, horizontal wings generate a vertical lift-force, using vertical airfoils it is possible to obtain a horizontal force to propel a water- or land-vehicle [1, 4, 6, 7]. The paper proposes different wind energy-conversion configurations that can be employed for efficient propulsion of robotic land vehicles. The proposed system, shown schematically in Fig. 1, is based on a vertical multi-wing device that can be mechanically reconfigured to work in different propulsion modes. Specifically, three working configurations are possible:

M. Foglia
Politecnico di Bari, Bari, Italy
e-mail: mario.foglia@poliba.it

G. Reina (✉)
University of Salento, Lecce, Italy
e-mail: giulio.reina@unisalento.it

G. Boschetti
University of Padova, Padua, Italy
e-mail: giovanni.boschetti@unipd.it

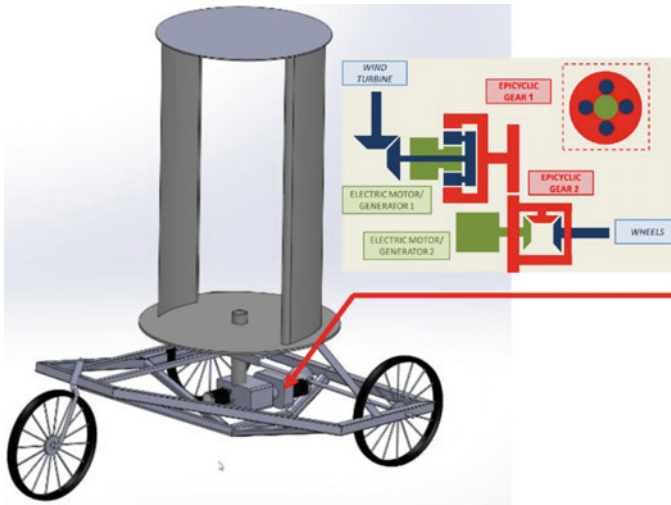


Fig. 1 Transmission tree for a wind-driven robot

- (1) Wind mill-mode: the multi-wing device rotates around its vertical axis, serving as a wind mill to generate electrical energy that is stored in the system.
- (2) Direct mode: the wind energy is turned into rotational mechanical energy that is made available directly at the vehicle wheels.
- (3) Sail-mode: by controlling the orientation of the multi-wing device, a horizontal lift-force can be appropriately generated to propel the vehicle.

System reconfiguration is performed through the use of epicyclical transmission, electrical motors/generators, and brakes/clutches. The choice for the best propulsion mode along the planned route towards the final goal will depend upon wind direction and intensity. For example, wind mill-mode will be used when the vehicle has low battery and does not need to move or the apparent wind angle relative to the course is not favorable, i.e. smaller than about 40° . In the latter case, vehicle propulsion will be based on the onboard electrical motors. In the direct mode, the robot does not require electrical power, but only mechatronic governance. The wind speed range should be between 3 and 15 m/s and the apparent wind angle may range from 0° to 180° in theory. The sail mode has higher efficiency when apparent wind angle ranges between 40° and 150° . Nevertheless, this propulsion mode needs appropriate ground friction since large forces can be exchanged by the wheels.

The direct and sail modes can be also considered as safe operating modes in the case of drive motor failure.

2 Power Transmission

With reference to the inset of Fig. 1 and to the block diagram of Fig. 2, the motor-generator MG_1 and the epicyclical gear train E_1 allow the three different propulsion settings to be switched off. The second epicyclical gear train E_2 allows the power flow to the wheels to be reconfigured according to two alternative configurations: (i) the wheels are electrically powered; (ii) the wheels are mechanically powered. During wind-based propulsion, regenerative braking will be also possible.

2.1 Main Components

The most important components of the proposed power transmission are the Electric Motor/Generators (MG) and the epicyclical gearings (E). These first devices convert power from the electric to mechanical form, and vice versa. (Energy losses are functions of the device power and speed). The devices considered in the present study belong to the brushless permanent magnet electric motor/generator family. A battery pack powers these devices and/or connects them when they work in different modes (one generates, the other drains electricity).

The first epicyclical gearing E_1 consists in a planetary gear unit, which mechanically connects the power derived from the two power sources, and it has been used as a speed-coupling device. It has the function of coupling the speeds of the two different power sources that enter the device separately and of providing the output torque to the shaft towards the second epicyclical gear. This device consists

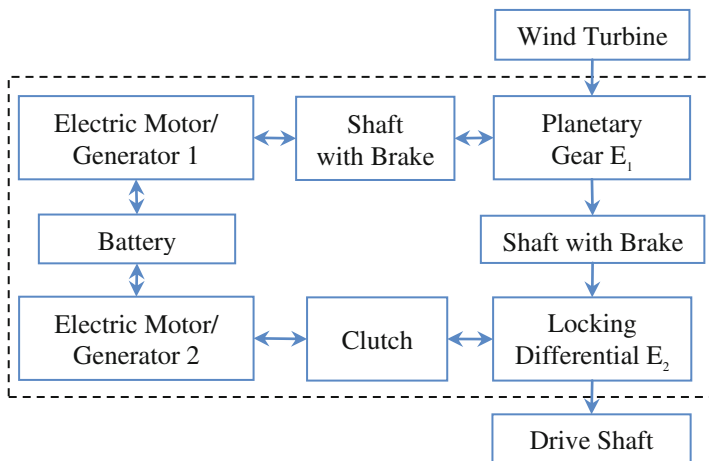


Fig. 2 Power transmission block diagram

of three rotating nodes, namely a sun gear, a ring gear and a carrier gear, as shown in Fig. 1, which are linked by a few small pinion gears. A second function of this device is obtained by locking the ring gear. In such a configuration the device (losing one degree of freedom) works as an epicyclical reductor where the carrier rotation is slower with respect to the sun rotation.

The second epicyclical gearing E_2 mechanically connects the output shaft of the first planetary gear (i.e. the ring), the second motor/generator and the drive shaft towards the wheels. Such a device never works as a two-degree-of-freedom mechanism: either the carrier or the pinion is locked depending on the overall working configuration. Since in differentials [3], locking the pinion (bevel gear) is more widespread than in other devices, a reasonable choice can be a locking differential, as proposed in Fig. 1, instead of a second planetary gear.

2.2 Architecture

The wind mill-mode recalls the typical “serial hybrid transmission” configuration of modern hybrid vehicles [5], where the main power source (i.e. the engine) is connected to the wheels by an electrical node instead of the traditional mechanical connection. Similarly, in the proposed approach, there is no mechanical connection between the wind turbine and the wheels (See block diagram of Fig. 3).

In detail, the ring of the planetary gear (see the red part in Fig. 1) is locked by the connected shaft. Conversely, the wind turbine, connected to the planetary carrier, makes the sun rotating. Since the MG_1 is connected to the sun gear, it rotates acting as a generator and the battery pack can be charged. In this way, the battery can continuously power the MG_2 that, working as a motor, transmit the revolute motion to the drive shaft and hence to the wheels, as highlighted with red arrows in Fig. 3. Since the ring of the first planetary gear is directly connected to the carrier of

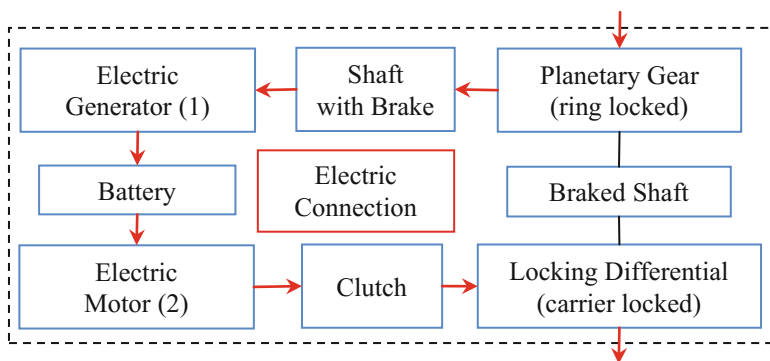


Fig. 3 Power flow in the first configuration

the differential, also the carrier is locked. Therefore the differential only keeps the rotation of the drive shaft inverted with respect to the rotation of the MG_2 .

The same scenario, in which the ring of the planetary gear is locked, is adopted for the sail-mode propulsion mode. This time the MG_1 is used to appropriately regulate the orientation of the sail with respect to the wind. At the same time, the MG_2 can be employed either as a motor to increase the speed if needed or as a generator by performing a regenerative braking. Finally, it can be also disconnected from the transmission, by means of a clutch, leaving the wheels free of spinning.

A different configuration is achieved with the direct propulsion mode which is similar to the “combined hybrid transmission” of modern hybrid vehicles [2]. In this case, the main power source, i.e. the wind turbine, the MG_1 and the output shaft are connected each other by means of a planetary gear acting as a speed-coupling device. Moreover in the proposed system, the differential is locked (i.e. the rotation of the pinion is not allowed). The rotation of the wind turbine and that of the MG_1 make the differential carrier to rotate.

Such a rotation is then transmitted to the wheels, as highlighted with red arrows in Fig. 4. Blue arrows of the same figure show that the MG_2 can work as either a motor or a generator (or it can be disconnected by means of the clutch).

In this scenario the MG_1 typically works as a motor; the planetary gear employed as a speed coupling device, can work like a CVT gearbox. Therefore a proper speed of the MG_1 , depending on the speed of the wind turbine, can lead to a null velocity of the wheels. This can be the state of the whole transmission when the vehicle stops. Then, by reducing the MG_1 speed the vehicle gradually starts moving while the wind turbine keeps rotating at a constant speed (Fig. 4: green arrows). A suitable cruise speed is achieved when the MG_1 has a null speed. Then, in order to reduce battery consumption, the sun of the planetary gear (or the connected shaft) should be locked until a speed reduction of the vehicle is needed.

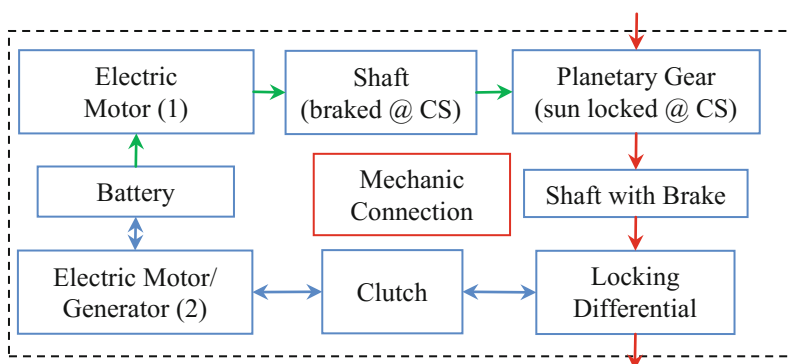


Fig. 4 Power flow in the second configuration

3 Sail-Mode

In previous work by the authors [8], it was presented the model of a three-wheel land robot featuring a sail-mode propulsion configuration, as shown in Fig. 5. The wind lift L (and so the wind thrust) is directly related to the apparent wind speed (AWS), i.e., the vector difference of the true wind speed (TWS) and the vehicle speed (VS). In Fig. 6, the main ground forces and total weight force are shown in their application points.

By appropriately controlling the sail orientation with respect to the incoming wind and the front steer angle, it is possible to propel the robot towards the desired point of interest. The model allows the main dynamic and aerodynamic aspects of

Fig. 5 Wind-driven robot in sail-mode configuration

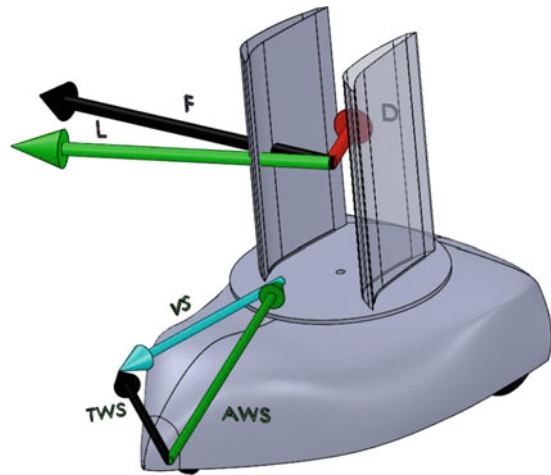


Fig. 6 Ground reaction forces and total weight force

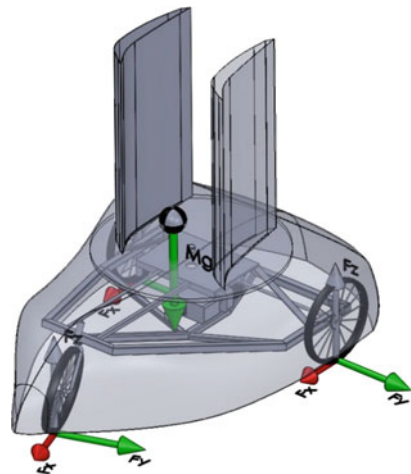
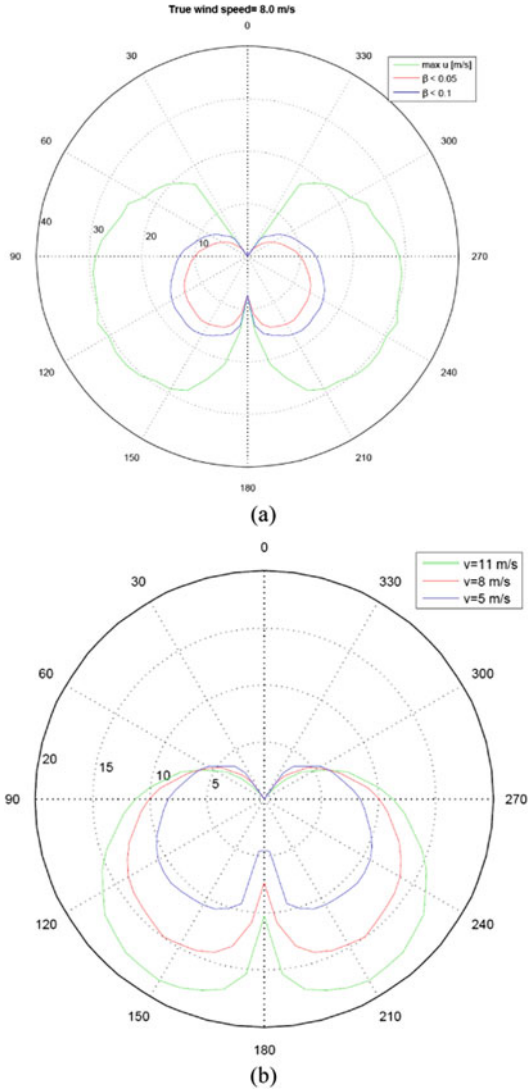


Fig. 7 VPP diagrams:
a response for a true wind intensity of 8 m/s,
b maximum velocity at different true wind intensities



the system response to be accounted for. For example, it is possible to draw Velocity Prediction program (VPP) diagrams that provide the performance of the robot under a given wind intensity. Figure 7a shows the VPP obtained for a true wind intensity of 8 m/s. Please refer to [8], for the geometric and mass properties used in the simulations. Polar coordinates are the maximum longitudinal speed of the vehicle and the relative orientation of the wind or true wind angle. Therefore, a velocity up to about 31 m/s can be reached by the robot with a true wind angle of about 118°. In Fig. 7a, three different cases are shown: (a) the vehicle sail trim is controlled to gain the maximum velocity with no constraint on the slip angle, β , of

the robot (green line), (b) and (c) the sail trim is controlled in order to keep constant slip angle, i.e. $\beta = 0.1$ rad (blue line) and $\beta = 0.05$ rad (red line). Finally, the comparison of the vehicle's response (maximum velocity) for three different wind intensities is shown in Fig. 7b.

4 Conclusions

This paper investigated different wind-based propulsion configurations. The idea is that of using a vertical multi-wing system that can be mechanically reconfigured to work in wind mill-, direct-, or sail-mode through the use of an epicyclical transmission. Details of the reconfigurable architecture are included. The performance of a robotic land yacht adopting sail-mode propulsion was also discussed in terms of velocity prediction programs or VPPs.

References

1. Chen J, Xie S, Luo J, Li H (2016) Wind-driven land-yacht robot mathematical modeling and verification. *Ind Robot: Int J* 43(1):77–90
2. Finesso R, Spessa E, Venditti M (2016) Cost-optimized design of a dual-mode diesel parallel hybrid electric vehicle for several driving missions and market scenarios. *Appl Energy* 177:366–383
3. Fostinger M, Bauer R, Hofer A (2015) Modelling and simulation of passive limited-slip differentials. *IFAC-PaperOnLine* 48(1):502–507
4. Hajos G, Jones J, Behar A (2005) An overview of wind-driven rovers for planetary exploration. In: *AIAA aerospace sciences meeting and exhibit*, pp 1–13
5. Houyu L, Guirong Z (2011) Hybrid electric vehicle drive control. *Proc Environ Sci* 10:403–407
6. Khayyat M, Rad M (2008) Comparison final velocity for land yacht with a rigid wing and cloth sail. In: *Proceedings of the world congress on engineering*, vol 2, pp 1–6
7. Mirzaei P, Rad M (2013) Toward design and fabrication of wind-driven vehicles: procedure to optimize the threshold of driving forces. *Appl Math Model* 37:50–61
8. Reina G, Foglia M (2016) On wind-driven land vehicles. In: *Proceedings of the international mechanical engineering congress and exposition (IMECE)*, pp 1–8

Anti-dive Front Suspension for Agricultural Tractors: Dynamic Model and Validation

Francesco Biral, Riccardo Pelanda and Alberto Cis

Abstract Off-highway market has recently shown the introduction of agricultural tractors equipped with a suspended front axle, whose benefits in term of improvement of dynamic performance might be disrupted by their tendency to increase the chassis pitch motion. Being agricultural tractors potentially loaded with many configurations and operating in a variety of terrain conditions, analysis of kinematics and dynamics performances, both numerical and experimental, is of paramount importance for system design and optimisation. The contributions of this study are mainly two: derivation of a set of analytical formulas to design an anti-dive suspension and of a validated model of the in-plane dynamics of an agricultural tractor fitted with an hydraulic semi-active front suspension.

1 Introduction

Agricultural tractors operate under loading conditions with large variability and on different surfaces (e.g. rough terrain, road, etc.). Semi-active suspensions have been identified as a technical solution to improve braking/tractive forces, to contrast chassis and ballasts induced static loads, improve vehicle stability (i.e. roll, yaw and pitch motions) and reduce unsprung mass oscillations due to tyre vertical deformation [1, 2, 4]. One possible configuration is the front axle suspended from the vehicle chassis with a four bar linkage in the symmetrical plane and an orthogonal pivoting axis to allow small roll angles. Despite the benefits of an improved comfort and han-

F. Biral (✉)

Department of Industrial Engineering (DII), University of Trento,
Via Sommarive 9, 38123 Povo, Trento, Italy
e-mail: francesco.biral@unitn.it

R. Pelanda

DII, University of Trento, Trento, Italy
e-mail: riccardo.pelanda@yahoo.it

A. Cis

Dana Holding Corporation, Via Linfano 1, 38062 Arco, Trento, Italy
e-mail: alberto.cis@dana.it

dling over rough terrain, the front suspension induces larger pitch motion of the sprung mass that may cause either the suspension to hit the end-stops and detrimental effects on the transient tyres' vertical loads and consequently vehicle manoeuvrability. General solution adopted to avoid this undesired situation requires more powerful, thus expensive, cylinders, which hardly cover all possible loading layouts due to the use of front and rear heavy ballasts that still may cause collision with the end-stops during hard braking/traction manoeuvres. An alternative or complementary solution optimizes the suspension geometry in order to reduce the sensibility of the suspension force to longitudinal load transfer. Such type of suspension are known as *anti-dive* suspensions whose design and optimisation is highly affected by tractor transmission type and loading conditions, which in general are not known by the axle manufacturer. Compared to scientific literature about anti-dive and anti-lift behaviour of cars and trucks not that much research is available for agricultural tractors. The most noticeable work [3] has extensively studied the analytical equations that yield anti-dive anti-lift conditions for different traction configurations (e.g. common brake architecture and two or four wheel drive systems). The present work extends the analysis deriving the relationship between suspension kinematics and forces sustained by the suspension arms and shock absorber. Additionally, a model of in-plane dynamics is developed and validated that also includes the hydraulic system of the semi-active suspension [5].

2 Dynamic Model of Agricultural Tractor with Front Suspension and Anti-dive Concept

The pitch motion is influenced both by road unevenness and by the presence of the longitudinal forces. Although the roll motion can induce pitch motion, the last is mainly a in-plane vehicle movement and can be well studied with a 2D model of the vehicle. If tyre vertical deformation is considered, the in-plane vehicle model has four degrees of freedom as shown in Fig. 1: x_r and z_r are respectively the horizontal

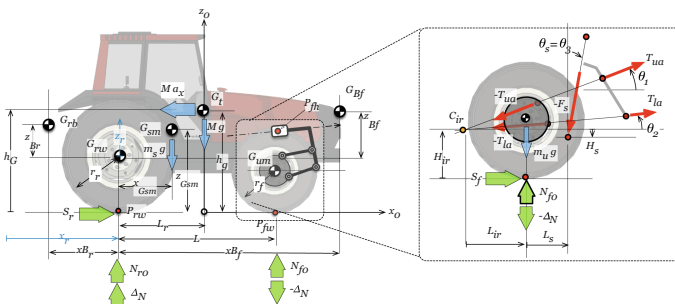


Fig. 1 Sketch shows centre of mass positions (G_{rb} and G_{fb} are respectively the rear and front ballasts), geometrical parameters, degrees of freedoms, the breakdown of internal and external forces and center of instantaneous rotation between sprung and unsprung

and vertical translations of the rear wheel from static condition, μ_r is the chassis pitch rotation and θ_1 upper arm rotation. The equations of motion are derived with a larger set of dependent coordinates $\mathbf{y}^d = [x_f(t), z_f(t), \mu_f(t), \theta_2(t)]^T$: x_f and z_f are respectively the horizontal and vertical translations of the front wheel from static condition, μ_f is the front axle pitch rotation, θ_2 is the lower arm rotation. The dependent coordinates \mathbf{y}^d can be obtained from the solution of the suspension kinematics equations: $\Phi(\mathbf{y}^i, \mathbf{y}^d, \mathbf{p}) = \mathbf{0}$. The symbolic equations of motion have been derived with the Newton-Euler approach using MBSymba package [6] in Maple © considering the suspension's arms as massless bodies. For sake of space the equations of motion are not here reported but more emphasis is given to the hydraulic and friction models of the suspension, which highly affect the dynamic response. The suspension force depends on hydraulic system, end-stop forces F_{es} and friction forces F_{fric} according to the following :

$$F_s(t) = p_p(t)A_p - p_r(t)(A_p - A_{rod}) + F_{es}(t) - F_{fric}(t) \quad (1)$$

The *anti* effect of a suspension is a term that describes the longitudinal to vertical force coupling between the sprung and unsprung masses [7]. The suspension *anti*'s behaviour determines the amount of longitudinal load transfer going through the suspension shock absorber and the pitch attitude of the vehicle (i.e. suspension deflection). A 100 % *anti*'s suspension has all the longitudinal load transfer and front brake forces carried by the suspension's arms: it is named as *anti-dive* when it prevents pitch motion during braking and *anti-lift* when it does it during acceleration.

The analytical condition of *anti*'s suspension behaviour can be derived by writing the Newton-Euler equations of the 2D multibody system in Fig. 1 which is made of the vehicle chassis with the attached ballasts (*sprung mass*) and the front axle with part of the suspension elements (*unsprung mass*). The relative motion of the sprung mass with respect to the unsprung mass is governed by the suspension kinematics via the position of the *center of instantaneous rotations (CIR)* which is the point the sprung mass instantaneously rotates around in its motion relative to the unsprung mass (see Fig. 1). Here, as a first approximation, steady state acceleration/braking condition is assumed for a given suspension configuration. The solution of the dynamics equations yields the suspension force F_s and the loads of the upper and lower suspension's arms T_{ua} , T_{la} as a sum of a static term and a dynamic term due to the longitudinal forces (Eq. (2)).

$$F_s = F_{s_0} + \Delta F_s, \quad T_{ua} = T_{ua_0} + \Delta T_{ua}, \quad T_{la} = T_{la_0} + \Delta T_{la} \quad (2)$$

For sake of space the expressions of static forces are not reported. On the contrary, it is interesting to analyse the dynamic terms which describe the change of the suspension force and arms' loads due to longitudinal forces.

$$\Delta_{F_s} = \left(\frac{(r_f - H_{ir})m_u}{Mb_0} - \frac{h_G L_{ir}}{Lb_0} \right) S + \frac{H_{ir}}{b_0} S_f \quad (3)$$

$$\Delta_{T_{ua}} = \left(-\frac{h_G}{L} \alpha_2 + \frac{m_u}{M} \beta_2 \right) S - \beta_2 S_f, \quad \Delta_{T_{ia}} = \left(\frac{h_G}{L} \alpha_1 - \frac{m_u}{M} \beta_1 \right) S + \beta_1 S_f \quad (4)$$

where $b_0 = (L_{ir} + L_s) \cos(\theta_3) - H_s \sin(\theta_3)$, $\alpha_i = \cos(\theta_i / (\sin(\theta_1 - \theta_2)))$ and $\beta_i = \sin(\theta_i / (\sin(\theta_1 - \theta_2)))$ with $i = 1, 2$. S is the total longitudinal force $S = a_x/M$ and S_f is the amount of longitudinal forces exerted by front tyre. Equation (3) says that the amount of change of the spring-damper force depends on the position of the CIR (L_{ir} and H_{ir}) and rear/front longitudinal force repartition. During braking, the front longitudinal force is a fraction K_B of the total braking force $S_f = -S K_B$ and the change of suspension force Δ_{F_s} reduces to:

$$\Delta_{F_s} = \underbrace{-\frac{H_{ir} K_B}{b_0} M a_x}_{\text{front brake force}} + \underbrace{\frac{H_{ir} - r_f}{b_0} m_u a_x}_{\text{front axle inertia}} + \underbrace{\frac{h_G L_{ir}}{L b_0} M a_x}_{\text{load transfer}} \quad (5)$$

Therefore, from Eq. (5), to have a 100 % anti-dive suspension Δ_{F_s} must be equal to zero in presence of longitudinal forces. The contribution of the front axle's force of inertia is cancelled if the vertical position of the IRC from ground is equal to the front wheel radius (i.e. $H_{ir} = r_f$). The remaining two terms of Eq. (5) can be set to zero if the longitudinal position of the IRC satisfies $L_{ir} = (r_f K_B L) / h_G$. In general the vehicle centre of mass height h_G is greater than front wheel radius and $K_B \leq 1$ thus the longitudinal position of the CIR that makes an anti-dive suspension is located between the two tyre contact points. K_B must be known to design a suspension with a desired anti-dive behaviour as concluded also in [3].

3 Suspension Hydraulics and Friction Model

The studied hydraulic system includes two accumulators of different size and two diskpacks devices that generate the damping effect with different characteristics in compression and extension not reported for sake of space. The hydraulic system also has a leveling control, which keeps the piston at the mid point of the extension range, when it is outside a pre-defined band for more than a given time threshold (e.g. 2s). There is also a pressure limiting device which extracts oil when the pressure exceeds a given threshold. Finally, 2-way solenoid valves are also used to change the damping characteristics whose governing algorithms are described in [4]. In this study the semi-active behaviour is not considered (i.e. valves locked). To derive the accumulators characteristics a polytropic transformation is used to obtain the gas volume and flow as follows:

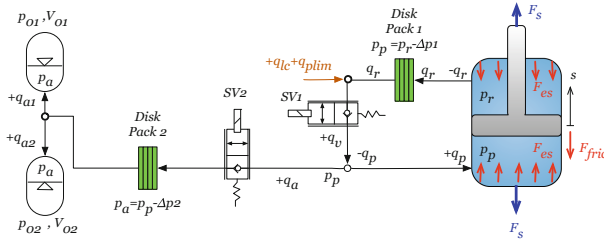


Fig. 2 Hydraulic system with double accumulators and disk packs (1 rebound and 2 compression). SV_1 SV_2 are 2-way solenoid valves normally closed which can provide additional damping features by acting on the current (PWM control)

$$V_{oil_1}(t) = V_{01} \left(1 - (p_{01}/p_a(t))^{\frac{1}{n}} \right), \quad V_{oil_2}(t) = V_{02} \left(1 - (p_{02}/p_a(t))^{\frac{1}{n}} \right) \quad (6)$$

where V_{01} , V_{02} and p_{01} , p_{02} are respectively the gas volume and pressure in pre-load conditions for the two accumulators and n is the polytropic transformation coefficient. Total accumulator volume is equal to gas volume where $V_{oil_1}(t)$ and $V_{oil_2}(t)$ are the oil volume of the accumulators (Fig. 2).

The oil flows $q_{a_1}(t)$ and $q_{a_2}(t)$ in the two accumulators are obtained from the following:

$$q_{a_1}(t) = V_{01} \left(\frac{p_{01}}{p_a(t)} \right)^{\frac{1}{n}} \frac{p'_a(t)}{n p_a(t)}, \quad q_{a_2}(t) = V_{02} \left(\frac{p_{02}}{p_a(t)} \right)^{\frac{1}{n}} \frac{p'_a(t)}{n p_a(t)} \quad (7)$$

where $p_a(t)$ is the accumulators pressure, $p_p(t)$ is the pressure on the piston side, $p_r(t)$ is the pressure on the rod side. The drop of pressure due to the disk-packs can be calculated by the following:

$$p_p(t) = p_r(t) - \Delta_{p1}(q_r(t)), \quad p_a(t) = p_p(t) - \Delta_{p2}(q_a(t)) \quad (8)$$

where $\Delta_{p1}(q_r(t))$ and $\Delta_{p2}(q_a(t))$ are the characteristics of the disk-packs systems as function of the flows and provided by the supplier. The flows through the orifices of piston's and rod's sides are respectively:

$$q_r(t) = -(A_p - A_{rod}) s'(t), \quad q_p(t) = A_p s'(t) \quad (9)$$

where $s(t)$ is the piston elongation. Additional equations of the hydraulic system describe the *leveling system* and *safety system* intervention. The first controls the suspension elongation $s(t)$ by driving it into a desired band around the static condition (i.e. middle position) by adjusting the oil quantity in the system $q_{lc}(t)$. The second controls the flow when pressure in the system goes over a given threshold (an oil quantity $q_{plim}(t)$ is subtracted from the plant). The related equations are:

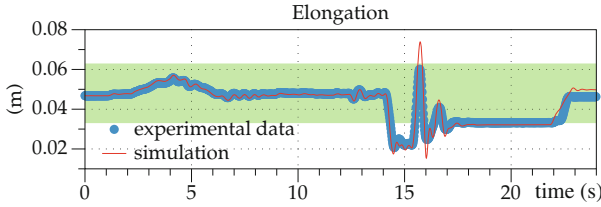


Fig. 3 Comparison between simulated and experimental cylinder elongation

$$q_v(t) = q_r(t) + q_{lc}(t) - q_{p_{lim}}(t), \quad q_a(t) = q_{a_1}(t) + q_{a_2}(t) \tag{10}$$

where the model for q_{lc} and $q_{p_{lim}}$ are:

$$q_{p_{lim}}(t) = \begin{cases} C_e A \sqrt{\frac{2\Delta p}{\rho}}, & \Delta p > 0, \\ 0, & \Delta p \leq 0. \end{cases}, \quad q_{lc}(t) = \begin{cases} -q_{lc0}, & s(t) > s_0 + s_{thlc}, \\ +q_{lc0}, & s(t) < s_0 - s_{thlc} \end{cases} \tag{11}$$

where ρ is the oil density, A is the orifice cross section, $\Delta p = p_r(t) - p_{lim}$. s_0 is the mid point of piston stroke and s_{thlc} is the threshold. The q_{lc0} is the flow increment/decrement. The hydraulic model was validated by using a known input history of the cylinder motion (i.e. excitation force). Figure 3 shows the comparisons between simulations and experimental data.

Since friction in the cylinder highly affects the suspension performance, a friction force model that depends on position, velocity of extension and cylinder pressure was introduced. The stationary value is:

$$F_{fric}(v, p_{stat}) = F_{f_c} + (F_{f_s} + F_{f_c}) e^{\left(\frac{v_s(t)}{v_0}\right)^{b_1}} + c_v v^{b_2} + k_p p_{stat} \tag{12}$$

with v is cylinder elongation velocity, p_{stat} is the static pressure, F_{f_s} is the static friction force, F_{f_c} is the kinetic friction force, v_0 and b_1 are respectively the Stribeck velocity and exponent, c_v , b_2 are viscous friction coefficient and exponent and k_p is the static pressure coefficient. The stationary value Eq. (12) was coupled with a LuGre friction model [8] for its ability to well describe transient behaviour and limited computational burden. Test bench experimental data, at different pressures and velocities, have been fitted with the friction model in Eq. (12) with a Least Square minimisation and a second set of experimental data was used to validate the LuGre model.

4 Identifications of Unknown Parameters and Model Validation

The procedure adopted to validate the model has used experimental data recorded on an agricultural tractor which mounts the suspension system with the following static load distribution: $N_r = 31250\text{ N}$, $N_f = 37850\text{ N}$ and total mass of $M = 6910\text{ kg}$. The experiments tested the system with three different load configurations: *high* with front ballast of 800 kg, *medium* with rear ballast of 800 kg and *low* with rear ballast of 2700 kg, where *high*, *medium*, *low* refer to level of front axle loading. The reader may note that due to the increase of vehicle mass in low load configuration the longitudinal load transfer increases of about 40 %, which causes the higher elongation rates during accelerations. The tractor was accelerated to a constant speed of 20 km/h in about 2 s and then around 12 s a hard brake manoeuvre was executed to stop it. The validation procedure was done into two steps: (*step 1*) static parameter identification, (*step 2*) model validation. Part of the experimental data set was used to identify, with a non-linear minimisation, some unknown or roughly known parameters, such as ballast exact positions, pitch moments of inertia and actual front/rear brake and traction repartition. Since the traction/braking forces are not experimentally measured those are estimated from the longitudinal accelerations and used as inputs. The remaining data set were used to evaluate the model performance in open-loop with respect to the experimental ones with longitudinal forces used as inputs. The Root Mean Square of the errors between the simulated and the experimental suspension elongation $L_s(t)$ and the hydraulic system pressures were used as accuracy metrics.

The results of the validation process show that the model is able to accurately reproduce the real system behaviour in high and medium load configurations (see Fig. 4). Qualitatively the comparison is fairly good and it is confirmed by the root mean square (RMS) error of the performance variables reported in table of Fig. 4. The error is less than 10 % for all performance variables. The oscillations of minor

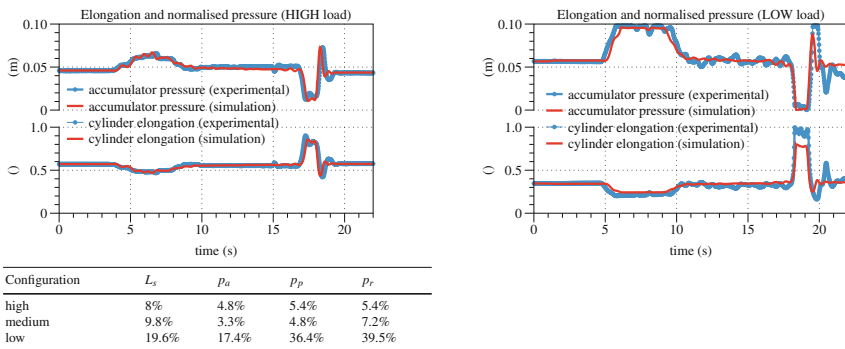


Fig. 4 Elongation and normalised accumulator pressure comparison between experimental and simulated, respectively from top, high and low load configurations. Table reports percentage RMS error of performance variables for the three load configurations

amplitudes and higher frequencies are due to the road unevenness which are not reproduced in the simulations. However, for low load configuration the model is less accurate especially during the hard braking manoeuvre, the main reason being the un-modelled diskpack characteristics which neglects the hysteretic effect that occurs at high stroke rates where the real behaviours is dominated by a saturation causing the real system to present a lower damping for this conditions. A better measurement of the damping diskpack sub-system will greatly improve the model also at low load configuration.

5 Conclusions and Design Considerations

A symbolic multibody model of the 2D vertical dynamics of an agricultural tractor was developed that includes a suspended front axle with semi-active suspension. Some considerations can be drawn from the validation results. First of all, the friction has a strong effect on the suspension performance affecting both static, stationary and the transient behaviour which can be improved with a better identification of the parameters of the friction model. Secondly, the un-modelled damping behaviour of the diskpack sub-system is the main cause of the poor performance of the model with configuration with low load on front axle. Finally, reducing the number of parameters that need to be identified will improve the overall accuracy.

A theoretical approach let us also find an analytical solution to design an anti-dive suspension that needs to be verified with the numerical dynamic model. This analytical equation can be used as a design guideline to define the kinematic suspension parameters.

References

1. Els P, Theron N, Uys P, Thoresson M (2007) The ride comfort vs. handling compromise for off-road vehicles. *J Terramech* 44(4):303–317
2. Giliomee C, Els P (1998) Semi-active hydropneumatic spring and damper system. *J Terramech* 35(2):109–117
3. Gobbi M, Mastinu G, Previati G (2014) Farm tractors with suspended front axle: anti-dive and anti-lift characteristics. *J Terramech* 56:157–172
4. Grott M, Biral F, Oboe R, Cis A, Vincenti E (2010a) Semi-active suspension systems for heavy-duty vehicles: Multibody model development, identification and control algorithm evaluation. In: ASME international mechanical engineering congress and exposition, proceedings, vol 10, pp 907–915
5. Grott M, Biral F, Sorniotti A, Oboe R, Vincenti E (2010b) Vehicle simulation for the development of an active suspension system for an agricultural tractor. *SAE Int J Commer Veh* 2(2):12–25
6. Lot R, Lio MD (2004) A symbolic approach for automatic generation of the equations of motion of multibody systems. *Multibody Syst Dyn* 12(2):147–172
7. Milliken WF, Milliken DL (1995) Race car vehicle dynamics. Society of Automotive Engineers
8. Pennestri E, Rossi V, Salvini P, Valentini PP (2016) Review and comparison of dry friction force models. *Nonlinear Dyn* 83(4):1785–1801

Dynamic Model of an Independent Carts System

Jacopo Cavalaglio Camargo Molano, Stefano Rossi,
Marco Cocconcelli and Riccardo Rubini

Abstract This paper focuses on the dynamic modelling of a recent mechatronic device called independent carts system. Different companies gave different commercial names, but the mechanics behind is the same: different linear motors on a closed loop, controlled individually to increase the flexibility but keeping the speed of dedicated solutions, such as mechanical cams or chains. The proposed model covers both the mechanical and control parts of the systems. In this paper the preliminary results are shown, and the model is validated on a real independent carts system by Rockwell Automation. The mechanical model is assumed to be a planar model and the moving carts are supposed to be rigid bodies moving along a rail. Friction and gravity effect are taken into account. The electrical model comprises three PID control loops. The aim of this model is to simulate the behavior of the system in order to evaluate different scenarios and architectures of new machines, decreasing the cost of development and the time to market.

Keywords Simulation · Dynamics · Linear motors · Mechatronics

J.C.C. Molano · M. Cocconcelli (✉) · R. Rubini
University of Modena and Reggio Emilia, Modena, Italy
e-mail: marco.cocconcelli@unimore.it

J.C.C. Molano
e-mail: 190802@studenti.unimore.it

R. Rubini
e-mail: riccardo.rubini@unimore.it

S. Rossi
Tetra Pak Packaging Solutions SpA, Modena, Italy
e-mail: stefano.rossi2@tetrapak.com

1 Introduction

Different studies [1] show how the technology of linear motors has improved in the last years. Thanks to these improvements some producers of automatic machines are introducing into the market new products based on independently actuated carts system (e.g. [2, 3]). This technology uses linear electrical motors in order to independently move carts along a closed modular track. It can be used to carry, rotate, block, screw and manipulate products. Great advantages of this new system have been identified [4] in comparison with the classic chain and belt drivers based on rotary motors, for example a high flexibility and a high velocity of the carts—the velocity that can be reached is about 4 m/s. This system is also different from the chain and belt drivers because the mechanical complexity is reduced in favor of the control complexity. As a matter of fact, it is no more necessary to design different chains or belts in order to synchronize and optimize the motion of machines, but it is necessary to develop more accurate algorithms to control several carts. In order to reduce the development time and cost of the new applications that use the new system it is possible to make dynamic simulations of machines. The simulation takes into account different studies in order to produce a model of the kinematics and dynamics of the mechanical structure [5]: a model of the electrical linear permanent magnet motors [1] and a model of the controller system ([6–8]).

This paper presents a dynamic model for an independent carts system focused on the iTRAK system developed by Rockwell Automation. The main contributions of this study are:

- Creation of a model that represents the kinematics and dynamics of the mechanical system and the model of the machine controller.
- Experimental analysis and validation of the model on the iTRAK system.
- Tuning and optimization of the model.

These points are essential to create a complete model of the machine that can be used for industrial and scientific knowledge.

The structure of the paper is the following. Section 2 describes the whole system. Section 3 shows the kinematic and dynamic model of the mechanical system. Section 4 discusses the model of the controller that has been implemented. Section 5 shows the validation and optimization of the system with respect to the experimental data of the real machine.

2 Independent Carts System

Independent Carts systems are basically linear motors with a more complex control system. Linear motors consist of two parts, a coil assembly and a magnet assembly. The coil assembly consists of copper windings within a core, which can be made of different materials. The magnet assembly consists of a set of rare-earth magnets

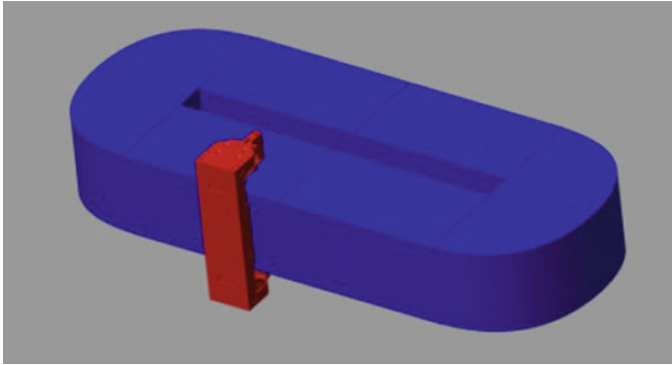


Fig. 1 Example of an independent cart system

mounted on a steel plate with alternating polarity. The magnetic field produced by magnets and the electrical field produced by current generate Lorentz's force. The current crossing the coil windings is controlled by a driver that imposes a magnitude and a direction such that the resultant Lorentz's force drives the rotor to the desired position. In this case the rotor as well as the stator can be made up either by coils or by magnets. The improvement of technology, especially as regards logic controllers, has enabled linear motors to perform more complex tasks. The Independent Carts system uses linear motors in order to control one or more movers that are constrained by rollers to follow a track. The track can have different shapes with curved and straight parts and it has a flexible architecture in order to build modular configurations. In this way a high performance flexible system can be produced, with this technology each mover can be controlled independently. The movers can accelerate, decelerate, take an absolute position and produce forces. The velocity of the movers can be very high with respect to rotary motors, each mover can move at a velocity of 4 m/s. The architecture of the machine is modular and it is possible to change the shape of the track and the numbers of the movers. Figure 1 shows a CAD model of an independent cart system, real machinery cannot be shown due to an NDA.

3 Mechanical Model

The model has been developed in Simulink environment, and it basically consists of two parts: the kinematic model comprising the geometry of the system and the dynamic model performing the simulation.

3.1 Kinematic Model

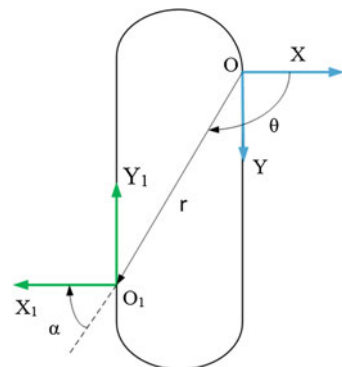
The case of study is the iTRAK machine that has an oval 3200 mm long track set in a longitudinal position. The track can be divided into four parts: two 800 mm long curves of 180° and two 800 mm long straight parts. The curves have a spline shape. There are two linear motors for each straight part and two linear motors for each curve. A mover is connected to the track by means of some rollers and it is driven by the variable magnetic field produced by the motors, which is concatenated with the magnetic field of the permanent magnets placed on the mover. The mover can move along the track through the rollers and it is constrained to follow the rail thanks to the preload of lateral rollers. When the cart moves along the curved parts, it covers a distance of 880 mm; when it moves along the straight parts, it covers a distance of 720 mm. This difference is due to the fact that the mover is constrained by the rail that has different lengths with respect to the track.

The model of the system is a two-dimensional model in which the cart is represented by a point that is constrained to move along the rail. In order to describe the kinematics of the system, two reference systems are chosen: a fixed polar reference system, the origin of which is set on the initial point of the straight part on the right, and a mobile reference system that is set on the mover. Being set on the mover, the mobile reference system is constrained to move along the track. In this way its Y_1 axis is always tangential to the track and its X_1 axis is always orthogonal to the track as shown in Fig. 2.

The fixed reference system determines the position of the mover through a polar angle θ and a radius r . In order to describe the position of the mobile reference system it is necessary to determine the value of the angle made up by the projection of the position vector on the X_1 axis of the mobile reference system. This angle is called α and it can be determined by the Eq. 1:

$$\alpha = \text{atan2}\left(-\frac{\dot{r}}{\dot{\theta}}, r\right) \quad (1)$$

Fig. 2 Fixed polar reference system (*light blue*) and mobile reference system (*green*)



Thanks to these choices it is possible to describe the position of the mover at each time instant by means of the values of α angle, θ angle and the polar radius.

3.2 *Dynamic Model*

The forces considered in the model are the driving force (F_m), the gravity force (F_g), the normal force (F_n), the inertia forces (F_j), the kinetic friction force (F_k) and the viscous friction force (F_v). The driving force F_m is produced by the magnetic field on the magnets, which are placed on the mover. It is considered to be always tangential to the track and to be always along the Y1 direction of the mobile reference system of the mover. The gravity force F_g always acts on the mover. Its direction is along the Y1 axis as regards the straight parts but it changes along the curves as regards the mobile reference system. The normal force F_n acts along the X1 axis of the mobile reference system. It is the sum of a constant part consisting in the preload of the rollers, which constrains the mover to move along the rail.

Inertia forces are taken into account but they are always balanced by the constraint produced by the architecture of the machine, since the rollers are forced to move only along the double rail on the frame. Two types of friction are considered: the kinetic friction and the viscous friction. In the kinetic friction model the friction force is proportional to the normal force by means of a coefficient μ_k . In the viscous friction model the force is always opposite to the direction of the motion and it is proportional to the speed of the mover by means of a viscous friction coefficient μ_v . The viscous friction coefficient is assumed to be 0.02, this value is provided by the carts producer. In the simulation a local coordinate system is taken on the cart, and all the components of forces are divided into tangential and normal forces.

4 **Controller Model**

The system supplier does not provide any information about the architecture of the real controller of the iTRAK system, for this reason it has been created a generic control system. The basic model of the control system is a PID controller, replicated for three control loops: the position control loop, the velocity control loop and the current control loop.

Each loop has three parameters that define the PID characteristics: K_p , K_i , K_d . In order to prevent the windup phenomenon that produces an excessive overshooting after the saturation of the motor, each loop also contains an anti-windup loop. The controller receives the desired position as input and produces a current signal as output. In order to model also the behavior of the electrical motor its transfer function is computed and it is equal to:

$$G(s) = \frac{K_m}{Le \cdot s + Re} \quad (2)$$

where K_m is the motor parameter, Le is the inductance parameter; Re is the resistance parameter [9].

The output signal of the controller is multiplied by the transfer function of the electrical motor and by the gain of the motor K_t .

5 Experimental Results and Validation of the Model

Validation and optimization of the model are based on tests performed on a straight and on a curved part of the system. In the tests the motion of the mover from a motor to another one is not considered because there is a little gap between each motor which does not allow a perfect control of the mover, since there is no coil in this area. Most of the parameters are available from direct measurements or data sheet. Other parameters—such as the friction coefficients and the gain parameters of the PID controllers—have been optimized by means of the Matlab Parameter Estimation. The setup configuration of the system is the same drawn in Fig. 2, the gravity force is opposite to the driving force.

Four tests are performed:

- (1) Standstill test along a straight part during which the control tends to block the mover in a command position. This test is useful to determine the static parameters of the mechanical and the control systems.
- (2) Trapezoidal motion test along a straight part during which the mover leaves from an initial position, reaches a final position and then come back to the initial position again. This test is performed at different velocities: 100, 500, and 1000 mm/s.
- (3) Standstill test along a curved part.
- (4) Trapezoidal motion test on the half of the curved part performed at three different velocities: 100, 500, and 1000 mm/s.

With the optimized parameters of the model it has been possible to validate the simulated machine. The Figs. 3 and 4 below shows the comparison between the current output of the model (red line) and of the real machine (blue line) in the trapezoidal motion along a straight part and in the trapezoidal motion along a curved part at a velocity of 1000 mm/s. In order to evaluate the performance of the model, the difference between the real current and the current of the model has been taken into consideration in the standstill parts of the cart motion. In this way it has been possible to compare the RMS values of the real current with the modelled current. The comparison between the two currents, when the mover is stopped in the different tests, is shown in Tables 1 and 2 for the straight and curved parts respectively. In the standstill parts the difference between the real and the model data lies on the fact that the discrete behavior of the driver in the model is not taken into account.

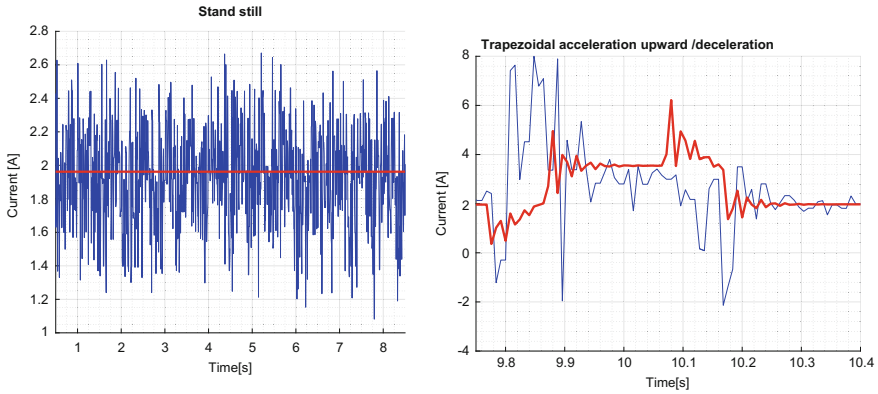


Fig. 3 Real (blue) and model (red) current along straight parts

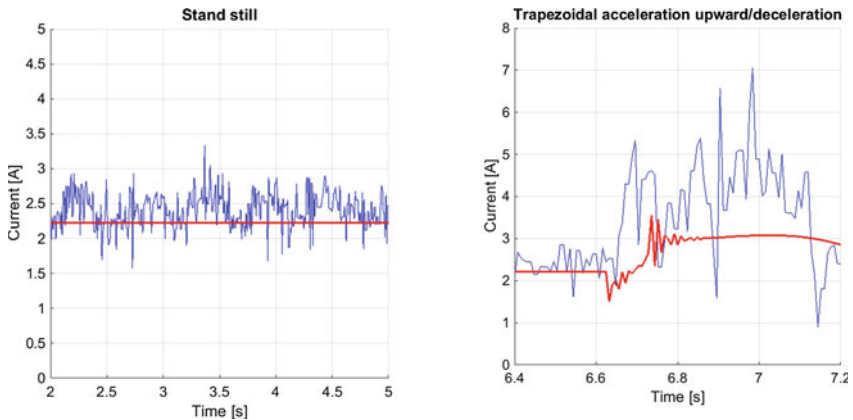


Fig. 4 Real (blue) and model (red) current along curved parts

Table 1 Comparison between the real and simulated RMS current along a straight part

Test type	Real RMS current [A]	Simulated RMS current [A]
Standstill	1.8	1.962
Trapezoidal 100 mm/s ²	1.8620	1.962
Trapezoidal 500 mm/s ²	1.98	1.962
Trapezoidal 1000 mm/s ²	1.9537	1.963

However, the higher difference between the experimental and model data is about 9 %. The difference in the acceleration and deceleration phases is mainly due to the different architecture and PID parameters of the controllers, since the supplier does not provide any information about the architecture of the real controller.

Table 2 Comparison between the real and simulated RMS current along a curved part

Test type	Real RMS current [A]	Simulated RMS current [A]
Standstill	2.3165	2.2072
Trapezoidal 100 mm/s ²	2.3963	2.24
Trapezoidal 500 mm/s ²	2.4259	2.24
Trapezoidal 1000 mm/s ²	2.4617	2.24

6 Conclusions

A dynamic model for an independent carts system has been proposed, tested and verified through a set of experimental results. The model simulates the most relevant mechanical aspects of the machine such as the forces acting on the carts and the shape of the track. The used controller is a theoretical one and its parameters have been tuned through the comparison between the experimental data and the model data. The results of the model are in good agreement with the experimental ones. As a matter of fact, the higher difference between the current of the model and the current of the real machine along the constant parts of the signal is about 9 %. The higher current error is in the acceleration and deceleration of the carts and it is due to the different architecture of the real machine controller and the model controller.

In general, the built model can be used to analyze the kinematics and dynamics of the system in order to realize new applications with this technology.

Acknowledgments The authors want to acknowledge Davide Borghi and Stefano Flore of Tetra Pak Packaging Solutions SpA for suggestions, fruitful discussions and technical support.

References

1. McLean GW (2008) Review of recent progress in linear motors. In: IEE proceedings B—electric power applications, pp 280–416
2. Beckhoff Automation. <http://www.beckhoff.com/XTS/>
3. Rockwell Automation. http://www.rockwellautomation.com/en_UK/products-technologies/itrak/overview.page
4. Fasih A (2015) Sviluppo di soluzioni innovative per l'alimentazione sincrona di macchine confezionatrici ad alte prestazioni. Ph.D. Thesis, University of Ferrara, in Italian
5. Cheli F, Pennestrì E (2010) Cinematica e dinamica dei sistemi multibody, vol 1–2, Casa Editrice Ambrosiana
6. Moscariello G et al (2006) Applications of a motion planning algorithm for funicular railways. WSEAS Trans Syst 5
7. Rossi C, Savino S (2013) Robot trajectory planning by assigning positions and tangential velocities. Robot Comput Integr Manuf 29:139–156

8. Siciliano B et al (2009) *Robotics: modelling, planning and control*. Springer-Verlag, London Limited
9. Polinder H et al (2002) Modelling a linear PM motor including magnetic saturation. In: *Proceedings of international conference on power electronics, machines and drives*, pp 632–637

Tyre-Road Adherence Conditions Estimation for Intelligent Vehicle Safety Applications

Mojtaba Sharifzadeh, Francesco Timpone, Arash Farnam,
Adolfo Senatore and Ahmad Akbari

Abstract It is well recognized in the automotive research community that knowledge of the real-time tyre-road friction conditions can be extremely valuable for intelligent safety applications, including design of braking, traction, and stability control systems. This paper presents a new development of an on-line tyre-road adherence estimation methodology and its implementation using both Burckhardt and LuGre tyre-road friction models. The proposed strategy first employs the recursive least squares to identify the linear parameterization (LP) form of Burckhardt model. The identified parameters provide through a Takagi-Sugeno (T-S) fuzzy system the initial values for the LuGre model. Then, it is presented a new large-scale optimization based estimation algorithm using the steady state solution of the partial differential equation (PDE) form of LuGre to obtain its parameters. Finally, real-time simulations in various conditions are provided to demonstrate the efficacy of the algorithm.

Keywords Vehicle longitudinal dynamics · State estimation · Tire force

M. Sharifzadeh · A. Akbari
Institute of Automatic Control, Sahand University of Technology, Tabriz, Iran
e-mail: m_sharifzadeh@sut.ac.ir

A. Akbari
e-mail: a.akbari@sut.ac.ir

F. Timpone (✉)
Department of Industrial Engineering, University of Naples Federico II, Naples, Italy
e-mail: francesco.timpone@unina.it

A. Farnam
SYSTeMS research group, Faculty of Engineering and Architecture, Ghent University,
Ghent, Belgium
e-mail: arash.farnam@ugent.be

A. Senatore
Department of Industrial Engineering, University of Salerno, Salerno, Italy
e-mail: a.senatore@unisa.it

1 Introduction and Motivation

Road-tyre forces are crucial in the control of vehicle dynamics, since they are the only forces that a ground vehicle experiences from the road. These forces significantly affect the longitudinal, lateral, yaw and roll behavior of the ground vehicle. Based on this principle, real-time road-tyre adherence estimation is useful in active stability control systems, intelligent driver support systems, adaptive cruise control, collision-avoidance systems and other intelligent vehicle safety systems [1–3].

When estimation methods based on vehicle dynamics, are not utilized, special sensors that directly attempt to measure adherence, are employed. One such approach [4], optical sensors installed at the front bumper of the vehicle, use the information from road reflections to predict the road surface conditions. All of the techniques such as this, have limitations with regard to robustness and reliability. Moreover, considering that, commercially available optical systems are quite expensive [5], it is clearly evident that, cost-effectiveness is another significant factor.

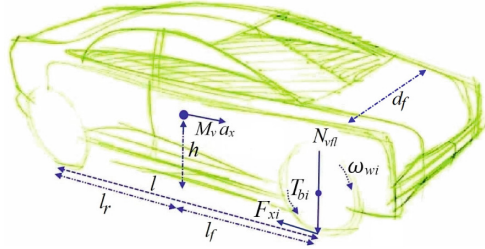
There are different vehicle-dynamics-based approaches and experimental studies to the solution of this problem [6]. One of the available solutions which is utilized in this work, is the well-known slip-based approach, which uses the road-tyre friction interaction models based on the wheel slip [7]. Most of the existing slip-based methods have employed simple vehicle dynamics because of estimation accuracy problem on a more complex vehicle dynamic models. Thus, considering that limited works have been reported for a real-time and robust detection of road-tyre conditions, we are focused on implementing computationally efficient method for on-line identification of surface conditions in different tyre types and road surface conditions during braking.

2 System Description

A simple but effective four-wheel vehicle considering vehicle/tyre/road dynamics is described in this section [6, 8]. The vehicle dynamic is given by summing the total forces applied to the vehicle with braking operation. Ignoring the road gradient and wind speed it is represented as $\dot{v}_v = - [\sum F_{xi} + B_v v_v + D_a v_v^2] / M_v$, where $v_v[m/s]$ is the longitudinal velocity of the vehicle; $F_{xi}[N]$ denotes the road-tyre friction force for the wheel $\{i = fl, fr, rl, rr\}$, ($f = front/r = rear, l = left/r = right$); B_v is the vehicle viscous friction; D_a is the aerodynamic drag force.

The road-tyre friction force for the i th wheel, is given by $F_{xi} = \mu(\lambda)F_{Ni}$, where the adherence μ is a function of the slip λ ; and $F_{Ni}[N]$ denotes the vertical wheel reaction force applied to the wheel. The i th wheel dynamic by summing the rotational torque yields to $\dot{\omega}_{wi} = \frac{1}{J_w} [-T_{bi} \text{sign}(\omega_{wi}) + R_w F_{xi} + T_e]$, where $\omega_{wi}[rad/s]$ is the angular velocity of the i th wheel, $T_{bi}[N.m]$ is the braking torque on the i th wheel, and $T_e[N.m]$ is main shaft torque on the wheel [9], see Fig. 1. Longitudinal Slip λ is

Fig. 1 Vehicle dynamics schematic (sketched)



the difference between vehicle actual longitudinal velocity and wheel circumferential velocity, is defined as, $\lambda = (v_v - v_w) / \max \{v_v, v_w\}$ with $v_w = R_w \omega_w$.

One of the widely-used models for friction, is the Burckhardt Model, which is easy to linearize for applying recursive least squares (RLS) identification method and allows a good correlation to be obtained with experimental results. This model is given as, $\mu(\lambda; c_\theta) = c_1(1 - \exp(-\lambda c_2)) - \lambda c_3$ where the Burckhardt elements vector is $c_\theta = [c_1 \ c_2 \ c_3]^T$;

On the other hand, increasing the vehicle speed, reduce the adherence for a given road condition, which is a fact that is generally not considered in these formulas [10]. Therefore in order to consider the adherence dependence on velocity and also to involve more properties of real friction behavior such as tyre situation, LuGre dynamic friction model [10, 11], is chosen in addition to the Burckhardt Model.

Assuming that the wheel radius (R_w) remains constant during braking, ignoring main shaft torque, summing the total vertical wheel reaction forces, considering the characteristics in real-time and applying some mathematical calculations [12], yields to

$$\mu(\lambda_i; i) = \frac{\frac{T_{bi}(t) \text{sign}(\omega_{wi}(t))}{J_w} - \Xi_3(t) \dot{\lambda}_i(t) - \frac{(D_a R_w \Xi_3(t) + B_v) \omega_{wi}(t)}{M_v}}{\frac{g \omega_{wi}(t)}{R_w \Xi_3(t)} + \frac{R_w M_v}{2 J_w l} \Xi_{1i}(t) (1 + \Xi_{2i}(t))}}, \quad (1)$$

$\{i = fl, fr, rl, rr\}$

$$\begin{pmatrix} \Xi_{1fl}(t) \\ \Xi_{1fr}(t) \\ \Xi_{1rl}(t) \\ \Xi_{1rr}(t) \end{pmatrix} = \begin{pmatrix} 1 & 0 \\ 1 & 0 \\ 0 & 1 \\ 0 & 1 \end{pmatrix} \begin{pmatrix} l_r g + h a_x(t) \\ l_f g - h a_x(t) \end{pmatrix}, \quad \begin{pmatrix} \Xi_{2fl}(t) \\ \Xi_{2fr}(t) \\ \Xi_{2rl}(t) \\ \Xi_{2rr}(t) \\ \Xi_3(t) \end{pmatrix} = \text{diag}(1, 1, 1, 1, \omega_{wi}(t)) \begin{pmatrix} 1 + \frac{2h a_y(t)}{d_f g} \\ 1 - \frac{2h a_y(t)}{2h a_y(t)} \\ 1 + \frac{d_f g}{2h a_y(t)} \\ 1 - \frac{d_f g}{2h a_y(t)} \\ \frac{1}{1 - \lambda_i(t)} \end{pmatrix}$$

3 Estimator Design

3.1 Burckhardt Parameters Estimation/Setting the Initial Conditions

As was shown, the Burckhardt model is nonlinear due to the exponential term in c_2 . If the linear form of μ Burckhardt model is determined, its unknown parameters will be estimated by linear least-squares methods. Therefore the problem is finding an optimal linear parameterization (LP) for the single nonlinear term $f(\lambda, c_2) = e^{-c_2\lambda}$ with the approximating domain $[0, \bar{\lambda}] \times D$, as $\hat{f}(\lambda, w, \beta) = [g_1(\lambda, w), \dots, g_n(\lambda, w)]\beta = G(\lambda, w)^T\beta$, where the principal functions for LP are the exponential as $G_E(\lambda, w) = [e^{w_1\lambda}, e^{w_2\lambda}, \dots, e^{w_m\lambda}]^T$ and the logistic sigmoid as $G_L(\lambda, w) = \left[\frac{1}{1+e^{-w_1\lambda-w_2}} \dots, \frac{1}{1+e^{-w_{m-1}\lambda-w_m}} \right]^T$, with $w = [w_1 w_2 \dots w_m] \in \mathfrak{R}^m$. Even though both functions can produce a reasonable LP results, the number of the parameters of exponential function is less than logistic sigmoid.

It is considerable that, reducing the number of the exponential functions can speed up the estimation. Therefore, in this paper, the exponential functions was implemented for the real-time estimation with the optimum w as $G(\lambda) = [e^{-5.02\lambda} \ e^{-18.39\lambda} \ e^{-65.59\lambda}]^T$. This approximation reduces the number of exponential functions to $n = 3$ and is as accurate as the complex slower LP forms presented in [6].

As a result the LP is as follows $\hat{\mu}(\lambda; t) = a_1 - a_2\lambda + a_3e^{-4.99\lambda} + a_4e^{-18.43\lambda} + a_5e^{-65.62\lambda}$, which can be described using linear regression as $\hat{\mu}(\lambda; t) = \phi(\lambda)^T a$ with $a = [a_1 \ a_2 \ \dots \ a_5]^T$ and $\phi(\lambda; t) = [1 \ -\lambda \ e^{-4.99\lambda} \ e^{-18.43\lambda} \ e^{-65.62\lambda}]^T$. where a_1 and a_2 equal c_1 and c_3 in Burckhardt model. Therefore, the recursive least squares (RLS) algorithm, can be used to update the unknown parameter vector of a iteratively, using the past input-output data contained within the measured regressor vector $\phi(t)$.

The structure of the proposed algorithm is shown in Fig. 2a. As shown in this structure, in order to complete the identification steps Burckhardt road type characteristics should be converted to LuGre road-tire parameters. The proposed formulation for this case is an instance of the Takagi-Sugeno (TS) fuzzy system (see Fig. 2b). Hence the rule base for this model can be written using the set of M rules as, $R = \{R^1_{Bklg}, R^2_{Bklg}, \dots, R^M_{Bklg}\}$ where the k th rule has the following format:



Fig. 2 Proposed algorithm architecture (a), and the Fuzzy logic based parameter conversion (b)

$R_{Bklg}^k : \mathbf{IF} C_1 \text{ is } \tilde{A}_1^k \text{ OR } C_2 \text{ is } \tilde{A}_2^k \text{ OR } C_3 \text{ is } \tilde{A}_3^k, \mathbf{THEN}$
 $\theta_{up} \text{ is } \tilde{B}_1^k \text{ AND } \theta \text{ is } \tilde{B}_2^k \text{ AND } \theta_{low} \text{ is } \tilde{B}_3^k, k = 1, \dots, M$

where \tilde{A}_j^k are the classified inputs and \tilde{B}_j^k are fuzzy sets defined by multivariate membership functions using experimental results of Burckhardt and LuGre models [6, 10].

3.2 LuGre Parameters Estimation

Theorem 1 For any given road conditions and tire type if v, ω are assumed to be constant during each estimation period and conditions of braking case hold then the following static form can be used to identify LuGre tire-road friction parameters by fitting the model to experimental data, i.e.,

$$\mu_b(\lambda) = \frac{g(\lambda)}{\theta} \left[1 + \frac{g(\lambda)(\lambda+1)}{\theta\sigma_0\lambda L} \left(e^{-\frac{\sigma_0\lambda L\theta}{g(\lambda)(\lambda+1)}} - 1 \right) \right] + \sigma_2\lambda v_v, \quad g(\lambda) = \mu_c + (\mu_s - \mu_c)e^{-\left| \frac{\lambda v}{v_0} \right|^{1/2}} \tag{2}$$

Proof The LuGre distributed models can be represented by the following PDE equations

$$\begin{cases} \frac{dz}{dt}(\zeta, t) = v_r - \frac{\theta\sigma_0|v_r|}{g(v_r)z} \\ F_{xi} = \frac{F_{Ni}}{L} \int_0^L (\sigma_0 z(\zeta, t) + \sigma_1 \dot{z}(\zeta, t) + \sigma_2 v_r) d\zeta \end{cases} \tag{3}$$

with boundary conditions $z(0, t) = z(L, t) = 0, \forall t \geq 0$, where $z(\zeta, t)$ denotes the corresponding friction state and the patch L represents the projection of the part of the tire that is in contact with the road, with ζ -axis along the length of the patch in the direction of the tire rotation. Assuming that v_v and ω_{wi} are constant, $\dot{\zeta} = |R_w\omega_{wi}|$ and by setting within an small enough interval of time $\frac{\partial z}{\partial t}(\zeta, t) = 0$ applying these conditions in equation $\frac{dz}{dt}(\zeta, t) = \frac{\partial z}{\partial t}(\zeta, t) + \frac{\partial z}{\partial \zeta}\dot{\zeta}$ gives $\frac{dz}{d\zeta}(\zeta) = \frac{1}{R_w\omega_{wi}} \frac{dz}{dt}(\zeta, t)$

$$\frac{dz}{d\zeta}(\zeta) = \frac{v_r}{R_w\omega_{wi}} - \frac{\sigma_0|v_r|}{g(\lambda)R_w\omega_{wi}}z, \quad \zeta \in [0, L] \tag{4}$$

Solving the Eq. 4 for $z(\zeta)$ with initial conditions $z(\zeta) = \zeta = 0$, one obtains

$$z(\zeta) = \begin{cases} \frac{g(\lambda)}{\sigma_0} \left(\exp\left(-\frac{\sigma_0\lambda\theta}{(1+\lambda)g(\lambda)}\zeta\right) - 1 \right), & 0 \leq \zeta \leq \frac{L}{2} \\ \frac{g(\lambda)}{\sigma_0} \left(\exp\left(-\frac{\sigma_0\lambda\theta}{(1+\lambda)g(\lambda)}(L - \zeta)\right) - 1 \right), & \frac{L}{2} \leq \zeta \leq L \end{cases} \tag{5}$$

Noticing that $\mu(\lambda_i) = F_{xi}/F_{Ni}$ and using the Eqs. 3 and 5, one obtains

$$\begin{aligned} \implies \mu(\lambda_i) &= \frac{\sigma_0}{L} \left[\frac{Lg(\lambda_i)}{\theta\sigma_0} \left(1 + \frac{2g(\lambda_i)(1+\lambda_i)}{\sigma_0\lambda_iL\theta} \left(e^{-\frac{\sigma_0\lambda_iL\theta}{2g(\lambda_i)(1+\lambda_i)}} - 1 \right) \right) \right] + \sigma_2v_r \\ + \frac{\sigma_1}{L} \left[\frac{2v_vg(\lambda_i)}{\theta\sigma_0} \left(1 - e^{-\frac{\sigma_0\lambda_iL\theta}{2g(\lambda_i)(\lambda_i+1)}} \right) \right] &\approx \frac{g(\lambda_i)}{\bar{\theta}} \left[1 + \frac{g(\lambda_i)(\lambda_i+1)}{\bar{\theta}\sigma_0\lambda_iL} \left(e^{-\frac{\sigma_0\lambda_iL\bar{\theta}}{g(\lambda_i)(\lambda_i+1)}} - 1 \right) \right] \\ + \sigma_2\lambda_iv_v \text{ where } g(\lambda_i) &= \mu_c + (\mu_s - \mu_c)e^{-\left| \frac{\lambda_iv_v}{v_0} \right|^{1/2}} \end{aligned} \tag{6}$$

□

Let $\mu_a \in \mathfrak{R}^N$ to be the vector of adherence which is calculated from the Eq. (1) for different values of λ_i and $\hat{\mu}_b(\lambda_i, \Theta) \in \mathfrak{R}^N$ be the vector of LuGre friction model (2) with unknown parameters and the sample vector of λ_i . Now the LuGre unknown parameters are available by minimizing the estimation error $f_\epsilon(\Theta) = |\mu_a - \hat{\mu}_b(\lambda_i, \Theta)|$. In order to solve estimation problem an interior Trust-Region method [12], is utilized in the present work. The proposed identification method is summarized in algorithm 1. The convergence of the algorithm is proven in [12].

Algorithm 1 Trust-Region based recursive identification algorithm for this problem

- 1: Initialisation of the Burckhardt parameter vector
- 2: **repeat**
- 3: Measure $\mu_a \in \mathfrak{R}^N$ and calculate $\lambda_i \in \mathfrak{R}^N$ using (1)
- 4: Determine the Burckhardt parameter vector using RLS method
- 5: Calculate $f_\epsilon(\Theta) = \mu_a - \hat{\mu}_b(\lambda_i, \Theta)$
- 6: Obtain $\Theta_1, l_{lo}, l_{up} \in \mathfrak{R}^N$ using T-S fuzzy,
- 7: Given $\Delta_1 > 0$ let $k = 1$,
- 8: **while** (Not converged) **do**
- 9: 8.1) Solve subproblem $(\min_{s \in \mathfrak{R}^N} s^T \nabla f_\epsilon(\theta_k) + \frac{1}{2} s^T \nabla^2 f_\epsilon(\theta_k) s \text{ such that } \|s\|_2 \leq \Delta_k)$
- 10: 8.2) Update Θ_k , i.e.

$$\Theta_{k+1} = \begin{cases} \Theta_k & \text{if } \Theta_k + s_k \notin [l_{lo}, l_{up}] \text{ or } f_\epsilon(\Theta_k) \leq f_\epsilon(\Theta_k + s_k) \\ \Theta_k + s_k & \text{otherwise,} \end{cases} \tag{7}$$

- 11: 8.3) Trust region radius update. Set

$$r_k = (f_\epsilon(\Theta_k) - f_\epsilon(\Theta_k + s_k)) / \psi_k(s_k); \quad \Delta_{k+1} \in \begin{cases} [\tau_3 \|s_k\|_2, \tau_4 \Delta_k] & \text{if } r_k < \tau_2, \\ [\Delta_k, \tau_1 \Delta_k] & \text{otherwise;} \end{cases}$$

- 12: 8.4) Update g_k, H_k and $k = k + 1$
 - 13: **end while**
 - 14: Update inputs
 - 15: **until** (there are no more input data available)
-

4 Simulation Results

This section presents simulation results to validate the proposed non-linear model in estimating the longitudinal friction curve and other adherence characteristics with the presented method.

The sampling time of the simulation was set to 5 ms and in order to consider more realistic settings, the prediction has been done on noisy simulation data. Zero mean white noises have been added to the wheel speed with $\sigma_{\omega}^2 = 0.01 \text{ rad}^2/\text{s}^2$, to the braking torque with $\sigma_{T_b}^2 = 10 \text{ N}^2\text{m}^2$, and to the rubber stiffness with $\sigma_{\sigma_0}^2 = 15 \text{ 1/m}^2$, due to the measurement noise by wheel encoder, EM-brakes and rubber stiffness uncertainty, respectively (Fig. 3).

In order to benchmark the results, two different driving scenarios are considered during braking for this case, where the desired vehicle longitudinal speed is changed from 25 m/s (90 km/h) to 16 m/s (56 km/h) on dry asphalt during braking and deceleration/braking from 25 to 23 m/s on snow (Figs. 4 and 5), respectively.

Both Burckhardt based identification [6] and proposed identification results have been illustrated for this scenarios. Figure 5 clearly shows that the combined method using both Burckhardt and LuGre models gives better results for the different surfaces. It also can be justified by noting that, combined NLLS method considers more realistic features, such as changes of tyre friction characteristics and vehicle longitudinal velocity.

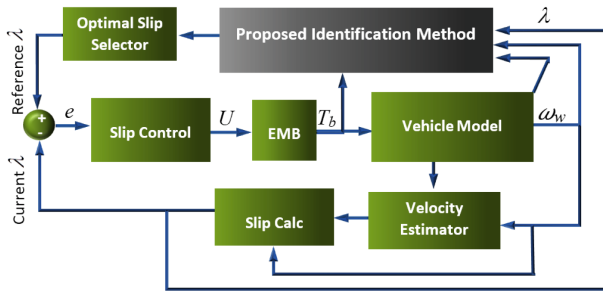


Fig. 3 Implementation of the proposed NLLS

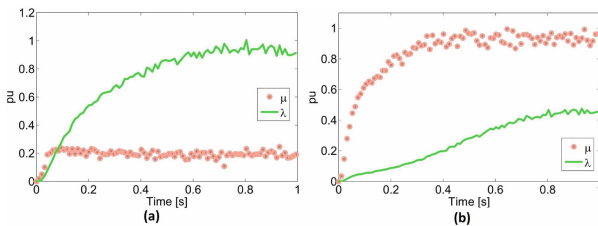


Fig. 4 Wheel slip (λ) and adherence (μ) on dry asphalt (b), hard-packed snow (a)

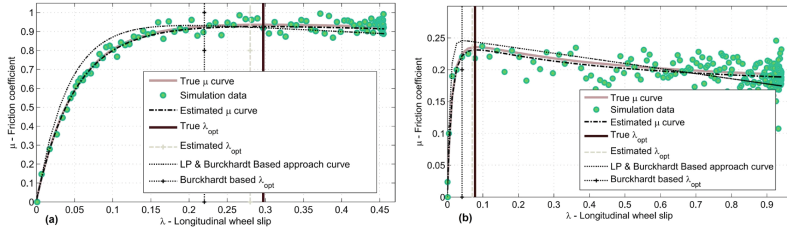


Fig. 5 Curve fitting results for adherence estimation on dry asphalt (a), hard-packed snow (b)

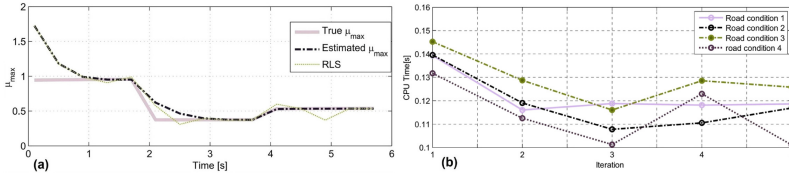


Fig. 6 $\hat{\mu}_{max}$ estimation results on time-varying road friction condition (a), CPU time results (b)

In order to validate the effectiveness of proposed friction estimator, a mixed- μ road test is simulated. Hence, the remaining work is passed on to the variable tyre/road monitoring.

The optimal value of the slip $\hat{\lambda}_{i_{opt}}$ is obtained by computing the estimated maximum adherence (μ_{max}). By using $\hat{\lambda}_{i_{opt}} = arg\ max\ \{\hat{\mu}_b(\lambda_i, v_v, \Theta)\}$ the results of peak adherence coefficient and its own slip value can be computed (see Fig. 6a). Figure 6b shows the CPU time results.

As shown in Fig. 6a, it is indicated that both presented NLLS approach and RLS friction estimator are available for the quick-changes of the road condition and have a good convergence rate. However, with respect to the RLS method [6], from the above results, it can be observed that the NLLS estimated values has a better fit to the real data. This also can be justified by the fact that although the RLS is fast but it assumes multiple linear regression model and has linearization error in this case. NLLS approach doesn't need to approximate the nonlinear models and is more robust to noise.

5 Conclusions

In this work an on-line algorithm for the estimation of $\hat{\mu}$ of road surface adherence, considering various tyre friction conditions and different vehicle speeds has been presented. In order to initialize and have a faster algorithm, the parameters of Burckhardt LP form have been identified using RLS and then converted to the LuGre parameters by using the fuzzy rules. The LuGre model is a static one obtained by the LuGre dis-

tributed model. Eventually, a new LuGre model-based NLLS parameter estimation algorithm has been presented. The convergence of NLLS method has been proved and also the total algorithm performance has been tested when it used in different road profiles. The effectiveness of proposed algorithm is demonstrated through simulation results and thus the proposed longitudinal road-tyre frictional condition estimation is valuable for intelligent vehicle control and autonomous vehicle systems. Although, this estimator used normal vehicle sensors, it still brought relatively good results when compared with the values obtained from the real data. In the future, the presented approach will be validated by our experiments.

Appendix

Vehicle nominal parameters are listed below [6, 10].

R_w : Radius of the wheel = 0.3 [m]	J_w : Rotation inertia of the wheel = 1 [kg.m ²]
l_f : Distance from CG to front axles = 1.3 [m]	l_r : Distance from CG to rear axles = 1.4 [m]
d_f, d_r : Distances between front/rear wheels = 0.9 [m]	h : Height of CG = 0.5 [m]
M_v : Mass of the vehicle at CG = 900 [kg]	L : Road/tyre patch length = 0.2 [m]
ω_{rot} : Model parameter of EMB dynamic = 70 [rad/s]	μ_c : Normalized coulomb friction = 0.8
σ_0 : Rubber longitudinal lumped stiffness = 181.54 [1/m]	μ_s : Normalized static friction = 1.55 [m]
σ_1 : Rubber longitudinal lumped damping = 4.94 [s/m]	σ_2 : Viscous relative damping = 0.0018 [s/m]
τ_M : Delay parameter of EMB dynamic = 10 [ms]	v_0 : Stribeck relative velocity = 6.57 [m/s]
c_1 : Maximum value of friction curve = [0.19, 1.28]	c_3 : $\mu(\lambda_{opt}) - \mu(1) = [6.46, 94.13]$
c_2 : Maximum value of friction curve shape = [0.06, 0.67]	

References

1. Farroni F, Giordano D, Russo M, Timpone F (2014a) Trt: thermo racing tyre a physical model to predict the tyre temperature distribution. *Meccanica* 49(3):707–723
2. Farroni F, Russo M, Russo R, Timpone F (2014b) A physical-analytical model for a real-time local grip estimation of tyre rubber in sliding contact with road asperities. *Proc Inst Mech Eng Part D: J Automobile Eng* 228(8):955–969
3. Sharifzadeh M, Ebrahimi S, Akbari A (2014) Analysis on vehicle stability in active braking: a comparative study of different approaches. In: *Regional conference on electrical and computer engineering, Civilica*, pp 58–69

4. Breuer B, Eichhorn U, Roth J (1992) Measurement of tyre/road-friction ahead of the car and inside the tyre. In: International symposium on advanced vehicle control, 1992. Yokohama, Japan
5. AB-Dynamics (2015) Corrsys-Datron optical sensors. http://abd-mf-jp.com/item/index_e.html
6. Savaresi SM, Tanelli M (2010) Active braking control systems design for vehicles. Springer Science & Business Media
7. Gustafsson F (1997) Slip-based tire-road friction estimation. *Automatica* 33(6):1087–1099
8. Ulsoy AG, Peng H, Çakmakci M (2012) Automotive control systems. Cambridge University Press
9. Pisaturo M, Cirrincione M, Senatore A (2015) Multiple constrained mpc design for automotive dry clutch engagement. *IEEE/ASME Trans Mechatron* 20(1):469–480
10. de Wit CC, Tsiotras P, Velenis E, Basset M, Gissinger G (2003) Dynamic friction models for road/tire longitudinal interaction. *Veh Syst Dyn* 39(3):189–226
11. Freidovich L, Robertsson A, Shiriaev A, Johansson R (2010) Lugre-model-based friction compensation. *IEEE Trans Control Syst Technol* 18(1):194–200
12. Sharifzadeh M, Akbari A, Timpone F, Daryani R (2016) Vehicle tyre/road interaction modeling and identification of its parameters using real-time trust-region methods. *IFAC-PapersOnLine* 48(3)

Part VIII
Tribology

Tilting Pad Journal Bearing TEHD Analysis: An Innovative Model

Amedeo Frilli, Enrico Meli, Daniele Nocciolini, Simone Panconi,
Luca Pugi, Andrea Rindi and Stefano Rossin

Abstract Tilting Pad Journal Bearings (TPJBs) are widely used in the turbomachinery field due to their superior dynamical performances, but their operation involves several different physical phenomena. In this research work the authors propose an innovative 3D ThermoElastoHydroDynamic (TEHD) model for the analysis of TPJBs behaviour developed and experimentally validated in cooperation with General Electric Nuovo Pignone: the model is able to perform a nonlinear transient coupled analysis taking into account fluid dynamical, thermal and elastic effects and reaches a good compromise between the accuracy of the results and the computational efficiency.

1 Introduction

In the last years, the development trend in the turbomachinery field has pushed towards ever higher rotational speeds and loads [13, 14]. In this scenario, Tilting Pad Journal Bearings (TPJBs) have almost completely substituted the more unstable

A. Frilli · E. Meli · D. Nocciolini · S. Panconi · L. Pugi (✉) · A. Rindi
Department of Industrial Engineering, University of Florence, Florence, Italy
e-mail: luca.pugi@unifi.it

A. Frilli
e-mail: amedeo.frilli@unifi.it

E. Meli
e-mail: enrico.meli@unifi.it

D. Nocciolini
e-mail: daniele.nocciolini@unifi.it

S. Panconi
e-mail: simone.panconi@unifi.it

A. Rindi
e-mail: andrea.rindi@unifi.it

S. Rossin
GE Oil & Gas, Florence, Italy
e-mail: stefano.rossin@ge.com

© Springer International Publishing AG 2017

G. Boschetti and A. Gasparetto (eds.), *Advances in Italian Mechanism Science*,
Mechanisms and Machine Science 47, DOI 10.1007/978-3-319-48375-7_43

Fixed Geometry Journal Bearings. TPJBs are particular fluid dynamical bearings where the supporting action exerted on the rotor is due to the pressure field generated by the rotor rotation in a set of lubricant films interposed between the rotor and the bearings tilting pads. TPJBs, due to their intrinsic stability properties, strongly reduce the risk of fluid dynamic induced vibrations like the Oil Whirl and the Oil Whip and, thanks to their ability to dynamically follow the rotor motion, are suitable for high speed and high load applications. However, their dynamic behaviour is influenced by many different physical phenomena and hence an accurate modelling of TPJBs operation is mandatory in order to safely design and operate such a rotor dynamic system. Furthermore, the numerical efficiency of a TPJB model must be accurately considered in order to develop a tool suitable to meet the industry requirements.

The developed model is based (regarding the technical and experimental data) on a test rig rotor supported by two five pads TPJBs and it is composed by the following components:

1. the oil film model provides the forces and moments both on the pads and on the rotor due to the pressure and temperature fields;
2. the pad FEM model provides the pad kinematic quantities and deformations and the pad temperature field;
3. the lubricant supply sump model is used to calculate the inlet temperature and pressure for each film;
4. the rotor FEM model is used to calculate the rotor kinematic quantities and deformations and the correspondent temperature.

2 Model Description

The TPJB architecture is visible in Fig. 1 where S_A , S_{pad} , S_1 , S_3 , S_2 , S_4 represent respectively the rotor and pad surfaces, the control volume boundaries correspondent to pads leading and trailing edges and the side boundaries where the oil flow leaks outwards. The oil film sub-model receives as inputs the kinematic quantities of rotor and pads and their elastic displacements and velocities (included in the FEM generalized displacements and velocities): \mathbf{q}_A^j , $\dot{\mathbf{q}}_A^j$, \mathbf{q}_{pad}^{ij} , $\dot{\mathbf{q}}_{pad}^{ij}$. Furthermore, it receives as inputs the rotor and pad temperature T , and the sumps temperature and pressure T^{ij} and p^{ij} .

The mesh has been built using bidimensional QUAD elements (justified by the hypotheses underlying the Reynolds equation), in order to obtain accurate results maintaining acceptable performances (in terms of numerical efficiency). To allow the correct coupling between the components of the model, it has been necessary to express all the kinematic and geometrical quantities, like the oil film thickness, in a common reference system with the origin in the bearing center (see Fig. 2). Considering the pressure field p and the velocity field $\mathbf{v} = (u \ v \ w)^T$ inside the oil

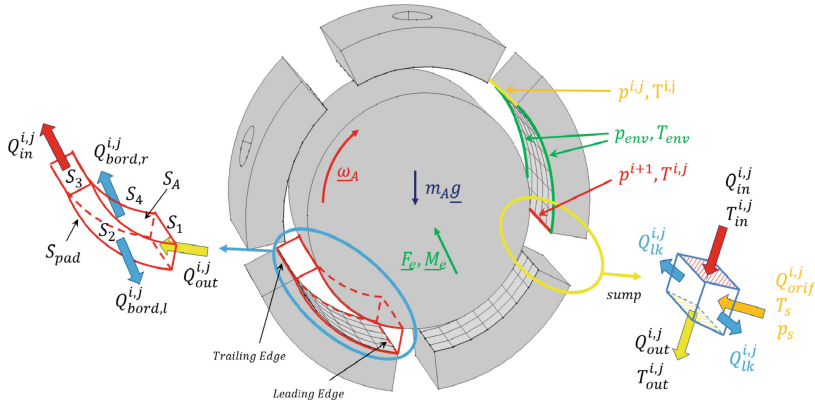
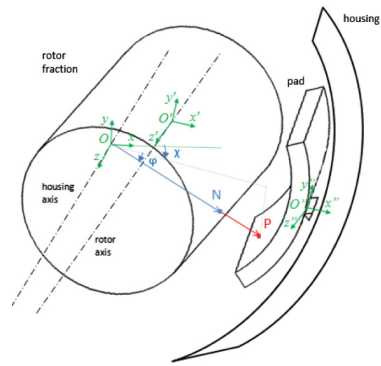


Fig. 1 TPJB structure, lubricant supply plant and control volume

Fig. 2 Geometric and kinematic representation of the oil film



film, the Reynolds equation can be written respect to the system O_{xyz} in the following form [4–6]:

$$\frac{\partial}{\partial x} \left(\frac{\rho h^3}{12\mu(T_f)} \frac{\partial p}{\partial x} \right) + \frac{\partial}{\partial z} \left(\frac{\rho h^3}{12\mu(T_f)} \frac{\partial p}{\partial z} \right) = \frac{\partial}{\partial x} \left[\frac{\rho h(u_{pad} + u_A)}{2} \right] + \frac{\partial}{\partial z} \left[\frac{\rho h(w_{pad} + w_A)}{2} \right] + \frac{\partial \rho h}{\partial t}, \tag{1}$$

where \mathbf{v} depends on p [4–6]; $\mu(T_f)$ is the lubricant dynamic viscosity, dependent on the fluid temperature T_f : the viscosity and the velocity field represent the coupling quantities between the Reynolds equation and the energy equation.

The lubricant viscosity itself and the specific volume have been modelled using polynomial equations [7], taking into account both the influence of temperature and pressure. Then, considering the velocity field obtained through the fluid dynamic analysis, the temperature field inside the oil film can be calculated according to the energy equation:

$$\rho C_p \frac{\partial T_f}{\partial t} + \nabla \cdot (-\lambda \nabla T_f) + \boldsymbol{\beta} \cdot \nabla T_f = \nabla \cdot (\mathbf{v} \cdot \boldsymbol{\tau}), \quad (2)$$

where C_p is the fluid specific heat capacity at constant pressure, λ is the fluid thermal conductivity, $\boldsymbol{\beta}$ is the convection coefficient and $\boldsymbol{\tau}$ is the stress tensor. The boundary conditions imposed at the leading edge of the control volume include an inlet temperature equal to the previous sump temperature, and a heat exchange equal to zero at the trailing edge and on the other side of the control volume. Loads, flow rates and temperatures are the outputs of the oil film sub-model.

The outputs of the previous sub-model are used in the pad FEM model in order to simulate both the thermal-elastic behaviour and the motion about the spherical pivot (2 DOFs) of each pad: each pad is in fact subjected to the oil film temperature and pressure T_f and p .

The equation governing the coupled thermal-structural analysis can be expressed as follows:

$$\begin{bmatrix} \mathbf{M}_{pad} & \mathbf{0} \\ \mathbf{0} & \mathbf{0} \end{bmatrix} \begin{Bmatrix} \ddot{\mathbf{q}}_{pad} \\ \ddot{\mathbf{T}}_{pad} \end{Bmatrix} + \begin{bmatrix} \mathbf{C}_{pad} & \mathbf{0} \\ \mathbf{C}_{pad}^{tu} & \mathbf{C}_{pad}^t \end{bmatrix} \begin{Bmatrix} \dot{\mathbf{q}}_{pad} \\ \dot{\mathbf{T}}_{pad} \end{Bmatrix} + \begin{bmatrix} \mathbf{K}_{pad} & \mathbf{K}_{pad}^{ut} \\ \mathbf{0} & \mathbf{K}_{pad}^t \end{bmatrix} \begin{Bmatrix} \mathbf{q}_{pad} \\ \mathbf{T}_{pad} \end{Bmatrix} = \begin{Bmatrix} \mathbf{f}_{pad} \\ \mathbf{Q}_{pad} \end{Bmatrix}, \quad (3)$$

where \mathbf{C}_{pad}^t is the specific heat matrix, \mathbf{K}_{pad}^{ut} is the thermo-elastic stiffness matrix, \mathbf{C}_{pad}^{tu} is the thermo-elastic damping matrix, \mathbf{q}_{pad} is the vector of the pad FEM generalized displacements and \mathbf{Q}_{pad} is the heat source due to the presence of the oil film.

The model considers a convective heat exchange boundary condition on the interface between pads and oil films, an absence of heat exchange and a spherical constraint in the pad-pivot interface and a further convective heat exchange condition on the remaining surfaces, where the pads are surrounded by steady lubricant at the supply temperature. The outputs of the model are the pad positions, velocities and deformations \mathbf{q}_{pad}^{ij} , $\dot{\mathbf{q}}_{pad}^{ij}$ and the pad temperature T_{pad} .

The lubricant supply sump model simulates the behaviour of the ducts-sump system which feeds the bearing with the needed lubricant flow rate. This sub-model is based on the Bond-Graph modelling approach [9] and receives as inputs the supply and environment pressures p_s and p_{env} , the supply temperature T_s , the inlet and outlet flow rates Q_{in}^{ij} , Q_{out}^{ij} (from the adjacent oil films) and the temperature T_{in}^{ij} correspondent to the inlet flow rate. The sump pressure (used as a boundary condition in the oil film model) can be calculated as follows:

$$\frac{dp^{ij}}{dt} = \frac{K}{Vol} \left(Q_{in}^{ij} - Q_{lk}^{ij} - Q_{out}^{ij} + Q_{orif}^{ij} \right), \quad (4)$$

in which K is the lubricant Bulk modulus and Vol is the sump volume.

The energy balance is used in the sump model in order to describe the energy mixing between the abovementioned flow rates. This way it is possible to calculate the temperature to be applied as boundary condition for the oil film inlet:

$$T^{i,j} = \frac{Q_{in}^{i,j}}{Q_{out}^{i,j}} T_{in}^{i,j} + \frac{Q_{orif}^{i,j}}{Q_{out}^{i,j}} T_s, \quad (5)$$

where $T_{in}^{i,j}$ is the temperature of the lubricant flow from the previous oil film and $T^{i,j}$ is the sump temperature which will be used as the inlet temperature for the following oil film. The outputs of the lubricant supply sump model are the sump pressure and temperature $p^{i,j}$ and $T^{i,j}$ and the supply and leakage flow rates $Q_{orif}^{i,j}$ and $Q_{lk}^{i,j}$.

The rotor FEM model is discretized through 3D BEAM elements (2 nodes with 6 DOFs per node [4], to reduce the computational effort) and through 3D BRICK elements, used to model the solid sections of the rotor enclosed in the bearings where the thermal-structural loads, due to the oil film, are applied. The rotor axis, at the initial time and in the undeformed position is coincident with the z -axis of the O_{xyz} reference system. The dynamical equations of the BEAM rotor model can be expressed as follows [3, 4]:

$$\mathbf{M}_A \ddot{\mathbf{q}}_A(t) + (\mathbf{C}_A + \mathbf{G}_A) \dot{\mathbf{q}}_A(t) + (\mathbf{K}_A + \mathbf{H}_A) \mathbf{q}_A(t) = \mathbf{f}_A(t), \quad (6)$$

where \mathbf{M}_A , \mathbf{C}_A , \mathbf{K}_A , \mathbf{H}_A , are respectively the mass, the damping, the stiffness and the circulatory matrices, and \mathbf{G}_A is the gyroscopic matrix, which takes into account the effects due to the shaft rotational velocity.

Similarly to the pad FEM model, the two rotor fractions are modelled to take into account both thermal and structural loads. Their dynamical equation include both the elastic and thermal effects and can be expressed as follows:

$$\begin{aligned} & \begin{bmatrix} \mathbf{M}_{A,frac} & \mathbf{0} \\ \mathbf{0} & \mathbf{0} \end{bmatrix} \begin{Bmatrix} \ddot{\mathbf{q}}_{A,frac} \\ \ddot{\mathbf{T}}_{A,frac} \end{Bmatrix} + \begin{bmatrix} \mathbf{C}_{A,frac} & \mathbf{0} \\ \mathbf{C}_{A,frac}^{tu} & \mathbf{C}_{A,frac}^t \end{bmatrix} \begin{Bmatrix} \dot{\mathbf{q}}_{A,frac} \\ \dot{\mathbf{T}}_{A,frac} \end{Bmatrix} + \\ & + \begin{bmatrix} \mathbf{K}_{A,frac} & \mathbf{K}_{A,frac}^{ut} \\ \mathbf{0} & \mathbf{K}_{A,frac}^t \end{bmatrix} \begin{Bmatrix} \mathbf{q}_{A,frac} \\ \mathbf{T}_{A,frac} \end{Bmatrix} = \begin{Bmatrix} \mathbf{f}_{A,frac} \\ \mathbf{Q}_{A,frac} \end{Bmatrix}, \end{aligned} \quad (7)$$

where $\mathbf{C}_{A,frac}^t$ is the rotor fraction specific heat matrix, $\mathbf{K}_{A,frac}^{ut}$ is the thermo-elastic stiffness matrix and $\mathbf{C}_{A,frac}^{tu}$ is the thermo-elastic damping matrix.

Furthermore the two rotor fractions are connected to the BEAM elements through rigid links. This way it is possible to couple the thermal-structural deformation of the rotor fractions to the rotor dynamical behaviour of the BEAM elements.

The boundary conditions used for the temperature fields are convective heat exchange in correspondence of the oil films interface and a conductive heat exchange in the other surfaces. The outputs of the model are the rotor displacements, needed to calculate the oil film thickness, and the rotor temperatures.

3 Validation and Results

The analyzed test rig consists of a rotor supported by two TPJBs fed with the mineral oil ISO VG 32. Each bearings is composed of five pads in the LOP configuration, and the rotor is subjected to an unbalance mass arranged at the rotor overhung.

Figure 3a shows the comparisons between the experimentally measured pressure and the one obtained through the proposed model by performing an unsteady analysis. The comparison between the experimental temperature and the numerical one is visible in the Fig. 3b. All the quantities are measured circumferentially on the oil film mean lines and are referred to the final step of the simulation (i.e. 240 s) with a rotor angular velocity equal to 8000 rpm.

The temperature for all the pads increases from the leading edge to the trailing edge. This is due to the viscous shear stresses which are higher where the film is thinner. Furthermore the most heavily loaded pads are subjected to a greater temperature and pressure [8, 10, 11]. For the pressure and temperature fields it is possible to highlight how the numerical results obtained with the proposed TEHD model are in good agreement with the experimental values; furthermore the results accuracy is increased with respect to the previous HD [1] and THD models.

In Fig. 4 the three dimensional representation of the pads temperature fields and the deformation due to the elastic and thermal loads are reported. The results shown are referred to the Non-Drive-End bearing, with a rotor speed equal to 8000 rpm. The temperature stress are greater than the elastic one, in fact the most deformed sections are the pad trailing edges where the oil films reach the highest temperature. Furthermore, it is possible to highlight how the minimum displacements can be found in correspondence of the pads pivots, while the displacements in correspondence of the pads leading and trailing edges are quite higher [15]. Figure 5a shows the three dimensional representation of the rotor fraction temperature fields, represented using a color scale. It is possible to highlight the presence of a cold spot and a hot spot

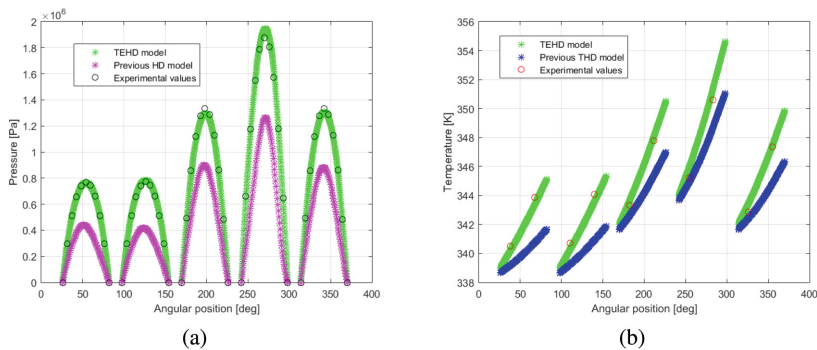


Fig. 3 Comparison between the pressure field (a) and the temperature (b) obtained with the proposed TEHD model, a previously developed HD model and the experimental measures

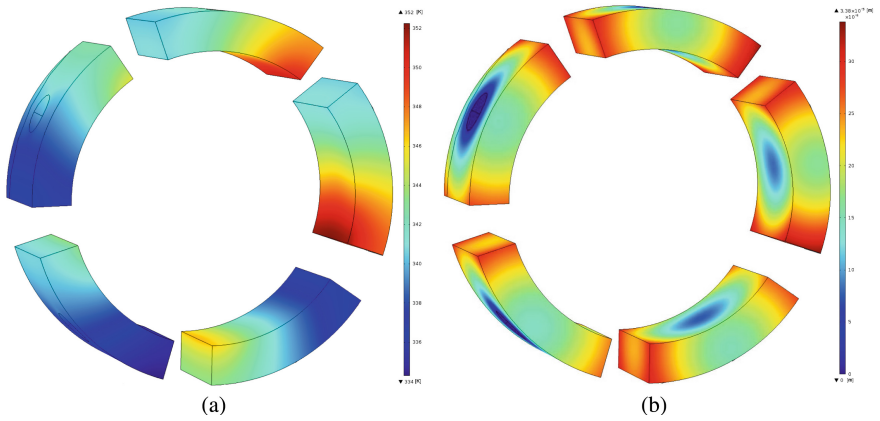


Fig. 4 3D representation of the pad. **a** Temperature and **b** thermo-elastic deformation fields (Non-Drive-End bearing location, 8000 rpm, bearing load equal to half the rotor mass)

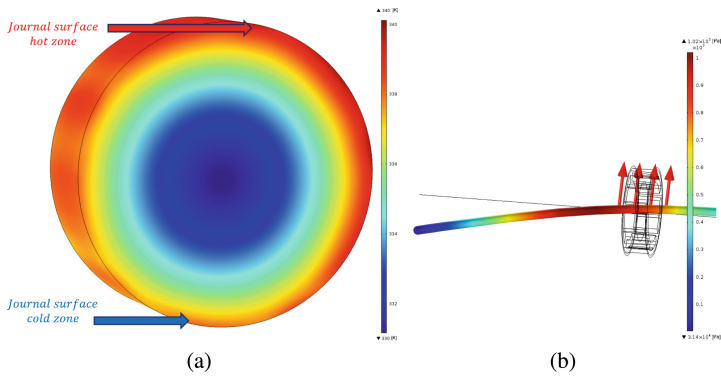


Fig. 5 3D representation of the rotor. **a** Temperature field and **b** stress field and temperature gradient (Non-Drive-End bearing location, 8000 rpm, bearing load equal to half the rotor mass)

consistently with the results found in literature [12]. This is due to the synchronous orbit of the rotor about its rotation axis. For the sake of synthesis, the correspondent rotor fraction thermo-elastic deformation field is not reported. The deformation of the rotor due to the asymmetric temperature field is visible in the Fig. 5b. Since the rotor fraction rotates about its z-axis and has a sinusoidal temperature distribution, the temperature gradient applied on the BEAM element is a rotating vector; this coupling is the base of the onset of the thermal phenomenon known as Morton Effect [2]. Figures 4 and 5 are referred to the final step (i.e. 240 s) of a transient simulation and the angular velocity of the rotor is equal to 8000 rpm.

4 Conclusions and Future Developments

In this research work, the authors proposed an innovative TPJB ThermoElastoHydroDynamic model which includes both the dynamic and the thermal phenomena typically involved in TPJBs operation.

The TPJB model has been developed and validated in collaboration with *Nuovo Pignone General Electric S.p.a.* which provided the technical and experimental data. The results provided by the proposed model are in good agreement with the experimental measures: the TEHD calculation of the oil film quantities obtained with the proposed model well matches the experimental results. Finally, the computational efficiency of the model proved to be very good, allowing the simulation of long transient operations with low computational times.

This research activity will continue in order to further validate the proposed model, proving its accuracy with different test cases and different operating situations. The model will also be further developed to include the modelling of the pivot thermo-elastic behaviour and it will be used to develop innovative heuristic relationships.

References

1. Conti R, Frilli A, Galardi E, Meli E, Nocciolini D, Pugi L, Rindi A, Rossin S (2015) An efficient quasi-three-dimensional model of tilting pad journal bearing for turbomachinery applications. *J Vib Acoust* VIB-14-1434
2. De Jongh FM, Morton PG (1994) The synchronous instability of a compressor rotor due to bearing journal differential heating. In: ASME 1994 international gas turbine and aeroengine congress and exposition
3. Friswell MI, Penny JET, Garvey SD, Lees AW (2010) Dynamics of rotating machines. Cambridge University Press, Cambridge, UK
4. Genta G (1993) Vibration of structures and machines—practical aspects. Springer-Verlag, New York, NY, USA
5. Genta G (2005) Dynamics of rotating systems. Springer, New York, NY, USA
6. Hamrock BJ (2004) Fundamentals of fluid film lubrication. Mc-Graw-Hill-International Editions, London, UK
7. Incropera FP, DeWitt DP (1996) Fundamentals of heat and mass transfer. John Wiley & Sons, New York, NY, USA
8. Knight JD, Barrett LE (1988) Analysis of tilting pad journal bearings with heat transfer effects. *J Tribol* 110(1):128–133
9. Kulakowski BT, Gardner JF, Shearer JL (2007) Dynamic modelling and control of engineering systems. Cambridge University Press, Cambridge, UK
10. Monmousseau P, Fillon M, Frene J (1998) Transient thermoelastohydrodynamic study of tilting-pad journal bearings under dynamic loading. *J Eng Gas Turbines Power* 120:405–409
11. Monmousseau P, Fillon M (1999) Frequency effects on the TEHD behaviour of a tilting-pad journal bearing under dynamic loading. *ASME J Tribol* 121:321–326
12. Murphy BT, Lorenz JA (2010) Simplified Morton effect analysis for synchronous spiral instability. *J Vib Acoust* 132
13. Nicholas JC (1994) Tilting pad bearing design. In: Proceedings of the twenty-third turbomachinery symposium, turbomachinery laboratory, Texas A & M University, College Station, Texas, pp 179–194

14. Nicholas JC (2003) Lund's tilting pad journal bearing pad assembly method. *J Vib Acoust* 125:448–454
15. San Andrés L, Li Y (2015) Effect of pad flexibility on the performance of tilting pad journal bearings: benchmarking a predictive model. In: *Proceedings of the ASME turbo expo 2015: turbine technical conference and exposition, Montreal, Quebec, Canada, 15–19 June 2015*

Thermo-Hydrodynamic Analysis of Tilting Pad Journal Bearing with General Purpose CFD Software

Marco Del Chiaro, Paola Forte, Francesco Torrigiani and Enrico Ciulli

Abstract This paper presents a prediction model for tilting pad journal bearings (TPJB), based on a general-purpose CFD software. Currently, the industrial manufacturers use *ad-hoc* proprietary codes for the design of TPJB and the prediction of their performance. However, apart from the input parameters defined by the code developer, the user can not modify the model. On the contrary, with a general-purpose software the user can implement modifications and exploit well developed toolboxes. In particular one can adopt up-to-date turbulence models and study fluid structure interaction with specific tools. A procedure was developed, based on ANSYS-CFX, to predict the static characteristic of a TPJB, such as load capacity, film temperature, flow rate and friction torque. A thermohydrodynamic model is presented and results, obtained with different boundary conditions, are compared.

Keywords Tilting pad journal bearing · General purpose CFD software · Thermohydrodynamic model · Static characteristic

1 Introduction

Due to their intrinsic stability features, tilting pad journal bearings (TPJB) are often used in high-speed rotating machinery. Characterization of the bearing static and dynamic response is fundamental for an optimal design of high speed rotation machines.

M. Del Chiaro · P. Forte · F. Torrigiani (✉) · E. Ciulli
Department of Civil and Industrial Engineering, University of Pisa,
Largo L. Lazzarino, 56122 Pisa, Italy
e-mail: francesco.torrigiani@ing.unipi.it

M. Del Chiaro
e-mail: marco.delchiaro1988@gmail.com

P. Forte
e-mail: p.forte@ing.unipi.it

E. Ciulli
e-mail: ciulli@ing.unipi.it

In 1964 Lund [1] presented an assembly method for the dynamic analysis of TPJB. Before this fundamental paper, studies consisted of steady-state analyses which were limited to determining load capacity and power loss. Lund calculated the stiffness and damping coefficients of a single fixed bearing pad and then summed the contribution of each pad to find the assembly coefficients. The results shown in [1] were obtained with a synchronous reduction procedure, but Lund's assembly method can be successfully used also for non-synchronous analysis, as shown by Nicholas [2].

After the landmark work of Lund, researchers extended the analysis of TPJB. Orcutt [3] was the first to use a turbulence model for the analysis of tilting pad bearings. Ettles [4] developed a thermo-elastic-hydrodynamic (TEHD) model. Turbulence effects were included by means of a generalized Reynolds equation. The temperature distribution inside the film thickness, thus the local value of viscosity, was determined by the energy balance. Moreover, by using the model of a curved beam, Ettles considered pad deformation due to elastic and thermal effects, to have the correct distribution of film thickness. Hashimoto et al. [5] studied large scale tilting pad bearings with a TEHD model. In particular they compared the results of laminar and turbulent flow. They observed a significant difference, from 20 to 100 percent on stiffness and damping coefficients. Also Hopf and Schüeler [6] investigated large tilting pad bearings and stated the importance of turbulence transition for this kind of bearings.

Nowadays the most advanced codes for the analysis of TPJB are MAXBRG [7] and XLTFPBeg, developed respectively by the University of Virginia and by the Texas A&M University. MAXBRG is based on a generalized Reynolds equation; turbulence is considered by adding to the laminar viscosity an eddy term. The code can also deal with the cavitation near the leading edge. XLTFPBeg, on the other hand, allows to take into account the lubricant inertia, but in this case the Reynolds model is replaced by a bulk-flow CFD approach. Turbulence is introduced in the model by means of the empirical Hirs' laws. However, both these codes are closed codes while the aim of this work is to develop a tool based on a general-purpose software.

2 Method

Following Lund's method, one can study a single pad and build a database of pad features for different values of eccentricity. Then, the characteristics of the whole bearing are obtained by a vectorial sum of each pad contribution.

2.1 Pad Database

Without loss of generality the single pad in a LOP (load on pad) configuration is considered. The shaft is moved along the line connecting the bearing center and the

where t is the pad thickness and

$$r_i = \sqrt{(R_b + t)^2 + e^2 - 2e(R_b + t)\cos(\psi_i - \phi)}. \tag{2}$$

With the eccentricity e_i , or the distance r_i , one can enter in the database and extract the forces on the pad and the pad tilt angle γ_{Ri} .

Knowing the bearing geometry and the loads on each pad, one can report these forces on the global reference system and calculate the total load on the shaft. Fixing a value of eccentricity, one can iteratively calculate the equilibrium attitude angle of the rotor by posing that the force on the shaft in the global direction X is null.

2.3 THD Lubrication Models

Consider a thermo-hydrodynamic (THD) lubrication model. The analysis domain is the thickness between the pad and the shaft, as depicted in Fig. 2. The symmetry of the bearing about the mid-cross-section allows one to study just half of the pad.

In a THD model the temperature is variable in the flow domain. In particular, because of the dissipation, the temperature inside the fluid film increases from the leading edge to the trailing edge of the pad. This affects oil density and viscosity and thus velocity and pressure in the domain. In order to consider this effect the energy equation is needed, thus Navier-Stokes equations, with flow and thermal boundary conditions, are used.

The no-slip boundary condition is adopted for the shaft and the pad wall. At the axial outlet surface the ambient pressure is imposed. The pressure at the pad leading and trailing edge depends on the hydraulic system; without specific information ambient pressure is imposed also on these surfaces. Conduction is imposed on the interface between the pad and the flow while the other pad surfaces are in contact with still oil at the supply temperature, see Fig. 2.

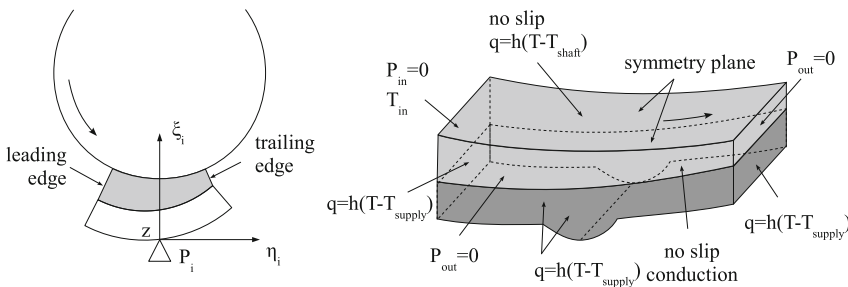


Fig. 2 THD model: domain, flow and thermal boundary conditions

The boundary condition on the shaft wall is more complex. Experiments show that the shaft temperature is constant along the circumferential direction. Szeri [8] proposes two different conditions. For a low angular speed, one can consider the portion of the shaft in contact with the oil film at constant temperature equal to the average temperature in the film, while for a high rotational speed the shaft is globally adiabatic. Two different conditions will be compared: a locally adiabatic shaft and a shaft with a constant imposed temperature.

The boundary condition on the inlet flow temperature is even more complex. In the groove, the outflow from the previous pad and the supply flow are mixed. The inclusion of the groove volume, in the analysed flow domain, is complicated, because the height of this volume is three orders of magnitude greater than the thickness of the film. Temperature balance can be used to calculate the average temperature in the groove. Moreover the outlet flow rate and temperature of the previous pad must be known, and this can be achieved only with another iteration loop.

Two different simplified models can be defined. In the first model, THD-COLD, the whole inlet flow is assumed coming from the supply, hence the supply temperature at the leading edge is imposed. In the second model, THD-HOT, the inlet flow comes from the previous pad, Q_{out}^{i-1} . If this flow rate is lower than the necessary inlet flow rate, Q_{in}^i , there is an additional flow from the supply. Thus the temperature at the leading edge is

$$T_{in}^i = \frac{Q_{out}^{i-1} T_{out}^{i-1} + (Q_{in}^i - Q_{out}^{i-1}) T_{supply}}{Q_{in}^i} . \quad (3)$$

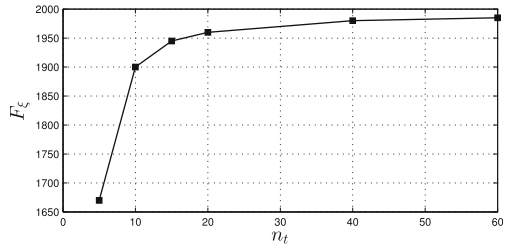
In this way an upper and a lower bound of the real behaviour of the bearing is obtained.

2.4 Software Implementation

The single pad simulations for each model were performed with ANSYS-CFX. The iteration on the single pad was managed by a journal file written in Python. While the iterative procedure to determine the assembly equilibrium configuration was implemented in a Matlab code.

Regarding the CFX model, a structured mesh with hexahedral elements was adopted. A sensitivity analysis on the number of mesh elements was performed. This analysis highlights the importance of the partition number in the thickness direction with respect to the other directions. A number of 60 elements in the thickness direction is a good compromise between accuracy and calculation time. Figure 3 shows the convergence of the normal force on pad, F_{ξ} , increasing the number of elements in this direction, n_t .

Fig. 3 Sensitivity study to the number of elements in the thickness direction



3 Results

The results reported in this section refer to the data collected in Tables 1 and 2. In Fig. 4 results obtained with the THD-COLD model are shown. On the left the trend of the friction torque on the shaft is depicted. It is monotonically increasing¹ with the

Table 1 Characteristics of the studied bearing

Description	Symbol	Value
Shaft diameter	D_s	109.808 mm
Bearing axial length	L	44 mm
Number of pads	n	5
Load configuration	LOP	
Pad length angle	β	60°
Pivot-Leading edge angle	α	30°
Pivot offset	β/α	0.5
Bearing clearance	$C_b = R_b - R_s$	0.1 mm
Pad clearance	$C_p = R_p - R_s$	0.121 mm
Preload	$m = 1 - C_b/C_p$	0.16
Pad thickness	t	17 mm
Pad moment of inertia	I_p	$9.67 \times 10^{-5} \text{ kgm}^{-2}$

Table 2 Oil characteristics

Description	Unit	Value
Kinematic viscosity at 40 °C	mm ² /s	46
Kinematic viscosity at 100 °C	mm ² /s	8
Density at 15 °C	kgm ³	871
Thermal conductivity	W(mK)	0.14
Specific heat	J/(kgK)	2000
Thermal exchange coefficient	W/(m ² K)	589

¹The minus sign is due to the reference axis z, that is in the shaft angular velocity direction.

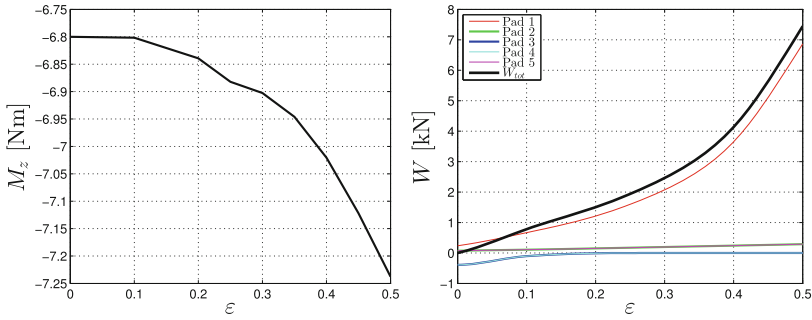


Fig. 4 Friction torque on shaft and load capacity at 7000 rpm for the THD-COLD model

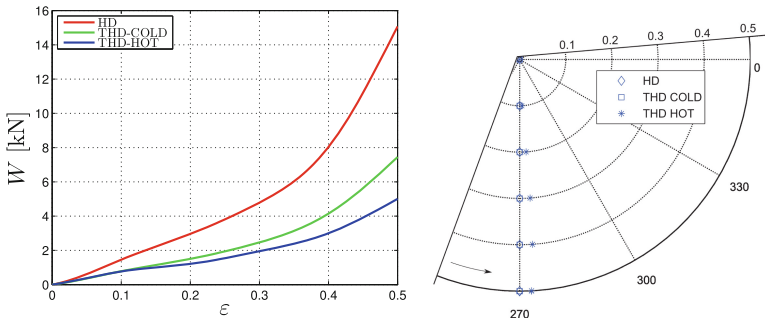


Fig. 5 Comparison between developed models in terms of load capacity and equilibrium position

non dimensional eccentricity $\epsilon = e/C_p$, as expected. The graph on the right of Fig. 4 represents the load supported by each pad and the total load capacity of the bearing. The pads are numbered from 1 to 5 starting from the one in the load direction and proceeding in the direction of rotation. The greater part of the total load is carried by the first pad. Note that due to a positive preload, $m = 0.16$, the load on pads 1, 3 and 4 is different from zero also for a null eccentricity, that is for zero external load. Moreover, the load on pads 2 and 3 is respectively equal to the load on pads 4 and 5 for every value of eccentricity. This symmetry is due to the approximation on thermal effects; the THD-HOT model instead takes into account the non symmetric behaviour of the bearing. Figure 5 shows a comparison between the two models. In the THD-HOT model the average temperature in the fluid domain is higher than in the THD-COLD model, especially for the lower pads. For this reason the load capacity of the THD-HOT model is lower than the one of the THD-COLD model, see Fig. 5 on the left. The real behaviour of the bearing is within the range of these two lines. The shown trends are qualitatively in agreement with the literature works, see for example [9].

On the right side of Fig. 5 the equilibrium position, for different non dimensional eccentricity, is represented. As already pointed out, the non symmetrical behaviour can be obtained only if recirculation is considered. Thus, the THD-COLD model has

Table 3 Comparison based on shaft thermal boundary conditions

		$T_a = 353 \text{ K}$	$T_a = 358 \text{ K}$	$T_a = 363 \text{ K}$	Adiabatic
$\varepsilon = 0.1$	$F_\xi [\text{N}]$	333.4	333.4	333.4	333.4
$\varepsilon = 0.3$	$F_\xi [\text{N}]$	1218	1247	1271	1039
$\varepsilon = 0.5$	$F_\xi [\text{N}]$	3171	3134	3089	3434
$\varepsilon = 0.1$	$T_{out} [\text{K}]$	334	334	334	334
$\varepsilon = 0.3$	$T_{out} [\text{K}]$	345	346	348	339
$\varepsilon = 0.5$	$T_{out} [\text{K}]$	361	363	366	355

a null attitude angle, while for the THD-HOT model a small positive attitude angle is obtained. Also this result is in agreement with previous works, for example [10].

For the THD-HOT model the thermal boundary condition on the shaft surface is a critical point. Two different conditions were compared: the first has a constant temperature on the shaft, while for the second an adiabatic condition on the shaft surface was used. In the first case three temperatures, that are consistent with the literature data for bearings of the same dimensions, were examined and a rotational speed of 7500 rpm was used. The analysis was performed for different eccentricities; the obtained load capacities and outlet temperatures are collected in Table 3. One can see that the difference between the models becomes significant only for high eccentricities. For example with an eccentricity $\varepsilon = 0.1$ there is no difference between the load capacity F_ξ and the outlet flow temperature T_{out} obtained with different thermal boundary conditions.

4 Conclusions

A procedure, based on a general purpose software, was presented in order to evaluate the static performance of a tilting pad journal bearing. The thermo-hydrodynamic model utilizes on Navier-Stokes equations. Results obtained with different boundary conditions on the shaft temperature and on the inlet temperature were compared.

The approach has great potentialities that are still to be exploited. More realistic boundary conditions can be adopted. Moreover, the use of a general purpose software eases the implementation of some features, among others, the adoption of a turbulence model and the evaluation of the elastic and thermal deformation. Note that both these aspects modify the single pad analysis but do not affect the assembly method.

References

1. Lund JW (1964) Spring and damping coefficients for the tilting-pad journal bearing. *ASLE Trans* 7:342–352
2. Nicholas JC (2003) Lund's tilting pad journal bearing pad assembly method. *J Vib Acoust Trans ASME* 125:448–454
3. Orcutt FK (1967) The steady state and dynamic characteristics of the tilting pad journal bearing in laminar and turbulent flow regimes. *ASME J Lubr Technol* 89:392–404
4. Ettles CMM (1932) The analysis of the pivoted pad journal bearing assemblies considering thermoelastic and heat transfer effects. *Tribol Trans* 35:156–162
5. Hashimoto H, Wada S, Marukawa T (1985) Performance characteristics of large scale tilting-pad journal bearings. *Bull JSME* 28:1761–1776
6. Hopf G, Schüeler D (1989) Investigations on large turbine bearings working under transitional conditions between laminar and turbulent flow. *J Tribol* 111:628–634
7. He M, Allaire P (2003) Thermoelastohydrodynamic analysis of fluid film journal bearings. UVA Report No. UVA/643092/ MAE03/595
8. Szeri AZ (1998) *Fluid film lubrication theory & design*. Cambridge University Press, Cambridge
9. Forte P, Lisini GG, Toni P (1994) Applicazione di un codice FEM per la determinazione delle caratteristiche del cuscinio a pattini oscillanti. In: *III Convegno AIMETA di Tribologia* 35–42
10. He M, Cloud C H, Byrne J M (2005) Fundamentals of fluid film journal bearing operation and modeling. In: *Proceedings of the thirty-fourth turbomachinery symposium* 155–157

Multiple Holes Rectangular Gas Thrust Bearing: Dynamic Stiffness Calculation with Lumped Parameters Approach

Federico Colombo, Mona Moradi, Terenziano Raparelli,
Andrea Trivella and Vladimir Viktorov

Abstract A lumped parameters model of a rectangular air pad is developed for dynamic analysis. The model is valid for different geometries of the pad, which is supplied through multiples orifices positioned on a supply rectangle. The dynamic stiffness is analytically obtained by linearizing the system around the steady equilibrium condition. In this paper the model is validated with a distributed parameters model in static conditions.

Keywords Aerostatic thrust bearing · Lumped parameters model · Dynamic stiffness

1 Introduction

Air pads are widely used in metrology and high precision motion machines in order to have no friction and high stiffness. In literature, most of the air bearings are analyzed with Distributed Parameters (DP) methods, using finite difference technique [1, 2] or finite element method [3, 4].

These methods are enough accurate as they allow to calculate the pressure distribution under the pad after discretization of the problem with a sufficiently fine

F. Colombo (✉) · M. Moradi · T. Raparelli · A. Trivella · V. Viktorov
Politecnico di Torino, Turin, Italy
e-mail: federico.colombo@polito.it

M. Moradi
e-mail: mona.moradi@polito.it

T. Raparelli
e-mail: terenziano.raparelli@polito.it

A. Trivella
e-mail: andrea.trivella@polito.it

V. Viktorov
e-mail: vladimir.viktorov@polito.it

grid. Nevertheless they often require long computational time, especially in the cases in which the dynamic stiffness is needed to be calculated. On the contrary, models based on few Lumped Parameters (LP) have faster implementations and solutions. Moreover, with LP models it is easier to perform the sensitivity analysis of a geometrical parameter on the pad performance in comparison with DP models.

A static LP model of rectangular air pads is described in [5]. The present paper extends that model to the dynamic analysis. A comparison with a distributed parameters model is performed in static conditions to validate the lumped model.

2 The LP Model

2.1 Geometry of the Pad

Figure 1a depicts the pad geometry. The supply holes, of diameter d_s , are positioned at distance l from the borders of the pad and distance w from each other. The number of holes along x and y directions can be easily deduced from the pad geometry: $N_x = \frac{L_x - 2l}{w} + 1$ and $N_y = \frac{L_y - 2l}{w} + 1$.

2.2 Hypothesis on the Pressure Distribution

In dynamic conditions, two pressure values are considered under the pad: pressure p_1 inside volume V_1 (Fig. 1b) and pressure p_2 along the supply rectangle perimeter.

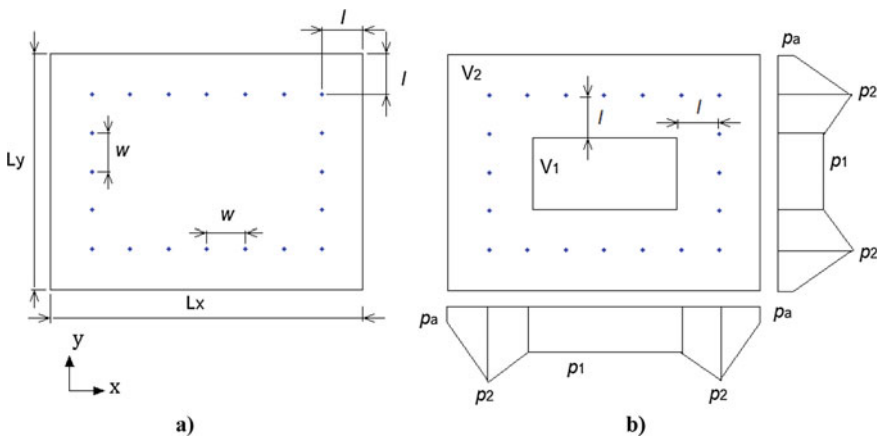


Fig. 1 Sketch of the pad under study (a) and hypothesis on the pressure distribution (b)

In steady state conditions, these pressures coincide with the static value p_0 , which is supposed to be constant inside the supply rectangle: $p_2 = p_1 = p_0$.

In dynamic conditions, due to the distributed resistance and capacity effects inside the air gap, the two pressures are different and a linear pressure distribution inside volume V_2 is supposed.

2.3 Air Mass Flow Rates

Air flow G_1 from volume V_2 to V_1 and air flow G_2 from V_2 to the exhaust can be calculated considering the formula for rectangular channels:

$$G_1 = Ah^3(p_2^2 - p_1^2) \quad (1)$$

$$G_2 = Bh^3(p_2^2 - p_a^2) \quad (2)$$

where

$$A = \frac{1}{6\mu RT} \left(\frac{L_y - 2l}{L_x - 2l} + \frac{L_x - 2l}{L_y - 2l} \right) \quad (3)$$

$$B = \frac{1}{12\mu RT} \left(\frac{L_y - 2l}{l} + \frac{L_x - 2l}{l} \right) \quad (4)$$

The input flow through the supply orifices is calculated applying a discharge coefficient to the isentropic expansion formula

$$G_{in} = c_1 c_d p_s \sqrt{1 - \Phi^2} \quad (5)$$

In subsonic conditions the following pressure ratio is defined

$$\Phi = \frac{p_c/p_s - b}{1 - b} \quad (6)$$

where p_c is the supply hole downstream pressure and b is the critical ratio [5]. In case of sonic flow $\Phi = 0$. The conductance is

$$c_1 = k_T \Psi \frac{\pi d_s^2}{4} (2N_x + 2N_y - 4) \quad (7)$$

where the temperature ratio k_T is $k_T = \sqrt{\frac{T_0}{T}}$ and coefficient Ψ is defined by $\Psi = \frac{0.685}{\sqrt{R \cdot T}}$.

2.4 Mass Balance Equations

Applying the mass conservation law to volumes V_1 and V_2 , the following equations are obtained:

$$G_{in} - G_1 - G_2 = \dot{m}_2 \quad (8)$$

$$G_1 = \dot{m}_1 \quad (9)$$

where m_1 and m_2 are the air masses inside volumes V_1 and V_2 respectively. Masses m_1 and m_2 are obtained integrating the air density over the volumes:

$$m_1 = \frac{1}{RT} \int_{V_1} p dV = Chp_1 \quad (10)$$

$$m_2 = \frac{1}{RT} \int_{V_2} p dV = h(Dp_2 + Ep_1 + Qp_a) \quad (11)$$

where

$$C = \frac{1}{RT} \frac{L_x - 2l}{2} \frac{L_y - 2l}{2} \quad (12)$$

$$D = \frac{1}{RT} \left[l(L_x + L_y - 4l) + l^2 + \frac{7}{16} (L_x - 2l)(L_y - 2l) \right] \quad (13)$$

$$E = \frac{5}{16RT} (L_x - 2l)(L_y - 2l) \quad (14)$$

$$Q = \frac{l}{RT} [L_x + L_y - l] \quad (15)$$

The non-linear system is thus obtained:

$$\begin{cases} c_1 c_d p_s \sqrt{1 - \Phi^2} - Ah^3 (p_2^2 - p_1^2) - Bh^3 (p_2^2 - p_a^2) = \frac{d}{dt} [h(Dp_2 + Ep_1 + Qp_a)] \\ Ah^3 (p_2^2 - p_1^2) = \frac{d}{dt} [Chp_1] \end{cases} \quad (16)$$

2.5 Linearization of the Problem

The system is linearized around the steady condition using the perturbation method. The perturbed air gap and pressures become

$$\begin{aligned}
 h &= h_0 + \Delta h \\
 p_1 &= p_{1,0} + \Delta p_1 \\
 p_2 &= p_{2,0} + \Delta p_2
 \end{aligned} \tag{17}$$

In the steady condition, the pressure values coincide as there is no flow between volumes V_2 and V_1 :

$$p_{2,0} = p_{1,0} = p_0 \tag{18}$$

The continuity equations assume the expressions below:

$$G_{1,0} + \Delta G_1 = \dot{m}_1 \tag{19}$$

$$G_{in,0} + \Delta G_{in} - G_{1,0} - \Delta G_1 - G_{2,0} - \Delta G_2 = \dot{m}_2 \tag{20}$$

The steady terms eliminate each other and the system is simplified into the following:

$$\Delta G_1 = \dot{m}_1 \tag{21}$$

$$\Delta G_{in} - \Delta G_1 - \Delta G_2 = \dot{m}_2 \tag{22}$$

All parameters are linearized arresting the first order Taylor expansion:

$$G_1 = 2Ah_0^3 p_0 (\Delta p_2 - \Delta p_1) \tag{23}$$

$$G_2 = G_{20} + 3Bh_0^2 (p_0^2 - p_a^2) \Delta h + 2Bh_0^3 \Delta p_2 \tag{24}$$

$$G_{in} = G_{in0} + H \Delta p_2 \tag{25}$$

where

$$H = - \frac{c_1 c_d \left(\frac{p_0 - b p_s (-0.148\gamma + 1)}{p_s (-0.148\gamma + 1)^2 (1-b)^2} \right)}{\sqrt{1 - \left(\frac{p_0}{p_s (-0.148\gamma + 1)} - b \right)^2}} \tag{26}$$

So it is

$$\dot{m}_1 = \dot{C} h p_0 + C h_0 \Delta \dot{p}_1 \tag{27}$$

$$\dot{m}_2 = \dot{h} ((D + E) p_0 + Q p_a) + h_0 (D \Delta \dot{p}_2 + E \Delta \dot{p}_1) \tag{28}$$

The time derivative of the air gap coincides with the time derivative of the perturbation term: $\dot{h} = \Delta\dot{h}$

The following linear system is thus obtained:

$$\begin{bmatrix} Ch_0 & 0 \\ Eh_0 & Dh_0 \end{bmatrix} \begin{bmatrix} \Delta\dot{p}_1 \\ \Delta\dot{p}_2 \end{bmatrix} = \begin{bmatrix} -2Ah_0^3p_0 & 2Ah_0^3p_0 \\ 2Ah_0^3p_0 & -2Ah_0^3p_0 + H - 2Bh_0^3 \end{bmatrix} \begin{bmatrix} \Delta p_1 \\ \Delta p_2 \end{bmatrix} + \begin{bmatrix} 0 & -Cp_0 \\ -3Bh_0^2(p_0^2 - p_a^2) & -(D+E)p_0 - Qp_a \end{bmatrix} \begin{bmatrix} \Delta h \\ \Delta\dot{h} \end{bmatrix} \quad (29)$$

2.6 Dynamic Stiffness

The aim of the analysis is to obtain the transfer function between the air gap and the load capacity:

$$\frac{\Delta F(s)}{\Delta h(s)} = k + cs \quad (30)$$

The load capacity is obtained integrating the pressure distribution over the pad and the result is:

$$F = (p_1 - p_a)M + (p_2 - p_a)N \quad (31)$$

where

$$M = 9 \frac{(L_x - 2l)(L_y - 2l)}{16} \quad (32)$$

$$N = l(L_x + L_y - 2l) + \frac{7}{16}(L_x - 2l)(L_y - 2l) \quad (33)$$

The perturbed force is

$$\Delta F = M\Delta p_1 + N\Delta p_2 \quad (34)$$

Rewriting the linear system using Laplace transform one obtains

$$\begin{bmatrix} -2Ah_0^3p_0 - Ch_0s & 2Ah_0^3p_0 \\ 2Ah_0^3p_0 - Eh_0s & -2Ah_0^3p_0 + H - 2Bh_0^3 - Dh_0s \end{bmatrix} \begin{bmatrix} \Delta p_1(s) \\ \Delta p_2(s) \end{bmatrix} = \begin{bmatrix} Cp_0s \\ 3Bh_0^2(p_0^2 - p_a^2) + [(D+E)p_0 + Qp_a]s \end{bmatrix} \Delta h(s) \quad (35)$$

The perturbed pressures are thus obtained

$$\begin{aligned} & \begin{bmatrix} \Delta p_1(s) \\ \Delta p_2(s) \end{bmatrix} \\ &= \frac{1}{det} \begin{bmatrix} +2Ah_0^3p_0 - H + 2Bh_0^3 + sDh_0 & 2Ah_0^3p_0 - sEh_0 \\ 2Ah_0^3p_0 & 2Ah_0^3p_0 + sCh_0 \end{bmatrix} \begin{bmatrix} -Cp_0s \\ -3Bh_0^2(p_0^2 - p_a^2) - s((D+E)p_0 + Qp_a) \end{bmatrix} \Delta h(s) \end{aligned} \quad (36)$$

where

$$det = (2Ah_0^3p_0 + sCh_0) (+2Ah_0^3p_0 - H + 2Bh_0^3 + sDh_0) - (2Ah_0^3p_0 + sEh_0)2Ah_0^3p_0 \quad (37)$$

The dynamic stiffness of the pad is finally calculated:

$$\frac{\Delta F(s)}{\Delta h(s)} = M \frac{\Delta p_1(s)}{\Delta h(s)} + N \frac{\Delta p_2(s)}{\Delta h(s)} \quad (38)$$

The final expression is

$$\begin{aligned} & \frac{\Delta F(s)}{\Delta h(s)} \\ &= \frac{M[-DhCp_0 + Eh(Dp_0 + Ep_0 + Qp_a)] - NCh(Dp_0 + Ep_0 + Qp_a)}{det} s^2 \\ &+ \frac{M[-C2Ah^3p_0^2 + HCp_0 - C2Bh^3p_0 - 2Ah^3p_0(Dp_0 + Ep_0 + Qp_a) + Eh3Bh^2(p_0^2 - p_a^2)]}{det} s \\ &- \frac{N[Cp_0^22Ah^3 + 3Bh^3(p_0^2 - p_a^2)C + (Dp_0 + Ep_0 + Qp_a)2Ah^3p_0]}{det} s + \frac{-6Ah^5p_0B(p_0^2 - p_a^2)(M+N)}{det} \end{aligned} \quad (39)$$

3 Validation of the Model in Static Conditions

The lumped model has been compared with a distributed parameters model in static conditions. Figure 2 shows the static characteristics of a pad, which geometry is defined in Table 1 using both models. The accuracy of the lumped model is good.

Fig. 2 Comparison of the static characteristics of the pad defined in Table 1 using lumped and distributed models; abs. supply pressure $p_s = 0.6$ MPa

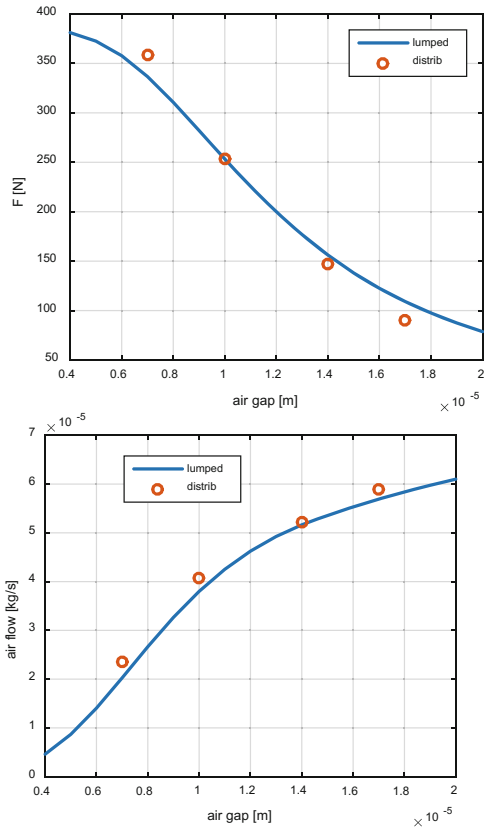


Table 1 Geometry of the pad relative to Fig. 1

L_x (mm)	L_y (mm)	w (mm)	l (mm)	ds (mm)
60	30	15	7.5	0.1

4 Conclusion

A lumped parameters model of rectangular gas thrust bearings has been developed in order to simulate the bearing in dynamic conditions. After linearization of the problem around a given operating point, the transfer function from the air gap to the load capacity has been obtained in analytical form. This can be useful to give information about the stiffness and damping of the bearing without the need of simulating the pad with distributed parameters numerical models.

Further work will consist in the development of a distributed parameters model in dynamic conditions in order to evaluate the accuracy of the lumped model also in these conditions.

References

1. Stout KJ, El-Ashkar S, Ghasi V, Tawfik M (1993) Theoretical analysis of two configurations of aerostatic flat pad bearings using pocketed orifice restrictors. *Tribol Int* 26:265–273
2. Zhang H, Zhu C, Yang Q (2008) Approximate numerical solution of hydrodynamic gas journal bearings. ICIRA 2008, Part II, LNAI 5315. Springer, Berlin, Heidelberg, pp 260–268
3. Fourka M, Tian Y, Bonis M (1996) Prediction of the stability of air thrust bearings by numerical, analytical and experimental methods. *Wear* 198:1–6
4. Li YT, Ding H (2007) Design analysis and experimental study of aerostatic linear guideways used in a high acceleration and high precision xy stage. In *Proceedings of IMechE*, vol 221 Part J, *Engineering Tribology*, 2007
5. Colombo F, Raparelli T, Trivella A, Viktorov V (2015) Lumped parameters models of rectangular pneumatic pads: static analysis. *Precis Eng* 42:283–293

Theoretical and Experimental Study of a Rectangular Grooved Pocketed Air Pad

Federico Colombo, Danial Ghodsiyeh, Tereziario Raparelli,
Andrea Trivella and Vladimir Viktorov

Abstract In this work, a numerical lumped model is developed to simulate static characteristics of an externally pressurized grooved air pad. In addition, an experimental study is performed with one sample pad to evaluate the accuracy of the model.

Keywords Grooved air pad · Lumped model

1 Introduction

Aerostatic bearings have some significant advantage over other types of bearing like negligible friction, no pollution, high positioning accuracy and long life. Furthermore, no noise and heat is generated in this type of bearings. Due to these advantages, aerostatic bearings are widely used in high precision applications such as machine tools, coordinate measuring machines (CMM) and wafer-steppers.

The study of aerostatic systems is in continuous progress; static and dynamic performance of these systems are depending on several geometric parameters, i.e., number and diameter of supply holes, bearing geometry, and grooves on bearing. Design of these parameters can affect significantly bearing characteristics like load capacity, stiffness and air flow consumption. In particular the stiffness of the bearing is very important to ensure the precision of the device.

A commonly used method to improve the stiffness and the load capacity is to machine on the bearing surface thin grooves. There are several studies which evaluate the effect of the grooves and compare them with other types of supply compensation.

Belforte et al. [1] studied grooved circular thrust bearings experimentally and using a numerical model based on Reynolds' equation. In another study Belforte et al. [2] compared the performance of circular grooved and plane aerostatic thrust

F. Colombo · D. Ghodsiyeh · T. Raparelli · A. Trivella (✉) · V. Viktorov
Department of Mechanical and Aerospace Engineering, Politecnico di Torino, Turin, Italy
e-mail: andrea.trivella@polito.it

bearings. It was found that the circumferential groove presence increases the load carrying capacity and the stiffness of the pad, especially at low clearance.

There are few major studies about rectangular pads which numerical models use the resistance network method (RNM) to take into account the groove presence. Kogure et al. [3] made the first analysis of the horizontal grooves by the RNM. Nakamura [4] made a theoretical analysis for static tilt characteristics of rectangular double-pad thrust bearings with horizontal and vertical grooves. Chen and Lin [5] investigated static behavior and dynamic stability of rectangular thrust bearings with X shaped grooves using RNM and it was found that the grooves provide greater stiffness and load capacity but may cause pneumatic hammer with too large width or depth.

Lumped models can be successfully applied on every pneumatic system to quickly describe static and dynamic behavior with good precision [6, 7]. In [8, 9] lumped parameters were used to describe the behavior of air bearings.

In this paper the static behavior of a rectangular grooved commercial pad, equipped with deep conical pockets is analyzed experimentally and numerically with a lumped model. The work is a part of a larger study conducted at the Politecnico di Torino to realize a pneumatic control system to increase the stiffness of air bearings [10, 11].

The numerical lumped model, based on the integration of the differential Reynolds' equation, is used to study the thrust-bearing performance in terms of load capacity and air flow consumption. A static test bench is used to investigate thrust-bearings at different air gaps. Experimental and numerical results are compared and discussed.

2 The Tested Pad

Figure 1 shows the rectangular pad under study, of dimensions 60 mm \times 30 mm. It includes four supply holes of diameter $d = 0.18$ mm which are placed in the center of the rectangle sides at a given distance of the borders. The holes are pocketed and connected by a closed rectangular groove of dimensions 43 mm \times 19 mm.

Fig. 1 Configuration of the aerostatic thrust bearing with rectangle—shaped groove

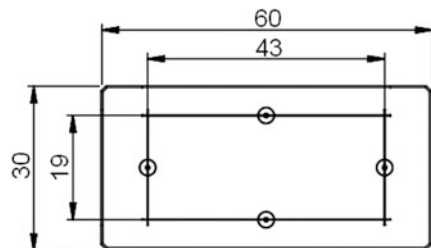


Fig. 2 Nominal cross-sectional sketch of supply orifice and pocket

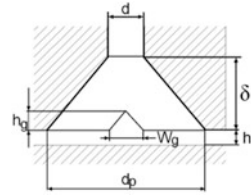


Fig. 3 Enlargement of orifice diameter (a) and pocket diameter (b)

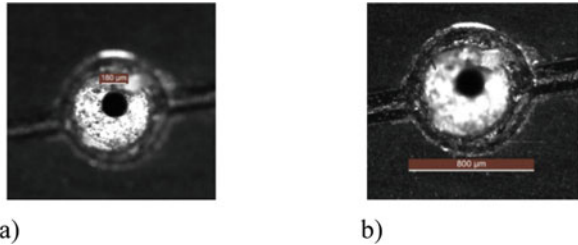


Figure 2 shows the nominal cross section sketch of the supply orifice with the pocket and the triangular groove (the sketch is not in scale). The groove, of 200 μm width (w_g) and 60 μm depth (h_g), is endowed of a conical pocket of diameter $d_p = 800 \mu\text{m}$ and depth $\delta = 300 \mu\text{m}$. The supply orifices and pocket diameters were checked with a microscope as Fig. 3 shows. The pad, of aluminum, is treated with an oxidation process to increase the surface hardness. The treatment, made before machining the holes and the pockets, gives a dark color to the component and also acts to a certain depth, as is visible in figure.

The profile shapes of the pocket and the groove were verified by a rugosimeter. Figure 4 shows the measured profiles.

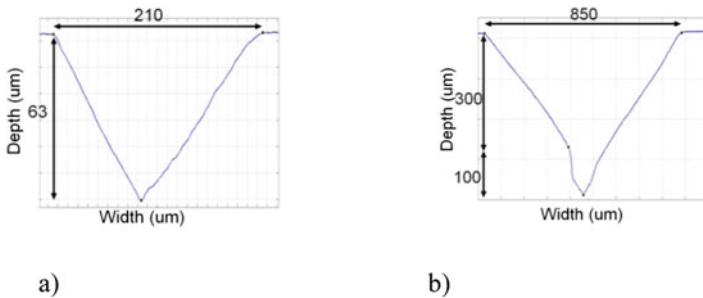


Fig. 4 Groove a and pocket b profile measured with a rugosimeter

3 Mathematical Model

The mathematical model developed represents the inlet holes as two lumped resistances in series whose conductance depends on the size of the holes and on the geometry of the pockets. In [12, 13] the flow discharge coefficients of the supply holes were identified for diameters d up to 0.5 mm, with or without cylindrical pocket of diameter d_p equal to 2 mm and 4 mm. Figure 5 shows the sketch of those feeding systems.

It was verified that the inlet resistance of the hole can be described as the series of two lumped resistances each of which leads a given drop of pressure. The first drop is due to the presence of the supply hole and the supply pressure P_S drops to pressure P_P inside the pocket. The conductance of this first resistance is given by formula:

$$C_d = \pi \frac{d^2}{4} \psi c_d \quad (1)$$

Where d is the diameter of the supply hole, $\psi = \frac{0.685}{\sqrt{RT}}$ considering an isentropic expansion, c_d is the hole's discharge coefficient for circular cross section, assumed to be a function of the hole dimension and of the Reynolds numbers Re calculated at the supply hole cross section [12, 13]:

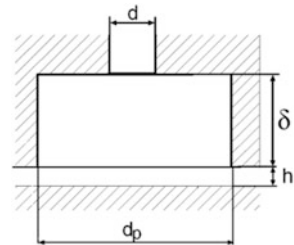
$$c_d = 0.85 \left(1 - e^{-8.2 \frac{h+\delta}{d}} \right) \left(1 - 0.3 e^{-0.001 Re \frac{h+\delta}{h+4\delta}} \right); \quad Re = \frac{4G}{\pi \mu d} \quad (2)$$

Where μ is the dynamic viscosity of air ($\mu = 17.89 \cdot 10^{-6}$ Pa s), h is the air gap height.

The second pressure drop occurs at the inlet of the air gap due to the restriction of the air section after the cylindrical pocket. The pressure drops to value P_C just after the annular surface of the pocket. The conductance of the second lumped resistance is given by the formula:

$$Ca = (\pi d_p h) \psi c_a \quad (3)$$

Fig. 5 Cross-sectional sketch of supply orifice and pocket studied in [12]



Where c_a is the discharge coefficient for the annular cross section, assumed to be function of the annular Reynolds numbers Re_a :

$$c_a = 1.05(1 - 0.3 e^{-0.005 Re_a}); \quad Re_a = \frac{G}{\pi \mu d_p} \tag{4}$$

In the present work, as a first approach of study, the same formulations of the flow discharge coefficients are adopted also for the current feeding system’s geometry. In particular the expressions of C_a and Re_a are modified in the Eq. (5) to take into account the presence of the groove intersecting the pockets:

$$C_a = (\pi d_p h + w_g h_g) \psi c_a; \quad Re_a = \frac{G h}{\pi \mu d_p h_{eq}}; \quad h_{eq} = \frac{\pi d_p h + w_g h_g}{\pi d_p}; \tag{5}$$

where w_g and h_g are width and maximum depth of the groove and h_{eq} is the height of the equivalent annular section due to the presence of the groove.

Mass flow rate G through each lumped resistance can be described by the ISO formula 6358. Defining P_1, P_2 the absolute supply hole upstream and downstream absolute pressures, one has:

$$G = K_T C P_1 \sqrt{1 - \varphi^2} \tag{6}$$

Where $K_T = \sqrt{\frac{T_0}{T}}$, T is the absolute air temperature, ($T_0 = 293K$), C is the conductance of the resistance, $\varphi = \frac{P_2 - b}{P_1 - b}$ for subsonic flow, and $\varphi = 0$ for sonic flow, b is the pressure critical ratio, assumed equal to the theoretical value 0.528, C is the conductance, equal to C_d and C_a for the first and the second lumped resistance respectively.

From the equilibrium of an infinitesimal element of dimensions dx and dy and by considering the laminar flow mass trough a generic section of height h it results:

$$\frac{dP}{dx} + \frac{12\mu}{RT} \frac{g_x}{Ph^3} = 0; \quad \frac{dP}{dy} + \frac{12\mu}{RT} \frac{g_y}{Ph^3} = 0. \tag{7}$$

where P is the pressure in the air gap, g_x, g_y are the mass flow rates in the given directions per unit of width.

A multiple lumped parameter circuit is adopted to define the pressure distribution in the gap. The contours of the pockets are squares of side d_p and the internal pressure P_p is considered uniform. The region surrounding the pockets is discretized in several regular areas by a grid of a given number of subdivisions. The step of the grid is not constant, it decreases near the pocket and the groove in order to cover their boundaries.

Δx and Δy are the dimensions of each discretized area; i, j are the index on the grid points along x and y directions. Figure 6 shows the nodal pressure $P_{i,j}$, the

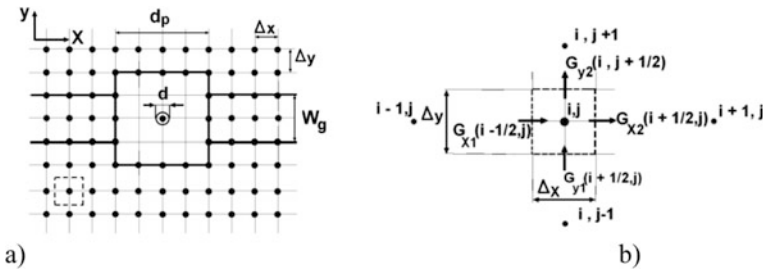


Fig. 6 Sketch of the grid near the pocket (a) and control volume to which the continuity equation is applied (b)

incoming masses air flow $G_{x,1}$, $G_{y,1}$ and the outgoing masses air flow $G_{x,2}$, $G_{y,2}$ through the boundary surrounding each node.

Considering isothermal flow and by integrating Eq. (7) in x and y directions one obtains:

$$\begin{aligned}
 G_{x,1} &= \left(P_{i-1,j}^2 - P_{i,j}^2 \right) \frac{h_{1,y^3}}{24\mu RT} \frac{\Delta y}{\Delta x}; & G_{x,2} &= \left(P_{i,j}^2 - P_{i+1,j}^2 \right) \frac{h_{2,y^3}}{24\mu RT} \frac{\Delta y}{\Delta x} \\
 G_{y,1} &= \left(P_{i,j-1}^2 - P_{i,j}^2 \right) \frac{h_{1,x^3}}{24\mu RT} \frac{\Delta x}{\Delta y}; & G_{y,2} &= \left(P_{i,j}^2 - P_{i,j+1}^2 \right) \frac{h_{2,x^3}}{24\mu RT} \frac{\Delta x}{\Delta y}
 \end{aligned}
 \tag{8}$$

Due to the presence of the groove, the air gap height isn't equal for all the nodes: $h_{1,x}$, $h_{1,y}$ and $h_{2,x}$, $h_{2,y}$ are the mean values of the air gap in each boundary section crossed by the flow.

The pressure P_P at the centre of each pocket and the pressures in each grid point are calculated by solving iteratively the continuity of the incoming and outgoing flow rates G_{in} and G_{out} through each control volume till the convergence of the solution:

$$P_{i,j^{t+1}} = P_{i,j^t} + (G_{in} - G_{out})_{i,j} \Delta t
 \tag{9}$$

where Δt is an appropriate constant able to obtain the convergence. Therefore the air flow consumption G of the pad is determined and the load capacity F is obtained by integration of the pressure field.

In [12] was experimentally proved that in case of holes without pocket and holes with shallow cylindrical pocket only the drop of pressure $P_S - P_P$ is significant, while the second lumped resistance of the supply hole could be neglected ($P_C = P_P$). In this case only the c_d coefficient can be used in simulations. For this reason, the present work is aimed to verify numerically the best suitability of the adopted discharge coefficients formulations to the current geometry of the supply holes. In particular two different lumped models I and II are here analyzed. The model I assumes significant the pressure drop $P_S - P_P$ and only the coefficient c_d is considered. The model II considers significant also the pressure drop $P_P - P_C$ and both

coefficients c_d and c_a are considered. The numerical results for both the models are then compared with the experimental ones to evaluate which is more accurate.

4 Results and Discussion

A specific test procedure was adopted in order to ensure the repeatability of the measurements. During the test the air gap height was increased from zero to 20 microns with steps of about 2 microns. The pressure force, the air flow rate and the air gap height were registered. The air gap height was measured by two inductive micrometer probes, positioned at the center and at the outer edge of the pad and the average value was considered.

Figures 7 and 8 show the numerical and experimental results of the load capacity and the air flow rate of the pad for the supply gauge pressure $p_s = 4$ bar. The experimental curves are fitted with continuous lines. As visible, the model that gives the better approximation to experimental results is model II, which considers both drops of pressure.

Fig. 7 Force versus air gap height

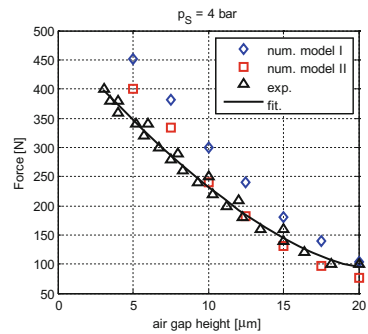
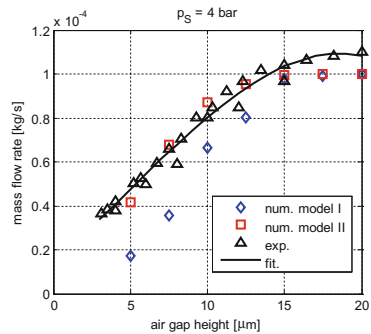


Fig. 8 Air consump. versus air gap height



5 Conclusions

In this work a numerical lumped model based on the integration of the Reynolds equation was used to study the static load capacity and the air flow consumption for a rectangular grooved air pad. The discharge coefficient formulas validated for feeding systems without groove and cylindrical pocket were modified for the current geometry of feeding system and groove. The numerical results of two models I and II were compared with the experimental ones. In model I only the discharge flow coefficient c_d is considered, in model II both the discharge flow coefficients c_d and c_a are used. The comparison with the experimental data shows a better suitability of the model II to represent the behavior of the pad. Further studies with CFD models will be carried out to better identify the influence of the geometry and dimensions of the pockets and the groove on the static behavior of the pad.

References

1. Belforte G, Colombo F, Raparelli T, Trivella A, Viktorov V (2010) Performance of externally pressurized grooved thrust bearings. *Tribol Lett* 37:553–562
2. Belforte G, Colombo F, Raparelli T, Trivella A, Viktorov V (2011) Comparison between grooved and plane aerostatic thrust bearings: static performance. *Meccanica* 46:547–555
3. Kogure K, Kaneko R, Ohtani K (1982) A study on characteristics of surface-restriction compensated gas bearing with T-shaped grooves. *Bull JSME*
4. Nakamura T, Yoshimoto S (1996) Static tilt characteristics of aerostatic rectangular double compound restrictors. *Trib Int* 2:145–152
5. Chen MF, Lin YT (2002) Static behavior and dynamic stability analysis of grooved rectangular aerostatic thrust bearings by modified resistance network method. *Trib Int* 35:329–338
6. Pugi L, Malvezzi M, Allotta B, Banchi L, Presciani P (2004) A parametric library for the simulation of a Union Internationale des Chemins de Fer (UIC) pneumatic braking system. In *Proceedings of the institution of mechanical engineers, part F: journal of rail and rapid transit*, vol 218(2), pp 117–132
7. Subramanian SC, Darbha S, Rajagopal KR (2004) Modeling the pneumatic subsystem of an S-cam air brake system. *J Dyn Syst Meas Control* 126(1):36–46
8. Raparelli T, Viktorov V, Trivella A (1998) Static and dynamic analysis of pneumatic support. In *7th international workshop on robotics—RAAD 98*. Smolenice Castle, June 26–28, 405–410
9. Colombo F, Raparelli T, Trivella A, Viktorov V (2015) Lumped parameters models of rectangular pneumatic pads: static analysis. *Precis Eng* 42:283–293
10. Raparelli T, Viktorov V, Manuello Bertetto A, Trivella A (2000) Air bearing with pneumatic active control. In *AIMETA international tribology conference*, L'Aquila, September 20–22, 693–700
11. Colombo F, Ghodsiyeh D, Raparelli T, Trivella A, Viktorov V (2015) A pneumatic active control for air pads. In *Ecotrib 2015*. ISBN: 9788890767036
12. Belforte G, Raparelli T, Viktorov V, Trivella A (2007) Discharge coefficients of orifice-type restrictor for aerostatic bearings. *Trib Int* 40:512–521. ISSN 0301-679X

13. Colombo F, Raparelli T, Trivella A, Viktorov V (2013) Investigation on the discharge coefficient of supply micro holes for gas bearings. In Proceedings of 5^o world tribology congress 2013, September 8–13, Torino

Experimental Identification of an Aerostatic Thrust Bearing

Federico Colombo, Luigi Lentini, Terenziano Raparelli
and Vladimir Viktorov

Abstract Conventional approaches to design aerostatic bearings are based on their static characteristics. However, dynamic predictions are fundamental in order to obtain very precise positioning since air bearings are frequently subjected to dynamic load variations. This paper presents a simple linear time invariant model for aerostatic thrust bearings and the related experimental identification procedure. The experimental procedure identifies the stiffness and damping coefficients of the air gap model. The model validation was obtained comparing the experimental and theoretical bode diagrams of the studied system. The comparison demonstrates that the model leads to good results when neighbours of equilibrium conditions are considered.

1 Introduction

Aerostatic thrust bearings are characterized by low friction, high precision and they represent a competitive clean alternative to conventional rolling and oil bearings. For this reason, aerostatic bearings are widely used in applications where high level of accuracy is required, e.g., measuring and tool machines. Conventional approaches to design aerostatic thrust bearings are based on their static characteristics. However, the prediction of their dynamic features is fundamental to obtain high precision bearings since they are frequently subjected to dynamic load variations. Literature presents several kinds of analytical and numerical approaches [1] to predict the

F. Colombo · L. Lentini (✉) · T. Raparelli · V. Viktorov
DIMEAS Politecnico di Torino, Corso Duca Degli Abruzzi 24, 10129 Turin, Italy
e-mail: luigi.lentini@polito.it

F. Colombo
e-mail: federico.colombo@polito.it

T. Raparelli
e-mail: terenziano.raparelli@polito.it

V. Viktorov
e-mail: vladimir.viktorov@polito.it

dynamic behaviour of air bearings. In particular, the identification of the air gap stiffness and damping coefficients represents the main goal of this kind of study. Aguirre et al. [2] and Al-Bender [3] proposed a multi-physical FE model of an active aerostatic thrust bearings with a conicity compensation. In their work, they investigate the air bearing dynamic behaviour considering the interactions among mechanical, electrical and pneumatic phenomena. Matsumoto et al. [4, 5] developed a physical model of an ultra precision straight motion system with many degrees of freedom.

Air gap models are often experimentally verified and investigated through different techniques. Impact hammer [6] and modal exciters [7] are currently adopted for the dynamic identification of bearing stiffness and damping coefficients. These two techniques mainly differ in the amplitude of the excited frequency bandwidths and the measured signal-to-noise ratio of the system's responses. When impact hammer tests are carried out, large bandwidth of frequencies are excited. However, the dynamic identification of the stiffness and damping coefficients is hard task due to the low signal-to-noise ratio of the measured spectrum. Conversely, shakers can be used to excite systems in a controlled frequency bandwidth. The amplitude of the excited bandwidth depends on the basis of the selected excitation function, e.g., sweep, pseudo-random periodic signal, chirp. In this case, the identification limitations are due to the interactions between the modal frequencies of the test rig and investigated system.

This paper introduces an experimental procedure to identify dynamic coefficients of an aerostatic thrust bearing by using a step force excitation. After illustrating the identification procedure, the dynamic coefficients are used to built a simple linear time invariant model of the air system. In the first parts of the paper, the main features of the aerostatic bearing and the test rig are discussed. Subsequently, the system physical model and its governing equation are described. Finally, the experimental identification and validation tests are shown.

2 The Active Aerostatic Thrust Bearing

The proposed experimental identification procedure has been performed on the active aerostatic bearing shown in Fig. 1. This bearing consists of a conventional air pad 1 integrated with a multilayer piezo actuator 2 (see Fig. 1a). This integration is possible thanks a compliant mechanism 3 and two supporting element 4 which hold the air pad and actuator together. Moreover, the compliant mechanism has the function to guide and preload the actuator when is running out. As it is possible to see, (Fig. 1b) the air pad has a rectangular base of $60 \times 30 \text{ mm}^2$ and two exhaust holes each one inside a "C shaped" groove.

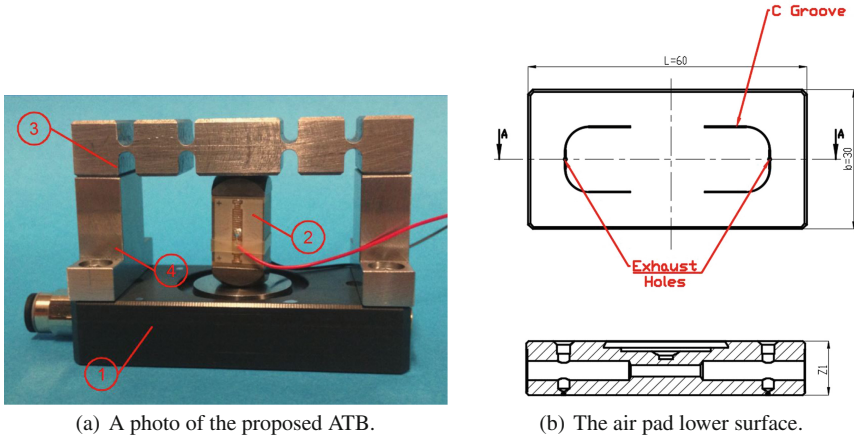


Fig. 1 The proposed active aerostatic thrust bearing

3 Experimental Set-Up

A scheme of the adopted experimental set-up is shown in Fig. 2a. The test bench consists of a moving and stationary parts. The moving part has a mass m_v and is composed of two horizontal and two vertical crossbars which have rectangular and circular cross sections respectively. The presence of two air bushings allows vertical motions of the moving part with respect to the stationary one. The bearing was placed between the upper crossbar of the movable structure and the bearing counter surface. External static loads are imposed on the system through the weight of mass m_s , which is fixed on the top of the moving structure. The load acting on the system is currently measured by means of three load cells (KISTLER Type 9313 AA1) which are circumferentially and symmetrically bolted between the air pad counter surface and the stationary part.

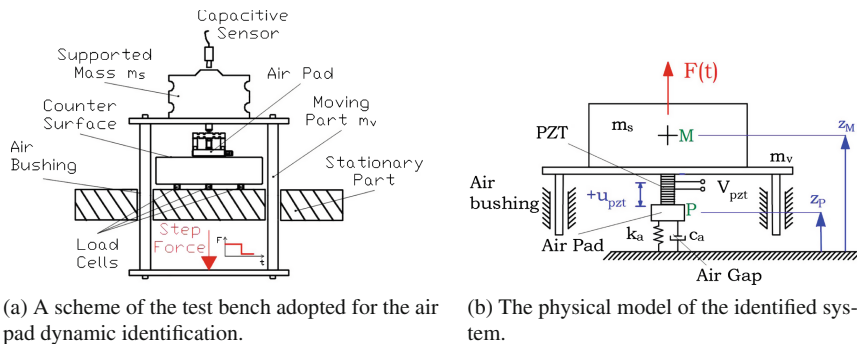


Fig. 2 System mechanical and physical configurations

System displacements are measured at the center of the supported mass by means of a capacitive sensor (MICROSENSE 8810 with a 2823 probe). The dynamic identification test was performed by applying a broad band excitation to the system and by evaluating its response in the frequency domain. In particular, step force excitations were chosen in order to exploit the test bench features and because this simple procedure makes it possible to impose an almost identical input to the air pad. Step force was obtained by suspending a small weight to a rope at the lower rectangular cross bar of the moving part. A negative step force occurs almost instantaneously when the connection rope is cut.

4 System Modelling

The motion of the system is described considering only its vertical translation as degree of freedom, due to the presence of two air bushings. In fact, these frictionless constraints do not allow additional displacements and rotations. The independent physical coordinate to describe the motion of the system can be arbitrary chosen among the absolute displacements z_p or z_m which are relative to the air pad (point P) and mass (point M). Relative displacements u_{pzl} correspond to the piezo actuator stroke changes and allow air gap variations to be compensated for. Changes of the actuator stroke are achieved by modifying the actuator control voltage V_{pzl} on the basis of the piezo electric material features. In this instance, z_m has been selected to describe the system motion. The relationship among displacements z_m , z_p and u_{pzl} is the following:

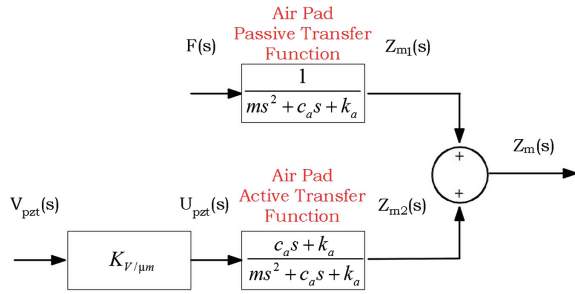
$$z_m = z_p + u_{pzl} \quad (1)$$

Concerning the model's parameters, the mass $m = m_s + m_v$ is the total and only one considered. It is realistic to treat the air pad and the piezo actuator ($k_{pzl} = 267 \cdot 10^6$ N/m) as rigid bodies. The air gap was modelled as a spring-damper system which has k_a and c_a as stiffness and damping coefficients respectively. $F(t)$ represents the external force acting on the system. By considering the non-linear nature of the air gap features, the presented physical model is feasible only in neighbourhoods of an equilibrium conditions. The system governing Eq. 2 can be easily achieved through a suitable combination of the equilibrium equations and by applying the Laplace transform.

$$Z_m(s)[ms^2 + c_a s + k_a] = F(s) + U_{pzl}(s)[c_a s + k_a] \quad (2)$$

Figure 3 shows the block diagram representation of the investigated system which is considered as MISO (Multiple Input Single Output). Indeed, the mass displacement $Z_m(s)$ is expressed as the sum of two contributions relative to external force disturbances $F(s)$ and the actuator stroke $U_{pzl}(s)$. The actuator strokes is proportional to the control voltage $V_{pzl}(s)$ applied at the actuator terminals. $K_{V/\mu m}$ is the static gain between the actuator control voltage $V_{pzl}(s)$ and its resulting stroke $U_{pzl}(s)$.

Fig. 3 The block diagram of the investigated system



5 Identification

The aim of the presented experimental identification procedure is to assess the stiffness and damping coefficients (k_a and c_a) of the above described physical model in a neighbour of an equilibrium condition ($P_s = 4$ absolute bar and an air gap height of $10 \mu\text{m}$). Figure 2a shows the scheme of the adopted test bench. The experimental identification was performed by imposing a step force to the moving part of the test bench (as described in Sect. 3) and measuring the time responses $z_{m,Air}(t)$ and $z_{m,NoAir}(t)$ which correspond respectively to the responses in presence and absence of the air pad supply. The power spectra of these two responses were compared in order to identify the first natural frequency of the air physical model. These spectra are shown in Fig. 4 and they are obtained by using the MATLAB[®] pwelch function.

The first natural frequency ω_n of the system was identified at 683.6 rad/s whereas, other spectra are related to the test bench modes. Given $m = 20.40$ kg, it is possible to compute the stiffness coefficient of the air gap k_a as:

$$k_a = \omega_n^2 \cdot m = 9.531 \cdot 10^6 \text{ N/m} \tag{3}$$

The air gap damping coefficient was computed estimating the damping ratio ζ by using the half-power bandwidth method (also called 3 dB method) [8]:

$$\zeta \simeq \frac{\Omega_2 - \Omega_1}{2\omega_n} = 0.04182 \tag{4}$$

$$c_a = \zeta \cdot 2\sqrt{k_a m} = 1.166 \cdot 10^3 \text{ Ns/m} \tag{5}$$

where, $\Omega_2 = 711.3$ rad/s and $\Omega_1 = 654.1$ rad/s are the frequencies corresponding to a magnitude of -3 dB with respect to the amplitude at the natural frequency ω_n . This method is a consolidate frequency domain method for damping estimation in presence of several different peaks in FRFs.

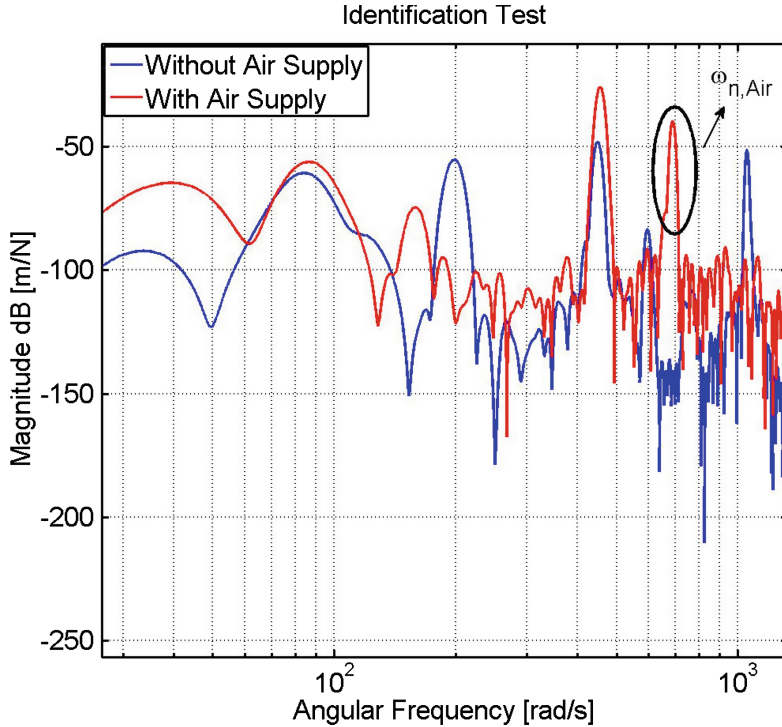


Fig. 4 The power spectra of the responses in presence and absence of the air pad supply and their difference

6 Experimental Validation

The system model was validated by comparing bode diagrams of the theoretical and experimental FRFs of the active transfer function (see Fig. 3):

$$G_{Active}(s) = \frac{Z_{m2}(s)}{U_{pzt}(s)} = \frac{K_{V/\mu m}(c_a s + k_a)}{ms^2 + c_a s + k_a} \quad (6)$$

The theoretical FRF was obtained through a MATLAB[®] LTI (Linear Time Invariant) model by considering the estimated k_a and c_a coefficients. On the other hand, the experimental bode diagram was obtained by imposing sine control voltage waves $v_{pzt}(t) = A \sin(\omega t)$ as input to the system and evaluating the output $z_{m2}(t)$. The imposed sine waves have small amplitudes ($A = 10$ V) in order to study the neighbourhood of an equilibrium condition and an excitation angular frequency ω . After this, the FFTs (Fast Fourier Transform) of $v_{pzt}(t)$ and $z_{m2}(t)$ signals were performed at each ω . Magnitudes were obtained by computing the ratio $\text{Abs}[\text{FFT}(z_{m2}(t))] / \text{Abs}[\text{FFT}(v_{pzt}(t))]$ at the considered excitation frequencies. Similarly, the associated

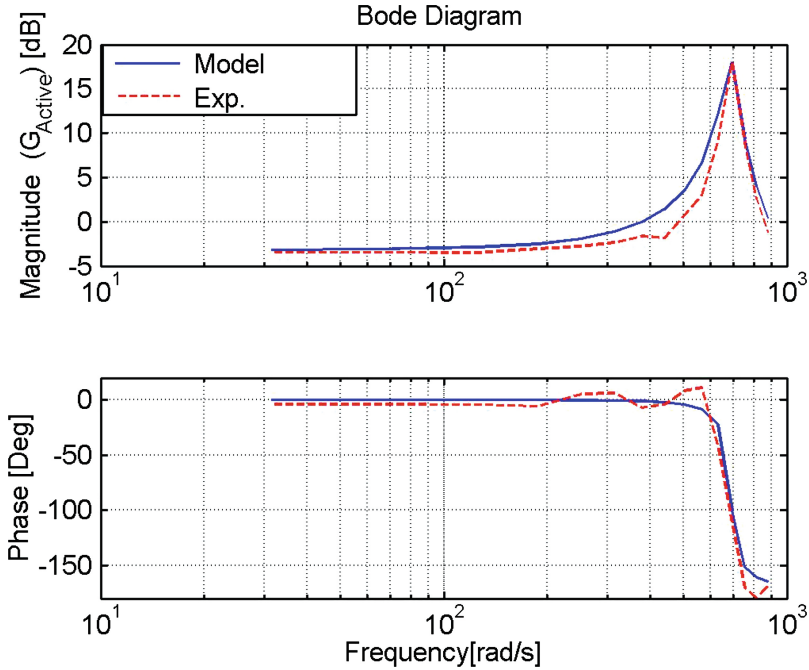


Fig. 5 The theoretical and experimental Bode diagrams

phases were assessed by computing the difference between the $\text{Angle}[\text{FFT}(z_{m2}(t))]$ and $\text{Angle}[\text{FFT}(v_{pzl}(t))]$. Figure 5 shows both the theoretical and experimental Bode diagrams. As it appears from the results, the adopted system model is in good agreement with the experimental data.

7 Conclusion

This paper presents a physical model of an aerostatic thrust bearing. This simple LTI model results feasible in neighbourhoods of equilibrium positions. An experimental identification procedure has been developed in order to identify the system’s stiffness and damping coefficients. This procedure consists in the application of a step force to the system both in presence and absence of the air supply and by computing the power spectrum of the responses. Firstly, the system’s natural frequency was evaluated by comparing the computed spectra. Secondly, the air gap stiffness and damping coefficients were identified using the half power bandwidth method. Concerning the system modelling, the active transfer function $G_{Active}(s)$ was theoretically and experimentally by the respective Bode diagrams. The comparison shows that the physical model results are in good agreement with the experimental ones.

References

1. Colombo F, Raparelli T, Viktorov V (2009) Externally pressurized gas bearings: a comparison between two supply holes configurations. *Tribol Int* 42(2):303–310
2. Aguirre G, Al-Bender F, Van Brussel H (2010) A multiphysics model for optimizing the design of active aerostatic thrust bearings. *Precis Eng* 34(3):507–515
3. Al-Bender F (2009) On the modelling of the dynamic characteristics of aerostatic bearing films: from stability analysis to active compensation. *Precis Eng* 33(2):117–126
4. Aoyama H, Watanabe I, Akutsu K, Shomokohbe A (1988) An ultra precision straight motion system (1st report). *J Jpn Soc Precis Eng* 54(3):558–563
5. Matsumoto H, Yamaguchi J, Aoyama H, Shomokohbe A (1988) An ultra precision straight motion system (2nd report). *J Jpn Soc Precis Eng* 54(10):1945–1950
6. Matta P, Arghir M (2012) Identification method for rotordynamic coefficients of cylindrical air bearing using an impact hammer. *J Eng Tribol* 226(3):199–212
7. Matta P, Arghir M, Bonneau O (2010) Experimental analysis of cylindrical air-bearing dynamic coefficients. *Tribol Trans* 5:329–339
8. Papagiannopoulos GA, Hatzigeorgiou GD (2011) On the use of the half-power bandwidth method to estimate damping in building structures. *Soil Dyn Earthquake Eng* 31(7):1075–1079

Experimental Analysis of the Influence of the Electrical Arc on the Wear Rate of Contact Strip and Contact Wire in a.c. System

Giuseppe Bucca, Andrea Collina and Ezio Tanzi

Abstract The transfer of electrical power from the overhead line to the train is carried out through the sliding contact between the pantograph's contact strip and the overhead line's contact wire. The state of the contact is defined by the current collection quality, where electrical arcs play a predominant role. Indeed, electrical arcs are generated when, during current collection, contact losses occur due to the dynamics of pantograph-catenary interaction. The main effects of the electrical arcs are electromagnetic disturbances and high values of local temperature on the strip and on the wire, which in turn cause an increase of wear rate on contact strip and contact wire. The aim of this paper is to analyze, by means of laboratory tests, the effect of electrical arc occurrence on the wear of strip and wire. Two different kinds of carbon based strip are considered: plain carbon strip and copper impregnated carbon strip. The contact wire considered in this work is a pure copper wire.

Keywords Electrical arcs · Pantograph-catenary interaction · Wear rate · Plain and impregnated carbon strips

1 Introduction

One of the index used to assess the quality of current collection related to the sliding contact between pantograph and catenary is the percentage of contact loss. To assess the quality of current collection, the EN50317 [1] introduces the parameter "percentage of arcing", defined as the ratio between the sum of arcs' duration and the total time of observation, with a collected current greater than 30 % of the

G. Bucca (✉) · A. Collina · E. Tanzi
Dipartimento di Meccanica, Politecnico di Milano, Milan, Italy
e-mail: giuseppe.bucca@polimi.it

A. Collina
e-mail: andrea.collina@polimi.it

E. Tanzi
e-mail: ezio.tanzi@polimi.it

nominal current. Typical values of the percentage of arcing defining a good quality of current collection are values less than 0.1 %.

The effects of the electrical arcs are mainly electromagnetic disturbances and high values of instantaneous temperature on the strip and on the wire that cause an increase of wear on the contact strip and on the contact wire [2–4]. The final result of this phenomenon is an important impact on the maintenance cost of the rolling stock due to a more frequent substitution of the pantograph's strips and of the infrastructure related to a reduction of the contact wire's life. For this reason, it is essential to reduce the occurrence of the electrical arcs by improving the contact quality.

In this paper, two different kinds of carbon based strip, i.e. plain carbon strip and impregnated copper carbon strips, and a pure copper contact wire were considered and first attempts to quantify this effect on the wear of the contact strip and contact wire were presented. For this aim, experimental tests were carried out on a specific test bench, developed to reproduce the electro-mechanical contact condition between the strip and the wire [4–6].

In the following sections, after a description of the test bench and test conditions, the experimental results are presented and commented.

2 The Test Bench and the Measurement Setup

In order to study the wear behavior of both contact strips and contact wire, tests were carried out using the test bench for the analysis of strip-wire contact, called CCTB (Current Collection Test Bench), designed by researchers of Department of Mechanics of Politecnico di Milano [4–6]. The CCTB enables the testing of a full-scale collector strip at speed up to 220 km/h with a level of electrical current up to 1400 A d.c., 500 A a.c. 16_{2/3} Hz and 350 A a.c. 50 Hz, in order to reproduce the typical European railway power supply types. The main element of the test rig (Fig. 1) is a fiber-glass wheel, with a 2 m radius, rotating around a vertical axis. A contact wire is elastically connected along its perimeter by means of 36 supports. The collector strip is mounted on two suspensions connected to a platform moving along the radial direction of the fiber-glass wheel, then reproducing the relative motion due to the staggering of the contact wire. The combination of the peripheral speed of the wheel, corresponding to the train speed, and the transversal motion imposed to the strip, corresponding to the stagger, represents the sliding speed between the contact wire and the strip. A ventilation apparatus conveys an air flow on the strip–wire contact zone, at the same speed of the test in order to correctly reproduce the thermal conditions on the contact zone.

The vertical contact force between the collector and the contact wire is applied by means of a hydraulic actuator mounted on the moving platform.

A fundamental aspect of the test rig is its measurement setup. The vertical and longitudinal components of contact forces are measured using four load cells, two

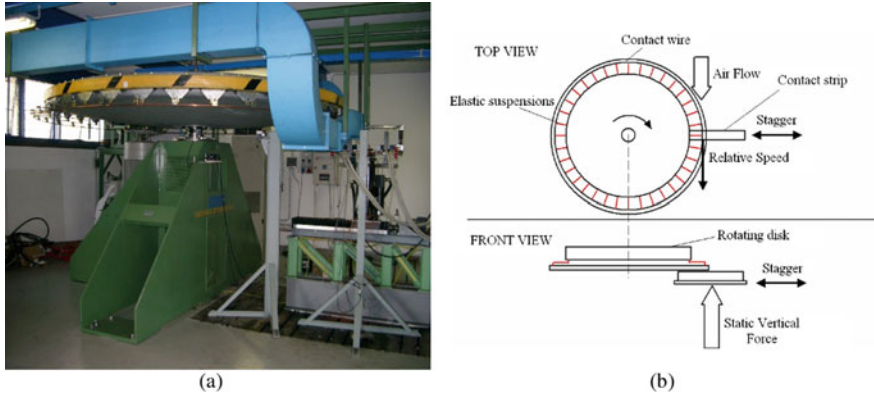


Fig. 1 The test rig for current collection investigation

for the measurement of the left and right vertical contact forces and two for the measurement of the left and right longitudinal contact forces (Fig. 2a).

The contact strip temperature is measured by means of a thermocouple placed in the center of the contact strip at the connection between the aluminum support and the carbon part (Fig. 2b), inside a cavity machined into the carbon volume.

The vertical acceleration of contact strip is measured by means of an accelerometer placed on the center of the contact strip. This measurement is important to verify the contact quality from the mechanical point of view. In particular, it is possible to correlate the r.m.s. value of the vertical acceleration with the percentage of arcing.

As far as the wear is concerned, strip wear rate is estimated from the strip mass difference before and after the test, while contact wire wear rate is estimated by the difference of the thickness between the end and the beginning of the test. The mass

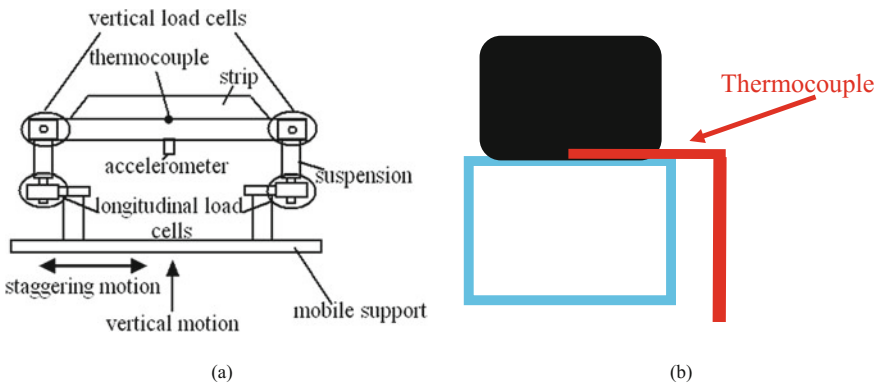


Fig. 2 a Scheme of the sensors applied on the strip; b scheme of the position of thermocouple on the strip

of contact strip is measured by means of a digital balance able to measure mass variation of 0.1 g. The thickness of the contact wire is measured in 180 sections (5 sections for each of the 36 supports) along the wire (Fig. 3) by means of a laser system with a resolution of about 3 μm . The wear of contact wire is expressed in terms of Normal Wear Rate (NWR) index [7], defined as the worn volume over the sliding distance (usual units of NWR are [mm^3/km]), and in worn area per million contact strip passages [$\text{mm}^2/10^6 \text{ csp}$] (csp = contact strip passage). Also the wear of contact strip is expressed in terms of Normal Wear Rate (NWR, [mm^3/km]).

The contact loss index is inferred from the voltage variation of the electrical circuit of the test rig, considering that those variations are due only to the variation of the contact force and then of the electrical contact resistance. The percentage of arcing is calculated analyzing the time history of contact voltage during tests. The mean value μ_V and the standard deviation σ_V of contact voltage are calculated and the range $\mu_V \pm 3 \cdot \sigma_V$ is defined (Fig. 4). If the instantaneous value of contact

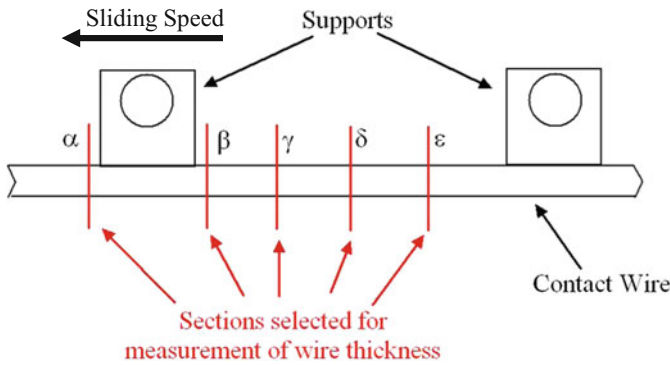


Fig. 3 Scheme of contact wire thickness measurement

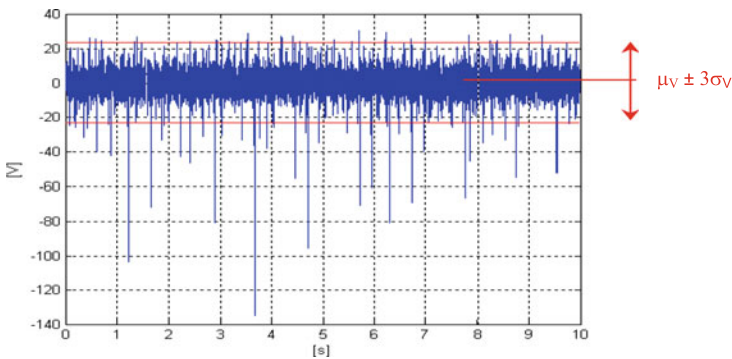


Fig. 4 Overall voltage drop and range for contact loss identification

voltage is out of this range the occurrence of the contact loss is considered. The percentage of arcing is calculated by means of the following relationship:

$$u\% = \frac{\sum_i \Delta t_i}{T} \cdot 100. \tag{1}$$

where T is the total time of observation while Δt_i is the time of contact loss occurrence. Although the calculation of percentage of arcing is the one reported in [1], the values calculated as indicated above are not directly comparable with that calculated in the real operation. The latter is evaluated by means of optical measurements in a narrow wavelength range corresponding to copper emission.

3 The Test Conditions

During the tests, pure copper contact wire with 100 mm² section and plain carbon and impregnated carbon strips were considered. For the impregnated carbon strip, the considered range of copper impregnation was 20–35 % and all the strips were 35 mm width.

The value of the speed is an important parameter that affects the dynamics of the strip-wire contact. A higher sliding speed causes a higher vertical acceleration of the strip, in sliding contact with the wire, and, then, a higher value of percentage of arcing. This relationship is shown in Fig. 5a, which reports the r.m.s. value of the vertical acceleration of the strip for different test speed values. This dependence is for all the types of contact strips independently on the copper percentage. Two different values of speed were mainly considered for the tests: 185 and 200 km/h. The first value was chosen to reproduce a current collection condition with low percentage of arcing while the second one was used to obtain a higher value of the percentage of arcing.

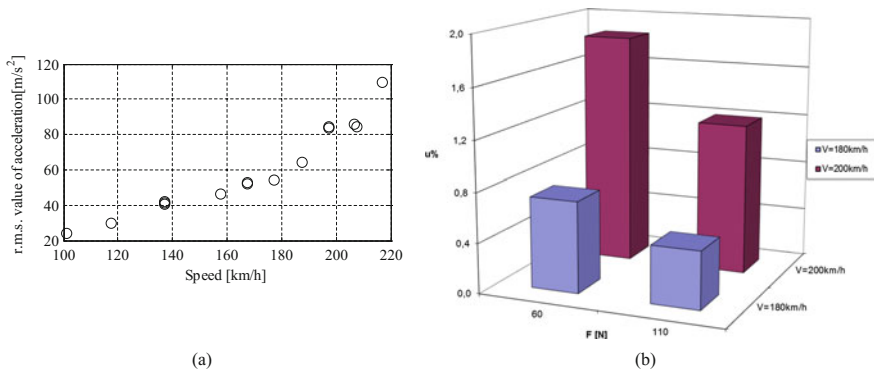


Fig. 5 **a** r.m.s. value of the vertical acceleration of the strip (0–500 Hz) versus the sliding speed; **b** percentage of arcing (u%) versus the sliding speed and the static vertical contact force

Another important parameter that influences the percentage of arcing is the static vertical force between the strip and the wire: a lower value of the static vertical contact force produces a higher value of the percentage of arcing. During the tests, two different values of static contact force were considered: 60 and 110 N. Figure 5b shows the combined effect of speed and static contact force on the value of percentage of arcing.

The value of the current during each tests was imposed at 280 A c.a. (r.m.s. value) at 50 Hz to obtain a current density equal to 8 A/mm, which is a typical value for the railway operation. Moreover, to avoid the introduction of different inertial effects during the interaction between strip and wire, the mass of the different strips tested was adjusted in order to be 2.3 kg.

4 The Test Results

In this section, the wear rate of both wire and strip, obtained during tests, are presented and discussed. The wear of the contact wire is obtained starting from the measurement of the difference of the wire thickness before and after the tests. The distribution of thickness variation due to the wear is not uniform along the ring shaped contact wire. Three thickness measurements for each of the 180 sections considered along the wire (see Sect. 2) were taken to analyze the repeatability. For the calculation of the wire thickness variation, the mean value of the three thickness measurements was considered and the corresponding 180 values were statistically analyzed building the corresponding histogram (see Fig. 6) Due to the dynamic behavior of the interaction between contact wire (elastically suspended) and contact strip, generally the contact wire wear is higher in the sections closest to the supports. Measurements are therefore divided in two classes, identified with blue and red color (see Fig. 6). The idea is to identify the thickness variations in the sections where electrical arcs occur from the other sections affected by sparking only. High thickness variation are obviously related to sections where electrical arcs occur: in

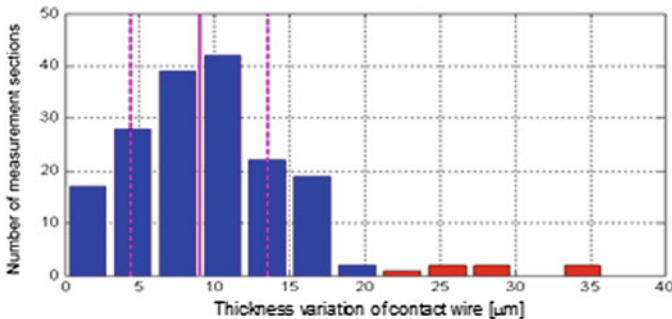


Fig. 6 Histogram of wire thickness variation

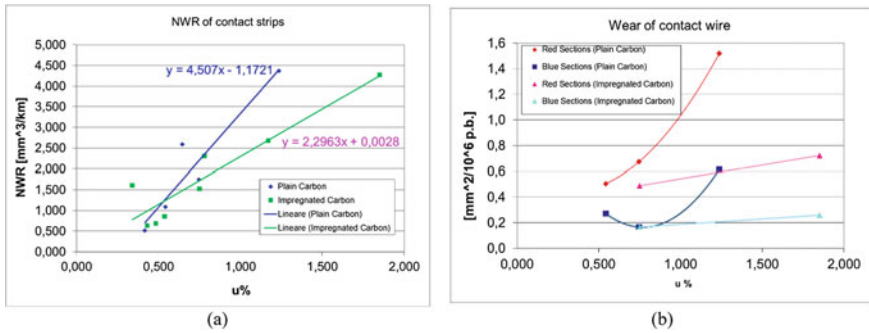


Fig. 7 **a** Wear of contact strip versus the percentage of arcing; **b** Wear of contact wire versus the percentage of arcing

the histogram the red measurement values refer to the sections with arcs, while the blue measurement values to the other sections. The continuous vertical line on the histograms represents the mean value of thickness for all blue sections while the two dotted vertical lines represent the mean value plus and minus the standard deviation of all blue sections.

For the analysis of wire wear, two different calculations were used for the worn volume: (i) the first calculation considers only the blue sections on the contribution of worn volume; (ii) the second calculation considers the red sections in order to point out the contribution on the wire wear due to the electrical arcs. Red sections, therefore, can be considered corresponding to the worst sections in the real catenary, i.e. sections under suspensions or in correspondence of heavy concentrated masses (junctions, insulating section, anchor mid-point).

The strip's wear (Fig. 7a) increases with the increase of the percentage of arcing, but a different trend can be noticed between the plain carbon strips and the impregnated ones. Indeed, the effect of the percentage of arcing on the wear of the strips is lower on the impregnated strips with respect to the plain carbon strips. Different behavior of the two kinds of strips can be observed (Fig. 7b) analyzing the results of the wire's wear: the plain carbon strip causes higher wear on the contact wire with respect to the impregnated carbon.

Possible reason for this different behavior of the two kinds of contact strips can be the lower electrical resistance of impregnated carbon strips.

5 Conclusions

This paper presented the results of laboratory tests aimed at analyzing the effect of the electrical arc occurrence on the wear of both pantograph's strips and contact wire for a.c. current collection. Two different kinds of contact strips were analyzed: plain carbon strips and copper impregnated carbon strips. The results show the

important influence of the parameter “percentage of arcing” on the wear of both strip and wire. In particular the following results were found: (i) the dependence of strip’s wear on the percentage of arcing is roughly linear; (ii) strips with percentage of copper impregnation up to 30 % are less prone to wear related to electrical arcs, by a factor of about two; (iii) copper impregnated strips cause low wear rate with respect to pure carbon; (iv) the dependence of the most worn sections of contact wire on the percentage of arcing is more than proportional.

References

1. CEI EN 50317—Railway applications—Current collection systems—Requirements for and validation of measurements of the dynamic interaction between pantograph and overhead line (2013)
2. Kubo S, Kato K (1999) Effect of arc discharge on the wear rate and wear mode transition of a copper-impregnated metallized carbon contact strip sliding against a copper disk. *Tribol Int* 32:367–378
3. Nagasawa H, Kato K (1998) Wear mechanism of copper alloy wire sliding against iron-base strip under electric current. *Wear* 216:179–183
4. Bucca G, Collina A (2015) Electromechanical interaction between carbon-based pantograph strip and copper contact wire: a heuristic wear model. *Tribol Int* 92:47–56
5. Bucca G, Collina A (2009) A procedure for the wear prediction of collector strip and contact wire in pantograph–catenary system. *Wear* 266:46–59
6. Bocciolone M, Bucca G, Collina A, Mapelli F (2004) A test rig for the comparative evaluation of the performance of collector strips. In *Railway engineering conference*, London, UK
7. Klapas D, Benson FA, Hackam R, Evison PR (1998) Wear in simulated railway overhead current collection systems. *Wear* 126:167–190

Part IX
Vibrations

Low-Cost Experimental Assessment of Forces in the Contact Bridge-Soundboard of Stringed Musical Instruments

Enrico Ravina

Abstract The paper describes the main results of an unconventional and non-industrial application of mechanics oriented to the experimental detection and monitoring of static and dynamic forces generated in the contact between bridge and soundboard in stringed musical instruments. Forces in bridge-soundboard contact are validated by low-cost experimental procedures, acquiring forces along the normal to the contact surfaces by means non-invasive thin film micro-sensors, interfaced to PC. Consequently, friction forces can be estimated, through the friction factor depending on the soundboard and bridge materials.

Keywords Mechanics of violin • Forces analysis • Stringed instruments • Experimental assessment

1 Introduction

In bowed and plucked musical instruments, the bridge plays a fundamental role for the generated sound, supporting the strings above the fingerboard from the nut to the tailpiece. It is not only a strength component supporting static and dynamic forces generated by the strings, but also a fundamental mechanical filter to vibrations generating sound. In the violins family the bridge needs to be fitted by carving its feet to match the curvature of the violin soundboard. It also needs to be adjusted so that it is the proper height for the violin, and usually it is placed even with the slash in the f-holes, opening holes having f-shape carved in the upper soundboard of the instrument. The feet of the bridge are placed over the sound post and the bass bar (Fig. 1). Geometries of violin bridges are very diversified and related to the dimensions of the instrument and to its mounting (baroque, classical, modern). Bridge is an asymmetrical component: one side is flat; the other is slightly tapered. The tapered side faces the tailpiece and the flat side faces the scroll. In this way, the

E. Ravina (✉)
University of Genova, Genova, Italy
e-mail: enrico.ravina@unige.it

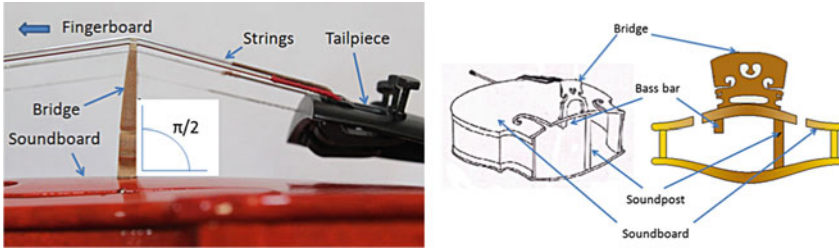


Fig. 1 Bridge mounting

thickness is variable matching small contact surfaces between strings and notches with a good stability at feet. The flat side should form a right angle with the violin’s soundboard; in addition, the bridge should be tilted away from vertical so the angles from bridge and both segments of the string will be equal. This posture equalizes the tensions on the opposite side of the string.

Actions generated by the strings to the bridge are both static and dynamic. Static actions are related to the tuning phase of the instrument, while dynamic actions are consequent to the motion on the bow on the string.

2 Static Forces Analysis

From the structural point of view, two of a violin’s most vulnerable areas are the points of contact between the sound post and the inside of the top, and between the bridge feet and the outside of the top. In both cases, large forces are brought to bear on small areas of relatively fragile wood. Moving the sound post to a slight angle from its point of true fit, as is commonly done during adjustments, tends to dent the inside of the top. The sliding motion itself, especially when done under full string pressure, can tear the grains of the spruce.

The bridge feet create similar problems (Fig. 2). When the top of the bridge is pulled toward the fingerboard during tuning, the downward force of the strings gets concentrated at the front edge of the feet, causing them to dig into the top. The bridge is then rocked back by the player and this rocking from edge to edge can lead to the indentations and cracks under the bridge feet of so many old instruments.

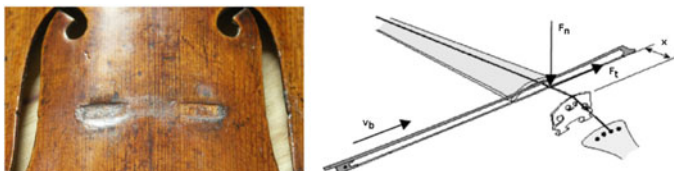


Fig. 2 Effects of bridge-soundboard contacts and actions on the bridge

The force distribution on the bridge is influenced by the tensions applied to the tuned strings and by the actions generated by the bow on the played strings. Tensions are related to the physical characteristics of the string and to the tuning frequency through the Mersenne’s relationship, Eq. (1):

$$T = 4 L^2 \mu f_0^2 \tag{1}$$

where f_0 is the fundamental frequency of the string, L its length measured from pegs and tailpiece, T the tension corresponding to the tuned condition and μ the linear density of the string.

The tension values for each strings assumes particular relevance in the violins family, determining the difference between baroque and modern instruments. Tensions define the pressure standing on the bridge and, consequently, the resultant of the forces transmitted from the bridge to the soundboard (usually called *down force*). This force is the result of two fundamental factors: the tension produced by the strings and the angle of the strings crossing the bridge. The string material, the string vibrating length, the tuning and the string diameter, determines tensions. The angle is influenced by the neck-fingerboard angle, the height of the bridge, the height of the arch and the shape of the tailpiece. In addition, differences from modern and baroque mountings include different values of tuning frequencies for each string and different materials (gut, steel, synthetic composite core with aluminum or silver wound, etc.), influencing the density of the strings. With reference to a modern violin, the tuning frequencies for each string are 660 Hz (E-string), 440 Hz (A-string), 294 Hz (D-string) and 196 Hz (G-string). Assuming the linear densities of the strings corresponding to a medium series of strings available on the market (e.g. $3.8 \cdot 10^{-4}$ kg/m for E string) and the length of strings equal to 350 mm, the static tensions are, respectively, 81.01 N (E-string), 65.10 N (A-string), 55.15 N (D-string) and 44.12 N (G-string).

Angles formed by string crossing the bridge can be geometrically evaluated, as shown in Fig. 3.

From the neck side $\theta_1^* = \arcsin (p_1/l_1)$ and, taking into account the slope of the bridge (θ_b) $\theta_1 = \theta_1^* - \theta_b$. From tailpiece side $\theta_2 = \arcsin (p_2/(h_b + h_{ta} - h_s))$, being h_{ta} the top arch dimension and h_s the saddle and gut dimension. Considering, for instance, typical dimensions as $l_1 = 330$ mm, $p_1 = 326$ mm, $p_2 = 160$ mm, $h_b = 31.5$ mm, $h_{ta} = 14.5$ mm and $h_s = 9$ mm the corresponding bridge angles are

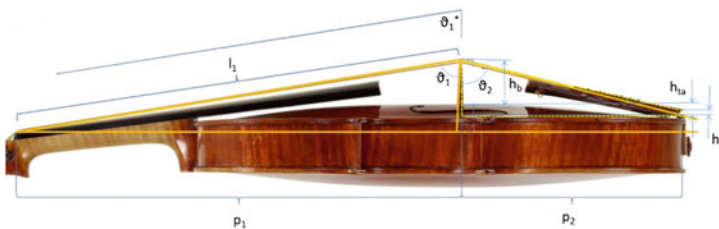


Fig. 3 String and bridge geometry

$\theta_1 = 78^\circ$ and $\theta_2 = 77^\circ$. Then the total bridge angle amounts, in this case, to 155° . More in general this angle is variable from 155° and 157° on modern violins and from 158° to 159° on baroque violins. For the down force evaluations we can consider, with good approximation, $\theta_1 = \theta_2$.

3 Forces on the Bridge

The static actions on the bridge are sketched in Fig. 4: for each string the tension T_i ($i = 1, 4$) generates the down force D_i . Is:

$$D_i = 2T_i \cos \theta / 2 \tag{2}$$

being, as previously assumed, $\theta = \theta_1 = \theta_2$.

The feet vertical reactions are different: the bass bar foot is less excited than the sound post E strings. In order to quantify these forces in Table 1 are collected the values corresponding to the example previously cited.

In order to evaluate the different normal forces at the base of the feet the geometry of the bridge must be considered. In Fig. 5 the main dimensions characterizing the violin bridge are collected.

Applying the cardinal equation of the statics (Fig. 5), the forces at sound post (R_S) and at bass bar (R_B) feet can be evaluated. Consequently, the friction forces between feet and sound posts can be calculated. About the friction coefficient must be noted that the contact is between bridge and sound post: when wood sliding on wood the friction coefficient is influenced by the sliding speed and by the moisture content [1]. For the purposes of this study the static friction value (maximum value) is assumed ($f_S = 0.8$).

In addition to static actions, dynamic forces induced in the bridge by the played string must be considered. The bowed string has two different ways of exerting driving forces on the bridge. The first comes about directly side-to-side oscillation

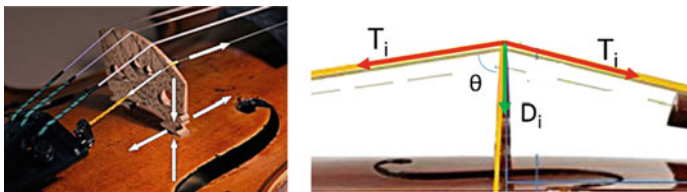
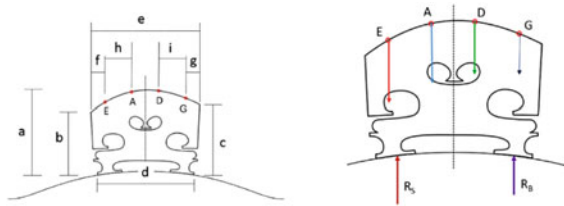


Fig. 4 Tensions and down forces

Table 1 Practical values of tensions and down forces

	<i>G string</i>	<i>D string</i>	<i>A string</i>	<i>E string</i>
Tension (N)	81.01	65.10	55.15	44.12
Down force (N)	18.15	19.13	21.09	29.43

Fig. 5 Bridge dimensions and static forces under feet



of the string in a direction parallel to the motion of the bow. This direct excitatory force is parallel to the surface of the top plate. It must be converted by the bridge into a force at right angles to the plate surface, in such a way it can effectively drive the body of the instrument. The second one depends on the tension variations: the tension of the played string goes through two cycles of variation during every cycle of the vibration, reaching maxima when the string moves to its extreme positions on either side of the rest position. This oscillating actions give rise to corresponding changes in the downward force exerted by the string on the bridge and consequently to the force which is ultimately applied to the soundboard. This indirect excitation takes place at twice the vibration frequency of the string.

These phenomena influence the actual forces generated in the bridge-soundboard contact. Different authors [2–4] propose bi-dimensional and three-dimensional models based on the evaluation of bridge mobility. Modelling the bridge as a simple lever the sound post acts a fulcrum. The bridge tends to rock, exerting a twisting force on the part of soundboard that lies between the f-holes. Assuming rigid the bass bar the bridge exerts up-and-down forces on the soundboard sections lying at its two ends. However, the validity of these hypotheses is limited to low frequencies. The theoretical evaluation of the actual forces transmitted by the bridge to the soundboard depends on the bridge geometry, on its stiffness and damping and to the attack conditions in the bow on the string.

The knowledge of the contact forces at the bridge feet is very important for measuring of tuning forces and for acquire information about the elastic deformation of the instrument and, consequently, to characterize, from the mechanical point of view, the bridge and the soundboard [5]. Experimental approaches able to detect the forces in the bridge-soundboard contacts are very attractive also to validate theoretical models.

4 Experimental Approach

The seat of contact is particularly critical for measurement. The prevalent action to be detected is the force generated by the bridge on the soundboard along the normal direction to the surface. The employment of conventional load cells located under the bridge is not acceptable because the thickness of the cell modify the relative position between bridge and strings. From the other hand, the reduction of the bridge height modifies the elastic response of the bridge. Other proposals [6] are based on

the customized load cells, expressly designed for this type of measurement, realizing an exact copy of the bridge under study (in iron) and equipped with extensometers. These solutions must be customized to the instrument under study and their cost can be justified only for mechanical characterization of valuable violins.

The proposal discussed hereafter is oriented to realize a low cost setup able to be applied on any bowed instrument. An improved and enhanced approach of measurement of the experimental analysis involves innovative thin film force sensors (Fig. 6). Sensors used are thin film tactile force sensors (Flexiforce, produced by Tekscan, Inc.). These extremely thin, less than 0.1 mm, and their flexible grid-based device are advantageous, allowing for minimally intrusive measurements, resulting in the least disturbance to the true pressure pattern. Each sensor consists on of a matrix of rows and columns of a semi-conductive material that changes its electrical resistance when force is applied to it. The dynamic response is very fast ($<5 \mu\text{s}$) and the force ranges (from 0 to 440 N) cover the field of interest. This solution applied to violins allows the use of standard bridges, because the relative positions and inclination of the string are not influenced by the presence of the sensors. A couple of sensors are interposed between bridge and soundboard, in order to detect the also the differential force under the feet.

The proposed solution is cheaper, not intrusive and good repeatable. Sensing area consists on a circle of 9.5 mm of diameter. Sensors can be connected to PC through electronic interface: wireless connection has been also tested. One sensor is placed under each bridge foot: foot surface is geometrically different to the sensing area. In order to develop a low cost approach the option to require customized sensors, tailored on particular surfaces, is not followed. The problem is solved implementing an original calibration procedure. Sensitive surface is a circle (diameter D_S equal to 9.5 mm in experiments here described), while the bridge foot is a rectangle (Fig. 7 (base b_F and height h_F , equal to 12.5×5 mm in the example detailed hereafter).

A correction based on the effective sensor and feet areas is implemented. Is:

$$F_d = p A_e = (F_a / A_s) A_e \quad (3)$$

being A_s the sensor area, A_e the effective area, F_a the external applied force, F_d the detected force, and p the contact pressure. In order to obtain $F_a = F_d$ during the setting it is necessary to introduce a correction factor corresponding to A_s / A_e . The effective area A_e is evaluated, with good approximation, as follows:

$$A_e = h_F (D_S - 2h) + 2A_s; A_s = 0.5 R^2 [\alpha - \sin(\alpha)]; R = D_S / 2; R = h + d; \\ c = 2 R \sin(\alpha / 2); d = R \cos(\alpha / 2)$$

Fig. 6 Thin film force sensors

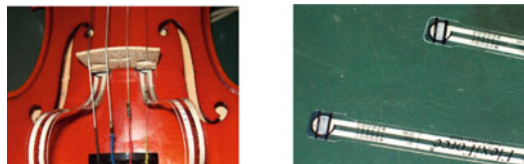
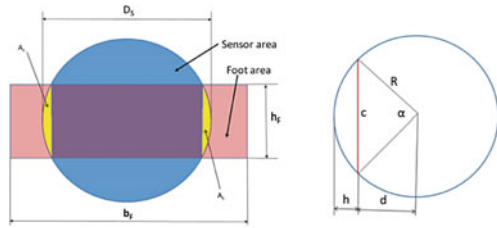


Fig. 7 Geometries of sensor and bridge foot



In the present application the correction factor is $A_s/A_e = 1.53$. The calibration of the sensors is obtained mounting of the sensors below the bridge feet and applying known forces using a pneumatic equipment: the air pressure is proportional to the actual force generated. Good results are obtained, checked also following the classical procedure of violin tuning. Different correction factors can be evaluated for other geometries of bridges (violas, cellos...). Some results of the experimentation are reported hereafter. Figure 8 shows a phase of tuning of a violin: forces under bass bar foot (red line) and sound post foot (blue line) are monitored versus time. We can observe that, in steady state conditions, the vertical force under the bass bar foot is greater than the force under sound post foot, but during the tuning phase the curves have intersections, due to the applied tuning technique.

Different conditions of string attack are tested: *continuo*, *spiccato*, *saltato*, *pizzicato*. Figure 9 shows an example of forces monitoring playing the D-strings in *pizzicato* attack. Dynamic forces are significantly different with respect to static ones, demonstrating the importance of a correct assessment of the internal forces.

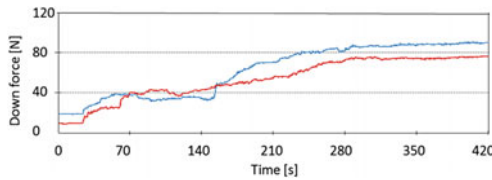


Fig. 8 Example of tuning monitoring

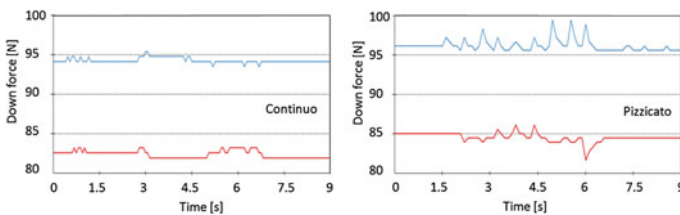


Fig. 9 Example of D-string in *continuo* and *pizzicato* attacks

5 Conclusions

A low-cost experimental approach oriented to the assessment of the forces in the contact bridge-soundboard of a violin has been described. The approach can be applied to other stringed musical instruments (e.g. viola, cello and double bass). Force monitoring is particularly important for studies related to the historical transformation of the violins family. In addition, it makes available fundamental information supporting structural analyses and identification approaches on the generated sound and of sound persistence. Finally, this monitoring is very significant to support tests oriented to correlate sound and dynamic forces generated in bowed musical instruments. Further development of the activity will be oriented to specific analyses and experiments detecting the influence of different kinds of bridges and of different tilt angles of the string on modern and baroque assembling, using metallic or gut strings.

References

1. McKenzie WM, Karpovich H (1968) The frictional behaviour of wood. *Wood Sci Technol* 2:139–152
2. Elie B, Gautier F, David B (2014) Acoustic signature of violins based on bridge transfer mobility measurements. *J Acoust Soc Am* 136(3):1385
3. Jansson JV (2004) Violin frequency response—bridge mobility and bridge feet distance. *Appl Acoust* 65:1197–1205
4. Pan J, Wilkins R (2007) A study of input mobility functions at a violin bridge. In *Proceedings of 14th international congress on sound and vibrations, ICSV14, Cairns, Australia*
5. Woodhouse J (2014) *The acoustics of the violin: a review. reports on progress in physics*, 42p. IPO publishing
6. Fioravanti M, Mazzanti P, Goli G, Rognoni GR, Sodini N (2008) Physical and mechanical characterization of ancient wooden musical instruments for conservation purposes. In *Proceedings of international conference on wood science for conservation of cultural heritage, Braga, Portugal*, pp 186–191

Vibration Modes of Piezoelectric Bimorphs: A Sensitivity Analysis

Alberto Borboni, Cinzia Amici, Valter Cappellini and Rodolfo Faglia

Abstract The paper presents a sensitivity study on the first five vibration modes of a bimorph piezoelectric beam. More in detail, the analysis focuses on the kinematic response of these kind of strips to uncertainties in the identification of electric, piezoelectric and mechanical parameters. The study defines these uncertainties as input errors in the identification process of the first five natural frequencies. The free vibration problem for bimorph piezoelectric beam constrained by simple supports has been solved, and results have been compared with the exact two-dimensional solution. Numerical simulations have also been implemented and data analyzed according to the Weibull distribution theory; eventually, high order functions have been identified, enabling to foresight the final frequency identification error.

Keywords Piezoelectric beam · Vibration modes · Bimorph strip

1 Introduction

Piezoelectric devices are nowadays broadly spread and commonly adopted in various industrial fields. In the last years, bimorph piezoelectric systems are gathering great attention by scholars and technicians as interesting actuators, able to perform mechanical motion or, in particular, vibration [1–8].

In 2005, Zhou et al. [9] presented semi-analytic approach for the evaluation of the eigenfrequencies of a piezoelectric bimorph based on an improved first-order shear deformation theory (FSDT) beam model.

In 2013, Borboni and Faglia [10] described how uncertainties on the knowledge of mechanical, piezoelectric or electric parameters reflect on the first vibration mode of a simply supported piezoelectric bimorph. Nevertheless, good practice for finest machine design would require a thorough awareness of the non-ideal responses of

A. Borboni (✉) · C. Amici · V. Cappellini · R. Faglia
Mechanical and Industrial Engineering Department,
Università degli Studi di Brescia, Brescia, Italy
e-mail: alberto.borboni@unibs.it

the system until the fifth vibration mode: for this reason, the present paper aims to investigate the previous models to the fifth vibration mode, thanks to a stochastic evaluation of the free vibrations of the piezoelectric bimorph.

2 Model Definition

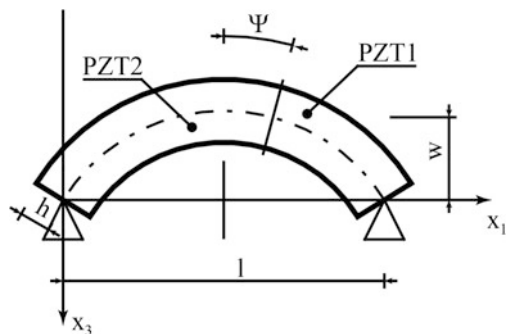
The basic system is composed of two piezoelectric layers, mechanically connected, and is constrained by simple supports; the layers are also electrically connected thanks to a parallel arrangement for the electric circuit and the Timoshenko theory [11] is applied in order to study the beam deformation.

According to this theory, the beam deformation can be properly analyzed in a planar space, since the deflection can be reduced to a two-dimensional movement. Referring to Fig. 1, a beam l long and having two layers h thick each, performs a movement in the x_1Ox_3 plane, and the *neutral* axis of the beam overlaps the x_1 axis in the undeformed configuration. The selection of the Timoshenko theory implicates that: (i) displacement \mathbf{u} of the axis points only depends by the linear x_1 variable, (ii) consecutive segments, normal to the neutral axis, remain consecutive after the deformation, and (iii) segments normal to the neutral axis in undeformed configuration do not strictly remain normal to the axis under deflection, indeed they could perform an additional Ψ rotation around the axis itself, as a consequence of the shear strain.

Under the effect of mechanical and/or electric actions, the beam deflects as presented in Fig. 1: in the deformed configuration, the bender presents for each section a w displacement along the x_3 direction and a Ψ rotation around x_2 .

Under the hypotheses of small deflection and plane stress state, the equilibrium equations along the i th direction ($i = 1, 3$) for an infinitesimal portion of the beam are described by Eq. (1), according to the definitions introduced by Eqs. (2)–(4), where σ and τ are components of the stress tensor is the stress tensor, f is a body force, ρ is the mass density of the bar, \bar{c} and are \bar{e} the components of the stiffness

Fig. 1 Simply supported piezoelectric bimorph



and piezoelectric matrix, ε and γ are the components of the strain tensor and E are the components of the electric field.

$$\frac{\partial \sigma_{xi}}{\partial x_i} + \frac{\partial \tau_{x1x3}}{\partial x1} + f_{xi} = \rho \frac{\partial^2 u_{xi}}{\partial t^2} \quad (1)$$

$$\sigma_{x3} = \bar{c}_{13} \varepsilon_{x1} + \bar{c}_{33} \varepsilon_{x3} - (-1)^r \bar{e}_{31} E_{x3} \quad (2)$$

$$\sigma_{x1} = \bar{c}_{11} \varepsilon_{x1} + \bar{c}_{13} \varepsilon_{x3} - (-1)^r \bar{e}_{31} E_{x3} \quad (3)$$

$$\tau_{x1x3} = \bar{c}_{55} \gamma_{x1x3} - (-1)^r \bar{e}_{15} E_{x1} \quad (4)$$

Since no external electrical charge is applied to the beam, the divergence and Gauss theorems led to Eq (5), where the components of the electric displacement matrix D_{x3} and D_{x1} are defined according to Eqs. (6) and (7), where $\bar{\varepsilon}$ are the components of the dielectric matrix.

$$\frac{\partial D_{x1}}{\partial x1} + \frac{\partial D_{x3}}{\partial x3} = 0 \quad (5)$$

$$D_{x3} = (-1)^r (\bar{e}_{31} \varepsilon_{x1} + \bar{e}_{33} \varepsilon_{x3}) + \bar{\varepsilon}_{33} E_{x3} \quad (6)$$

$$D_{x1} = (-1)^r (\bar{e}_{15} \gamma_{x1x3}) + \bar{\varepsilon}_{11} E_{x1} \quad (7)$$

Moreover, Eqs. (8)–(12) describe the relation of kinematics with displacement and electric potential ϕ .

$$\varepsilon_{x1} = \frac{\partial u_{x1}}{\partial x1} \quad (8)$$

$$\varepsilon_{x3} = \frac{\partial u_{x3}}{\partial x3} \quad (9)$$

$$\gamma_{x1x3} = \frac{\partial u_{x1}}{\partial x3} + \frac{\partial u_{x3}}{\partial x1} \quad (10)$$

$$E_{x1} = - \frac{\partial \phi}{\partial x1} \quad (11)$$

$$E_{x3} = - \frac{\partial \phi}{\partial x3} \quad (12)$$

Finally, according to the first-order shear deformation theory, the final mechanical displacement can be presented as in Eqs. (13) and (14); merging those definitions with the previous relations, the final Eqs. (15) and (16) can be obtained, where w and ψ are the translation and rotation of a cross section.

$$u_{x3}(x1, x3, t) = w(x1, t) \quad (13)$$

$$u_{x1}(x1, x3, t) = -x3\psi(x1, t) \quad (14)$$

$$\varepsilon_{x1} = -x3 \frac{\partial \psi}{\partial x1} \quad (15)$$

$$\gamma_{x1x3} = -\psi + \frac{\partial w}{\partial x1} \quad (16)$$

Under the further hypothesis of parallel electric configuration, Eqs. (17)–(21) can be written to approximate Eqs. (1) and (2), where m and p are the applied torque and force, M_x and Q_x are the bending moment and the shear force.

$$\frac{\partial M_{x1}}{\partial x1} - Q_{x1} - \int_{-h}^h \rho z \frac{\partial^2 u_{x1}}{\partial t^2} dx3 = m \quad (17)$$

$$- \frac{\partial Q_{x1}}{\partial x1} + \int_{-h}^h \rho \frac{\partial^2 u_{x3}}{\partial t^2} dx3 = p \quad (18)$$

$$\int_0^h \left(\frac{\partial D_{x1}}{\partial x1} + \frac{\partial D_{x3}}{\partial x3} \right) dx3 = 0 \quad \circ \quad \int_{-h}^0 \left(\frac{\partial D_{x1}}{\partial x1} + \frac{\partial D_{x3}}{\partial x3} \right) dx3 = 0 \quad (19)$$

$$M_{x1} = \int_{-h}^0 x3 \sigma_{x1} dx3 + \int_0^h x3 \sigma_{x1} dx3 \quad (20)$$

$$Q_{x1} = \int_{-h}^0 \tau_{x1x3} dx3 + \int_0^h \tau_{x1x3} dx3 \quad (21)$$

The initial conditions are then described by Eqs. (22)–(24), and expanding in Fourier series, the solving system in Eq. (25) can be defined: Eqs. (26)–(35) collect the definition of the A matrix coefficients, where b are the components of a parameter matrix opportunely dependent on the shear coefficient k and on different parameters of the model, as shown in [9]

$$w|_{x1=0, l} = 0 \quad (22)$$

$$\sigma_{x1}|_{x1=0, l} = 0 \quad (23)$$

$$\Phi|_{x1=0, l} = 0 \quad (24)$$

$$\begin{bmatrix} a_{11} & a_{12} & a_{13} \\ a_{21} & a_{22} & a_{23} \\ a_{31} & a_{32} & a_{33} \end{bmatrix} \begin{pmatrix} W_n \\ \Psi_n \\ \Phi_n \end{pmatrix} = \begin{pmatrix} a_{14} V_n \\ P_n + a_{24} V_n \\ a_{34} V_n \end{pmatrix} \quad (25)$$

$$a_{12} = -b_{21}\left(\frac{n\pi}{l}\right)^2 - b_{12} + b_{41}\omega_n^2 \quad (26)$$

$$a_{13} = (b_{22} - b_{13})\frac{n\pi}{l} \quad (27)$$

$$a_{21} = b_{11}\left(\frac{n\pi}{l}\right)^2 - b_{42}\omega_n^2 \quad (28)$$

$$a_{22} = b_{12}\frac{n\pi}{l} \quad (29)$$

$$a_{23} = b_{13}\left(\frac{n\pi}{l}\right)^2 \quad (30)$$

$$a_{31} = -b_{31}\left(\frac{n\pi}{l}\right)^2 \quad (31)$$

$$a_{32} = -b_{32}\frac{n\pi}{l} \quad (32)$$

$$a_{33} = -b_{33}\left(\frac{n\pi}{l}\right)^2 + b_{35} \quad (33)$$

$$a_{24} = -b_{14}\left(\frac{n\pi}{l}\right)^2 \quad (34)$$

$$a_{34} = -b_{34}\left(\frac{n\pi}{l}\right)^2 \quad (35)$$

The determinant of the system in Eq. (25) solved for the n th value allows to define the n th eigenvalue.

3 Stochastic Approach

In order to obtain comparable results, the same stochastic approach introduced by Borboni and Faglia in 2013 [10] has been adopted in the sensitivity analysis of the variable parameters collected in the \mathbf{Z} vector: the mechanical stiffness \mathbf{C} , and the piezoelectric parameters \mathbf{e} and $\boldsymbol{\epsilon}$.

Once defined μ_{ij} the nominal value of the ij th element of \mathbf{Z} , and Δ_z the maximum allowed error (i.e. the maximum implemented variation of the parameter), the variance ζ can be described as Eqs. (36) and (37) present.

$$\delta_{ij}(z_{ij}) = \begin{cases} \frac{1}{2\mu_{ij}\Delta_z}, & \mu_{ij}(1 - \Delta_z) \leq z_{ij} \leq \mu_{ij}(1 + \Delta_z) \\ 0, & \text{elsewhere} \end{cases} \quad (36)$$

$$3\zeta_{ij}^2 = \mu_{ij}^2 \Delta_z^2 \quad (37)$$

Table 1 PZT-5A: nominal values of the main material property

Parameter	Tested values				
Input	C	e	ϵ	C, e and ϵ	
Δ_{Input}	0.01	0.02	0.03	0.04	0.05
λ	5	10	20	50	100
$k\rho$	0.8333	0.8472	0.8611	0.8750	0.8889

The aims of the work is to test the sensitivity of the model, in terms of ability to quantify the natural frequencies of the system, to parametric errors. The numerical simulations are performed for: five values of the geometric ratio λ , five values of the shear coefficient k , five values of the maximum error Δ_{Input} and four types of error conditions, as shown in Table 1. Each test is statistically repeated 1000 times, according to (36) and (37), for each natural frequency from the 1st to the 5th.

Table 1 collects the testing conditions of the stochastic simulations.

4 Numerical Results and Discussion

Numerical evaluation have been performed under the hypothesis of PZT-5A; the main characteristics of this material are collected in Table 2.

The main result is that the influence of the electric and piezoelectric error on the frequency evaluation is limited, less than 0.5 %, whereas the mechanical parameters are predominant. Although the shear coefficient is an important parameter, when its value is chosen within the range proposed by Cowper [11], the error produced on the frequency evaluation is limited. The error on the geometric ratio λ is relevant starting from the 2nd frequency and the instability of the model increases with increasing vibrational modes (Fig. 2).

Table 2 PZT-5A: nominal values of the main material property

Property	Value	Measurement unit
c_{11}	105	[GPa]
c_{12}	54.6	[GPa]
c_{13}	52.7	[GPa]
c_{33}	86.8	[GPa]
c_{55}	22.2	[GPa]
e_{15}	12.2	[C/m ²]
e_{31}	-9.78	[C/m ²]
e_{33}	13.8	[C/m ²]
ϵ_{11}	16.4	[nF/m]
ϵ_{33}	15.1	[nF/m]
ρ	7800	[kg/m ³]

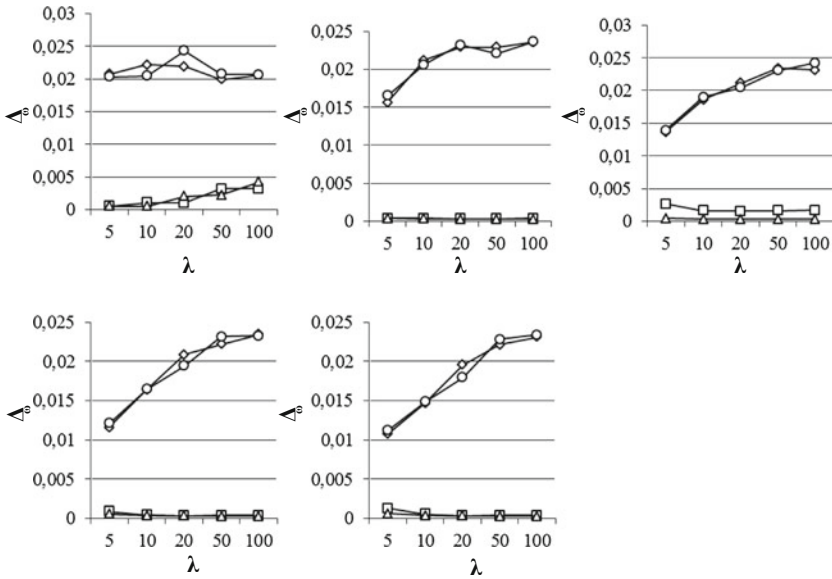


Fig. 2 $\Delta\omega$ with respect to λ . The results of mechanical (*diamond*), piezoelectric (*square*), electric (*triangle*) and all (*dot*) parameters variations are presented, under the hypotheses of 1 % input error and $k = 5/6$. The first diagram on the top left is the 1st vibration mode, the consequent diagrams are associated to increasing vibration modes

5 Conclusions

The problem of the computation of the natural frequencies for the 1st–5th modes of a simply supported piezoelectric bimorph beam was investigated in presence of evaluation errors in mechanical, piezoelectric and electric parameters. The analysis was performed on a PZT-5A device. Under some limitations, we can conclude that: the effect of the errors on mechanical stiffness is predominant with respect to the piezoelectric and electric errors. The correlation between mechanical errors and natural frequencies can be represented with simple empirical expressions. These results was known for the first vibration mode and this work extends the previous result to the 1st–5th vibration modes. We must also observe that the model is stable for the first modes, where the effect of the errors on the parameters and of the number of tests is limited on the natural frequencies. Increasing the number of modes the model becomes more and more unstable and its ability to predict the vibrational frequencies of the devices becomes really dependent on the ability to estimate, particularly its mechanical parameters. Thus a superficial analysis is not sufficient and a deep mechanical analysis of the device is necessary to accurately predict high order vibrational behavior of the device.

References

1. Jafferis NT, Lok M, Winey N, Wei G-Y, Wood RJ (2016) Multilayer laminated piezoelectric bending actuators: design and manufacturing for optimum power density and efficiency. *Smart Mater Struct* 25 (5), art. no. 055033
2. Vidal P, Gallimard L, Polit O (2016) Modeling of piezoelectric plates with variables separation for static analysis. *Smart Mater Struct* 25 (5), art. no. 055043
3. Jang HS, Cha YT, Lee HS, Choi SJ, Park J (2016) An optimal study of wind measurement device using piezoelectric unimorph benders. *Int J Precis Eng Manufact* 17(4):511–515
4. Feri M, Alibeigloo A, Pasha Zanoosi AA (2016) Three dimensional static and free vibration analysis of cross-ply laminated plate bonded with piezoelectric layers using differential quadrature method. *Meccanica* 51(4):921–937
5. Nam J, Kim Y, Jang G (2016) Resonant piezoelectric vibrator with high displacement at haptic frequency for smart devices. *IEEE/ASME Trans Mechatron* 21(1):394–401, art. no. 7147801
6. Li HB, Wang X (2016) Nonlinear dynamic characteristics of graphene/piezoelectric laminated films in sensing moving loads. *Sens Actuators, A* 238:80–94
7. Rios SA, Fleming AJ (2016) Design of a charge drive for reducing hysteresis in a piezoelectric bimorph actuator. *IEEE/ASME Trans Mechatron* 21(1):51–54, art. no. 7283638
8. Jiaqiang E, Qian C, Liu T, Liu G (2016) Chaos analysis on the acceleration control signals of the piezoelectric actuators in the Stewart platform. *Shock Vib*, art. no. 8087176
9. Zhou Y-G, Chen Y-M, Ding H-J (2005) Analytical solutions to piezoelectric bimorphs based on improved FSDT beam model. *Smart Struct Syst* 13:309–324
10. Borboni A, Faglia R (2013) Stochastic evaluation and analysis of free vibrations in simply supported piezoelectric bimorphs. *J Appl Mech* 80(2):021003
11. Cowper GR (1966) The shear coefficient in Timoshenko's beam theory. *J Appl Mech* 33 (2):335–340

Concurrent Active Control and Dynamic Structural Modification in the Design and the Optimization of Vibrating Systems

Roberto Belotti, Roberto Caracciolo and Dario Richiede

Abstract The simultaneous optimization of the mechanical design and of the controller in vibrating systems is of great importance in order to improve the system dynamic performances. Due to the mutual interaction, the two tasks should be performed in a concurrent way. In order to overcome the limitations of traditional decoupled approaches, this paper proposes a method for the simultaneous synthesis of the state feedback controller and of the modifications of the inertial and elastic parameters. The performance optimization is obtained by assigning some desired eigenvectors and eigenvalues to the controlled systems, so that a desired dynamic behaviour is featured. Indeed, the eigenvalues determine damping and speed of response, while the eigenvectors set the sensitivity of the eigenvalues and the spatial shape of the vibration. By properly combining active control and structural modification, the capability to assign the desired eigenpairs is enlarged since passive control shapes the allowable subspace so that the desired eigenpairs can be assigned through active control. The numerical results show the effectiveness of the proposed method and the great potential advantages of the concurrent use of structural modification and active control over traditional design methods.

Keywords Vibrating system · Dynamic response · Eigenstructure assignment · Active control · Structural modification

R. Belotti · R. Caracciolo · D. Richiede (✉)
Università degli Studi di Padova, Padua, Italy
e-mail: dario.richiede@unipd.it

R. Belotti
e-mail: belotti@gest.unipd.it

R. Caracciolo
e-mail: roberto.caracciolo@unipd.it

1 Introduction

The ever growing interest towards increasing the dynamic performances of mechanical and mechatronic systems, while reducing their cost and the actuation effort, imposes a control-oriented approach since the early stages of the design. Indeed, design choices should address the interactions between the mechanical issues and the control synthesis [6]. Indeed, while, a badly designed mechanical system will barely enable high performances even with sophisticated controllers, on the other hand the knowledge of the controller performances allows for cost effective mechanical constructions [11]. Traditional sequential design approaches do not optimally tackle most of these interactions and often neglect the relations between the achievable performances of the controlled system and the mechanical properties. Hence, time-consuming trial-and-error approaches should be adopted. To overcome this limitation, the recent literature has often highlighted the need for concurrent approaches, but there is still a partial lack of practical methods supporting a control-oriented design of the mechanical part. The limits of sequential design approaches are exacerbated in the presence of flexible mechanical components. Both passive and active methods have been suggested to optimize their vibrational behavior, by imposing the desired eigenstructure, i.e. the eigenvalues (the poles) and/or eigenvectors (the mode shape), through the so called eigenstructure assignment (EA). The poles set the frequency and the damping of the vibrational modes, and therefore also the speed of response and the settling time. The eigenvectors fix the robustness of the eigenvalues with respect to the parameter variability and determine the spatial shape of the vibration. Shaping eigenvectors is for instance effective for redistributing vibrations along the system, for confining them to parts of the system where they are admissible or desirable [10], as well as to optimize the generation of the vibrations in resonators [2].

Passive approaches to the optimal design of mechanical and mechatronic systems in the presence of component flexibility have been investigated within the frame of the “dynamic structural modification” (DSM) [2]. DSM aims at calculating mass, stiffness and, sometimes damping, modifications to be applied to a first-trial design of the system, in such a way that the desired eigenstructure is obtained. Although DSM does not require additional sensors and actuators, its performances are intrinsically limited because of the presence of technical and economical constraints on the feasible modifications. Additionally, the symmetric nature of the passive modifications is an another intrinsic limitation.

A different approach in the optimization of the dynamic behavior of vibrating systems is active control, which can be exploited to obtain the desired eigenstructure of closed-loop controlled system. A typical approach in vibrating systems is the use of active controllers aimed at assigning the closed loop system poles (the eigenvalues), since poles set damping, stability and the speed of response (see [9]). The control forces exerted by the motor should then ensure the desired dynamic response by behaving as active masses, springs and dampers. One of the reasons for the wide use of the mentioned pole placement methods is that they just need the

system to be controllable and observable. In contrast, controllability does not ensure that any desired eigenstructure could be obtained, if the system is underactuated [1, 7], as often occurs in the case of vibrating systems.

The concurrent combination of active control and passive modifications is therefore a promising approach to overcome the limitations of the single use of either the approaches and hence boost the achievement of the desired dynamic behaviour. The simultaneous use of active and passive control has been named “hybrid control”. For example, the idea of “hybrid control” has been successfully exploited in [8] through a suitable combination of DSM and active control, to improve pole placement, by performing the two stages of the design in a sequential way. A great improvement in the results achieved through hybrid control can be obtained through a concurrent approach, where the synthesis of the mechanical properties and of the controller gains are performed simultaneously. The inclusion of the controlled system expected performances in the design process decreases the need of iterating and hence allows to handle more complicated problems.

Despite the possible improvement of the closed loop performances, the issue of hybrid control to EA has been only marginally investigated. In this research field, this paper proposes and validates a novel method for the concurrent synthesis of the structural modifications and the active controller gains.

2 Dynamic Structural Modification (DSM)

Let us consider a N -dimensional undamped vibrating system modelled as

$$\mathbf{M}\ddot{\mathbf{q}}(t) + \mathbf{K}\mathbf{q}(t) = \mathbf{B}\mathbf{v}_A(t) \tag{1}$$

with \mathbf{M} , \mathbf{K} the mass and stiffness matrices, $\mathbf{q}(t)$ the displacement vector, $\mathbf{v}_A(t)$ the control force vector, \mathbf{B} the control force distribution matrix. It is assumed that the control forces are not redundant (i.e. \mathbf{B} is full rank) and that \mathbf{B} cannot be modified. DSM of undamped systems aims at calculating mass and stiffness modifications (denoted $\Delta\mathbf{M}$ and $\Delta\mathbf{K}$) to be applied to the original system so that desirable eigenpairs are met. The desired dynamic behaviour is therefore specified through the real eigenpairs $(\tilde{\omega}_i^2, \tilde{\mathbf{u}}_i)$, where $\tilde{\omega}_i$ is the natural frequency of the mode with shape $\tilde{\mathbf{u}}_i$. Hence, for any desired eigenpair the following equation must hold:

$$\tilde{\omega}_i^2[\Delta\mathbf{M} + \mathbf{M}]\tilde{\mathbf{u}}_i = [\Delta\mathbf{K} + \mathbf{K}]\tilde{\mathbf{u}}_i \tag{2}$$

The topologies of the symmetric modification matrices $\Delta\mathbf{M}$ and $\Delta\mathbf{K}$ are a priori assumed on the basis of design requirements and practical constraints. Other technical requirements impose bounds on the values of the system modifications, which defines the feasible domain Γ to which $\Delta\mathbf{M}$ and $\Delta\mathbf{K}$ should belong.

3 Active Control

EA through state feedback aims at computing the controller gains ensuring the achievement of the desired eigenpairs. The control force is defined as follows:

$$v_A(t) = -\mathbf{F}^T \dot{q}(t) - \mathbf{G}^T q(t) \quad (3)$$

\mathbf{F} and \mathbf{G} are the control gains to be computed such that the closed loop system features a prescribed set of eigenpairs $(\tilde{\lambda}, \tilde{\mathbf{u}})_i$. The pair $(\tilde{\lambda}, \tilde{\mathbf{u}})_i$ is an eigenpair if (and only if) it is a solution of the following equation.

$$\left[\mathbf{M} \tilde{\lambda}_i^2 + \mathbf{K} \right] \tilde{\mathbf{u}} = -\mathbf{B} \left[\tilde{\lambda} \mathbf{F}^T \quad \mathbf{G}^T \right] \tilde{\mathbf{u}} \quad (4)$$

which dictates that any assignable eigenvector must belong to the vector space $\Psi(\tilde{\lambda}_i)$, named the allowable subspace, and defined as follows:

$$\tilde{\mathbf{u}}_i \in \text{span} \left\{ \left[\mathbf{M} \tilde{\lambda}_i^2 + \mathbf{K} \right]^{-1} \mathbf{B} \right\} = \Psi(\tilde{\lambda}_i). \quad (5)$$

Since $\dim \Psi(\tilde{\lambda}_i) = \text{rank}(\mathbf{B})$, it is not always possible to assign any arbitrary eigenvector by employing only state feedback control in the case of underactuated systems [1, 7].

4 Hybrid Control

Let us suppose that it is wanted to assign the eigenpair $(\tilde{\lambda}, \tilde{\mathbf{u}})_i$; the extension for an arbitrary number is almost straightforward and it is omitted for brevity. The hybrid control approach consists in modifying the allowable subspace $\Psi(\tilde{\lambda}_i)$ by means of $\Delta \mathbf{M}$ and $\Delta \mathbf{K}$ to obtain new subspace $\hat{\Psi}(\tilde{\lambda}_i)$ to which the desired eigenvector should belong.

$$\tilde{\mathbf{u}}_i \in \text{span} \left\{ \left[(\mathbf{M} + \Delta \mathbf{M}) \tilde{\lambda}_i^2 + (\mathbf{K} + \Delta \mathbf{K}) \right]^{-1} \mathbf{B} \right\} = \hat{\Psi}(\tilde{\lambda}_i) \quad (6)$$

The computation of the modification matrices can be formulated as a rank minimization problem. This formulation is advantageous, in fact, since rank minimization problems have many applications in different fields, there are several effective numerical algorithms. Additionally, it does not require the inversions of the matrices collecting the unknowns. By defining the real vectors of the coefficients of the span in Eq. (6), denoted \mathbf{x}_i , Eq. (6) is equivalent to the following condition:

$$\mathbf{B}\mathbf{x}_i = \left[(\mathbf{M} + \Delta\mathbf{M})\tilde{\lambda}_i^2 + (\mathbf{K} + \Delta\mathbf{K}) \right] \tilde{\mathbf{u}}_i \tag{7}$$

which is a linear system with \mathbf{x}_i the unknown vector. On the basis of the well-known Rouché-Capelli theorem, such system can be solved if and only if the rank of \mathbf{B} is equal to the rank of $\left[\mathbf{B} \left[(\mathbf{M} + \Delta\mathbf{M})\tilde{\lambda}_i^2 + (\mathbf{K} + \Delta\mathbf{K}) \right] \tilde{\mathbf{u}}_i \right]$, named the augmented matrix. Since \mathbf{B} has maximum rank, denoted N_b , the rank of the augmented matrix instead could be either N_b or $N_b + 1$, depending on the modification matrices $\Delta\mathbf{M}$ and $\Delta\mathbf{K}$. Hence, the computation of the modification of the allowable subspaces consists in finding the matrices $\Delta\mathbf{M}$ and $\Delta\mathbf{K}$ such that:

$$\text{rank} \left(\left[\mathbf{B} \left[(\mathbf{M} + \Delta\mathbf{M})\tilde{\lambda}_i^2 + (\mathbf{K} + \Delta\mathbf{K}) \right] \tilde{\mathbf{u}}_i \right] \right) = N_b \tag{8}$$

Since the presence of the constraints on the feasible modifications do not allow for any arbitrary modification, the existence of a solution of problem in Eq. (8) is not guaranteed. Therefore, it is convenient to use an approximated optimization-based formulation, which casts the hybrid control problem as finding the modification matrices as those solving the following constrained problem:

$$\min_{\Delta\mathbf{M}, \Delta\mathbf{K} \in \Gamma} \left\{ \text{rank} \left(\left[\mathbf{B} \left[(\mathbf{M} + \Delta\mathbf{M})\tilde{\lambda}_i^2 + (\mathbf{K} + \Delta\mathbf{K}) \right] \tilde{\mathbf{u}}_i \right] \right) \right\}. \tag{9}$$

If the matrix is rectangular, in [4] it is proposed to exploit the semidefinite embedding lemma to recast the problem as minimization of the rank of a positive semidefinite square matrix. In such a way, the problem can be formulated in an approximated way by taking advantage of the so called trace heuristics [4], which consists in replacing the rank with the trace. The justification is intuitive, although a more rigorous interpretation is given in [5]. Indeed, the rank is the number of non-zero eigenvalues, while the trace is the sum of the eigenvalues. Since the matrix considered in the problem is positive semidefinite, then all its eigenvalues are greater or equal to 0, and therefore it is reasonable to assume that a small trace “forces” the rank to be low.

Once the modifications matrices have been computed through the solution of the problem in Eq. (9), the feedback gains should be finally calculated through any of the methods available in the literature. If the achievable eigenvector does not match exactly the desired one, the gains should be computed as those allowing for the orthogonal projection of the desired eigenvector in the modified allowable subspace, which is the best allowable approximation.

5 Test Case

In order to validate the proposed method, it is applied in the optimization of a cantilever beam. The system has 6 degrees-of-freedom, since it is modelled by three Euler-Bernoulli beam elements of equal length (see Fig. 1). The cross section is supposed to be circular and the physical quantities that characterize the dynamical properties of the beam are listed in Table 1. The system parameters that are supposed to be modifiable are the linear mass density of each beam element, denoted as ρA_i , and the product of the Young’s modulus and the moment of inertia, denoted as EJ_i . Moreover, it is supposed that three concentrated masses m_i can be placed at the free end of the beam and also at the distance of 0.3 and 0.6 m from the free end. The values of the system parameters in the original design are stated in Table 2, together with the bounds on the feasible modifications.

It is wanted that the system features a mode at the frequency of 500 Hz with a node at 0.3 m from the clamped end of the beam. In particular, the desired eigenstructure is shown in Table 3, as well as the closest eigenpair of the original system. Concerning the actuation characteristics of the considered system, it is supposed that two independent control forces are exerted, as shown in Fig. 1.

The desired eigenstructure has been assigned by four different techniques: by DSM, as for example in [2], by active control, as in [3], using active control on the system modified by DSM and finally with the proposed hybrid method. The computed structural modifications and/or feedback gains are omitted for brevity. The obtained eigenstructure in the four cases can be assessed evaluating the absolute error of the obtained frequency, with respect to the desired one, and the cosine of the angle between the desired eigenvector and the obtained one. Such quantities are shown in Table 4, together with the norms of the modification matrices $\Delta\mathbf{M}$ and $\Delta\mathbf{K}$, and of the controller gain \mathbf{G} . The results of Table 4 prove

Fig. 1 Cantilevered beam model

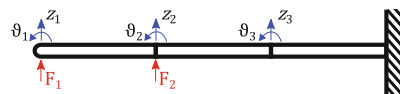


Table 1 Physical properties

	Symbol	Value
Mass density	ρ	7860 kg/m ³
Young’s modulus	E	200 GPa
Cross section radius	r	0.02 m
Beam length	L	0.90 m

Table 2 System modifications

	Original value	Constraints
ρA_i (kg/m)	9.8772	[0, +29.632]
m_i (kg)	0	[0, +10]
EJ_i (kNm ²)	25.133	[0, +25.133]

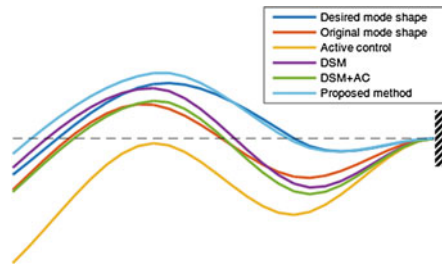
Table 3 Desired eigenstructure

	Original	Desired
ω (Hz)	619.13	500
u_1	-0.6740	-0.10
u_2	5.9530	1.00
u_3	0.4422	0.15
u_4	-0.9501	0.20
u_5	-0.5015	0.00
u_6	-1.2447	-0.80

Table 4 Eigenstructure comparison

	DSM [2]	Active control [3]	DSM+AC	Proposed method
$ \omega_{des} - \omega_{obt} $ (Hz)	29.29	0.0000	0.0000	0.0000
$\cos(\mathbf{u}_{des}, \mathbf{u}_{obt})$	0.9577	0.7349	0.9499	0.9890
$\ \Delta\mathbf{M}\ $	1.4659	-	1.4659	30.7459
$\ \Delta\mathbf{K}\ $	2.2843×10^7	-	2.2843×10^7	2.2843×10^7
$\ \mathbf{G}\ $	-	2.6807×10^7	1.0527×10^7	1.5329×10^7

Fig. 2 Mode shape comparison



that neither DSM or active control are capable of assigning the desired eigenstructure. The employment of both the approaches together can be an effective way to achieve the desired specifications. Of the two tested hybrid approaches, the proposed method is the one that gives the best results in terms of attainment of the desired eigenvector. A comparison of the mode shapes in the four cases of interest is provided by Fig. 2, as a further proof that the proposed hybrid approach is the only one that allows to obtain the node in the desired location.

6 Conclusions

This paper proposes a novel method for the optimization of the dynamic behaviour of vibrating systems through the concurrent synthesis of passive modifications and active state feedback control gains. The presence of passive modifications of the

inertial and elastic parameters modifies the set of eigenvectors that can be achieved through state feedback control, by overcoming the limitation of either the sole active EA or the DSM. The problem is formulated as a constrained rank minimization problem, by taking advantages of some mathematical theorems recently proposed in the literature, that allow for a simple problem formulation and solution. The method is validated through a numerical test case, that has proved its effectiveness in boosting the achievement of the desired performances. Indeed, the obtained eigenpair is very close to the desired one both in terms of frequency and mode shape, despite the fact that the system is underactuated.

Acknowledgments The first Author acknowledges the financial support of the FSU foundation (“Fondazione Studi Universitari” — Vicenza) through a Ph.D. scholarship.

References

1. Andry AN Jr et al (1983) Eigenstructure assignment for linear systems. *IEEE Trans Aerosp Electron Syst* 19(5):711–729
2. Caracciolo R et al (2015) Designing vibratory linear feeders through an inverse dynamic structural modification approach. *Int J Adv Manuf Technol* 80(9–12):1587–1599
3. Datta BN et al (2000) Partial eigenstructure assignment for the quadratic pencil. *J Sound Vib* 230:101–110
4. Fazel M et al (2003) Log-det heuristic for matrix rank minimization with applications to Hankel and Euclidean distance matrices. In: *Proceedings of the American control conference, 2003*, vol 3, pp 2156–2162
5. Fazel M et al (2001) A rank minimization heuristic with application to minimum order system approximation. In: *Proceedings of the American control conference, 2001*, vol 6, pp 4734–4739
6. Hehenberger P et al (2010) Hierarchical design models in the mechatronic product development process of synchronous machines. *Mechatronics* 20:864–875
7. Moore BC (1976) On the flexibility offered by state feedback in multi-variable systems beyond closed-loop eigenvalue assignment. *IEEE Trans Autom Control* AC-21(5):689–692
8. Ouyang H (2011) A hybrid control approach for pole assignment to second-order asymmetric systems. *Mech Syst Signal Process* 25:123–132
9. Ouyang H et al (2013) Pole assignment for control of flexible link mechanisms. *J Sound Vib* 332(12):2884–2899
10. Richiedei D, Trevisani A (2013) Vibration confinement in lightly damped multibody systems: an hybrid active-passive approach. In: *Proceedings of the ECCOMAS thematic conference on multibody dynamics, Zagreb*
11. van Amerongen J (2003) Mechatronic design. *Mechatronics* 13:1045–1066

A Vibration Isolator Based on Magneto-Rheological Elastomer

Renato Brancati, Giandomenico Di Massa and Stefano Pagano

Abstract The paper presents an investigation about a magneto-rheological elastomeric (MRE) pad to be adopted as seismic semi-active isolator for lightweight structures. MRE pad may change its stiffness if immersed in a magnetic field. This characteristic allows to real time shift the fundamental frequency of the isolated structure. In this way it is possible to drive away the structure fundamental frequency from the exciting frequencies and therefore to reduce accelerations induced by the ground motion. The isolator includes a ball transfer unit (BTU) to sustain the vertical load so that MRE pad must only exert horizontal restoring forces and it may have a slender geometry without concern regarding buckling.

Keywords Vibration isolator • Magneto-rheological elastomer • Nonlinear dynamics • Semi-active control

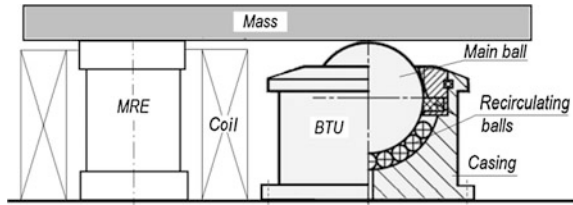
1 Introduction

Seismic isolators are adopted to protect structures from damage caused by earthquake attack. Their effect is to decouple the structure from the ground and to reduce the fundamental frequency of the isolated structure to a value outside the range of frequencies containing the main earthquake energies. As a result, they experience higher displacements but lower accelerations and hence lower forces.

Isolators must be able to support the structure weight and to exert a restoring force to re-centre the isolated structure.

Recently, many research activities are focused on MRE isolators whose mechanical properties change if immersed in a magnetic field [1, 2]. In case of lightweight structures, like cabinets or racks containing equipment sensitive to accelerations, low fundamental frequencies may be achieved adopting slender isolators; to overcome the isolator buckling, rolling devices can be adopted to

R. Brancati (✉) · G. Di Massa · S. Pagano
Università di Napoli Federico II, Napoli, Italy
e-mail: renato.brancati@unina.it

Fig. 1 Scheme of the isolator

sustain the vertical load so that the elastomeric elements can be freely chosen to meet the desired horizontal fundamental frequency [3, 4].

Ball transfer units (BTU) are omni-directional rolling support constituted by a main ball, sustained by small recirculating balls. Figure 1 shows the scheme of the proposed isolator constituted by a MRE pad and a BTU support. The BTU is mounted in ball-up configuration, i.e. with the main ball facing up, so that debris cannot settle on the rolling surface and cannot affect the regular main ball rolling.

The system combines the positive aspects of passive elastomeric isolators that are considered more reliable as they do not require power supply, which may not be available during a seismic event, with the advantages of controlled devices. In fact, this isolator operates as:

- passive system, in absence of external power. In this case, it is an open-loop device since its action does not depend on the system dynamics;
- semi-active system if it is immersed in a magnetic field, generated by suitable coils, whose intensity may be real time adjusted. In this way, detecting the system state motion, the pad stiffness may be adjusted with the aim of reducing its acceleration.

In this paper, the design and the construction of the MRE pad are investigated.

2 Elastomeric Pad

Some important considerations about elastomeric isolators can be carried out adopting the *simple two-spring model* [5, 6]. The isolator is represented (Fig. 2a) by means of two intermediate massless rigid bodies (I_1 , I_2), connected by a linear guide; their relative translational motion (s) is counteract by a linear spring (k_s). Two massless end-plates (P_1 , P_2) linked to the intermediate bodies by means of hinges; the corresponding relative rotations (q) are counteract by two rotational springs ($k_b/2$). Lumped parameters, k_s and $k_b/2$, represent shear and bending isolator stiffness, respectively. The model shows that bending and shear stiffness act in series and therefore the overall lateral stiffness is:

$$k = \frac{1}{\frac{1}{2k_b} + \frac{1}{k_s}} = \frac{1}{\frac{\beta}{12EI} + \frac{1}{GA}} \quad (1)$$

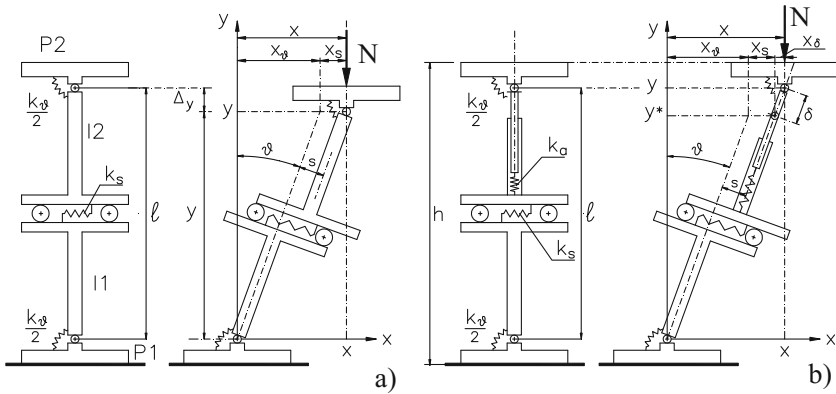


Fig. 2 Simple two-spring model. **a** without BTU; **b** with BTU

For cylindrical isolator with height-diameter ratio close to one, both terms (shear and bending) must be considered; if, instead, the diameter is at least 3 times greater than the height, the bending term may be neglected.

Lateral stiffness decreases with vertical load N ; it is so possible to define the value at which the buckling occurs.

If the elastomeric pad acts in combination with a BTU, the upper plate cannot vary its quota, as it is constantly equal to the BTU height (h). Therefore, a lateral displacement of the upper plate induces an elongation δ of the elastomeric pad (Fig. 2b); the pad axial force has a horizontal restoring component and therefore, indicating with k_a the axial stiffness, the overall lateral stiffness results:

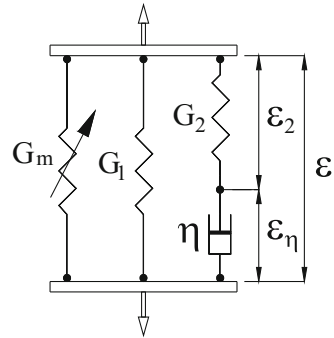
$$k = \frac{1}{\frac{1}{2k_g} + \frac{1}{k_s} + \frac{1}{k_a}} = \frac{1}{\frac{\beta}{12EI} + \frac{l}{GA} + \frac{l}{EA} \text{sen}\theta} \tag{2}$$

In the proposed device, the pad is pre-loaded by the structure weight, as its free load length is higher than the BTU one. The k_a spring gives a negative force (i.e. it shifts away the structure from the centred position) until it is compressed.

3 Magneto-Rheological Effect

The MRE is compound with suspended magnetizable particles (size 3–10 μm) in a non-magnetic matrix. Its mechanical and rheological properties can be reversibly changed by means of a suitable magnetic field [7]. The physical material property, that undergoes a significant variation depending on the magnetic field, is the shear elastic modulus, G ; it is so possible to realize pads with a controllable stiffness. The *magneto-rheological effect* concerns the shear modulus change with respect to the value it assumes in absence of magnetic field. This effect is maximized for particle concentrations in a volume ranging from 20 to 30 %.

Fig. 3 MRE rheological model



These materials are excellent candidates to be used in isolation-controlled devices as they give large modulus changes, fast response time, stability, compatibility with mechanical components and reasonably low power requirements.

The magnetic field can be generated by means of permanent magnets or coils. The MRE pad becomes a part of the magnetic circuit. In absence of magnetic field, pad shear modulus is evaluated with the following formula [8]:

$$G = G_0(1 + 1.25\varphi + 14.1\varphi^2) \tag{3}$$

being G_0 the matrix module and φ the volume percentage of magnetic particles.

MRE dynamic behavior can be described by means of the Chen model [9] schematically represented in Fig. 3. It is constituted by the standard linear model, characterized by springs having shear modulus G_1 , G_2 and damping η , arranged as in the standard linear solid (SLS) model [10], in parallel with a spring, G_m , whose value depends on the magnetic field, H . This modulus may be determined by means of the following expression [11]:

$$G_m(H) = \frac{6\varphi^2\mu_0(\mu_p - 1)^2 M_S^2 H^2 (4 - \varepsilon^2)}{8\pi\mu_1 [M_S + (\mu_p - 1)H]^2 (1 + \varepsilon^2)^{7/2}} \tag{4}$$

being: μ_0 = vacuum permeability; μ_1 = relative permeability of the medium; μ_p = relative permeability of particles; M_S = saturated magnetization; ε = pad deformation.

4 MRE Pad Definition

A set of MRE pads have been realized mixing silicon rubber with iron particles into a homogenous mixture. The particles are iron-carbonyl (supplied by Metalpolveri; type FECARB) with diameter range from 4 to 6 μm and density 3.9 g/cm^3 while for the silicon rubber it was used the three components *Axson UPX8400* that

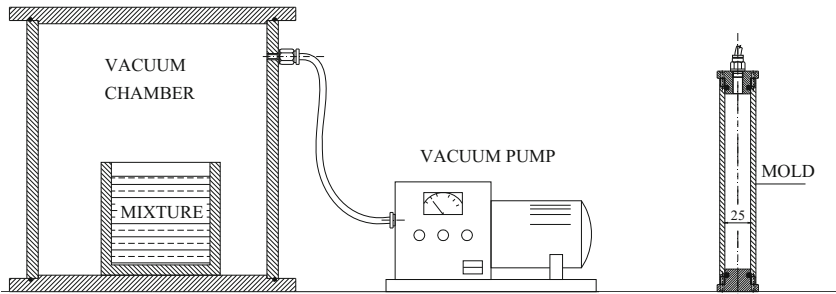


Fig. 4 Mixture in vacuum chamber and mold

permits to obtain several values of the rubber modulus. In this case study, the following components have been adopted: 20 % polyol, 20 % isocyanate, 60 % extender and particles 20 %. MRE mixture may be anisotropic if during the curing phase it is immersed in a magnetic field; otherwise, it will be isotropic.

In particular, the equipment adopted to form the MRE pads comprises a vacuum pump, a vacuum chamber and a mold. In fact, it is necessary to remove air bubbles from the mixture and therefore, the pads are formed in a mold, obtaining a uniform material, with a higher permeability.

A steel pipe, closed at the ends with two plates, constitutes the *vacuum chamber* (Fig. 4); in the contact zone between pipe and plates, there is an O-ring to ensure the air-tightness. On the chamber lateral surface, there is a quick compression coupling for connecting the chamber volume with the vacuum pump. When the pump starts to suck the air, the plates are squeezed on the tube and therefore no device to connect plates and pipe are required.

In the vacuum chamber, it is arranged the mixture to form the MRE pad. From the constructive point of view, the mold is similar to the vacuum chamber; in fact, it is constituted by a pipe closed at the ends by two plugs. Even in this case, between each plug and the tube, there is an O-ring.

One of the two plugs is open to pour into the liquid mixture. To prevent the bonding between the elastomeric pad and internal mold surface and to easily extract the formed pad from the mold, a release agent is used.

The liquid mixture is so poured into the mold and cured at constant temperature (70 °C) for about 3 h. The mold allows forming a single long element that is then sliced to obtain several pads of suitable height.

5 Coils Characteristics and Magnetic Circuits

To modify the stiffness of MR pad in controllable way it is necessary to provide a proper magnetic field; for this purpose an electromagnetic coil is used. It is well known that varying the applied current, the magnetic induction through the field-sensitive material changes. A proper design of the magnetic circuit allows to

maximize the MR effect. In fact, if the magnetic field flux is perpendicular to the motion of MRE, the MR effect can be fully utilized. The proposed isolator uses the configuration, with the MRE placed inside the magnetic coil, as core of the magnetic circuit.

The greatest advantage of this design is that it provides a large active area, a strong and uniform magnetic field. Therefore, the MRE inside the coil can be fully energized by a uniform magnetic field. However, due to the low permeability of the MRE material it is necessary to place one steel element under the MRE to increase the magnetic conductivity of the magnetic core.

A FEM model, in *Ansys Maxwell*[®] environment was developed. A first configuration consist of a cylindrical MRE element having a diameter of 24 mm and a height of 20 mm, over a steel cylindrical element with a diameter of 60 mm and a height of 37 mm. These two elements are inserted inside a coil having the following characteristics: inner diameter, 60 mm; outer diameter, 108 mm and height 54 mm (Fig. 5a). The saturation value of magnetic field in MRE is about 800 mT and, for this configuration, to obtain it are necessary 10,000 A-turns.

To optimize the magnetic flux, the cylindrical steel element has been replaced with a conical one having the following dimensions: bottom diameter, 60 mm; top diameter, 24 mm; height, 37 mm (Fig. 5b). To obtain the saturation value of magnetic field it are necessary only 6000 A-turns.

The materials of the isolator components adopted for the simulations are: steel Aisi-1008 for the plates and the core; copper for the coil; rubber and iron powder for the MRE pad. Figure 6 shows the magnetization curve for steel and MRE components; it also shows the FEM model adopted for the simulations.

Figure 7 shows the value of magnetic field inside the MRE pad. Adopting the second configuration, for a maximum current of 4A, the coil requires 1500 turns, made with a 1.02 mm diameter cable (AWG17), having an overall length equal to 310 m (resistance equal to 6.9 Ω , with a maximum dissipated power of 109 W).

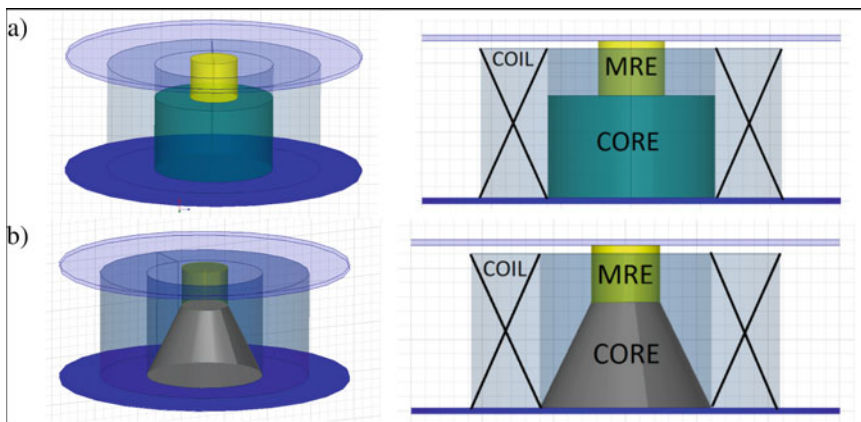


Fig. 5 FEM device model: **a** cylindrical core; **b** conical core

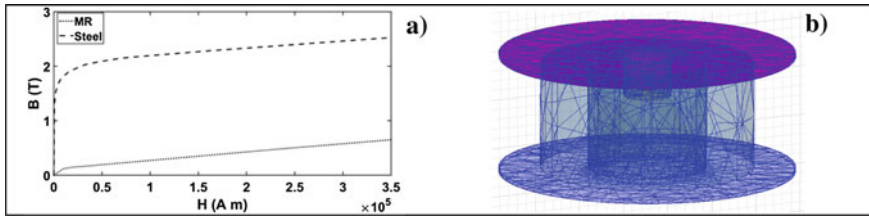


Fig. 6 a Magnetization curves for steel and MRE pad; b FEM model for the device with conical core

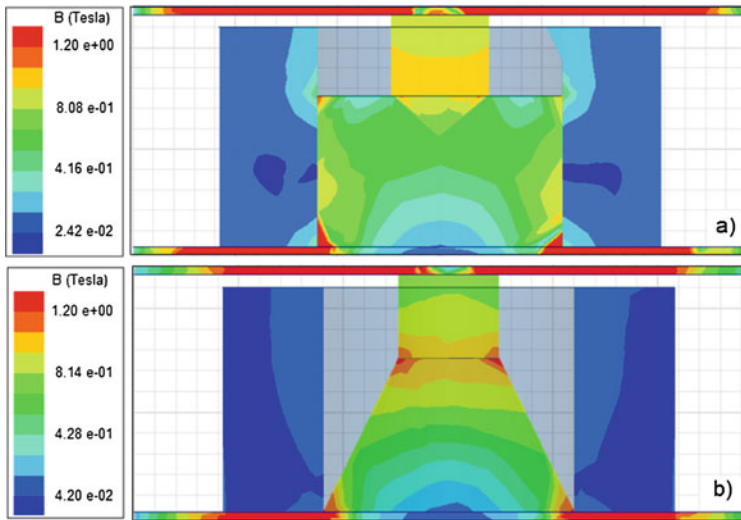


Fig. 7 Magnetic field: a cylindrical core, b conical core

6 Conclusions

The paper describes the design of an isolator based on a MRE pad in combination with a rolling device (BTU) to decouple the horizontal restoring force from the vertical reaction. Slender MRE pads may be adopted to achieve low horizontal fundamental frequencies that can be adjusted in suitable way to minimize the suspended structure acceleration. By means of a FEM code, it was found that a conical core allows reducing the number of turns of the coil. By assigning the saturation value of magnetic field, it was possible to define the number of turns and the wire diameter to be used for the coil. Furthermore, the equipment adopted to realize the MRE pad and the mixture components of the MRE itself, are described.

References

1. Yang CY, Fu J, Yu M, Zheng X, Ju BX (2015) A new magneto rheological elastomer isolator in shear–compression mixed mode. *J Intell Mater Syst Struct* 26(10):1290–1300. doi:[10.1177/1045389X14541492](https://doi.org/10.1177/1045389X14541492)
2. Jolly MR, Carlson JD, Munoz BC (1996) A model of the behaviour of magnetorheological materials. *Smart Mater Struct* 5:607–614
3. Behrooz M, Wang X, Gordaninejad F (2014) Modeling of a new semi-active/passive magneto rheological elastomer isolator. *Smart Mater Struct* 23:045013 (7 pp)
4. Brancati R, Di Massa G, Pagano S, Rocca E, Strano S (2013) Experimental investigation of the performances of a WRS-BTU seismic isolator. In: *World Congress on Engineering (WCE)*, London, U.K., 3–5 July 2013. ISBN: 978-988-19251-0-7
5. Forcellini D, Kelly J (2014) Analysis of the large deformation stability of elastomeric bearings. *J Eng Mech* 04014036. doi:[10.1061/\(ASCE\)EM.1943-7889.0000729](https://doi.org/10.1061/(ASCE)EM.1943-7889.0000729)
6. Chen L, Jerrams S (2011) Rheological model of the dynamic behaviour of magnetorheological elastomers. *J Appl Phys* 110:013513. doi:[10.1063/1.3603052](https://doi.org/10.1063/1.3603052)
7. Guth EJ (1945) Theory of filler reinforcement. *J Appl Phys* 16(1):20–25. doi:[10.1063/1.1707495](https://doi.org/10.1063/1.1707495)
8. Kallio M (2005) The elastic and damping properties of magnetorheological elastomers. Thesis for the degree of Doctor of Technology, VTT Technical Research Centre of Finland. ISBN: 9513864472
9. Brancati R, Di Massa G, Pagano S, Strano S (2015) A seismic isolation system for lightweight structures based on MRE devices. In: *Proceedings of the world congress on engineering 2015 (WCE 2015)*, London, U.K., 1–3 July 2015. ISBN: 978-988-14047-0-1, ISSN: 2078-0966
10. de Haan YM, Sluimer GM (2001) Standard linear solid model for dynamic and time dependent behavior of building materials. *HERON* 6(1). ISSN: 0046-7316
11. Koh CG, Kelly JM (1987) Effects of axial load on elastomeric isolation bearings. Rep. No. UCB/EERC-86/12. Earthquake Engineering Research Center, University of California, Berkeley

A Physical Analytical Model to Study the Elasto-Kinematic Behaviour of a MacPherson Suspension

Francesco Timpone

Abstract This paper describes a physical analytical model able to characterize the elasto-kinematic behaviour of a MacPherson suspension for automotive applications. The presented model allows to determine the position and the orientation of the wheel upright as a function of the generalized three-dimensional loads applied to the center of the tire-road contact patch, and consequently to determine the variation of the characteristic suspension parameters of main interest: wheel base, track, camber and toe. All the steps carried out to build the model are described, starting from the kinematic analysis, ongoing with the static and finally with the elasto-kinematic ones, describing how compliance has been taken into account in equilibrium conditions. The kinematic and static analyses have been validated by comparing the results with the ones of a multibody model. In order to obtain the desired elasto-kinematic curves it is possible to act both on the geometry of the suspension, and on the stiffness of the bushings and of the arms, which cause compliance, modifying the positions of the various elements of the suspension and ultimately of the hub. By means of the proposed model it is possible to rapidly evaluate the effects of these variations. Numerical examples relative to a suspension for the front axle of a vehicle are presented.

Keywords Vehicle suspension • Macpherson • Elasto-kinematic behaviour • Compliance • Suspension analysis

1 Introduction

Almost all road vehicles are equipped with flexible suspensions with the double aim to isolate the sprung mass from the vibrations caused by road irregularities and to manage tire position and orientation. So suspensions should provide at the same

F. Timpone (✉)
University of Naples, Naples, Italy
e-mail: francesco.timpone@unina.it

time the tire optimal position respect to the ground for grip purposes and the vehicle's comfort and stability in all driving conditions such as the cornering or braking. As known, the improvement of one of these two aspects penalizes the other: a rigid suspension setting is optimal for the handling, but not for the comfort, vice versa a soft calibration. Hence, in the case of standard cars, it is necessary to reach a stiffness value of the system elements representing a good compromise between the two conflicting requirements. It is easy to understand that, however, in the case of sports cars, there is a tendency to prefer stiffer springs in order to enhance the stability requirements even under the harshest driving conditions. Since the suspension allows the wheel to perform extensive vertical movements and small kinematic and elastic movements around well-defined axis, the placement parameters of the wheel relative to the ground vary with driving conditions. In order to choose the right suspension for each type of vehicle it is extremely important to know the laws of variation of the above parameters to vary the shaking and the stresses coming from the tire-road interaction, this also with reference to tire thermal effects [1].

The present work proposes a model for the analysis of the elasto-kinematic behaviour of a MacPherson suspension in order to facilitate the designer in the creation of the most suitable suspension system [2] or, alternatively, to constitute a valid diagnostic tool for already existing suspensions. The bushings, being easy to replace, can be used to improve or modify the behaviour of a suspension with a given geometry: this algorithm is able to aid the designer in the choice of their stiffness. Alternatively, when the elasto-kinematic behaviour is acquired through experimental tests, the algorithm can be used to estimate the stiffness of the suspension bushings.

In the literature, several authors have studied the kinematics and elasto-kinematics suspension, dealing mainly with multilink schemes.

J. Knapczyk and M. Maniowski in [3] describe an algorithm for the analysis of elasto-kinematics of a multilink suspension.

J. Knapczyk and S. Dzierżek in [4] present an algebraic vector method to analyze the kinematics of a multi-link suspension and illustrate an iterative process that allows you to incorporate the compliance of the bushings in the analysis of the displacements suffered by the hub.

E. Rocca and R. Russo in [5] use the method proposed in [4] to develop a procedure for the identification of the stiffness of the bushings based on a nonlinear least-squares solution to the problem.

Figliolini and P.G. Rea in [6] use the distances of the method presented to develop a procedure of calculation in Matlab for a multilink suspension.

This kind of approaches have also been used in other fields such as robotics and the study of the ancient throwing machines [7–11]

In this paper it is firstly developed a kinematic study with the aim to define the geometry of the various organs of the suspension. Successively a static study is conducted to find out the distribution of loads and stresses acting on the different

suspension parts (arms, bushings, etc.). Finally the elasto-kinematic study is carried on, evaluating the elasticity of the various supporting bodies (arms and bushings) of the suspension.

2 The MacPherson Suspension

The Macpherson, under the kinematic point of view, is an independent wheel suspension, since it connects the hub to the sprung mass allowing one d.o.f.

The scheme considered for this study is reported in Fig. 1 together with the main reference system, the coordinates of the characteristic points are reported in Table 1. The coordinates refer to a front right wheel (these coordinates can be obtained by means of laser scanner techniques [12]).

The tire considered for this study is a 205/60R15.

Vehicle suspensions can be characterized from the kinematic, static and elasto-kinematic point of view. In the following paragraph the first of these approaches will be described for the suspension under examination.

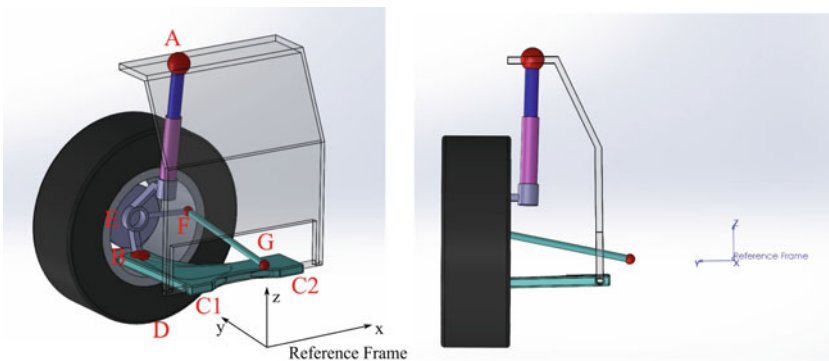


Fig. 1 MacPherson suspension scheme

Table 1 Suspension characteristic points coordinates

Point suspension	x	y	z
Upper strut joint (A)	31.8	593	604
Lower outer joint (B)	-9.1	725	-60
Lower front joint (C1)	-10	400	-55
Lower rear joint (C2)	311	400	-50.4
Contact point (D)	-1.6	773.5	-226.8
Wheel center (E)	-1.6	768.4	65.1
Tie rod outer joint (F)	136.9	682.7	88.5
Tie rod inner joint (G)	170	310	9
Origin of main reference frame	0	0	0

2.1 Kinematic Analysis

The kinematic study aims to determine, under the hypothesis of rigid bodies, the variation of the main quantities [13] (toe, camber, wheel base, track) characterizing wheel position and orientation respect to the road as a function of the wheel center travel.

To determine these quantities a physical analytical model of the MacPherson suspension has been built.

To conduct the kinematic study two main hypothesis have been adopted: the arms of the suspension have been supposed perfectly rigid and the joints backlashes have been considered null. The point of interest for this study are B, E, F.

Since in C1 there is a revolute joint and in C2 a spherical joint, point B describes a circular trajectory having a radius equal to:

$$R_{BC3} = R_S = \sqrt{BC_1^2 - C_1C_3^2} = \sqrt{BC_2^2 - C_2C_3^2} = \sqrt{BC_2^2 - (C_1C_2 - C_1C_3)^2} \quad (1)$$

(where C3 is the intersection of the perpendicular from point B to the segment C1–C2) whose equations are:

in the general case ($Y_{C1} \neq Y_{C2}$)

$$\begin{aligned} A_S &= \frac{Z_{C2} - Z_{C1}}{X_{C2} - X_{C1}} & B_S &= \frac{Y_{C2} - Y_{C1}}{X_{C2} - X_{C1}} \\ X_B(u) &= X_{C_S} + R_S \cdot \left[\frac{-A_S \cdot \sin(u) - B_S \cdot S \sqrt{\cos(u)^2 \cdot (1 + B_S^2) - \sin(u)^2 \cdot A_S^2}}{1 + B_S^2} \right] \\ Y_B(u) &= Y_{C_S} + R_S \cdot \left[\frac{-A_S \cdot B_S \cdot \sin(u) - \sqrt{\cos(u)^2 \cdot (1 + B_S^2) - \sin(u)^2 \cdot A_S^2}}{1 + B_S^2} \right] \\ Z_B(u) &= Z_{C_S} + R_S \cdot \sin(u) \end{aligned} \quad (2)$$

In the particular case under examination ($Y_{C1} = Y_{C2}$)

$$\begin{aligned} X_B(u) &= X_{C_S} + R_S \cdot \left[-\sin(u) \cdot \frac{Z_{C2} - Z_{C1}}{\cos(u)(X_{C2} - X_{C1})} \right] \cdot \cos(u) \\ Y_B(u) &= \left[Y_{C_S} + R_S \cdot \sqrt{1 - \left[(-\sin(u)) \cdot \frac{Z_{C2} - Z_{C1}}{\cos(u)(X_{C2} - X_{C1})} \right]^2} \cdot \cos(u) \right] \\ Z_B(u) &= Z_{C_S} + R_S \cdot \sin(u) \end{aligned} \quad (3)$$

Having indicated with $\vartheta = u$ the angle in Fig. 2.

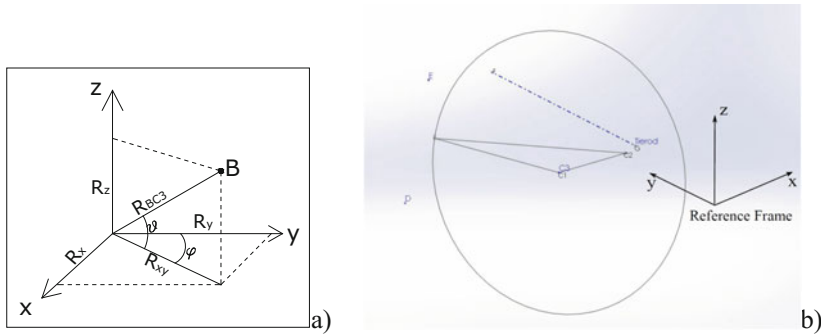


Fig. 2 Reference frame for equations ($\vartheta = u$ angle definition) (a) Circular trajectory of point B (b)

Clearly in this study the angle u varies in a small range because the vertical coordinate of the wheel center has a variation of ± 8 cm starting from its initial position.

The variable u in the equations practically is the angle between the lower triangle of the suspension and the reference plane xy and it will be the independent variable of the whole system, so also E and F coordinates will be expressed as functions of this variable.

As concerns the points E and F , the first one describes a circular trajectory as well, while the second moves on a sphere having radius FG .

To determine these trajectories it is necessary to introduce three more reference systems (Fig. 3).

The first reference system, integral with the hub (Reference Strut), has the origin in B , x axis oriented as the vector $(F-B)$, y axis perpendicular to the plane

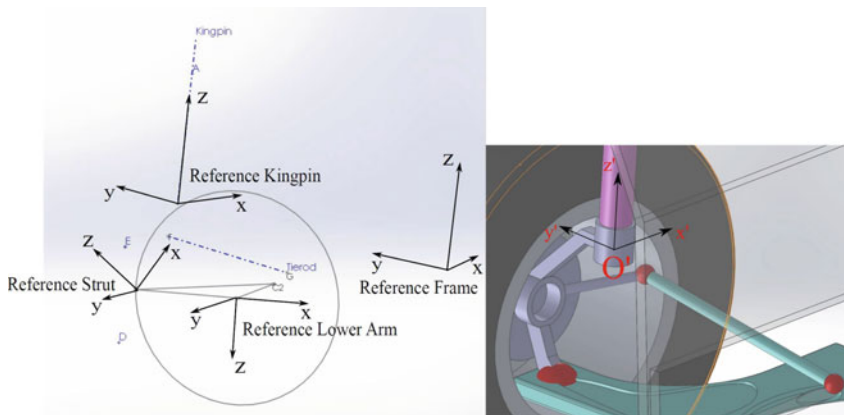


Fig. 3 Auxiliary reference frames

containing B, E and F points, z axis directed to form a left-handed orthogonal reference frame.

Clearly E, F and B points have constant positions relative to this reference frame, while the rotation matrix to pass to the main reference frame changes during wheel travel.

The second reference frame, integral with the shock absorber (Reference Kingpin), has the origin in the lower extreme of this component O', x axis directed as the vector (P5-O'), y axis as (P4-O'), z axis to form a left-handed orthogonal reference frame. The points P4 and P5 have been chosen in the space integral with the shock absorber reference frame which is also integral to the hub, only the shock absorber inclination referred to the main frame varies.

The third reference frame, integral with the lower arm (Reference Lower Arm), has the origin in C3, x axis directed as (C3-B), y axis along (C1-C2), z axis to form a left-handed orthogonal reference frame.

To determine the trajectories of points E and F as functions of the angle u the following conditions have been used:

- The distances BE, BF, EF are constant when angle u varies;
- The distance FG is constant because of the hypothesis of infinitely rigid arms;
- The direction of the shock absorber is constant if referred to the hub.

$$\left\{ \begin{array}{l} \frac{(X_{AWC} - X_{O'WC})}{\text{mod}AO'} - \cos t1 = 0 \\ \frac{(Y_{AWC} - Y_{O'WC})}{\text{mod}AO'} - \cos t2 = 0 \\ \frac{(Z_{AWC} - Z_{O'WC})}{\text{mod}AO'} - \cos t3 = 0 \\ \sqrt{(X_B - X_E)^2 + (Y_B - Y_E)^2 + (Z_B - Z_E)^2} - BE = 0 \\ \sqrt{(X_B - X_F)^2 + (Y_B - Y_F)^2 + (Z_B - Z_F)^2} - BF = 0 \\ \sqrt{(X_E - X_F)^2 + (Y_E - Y_F)^2 + (Z_E - Z_F)^2} - EF = 0 \\ \sqrt{(X_F - X_G)^2 + (Y_F - Y_G)^2 + (Z_F - Z_G)^2} - FG = 0 \end{array} \right. \quad (4)$$

where X_{AWC} , Y_{AWC} and Z_{AWC} are the coordinates of point A in the reference frame integral to the hub (Reference Strut).

The Eq. (4) are solved in their implicit form with an iterative nonlinear numeric algorithm (trust-region-dogleg), so the position of all the points of the suspension is expressed as a function of the angle u only.

2.2 Static Analysis

The objective of the static analysis is to find out the suspension configuration and the forces acting in the suspension elements when a three-dimensional generalized force and/or torque are applied to the tire contact patch center.

In this analysis the suspension components are still supposed rigid and there are no backlashes in the joints.

To this aim different equilibrium equations are used, considering that in the lower control arm there are two reactions in the plane containing the three joints and they are directed along the lines joining the joint on the hub with the two joints on the chassis; the same consideration is valid for the steering link.

The shock absorber and the hub have to be considered together because in O' they are constrained, the only d.o.f. allowed is the rotation of the shock absorber along its axis.

The translational and rotational (around D) equilibrium equations of the hub are:

$$\begin{aligned} \vec{R}_{FG} + \vec{R}_{BC1} + \vec{R}_{BC2} + \vec{F}_G + \vec{F}_{EXT} &= \vec{0} \\ \vec{R}_{FG} \wedge (\vec{F} - \vec{D}) + \vec{R}_{BC1} \wedge (\vec{B} - \vec{D}) + \vec{R}_{BC2} \wedge (\vec{B} - \vec{D}) + \vec{F}_G \wedge (\vec{O}' - \vec{D}) + \vec{M}_G + \vec{M}_{EXT} &= \vec{0} \end{aligned} \tag{5}$$

where R_{ij} is the reaction force directed along the line joining the joints i and j ; F_G and M_G are the reaction force and the reaction torque in O'; F_{EXT} and M_{EXT} are the generalized three-dimensional external force and moment acting in D.

Since the shock absorber can rotate around its axis the component of M_G along this axis is null.

$$M_{gZSA} = h_\alpha \cdot M_{gXMR} + h_\beta \cdot M_{gYMR} + h_\gamma \cdot M_{gZMR} = 0 \tag{6}$$

where h_α , h_β , and h_γ are the direction cosines of the shock absorber (SA) axis in the main reference system (MR).

The last two equations are the rotational equilibriums around x and y axis of the shock absorber reference frame choosing as moments point A:

$$\begin{aligned} M_{gXSA} + F_{gYSA} \cdot Z_{AS} &= 0 \\ M_{gYSA} + F_{gXSA} \cdot Z_{AS} &= 0 \end{aligned} \tag{7}$$

The equilibrium of the system is reached when the spring force is equal to the component of the force exerted by the system along the shock absorber direction.

For each equilibrium condition it is possible to find out an angle u and so a configuration of the suspension.

2.3 Elasto-Kinematic Analysis

To conduct the elasto-kinematic analysis it is necessary to consider suspension compliance due to arms and bushings elasticity. Compliance causes a displacement variation in the loaded system respect to the static scheme.

To simplify the model all the compliance is supposed to be allocated in the bushings connecting the arms to the chassis, so in the two joints of the lower control arm and in the single upper strut mount joint of the shock absorber.

Starting from the static analysis it is possible to determine the joints displacements due to compliance, which cause a configuration variation and so modify equilibrium equations. The new equilibrium modifies the forces and so the displacements. The procedure is iterative and it stops when the difference between the actual and the previous configuration is smaller than a fixed little value (in the results showed in the following it has been supposed equal to 10^{-5} mm)

The equations to determine the displacements are the equilibrium conditions of the lower control arm along x and y directions and the rotational equilibrium respect to the point C2 (Fig. 4).

Since the arms are supposed to be rigid other three equations express the constancy of distances C1–C2, B–C1 and B–C2, as an example the equation for B–C1 is:

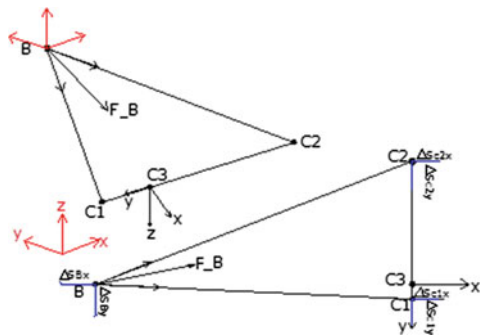
$$(X_B + \Delta s_{BX} - X_{C1} - \Delta s_{C1X})^2 + (Y_B + \Delta s_{BY} - Y_{C1} - \Delta s_{C1Y})^2 + (Z_B + \Delta s_{BZ} - Z_{C1} - \Delta s_{C1Z})^2 - BC_1^2 = 0 \tag{8}$$

So it is possible to determine the displacements in the lower control arm.

As concerns the shock absorber it is possible to write its translational equilibrium taking into account the compliance (and then the bushing stiffness) in A

$$\vec{F}_{gSA} + \begin{Bmatrix} K_{AXSA} \cdot \Delta s_{AXSA} \\ K_{AYSA} \cdot \Delta s_{AYSA} \\ K_{AZSA} \cdot \Delta s_{AZSA} \end{Bmatrix} = \vec{0} \tag{9}$$

Fig. 4 Compliance of joints in C1 and C2



3 Results

In this paragraph some of the results of the kinematic, static and elasto-kinematic analyses are reported. The reported diagrams are relative to camber and toe variations in the three analyses; analogous considerations can be made for the wheel-base and the track variations.

To conduct the kinematic study a variation (± 8 cm starting from its nominal position) of point E absolute z coordinate has been imposed.

To conduct static and elasto-kinematic analyses, for simplicity, a vertical force variable between -630 and 13000 N, has been applied to the tire-road contact point (D), clearly the developed model allows to apply a generalized three-dimensional force and/or a generalized three-dimensional moment (Eq. (5)).

As concerns spring stiffness it has been supposed constant and equal to 71845 N/m, while the principal components of the constant bushings stiffness parameters are reported in (10).

$$\begin{cases} K_A = [4.52 \cdot 10^7, 1.13 \cdot 10^6, 1.2 \cdot 10^7] \\ K_{C_1} = [1.71 \cdot 10^7, 2.25 \cdot 10^7, 1 \cdot 10^8] \\ K_{C_2} = [1.61 \cdot 10^7, 6.36 \cdot 10^6, 1 \cdot 10^8] \end{cases} \quad (10)$$

The results of kinematic and static analyses have been validated by comparison with the ones of a multibody model of the same suspension built with a commercial code (MSC Adams) (Fig. 5); while the elasto-kinematic results have been compared with the static ones to highlight the effects of compliance (Fig. 6).

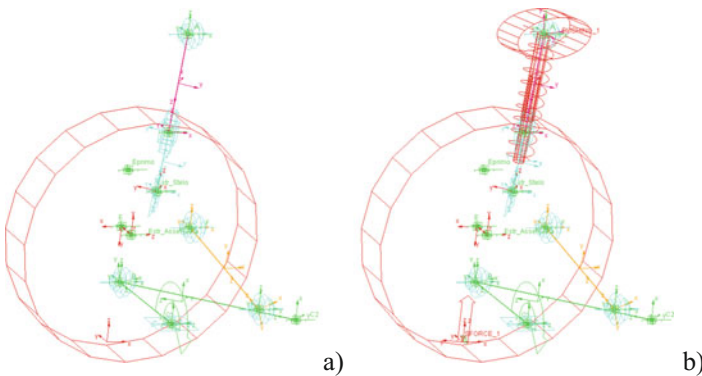


Fig. 5 Multibody models of MacPherson suspension for kinematic **a** and static **b** analyses

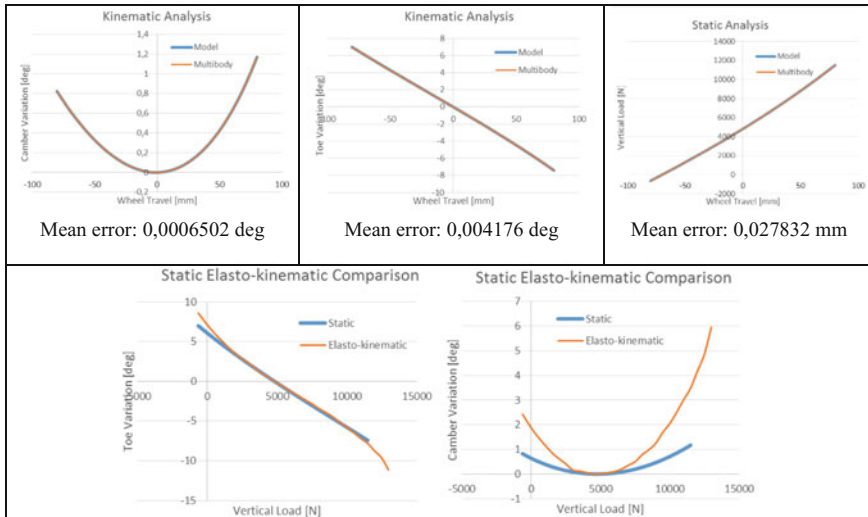


Fig. 6 Kinematic, static and elasto-kinematic results

4 Conclusions

In this paper a physical analytical model to characterize the kinematic, static and elasto-kinematic behaviour of a MacPherson suspension for automotive applications has been presented with the aim to facilitate the suspension designer in the creation of the most suitable suspension system or, alternatively, to constitute a valid diagnostic tool for already existing suspensions. The kinematic and static behaviour have been validated by comparison with the results of a multibody model built with a commercial code finding an almost perfect agreement, while the elasto-kinematic results have been compared with the kinematic ones, highlighting the possibility to evaluate the effects of compliance on characteristic suspension quantities.

References

1. Allouis C, Amoresano A, Giordano D, Russo M, Timpone F (2012) Measurement of the thermal diffusivity of a tire compound by mean of infrared optical technique. *Int Rev Mech Eng* 6(6):1104–1108
2. Rocca E, Timpone F (2016) Analysis of multilink suspension characteristics due to the rods length variations. In *Proceedings of the world congress on engineering 2016 Vol II WCE 2016, June 29–July 1, London, U.K.*, pp 107–1021
3. Knapczyk J, Maniowski M (2006) Elastokinematic modeling and study of five-rod suspension with subframe. *Mech Mach Theor* 41:1031–1047

4. Knapczyk J, Dzierżek S (1995) Displacement and force analysis of five-rod suspension with flexible joints. *Trans ASME, J Mech Des* 117:532–538
5. Rocca E, Russo R (2002) A feasibility study on elastokinematic parameter identification for a multilink suspension. *Proc IMechE vol 216 Part D: J. Automobile Eng* 153–160
6. Figliolini G, Rea P (2006) Synthesis and simulation of a multilink suspension mechanism. *Mech Manipulators* 5(2):55–60
7. Carbone G, Rossi C, Savino S (2015) Performance comparison between FEDERICA Hand and LARM Hand. *Int J Adv Robot Syst* 12
8. Niola V, Penta F, Rossi C, Savino S (2015) An underactuated mechanical hand: theoretical studies and prototyping. *Int J Mech Control* 16(1):11–19. ISSN: 15908844
9. Niola V, Rossi C, Savino S (2014) A new mechanical hand: theoretical studies and first prototyping. *Int Rev Mech Eng* 8(5):835–844. doi:<http://dx.doi.org/10.15866/ireme.v8i5.1755>
10. Rossi C, Pagano S (2011) A study on possible motors for siege towers. *J Mech Des Trans ASME* 133(7), art. Num. 71009
11. Rossi C, Savino S (2013) Mechanical model of a single tendon finger. In *Proceedings of 11th international conference of numerical analysis and applied mathematics 2013, ICNAAM 2013, Rhodes; Greece; 21 September 2013 through 27 September 2013*, vol 1558, pp 1286–1292
12. Niola V, Rossi C, Savino S (2010) A new real-time shape acquisition with a laser scanner: first test results. *Robot Comput-Integr Manuf* 26(6):543–550
13. Guiggiani M (2014) *The science of vehicle dynamics*. Springer

A Smart System for Shock and Vibration Isolation of Sensitive Electronic Devices On-Board a Vehicle

M. De Michele, G. Di Massa, G. Frisella, S. Lippolis, S. Pagano, G. Pisani and S. Strano

Abstract The paper presents an innovative system for shock and vibration isolation of a set of racks on-board vehicles containing equipment sensitive to accelerations. The suspension system is composed of air springs so that the isolation efficiency and the rack attitude do not vary if some devices are replaced with other ones having different inertial characteristics. As the air springs have a low level of damping, the suspension system is equipped with four magnetorheological dampers whose damping may be adjusted in real time to minimize rack accelerations. The suspension system also includes stabilizers in order to contain roll and pitch motions of the racks.

Keywords Air springs · MR dampers · Shock isolation · Vibration isolation

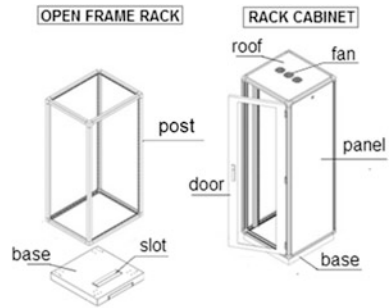
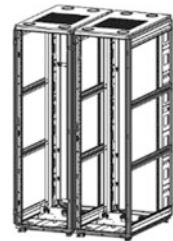
1 Introduction

Electrical and electronic equipment (audio, video, networking, etc.) are often housed in rack cabinets of standard dimensions. The adoption of the rack allows to reduce the overall dimensions of the equipment as installable without own case; moreover, thanks to the devices size standardization and fastening systems, it is easy to remove units for maintenance or for replacement in case of failure or for upgrading. Devices stored in rack have standard dimensions; the most common standard is the 19-inch rack, being 19" the distance between posts to which equipment are bolted. The depth of the rack (distance from front to back) is not standardized while the devices height must be a multiple of 1.75" (rack unit).

The commonly adopted rack structure are (Fig. 1): (a) *open frame rack*; (b) *rack cabinet (or rack enclosure)*. Rack cabinets can better preserve equipment as they

M. De Michele · G. Di Massa · S. Pagano (✉) · G. Pisani · S. Strano
Università di Napoli "Federico II", Napoli, Italy
e-mail: stefano.pagano@unina.it; pagano@unina.it

G. Frisella · S. Lippolis
MBDA Italia S.p.A., Rome, Italy

Fig. 1 Racks**Fig. 2** Set of two racks

are closed with doors and panels that allow the control of the internal temperature and the equipment protection from damage caused by dust, water and other debris.

To accommodate a large number of devices, two or more racks, can be connected (*set of racks*) (Fig. 2).

Racks are mounted even inside motor vehicles (Fig. 3) that are sources of mechanical shocks and vibrations caused by roughness of the road. It is the case of mobile laboratories, mobile remote broadcast television studio or military mobile shelters.

The choice of the suspension system requires the knowledge of the inertial characteristics of the suspended mass constituted by the rack structure and by the stored devices.

The rack structure mass depends on the dimensions and on the structure type (open or closed structure, with or without air-conditioning system, etc.). The rack structure mass of a 19" rack for 42 rack units may range between 60 and 180 kg. The corresponding total mass, comprising the installed devices, may range in a

**Fig. 3** **a** Mobile remote broadcast television studio; **b** Military shelter on truck

wide interval; it can be considered that, for example, a disk drive may have a mass of 0.75 kg while a power supply may even exceed 30 kg.

Very often, it is necessary to add or to replace some devices and it can lead to a marked variation of the inertial rack properties. In this (frequent) case, to avoid a worsening of the isolation efficiency and an evident variation of the rack attitude the suspension system must be adapted.

The most widely used suspension system, mainly in military field, is constituted by a set wire rope springs (WRS) [1, 2]. This paper evaluates the possibility of suspending the rack on an air springs suspension system that can be adjusted in function of the suspended mass.

2 Isolation System Description

In the following, a set of three racks transported inside a shelter fixed on a truck, is considered; each rack has a mass of about 250 kg. The suspension system is constituted by the following elements (Fig. 4):

- (a) six double convoluted air spring (Firestone mod. 25) placed between racks and shelter floor;
- (b) two wire rope springs placed between the top of the racks and the shelter wall, called “stabilizers”, to reduce the roll and pitch motion amplitude;
- (c) some puffers to soften the impact between the rack walls when the relative motion between racks and shelter achieves too large displacements;
- (d) four magnetorheological (MR) dampers (Lord. mod. RD 8040); two dampers are arranged along the transverse direction so that they mainly exert their action to dampen transverse, yaw and roll motion; the other two dampers are displaced in the longitudinal plane to dampen longitudinal, pitch and bounce motions. MR dampers extremities are equipped by means of spherical joints.

MR dampers are constituted by a cylinder-piston system whose two chambers communicate through a calibrated hole formed in the piston. Around the hole, an



Fig. 4 a Convoluted two-lobe air spring; b wire rope spring; c puffer; d MR damper

electric coil induce a magnetic field in the fluid that passes through the hole. Thanks to the presence of iron particles (1 to 10 μm) in suspension in the fluid, varying the current intensity, it is possible to adjust the fluid viscosity and therefore the damping characteristics [3]. This technology allows to change the damping coefficient in a very short time (about 1 ms) making it possible to adjust it on the base of the motion characteristics of the suspended mass [4].

To evaluate the efficiency of the suspension system, a demonstrator was adopted. The set of racks was simulated by means of a steel rigid frame (green, in Fig. 5a) having the following external dimensions: $1446 \times 450 \times 1780$ mm. It can be ballasted by means of additional masses, bolted on the frame. The pavement and the wall of the shelter are simulated by means of the *base frame* (red) and *castle frame* (blue), respectively. Air springs, MR dampers and puffers are placed between the base frame and the rack; stabilizers are instead placed between rack and castle frame that can be considered rigid for forcing frequency lower than 15 Hz.

Air springs were selected taking into account the suspended mass and the target natural frequencies. Manufacturers provide the axial stiffness characteristics but, in general, are not exhaustive about transverse characteristics. The transverse stiffness depends on the axial load and, generally, it decreases with the axial load until the static instability. For this reason, it is necessary to carry out a preventive investigation to characterize the shear reaction of the air springs.

The air springs are supplied with a compressor equipped with a small tank (0.7 L). Six solenoid valves, independently for each air spring, control the airflow.

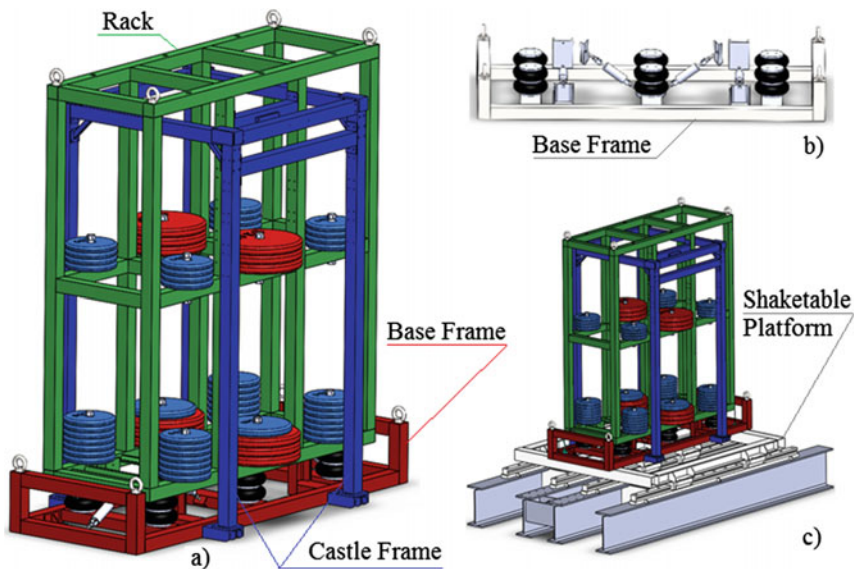


Fig. 5 a Demonstrator; b air springs and MR dampers; c demonstrator on shaking-table

Two power supplies (12 V DC 30A) feed the following units:

- (PS1) an air compressor (18A) and the MR dampers ($4 \times 2 = 8A$), which do not work simultaneously;
- (PS2) an acquisition and control system (Autobox D-Space DS1103 PPC Controller Board with Panel Connector 1103 (25A) and measurement instrumentation (max 1A):
 - four draw-wire displacement sensors (Micro-Epsilon, Mod. WPS-MK30-250-P25) to detect the displacement between the four lower corner of the rack and the base frame;
 - two tri-axial accelerometers (range ± 20 g), to evaluate the acceleration transmissibility. An accelerometer is placed on the base; the other one on the rack;
 - an inertial measurement unit (IMU, LandMark MRM10 6-axis analog output ± 5 V), placed on the top of the rack.

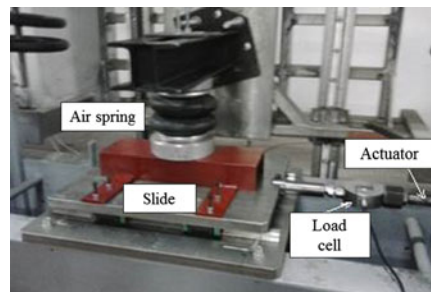
3 Air Spring Experimental Characterization

The first part of the experimental activity has regarded the experimental transverse characterization of the convoluted air springs; to this end, the springs were subjected to a constant compression and variable shear load. The tests were carried out on a press (Fig. 6) equipped with a horizontal slide driven by a mechanical actuator able to impose a horizontal harmonic motion to the slide. For a fixed value of the height of the spring and of the initial pressure, it was measured:

- (1) the axial force exerted by the spring for different values of the spring squashing; the test was repeated for different values of the inflation pressure;
- (2) the horizontal force (shear) while the slide moves; the corresponding hysteresis cycles are shown below.

The spring were characterized for the following three pressure values: 2, 3 and 4 bar (absolute pressure). The squashing has been adjusted in the range of

Fig. 6 Convoluted air spring under test



150–80 mm while the transverse displacement amplitude was equal to 7.5 mm (in both directions).

In the following, the results of several tests conducted on double convoluted air spring (Firestone mod. 25) at constant pressure (2 bars) and for different values of the squashing.

In the first set of tests, pressure can be considered constant during the squashing since the spring is in communication with the compressed air tank. Diagrams in Fig. 7 show that the shear force, exerted by the spring, varies with an almost linear trend with the transversal deformation. When the slide motion reverses, the diagram shows the characteristic discontinuity due to the friction in the guide of the slide; the slope of the two branches represents the transverse stiffness of the spring. The relation between the horizontal stiffness and the spring height is shown in Fig. 8. It can be noted that the shear stiffness decreases until it assumes null value; then, for a further reduction of the height of the spring, the stiffness becomes negative (static instability).

Figure 9 shows the trend of the transverse stiffness for different heights of the spring and for different pressure values; in these tests the communication between air spring and tank is closed.

The spring behavior is similar even if the pressure does not remain constant but increases with the compression of the spring and the instability appears for smaller

Fig. 7 F-D cycle for $p = 2 \text{ bar} = \text{constant}$

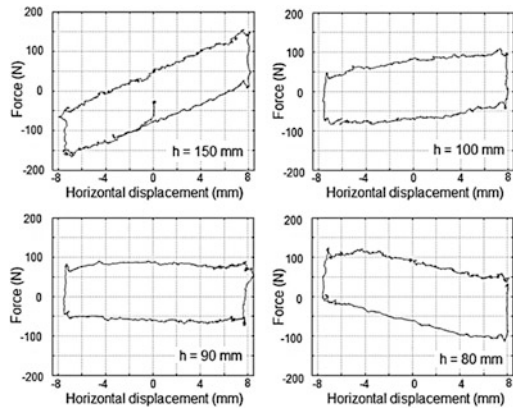


Fig. 8 Transverse-stiffness versus spring height

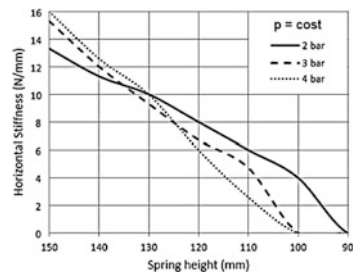


Fig. 9 F-D cycle for $p = 2$ bar at $h = 140$ mm

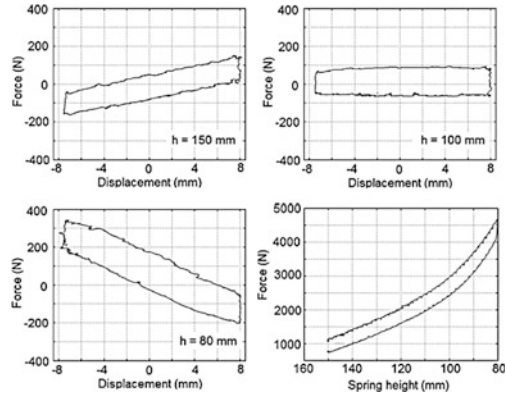
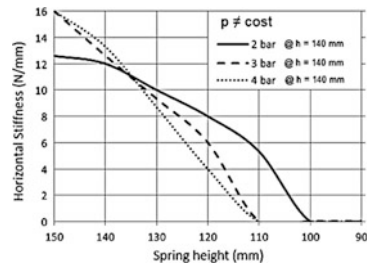


Fig. 10 Transverse-stiffness versus spring height



values of the spring height; the two branches of the force diagram are horizontal for $h = 100$ mm (rather than 90 mm as in the case of $p = \text{constant}$). This means that an increase of the pressure has a negative effect on system stability (Fig. 10).

4 First Tests on Shaking Table

Some tests were planned on a shake-table [5], exciting a horizontal movement of the base frame (Fig. 11), which involves shear and axial springs reactions.

The experimental results, obtained by assigning to the moving platform of the shaking table a sweep frequency or a harmonic motion, are shown in the following. In particular exciting a sweep motion, characterized by a displacement amplitude of 5 mm and a frequency variation of 0.02 Hz/s, in the 0–5 Hz range, it was noted that:

- the acceleration amplitude of the base frame grows with parabolic law (Fig. 12) reaching, at 5 Hz, the value of about 13 m/s^2 ;
- the acceleration amplitude of the demonstrator (Fig. 12) does not exceed the value of 4 m/s^2 . There is an amplitude amplification for two time values: $t = 65$ s, which corresponds to a frequency excitation of $65 \times 0.02 = 1.3$ Hz, and $t = 130$ s which corresponds to a frequency of 2.6 Hz;

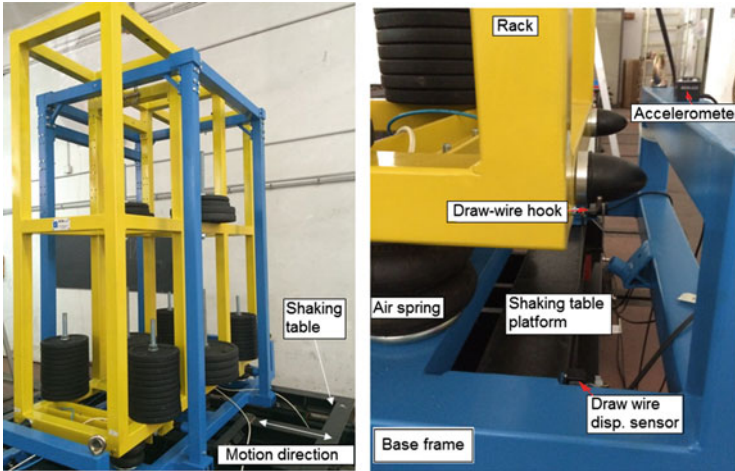
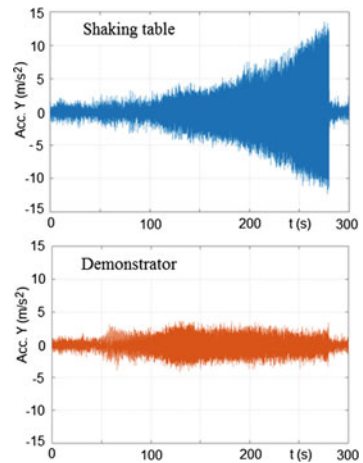


Fig. 11 Demonstrator on the shaking table

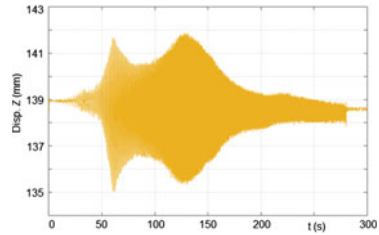
Fig. 12 Sweep test: horizontal acceleration



- the displacement sensor signals (Fig. 13) show more clearly the amplification of motion at the two frequencies (1.3 and 2.6 Hz) representing two natural frequencies: roll motion and translational motion of the demonstrator in the excitation direction.

Both eigen-modes are characterized by natural frequencies sufficiently lower than the frequency excited by the motion of the truck on the road which value can be considered equal to about 10 Hz. In both cases, the maximum amplitude of the displacement sensor measurements was approximately 4 mm.

Fig. 13 Sweep test: vertical displacement



5 Conclusions

The design and the experimental verification of an innovative system for shock and vibration isolation of sensitive electronic devices on-board a vehicle has been presented. The suspension system is composed of air springs and magnetorheological dampers. The main idea of the proposed solution is to use shock and vibration isolation properties of air springs in addition with the possibility to control the damping in order to optimize the isolation performance for a wide range of excitation frequencies. A mechanical characterization testing of the adopted air springs have allowed a detailed analysis of their behavior in compression and shear. Successively, several experimental tests on shaking table have been conducted to verify the performance of the smart isolation system. The experimental results have shown good performance of the proposed solution with reference to the excitation frequencies to be considered for sensitive equipment on-board vehicles.

Acknowledgments The authors are grateful to Angelo Fornaro (AR.TER. S.r.l.) and to Marco Di Pilla, Giuseppe Iovino, Gennaro Stingo for their collaboration during the demonstrator construction and the execution of laboratory tests.

References

1. Demetriades GF, Constantinou MC, Reinhorn AM (1993) Study for wire rope systems for seismic protection of equipment in buildings. *Eng Struct* 15(5):321–334
2. Di Massa G, Pagano S, Strano S (2014) Cabinet and shelter vibration isolation: numerical and experimental investigation. *Eng Lett* 22(4):149–157
3. Kordonsky W (1993) Magnetorheological effect as a base of new devices and technologies. *J Magn Magn Mater* 122:395–398
4. Kordonsky W (1993) Elements and devices based on magnetorheological effect. *J Intell Mater Syst Struct* 4:65–69
5. Pagano S, Russo M, Strano S, Terzo M (2014) Seismic isolator test rig control using high-fidelity non-linear dynamic system modeling. *Meccanica* 49(1):169–179

Wavelet Analysis of Gear Rattle Induced by a Multi-harmonic Excitation

Renato Brancati, Ernesto Rocca, Sergio Savino
and Francesco Timpone

Abstract The paper reports a feasibility study for the detection of automotive gear rattle induced by multi-harmonic excitation through the use of a wavelet multi-resolution analysis. The analysis adopts experimental data coming from a helical gear pair under unloaded conditions. The excitation of gear rattle is of periodic type with two harmonic components, which is similar to the excitation of an actual automotive I.C. engine. The dynamic behavior of the gear pair has been analyzed by varying the second order harmonic amplitude of the excitation, for two mean speed values. The analysis gives useful information to develop an index of performances based on the wavelet theory that could be adopted for comparative analyses with respect to the severity of the tooth impacts occurring during the rattle phenomenon.

Keywords Automotive transmission · Gear rattle · Multi-harmonic · Wavelet analysis

1 Introduction

The gear rattle phenomenon of the automotive gear box is one of the main issues of research for the industrial noise and vibration sectors, being perceived as a quality parameter for the acoustic comfort in cars. This aspect becomes fundamental so in

R. Brancati · E. Rocca (✉) · S. Savino · F. Timpone
University of Napoli “Federico II”, Napoli, Italy
e-mail: ernesto.rocca@unina.it

R. Brancati
e-mail: renato.brancati@unina.it

S. Savino
e-mail: sergio.savino@unina.it

F. Timpone
e-mail: Timpone@unina.it

the highly competitive automotive market. It strongly depends on the torque fluctuations of the I.C. engine, and is due to repeated tooth impacts inside the gearbox regarding only the unloaded gear pairs [9, 14].

The use of the wavelet Transform in various type of scientific researches is today increasingly widespread. It permits to analyze a particular event in the time and frequency domains. Many examples of applications can be cited, starting from the image compression technology up to the diagnostics of industrial machinery [1, 2, 12]. There are many applications of this technique that aim to prevent malfunctions and failures of transmission gear systems [8, 11, 13].

The method generally adopted to investigate vibrations in the industrial field is based on the decomposition of a signal by the wavelet multi-resolution analysis.

As regard to the specific problem of gear rattle in gear box, solutions are often oriented to attenuate its effect by means of mechanical devices such as multistage clutches or by dual mass flywheels, or by adopting suitable lubrication techniques in gears [5, 9, 14].

Many experimental and theoretical studies about gear rattle have given contribution in the last years to propose solutions to the problem [5, 6, 9]. Some recent studies begin to analyze the use of the wavelet based techniques to detect noise problems in gears [4, 7].

As regard to the modeling of the rattle excitation it is known that the law of motion of the primary shaft of an automotive gear box depends on the number of cylinders and on the engine technology. Moreover the law of motion of the input shaft, due to the discontinuous combustion in the engine, cannot be considered as purely of harmonic type. In fact, recent studies consider the multi-harmonic excitation of the rattle as a better approach to correctly analyze the problem [3, 6].

In the paper an experimental study is conducted by considering a multi-harmonic excitation for the pinion gear, consisting in a sum of two harmonic components.

The development of indices of performances in this field of investigation has a fundamental importance and so the development of an index based on the wavelet multi-resolution analysis can be considered particularly useful [4].

The present wavelet based analysis, adopted by the authors in previous experimental works to investigate the influence of some aspects of vibration in gear, aims to show interesting perspectives in detecting the severity of tooth impacts in gear rattle context, in the case of multi-harmonic excitation.

2 The Experimental System

The analysis has been conducted on an experimental test rig constituted by a helical gear pair coming from an automotive gear box. The gear is driven by a speed controlled brushless motor by a suitable law of speed. The gear pair operates under unloaded conditions to reproduce the gear rattle phenomenon. The Fig. 1 shows the scheme of the test rig adopted for the tests.

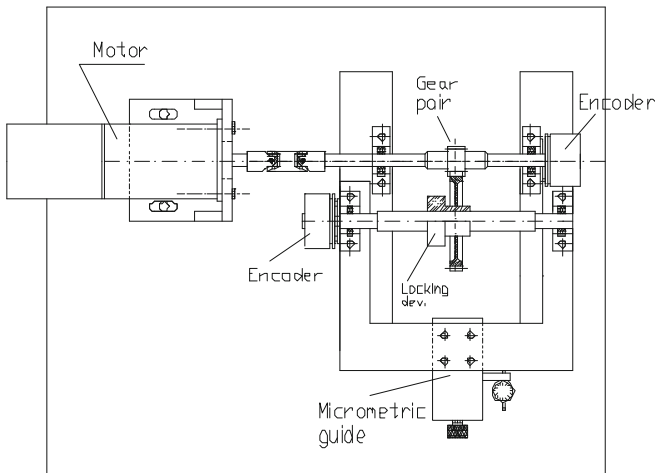


Fig. 1 The experimental test rig

The time histories of the gears relative angular motion are acquired by the use of two incremental encoders with high resolution (10,000 pulses/rev). By virtue of a quadrature detection, each encoder provides a resolution of 40,000 pulses/rev ($1.57e-4$ rad).

The relative angular motion $\Delta\theta(t)$ is measured by combining the absolute rotations θ_1 and θ_2 of the wheels. This relative motion, defined also as the Transmission Error (TE), is given by:

$$\Delta\theta(t) = \theta_1(t) - \theta_2(t) \frac{r_2}{r_1} = \theta_1(t) - \theta_2(t) \frac{z_2}{z_1} \quad (1)$$

In the Eq. (1) r_1 , r_2 , and z_1 , z_2 indicate respectively the pitch radii and the tooth number of the pinion (1) and wheel gear (2). The gear pair adopted for the tests has the following transmission ratio: $\varepsilon = z_2/z_1 = 33/37 = 0.89$. The rig enables moreover the shafts to be distanced in order to increase or decrease the gear backlash: in the present tests the distance between axes is 65.5 mm. So the measured angular backlash has a mean value of about $1.01e-4$ rad. Because of assembly errors the angular backlash varies with a periodic fluctuation between a minimum value of $8.6e-5$ rad and a maximum of $1.17e-4$ rad. The law of speed for the driving gear is multi-harmonic, composed of two components:

$$\Omega(t) = \Omega_m + \sum_{k=1}^2 \Delta\Omega_k \sin(2\pi kft) \quad (2)$$

In Eq. (2) Ω_m represents the speed mean value; $\Delta\Omega_k$ is the amplitude of the two speed fluctuation components; f is the fundamental frequency of the rattle cycle.

The tests were conducted for two constant mean speed values: 500 and 600 rpm. The fundamental frequency chosen for the rattle excitation is $f = 5$ Hz; while the two $\Delta\Omega_k$ fluctuation components of the speed have been varied in the following way: the $\Delta\Omega_1$ component has been set as 20 % of the mean speed, while the second order component $\Delta\Omega_2$ has been varied among 10 and 100 % of the $\Delta\Omega_1$ component one, with step equal to 10 %.

All the tests were conducted without lubricant interposed between teeth.

3 The Wavelet Multi-resolution Analysis

The wavelet multi-resolution analysis has high capability to analyze signals characterized by discontinuities due to impulsive events [10], so it represents a good tool to individuate non-stationary phenomena in the gearbox fault diagnosis [4, 8]. The tool is based on the discrete wavelet transform (DWT), that performs a decomposition of a given signal s with n samples [10]. The multi-resolution decomposition consists of $k = \log_2(n)$ stages. Starting from s , the first stage produces two sets of coefficients: approximation coefficients CA_i , and detail coefficients CD_i . These vectors are obtained by convolving s respectively with a low-pass filter Lo_D for approximation, and with a high-pass filter Hi_D for detail, followed by a dyadic decimation (downsampling) [10].

The coefficients CA_i and CD_i allow to reconstruct the single level i of the wavelet decomposition obtaining two vectors: A_i (approximation), and D_i (detail). In this way a signal s can be reconstructed as a sum of $(k + 1)$ components:

$$s = A_k + D_k + D_{k-1} + D_{k-2} + \dots + D_1 \quad (3)$$

The technique used in this paper consists in analyzing the detail vectors sum $\sum D_i$ of the wavelet decomposition conducted on the transmission error (TE) of the gear relative rotation, neglecting the approximation vector that contains information about the low frequencies, as presented in [4, 7]. For the present analysis the Haar wavelet has been adopted.

With this metric it is possible to highlight the tooth impacts, characterized by high frequencies, with respect to the entire signal.

By the DWT the s signal can be decomposed at level $m \leq k$, writing so:

$$s = A_m + D_m + D_{m-1} + D_{m-2} + \dots + D_1 = A_m + D_1^m \quad (4)$$

where:

$$D_1^m = \sum_{i=1}^m D_i \quad (5)$$

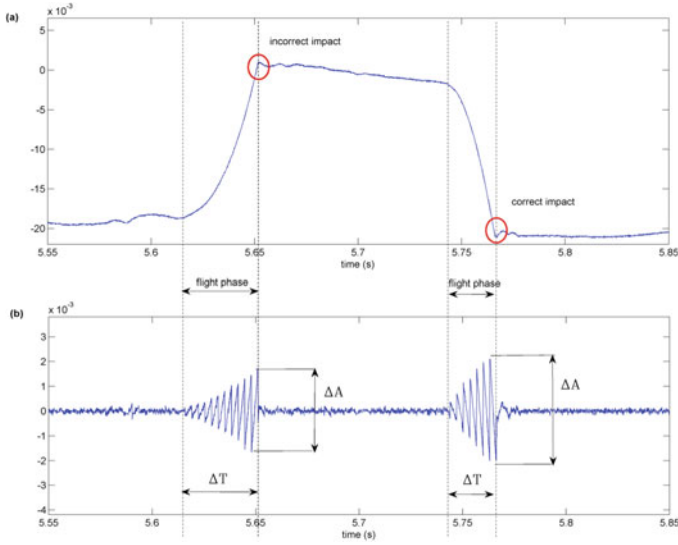


Fig. 2 Transmission Error TE (a), and related detail vector sum D_1^5 (b)

In the paper the minimum level that comprises all the frequencies useful to conduct a comparative analysis, has been fixed in $m = 5$.

In order to analyze the oscillations of D_1^5 , two parameters have been adopted:

- ΔA : represents the maximum value of the peak-valley distance;
- Δt : is the time duration of the oscillation.

The various impacts are qualitatively different and, analyzing the oscillations of the sum vector D_1^5 , it is possible to observe a difference, both in terms of amplitude (ΔA) and in terms of time interval (Δt), as function of intensity of the impact.

In the following Fig. 2 there are well represented the above parameters for the impacts on the two different sides of the teeth: the “correct impact” when the driving gear impacts on the driven one; the “incorrect impact” represents the condition where the driven wheel (idle) impacts on the driving wheel, due to its moment of inertia forces.

4 The Experimental Results

Some experimental tests have been conducted, under unloaded operative conditions, for the gear pair described in Sect. 2. The speed law imposed at the pinion gear is the one referred in Eq. (2).

The rattle excitation fundamental frequency chosen for the tests is equal to 5 Hz, and it is uncorrelated to the frequency of the 500 rpm mean speed test (8.33 Hz),

while it is equal to half of the frequency of the 600 rpm speed test (10 Hz). The amplitude of the first and the second order harmonics have been varied in percent in the way described in Sect. 2.

The following Fig. 3 shows, for a mean speed value of 500 rpm, $\Delta\Omega_1 = 100$ rpm and three different values of $\Delta\Omega_2$, the time histories of the gear relative motion (TE) and their Fast Fourier Transform (FFT) spectra. Some original aspects about the rattle with multi-harmonic excitation can be observed by varying the second order component of the excitation. Figure 3 refers to $\Delta\Omega_2$ amplitude values of 20, 50 and 90 % of the $\Delta\Omega_1$ speed fluctuation.

An evident bilateral rattle, with impacts on the two different sides of teeth, can be noted. When the second order harmonic $\Delta\Omega_2$ increases the dynamic behavior of the gear tends to a more heavy gear rattle. The time history in Fig. 3, related to $\Delta\Omega_2 = 90\%$, shows that the rattle cycle changed its frequency (10 Hz), equal to the value of the second order component. In fact the FFT shows, in this case, that the amplitude of component at 10 Hz exceeds the value of the fundamental one (5 Hz). This feature begins to occur already for a value of $\Delta\Omega_2 = 80\%$.

In the Fig. 4 the curves show the mean value of the wavelet based parameter ΔA , i.e. the peak to valley amplitude, evaluated in a time interval of about 10 s. It can be noted an increase of this parameter with the increase of the $\Delta\Omega_2$ amplitude, being generally constant in the range 30–70 %. The results are qualitatively similar for the mean speed value of 600 rpm and $\Delta\Omega_1 = 120$ rpm, shown in the same figure. Moreover it can be noted that the wavelet parameter is sensitive to the mean speed of the gear, because it increases as its value increases.

Results of the analysis have been compared with those of an investigation method, based on a harmonic analysis (FFT method), previously developed and tested by authors [6]. The comparisons confirm the reliability of the wavelet procedure when applied to rattle problems with multi-harmonic excitation.

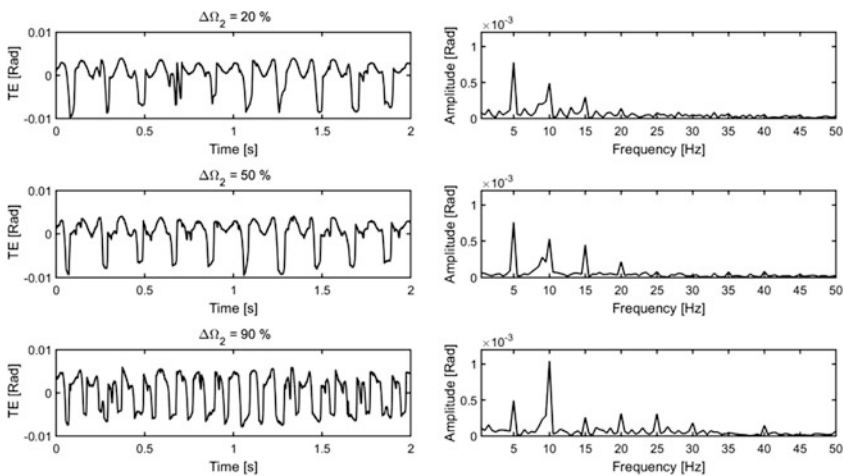


Fig. 3 TE time history and FFT spectra for 500 rpm

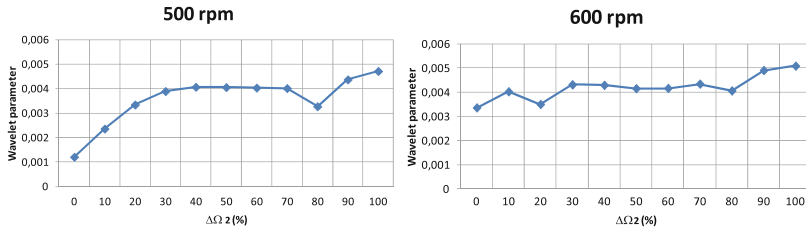


Fig. 4 The wavelet based parameter for 500 and 600 rpm

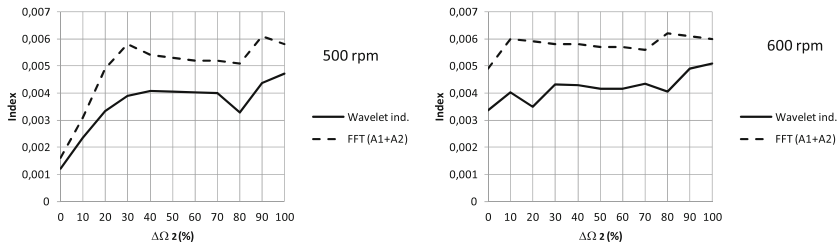


Fig. 5 Wavelet and FFT indexes comparison for 500 and 600 rpm

The diagrams in Fig. 5 show, in terms of trend of the curves, a qualitatively good agreement between the wavelet analysis results and those of the FFT technique. This last parameter, based on the harmonic analysis method, is calculated by summing the amplitudes of only the first and second harmonic components ($A_1 + A_2$) obtained through the FFT of the signals. This clarifies the numerical differences, in terms of index, between the two methods.

5 Conclusions

The analysis conducted in the paper, for an unloaded gear pair subjected to a multi-harmonic excitation, has evidenced that the quality of the gear rattle phenomenon can be evaluated by the use of an index of performance based on a wavelet multi-resolution analysis.

The advantage of the present technique consists in the possibility of evaluating the severity of the various impacts during the gear meshing, because of the peculiarity of the wavelet analysis in identifying an event in the time domain.

Results showed that the wavelet parameter is sensitive to the increase of the average speed values of gears. An increase of the index has been generally noted, in particular, when the amplitude of the second order excitation component reaches a value equal to about 70–80 % of the first component. This happens independently of the mean speed of the pinion, at least for the values adopted in the present

analysis. This dynamic behavior could be justified considering the increase in the wheel gear inertia forces with the 2nd order excitation component.

Moreover the results of the experimental analysis well agree with those obtained by the use of a method based on the FFT analysis, conducted on the same signals, confirming so the appropriateness of the wavelet based method in the detection of the gear rattle phenomenon.

References

1. Amoresano A, Avagliano V, Niola V, Quaremba G (2013) The assessment of the in-cylinder pressure by means of the morpho-dynamical vibration analysis—methodology and application. *Int Rev Mech Eng* 7(6):999–1006
2. Amoresano A, Niola V, Quaremba G (2012) A sensitive methodology for the EGR optimization: a perspective study. *Int Rev Mech Eng* 6(5):1082–1088
3. Barthod M, Hayne B, Tebec JL, Pin JC (2007) Experimental study of gear rattle excited by a multi-harmonic excitation. *Appl Acoust* 68:1003–1025
4. Brancati R, Rocca E, Savino S (2015) A gear rattle metric based on the wavelet multi-resolution analysis: experimental investigation. *Mech Syst Signal Process* 50–51:161–173
5. Brancati R, Montanaro U, Rocca E, Santini S, Timpone F (2013) Analysis of bifurcations, rattle and chaos in a gear transmission system. *Int Rev Mech Eng (IREME)* 7(4):583–591
6. Brancati R, Rocca E, Savino S, Timpone F (2015) Experimental analysis of the relative motion of a gear pair under rattle conditions induced by multi-harmonic excitation. In: *Proceedings of the world congress on engineering (WCE)*, vol II, pp 1016–1021
7. Brancati R, Rocca E, Savino S, Farroni F (2013) Analysis of gear rattle by means of a wavelet-based signal processing procedure. *Meccanica* 48–6:1399–1413
8. Dalpiaz G, Rivola A, Rubini R (2000) Effectiveness and sensitivity of vibration processing techniques for local fault detection in gears. *Mech Syst Signal Process* 14(3):387–412
9. Dogan SN, Ryborz J, Bertsche B (2006) Design of low-noise manual automotive transmissions. *Proc IMechE Part K J Multi-body Dyn* 220:79–95
10. Mallat S (1999) *A wavelet tour of signal processing*. Academic Press
11. Niola V, Quaremba G, Avagliano V (2009) Vibration monitoring of gear transmission. In: *Proceedings of 9th WSEAS international conference simulation, modelling and optimization, SMO'09*, 5th WSEAS international symposium on grid computing, *Proceedings of 5th WSEAS international symposium on digital libraries*, *Proceedings of 5th WSEAS international symposium data mining*, pp 74–79
12. Niola V, Quaremba G, Amoresano A (2009) A study on infrared thermography processed through the wavelet transform. In: *Proceedings of the 8th WSEAS international conference on system science and simulation in engineering, ICOSSE'09*, pp 57–62
13. Niola V, Quaremba G, Forcelli A (2008) The detection of gear noise computed by integrating the Fourier and Wavelet methods. *WSEAS Trans Signal Process* 4(3):60–67
14. Wang Y, Manoj R, Zhao WJ (2001) Gear rattle modeling and analysis for automotive manual transmissions. *Proc IMech J Automobile Eng* 215(Part D):241–258

Part X
Special Session in Honor of
Prof. Aldo Rossi for his 70th Birthday

Analytical and Multibody Modelling of a Quick-Release Hook Mechanism

Luca Bruzzone, Davide Bonatti, Giovanni Berselli
and Pietro Fanghella

Abstract Quick-Release Hooks (QRH) are particular accessories for connecting chains or metal ropes, that can be remotely unfastened under full-load conditions via application of an external force with limited magnitude. Despite their widespread use, and aside from a number of patents, the scientific literature related to QRH performance is rather limited. This paper reports about the modelling of a class of QRH, which relies on the use of a four-bar linkage mechanism operating in the proximity of a singularity configuration. Design graphs depicting the main functional parameters are reported. At last, a multibody model of the system is developed, which validates the analytical results while providing an insight of the frictional forces effect on the device modelling and performance.

Keywords Quick-Release hook · Kinematic analysis · Static analysis · Parameter design · Multibody modelling

1 Introduction

Practical devices for hoisting high loads while ensuring the possibility for a quick release under the action of a manual command are strongly required in several applications. An explicit example of this operational need can be found in the naval industry, where passenger ships are equipped with a number of lifeboats that must

L. Bruzzone (✉) · G. Berselli · P. Fanghella
University of Genoa, DIME, Genova, Italy
e-mail: bruzzone@dimec.unige.it

G. Berselli
e-mail: giovanni.berselli@unige.it

P. Fanghella
e-mail: pietro.fanghella@unige.it

D. Bonatti
Alioto Group, Castelnuovo Magra, Italy
e-mail: davide.bonatti@aliotogroup.com

be securely connected to the ship structure during normal cruising and may need to be quickly released in case of accidents [1]. Aside from the naval engineering field, Quick-Release Hooks (QRH) are also employed whenever a rapid and effective unfastening action is required, or when high-load lifting rigs are located in places which are hardly accessible by an operator. For obvious reasons, these hoisting devices must be carefully designed in order to be capable of withstanding high loads while maintaining quick-release capabilities and preventing unintentional opening.

In their most common embodiment design, QRHs comprise a four-bar linkage operating in the proximity of a singularity configuration. With reference to Fig. 1, which shows a pre-series industrial product, the four-bar linkage is dimensioned so as to provide a double rocker arrangement; the base link (1), the upper rocker arm (2), the connecting rod (3) and lower rocker arm (4) are connected by revolute joints at points O, A, B, C (the upper hole of body 1 allows the fixed connection to the rope). Frame link (1) and lower rocker arm (4), realized as latches with semicircular slot, share the external load (schematized as a force acting on point F). The QRH release operation is then actuated by applying an opening force (much lower than the external load) on the upper rocker arm (point D). Obviously, the magnitude of the opening force to be applied on point D depends on the mechanism geometry, with unavoidable frictional forces in the revolute joints.

Despite the relevant practical interest for QRH designs, the scientific literature dealing with the subject is quite limited. For instance, Häkkinen et al. [2, 3] reported about the consequences of unsuitable QRH designs for applications on safety systems. The authors clearly state that an optimal design solution, in terms of *efficiency* and *practicability*, should be effective enough to fulfil the intended safety function while practical and appropriate to prevent further hazards and operational delays in case of accidents. As a response to the need of more strict safety standards, recent international standards have been developed [4].

Within this scenario, this paper reports about the analysis and design of the mechanism, with the aim of providing an analytical model for further design optimizations, along with a better insight of the QRH mode of operations. For instance, the position of revolute joint A is taken as a design parameter, to evaluate

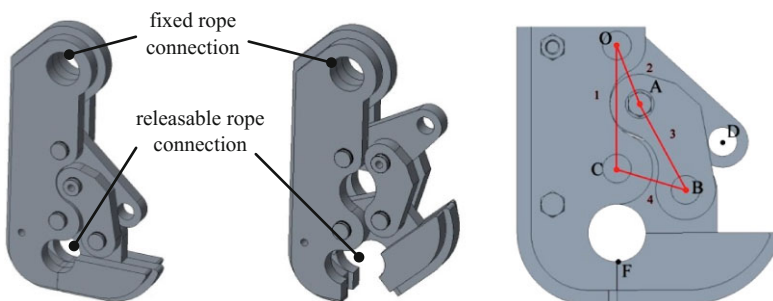


Fig. 1 Four-bar Quick Release Hook mechanism

the main characteristics of the mechanism. At last, frictional forces are accounted by means of a multibody model of the system and a detailed analysis of the obtained results is presented.

2 Kinematic Model

The kinematic scheme of the mechanism is shown in Fig. 2. With reference to the vectors shown in Fig. 2, the position analysis of the closed-loop chain is expressed by the following vector equation:

$$\mathbf{z}_2 + \mathbf{z}_3 + \mathbf{z}_4 - \mathbf{z}_1 = \mathbf{0} \tag{1}$$

Considering the angle θ_2 as the Lagrangian coordinate of the 1-DOF mechanism, it is possible to solve the direct position analysis starting from (1). The angle θ_2 can vary in the range between θ_{2i} (closure position, Fig. 2a) and θ_{2max} (maximum opening position, Fig. 2d). The maximum opening position is a mechanism singularity, with body 3 and 4 aligned. Another mechanism singularity is shown in Fig. 2b (blue), with body 2 and 3 aligned. This singularity is near to the initial closed position, since the angle $\delta = \theta_{3i} - \theta_{2i}$ (Fig. 2a) is small.

The angles θ_3 and θ_4 as functions of θ_2 are shown in Fig. 3, for the initial design configuration; this configuration is defined by the coordinates of the points A, B, C, D and F in the closure position, see Table 1.

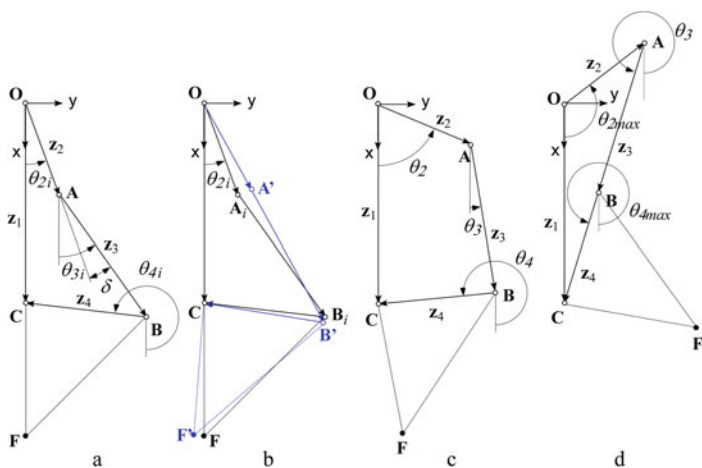


Fig. 2 Closed-loop chain of the four-bar mechanism: **a** closure position; **b** singularity position (blue), with extra-closure of the hook; **c** generic position; **d** maximum opening position (singularity)

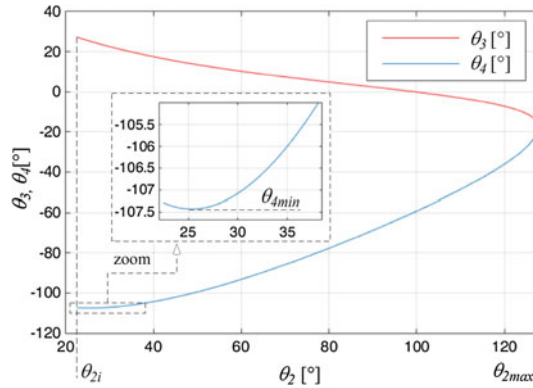


Fig. 3 Angles θ_3 and θ_4 as functions of θ_2 for the initial design configuration of Table 1

Table 1 Point coordinates in the closure position for the initial design configuration [mm]

x_A	y_A	x_B	y_B	x_C	y_C	x_D	y_D	x_F	y_F
20.32	8.41	50.54	24.00	43.07	0	33.70	36.93	75.57	0

The minimum value of the angle θ_4 (θ_{4min}) is in the singularity of Fig. 2b, when $\theta_2 = \theta_3$; let us note that this position corresponds to an extra-closure of the hook, with respect to the initial closed position; therefore, a proper clearance between the latches (tips of bodies 1 and 4) must be considered in the design phase to avoid interference. In the following we will call this singularity *extra-closure position*.

Therefore an important design parameter is the extra-closure displacement of the point F:

$$\Delta s_{ec} = \overline{CF}(\theta_{4i} - \theta_{4min}) \tag{2}$$

3 Static Analysis

The mechanism static analysis is carried out in two load cases:

- A. mechanism in closed position with load applied in F (Fig. 4a)
- B. mechanism in closed position with load applied in F, at the beginning of the opening manoeuvre (Fig. 4b)

For sake of simplicity, the internal reactions of the revolute joints are not shown in Fig. 4 in the static schemes of the complete mechanism. In the following, we will refer to R_{ij} as the reaction force applied by body i to body j . For both the load conditions, the component Q_x is about half the load weight (the load weight is

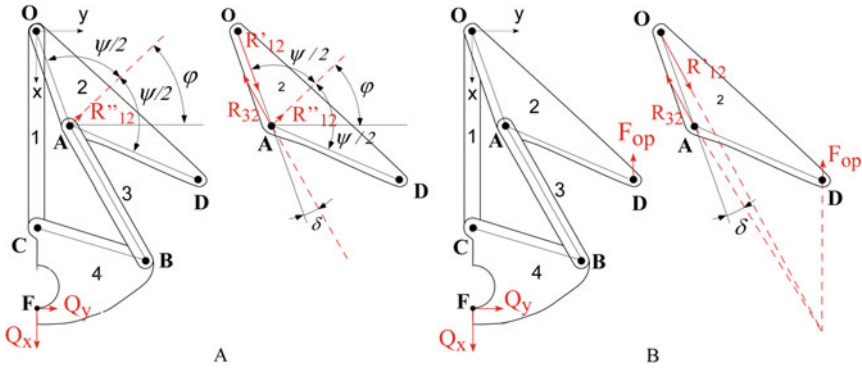


Fig. 4 Static equilibrium: **a** in closed position with load, complete mechanism and body 2; **b** in closed position with load, at the beginning of the opening manoeuvre, complete mechanism and body 2

supposed to be equally distributed on bodies 1 and 4, since these bodies have symmetrical internal profiles in contact with the load fastener). In the load case A, the maximum possible Q_y is supposed to be a percentage r_{xy} of Q_x ($Q_y = r_{xy}Q_x$). In the load case B, since body 4 has to move clockwise around C to reach the extra-closure position, Q_y can be evaluated by the static friction coefficient f between the hook and the load fastener ($Q_y = fQ_x$).

As regards body 2, in the load case A the reaction R_{32} is supported by the revolute joint reaction R'_{12} in O and by the unilateral contact force R''_{12} in A, which direction is supposed to coincide with the bisector of the angle ψ between \mathbf{z}_2 and \mathbf{z}_3 (Fig. 4a); in the load case B the opening force F_{op} starts to move the mechanism towards the extra-closure position, and R''_{12} is absent, because there is no more contact in A between bodies 1 and 2 (Fig. 4b).

By using the static equilibrium equations, it is possible to obtain the expressions of the reaction force R''_{12} in the load case A and of the opening force F_{op} in the load case B:

$$R''_{22} = \sqrt{\left(\frac{R_{32x}y_A - R_{32y}x_A}{x_A + y_A \tan \varphi}\right)^2 (1 + \tan^2 \varphi)} \tag{3}$$

$$= \sqrt{\left(\frac{Q_y(x_F - x_C)(y_A - x_A \tan \theta_3)}{((x_B - x_C) \tan \theta_3 - (y_B - y_C))(x_A + y_A \tan \varphi)}\right)^2 (1 + \tan^2 \varphi)}$$

$$F_{op} = \frac{R_{32x}y_A - R_{32y}x_A}{y_D} = \frac{Q_y(x_F - x_C)(y_A - x_A \tan \theta_3)}{y_D((x_B - x_C) \tan \theta_3 - (y_B - y_C))} \tag{4}$$

where $\varphi = \theta_{2i} + \delta/2$ (Fig. 4a).

Using Eqs. (3) and (4) it is possible to evaluate the influence of the design parameters on the static behaviour of the mechanism.

As an example, Fig. 5 shows the effects of variations of $\pm 15\%$ in the coordinates of A with respect to the values of Table 1 (the other coordinates are kept constant), for a load mass m_{load} of 4000 kg, therefore $Q_y = m_{load} g/2$. Moreover, the values $r_{xy} = 0.2$, $f = 0.3$ are supposed on the basis of the material properties. When x_A increases and y_A decreases, the point A is more distant from the segment OB; consequently, the angle δ and the extra closure displacement Δs_{ec} are higher, as the reaction force in A and the opening force. When A lies on the segment OB ($y_A/x_A = y_B/x_B$, red segments on the surfaces of Fig. 5), the initial position coincides with the extra-closure singularity; that is, the extra-closure displacement is null; in this condition all the four parameters of Fig. 5 are null, and the self-locking closure is at the limit of stability. On the contrary, when $y_A/x_A < y_B/x_B$, δ is negative, Δs_{ec} is null, the unilateral contact reaction R''_{12} is null, and the opening forces F_{op} changes direction (but this condition is not represented in Fig. 5, because the mechanism is not self-locking in the closure position).

In the design phase, it is necessary to obtain a proper compromise between sufficiently high values δ and Δs_{ec} , which are necessary for the closure stability, and not too high values of the opening force F_{op} .

A suitable design compromise is in the region with:

$$0.475x_A - 1.5 < y_A < 0.475x_A - 1 \quad (5)$$

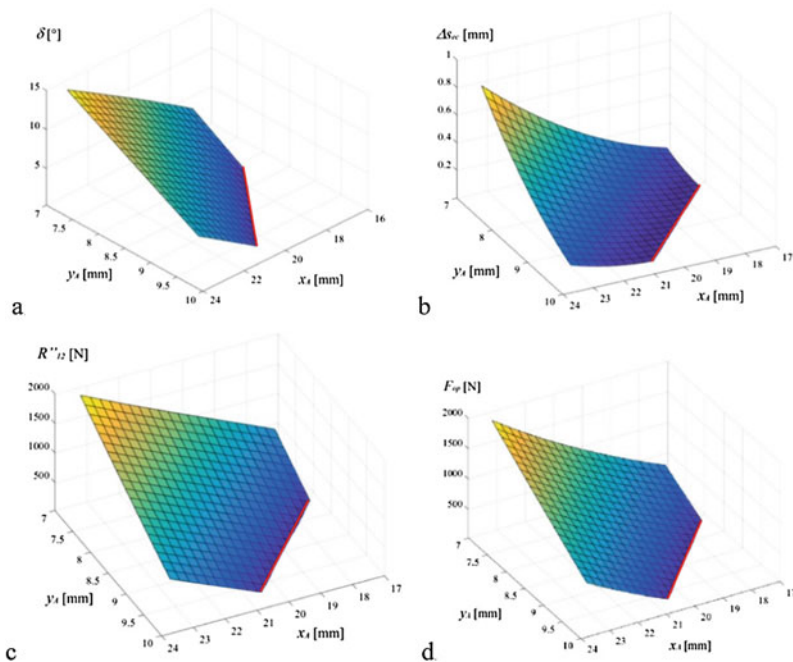


Fig. 5 Influence of x_A and y_A on δ (a), s_{ec} (b), R''_{12} (c), F_{op} (d)

In this range the angle δ is in the range between 4° and 6° , Δs_{ec} is in the range between 0.05 and 0.12 mm and the opening force F_{op} is in the range between 420 and 650 N. The design configuration of Table 1 is located about in the middle of this region ($F_{op} = 533$ N, $\Delta s_{ec} = 0.08$ mm, $\delta = 4.8^\circ$). This opening force can be applied manually, for example, with the interposition of a single luff tackle (with a mechanical advantage of 3).

4 Multibody Model

In order to validate analytical results and to explore more complex effects, a multibody model of the hook has been developed using the same CAD-CAE software tool used for its embodiment design. The four bar model is based on the reference configuration shown in Table 1, and has been simulated in the opening manoeuvre, in the ideal case, as discussed in Sect. 3, and in presence of friction in revolute pair between frame 1 and body 4 (pair C), which exerts a reaction force much higher than the others. The same external loads Q_x and Q_y on point F, discussed in Sect. 3, are applied to the multibody model. The initial equilibrium configuration is obtained through an angular limit of the pair O between frame body 1 and driving link 2; such additional constraint becomes active only when the pair is in the limit position, and a constraining torque is needed to prevent the mechanism motion beyond the allowed angle. The vertical opening force on point D (F_{op}) is assumed as linearly increasing with time, and the simulation is terminated through a logical condition as soon as the hook begins moving. The F_{op} ramp is sufficiently slow to make dynamic inertial effects negligible. In this way, the opening force without and with friction are determined: in the ideal case the hook begins opening for $F_{op} \approx 530$ N, value corresponding to that of the static analysis. The friction case has been evaluated according to actual working conditions of the hook, possibly with mating surfaces in joints in limit or absent lubrication, so static and friction coefficients $f_s = 0.3$ and $f_d = 0.25$ are assumed, along with a pin radius of 5 mm, corresponding to the actual geometry. As a result of friction application, the opening force required increases to $F_{op} \approx 660$ N.

In order to better understand multibody simulation results, let us consider the graphs in Fig. 6 showing respectively:

- the number of degrees of freedom and of redundant constraints in the mechanism, for the two considered cases (no friction and with friction);
- the locking torque due to the angular limit on pair O for both cases and the friction torque in pair C for the friction case.

By observing the two plots together, it can be recognized that the system behaviour for the no friction case can be subdivided into two distinct phases, corresponding to different constraint configurations:

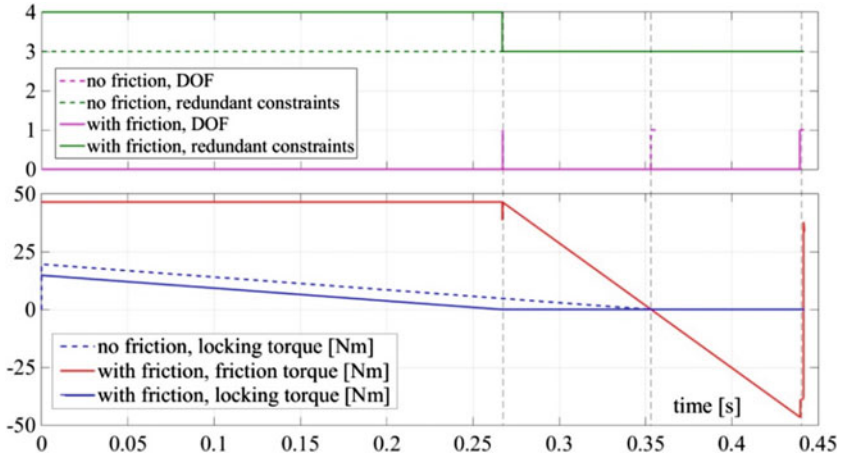


Fig. 6 Results from multibody model

- (1) from $t = 0$ to $t = T_2 = 0.35$ s: the value of the opening force (time ramp) is not sufficient to detach the hook from its stable configuration; the locking constraint on pair O is active (locking torque > 0 , see Fig. 6); in this phase, the number of d.o.f. is zero, due to the presence of the locking constraint. The three redundant constraints come out from a 3D closed loop formed by 4 revolute joints, and do not affect the planar motion of the mechanism.
- (2) as soon as the opening force F_{op} reaches the value necessary to open the hook and, correspondingly, the locking torque on pair O becomes zero ($t = T_2$), the mechanism becomes movable and the simulation terminates.

The case with friction is more complicated, as two locking effects act in parallel (angular limit on pair O, static friction on pair C). Four phases are present:

- (1) from $t = 0$ to $t = T_1 = 0.26$ s: both static friction and angular limit constraints are active, so the system is statically indeterminate in the plane (3 + 1 redundant constraints): the solver applies friction as an active force and use the angular constraint torque to balance static equilibrium (see Fig. 6);
- (2) from $t = T_1$ to $t = T_2 = 0.35$ s: the angular constraint becomes inactive and the system is statically determinate in the plane; static friction is used to prevent the hook overcoming the angular limit (*improper choice of the solver: friction should be zero and angular limit constraint should be active*);
- (3) from $t = T_2$ to $t = T_3 = 0.44$ s: the opening force reaches values sufficient to open the hook in the ideal case, so friction torque, having changed sign at T_2 , keeps the hook locked (*now correctly*);
- (4) $t = T_3 = 0.44$ s: due to the increase of the opening force ($F_{op} \approx 660$ N), the friction torque reaches its limit, the system becomes movable and the simulation terminates.

5 Conclusions

The model of a four-bar QRH has been discussed. In order to validate the analytical results and to consider also frictional effects, a multibody model of the hook has been developed. Analytical results confirms that better-behaved QRHs can be conceived by optimizing the mechanism geometry on the basis of an analytical or numerical model. Considering also the internal reaction forces and friction, a proper multi-objective index can be defined to optimize the functional and constructive design of the Quick Hook; this is the future direction of the research.

References

1. Goudey C (1982) A quick-release hook for lifeboats and offshore rigging. In: Proceedings of OCEANS 82, Washington, DC, USA, pp 728–731
2. Häkkinen K, Mäkeläinen J (1985) Efficiency and practicability of safety latches in lifting hooks. *J Occup Accid* 7(2):125–137
3. Häkkinen K (1978) Crane accidents and their prevention. *J Occup Accid* 1:353–361
4. IMO (2011) International Maritime Organization, Guidelines for evaluation of lifeboats release and retrieval systems, available online

Evolution of a Dynamic Model for Flexible Multibody Systems

P. Boscaroli, P. Gallina, A. Gasparetto, M. Giovagnoni, L. Scalera and R. Vidoni

Abstract In this paper the evolution of a dynamic model for flexible multibody systems is presented. This model is based on an equivalent rigid-link system (ERLS) and, in the first formulation, has been exploited together with a FEM approach for the modeling of planar flexible-link mechanisms. Subsequently, the model has been linearized in order to be applied for control purposes and then it has been extended to the three-dimensional case. In the last years, a modal approach has been developed and the ERLS concept has been applied in order to formulate the dynamics of spatial flexible mechanisms with a component mode synthesis (CMS) technique.

Keywords Dynamic model · Flexible multibody system · Equivalent rigid-link system · Linearization · Component mode synthesis

P. Boscaroli
University of Padova, Padua, Italy
e-mail: paolo.boscaroli@unipd.it

P. Gallina
University of Trieste, Trieste, Italy
e-mail: pgallina@units.it

A. Gasparetto (✉) · M. Giovagnoni · L. Scalera
University of Udine, Udine, Italy
e-mail: alessandro.gasparetto@uniud.it

M. Giovagnoni
e-mail: marco.giovagnoni@uniud.it

L. Scalera
e-mail: scalera.lorenzo@spes.uniud.it

R. Vidoni
University of Bolzano-Bozen, Bolzano, Italy
e-mail: renato.vidoni@unibz.it

1 Introduction

In the last 20 years, the demand for high speed operations of mechatronic systems has pushed the study of dynamic models and controllers for flexible multibody systems. An approach to model multibody dynamics is based on a rigid-body model of the mechanism, to which elastic deformations are added to take link flexibility into account: this yields a coupled set of non-linear partial differential equations. In order to obtain a finite-dimensional problem formulated by a set of ordinary differential equations from these partial differential equations, two approaches have been proposed in the literature, namely the “nodal” and the “modal” approach [7, 8, 14, 18–22, 24, 31].

Although very popular, the latter approach has the drawback to yield a system of coupled differential equations with no separation between the rigid-body motion and the elastic deformation of the flexible body. The authors of this paper carried out, throughout a period of almost 30 years, extensive research that led to the formulation and experimental validation of a dynamic model based on the nodal approach.

The model is based on the concept of Equivalent Rigid-Link System (ERLS), first introduced in [6, 26, 27]. The first studies and the original formulation of the model (2D case) were done by Giovagnoni and Rossi in the 1980s [15, 16]. Giovagnoni validated the model for a 4-link flexible mechanism in 1994 [17]. Gasparetto validated the model for a 5-link flexible mechanism [11], linearized the original model [10] and used the model to test some controllers [1–5, 9, 12, 23, 25, 32]. Vidoni et al. [28, 29] extended the model to the 3D case and developed an efficient simulator of flexible multibody systems based on the extended model [13]. Lately, the ERLS principle was used to develop a modal approach to the dynamic modelling of flexible multibody systems [30].

2 The Original Dynamic Model

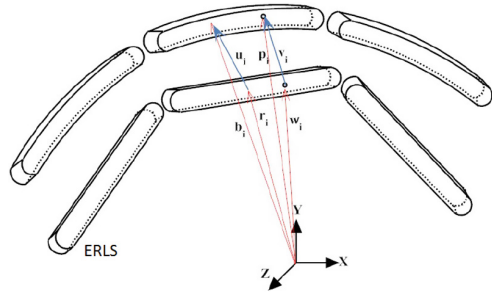
The dynamic model of flexible link multibody systems was originally developed for planar mechanisms [15, 16]. Every link is divided into finite elements, and the elastic displacements are defined with respect to an Equivalent Rigid Link Mechanism (ERLS), as shown in Fig. 1.

In Fig. 1, \vec{u} is the nodal displacement vector and the vector \vec{r} contains the positions of the nodes belonging to the ERLS. The vector \vec{p} of the position of the generic point of the finite element is given by adding the vector \vec{w} of the position of the corresponding point in the ERLS to the elastic displacement \vec{v} :

$$\vec{p} = \vec{w} + \vec{v} \quad (1)$$

Similarly, the displacements and the rotations at the nodes are given by the sum of the ERLS position and the elastic displacements:

Fig. 1 Model of the dynamic system



$$\vec{b} = \vec{u} + \vec{r} \tag{2}$$

Similar relations hold for the infinitesimal displacements $d\vec{p}$ and $d\vec{b}$.

The position, velocity and acceleration of the ERLS are functions of the vector \vec{q} of the free coordinates:

$$d\vec{r} = \vec{S}(\vec{q})d\vec{q} \tag{3}$$

$$\vec{r} = \vec{S}(\vec{q})\vec{q} \tag{4}$$

$$\vec{r} = \vec{S}(\vec{q})\vec{q} + \vec{S}(\vec{q}, \vec{q})\vec{q} = \vec{S}(\vec{q})\vec{q} + \left(\sum_k \dot{q}_k \frac{\partial \vec{S}}{\partial q_k} \right) \tag{5}$$

where $\vec{S}(\vec{q})$ is the matrix of the sensitivity coefficients for all the nodes. Once the kinematics has been defined, the dynamic equations of motion for the flexible mechanism can be obtained by applying the principle of virtual work:

$$dW^{inertia} + dW^{elastic} + dW^{external} = 0 \tag{6}$$

From Eq. (6), according to [5], two dynamic equations of motion can be obtained:

$$d\vec{u}^T \vec{M}(\vec{r} + \vec{u}) + 2d\vec{u}^T \vec{M}_C \vec{u} + d\vec{u}^T \vec{K} \vec{u} = d\vec{u}^T (\vec{f}_g + \vec{f}) \tag{7}$$

$$d\vec{r}^T \vec{M}(\vec{r} + \vec{u}) + 2d\vec{r}^T \vec{M}_C \vec{u} + d\vec{u}^T \vec{K} \vec{u} = d\vec{r}^T (\vec{f}_g + \vec{f}) \tag{8}$$

where \vec{M} is the mass matrix, \vec{M}_C the Coriolis matrix, \vec{K} the stiffness matrix of the mechanism; \vec{f}_g is the gravity vector and \vec{f} the vector of the external loads applied to the mechanism. Equation (7) formulates the nodal equilibrium, namely equivalent loads applied to every node must be in equilibrium. Equation (8) formulates the overall equilibrium, namely for any virtual displacement of the ERLS all the equivalent nodal loads produce no work. By expressing the infinitesimal displacements of the ERLS in terms of the sensitivity coefficient matrix, as in Eq. (3), the $d\vec{u}$'s and the $d\vec{r}$'s can be cancelled from Eqs. (7) and (8), thus obtaining:

$$\vec{M}(\vec{r} + \vec{u}) + 2\vec{M}_C \vec{u} + \vec{K} \vec{u} = (\vec{f}_g + \vec{f}) \tag{9}$$

$$d\vec{S}^T \vec{M}(\vec{r} + \vec{u}) + 2\vec{S}^T \vec{M}_C \vec{u} = \vec{S}^T (\vec{f}_g + \vec{f}) \tag{10}$$

which in matrix form can be written as:

$$\begin{bmatrix} \vec{M} & \vec{M}\vec{S} \\ \vec{S}^T\vec{M} & \vec{S}^T\vec{M}\vec{S} \end{bmatrix} \begin{bmatrix} \vec{\ddot{u}} \\ \vec{\ddot{q}} \end{bmatrix} = \begin{bmatrix} \vec{\Gamma}(\vec{u}, \vec{\dot{u}}, \vec{q}, \dot{q}) \\ \vec{S}^T\vec{\Gamma}(\vec{u}, \vec{\dot{u}}, \vec{q}, \dot{q}) \end{bmatrix} \tag{11}$$

Equation (11) can be imported in a simulation environment, thus computing the values of the accelerations at each step by solving the system, and obtaining the values of velocities and of displacements by integration.

The dynamic model described above was validated by means of experimental tests on real flexible-link mechanisms, by comparing the values of accelerations and elastic deformations experimentally measured with those obtained in simulation. The model was validated using a chain of four flexible bodies [17] and a five-link elastic mechanism, with two-degrees-of-freedom [11].

3 Linearization of the Model

A useful application of the dynamic model described above is the synthesis of controllers for reducing the vibrations of flexible multibody systems. To be able to do that, it is convenient to linearize Eq. (11), so as to bring the model into the state space form. The linearization of the model [10] will be briefly described in the following.

The augmented state-space vector is taken as: $\dot{x}(t) = [\vec{\dot{u}} \ \vec{\dot{q}} \ \vec{u} \ \vec{q}]^T$, so that Eq. (11) becomes:

$$\begin{bmatrix} \vec{M} & \vec{M}\vec{S} & 0 & 0 \\ \vec{S}^T\vec{M} & \vec{S}^T\vec{M}\vec{S} & 0 & 0 \\ 0 & 0 & \vec{I} & 0 \\ 0 & 0 & 0 & \vec{I} \end{bmatrix} \begin{bmatrix} \vec{\ddot{u}} \\ \vec{\ddot{q}} \\ \vec{\dot{u}} \\ \vec{\dot{q}} \end{bmatrix} = \begin{bmatrix} -2\vec{M}_G & -\vec{M}\vec{S} & \vec{K} & 0 \\ -2\vec{S}^T\vec{M}_G & \vec{S}^T\vec{M}\vec{S} & 0 & 0 \\ \vec{\Gamma} & 0 & 0 & 0 \\ 0 & \vec{\Gamma} & 0 & 0 \end{bmatrix} \begin{bmatrix} \vec{\dot{u}} \\ \vec{\dot{q}} \\ \vec{u} \\ \vec{q} \end{bmatrix} + \begin{bmatrix} \vec{M} & \vec{I} \\ \vec{S}^T\vec{M} & \vec{S}^T \end{bmatrix} \begin{bmatrix} \vec{g} \\ \vec{f} \end{bmatrix} \tag{12}$$

In a more compact form:

$$\vec{A}(\vec{x}(t))\vec{\dot{x}}(t) = \vec{B}(\vec{x}(t))\vec{x}(t) + \vec{C}(\vec{x}(t))\vec{v}(t) \tag{13}$$

where the matrices \vec{A} , \vec{B} and \vec{C} do not depend on the input vector \vec{v} . However, the system in Eq. (12) is still non-linear, because the matrix \vec{S} contains the values of the velocities $\vec{\dot{q}}$ of the free coordinates, so quadratic terms appear. If an equilibrium point \vec{x}_e, \vec{v}_e is chosen, we can write: $\vec{x}(t) = \vec{x}_e + \Delta\vec{x}(t)$, $\vec{v}(t) = \vec{v}_e + \Delta\vec{v}(t)$, so Eq. (13) becomes:

$$\vec{A}(\vec{x}_e)\Delta\vec{\dot{x}}(t) = \vec{B}(\vec{x}_e + \Delta\vec{x}(t))(\vec{x}_e + \Delta\vec{x}(t)) + \vec{C}(\vec{x}_e + \Delta\vec{x}(t))(\vec{v}_e + \Delta\vec{v}(t)) \tag{14}$$

where it has been taken into account that $\vec{\dot{x}}_e = 0$ for definition of equilibrium point, and the approximation: $\vec{A}(\vec{x}_e + \Delta\vec{x}(t))\Delta\vec{\dot{x}}(t) \cong \vec{A}(\vec{x}_e)\Delta\vec{\dot{x}}(t)$ has been used. The final expression for the system linearized about the equilibrium state is:

$$\vec{A}(\vec{x}_e)\Delta\vec{x}(t) = \left[\vec{B}(\vec{x}_e) + \left(\left. \frac{\partial \vec{B}}{\partial \vec{x}} \right|_{\vec{x}=\vec{x}_e} \otimes \vec{x}_e \right) + \left(\left. \frac{\partial \vec{C}}{\partial \vec{x}} \right|_{\vec{x}=\vec{x}_e} \otimes \vec{v}_e \right) \right] \Delta\vec{x}(t) + \vec{C}(\vec{x}_e)\Delta\vec{v}_e(t) \quad (15)$$

where the “ \otimes ” symbol is meant to indicate the inner product of each vector $\left[\frac{\partial B_{i,1}}{\partial x_j} \dots \frac{\partial B_{i,n}}{\partial x_j} \right]_{x=\vec{x}_e}$, for any i and j , by the vectors \vec{x}_e and \vec{v}_e . Once the equilibrium point \vec{x}_e is set, defining the matrices $\vec{A}(\vec{x}_e)$, $\vec{B}(\vec{x}_e)$ and $\vec{C}(\vec{x}_e)$ is straightforward, and the matrices $\left(\left. \frac{\partial \vec{B}}{\partial \vec{x}} \right|_{\vec{x}=\vec{x}_e} \otimes \vec{x}_e \right)$ and $\left(\left. \frac{\partial \vec{C}}{\partial \vec{x}} \right|_{\vec{x}=\vec{x}_e} \otimes \vec{v}_e \right)$ can be computed according to their definitions.

The dynamic model described above was then used in order to test in simulation several vibration controllers for flexible multibody systems. For instance, a PID regulator [9], an optimal controller [12], a model predictive controller [1, 2, 23], a delayed reference control [4], as well as hybrid controllers [3, 5, 25] were synthesized and tested, yielding good results. Moreover, the model could be employed in connection with innovative simulation techniques, such as the Hardware-in-the-Loop [32].

4 Extension to the 3D Case

The dynamic model described in this paper was originally intended for planar mechanisms. However, although planar mechanisms are an important category of multibody systems (many industrial machines are based on planar mechanisms), it was convenient to study a dynamic model for 3D mechanisms. As it is known, the extension from the 2D to the 3D case is not straightforward. The 3D dynamical model, based on the considerations above extended to the 3D case, was described in [28, 29]. The extension to the 3D system was done by collocating several reference frames along the kinematic chain, according to the Denavit-Hartenberg rules, and by defining the transformation matrices between any two consecutive frames. So, by using a local to global transformation matrix $\vec{R}_i(\vec{q})$, a block-diagonal rotation matrix $\vec{T}_i(\vec{q})$ and an interpolation function matrix $\vec{N}_i(\vec{x}_i, \vec{y}_i, \vec{z}_i)$, one can compute the virtual displacements in the fixed reference frame and the acceleration of a generic point inside the i -th finite element.

As in the 2D case, after defining the kinematics, the dynamic equations of motion can be computed by means of the principle of virtual work, by adding the inertial, elastic and external generalized force terms:

$$dW^{inertia} + dW^{elastic} = -dW^{external} \quad (16)$$

$$\sum_i \int_{v_i} \delta \vec{p}_i^T \vec{p}_i \rho_i d\vec{v} + \sum_i \int_{v_i} \delta \vec{E}_i^T \vec{D}_i \vec{\epsilon}_i d\vec{v} = \sum_i \int_{v_i} \delta \vec{p}_i^T \vec{g}_i \rho_i d\vec{v} + (\delta \vec{u}^T + \delta \vec{r}^T) \vec{f} \quad (17)$$

where ρ_i , \vec{D}_i and ε_i are the mass density, the stress-strain matrix and the strain vector for the i -th element, \vec{g} is the gravity acceleration vector and \vec{f} is the vector of the external forces and torques. As in the 2D case, the nodal elastic virtual displacements $\delta\vec{u}$ and virtual displacements of the ERLS $\delta\vec{r}$ are independent, which yields two set of equilibrium equations, namely those expressing the local and the global equilibrium at the nodes:

$$\vec{M}(\vec{\ddot{r}} + \vec{\ddot{u}}) + 2(\vec{M}_{G1} + \vec{M}_{G2})\vec{\ddot{u}} + (\vec{M}_{C1} + 2\vec{M}_{C2} + \vec{M}_{C3})\vec{\ddot{u}} + \vec{K}\vec{u} = (\vec{f}_g + \vec{f}) \quad (18)$$

$$\vec{J}^T \vec{M}(\vec{\ddot{r}} + \vec{\ddot{u}}) + 2\vec{J}^T(\vec{M}_{G1} + \vec{M}_{G2})\vec{\ddot{u}} + \vec{J}^T(\vec{M}_{C1} + 2\vec{M}_{C2} + \vec{M}_{C3})\vec{\ddot{u}} = \vec{J}^T(\vec{f}_g + \vec{f}) \quad (19)$$

where \vec{M} is the mass matrix, \vec{M}_{G1} and \vec{M}_{G2} are the Coriolis' terms, \vec{M}_{C1} , \vec{M}_{C2} and \vec{M}_{C3} the centrifugal stiffness terms, \vec{K} the stiffness matrix, \vec{J} the Jacobian matrix, and \vec{f}_g the vector of the equivalent nodal loads due to gravity. In order to make the model more realistic, Rayleigh damping was considered and inserted in the model, (α and β coefficients). In matrix form, one can write:

$$\begin{bmatrix} \vec{M} & \vec{M}\vec{J} \\ \vec{J}^T \vec{M} & \vec{J}^T \vec{M}\vec{J} \end{bmatrix} \begin{bmatrix} \vec{\ddot{u}} \\ \vec{\ddot{q}} \end{bmatrix} = \begin{bmatrix} -2(\vec{M}_{G1} + \vec{M}_{G2}) - \alpha\vec{M} - \beta\vec{K} & -\vec{M}\vec{J} & -(\vec{M}_{C1} + 2\vec{M}_{C2} + \vec{M}_{C3}) - \vec{K} \\ \vec{J}^T(-2(\vec{M}_{G1} + \vec{M}_{G2}) - \alpha\vec{M}) & -\vec{J}^T \vec{M}\vec{J} & -\vec{J}^T(\vec{M}_{C1} + 2\vec{M}_{C2} + \vec{M}_{C3}) \end{bmatrix} \begin{bmatrix} \vec{\ddot{u}} \\ \vec{\ddot{q}} \\ \vec{\ddot{q}} \end{bmatrix} + \begin{bmatrix} \vec{M} & \vec{I} \\ \vec{J}^T \vec{M} & \vec{J}^T \end{bmatrix} \begin{bmatrix} \vec{g} \\ \vec{f} \end{bmatrix} \quad (20)$$

which can be used to run the integration-based simulations.

The 3D model was validated by means of experimental tests, by comparing the measured accelerations and deformations with those provided by simulations [13].

5 From a Nodal to a Modal Approach

In the models described in the foregoing, either 2D or 3D, the ERLS concept has been exploited together with a FEM approach, namely a nodal approach. The latest studies developed an ERLS-based model which could be employed also within a framework based on a modal approach [30]. In this way, one can obtain a more flexible solution based upon a reduced-order system of equations. This is the first work in the literature in which the ERLS concept is used to formulate the dynamics of 3D flexible mechanisms with a component mode synthesis (CMS) approach. The core of the method lies in expressing the nodal displacements \vec{u}_i of the i -th link as functions of a given number of eigenvectors \vec{U}_i and modal coordinates \vec{q}_i , namely:

$$\vec{u}_i = \vec{U}_i \vec{q}_i \quad (21)$$

By introducing the local-to-local transformation matrix $\vec{T}_{i+1,i}(\theta)$ between the two reference frames of the ELRS associated to the two consecutive links i and $i + 1$:

$$\vec{u}_{i+1} = \vec{T}_{i+1,i} \vec{u}_i \tag{22}$$

one obtains the following equation:

$$\vec{S}_{i+1} \vec{U}_{i+1} \vec{q}_{i+1} = \vec{T}_{i+1,i}(\theta) \vec{S}_i \vec{U}_i \vec{q}_i \tag{23}$$

which can be rewritten as:

$$\left[-\vec{T}_{i+1,i}(\theta) \vec{S}_i \vec{U}_i \quad \vec{S}_{i+1} \vec{U}_{i+1} \right] \begin{bmatrix} \vec{q}_i \\ \vec{q}_{i+1} \end{bmatrix} = 0 \tag{24}$$

or:

$$\vec{C}(\vec{\theta}) \vec{q} = 0 \tag{25}$$

where \vec{S}_i is the joint displacements selecting matrix, $\vec{C}(\vec{\theta})$ is a band-diagonal matrix, \vec{q} is the modal coordinate vector and $\vec{\theta}$ is the joint parameter one. Starting from this, a quite long dissertation is carried out, in order to get a model. This was then validated by comparing the results of the simulator with those provided by ADAMS-Flex™ software for the same benchmark mechanism (a 3D L-shaped link).

6 Conclusions

In this work, the evolution of a dynamic model for flexible multibody systems, from the original formulation in the 1990s up to the latest developments, was presented. The model is based on an equivalent rigid-link system and originally has been exploited together with a FEM approach for the modeling of planar flexible-link mechanisms. Subsequently, the model has been linearized for control purposes and then it has been extended to the three-dimensional case. In the last years, a modal approach has been developed and the ERLS concept has been applied in order to formulate the dynamics of spatial flexible mechanisms with a component mode synthesis (CMS) technique. In this way, a more flexible solution based upon a reduced-order system of equations can be obtained.

References

1. Boscariol P, Gasparetto A, Zanotto V (2010) Active position and vibration control of a flexible links mechanism using model-based predictive control. ASME J Dyn Syst Measur Control 132(1)
2. Boscariol P, Gasparetto A, Zanotto V (2010) Model predictive control of a flexible links mechanism. J Intell Robot Syst 58(2)
3. Boscariol P, Gasparetto A, Zanotto V (2011) Simultaneous position and vibration control system for flexible link mechanisms. Meccanica 46(4)

4. Boschetti G, Richiedei D, Trevisani A (2012) Delayed reference control applied to flexible link mechanisms: a scheme for effective and stable control. *J Dyn Syst Measur Control* 134(1):011003
5. Caracciolo R, Richiedei D, Trevisani A, Zanutto V (2005) Robust mixed-norm position and vibration control of flexible link mechanisms. *Mechatronics* 15:767–791
6. Chang L, Hamilton J (1991) The kinematics of robotic manipulators with flexible links using an equivalent rigid link system (ERLS) model. *ASME J Dyn Syst Measur Control* 113:48–53
7. Dietz S, Wallrapp O, Wiedemann S (2003) Nodal vs. modal representation in flexible multi-body system dynamics. In: Jorge AC Ambrosio (ed) *Proceedings of ECCOMAS thematic conference multibody 2003—Advances in computational multi-body dynamics*, vol MB2003-044, Lisbon, Portugal: Instituto Superior Tecnico, IDMEC/IST, 1–4 July 2003
8. Dwivedy S, Eberhard P (2006) Dynamic analysis of flexible manipulators, a literature review. *Mech Mach Theory* 41:749–777
9. Gallina P, Gasparetto A, Rosati G, Rossi A (2002) Design of a PID controller for a flexible five-bar closed-chain planar manipulator. In: *Proceedings of the 14th CISM-IFTOMM symposium on robotics—RoManSy 2002*, Udine, 1–4 luglio 2002
10. Gasparetto A (2001) Accurate modelling of a flexible-link planar mechanism by means of a linearized model in the state-space form for design of a vibration controller. *J Sound Vib* 240(2):241–262
11. Gasparetto A (2004) On the modeling of flexible-link planar mechanisms: experimental validation of an accurate dynamic model. *ASME J Dyn Syst Measur Control* 126(2):365–375
12. Gasparetto A, Zanutto V (2006) Vibration reduction in a flexible-link mechanism through synthesis of an optimal controller. *Meccanica* 41(6):611–622
13. Gasparetto A, Kiaeian Moosavi SAH, Boscarì P, Giovagnoni M (2013) Experimental validation of a dynamic model for lightweight robots. *Int J Adv Robot Syst* 182:1–7
14. Ge S, Lee T, Zhu G (1997) Nonlinear feedback controller for a single-link flexible manipulator based on finite element model. *J Robot Syst* 14:165–178
15. Giovagnoni M, Piccoli H, Rossi A (1987) Finite elements and sensitivity coefficients in flexible planar linkage analysis. *Meccanica* 22:157–162
16. Giovagnoni M, Rossi A (1989) Transient analysis of a flexible crank. *Mech Mach Theory* 24(4):231–243
17. Giovagnoni M (1994) A numerical and experimental analysis of a chain of flexible bodies. *ASME J Dyn Syst Measur Control* 116:73–80
18. Kalra P, Sharan A (1991) Accurate modeling of flexible manipulators using finite element analysis. *Mech Mach Theory* 26:299–313
19. Martins J, Mohamed Z, Tokhi M et al (2003) Approaches for dynamic modelling of flexible manipulator systems. In: *Proceedings of the IEEE conference on control theory applications*, vol 150, July 2003, pp 401–411
20. Naganathan G, Soni A (1988) Nonlinear modeling of kinematic and flexibility effects in manipulator design. *ASME J Mech Transm Autom Des*
21. Nagarajan S, Turcic D (1990) Lagrangian formulation of the equations of motion for elastic mechanisms with mutual dependence between rigid body and elastic motions. Part I: Element level equations. *ASME J. Dyn Syst Measur Control*
22. Shabana A (1997) Flexible multibody dynamics: review of past and recent developments. *Multibody Syst Dyn* 1:189–222
23. Shojaei BE, Gasparetto A (2015) Predictive control of spatial flexible mechanisms. *Int J Mech Control* 16(1)
24. Theodore R, Ghosal A (1995) Comparison of the assumed modes method and finite element models for flexible multilink manipulators. *Int J Robot Res* 14:91–111
25. Trevisani A (2003) Feedback control of flexible four-bar linkages: a numerical and experimental investigation. *J Sound Vib* 268:947–970
26. Turcic D, Midha A (1984) Dynamic analysis of elastic mechanism systems. Part i: Applications. *ASME J Dyn Syst Measur Control*

27. Turcic D, Midha A (1984) Generalized equations of motion for the dynamic analysis of elastic mechanism systems. *ASME J Dyn Syst Measur Control*
28. Vidoni R, Gasparetto A, Giovagnoni M (2013) Design and implementation of an ERLS-based 3-D dynamic formulation for flexible-link robots. *Robot Comput Integr Manuf* 29:273–282
29. Vidoni R, Gasparetto A, Giovagnoni M (2014) A method for modeling three-dimensional flexible mechanisms based on an equivalent rigid link system. *J Vib Control* 20:483–500
30. Vidoni R, Gallina P, Boscariol P, Gasparetto A, Giovagnoni M (2015) Modeling the vibration of spatial flexible mechanisms through an equivalent rigid link system/component mode synthesis approach. *J Vib Control*. Published online before print on September 9, 2015
31. Wang D, Lu Y, Liu Y et al (1996) Dynamic model and tip trajectory tracking control for a two-link flexible robotic manipulator. In: *Proceedings of the IEEE conference on system, man and cybernetics*, Beijing, 14–17 October 1996, pp 1020–1024
32. Zanutto V, Gasparetto A, Lanzutti A, Boscariol P, Vidoni R (2011) Experimental validation of minimum time-jerk algorithms for industrial robots. *J Intell Robot Syst* 64(2):197–219

Anti-hedonistic Mechatronic Systems

Lorenzo Scalera, Paolo Gallina, Alessandro Gasparetto
and Marco Giovagnoni

Abstract In this paper the concept of anti-hedonistic mechatronic systems interacting with humans is discussed. Up to this time, people have used their creativity to design machines which could reduce human efforts (i.e. robots) or enhance the perceived pleasure (i.e. entertainment tools and virtual reality systems). Nowadays, new machines designed to prevent people from doing something are emerging. Examples are: intragastric balloons to prevent people from eating, timed cigarettes boxes to prevent people from smoking, bracelets to prevent people from nail biting, alcohol-testers connected to car starter to avoid driving under alcohol influence. The aim of this work is to present a survey about anti-hedonistic machines, providing general definitions and a possible classification. In particular a mechatronic system designed to motivate users to do push-ups exercises, by controlling the television energy supply, is presented.

Keywords Anti-hedonistic machine • Mechatronic systems • Human-machine interaction • Precommitment • Biomechanics

L. Scalera · A. Gasparetto · M. Giovagnoni
University of Udine, Udine, Italy
e-mail: scalera.lorenzo@spes.uniud.it

A. Gasparetto
e-mail: alessandro.gasparetto@uniud.it

M. Giovagnoni
e-mail: marco.giovagnoni@uniud.it

P. Gallina (✉)
University of Trieste, Trieste, Italy
e-mail: pgallina@units.it

1 Introduction

In the field of Human-Machine Interaction (HMI), the term *anti-hedonistic machines* (AHMs) refers to a new kind mechatronic systems designed to prevent people from feeling immediate pleasure. In other words, AHMs should be able to limit or inhibit the chance to reach an immediate and instinctive pleasure.

Every AHM needs the user to be aware about the aim of the machine itself before starting to use it. The initial awareness is fundamental for the correct functionality and efficiency of such a machine. In fact, people using AHMs need to know that, in a short time, their willpower would weaken and have to accept in advance the deprivation effects and the discomfort conditions which the machine would cause to them [5, 6].

This concept could be explained through the myth of Ulysses. According to the myth, the greek warrior ordered to the crew to be tied to the mast when his mind was still clear, in order to avoid to succumb to siren flatteries when his mind would have been benighted. Another example could be taken from italian literature. It is known the firm decision of Vittorio Alfieri, who ordered to his servant to be tied to his chair for the purpose of finish the tragedy he was writing as soon as possible. The playwright in fact kept putting off the tragedy writing because of his attractions for other pleasure situations [4]. In both Ulisse's and Alfieri's example it is possible to identify the ropes as a rudimental but efficient example of AHM.

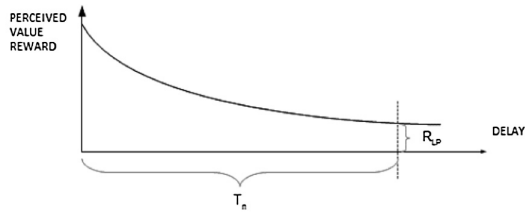
Taking advantage of an artifact planned in the present to modify or restrict someone's freedom of choice in the future is a concept that attracted considerable interest in the last few years, in particular referring to the notion of precommitment [5, 6, 16]. Using an AHM could be read as the outsourcing of a person own willpower: to delegate out of the mind choices which could be advantageous in the long future.

The main contribution of this paper is the definition of AHMs, providing the main operating principle and a possible classification. The concept is discussed for a real scenario, namely a mechatronic system designed to motivate users to do push-ups exercises based on precommitment concept.

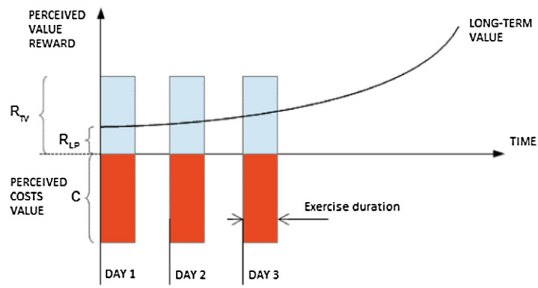
2 Operating Principles

To better understand AHMs operating principles first of all it is necessary to consider that every time someone have to make a choice, he assigns a value to all the possible alternatives he has. In most cases the perceived value associated to a reward decays according to the delay with which it is possible to benefit from the reward [11, 15]. This concept is explained in Fig. 1a. The horizontal axis indicates the reward delay and the vertical one shows the amount of value perceived for that reward. The more the delay increases, the more the perceived value is affected by a higher *temporal discount*. In literature curves that model the perceived value decay are characterised by an exponential or hyperbolic trend [1].

Fig. 1 Graphical visualization of *temporal discounting* concept



(a) Perceived value reward over time.



(b) Perceived value reward, costs and machine reward over time.

If an artifact or a machine interacts with someone to change his own choices and make the precommitment effective, not only the temporal discount but also the costs, which the subject have to pay to reach the reward, should be considered [14].

For example, going to the gym is for many people a way to gain an excellent physical condition, which is the reward pursued by them in the long term. The value perceived from this reward is not constant over time but it is subjected to a temporal discount. In fact, if only it was enough to do a single exercise to gain the perfect physical condition, the value perceived from the reward would be great. On the other side, if it was need to do exercises for years this value would definitely decrease. In particular, the degrowth of this value is proportional to the delay with which the result would appear.

For further explain AHMs role in precommitment scheme, the symmetrical to the vertical axis curve of temporal discounting is used (Fig. 1b). In this case, the value R_{LP} in $t = 0$ represents the discounted value of the reward for a delay equal to T_n , which is to the value assigned to the perfect physical condition.

Doing physical exercises involves a considerable amount of energy and a sort of discomfort that becomes a cost in the amount of motivations needed to take a decision. The cost C contrasts the motivational effect of the reward. As it is shown in Fig. 1b, this cost is constant during the exercise and is null after this one. The figure shows that at the beginning costs are higher than the long term reward.

$$R_{LP} + C < 0 \tag{1}$$

This inequality can explain that, if costs are higher than the perceived reward, the exercise would not be done.

The mechatronic system presented in Sect. 4 operates right at this stage, introducing a third contribute to Eq. (1). Having recognised the correct execution of the exercise (a set of push-ups in the presented case), the machine could allow the switching on of the television by means of control system. If instead the exercise has not been executed, the television will not be switched on. The possibility of watching television is to be considered a third reward, named *machine reward*. This last is indicated with R_{TV} and, for sake of simplicity, it could be considered a constant during the exercise execution (as the matter of fact R_{TV} could change over time). The machine reward increases the one related to the perfect physical condition. Finally, it is possible to conclude that someone would execute push-ups exercises only in the event in which Eq. (2) is verified.

$$R_{TV} + R_{LP} + C < 0 \tag{2}$$

In Sect. 3 a classification of different types of artifacts and mechatronic systems, which induce or drive away someone to do an action, is proposed.

3 Classification of Anti-hedonistic Machines

AHMs can operate in large variety of modalities, introducing a reward or a deterrent which could persuade someone from misbehaving. In Fig. 2 a classification (non-exhaustive) of these machines and systems is proposed.

The matrix columns indicate the manner in which AHMs operate: from a motivational reward to a inhibitory high cost, such as psychological discomfort or distress. The rows show the different ways in which an AHM could be implemented: autonomously, with human mediating, up to an artificial intelligence (AI) support.

To this regard, AI agents, such as chatbots or artificial personal assistants, could play a significant role in preventing undesired behaviours.

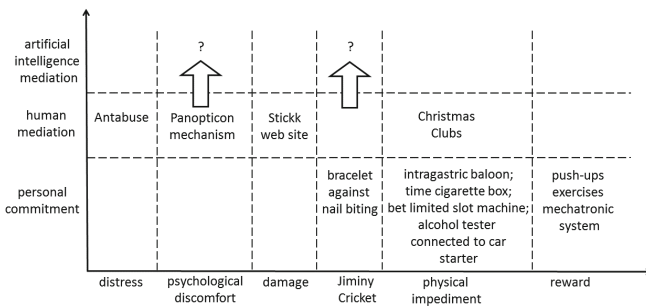


Fig. 2 Anti-hedonistic machines classification matrix

The push-ups exercises mechatronic system, integrated with television control, introduces a reward and does not need an external human mediator to operate. It is positioned in the right-bottom side of the matrix.

A machine for physical exercises could also be integrated with a software able to modify the present body shape of the user, virtually showing the benefit of a long term exercise training on his body [7]. This is a sort of virtual reward.

A second class of AHMs is based on the concept of physical impediment. In this category, intragastric balloon, time cigarette box, bet limited slot machine and alcohol tester connected to car starter could be found. The first is a technology developed to treat obesity and it consists in a balloon which partially fills the stomach and limits the food intake [8]. The intragastric balloon certainly constitutes an AHM developed to recover the imbalance caused by *evolutionary mismatch*: the mismatch between hereditary features of individuals, which are adapted for a past resource-poor environment, and the present context, unfit for that hereditary features [9, 12, 18].

The second artifact is a small box which prevents people from immoderately smoking, providing cigarettes only after a pre-set timing. Obviously, it is not possible to damage this kind of machine without introducing another cost.

Bet limited slot machines are a deterrent for pathological gambling, presetting the max upper game limit above which it is not more possible to bet [13].

Another impediment-based mechanical system is an alcohol-tester connected to car starter: before playing the engine it is necessary to blow in a pipe and if the detected alcohol level is higher than the permitted one, the car do not start.

In the same column, but in the “human mediation” row, it is possible to find an example of bank transfer which can be considered as an AHM. *Christmas Club* were deposit funds very popular in the USA during the recession of the 1930s. Every week a tiny amount of money was transferred on the fund and the total amount would be given back only during Christmas time [17].

On the left column *Jiminy Cricket* concept based machines could be found. The cricket acted as Pinocchio’s conscience; in the same manner, machines belonging to this category are *reminders* for people using them. An example is given by special non-removable bracelets which prevent people from nail biting [10].

Moving to the left in the matrix, AHMs developed for strong and persuasive actions can be found. Because of the potential dangerous impact of the machine, without the mediation of specialist staff, the “personal commitment” box in this column is empty. www.stickk.com is a website in which it is possible to publish a personal commitment. At the same time the user has to transfer to the website an amount of money, which would not be given back if the goal has not been reached [2].

Psychological discomfort-based machines operate by means of the *panopticon* mechanism [3]. The term means “to monitor everything” and it refers to the ethical and correct behaviour of someone who knows to be under control. *Lifelogging* is an example of this group of emerging technologies which include all wearable sensors enabled to collect visual and biometric informations about a person and make them available to community through social networks.

On the far left column of the matrix distress-based machines are allocated. Disulfiram, better known as Antabuse, is a medicine used in the treatment of chronic alco-

holism by producing the effects of a “hangover” if alcohol is consumed. It works as a real AHM which uses a chemical deterrent to prevent people from drinking alcohol. Human mediating, as the doctor who prescribes it, is strictly required.

4 Push-ups Exercises Mechatronic System

In the present section a push-ups exercises mechatronic system is presented.

As described in Sect. 2, this machine induces the user in doing push-ups introducing a reward (indicated with R_{TV} in Eq. (2)): the possibility of watching television if the exercises have been correctly done; or a deterrent: the impossibility of switching on the lighting or powering the fridge. In Fig. 3 an operating scheme of the AHM is shown.

The mechatronic prototype is composed by a gym push-ups tool, on which a measurement set-up is installed, a data acquisition system and a control device which activates the television energy supply. Data from fitness exercises are provided by two VISHAY BAK 200 strain gauges mounted on the metal bar of the tool, which are able to detect the bar deformation during the exercises.

The bar displacement is transduced into a voltage signal by means of strain gauges, which are integrated in a full Wheatstone bridge. This analogue signal is filtered and converted into a digital one in a EMANT 380 DAQ module and it is sent to a computer by means of a Bluetooth connection. The signal is analysed by a control software implemented in Python environment and based on a simple machine learning algorithm, which compares each training session with a reference one. This last has to be executed in a proper manner in the initial phase, when the user is determined and his willpower still strong.

After the signal analysis, the control system returns in output a boolean variable which closes or opens a switch depending on the outcome of the check. If the exercises are correctly executed, the switch will be closed and the television could be switched on. If no, the digital output consists in a *false* constant and the power line

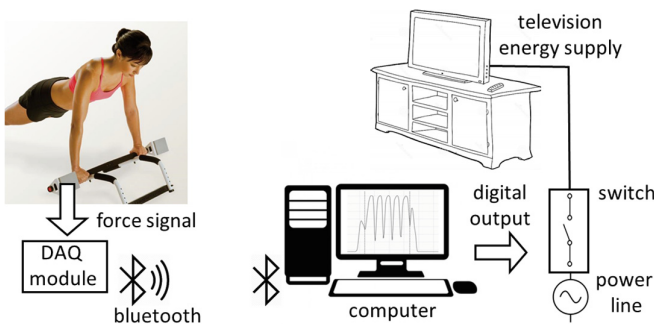


Fig. 3 Anti-hedonistic mechatronic system operating scheme

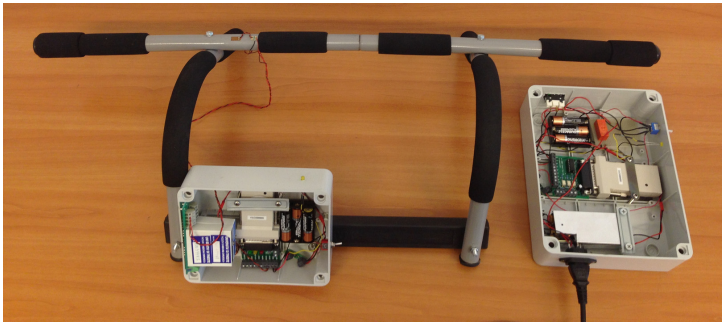
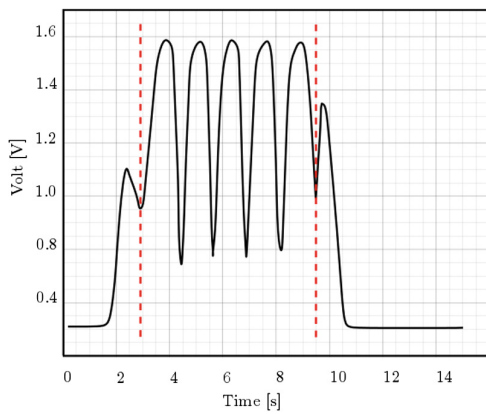


Fig. 4 Push-ups exercises mechatronic system

Fig. 5 Graphical representation of voltage trend during push-ups exercise



will be interrupted. Furthermore, the system is programmed in a way that it requires a daily amount of exercises.

In Fig. 4 a picture of the push-ups tool is shown. On the left-back side the DAQ module can be seen and, on the right side, the control system box with the switch of the 220 V electric current, is reported. The mechanical system has been developed in such a way to prevent the user from easily bypassing the switch.

Fig. 5 shows a graphical representation of strain gauges signal trend versus time during a push-ups exercise, related to an execution of five push-ups. The lowest points in the graph are related to the moments in which the slope of the push begins, while the peaks are correlated to the beginning of the rise, when the bending moment is maximum. As it can be seen from the graph, two fictitious peaks, the first and the last one, are present. These two are correlated to the load stage, in which the user grasps the tool with his hands, and the discharge phase, moment in which the exercise is finished. This two fictitious peaks have to be necessarily discarded. Therefore, the signal compared with the reference one is only the section included between the two red and dotted vertical lines.

5 Conclusions

In this paper the concept of anti-hedonistic machines interacting with humans has been proposed. A general definition and the operating principles of this new technologies have been provided and, in particular, the concepts of *precommitment*, *temporal discounting*, *cost* and *machine reward* have been investigated.

Different examples have been discussed and a classification (non-exhaustive) of these machines has been proposed. In this context, the manners in which artifacts operate and the ways in which they could be implemented have been exposed.

To validate the illustrated concept, a prototype of anti-hedonistic mechatronic system, designed to motivate users to do fitness exercises by controlling the television energy supply, has been developed.

References

1. Ainslie G (1992) *Picoeconomics: the strategic interaction of successive motivational states within the person*. Cambridge University, New York
2. Appel J, Karlan D (2011) More than good intentions. Dutton Press, pp 160–161
3. Bentham J (1995) The panopticon writings. In: Bozovic M (ed) London
4. D'ambra L (1938) *Il tragedia legato alla sedia*. Zanichelli Editore
5. Elster J (1979) *Ulysses and the sirens*. Cambridge University Press, Cambridge
6. Elster J (2000) *Ulysses unbound*. Cambridge University Press, Cambridge
7. Fox J, Bailenson JN (2009) Virtual self-modeling: the effects of vicarious reinforcement and identification on exercise behaviors. *Media Psychol* 12:1–25
8. Göttig S, Weiner RA, Daskalakis M (2009) Preoperative weight reduction using the intragastric balloon. *Obes Facts* 2:20–23
9. Kelley AE, Berridge KC (2002) The neuroscience of natural rewards: relevance to addictive drugs. *J Neurosci* 22:3306–3311
10. Koritzky G, Yechiam E (2011) On the value of nonremovable reminders for behavior modification: an application to nail-biting (onychophagia). *Behav Modif* 35:511–530
11. Mazur JE (1997) Choice, delay, probability, and conditioned reinforcement. *Anim Learn Behav* 25:131–147
12. Nesse RM, Berridge KC (1997) Psychoactive drug use in evolutionary perspective. *Science* 278:63–66
13. Nower L, Blaszczynski A (2010) Gambling motivations, money-limiting strategies and precommitment preferences of problem versus non-problem gamblers. *J Gambli Stud* 26:361–372
14. Paglieri F (2013) The costs of delay: waiting versus postponing in intertemporal choice. *J Exp Anal Behav* 99:362–377
15. Raiff BR, Yoon J (2010) From bench to bedside: a review of Impulsivity: the behavioral and neurological science of discounting. *Behav Process* 84:632–633
16. Schelling TC (1966) *Arms and influence*. Yale University Press, New Haven, CN
17. Strotz RH (1955) Myopia and inconsistency in dynamic utility maximization. *Rev Econ Stud* 23:165–180
18. Tooby J, Cosmides L (1990) The past explains the present: emotional adaptations and the structure of ancestral environments. *Ethol Sociobiol* 11:375–424

On the Use of Cable-Driven Robots in Early Inpatient Stroke Rehabilitation

G. Rosati, S. Masiero and A. Rossi

Abstract Cable-driven robots are a special class of manipulators in which the end-effector is actuated by cables, rather than by actuators connected to rigid links. Their use in early inpatient stroke rehabilitation has been extensively investigated by the research group led by Prof. Aldo Rossi at University of Padua, Italy. Both cable suspended solutions (NeReBot, MariBot) and planar designs (Sophia-3) have been considered. Among them the NeReBot, a prototype underactuated cable suspended robot, has been clinically tested in early upper-limb rehabilitation of severely impaired stroke survivors. Results were encouraging, both with additional and with substitutive robotic treatment protocols, in comparison to standard stroke rehabilitation therapy. This paper presents the concept, results and benefits provided by the use of cable robot technology in stroke rehabilitation.

1 Introduction

This paper presents an overview on the use of cable robot technology in rehabilitation of the proximal upper-limb post-stroke. Stroke is a leading cause of death and disability in the USA and Europe, and the number of stroke survivors requiring rehabilitation is climbing rapidly due to population aging [12]. Robots have been proposed in the recent past as adjunctive tools that increase the intensity of rehabilitation therapies in stroke patients [10, 11]. Not only rehabilitation robots allow a single therapist to assist several subjects together, but also they allow to enrich the sensorimotor experience of the patient, while increasing at the same time the repeatability of therapies and the measurability of outcome [19]. Such general concepts have been declined in disparate ways by researchers and companies, leading to the development of many different robotic solutions, ranging from exoskeletons to

G. Rosati (✉) · A. Rossi

Department of Management and Engineering, University of Padua,
via Venezia 1, I-35131 Padua, Italy
e-mail: giulio.rosati@unipd.it

S. Masiero

Department of Neuroscience, University of Padua, via Giustiniani 2, I-35128 Padua, Italy

© Springer International Publishing AG 2017

G. Boschetti and A. Gasparetto (eds.), *Advances in Italian Mechanism Science*,
Mechanisms and Machine Science 47, DOI 10.1007/978-3-319-48375-7_59

end-effector devices, from planar to three-dimensional architectures, from electrical to pneumatic actuation, etc. [26, 40].

Cable-driven parallel robots (CDPRs) are a special class of parallel manipulators in which the end-effector is directly actuated by cables [3, 23]. Applications of cable robots range from heavy load and large scale manipulation [1, 2] to rescue operations [21, 39] and entertainment [5]. CDPRs bring many peculiar advantages provided by their characteristics: they have a lightweight structure with small moving inertias and a large workspace, with a high potential in terms of modularity, adaptability and flexibility [9, 29], despite the reduced manufacturing and maintenance costs; they also possess intrinsically safe features due to cable flexibility, which allow for safe manipulation in close proximity to humans [4]. Disadvantages include redundancy (as cables are mono-lateral actuators) and interference between cables and environment.

2 Concept

The concept behind using cable robot technology in proximal upper-limb rehabilitation lies in the need for building simple and portable robotic devices, able to assist the patient in the execution of natural movements of the arm in a mechanically compliant way [14]. The rationale for building robotic devices that allow natural movements is that motor training shows specificity of learning; that is, people improve most at the movements they practice [37]. Compliance is a second, fundamental feature of rehabilitation robotic devices, not only because it allows for safe human-robot interaction, but mainly because it preserves the causal relationship between patient effort and resulting arm movement, even when robotic assistance is provided [41]. Moreover, robot compliance allows patients to make movement errors (that would not be permitted by a stiff controller), and this helps stimulate motor learning, which is an error-driven process [37]. From this perspective, simple, lightweight structures are preferable with respect to rigid robotic links, as the robot-mediated exercise must be as close as possible to the free motion of the arm.

2.1 *Rehabilitation of the Upper-Limb by Cable Suspended Devices*

The NeReBot [6, 15] was conceived to fit as much as possible such requirements. In this robot (Fig. 1a), the upper limb of the patient is supported and manipulated by three cables, operated independently by electric motors [32]. The main advantage of this design is, among others, that the compliance is given by the kinematic structure itself (which is under-actuated) and by the choice of using unilateral (cable) actuation. In this way, *compliance* is obtained *by design*: cables can assist the motion of

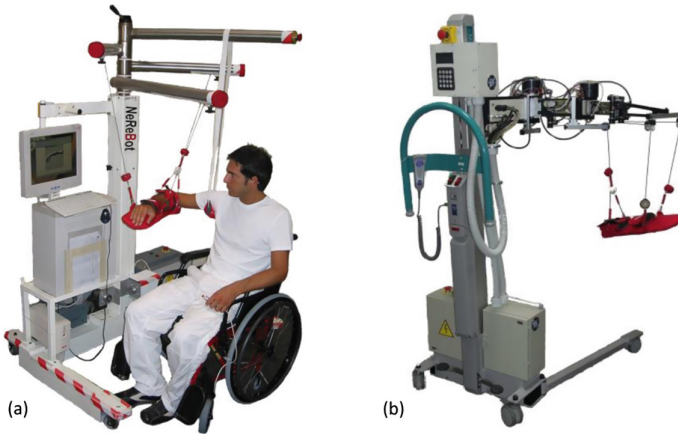


Fig. 1 Cable-suspended robots for upper limb rehabilitation: NeReBot **a** and MariBot **b**. In both robots, the upper limb of the patient is manipulated by three cables. The designs differ in the overhead structure, which in the case of MariBot is actuated. Also, the lower part of the robot is improved with respect to NeReBot, with a more compact design based on a commercial lifting device (Marisa by Arjo Ltd)

the patient's limb along a pre-planned three-dimensional trajectory, but, at the same time, out-of-path voluntary movements are permitted, even while robotic assistance is provided. Moreover, inertia of the parts connected to the patient's arm is minimized, requiring no sophisticated controls to recreate the feeling of a low-inertia robot. Such results could not have been obtained with traditional, non-cable based designs, such as end-effector based rigid link robots or robotic exoskeletons. In such systems, *compliance* can only be gained by *control* [41].

The lower part of NeReBot is wheeled (Fig. 1a), and can be easily deployed at bedside for early inpatient rehabilitation. The exercise is recorded by the therapist, who chooses a set of via-points to be interpolated by the machine. The overhead structure, from which the cables originate, can be manually adjusted by the therapist. In this way, the position of cable entry points, which affects robot force capabilities [7, 8], can be adapted to the specific motion to be exercised. Nonetheless, NeReBot has more control on movements in the vertical plane (like shoulder abduction/adduction), rather than in the horizontal plane.

To overcome such limitation, a second device was developed, the MariBot [33]. MariBot (Fig. 1b) implements the same principle of NeReBot, as it employs three cables to suspend the upper-limb of the patient. The main difference between the two robots lies in that the overhead structure of MariBot is actuated by two motors (like the shoulder-elbow portion of a SCARA manipulator), so it can automatically adapt the position of cable entry points according to the motion of the limb. This architecture, which represents the first example of *adaptive cable-driven robot* [29], yields greatly improved capabilities in controlling human upper-limb motion at joint level, also in the horizontal plane [28].

2.2 A Planar Adaptive Design

Another cable-driven device for upper-limb rehabilitation developed at the University of Padua is the Sophia-3 [43]. In this robot, which has a planar workspace, three cables are used to control the planar motion of a handle grasped by the patient (see Fig. 2a). Two cables are directly driven by fixed motors, whereas the third one originates from a moving motor-pulley block. The position of the moving block is adapted to that of the handle in real-time, optimizing the force capabilities of the robot and avoiding cable-limb interference at the same time [36]. As in the case of MariBot, we implemented here the concept of on-line adapting the geometry of cables to the position of the end-effector, with the aim of maximizing performance and usability of the cable robot.

With respect to other planar rehabilitation robots, the Sophia-3 shows very low and isotropic inertia (which in turn yields high transparency of the device), and possesses highly isotropic force capabilities [35]. Low inertia is a direct consequence of using cable technology, the other benefits derive from choosing and adaptive design rather than a traditional cable robot design.

Another characteristic which distinguishes Sophia-3 from other planar devices is that the plane of motion of the end-effector can be tilted (Fig. 2b). Thanks to this feature, the participation of patient's shoulder to the exercise can be on-line modulated not only by generating virtual forces on the handle, but also by exploiting the force of gravity. In this way, the patient's shoulder, which is one of the main targets of upper-limb rehabilitation post-stroke, can be thoroughly exercised.

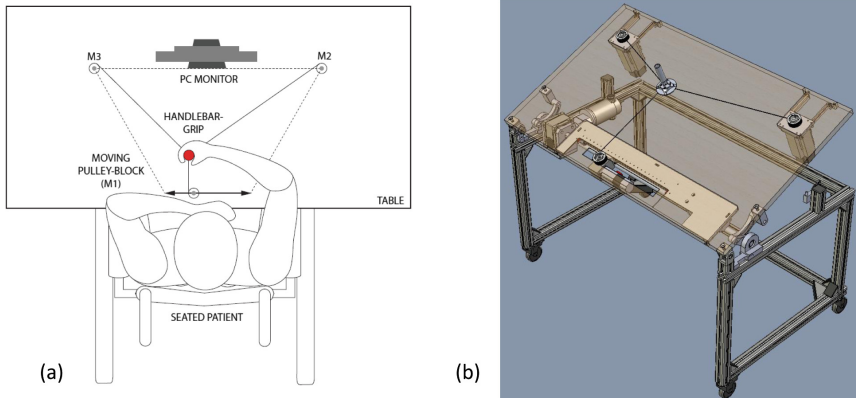


Fig. 2 Top **a** and 3-D **b** sketch of Sophia-3, a semi-adaptive planar cable-driven robot for upper-limb rehabilitation. The user interacts with a handle (to the left, in red) controlled by three cables. Two cables are directly driven by fixed motors, whereas the third one originates from a moving motor-pulley block **a**. The table can be tilted to increase the participation of patient's shoulder to the exercise **b**

3 Clinical Evidence

Despite the potential benefits of robotic rehabilitation after stroke, there is no evidence that robotic training brings improvements to the functional level versus standard therapy: although motor benefits have been noted, robotic approaches have disparate responses depending on rehabilitation problem, device used and patient characteristics [19, 20, 27].

As of our devices, NeReBot was tested in two different randomized controlled trials (RCT) [13, 16, 17]. Both studies involved hemiparetic subjects in the acute/subacute phase of their stroke, enrolled within 15 days after stroke. In this phase of recovery, the brain has added capacity for plasticity, so the benefits brought by rehabilitation are usually greater. NeReBot RCTs tested two different robotic protocols in comparison to standard rehabilitation, one using the robot *in addition* to the traditional treatment [16], one in partial *substitution* to the standard rehabilitation programme, with a dose-matched approach [13, 17].

Clinical results show that the substitutive treatment protocol with NeReBot could be considered comparable to the traditional one [13]. On the other hand, patients treated with the additional protocol developed a greater recovery of motor function and coordination than patients treated only with the standard protocol, both at the end of therapy and at follow-up [16]. These results allow to hypothesize that a *mixed robotic protocol*, in which additional robotic training is delivered in the very early stage post-stroke, while substitutive robotic exercises are delivered in the following weeks, may lead to anticipate patient discharge from hospital. Thanks to the low cost of cable robot technology, the cost of such a protocol, if delivered by a device like NeReBot or MariBot, could be comparable to that of conventional therapy [18].

4 Discussion

Robot-mediated movement training has not yet proven to be a better way of treating stroke survivors in comparison to traditional rehabilitation therapy [19, 20]. Nonetheless, the use of underactuated, cable suspended robots to exercise the upper-limb early post-stroke, as per our clinical experience, represents a valid instrument in addition or substitution of the upper-limb portion of traditional therapy. Despite the limited capabilities of such systems in controlling precisely the motion of the patient's limb, clinical results on severely affected patients were encouraging, thanks to the naturally compliant behavior of the cable robot. One interesting point is that, thanks to the simplicity and ease-of-use of the technical solution proposed, we were able to deliver robotic therapy to patients in the stage of recovery where access to patients is more difficult, but outcomes are likely to be greater. Another benefit, directly deriving from the use of cable robot technology, is that the cost of the device is comparably lower with respect to traditional robotic designs. As a consequence,

affordable early robotic protocols can be defined, potentially able to bring benefits to patients and generate savings for the National Health Care System at the same time.

Anyway, further steps are needed to strengthen the impact of robotics in stroke rehabilitation. A key enabling strategy to improve outcomes could be to adapt devices, exercises and protocols to user needs (patients, therapists, clinicians) [19]. In fact, robotic technology allows to implement very different solutions (in terms of kinematics, mechanical compliance, control and feedback), and to provide additional multi-sensory feedback to the subject with respect to physical rehabilitation. Our research is currently following this direction, with the aim of better understanding to what extent motor learning can be influenced by haptic [24], tactile [31], auditory [25, 30, 34, 38, 42] or action-related feedback [22].

Acknowledgments The authors gratefully acknowledge Dr. Mario Armani for his fundamental contribution to running NeReBot clinical trials.

References

1. Albus J, Bostelman R, Dagalakis N (1992) The NIST robocrane. *J Robot Syst* 10(5)
2. Bosscher P et al (2006) Wrench-feasible workspace generation for cable-driven robots. *IEEE Trans Robot* 22(5):890–902
3. Carricato M, Merlet J-P (2013) Stability analysis of underconstrained cable-driven parallel robots. *IEEE Trans Robot* 29(1):288–296
4. Castelli G, Ottaviano E (2010) Modelling, simulation and testing of a reconfigurable cable-based parallel manipulator as motion aiding system. *Appl Bionics Biomech* 7(4):253–268
5. Cone L (1985) Skycam: an aerial robotic camera system. *Byte* 10(10):122–132
6. Fanin C, Gallina P, Rossi A, Zanatta U, Masiero S (2003) Nerebot: a wire-based robot for neurorehabilitation. In: *Proceedings of the IEEE 8th international conference on rehabilitation robotics*. Seoul (Korea), p 2327
7. Gallina P, Rosati G (2002) Manipulability of a planar wire driven haptic device. *Mech Mach Theory* 37(2):215–228
8. Gallina P, Rosati G, Rossi A (2001) 3-d.o.f. wire driven planar haptic interface. *J Intell Robot Syst* 32(1):23–36
9. Gosselin C (2014) Cable-driven parallel mechanisms: state of the art and perspectives. *Mech Eng Rev* 1(1):1–17
10. Harwin W, Patton J, Edgerton V (2006) Challenges and opportunities for robot-mediated neurorehabilitation. *Proc IEEE* 94(9):1717–1726
11. Kwakkel G, Kollen BJ, Krebs HI (2007) Effects of robot-assisted therapy on upper limb recovery after stroke: a systematic review. *Neurorehabilitation Neural Repair* 22:111–121
12. Lloyd-Jones D et al (2009) Heart disease and stroke statistics-2009 update: a report from the american heart association statistics committee and stroke statistics subcommittee. *Circulation* 119:e21–e181
13. Masiero S, Armani M, Ferlini G, Rosati G, Rossi A (2014a) Randomized trial of a robotic assistive device for the upper extremity during early inpatient stroke rehabilitation. *Neurorehabilitation Neural Repair* 28(4):377–386
14. Masiero S, Carraro E, Ferraro C, Gallina P, Rossi A, Rosati G (2009) Upper limb rehabilitation robotics after stroke: a perspective from the University of Padua Italy. *J Rehabil Med* 41(12):981–985
15. Masiero S, Celia A, Armani M, Rosati G (2006) A novel robot device in rehabilitation of post-stroke hemiplegic upper limbs. *Aging Clin Exp Res* 18(6):531–535

16. Masiero S, Celia A, Rosati G, Armani M (2007) Robotic-assisted rehabilitation of the upper limb after acute stroke. *Arch Phys Med Rehabil* 88(2):142–149
17. Masiero S et al (2011) Upper-limb robot-assisted therapy in rehabilitation of acute stroke patients: focused review and results of new randomized controlled trial. *J Rehabi Res Dev* 48(4):355–366
18. Masiero S, Poli P, Armani M, Ferlini G, Rizzziello R, Rosati G (2014) Robotic upper limb rehabilitation after acute stroke by nerebot: Evaluation of treatment costs. *BioMed Res Int*
19. Masiero S, Poli P, Rosati G, Zanotto D, Iosa M, Paolucci S, Morone G (2014c) The value of robotic systems in stroke rehabilitation. *Expert Rev Med Devices* 11(2):187–198
20. Mehrholz J et al (2012) Electromechanical and robot-assisted arm training for improving generic activities of daily living, arm function, and arm muscle strength after stroke. *Cochrane Database Syst Rev (Online)* 6:CD006876
21. Merlet J-P, Daney D (2010) A portable, modular parallel wire crane for rescue operations, pp 2834–2839
22. Minto S, Zanotto D, Boggsy E, Rosati G, Agrawal S (2016) Validation of a footwear-based gait analysis system with action-related feedback. *IEEE Trans Neural Syst Rehabil Eng*
23. Mustafa S, Lim W, Yang G, Yeo S, Lin W, Agrawal S (2015) Cable-driven robots. *Handb Manuf Eng Technol*
24. Oscari F, Finetto C, Kautz S, Rosati G (2016) Changes in muscle coordination patterns induced by exposure to a viscous force field. *J NeuroEngin Rehabil*
25. Oscari F, Secoli R, Avanzini F, Rosati G, Reinkensmeyer DJ (2012) Substituting auditory for visual feedback to adapt to altered dynamic and kinematic environments during reaching. *Exp Brain Res* 221(1):33–41
26. Poli P, Morone G, Rosati G, Masiero S (2013) Robotic technologies and rehabilitation: new tools for stroke patients therapy. *BioMed Res Int* 2013(153872):1–8
27. Rosati G (2010) The place of robotics in post-stroke rehabilitation. *Expert Rev Med Devices* 7(6):753–758. Invited Paper
28. Rosati G, Andreolli M, Biondi A, Gallina P (2007) Performance of cable suspended robots for upper limb rehabilitation. In: *Proceedings of the IEEE 10th international conference on rehabilitation robotics*. Noordwijk, The Netherlands, pp 385–392
29. Rosati G et al (2011) On the design of adaptive cable-driven systems. *J Mech Robot-Trans ASME* 3(2):021004
30. Rosati G et al (2012) Effect of task-related continuous auditory feedback during learning of tracking motion exercises. *J NeuroEng Rehabil* 9(79)
31. Rosati G et al (2014) Effects of kinesthetic and cutaneous stimulation during the learning of a viscous force field. *IEEE Trans Haptics* 7(2):251–263
32. Rosati G, Gallina P, Masiero S (2007b) Design, implementation and clinical tests of a wire-based robot for neurorehabilitation. *IEEE Trans Neural Syst Rehabil Eng* 15(4):560–569
33. Rosati G, Gallina P, Masiero S, Rossi A (2005) Design of a new 5 d.o.f. wire-based robot for rehabilitation. In: *Proceedings of the IEEE 9th international conference on rehabilitation robotics*. Chicago, IL, USA, pp 430–433
34. Rosati G, Roda A, Avanzini F, Masiero S (2013) On the role of auditory feedback in robot-assisted movement training after stroke: review of the literature. *Comput Intell Neurosci* 2013(586138):1–15
35. Rosati G, Secoli R, Zanotto D, Rossi A, Boschetti G (2008) Planar robotic systems for upper-limb post-stroke rehabilitation. In: *Proceedings of the (2008) ASME international mechanical engineering congress & exposition*, Boston, MA, USA
36. Rosati G, Zanotto D, Secoli R, Rossi A (2009) Design and control of two planar cable-driven robots for upper-limb neurorehabilitation. In: *Proceedings of the IEEE 11th international conference on rehabilitation robotics*. Kyoto, Japan, pp 560–565
37. Schmidt R (1998) *Motor control and learning*. Human Kinetics Publishers
38. Secoli R, Milot M-H, Rosati G, Reinkensmeyer DJ (2011) Effect of visual distraction and auditory feedback on patient effort during robot-assisted movement training after stroke. *J NeuroEng Rehabil* 8(21)

39. Tadokoro S, Kobayashi S (2002) A portable parallel motion platform for urban search and surveillance in disasters. *Adv Robot* 16(6):537–540
40. Timmermans AA et al (2009) Technology-assisted training of arm-hand skills in stroke: concepts on reacquisition of motor control and therapist guidelines for rehabilitation technology design. *J NeuroEng Rehabil* 6(1)
41. Wolbrecht ET, Chan V, Reinkensmeyer DJ, Bobrow JE (2008) Optimizing compliant, model-based robotic assistance to promote neurorehabilitation. *IEEE Trans Neural Syst Rehabil Eng* 16(3):286–297
42. Zanotto D et al (2013) Effects of complementary auditory feedback in robot-assisted lower extremity motor adaptation. *IEEE Trans Neural Syst Rehabil Eng* 21(5):775–786
43. Zanotto D et al (2014) Sophia-3: a semiadaptive cable-driven rehabilitation device with a tilting working plane. *IEEE Trans Robot* 30(4):974–979